# Towards an NMR multiphase flowmeter

## Method development and performance evaluation for two-phase flow measurements

Daalmans, A.C.L.M.

**DOI**
10.4233/uuid:53a0f525-0131-424d-b610-7cd21cbca550

**Publication date**
2021

**Document Version**
Final published version

**Citation (APA)**
Daalmans, A. C. L. M. (2021). *Towards an NMR multiphase flowmeter: Method development and performance evaluation for two-phase flow measurements*. [Dissertation (TU Delft), Delft University of Technology]. https://doi.org/10.4233/uuid:53a0f525-0131-424d-b610-7cd21cbca550

# Towards an NMR multiphase flowmeter

*method development and performance evaluation for two-phase flow measurements*

**Annekatrien Daalmans**

# Stellingen

behorende bij het proefschrift
**Towards an NMR multiphase flowmeter**
method development and performance evaluation for two-phase flow measurements
door **Annekatrien Daalmans**

1. De kwaliteit van de $T_1$-relaxatietijd bepaling is doorslaggevend voor de prestatie van alle zuiver NMR gebaseerde meerfasen stromingsmeters.
   *Dit proefschrift, hoofdstuk 5.*

2. Het vloeistofstroommodel vervult een sleutelrol in de nauwkeurigheid van de in intermitterende regimes werkende niet-beeldvormende NMR stromingsmeters, zelfs wanneer de lokale snelheden direct worden gemeten.
   *Dit proefschrift, hoofdstuk 8.*

3. Sterk overlappende gevoelige volumes behorend bij de knooppunten van de wiremesh sensor zijn wel degelijk de hoofdoorzaak van de systematische signaaloverschatting van de vloeistof hold-up, in tegenstelling tot wat Prasser en Häfeli beweren.
   *Dit proefschrift, hoofdstuk 7; Prasser en Häfeli (2018).*

4. Productontwerp is als dansen op een slap koord; wie de balans doet doorslaan op één aspect kan alleen met kunst- en vliegwerk de zaak redden.

5. Ondanks de opmars van virtuele stromingsmetertechnologie als goedkoop alternatief voor reservoirbeheer, zijn meerfasen stromingsmeters het enige antwoord op fiscale allocatie in diepwater and ultra diepwater velden.

6. Het is een utopie om te denken dat door kunstmatige intelligentie te gebruiken in virtuele stromingsmeters de nauwkeurigheid van de geschatte debieten automatisch beter wordt.
   *Bikmukhametov en Jäschke (2020).*

7. Wetenschappelijk onderzoek zou alleen gepubliceerd moeten worden als de onderliggende reproductiemechanismen ook worden gedeeld; anders is het noch reproduceerbaar, noch bruikbaar.

8. Het Nieuwe Werken ontneemt de wetenschappelijke gemeenschap van de essentiële bouwstenen die noodzakelijk zijn voor het ontstaan van baanbrekende ideeën, zoals spontane interacties en kruisbestuiving.

9. Door het gebruik van digitale meters krijgen mensen een onterecht vertrouwen in de nauwkeurigheid van hetgeen gemeten is.

10. Deeldiensten die niet gebaseerd zijn op wegwerpeconomische principes, verrijken de samenleving werkelijk.

Deze stellingen worden opponeerbaar en verdedigbaar geacht en zijn als zodanig goedgekeurd door de promotor Prof. dr. R.F. Mudde en copromotor Dr. Eng. L.M. Portela.

# Propositions

accompanying the dissertation
**Towards an NMR multiphase flowmeter**
method development and performance evaluation for two-phase flow measurements
by **Annekatrien Daalmans**

1. The quality of the $T_1$ relaxation time determination is decisive for the performance of all pure NMR based multiphase flowmeters.
   *This dissertation, Chapter 5.*

2. The fluid flow model plays a key role in the accuracy of non-imaging NMR multiphase flowmeters operating in intermittent regimes, even when measuring the local velocities directly.
   *This dissertation, Chapter 8.*

3. Strongly overlapping nodal sensitive volumes of the wiremesh sensor are most definitely the main cause of the systematic overestimation of the liquid holdup, contrary to what Prasser and Häfeli claim.
   *This dissertation, Chapter 7; Prasser and Häfeli (2018).*

4. Product design is like dancing on a tightrope; those who tip the balance on one aspect can only save the case with acrobatics.

5. Despite the advance of virtual flowmetering technology as a low-cost alternative to reservoir management, multiphase flowmeters are the only answer to fiscal allocation in deep water and ultra-deep water fields.

6. It is a utopia to think that using virtual flowmeters based on artificial intelligence will automatically improve the accuracy of the estimated flowrates.
   *Bikmukhametov and Jäschke (2020).*

7. Scientific research should only be published if the underlying reproductive mechanisms are also shared; otherwise it is neither reproducible nor useful.

8. The New World of Work deprives the scientific community of the essential building blocks that are necessary for the creation of groundbreaking ideas, such as spontaneous interactions and cross-pollination.

9. The use of digital meters gives people misplaced confidence in the accuracy of what is measured.

10. Shared services that are not based on throwaway economic principles really enrich society.

These propositions are regarded as opposable and defendable, and have been approved as such by the promotor Prof. dr. R.F. Mudde and copromotor Dr. Eng. L.M. Portela.

# Towards an NMR multiphase flowmeter

method development and performance evaluation for two-phase flow measurements

# Towards an NMR multiphase flowmeter

method development and performance evaluation for two-phase flow measurements

PROEFSCHRIFT

ter verkrijging van de graad van doctor
aan de Technische Universiteit Delft,
op gezag van de Rector Magnificus Prof.dr.ir. T.H.J.J. van der Hagen,
voorzitter van het College voor Promoties,
in het openbaar te verdedigen op
woensdag 29 september 2021 om 12:30 uur

door

Anna Catharina Laurentia Maria DAALMANS

Natuurkundig ingenieur,
Technische Universiteit Delft, Nederland
geboren te Delft, Nederland

Dit proefschrift is goedgekeurd door de
promotor: Prof. dr. R.F. Mudde
copromotor: Dr. Eng. L.M. Portela

Samenstelling promotiecommissie:

| | |
|---|---|
| Rector magnificus, | voorzitter |
| Prof. dr. R.F. Mudde, | Technische Universiteit Delft, promotor |
| Dr. Eng. L.M. Portela, | Technische Universiteit Delft, copromotor |

Onafhankelijke leden:

| | |
|---|---|
| Prof. dr. ir. C. Poelma, | Technische Universiteit Delft |
| Prof. dr. ir. P.L.J. Zitha, | Technische Universiteit Delft |
| Prof. Dr.-Ing. habil. U. Hampel, | Helmholtz-Zentrum Dresden-Rossendorf, Technische Universität Dresden, Duitsland |
| Prof. dr. M.L. Johns, | The University of Western Australia, Australië |
| Dr. A.J. Sederman, | University of Cambridge, Verenigd Koninkrijk |

**e**conomie**e**cologie**t**echnologie

Het project is uitgevoerd met subsidie van het Programma E.E.T. (Economie, Ecologie en Technologie) een gezamenlijk initiatief van de Ministeries van Economische Zaken, Onderwijs, Cultuur en Wetenschappen en Volkshuisvesting, Ruimtelijke Ordening en Milieu. Het programma wordt uitgevoerd door het Programmabureau E.E.T., een samenwerkingsverband van Senter en Novem.



Printed by GVO drukkers & vormgevers B.V.

ISBN 978-94-6332-787-9
An electronic version of this dissertation is available at
`http://repository.tudelft.nl/`.

*wisdom begins in wonder*

free after Socrates by Plato, Theaetetus 155d

# Summary

There is an increasing demand from the petroleum industry for high accuracy subsea multiphase flowmeters to make the development of difficult to access deep water and ultra-deep water fields economically viable. Nuclear Magnetic Resonance (NMR) is a very powerful measuring principle, and is one of the few techniques considered to be capable of meeting the required high performance.
The work presented in this thesis is a first step in the development of a non-invasive, in-line, full-bore, nuclear magnetic resonance based, multiphase flowmeter without phase separation. The continued development of the investigated system has led to the commercial KROHNE M-PHASE 5000 flowmeter, which is based on an improved prototype. To keep maintenance as low as possible, the flowmeter consists of a permanent polarizing magnet with two measuring probes, operating at 14.1 MHz, at different streamwise positions. Pipelines with an inner diameter of up to 10 cm fit through the bore of the flowmeter prototype. Two NMR measurement concepts have been developed, each with a different underlying velocity measuring principle, to determine the liquid flowrate in a gas-liquid flow: (i) the $T_1$ Relaxation Residence Time (T1RRT) method utilizes the longitudinal relaxation principle to derive the velocity from the intensity of the NMR signal, which is a function of the residence time in the polarizing magnetic field; (ii) the Pulsed Gradient Spin Echo (PGSE) method exploits pulsed magnetic field gradients, to obtain the fluid velocity from the phase shift of a spin echo signal. Both flowmetering concepts resolve the fractions of the liquid components identically, from the multi-exponential course of the signal intensity associated with the different polarization lengths of the measuring probes. The measurement concepts have been tested for single-phase flow in 9.85 mm, 34 mm and 98.6 mm diameter pipes and for two-phase flow in a 98.6 mm diameter pipe.

The performance of the flowmetering concepts has been assessed on three aspects: (i) rangeability, (ii) whether the use of a plug flow model, which disregards the no-slip condition at the wall and phase slip in the case of multiphase flow, is justified and (iii) the capacity to capture the time scales of the multiphase flow structures. Errors and uncertainties of technical nature related to the flowmeter design are also extensively analyzed.

For practical reasons, the performance evaluation of the functional flowmeter model is limited to horizontal flow. As long as steady-state, pseudo-steady state or quasi-static, fully-developed, intermittent, multiphase flows are measured, the conclusions drawn are expected

to remain valid for a flowmeter installed vertically or at any other angle. However, since the flow patterns show great variation for other pipe orientations, the data processing software implemented in the flowmeter to reconstruct the flowrate, must be adapted to the prevailing flow regime.

The PGSE method is not suitable for multiphase flow regimes with fast moving flow structures, because a stable velocity is required over the different repetitions of the pulse sequence. The T1RRT method has a much better time resolution with a sampling frequency of a few Hz, and is, therefore, tested on both single-phase flow and two-phase air-water stratified and slug flow, at atmospheric pressure; the PGSE method test is limited to single-phase flow.
Since both measurement concepts are sensitive to changes in the $T_1$ relaxation time, a study with static dummies has been carried out, showing that the standard INVREC technique in combination with a bi-exponential curve fit model is not accurate enough to determine the $T_1$ relaxation times of oil and water simultaneously, over the full viscosity range. In the actual flowmeter application, it is recommended to implement a mapping technique, known from well-logging, which resolves a linear system of equations for a predefined $T_1$-range. Unlike the PGSE method, the T1RRT method is unsuitable for measuring the flowrates of highly viscous fluids with the current flowmeter prototype, since thermal equilibrium is reached before the liquids enter the first measuring probe.
Regarding the rangeability, the preliminary experiments performed with PGSE demonstrate that the method is able of determining the average streamwise velocity of single-phase flow with a reasonable accuracy in the range of 0 - 0.8 m $s^{-1}$. After correction for the eddy-currents, a measurement uncertainty better than 5% of the true velocity and a velocity bias of less than 2 cm $s^{-1}$ has been found.
For accurate velocity measurements with the T1RRT method, it is important that the flowmeter range falls within the steepest part of the signal fraction curve. When the velocity is made dimensionless, by scaling with the fraction of the $T_1$ relaxation time over the polarization length up to the first probe, the uncertainty by repeatability reaches a constant level, starting from a slope of 0.25 of the curve. For the current prototype, with measuring probes at 0.5 and 2.5 m from the magnet entrance, this corresponds to a bulk velocity range of 0.05 – 0.94 m $s^{-1}$ for tap water, with a typical $T_1$ of 2.5 s, and 0.84 – 15.7 m $s^{-1}$ for light oils, with a typical $T_1$ of 0.15 s.
The experimental results for both laminar and turbulent single-phase flow, and stratified flow, have been compared with numerical simulations of an artificial two-dimensional velocity profile of the liquid phase, to investigate whether prior knowledge of the velocity profile is required in the T1RRT method, or whether the plug flow approach is sufficient. This shows that the flowmeter routine should only be adjusted for slip in the case of laminar single-phase flow and that the plug flow model can be used without any problem for (i) turbulent single-phase flow, (ii) stratified smooth and (iii) stratified wavy flow with regular 2D waves.
The processing of the T1RRT data is adapted to horizontal slug flow, by using clustering to distinguish the slug section data from the film section data, after which the average liquid flowrate is calculated using the unit-cell concept. It has been shown that it is particularly important that the flowmeter algorithm incorporates the liquid shedding and pickup processes, which take place in slug flow. The incorrect assumption of a constant velocity during the

transit time through the flowmeter results in an underestimation of the liquid holdup in the film sections, and an overestimation of the liquid holdup in the slug sections. Since the phase fraction determination with the PGSE method, which obtains the average streamwise velocity directly from the NMR signal, irrespective of the velocity profile, is identical to the T1RRT method, it must be adjusted accordingly for phase slip.

The following technical factors have been identified as important sources of errors and uncertainties for a high-performing NMR flowmeter:

- Two problems arise from the choice to make the bore of the measuring probes only slightly larger than the outer diameter of the pipeline. First, magnetic field simulations have shown that this results in an inhomogeneous pulsed field, with a wider distribution of flip angles for a smaller coil-to-sample diameter ratio. The influence this has on the average 90° and 180° pulse lengths and the weighting of the local signal contribution has been tried to minimize by using calibration. Second, the poor uniformity of the gradient field due to the closely spaced gradient modules has major consequences for the accuracy of the PGSE measurements: a different effective gradient strength is found for each pipe diameter.

- Furthermore, the non-rectangular shape of the polarizing magnetic field, which starts already centimeters in front of the physical entrance of the flowmeter, must be taken into account. With Lagrangian simulations of the magnetization build-up, based on Hall-sensor measurements of the magnets entrance area, it has been found that the model used by the flowmeter is best adapted for the incorrect polarization length by raising it with the distance, equivalent to the asymptote of the effective field deviation when having a uniform field strength.

- Underestimation of the liquid holdup is recognized as a general problem of the flowmeter. The probe gets detuned and dematched when the filling factor changes, due to the dielectric losses by the organic material of which most samples consist. Much of the adverse effect this has on the probe efficiency has been successfully tackled by placing strip-shields between the sample and the coil, but loss of signal intensity cannot be completely prevented.
  In addition, the large distance between the coils makes it difficult to guarantee a constant water level in the flowmeter, which is assumed by the T1RRT method. There is clear evidence that the presence of a very weak gradient has a strong negative effect on the reliability of both the velocity and holdup measurements.

- Finally, the PGSE measurements are disturbed by eddy currents, which affect the effective gradient strength and cause a velocity bias.

A study of the accuracy shows that without improvements, the performance of the PGSE method is not good enough to meet the industry requirements, especially if the holdup has yet to be determined. Moreover, the high measurement frequency that is essential for multiphase flowmetering seems unfeasible. A disadvantage of the T1RRT method over the PGSE method

is that the velocity and fraction determination are correlated, such that the velocity bias is reinforced in the liquid holdup. However, the propagation of errors is limited if the probe, of which the NMR signal is used for the fraction determination, is placed far enough within the polarizing magnetic field. Repeatability, in particular in the velocity determination, is the largest contributor to the total accuracy of the T1RRT method. Based on repeatability of the flowrate, the T1RRT metering principle meets the stratified flow measurement requirements set by industry for reservoir management and well-testing; for higher liquid bulk velocities, the repeatability is also within the desired range for production allocation. The repeatability of the liquid holdup meets the upper limit of 2% in the water-cut, in almost all measurements. The accuracy of the T1RRT method can be further improved by using a better flow pattern-specific model for the velocity distribution.

With this investigation into the measurement possibilities of an NMR flowmeter prototype consisting of a permanent polarizing magnet with two measurement probes at different streamwise positions, important knowledge has been gathered for the realization of an NMR multiphase flowmeter to measure the flowrates of unseparated oil, water and natural gas streams. The power of NMR is that the same measuring principle can be used to determine both the velocity and the volume fraction of the components. The calibration procedure with the known methods, for which the production stream has to be interrupted, is still a challenge. The T1RRT method, with its good time resolution, is the most promising of the two measuring principles developed. Light and medium hydrocarbons do not appear a problem. With regard to the velocity determination of highly viscous crude oil, the results give reason to look for an alternative measuring principle such as the efflux method. The flow regime specific model has been identified as a critical factor in the performance of any NMR based flowmeter. The findings concerning the volume fraction determination are also relevant for flowmeters based on a different NMR velocity measuring principle. In order to reconstruct the volume fractions from the NMR signal, the velocity history of a flow element must be correctly captured during its trajectory across the flowmeter. There is strong evidence that a plug flow assumption offers sufficient accuracy for continuous, stable, flow regimes. For intermittent flow patterns, the flow model is a matter of concern. Especially, when a third phase is involved. Whether NMR can break through as a multiphase flowmetering technique for the petroleum industry depends on the degree to which it will be able to distinguish the oil and water components.

# Samenvatting

Vanuit de olie-industrie is er een toenemende vraag naar onderzeese meerfasen stromingsmeters met hoge nauwkeurigheid om de ontwikkeling van moeilijk toegankelijke velden in diep en ultra diep water economisch rendabel te maken. Nucleaire magnetische resonantie (NMR) is een zeer krachtig meetprincipe dat als een van de weinige technieken in staat wordt geacht om aan de vereiste hoge prestaties te voldoen.
Het werk dat in dit proefschrift wordt gepresenteerd, is een eerste stap in de ontwikkeling van een niet-invasieve, gealigneerde, op nucleaire magnetische resonantie gebaseerde meerfasen stromingsmeter met gelijkblijvende diameter zonder faseschеiding. Doorontwikkeling van het onderzochte systeem heeft geleid tot de commerciële KROHNE M-PHASE 5000 stromingsmeter, die is gebaseerd op het verbeterde prototype. Om het onderhoud zo laag mogelijk te houden, bestaat de stromingsmeter uit een permanente polarisatiemagneet met twee bij 14,1 MHz opererende meetsondes op verschillende stroomsgewijze posities. Door het stromingsmeter prototype passen pijpleidingen met een binnendiameter tot 10 cm. Er zijn twee NMR-meetconcepten ontwikkeld, elk met een ander onderliggend snelheidsmeetprincipe, om het vloeistofdebiet in een gas-vloeistofstroom te bepalen: (i) de $T_1$ Relaxatie Verblijftijd (T1RRT) methode gebruikt het longitudinale relaxatieprincipe om de snelheid af te leiden uit de intensiteit van het NMR-signaal, welke een functie is van de verblijftijd in het polariserende magneetveld; (ii) de Gepulste Gradiënt Spin Echo (PGSE) methode maakt gebruik van gepulste magnetische veldgradiënten om de vloeistofsnelheid te verkrijgen uit de faseverschuiving van een spinechosignaal. Beide stromingsmeetconcepten lossen de fracties van de vloeistof componenten identiek op uit het multi-exponentiële verloop van de signaalintensiteit behorende bij de verschillende polarisatielengtes van de meetsondes. De meetconcepten zijn getest voor éénfase-stroming in buizen met een diameter van 9,85 mm, 34 mm en 98,6 mm en voor tweefasen-stroming in een buis met een diameter van 98,6 mm.

De prestaties van de stromingmeetconcepten zijn beoordeeld op drie aspecten: (i) het meetbereik, (ii) of het gebruik van een propstromingsmodel gerechtvaardigd is welke de slipvrije toestand aan de wand en de slip tussen de fasen in het geval van meerfasenstroming negeert, en (iii) het vermogen om de tijdschalen van de meerfasenstroomstructuren vast te leggen. Fouten en onzekerheden van technische aard met betrekking tot het ontwerp van de stromingsmeter worden ook uitgebreid geanalyseerd.

Om praktische redenen is de prestatie-evaluatie van het functionele stromingsmetermodel beperkt tot horizontale stroming. Zolang stationaire, pseudo-stationaire of quasi-statische,

volledig ontwikkelde, intermitterende, meerfasenstroming wordt gemeten, is de verwachting dat de getrokken conclusies geldig blijven voor een stromingsmeter die verticaal of onder een andere hoek is geïnstalleerd. Aangezien de stromingspatronen grote variatie vertonen voor andere pijporiëntaties, dient de gegevensverwerkingssoftware, die in de stromingsmeter is geïmplementeerd om het debiet te reconstrueren, wel aangepast te worden aan het heersende stromingsregime.

De PGSE-methode is ongeschikt voor meerfasenstromingregimes met snel bewegende stromingsstructuren, omdat een stabiele snelheid is vereist over de verschillende herhalingen van de pulsreeks. De T1RRT-methode heeft een veel betere tijdsresolutie met een meetfrequentie van enkele Hz en wordt daarom getest op zowel éénfase-stroming als tweefasen lucht-water gelaagde en slugstroming bij atmosferische druk; de test van de PGSE-methode is beperkt tot éénfase-stroming.
Aangezien beide meetconcepten gevoelig zijn voor veranderingen in de $T_1$ relaxatietijd, is er een onderzoek met statische dummies uitgevoerd, waaruit blijkt dat de standaard INVREC-techniek in combinatie met een bi-exponentieel curve-fit model niet nauwkeurig genoeg is om de $T_1$ relaxatietijden van olie en water tegelijk over het volledige viscositeitsbereik te bepalen. Het wordt aanbevolen om een mathematische afbeeldingsprocedure, die bekend is uit de boorputgeofysica, in de daadwerkelijke stromingsmeter toepassing te implementeren welke een lineair systeem van vergelijkingen oplost voor een vooraf gedefiniëerd $T_1$-bereik. In tegenstelling tot de PGSE-methode, is de T1RRT-methode met het huidige prototype van de stromingsmeter niet geschikt voor het meten van de debieten van zeer viskeuze vloeistoffen, aangezien thermisch evenwicht wordt bereikt voordat de vloeistoffen de eerste meetsonde binnenkomen.
Wat het meetbare bereik betreft, tonen de voorlopige experimenten die met PGSE zijn uitgevoerd aan dat de methode in staat is om de gemiddelde stroomsnelheid van éénfase-stroming met een redelijke nauwkeurigheid te bepalen in het bereik van 0 - 0,8 m $s^{-1}$. Na correctie voor wervelstromen wordt een meetonzekerheid beter dan 5% van de werkelijke snelheid en een systematische fout kleiner dan 2 cm $s^{-1}$ gevonden.
Voor nauwkeurige snelheidsmetingen met de T1RRT-methode is het belangrijk dat het bereik van de stromingsmeter binnen het steilste deel van de signaalfractiecurve valt. Wanneer de snelheid dimensieloos wordt gemaakt door te schalen met de fractie van de $T_1$ relaxatietijd en de polarisatielengte tot aan de eerste sonde, bereikt de onzekerheid door herhaling een constant niveau vanaf een helling van 0,25 van de curve. Wat betreft het huidige prototype met meetsondes op 0,5 en 2,5 m van de magneetingang, komt dit overeen met een bulksnelheidsbereik van 0,05 - 0,94 m $s^{-1}$ voor leidingwater met een typische $T_1$ van 2,5 s en 0,84 - 15,7 m $s^{-1}$ voor lichte oliën met een typische $T_1$ van 0,15 s.
De experimentele resultaten voor zowel laminaire als turbulente éénfase-stroming en gelaagde stroming zijn vergeleken met numerieke simulaties van een kunstmatig tweedimensionaal snelheidsprofiel van de vloeistoffase om te onderzoeken of voorkennis van het snelheidsprofiel vereist is in de T1RRT-methode of dat de propstroming-benadering voldoende is. Dit liet zien dat de routine van de flowmeter alleen moet worden aangepast voor slip in het geval van laminaire éénfase-stroming en het propstroming-model zonder problemen gebruikt kan worden voor (i) turbulente éénfase-stroming, (ii) gelaagde gladde en (iii) gelaagde golfstroming met regelmatige 2D-golven.

De verwerking van de T1RRT-gegevens is aangepast aan horizontale slugstroming door clustering te gebruiken om de slug sectie-data te onderscheiden van de film sectie-data, waarna het gemiddelde vloeistofdebiet wordt berekend met behulp van het eenheidscel concept. Er is aangetoond dat het bijzonder belangrijk is dat de processen van vloeistof afstoten en opnemen die in slugstroming plaatsvinden in het algoritme van de stromingsmeter zijn verwerkt. De onjuiste aanname van een constante snelheid tijdens de doorgangstijd door de stromingsmeter resulteert in een onderschatting van de vloeistoffractie in de filmsecties en een overschatting van de vloeistoffractie in de slugsecties. Aangezien de bepaling van de fasefracties met de PGSE-methode, die de gemiddelde stroomsnelheid direct uit het NMR-signaal haalt, ongeacht het snelheidsprofiel, identiek is aan de T1RRT-methode, moet deze dienovereenkomstig worden aangepast voor slip tussen de fasen.

De volgende technische factoren zijn geïdentificeerd als belangrijke bronnen van fouten en onzekerheden voor een goed presterende NMR-stromingsmeter:

- Twee problemen komen voort uit de keuze om het boorgat van de meetsondes slechts iets groter te maken dan de buitendiameter van de pijpleiding. Ten eerste hebben magnetische veldsimulaties aangetoond dat dit resulteert in een inhomogeen gepulst veld met een bredere verdeling van omklaphoeken voor een kleinere verhouding van spoel tot monster diameter. De invloed hiervan op de gemiddelde 90° en 180° pulslengte en de weging van de lokale signaalbijdrage is getracht door kalibratie te verminderen. Ten tweede heeft de slechte uniformiteit van het gradiëntveld vanwege de dicht bij elkaar gelegen gradiëntmodules grote gevolgen voor de nauwkeurigheid van de PGSE-metingen: voor elke buisdiameter wordt een andere effectieve gradiëntsterkte gevonden.

- Verder moet rekening worden gehouden met de niet-rechthoekige vorm van het polariserende magneetveld, dat al centimeters voor de fysieke ingang van de stromingsmeter begint. Met Lagrangiaanse simulaties van de magnetisatie opbouw op basis van Hall-sensormetingen van het ingangsgebied van de magneet, is gebleken dat het model dat door de stromingsmeter wordt gebruikt, het beste wordt aangepast voor de onjuiste polarisatielengte door deze te verhogen met de afstand gelijk aan de asymptoot van de effectieve veldafwijking bij een uniforme magnetische veldsterkte.

- Onderschatting van de vloeistoffractie wordt erkend als een algemeen probleem van de stromingsmeter. De sonde raakt ontstemd en onaangepast wanneer de vullingsgraad verandert vanwege de diëlektrische verliezen door het organische materiaal waaruit de meeste monsters bestaan. Veel van het nadelige effect dat dit heeft op de efficiëntie van de sonde is met succes aangepakt door stripafschermingen tussen het monster en de spoel te plaatsen, maar verlies van signaalintensiteit kan niet volledig worden voorkomen. Bovendien maakt de grote afstand tussen de spoelen het moeilijk om een constant waterniveau in de stromingsmeter te garanderen, wat wordt aangenomen door de T1RRT-methode. Er is duidelijk bewijs dat de aanwezigheid van een zeer zwakke gradiënt een sterk negatief effect heeft op de betrouwbaarheid van zowel de snelheids- als de volumefractiemetingen.

- Ten slotte worden de PGSE-metingen verstoord door wervelstromen die de effectieve gradiëntsterkte beïnvloeden en een snelheidsafwijking veroorzaken.

Een onderzoek naar de nauwkeurigheid toont aan dat zonder verbeteringen de prestaties van de PGSE-methode niet goed genoeg zijn om aan de industriële eisen te voldoen, vooral als de volumefractie nog moet worden bepaald. Bovendien lijkt de hoge meetfrequentie die essentieel is voor het meten van meerfasenstroming onhaalbaar. Een nadeel van de T1RRT-methode ten opzichte van de PGSE-methode is dat de bepaling van snelheid en fractie zodanig gecorreleerd is dat de snelheidsafwijking in de vloeistoffractie wordt versterkt. De doorwerking van fouten is echter beperkt als de meetsonde, waarvan het NMR-signaal wordt gebruikt voor de fractiebepaling, ver genoeg binnen het polariserende magneetveld wordt geplaatst. Herhaalbaarheid, met name bij de bepaling van de snelheid, levert de grootste bijdrage aan de totale nauwkeurigheid van de T1RRT-methode. Gebaseerd op de herhaalbaarheid van het debiet, voldoet het T1RRT-meetprincipe voor de gemeten gelaagde stroming, aan de eisen die de industrie stelt aan reservoirbeheer en het testen van putten; voor hogere bulkvloeistofsnelheden ligt de herhaalbaarheid ook binnen het gewenste bereik voor productietoewijzing. De herhaalbaarheid van de vloeistoffractie voldoet in bijna alle metingen aan de bovengrens van 2% in het waterdeel. De nauwkeurigheid van de T1RRT-methode kan verder worden verbeterd door een beter stromingspatroon specifiek model te gebruiken voor de snelheidsverdeling.

Met dit onderzoek naar de meetmogelijkheden van een NMR stromingsmeter prototype bestaande uit een permanente polarisatiemagneet met twee meetsondes op verschillende stroomsgewijze posities is belangrijke kennis vergaard voor de verwezenlijking van een NMR meerfasen stromingsmeter om de debieten van niet-gescheiden olie-, water- en aardgasstromen te meten. De kracht van NMR is dat hetzelfde meetprincipe gebruikt kan worden voor de bepaling van zowel de snelheid als de volumefractie van de componenten. De kalibratieprocedure met de bekende methoden, waarvoor de productiestroom onderbroken moet worden, vormt nog een uitdaging. De T1RRT-methode is met zijn goede tijdresolutie het meest veelbelovend van de twee ontwikkelde meetprincipes. Lichte en middelzware koolwaterstoffen lijken geen probleem te vormen. Wat de snelheidsbepaling van hoogviskeuze ruwe olie betreft, geven de resultaten aanleiding om naar een alternatief meetprincipe zoals de efflux-methode uit te kijken. Het stromingsregime-specifieke model is geïdentificeerd als een kritische factor in de prestaties van elke op NMR gebaseerde stromingsmeter. De bevindingen betreffende de volumefractie bepaling zijn ook relevant voor stromingsmeters berustend op een ander NMR snelheids meetprincipe. Om de volumefracties uit het NMR-signaal te reconstrueren, is het belangrijk dat de snelheidsgeschiedenis van een stromingselement tijdens zijn traject door de stromingsmeter goed weergegeven wordt. Er zijn sterke aanwijzingen dat een aanname van propstroom voldoende nauwkeurigheid biedt voor continue, stabiele stromingsregimes. Voor intermitterende stromingspatronen is het stromingsmodel een punt van zorg. Vooral als er een derde fase bij betrokkken is. Of NMR kan doorbreken als meerfasen stromingsmeettechniek voor de petroleumindustrie hangt af van de mate waarin het de olie- en watercomponenten kan onderscheiden.

# Contents

# Nomenclature

### Latin

| | | |
|---|---|---|
| $A$ | amplitude of the induced voltage in the time domain | - |
| $\mathbf{A}$ | vector potential | T m |
| $A_{3se}$ | amplitude third spin echo | - |
| $A_G$ | corss-sectional area occupied by the gas phase | $m^2$ |
| $A_L$ | corss-sectional area occupied by the liquid phase | $m^2$ |
| $A_{pe}$ | amplitude primary echo | - |
| $A_{RMS}$ | RMS amplitude of the waves in stratified flow | m |
| $A_{ste}$ | amplitude stimulated echo | - |
| $a$ | amplitude of the r.f. pulse in the time domain | - |
| $a$ | coil radius | m |
| $\mathbf{B}$ | magnetic field | T |
| $\mathbf{B_0}$ | permanent magnetic field | T |
| $\mathbf{B_1}$ | oscillating magnetic field | T |
| $\mathbf{B}_{ec}$ | magnetic field generated by eddy-currents | T |
| $\mathbf{B}_{\text{eff}}$ | effective magnetic field | T |
| $\mathbf{B}_{\text{grad}}$ | gradient magnetic field | T |
| $B_i$ | field deviation of the nominal $\mathbf{B}_0$ field | T |
| $B_z$ | magnetic field component in direction permanent magnetic field | T |
| $b$ | group indicator | - |
| $C$ | capacitor | F |
| $C_1$ | lossless capacitance from r.f. coil to sample | F |
| $C_2$ | dielectric capacitance of lossy sample | F |
| $C_d$ | distributed capacity of the r.f. coil | F |
| $C_t$ | variable tuning capacitor | F |
| $C_m$ | matching capacitor | F |
| $C_\beta$ | gradient in the liquid holdup | $m^{-1}$ |
| $c$ | speed of light | m $s^{-1}$ |
| $c_{\{1,2,3,4,5\}}$ | fit estimators | - |
| $D$ | diffusion coefficient | $m^2$ $s^{-1}$ |
| $D_{\{1,2\}}$ | time delay between two gradient pulses in Fieldmap | s |

| | | |
|---|---|---|
| $D_c$ | r.f. coil diameter | m |
| $D_{\{hG,hL\}}$ | hydraulic diameter of the gas or the liquid phase | m |
| $D_p$ | pipe diameter | m |
| $D_{pz}$ | pipe diameter on a horizontal chord | m |
| $D_s$ | sample diameter | m |
| $dv^*$ | systematic error in the dimensionless streamwise velocity | - |
| $d\alpha_{L,\{1,2\}}$ | systematic error in the liquid holdup | - |
| $E_{m_I}$ | spin magnetic energy | J |
| $f_{\{-1,0,1\}}$ | function values | - |
| $f_m$ | measurement frequency | $s^{-1}$ |
| $f_p$ | primary peak frequency | $s^{-1}$ |
| $f_s$ | sample frequency | $s^{-1}$ |
| $G$ | gradient of permanent magnetic field | $T\ m^{-1}$ |
| $\mathbf{G}_y$ | gradient of permanent magnetic field in y-direction | $T\ m^{-1}$ |
| $\mathbf{G}_{y,\max}$ | maximum gradient strength in y-direction | $T\ m^{-1}$ |
| $G^{de\phi}$ | dephasing gradient | $T\ m^{-1}$ |
| $G^{re\phi}$ | rephasing gradient | $T\ m^{-1}$ |
| $\mathbf{g}_0$ | gradient due to inhomogeneities of permanent magnetic field | $T\ m^{-1}$ |
| $\mathbf{g}_y$ | gradient of permanent magnetic field in y-direction | $T\ m^{-1}$ |
| $H_L$ | Fourier Transform of liquid level $h_L$ | $m\ s^{-1}$ |
| $h$ | Planck's constant | Js |
| $h$ | integration step | - |
| $h$ | Gaussian kernel | - |
| $\hbar$ | reduced Planck's constant | $J\ s\ rad^{-1}$ |
| $h_L$ | liquid level | m |
| $h'_L$ | liquid level fluctuation | m |
| $h_{L\{1,2\}}$ | liquid level at the r.f. probe | m |
| $h_{\mathrm{L,WM}}$ | liquid level measured by the wiremesh sensor | m |
| $I$ | nuclear spin quantum number | - |
| $I$ | amplitude of r.f. pulse modulated with cosine carrier function | - |
| $I$ | current | A |
| $i, j, k, n, r$ | indices matrix elements | - |
| $i_{\max}$ | index mode velocity | - |
| $\mathbf{J}$ | current density | $A\ m^2$ |
| $j_{n,\mathrm{WM}}$ | index nose of the bubble in the wiremesh signal | - |
| $j_{t,\mathrm{WM}}$ | index tail of the bubble in the wiremesh signal | - |
| $K$ | number of segments | - |
| $k$ | Boltzmann's constant | $J\ K^{-1}$ |
| $k_{0,1}$ | proportionality factor eddy-current fields | - |
| $L$ | inductance | H |
| $L$ | axial position coil filament | m |
| $L$ | window length | - |
| $L_B$ | chord-length bubble | m |
| $L_c$ | coil length | m |

| | | |
|---|---|---|
| $L_M$ | mixing length | m |
| $L_S$ | chord-length slug | m |
| $L_s$ | sample length | m |
| $L_{sp,i}$ | transversal length controlled by liquid pickup | m |
| $L_{ss,i}$ | transversal length controlled by liquid shedding | m |
| $\mathbf{M}$ | net magnetic moment | J $T^{-1}$ $m^{-3}$ |
| $M_0$ | thermal equilibrium magnetization | J $T^{-1}$ $m^{-3}$ |
| $m_{\{1,2\}\{1,2,3\}}$ | cluster mean | - |
| $m_I$ | azimuthal nuclear spin quantum number | - |
| $N$ | number of acquired data points | - |
| $N_+$ | nuclei with magnetic moment parallel to the magnetic field | - |
| $N_-$ | nuclei with magnetic moment antiparallel to the magnetic field | - |
| $N_B$ | number of cells in the polarizing magnet domain | - |
| $N_b$ | number of bubbles detected by the second tip-sensor | - |
| $N_{bG}$ | number of bubbles | - |
| $N_{c,\{1,2\}\{1,2,3\}}$ | number of objects in the cluster | - |
| $N_i$ | number of phase changes | - |
| $N_s$ | number of flow measurements | - |
| $N_v$ | number of discrete velocities | - |
| $N_y$ | number of cells in the streamwise probe domain | - |
| NFFT | number of discrete Fourier Transform points | - |
| $NxhL$ | number of cells within the pipe in the x-direction | - |
| $NzhL$ | cells containing the liquid level in stratified flow | - |
| $n$ | exponent of the power law model | - |
| $n_c$ | number of turns of the solenoidal coil | - |
| $P_{h_L h_L}$ | PSD estimate of the interfacial waves | $m^2 s^{-1}$ |
| $\bar{P}_{h_L h_L}$ | average PSD estimate of the interfacial waves | $m^2 s^{-1}$ |
| $P_{\{G,L\}}$ | wetted perimeter of the gas or the liquid phase | m |
| $P_i$ | width of the gas-liquid interface | m |
| $Q$ | amplitude of r.f. pulse modulated with sine carrier function | - |
| $q_L$ | liquid flowrate | $m^3$ $s^{-1}$ |
| $q_{\mathrm{NMR}}$ | liquid flowrate measured by NMR | $m^3$ $s^{-1}$ |
| $R$ | resistance | Ω |
| $R$ | distance to current element | m |
| $R$ | number of non-overlapping elements | - |
| $Rs$ | signal strength difference | - |
| $R_d$ | parallel dielectric resistance | Ω |
| $R_{d,s}$ | serial dielectric resistance | Ω |
| $R_{ext}$ | external resistor | Ω |
| $R_m$ | magnetic loss resistance | Ω |
| $r$ | radial cylindrical coordinate | m |
| $r_x$ | radial coordinate on a horizontal chord | m |
| $r_z$ | radial coordinate on a vertical chord | m |
| $\mathbf{S}$ | spin angular momentum | J s |

| | | |
|---|---|---|
| $S_{Im}$ | dispersion spectrum | - |
| $S_{Re}$ | absorption spectrum | - |
| $S_{tot}$ | magnitude total spin angular momentum | J s |
| $S_z$ | spin angular momentum in direction of permanent magnetic field | J s |
| $\mathbf{s}$ | detected NMR signal | - |
| $\mathbf{s}^*$ | dimensionless NMR signal strength | - |
| $s_0$ | thermal equilibrium attenuation of the detected signal in time space | - |
| $s_{100\%}$ | initial signal intensity of pure sample | - |
| $s_{F,i}$ | signal strength for a residence time $\tau_{F,i}$ | - |
| $s_{Im}$ | imaginary part of the detected signal in time space | - |
| $s_{Re}$ | real part of the detected signal in time space | - |
| $s_{S,i}$ | signal strength for a residence time $\tau_{S,i}$ | - |
| $s_{sp,i}$ | average signal level for the entire slug section | - |
| $s_{ss,i}$ | average signal level for the entire film section | - |
| $s_{t,\{1,2\}}$ | tip-sensor signal | V |
| $T$ | temperature | K |
| $T$ | half-width pulse | s |
| $T_1$ | longitudinal relaxation time | s |
| $T_2$ | transverse relaxation time | s |
| $T_2^*$ | effective transverse relaxation time | s |
| $T_G$ | temperature gas phase | K |
| $T_L$ | temperature liquid phase | K |
| $t$ | time | s |
| $t$ | residence time | s |
| $t^*$ | dimensionless residence time | - |
| $t_{echo}$ | time of maximum echo amplitude | s |
| $t_{\{n,n1,n2\}}$ | arrival time bubble nose at the tip-sensor | s |
| $t_p$ | pulse time | s |
| $t_{\mathrm{ST}\ 0.025}$ | coverage factor using Student's t distribution for a 95% confidence level | - |
| $t_t$ | arrival time bubble tail at the tip-sensor | s |
| $U$ | expanded uncertainty | |
| $U$ | strength wiremesh signal | V |
| $U$ | normalizing constant for the windowing operation | - |
| $U_{ADC}$ | wiremesh signal before being digitized by the AD converter | V |
| $< U^G >$ | time-averaged wiremesh signal for pure gas | V |
| $U_{LJ}$ | voltage applied by output line LabJack | V |
| $U_{pulse}$ | voltage of the pulse by the wiremesh transmitter amplifier | V |
| $U_{\{s1,s2\}}$ | tip-sensor voltage across the external resistor | V |
| $< U^W >$ | time-averaged wiremesh signal for pure water | V |
| $u$ | standard uncertainty | |
| $v_B$ | bubble velocity | m $s^{-1}$ |

| | | |
|---|---|---|
| $\langle v_B \rangle$ | average bubble velocity Gaussian model assumed | m s$^{-1}$ |
| $v_{\mathrm{BG}}$ | gas bulk velocity | m s$^{-1}$ |
| $v_{BG}$ | velocity in the elongated bubbles | m s$^{-1}$ |
| $v_{\mathrm{BL}}$ | liquid bulk velocity | m s$^{-1}$ |
| $v^*_{\mathrm{BL}}$ | dimensionless liquid bulk velocity | - |
| $v_{BS}$ | velocity of the dispersed bubbles in the liquid slug | m s$^{-1}$ |
| $v_{\mathrm{EMF}}$ | streamwise flow velocity measured with a calibrated flowmeter | m s$^{-1}$ |
| $v_F$ | film velocity | m s$^{-1}$ |
| $v_H$ | velocity head | m |
| $v_{mix}$ | mixture velocity | m s$^{-1}$ |
| $v_{\mathrm{NMR}}$ | streamwise flow velocity measured with NMR | m s$^{-1}$ |
| $v^*_{\mathrm{NMR}}$ | dimensionless streamwise flow velocity measured with NMR | - |
| $v_{\mathrm{NMR,\{F,S\}}}$ | streamwise flow velocity measured with NMR | m s$^{-1}$ |
| $v_S$ | slug velocity | m s$^{-1}$ |
| $v_{\mathrm{SG}}$ | superficial gas velocity | m s$^{-1}$ |
| $v_{\mathrm{SL}}$ | superficial liquid velocity | m s$^{-1}$ |
| $v_y$ | streamwise flow velocity | m s$^{-1}$ |
| $v^*_y$ | dimensionless streamwise flow velocity | - |
| $vyz0$ | streamwise velocity along the z-axis | m s$^{-1}$ |
| $W$ | half bandwidth r.f. pulse | rad s$^{-1}$ |
| $w$ | weight coefficient wiremesh | - |
| $w$ | window | - |
| X | 1$^{\mathrm{st}}$ order shim gradient of $B_z$ in x-direction | T m$^{-1}$ |
| $x, y, z$ | cartesian coordinates | m |
| $x', y', z'$ | rotating frame cartesian coordinates | m |
| $xv$ | position x-direction | m |
| Y | 1$^{\mathrm{st}}$ order shim gradient of $B_z$ in y-direction | T m$^{-1}$ |
| $y_{c,\{1,2\}}$ | probe position | m |
| $Z^0$ | 0$^{\mathrm{th}}$ order shim gradient of $B_z$ in z-direction | T m$^{-1}$ |
| Z | 1$^{\mathrm{st}}$ order shim gradient of $B_z$ in z-direction | T m$^{-1}$ |
| $Z^2$ | 2$^{\mathrm{nd}}$ order shim gradient of $B_z$ in x-direction | T m$^{-1}$ |
| $zv$ | position z-direction | m |

**Greek**

| | | |
|---|---|---|
| $\alpha$ | flip angle | $^\circ$ |
| $\alpha_L$ | liquid holdup | - |
| $\alpha_{\mathrm{LF}}$ | liquid holdup in the film region | - |
| $\alpha_{\mathrm{L,NMR}}$ | liquid holdup measured with NMR | - |
| $\alpha_{\mathrm{L,WM}}$ | liquid holdup measured with the wiremesh sensor | - |
| $\alpha_{\mathrm{LS}}$ | liquid holdup in the slug region | - |
| $\alpha_{\mathrm{NMR,\{1,2\}}}$ | liquid holdup measured with NMR | - |
| $\alpha_{\mathrm{NMR,\{F,S\}\{1,2\}}}$ | liquid holdup measured with NMR | - |

| | | |
|---|---|---|
| $\beta$ | elevation angle | rad |
| $\gamma$ | gyromagnetic ratio | rad $T^{-1}s^{-1}$ |
| $\gamma$ | top angle stratified flow | rad |
| $\Delta$ | phase shift | rad |
| $\Delta B_0$ | offset of the uniform $B_0$-field | T |
| $\Delta E$ | energy difference between adjacent energy levels | J |
| $\Delta f$ | frequency resolution | $s^{-1}$ |
| $\Delta_G$ | inter gradient pulse spacing | s |
| $\Delta g$ | additional linear gradient field | T $m^{-1}$ |
| $\Delta l$ | added length of the replacement magnetic field | m |
| $\overline{\Delta l}$ | average added length of the replacement magnetic field | m |
| $\Delta l_{\text{ref}}$ | added length reference of the replacement magnetic field | m |
| $\Delta t$ | residence time resolution | s |
| $\Delta t_p$ | pulse length | s |
| $\Delta y$ | spatial resolution y-direction | m |
| $\Delta y_{f2,\text{WM}}$ | mutual distance second tip-sensor – wiremesh | m |
| $\Delta y_{tip}$ | mutual distance tip-sensors | m |
| $\Delta\phi$ | phase shift | rad |
| $\Delta\hat{\phi}$ | filtered phase shift | rad |
| $\Delta\omega_0$ | offset frequency with respect to the Larmor frequency | rad $s^{-1}$ |
| $\delta$ | sampling interval | s |
| $\delta\alpha_{\text{LF},ss}$ | bias in the liquid holdup of the film section by the liquid shedding process | - |
| $\delta\alpha_{\text{LS},sp}$ | bias in the liquid holdup of the slug section by the liquid pickup process | - |
| $\delta v_{F,ss}$ | velocity bias by the liquid shedding process | m $s^{-1}$ |
| $\delta_G$ | gradient pulse width | s |
| $\delta v_{\{\text{BG,BL}\}}$ | systematic error in the gas or the liquid bulk velocity | m $s^{-1}$ |
| $\delta v_F$ | systematic error in the film velocity | m $s^{-1}$ |
| $\delta v_S$ | systematic error in the slug velocity | m $s^{-1}$ |
| $\delta v_{S,sp}$ | velocity bias by the liquid pickup process | m $s^{-1}$ |
| $\delta v_y$ | error in the velocity reading | m $s^{-1}$ |
| $\delta\alpha_L$ | liquid holdup overestimation | - |
| $\epsilon_0$ | vacuum permittivity | F $m^{-1}$ |
| $\epsilon_r$ | relative permittivity | - |
| $\Theta$ | polar angle | rad |
| $\theta$ | azimuthal coordinate | rad |
| $\lambda$ | wavelength | m |
| $\boldsymbol{\mu}$ | nuclear magnetic moment | $JT^{-1}$ |
| $\mu_0$ | magnetic permeability of vacuum | $Hm^{-1}$ |
| $\mu_{\{G,L\}}$ | dynamic viscosity of the gas or the liquid phase | Pa s |
| $\mu_z$ | nuclear magnetic moment in permanent magnetic field direction | $JT^{-1}$ |
| $\nu$ | degrees of freedom | - |

| | | |
|---|---|---|
| $\nu$ | frequency | $s^{-1}$ |
| $\nu$ | kinematic viscosity | $m^2\ s^{-1}$ |
| $\nu_{\text{eff}}$ | effective degrees of freedom | - |
| $\nu_L$ | resonance frequency electromagnetic radiation | $s^{-1}$ |
| $\xi$ | induced NMR signal strength | $J\ s^{-1}m^{-3}$ |
| $\rho$ | radial spherical coordinate | m |
| $\rho_{\{G,L\}}$ | density of the gas or the liquid phase | $kg\ m^{-3}$ |
| $\sigma$ | standard deviation | - |
| $\sigma_s$ | specific conductivity of the sample | $S\ m^{-1}$ |
| $\tau$ | time delay | s |
| $\tau$ | loss factor of the sample | - |
| $\tau_{\{0,1,2\}}$ | time delay | s |
| $\tau_{F,i}$ | residence time in $\mathbf{B}_0$ of the liquid in the film section | s |
| $\tau_i$ | time constant eddy-currents | s |
| $\tau_{S,i}$ | residence time in $\mathbf{B}_0$ of the liquid in the slug section | s |
| $\tau_{t,\text{WM}}$ | delay of the tip-sensor relative to the wiremesh measurement | s |
| $\Phi_S$ | magnetic flux | Wb |
| $\phi$ | phase NMR signal | rad |
| $\phi$ | azimuthal angle | rad |
| $\hat{\phi}$ | filered phase NMR signal | rad |
| $\phi_0$ | phase offset due to experimental conditions | rad |
| $\phi_R$ | receiver phase | rad |
| $\phi_T$ | transmitter phase | rad |
| $\psi$ | phase describing the r.f. pulse shape | rad |
| $\psi$ | difference in azimuthal angle | rad |
| $\Omega$ | reduced frequency with respect to the carrier frequency | $rad\ s^{-1}$ |
| $\omega$ | angular frequency | $rad\ s^{-1}$ |
| $\omega_0$ | Larmor frequency | $rad\ s^{-1}$ |
| $\omega_1$ | precession frequency about oscillating magnetic field | $rad\ s^{-1}$ |
| $\omega_{\text{eff}}$ | precession frequency about effective magnetic field | $rad\ s^{-1}$ |
| $\omega_{osc}$ | resonance frequency of probe circuit | $rad\ s^{-1}$ |
| $\omega_r$ | carrier frequency | $rad\ s^{-1}$ |

**Abbreviations**

| | |
|---|---|
| CPMG | Carr-Purcell-Meiboom-Gill |
| DFT | Discrete Fourier Transform |
| ECT | Electrical Capacitance Tomography |
| emf | electromotive force |
| EPI | Echo Planar Imaging |
| ERT | Electrical Resistance Tomography |
| ESR | Electron Spin Resonance |
| FID | Free Induction Decay |

| | |
|---|---|
| FFT | Fast Fourier Transform |
| FPSO | floating production, storage and offloading unit |
| GE | gradient echo |
| GERVAIS | Gradient Echo Rapid Velocimetry and Acceleration Imaging Sequence |
| GVF | gas volume fraction |
| GX | gradient channel |
| HI | hydrogen index |
| Im | imaginary signal component |
| INVREC | Inversion Recovery |
| LA | large amplitude stratified wavy flow |
| lab | laboratory frame of reference |
| LP | low pass |
| MRFO | marine residual fuel oil |
| MRV | Magnetic Resonance Velocimetry |
| N | north pole permanent magnetic field |
| NMR | Nuclear Magnetic Resonance |
| P180 | 180° pulse length |
| P90 | 90° pulse length |
| $P90_{3se}$ | 90° pulse length obtained from third spin echo |
| $P90_{ste}$ | 90° pulse length obtained from stimulated echo |
| $P90_{ste/pe}$ | 90° pulse length obtained from ratio of stimulated to primary echo |
| PFG | pulsed field gradient |
| PGSE | pulsed gradient spin echo |
| PGSEG | pulsed gradient spin echo in which $G_y$ is altered |
| PGSET | pulsed gradient spin echo in which $\delta_G$ is alterd |
| PNA | Pulsed Neutron Activation |
| PSD | phase sensitive detector |
| RARE | Rapid Acquisition with Relaxation Enhancement |
| Re | real signal component |
| Re | Reynolds number |
| $Re_{\{G,L\}}$ | Reynolds number of the gas or the liquid phase |
| r.f. | radio frequency |
| RFA0 | r.f. pulse amplitude parameter |
| rot | rotating frame of reference |
| RX | receiving channel |
| S | south pole permanent magnetic field |
| SA 2D | small-amplitude two-dimensional stratified wavy flow |
| SE | spin echo |
| SEMI-RARE | Single Excitation Multiple Image RARE |
| SS | stratified smooth flow |
| SW | stratified wavy flow |
| T1RRT | $T_1$ relaxation residence time |
| TX | transmitting channel |
| WM | wiremesh sensor |

# Chapter 1

# Introduction

## 1.1 Motivation

Multiphase flowmeters are increasingly seen as a facilitator for the exploitation of, in particular, deep water and ultra-deep water oil fields. The most promising offshore projects are the Gulf of Mexico, South Chinese Lake and near Brazil. Cost-efficient development of the North Sea marginal fields gave reason in the 1980s to investigate the deployability of multiphase flowmeters. Jamieson [116] argued that "without high-performance multiphase flowmetering it will simply not be economically worthwhile for oil companies to develop small accumulations of hydrocarbons in the North Sea." Producing the new reserves would only be viable by developing them as unmanned platforms, subsea tie-backs, or satellite fields, utilizing the processing capacity on the nearest host platform, either on- or offshore, rather than building new installations for each field.

Multiphase flow measurements are required for field development, reservoir management, and production allocation, among others. Traditionally, well tests are carried out periodically, with a test separator, as shown in Figure 1.1, which separates the three phases based on their specific gravity difference, after which the individual gas, oil and water flows can be measured. These cylindrical vessels are huge in size, typically ranging from 4.6 – 9.1 meter in length, 2.4 – 4 meter in height and weighing up to $9.1 \cdot 10^3$ kg, at the expense of the ever-scarce space on offshore platforms, and their price is correspondingly high [10].
To monitor the production of the individual wells connected to the same manifold, dedicated test lines are used, which allow testing the wells one at a time, without shutting down the other wells. However, the limitations of this form of well testing are considerable. Test separators have difficulties measuring dynamic flow regimes, because stable processing conditions are needed. Due to the large distances to the production manifolds, extended stabilization periods between the tests are, therefore, often inevitable. Another drawback is that during testing the back pressure experienced by the well often differs from the normal production conditions. The vessel must also have sufficient capacity to accommodate the largest occurring slugs. The installation costs are thus high, while the quality of the measurements is limited [117].

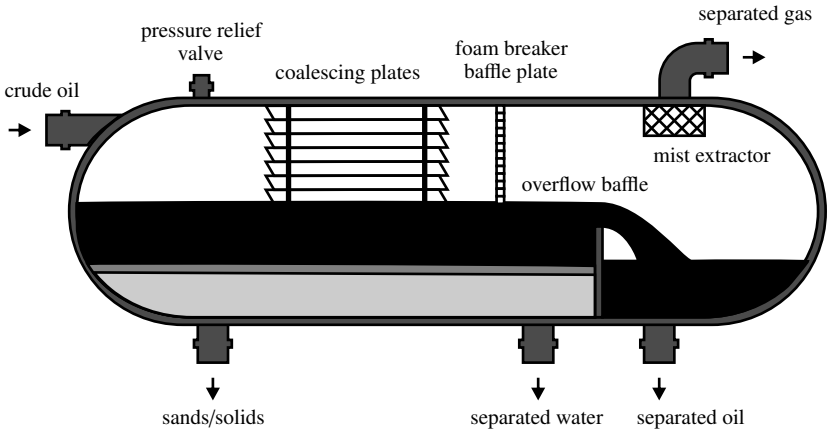


**Figure 1.1**: Typical test separator, in which gravity settling is used to separate the crude oil into individual gas, water and oil streams, after which the flowrates of the gas and liquid phases, upon leaving the vessel, are usually measured with orifices and mechanical meters, respectively, before recombining and returning to the flowline.

Replacing the topside offshore separators with a relatively cheap multiphase flowmeter leads already to significant savings. Other advantages are that multiphase flowmeters involve less intervention and maintenance than gravity separators, and their compact design dramatically reduces platform space and load requirements. In addition, onshore processing of the total production of the wells allows for more efficient separation of the flows and will reduce the volume of discharged oil-polluted water that is routed back into the sea. Subsea metering is of strategic importance for the future of oil field exploitation, as it resolves technical and economic bottlenecks related to the difficult accessibility of subsea developments. The layout of the production facilities can be extremely simplified, if use is made of stand-alone subsea multiphase flowmeters. Removal of the infrastructure of manifold and test lines associated with the topside offshore separator results in huge savings, in both capital and operational expenditures [221].

However, it is not just the costs in which multiphase flowmetering technology has added value. Multiphase flowmeters make it possible to perform well tests over longer time periods, and on a more frequent basis, as test results are delivered a few minutes after switching to the well, while in a conventional test separator it can take hours for the fluids to stabilize sufficiently to be measured. In addition, they allow to test the well close to actual producing conditions.
The fact that multiphase flowmeters provide near real-time, continuous production monitoring is a major improvement for reservoir management. Because the produced flowrates can span up to three decades over the lifetime of a well, as Slijkerman et al. [234] show on the basis of a selection of practical examples, the multiphase flowmeter is an important source

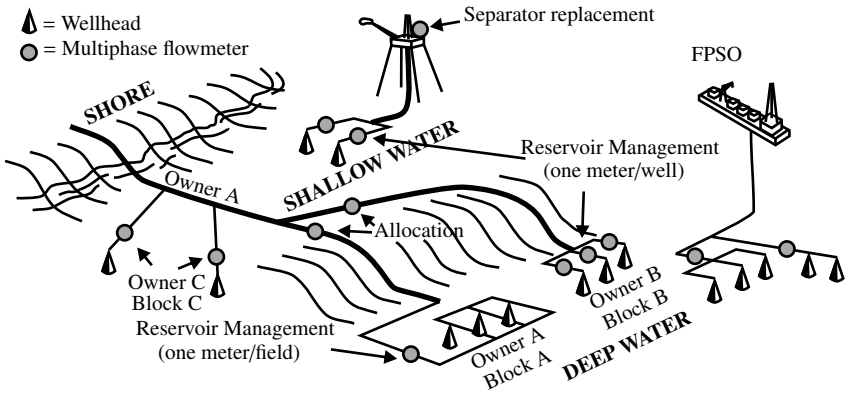


**Figure 1.2**: Typical field configuration adapted from Pinguet et al. [201]. The production of block B and two wells of operator C are tied back to the existing subsea pipeline owned by operator A. To reduce the uncertainty in the partner allocation, each company, A and B, has a meter before commingling the production. Due to the size of the satellite fields in block C, a redundancy measurement is not feasible, making the accuracy of the multiphase flowmeters a critical factor in the custody transfer between the companies A and C. In deep water (depths greater than 300 m), a floating production, storage and offloading (FPSO) unit usually serves as the surface facility to which the hydrocarbons produced from different wells are commingled.

of information for the development of dynamic reservoir models. The data leads to better reserve estimates and production forecasts, and helps to limit the number of production interruptions. Many wells produce at high water-cuts, above 90%. Accurate monitoring of the water-oil ratio helps to determine whether production is still profitable, or whether it is better to shut the well. The multiphase flowmeter data also contributes to a greater quality in the decision-making regarding production optimization. Immediate action can be taken on changes in well productivity, and the water and gas injection in artificial lift operations can be continuously adjusted to optimize field performance.

One of the applications that require multiphase flowmetering is in the allocation of hydrocarbons. Different owner structures are increasingly used, whereby the production of new developments is commingled to the nearest shared production facility or floating production, storage and offloading (FPSO) unit. Pinguet et al. [201] address the benefits of permanent monitoring with multiphase flowmeters, for fiscal allocation in the light of a number of typical field configurations. In the case of partnership allocation, where the owner connecting his production to another owner's pipeline is in the same field, such as company A and B in Figure 1.2, production uncertainty is greatly reduced when both companies have an additional flowmeter before the production is commingled, implying that smaller safety margins can be maintained in the settlement. In the scenario like that of company C with two satellite fields tied back to the subsea pipeline owned by company A, the value of a high performance flowmeter is even greater, because backup measurements are not an option due to the small scale of the field. As long as there are no affordable alternatives with single-phase fiscal me-

tering accuracy that do not jeopardize the development or profitability of new fields, Pinguet et al. [201] conclude that "authorities are moving away from considering the use of multiphase flowmeters as a second solution or lower alternative."

Worldwide the application of multiphase flowmeters is growing. As the multiphase flowmeters become mainstream and, therefore, more affordable, more and more companies, like TOTAL [49], have the policy of installing one meter per well, instead of one meter per field. With the increasing depletion of offshore production in global shallow water deposits, deep water, or even ultra-deep water projects, are becoming more common and a high-performance multiphase flowmeter is, therefore, essential. The main motivation for this project, associated with developing a new type of subsea multiphase flowmeter, is the high accuracy which can be reached with NMR.

## 1.2 Multiphase Flow Patterns

Multiphase flowmetering is so challenging because multiphase flow is a highly complex phenomenon. Many flow regimes can occur, where the complicated interaction between the flow in each of the phases determines their configuration in space and time. Moreover, the physical understanding is in general insufficient to predict which flow regime will exist under the prevailing operating conditions. Factors leading to regime transitions are the diameter and the orientation of the pipeline, the flowrates, and the fluid properties (in particular the liquid-gas density ratio, the viscosity and the surface tension). Although the flow structures may change strongly with the inclination of the pipe, we limit our study at this stage, for practical reason, to a pure horizontal alignment of the flowmeter. NMR is insensitive to the position of the hydrogen protons in the measurement section. It is therefore expected that the flowmeter can also be installed vertically or at any other angle, as long as the flow regimes are steady-state, pseudo steady-state or quasi-static, fully-developed, intermittent. The developed flowmetering principles are as yet unsuitable for measuring flow regimes with abrubt regime changes. Apart from churn flow in which irregular and relatively unstable slugs of gas move up through the center of the pipe, we believe that measuring vertical multiphase flows will be less difficult due to the more common rotational symmetry of the flow patterns.
Figure 1.3 shows the flow map of the basic flow patterns in horizontal two-phase gas-liquid flow, namely bubble flow, stratified smooth or wavy flow, intermittent flow (plug or slug flow) and annular flow. For a description of the characteristics of the different flow regimes is referred to the text books on the fundamentals of multiphase flow by Brennen [31], Ghiaasiaan [78] and Govier and Aziz [85].
Compared to gas-liquid two-phase flow, little research has been done into three-phase oil-water-gas flow. Three-phase flow patterns are more complex, because oil and water have different gradations of mixing, with fully separated and homogeneously dispersed flow as extremes. Overall, the horizontal three-phase flow patterns can be grouped into the same four major categories as found for two-phase flow. Because of the presence of the third phase, Açikgöz et al. [3] observed many variations of the flow patterns for three-phase horizontal oil-water-air flow in a 1.9 cm diameter pipe, which were not seen in two-phase flow. One

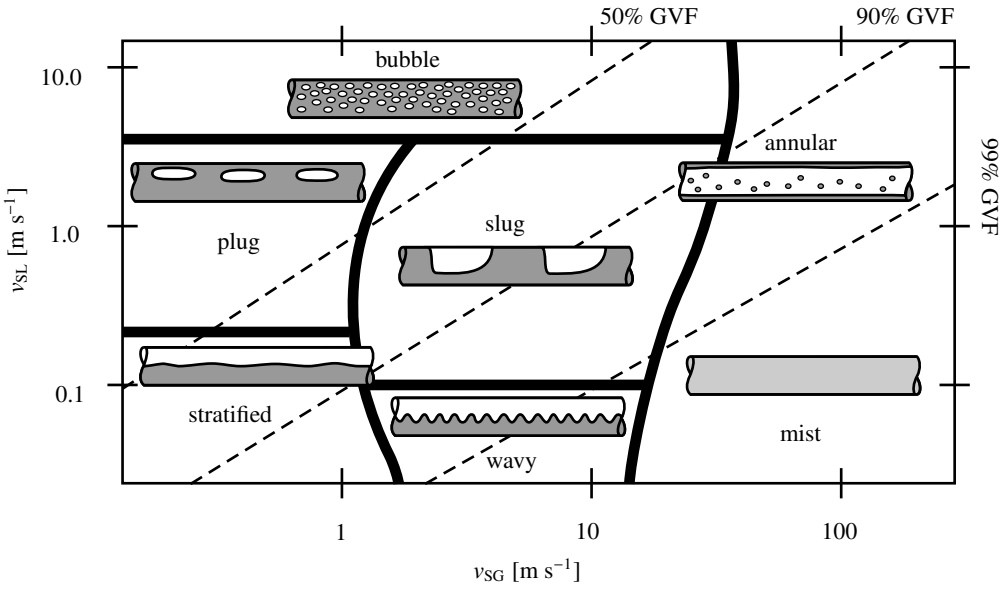


**Figure 1.3**: Generic two-phase horizontal flow map after the American Petroleum Institute (API) [5] based on experiments in a 4" horizontal diesel-air system operating at low-pressure.

of their findings was that oil dominated flow regimes bring a new variety of sub-patterns that do not occur in water dominated flow. The classification they have devised to facilitate the development of three-phase flow models, therefore, consists of a wide range of possible subcategories as illustrated in the Figures 1.4 and 1.5. Lee et al. [151] have investigated the influence of two different viscosities of the oil on the flow pattern maps of three-phase oil-water-carbon dioxide mixtures in a 10 cm diameter horizontal pipe. The results confirm that the liquid composition has a major effect on the flow regime transitions and that these are not predicted by the most commonly used models. Spedding et al. [236] report the flow regimes for horizontal three-phase oil-water-air pipe flow for a 2.59 cm and a 5.01 cm diameter pipe and have developed a "universal" flow regime map that they claim can predict the major pattern types for both two and three phase macro-scale, co-current, horizontal pipe flow systems. However, some nuance is necessary, since no present flow regime map is robust enough to accurately predict the regime changes for a wide variety of geometries and phase physical properties.

According to the American Petroleum Institute [5], oil fields generally operate in a gas volume fraction (GVF) range between 40% (high pressure operation) and 90 – 95% (low pressure and gas lift operation). Oil wells predominantly operate in the slug flow regime, in the middle of the flow map of Figure 1.3, in which the GVF is indicated by the diagonal lines. Bubble and annular flow regimes associated with the high flowrates of higher produc-

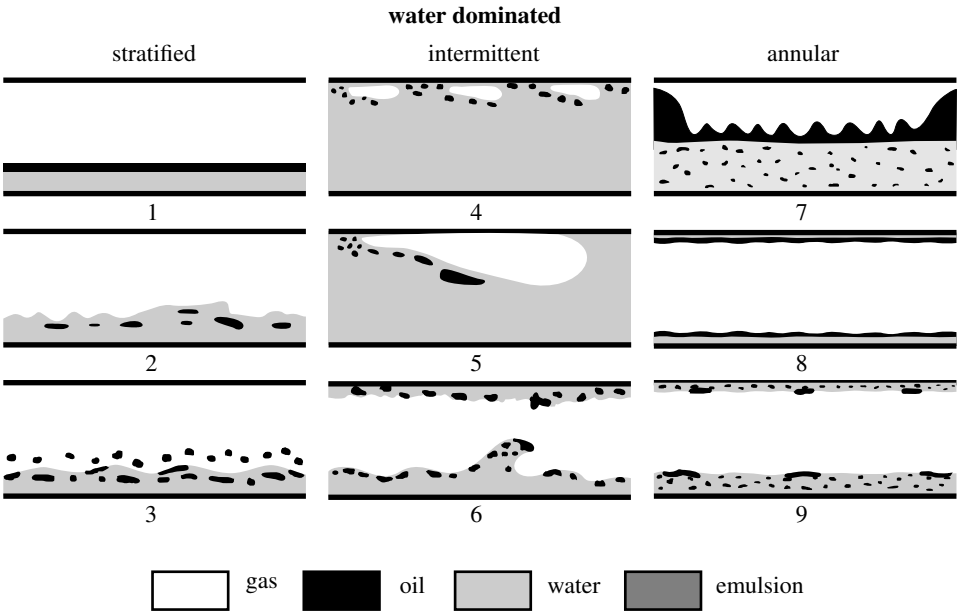


**Figure 1.4**: Water dominated co-current three-phase flow regimes adapted from Açikgöz et al. [3] and Spedding et al. [236], where (1) smooth stratified separated flow, (2) stratified wavy separated flow, (3) stratified roll-wave droplet dispersed flow, (4) plug dispersed flow, (5) slug dispersed flow, (6) blow through slug flow, (7) incipient stratifying-annular separated/dispersed flow, (8) annular separated flow and (9) annular dispersed flow.

tivity wells are undesirable because of the higher maintenance costs due to the mechanical vibration load and erosion of the production facilities. From an economic point of view, the stratified flow regimes on the other end of the production spectrum, a consequence of oversized flow lines, have too low yields and should therefore also be avoided.
Multiphase flowmeters are primarily a solution for moderate GVF in the range of 25 – 85%. The single-phase flowmeters that in many cases still provide sufficient measurement performance at low GVF < 25% are no longer cost-effective under these circumstances. Multiphase flowmeters become less reliable for high GVF > 85%, as the measurement uncertainties increase rapidly with the gas fraction while the oil fraction decreases. The financial risk is generally too high, which is why partial separation is sometimes used to bring the GVF back into the moderate GVF range [48].

Two aspects of multiphase flow are very important for multiphase flowmetering: the unsteadiness of the flow structures and phase slip. Depending on the flow regime, multiphase flows can have strong non-uniformities, in space and time, within each phase as well as in the phase pattern. It is inherent to multiphase flow that the flow pattern evolves continuously, even within a flow regime.

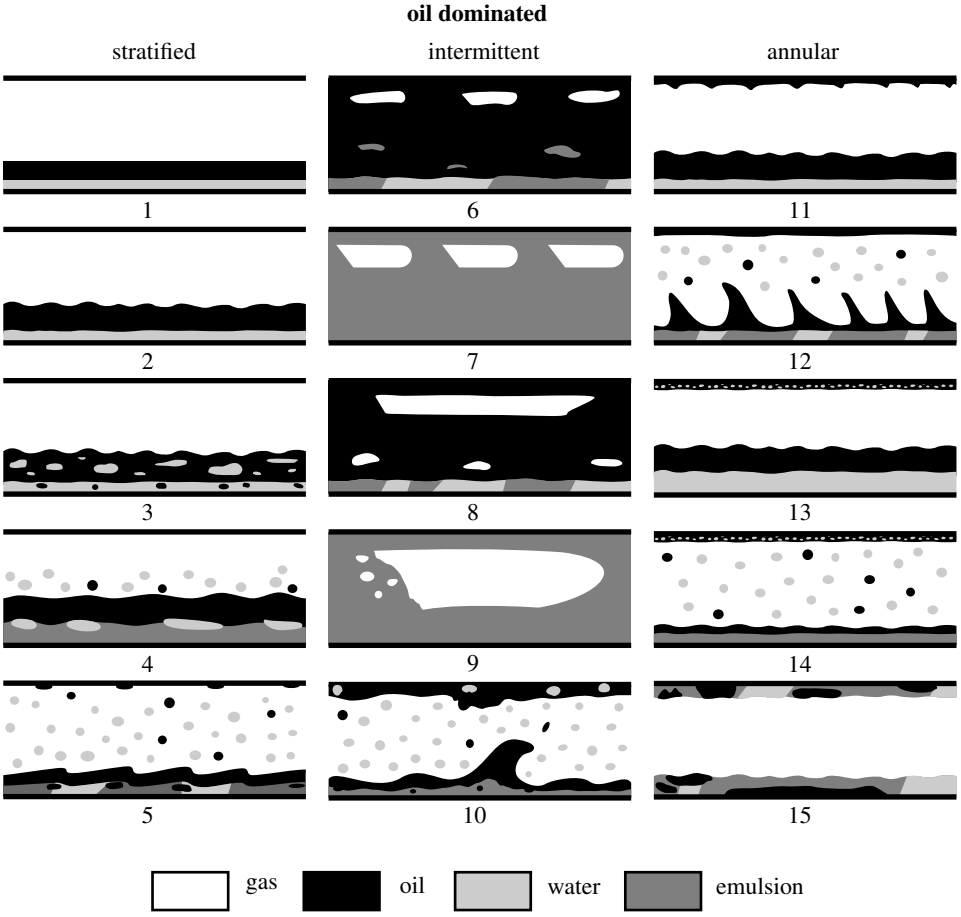


**Figure 1.5**: Oil dominated co-current three-phase flow regimes adapted from Açikgöz et al. [3] and Spedding et al. [236], where (1) smooth stratified separated flow, (2) stratified wavy separated flow, (3) stratified wavy dispersed flow, (4) stratified roll-wave dispersed flow, (5) roll-wave dispersed flow, (6) plug separated flow, (7) plug dispersed flow, (8) slug separated flow, (9) slug dispersed flow, (10) blow through slug flow, (11) annular separated flow, (12, 13) stratifying-annular separated/dispersed flow, (14) annular dispersed flow and (15) broken film regime at the inversion between oil and water dominated flow.

Phase slip arises from the different densities and viscosities of the three phases, causing each of them to travel at a different velocity in a pipe flow. Gas tends to flow at a much higher velocity than the liquid phases due to its much lower density. Although smaller, phase slip is also present between the oil and water phases. In addition to this velocity difference, the multiphase measurement technique must also take into account that, owing to the phase slip between liquid and gas, the liquid holdup will be larger than the liquid-cut. Oddie et al. [184] conclude based on a comparison of shut-in liquid holdup measurements versus the liquid-cut between two-phase water-nitrogen and three-phase kerosene-water-nitrogen flow in a 15 cm diameter pipe that the results are reasonably close to treat oil and water in three-phase systems as one liquid phase. However, in liquid-liquid kerosine-water systems, the slip they detect between the oil and the water at low and modest oil flowrates up to 10 $m^3\ h^{-1}$ is still quite substantial, even though it is much less than that observed for liquid-gas systems. Phase slip is an important issue, which is quite dependent on the inclination of the pipe. Both issues can pose serious challenges for the multiphase flowmeter.

The challenge for multiphase flowmeters compared to conventional flowmeters in that they must be able to identify the proportions of each particular component in presence of complex structures. As the important flow parameters such as the gas volume fraction and the local velocities can fluctuate very quickly, this can affect the reconstruction of the flowrates from the NMR signal. The flowmeter's measurement frequency must be adapted to these rapid fluctuations in order to determine the key parameters with sufficient accuracy.
In the case of pseudo-steady flow, for example stratified or annular flow, the flowrates can be calculated as a simple time average of the raw data. For the more complex or even discontinuous regimes such as slug flow, all multiphase flowmeters rely on some degree of flow modeling. The flowmeter will therefore only work properly if the correct model is selected for the prevailing flow regime.

With regard to phase slip, the challenge resides first of all in overcoming the effect that the non-uniform velocity profiles within each phase have on the NMR signal. Second, the measuring method must be able to distinguish the oil and water components of the liquid phase, which is complicated by phase slip. At the highest water and oil flowrates, there is very little slip at any pipe inclination because oil and water are well mixed at high flowrates and form homogeneous dispersions or emulsions. For dispersed flow, it seems therefore justified to assume no-slip between the two liquid phases, but for an optimal performance of the flowmeter at separated or dual-continuous flows, the stratified flow patterns with mixing at the interface, it is better if the multiphase flowmeter can determine both the individual oil and water velocities.

## 1.3 State-of-the-art in multiphase flowmetering

The multiphase flowmetering solutions that have been developed for the petroleum industry are very diverse. In order to meet the production conditions that have become more challenging, the focus of the latest developments, as explained by Thorn et al. [243], is on increasing

the operational envelope, reducing the measurement uncertainty and improving the longterm reliability. The systems can be classified into two categories according to their approach to measure the flowrates of a three-phase flow, as is illustrated in Figure 1.6 [64].

In the first, also known as virtual flowmeters [23, 90], the flowrates are determined indirectly by using functions that relate the flowrate to the measured parameters. These flowmeters usually consist of a combination of a differential pressure meter, mostly a venturi tube or an orifice plate, with technology to determine the GVF and density of the mixture. As pointed out by Oliemans [185], the 'inverse' models developed to predict the flowrates of three-phase flow based on the measurements of the pressure drop and the liquid holdup are thus far by no means of the level of sophistication as the two-phase models, because the physics of three-phase flow is insufficiently understood, so that the uncertainties in the obtained flowrates are unacceptably large. In the absence of theoretical predictions, the functional interrelationships must be established by calibration. Although virtual flowmeters provide a cheap solution to the petroleum industry by being based on simple instrumental equipment, the disadvantage is that the reliability of the empirical algorithms is only guaranteed for the range that has been calibrated, which is usually not over the full range of conditions.

The second approach involves the direct measurement of the essential parameters of the component velocities and component fractions or of quantities that are unambiguously associated with these [64]. To determine the individual flowrates of the oil, water and gas components, five measurements are needed, namely three velocities and two phase fractions. The third phase fraction can be obtained from the condition that the sum of all three phase fractions must be equal to one.
In order to reduce the difficulty of the measurement problem, various manufacturers resort to partial separation or homogenization of the flow. By full two-phase separation into gas only and liquid only streams, the need to determine the GVF disappears and conventional single and two-phase technology, such as Coriolis mass flowmeters and Vortex shedding meters, can be used to determine the three flowrates. Since one of the main objectives of applying multiphase flowmeters is to replace the gravity separators, flow diverters and inline swirl separators are preferred to divert most of the free gas into a bypass loop. The drawback of inline separators is the increased pressure drop that the device produces and the limitation it imposes on pigging the pipeline.
Homogenization prior to the measurements makes the velocity the same for all phases, so that the number of unknowns to be measured comes down to three. The inline mixers commonly used for this purpose have the same disadvantages as the inline separators. In addition, care should be taken not to mix too far upstream of the measurement section. As mentioned by Ashkuri and Hill [8], it only takes a few diameters after the multiphase flow in the pipeline is well mixed for some gas and liquid velocity difference to be found due to phase separation.

The existing multiphase flowmetering systems are usually an integrated solution of instruments based on different measurement techniques. This has the major drawback that the errors of the different measurement principles add up to a large total error.

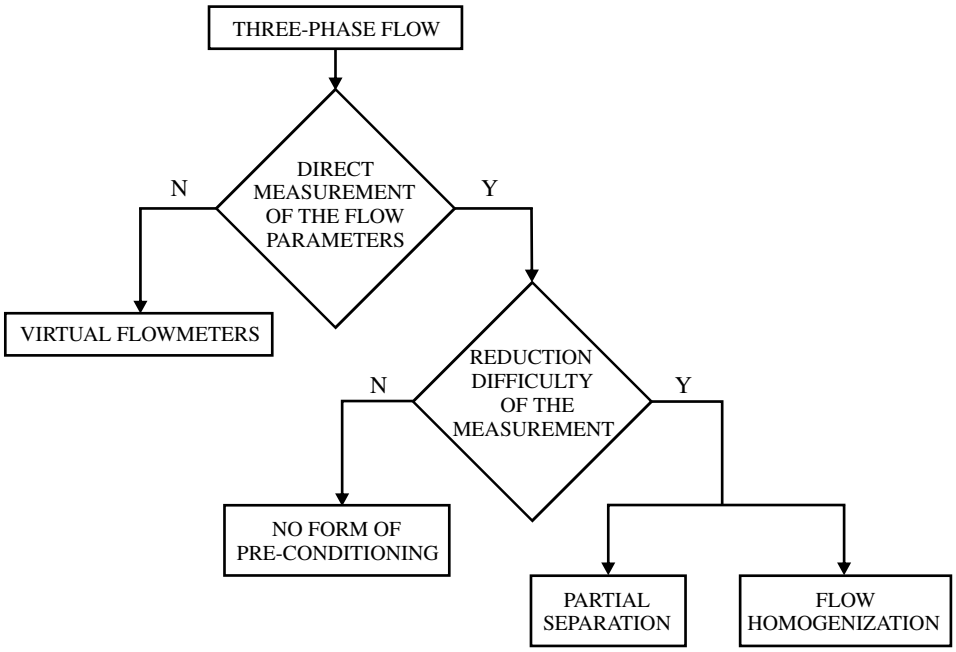


**Figure 1.6:** Classification system for three-phase flowmeters.

To determine the phase volume fractions, the most commonly used methods are gamma densitometery and electrical impedance techniques [242, 243].
Gamma densitometry is a reliable, non-intrusive method that uses one or two radioactive sources of different intensity to measure either the GVF or all three phase volume fractions. The main disadvantage is that radiation hazards are involved for which safety measures must be taken. Another limitation is a changing salinity content of the water, which Slijkerman et al. [234] have shown could change significantly in a short period of time, causing errors in the measurements unless this is compensated for. As a recent study by Hansen et al. [90] concluded that phase fraction measurement methods with radioactive sources tend to have a much better accuracy than those without, it is not surprising that gamma densitometry is currently a well-established technique, widely accepted in field applications.
Electrical impedance techniques exploit the differences in electrical behavior of oil and water to a voltage applied by electrodes integrated in the pipe wall. Oil is a dielectric, acting like a capacitor. Water, on the other hand, is a conductor. Depending on the composition of the flowing medium, the impedance is formed by capacitance, resistance or both. Electrical Capacitance Tomography (ECT) determines the oil distribution based on the measured capacitance, which changes when the distribution of the dielectrical material changes, while the Electrical Resistance Tomography (ERT) determines the water distribution based on the measured resistance; the quantities being a direct function of the flow's component ratio.

Because water can short-circuit a sensor that measures the capacitance, while the insulating property of oil (or air) can block the conductance measurements of an ERT sensor, it is essential to know whether oil or water is the continuous phase of an oil-water mixture before selecting the operating principle. A strong variation of the GVF, such as in slug flow between 0 and 100%, presents a challenge to ERT methods, as there can be no guarantee that the continuous phase will maintain direct contact with the electrodes at all times. To function under both water continuous and oil continuous conditions, the ERT and ECT technology are often combined in a dual-modal sensor [90]. The methods have the advantage over gamma densitometry that an almost instantaneous dynamic response can be achieved while avoiding the need of radioactive sources. This makes them very suitable for measuring transient multiphase flow phenomena. Moreover, impedance meters are relatively cheap. Despite good experiences with two-phase flow, Falcone et al. [64] question the general applicability of the devices in three-phase flows. The principal difficulty is that the technique is flow regime dependent, making the method unsuitable for applications where the regime is unknown or unstable. Related to this is the poor performance achieved when the production line operates in the vicinity of the inversion point, usually between 40 and 60% water-cut [64], at which an oil-water mixture can switch from oil continuous into water continuous flow as it passes through the meter. ERT sensors also have difficulties in accurately measuring emulsions. For oil dispersed in water, but emulsified, the sensor will only measure the free water and not the total water fraction. Due to the insulating effect of oil, the emulsified water in oil will not be detected. In addition, the ERT sensor is sensitive to changes in the conductivity of water, which can fluctuate significantly with the salinity. For a comprehensive literature review of the latest electrical impedance methods, see Hansen et al. [90].
Alternative techniques for determining the phase fraction that have also been developed for commercial use are microwave attenuation and infrared absorption, but Falcone et al. [65] indicate that these techniques are unlikely to be reliable in the presence of gas and that they are potentially limited to small-scale applications.

In multiphase flowmetering solutions that do not require flow separation, the flow velocity is mainly determined with venturi meters or cross-correlation techniques using a variety of sensors such as capacitance, gamma-ray and microwave. The weakness of both measuring principles is the flow model needed in order to determine the bulk velocities in the presence of slip between the gas and the liquid phase. Only homogeneous conditions lend themselves well for direct measurement with differential pressure devices such as the venturi meter. Although cross-correlation techniques are not as dependent on calibration since they directly monitor the velocity belonging to a specific feature of the flow, usually the slug velocity, the accuracy also strongly depends on the validity of the model that connects this specific velocity to the bulk velocities. A further shortcoming in relation to three-phase flow measurements is the fact that in general no distinction can be made between the liquid phases, so that a homogeneous oil-water mixture should be pursued.

As far as is known, Nuclear Magnetic Resonance (NMR) and Pulsed Neutron Activation (PNA) are the only single sensing principle technologies that can directly measure the velocity of the individual components as well as their phase fractions without the need of pre-

conditioning the production stream. A decrease in the number of sensing principles used has the advantage that it reduces the number of sources of potential errors. Although the techniques are highly complex and expensive in comparison, they do offer an inline, full-bore, robust, non-intrusive total solution that is indifferent to the flow regime and allows more compact flowmeters. It is particularly beneficial that the bore of the sensor, unlike the venturi tube and orifice plate, is a straight section of the same diameter as the rest of the pipeline, as it remains possible to remove wax and other obstructions by pigging the system. This keeps the flowmeter functional and maintenance free. While PNA involves using a pulsed neutron source to activate one or more components within the mixture, NMR has the considerable advantage that it is not a nuclear technique. According to Falcone et al. [64], NMR and PNA are the only two methods that could eventually meet the strict requirements for fiscal metering. These prospects motivate important research efforts towards the development of an NMR multiphase flowmeter.

For a comprehensive review of the pros and cons of the different measurement principles, see the handbook about multiphase flowmetering by Falcone et al. [65]. Detailed technical comparisons of commercial and non-commercial multiphase flowmetering systems can be found in Thorn et al. [242, 243], Falcone et al. [64], and Hansen et al. [90]. Nevertheless, some multiphase flowmetering systems have since disappeared from the market due to the changing demands from the industry.

## 1.4 State-of-the-art in NMR flowmetering

Despite the wide variety of multiphase flowmeters available, discussed in section 1.3, there is a great demand for NMR flowmeters. Many disciplines are looking for methods that do not require mechanical or electrical contact with the flow and hence do not disturb the flow pattern. This non-invasive nature is especially important for medical diagnostics such as angiography, which measures the flow in blood vessels, but also for industrial applications where additionally obstructions cause large pressure drops. In addition, it allows measurements on explosive or abrasive substances without damaging the flowmeter. Furthermore, NMR does not generate measurement signals with harmful ionizing radiation, used by X-ray or $\gamma$-ray methods, which require special safety precautions. Moreover, NMR is, contrary to optical probes, not limited to transparent media. One limitation are ferromagnetic fluids, because their intrinsic magnetism can produce interfering NMR emission. The greatest strength of NMR lies, however, in its ability to distinguish between different states of matter and different chemical species independent of gas and solid entrainment. A property that provides the basis for the development of techniques for multiphase and multicomponent flow measurements.
Primitive NMR methods use only the bulk magnetization, making them the least demanding on computing resources. Well-logging exploits the bulk magnetization to analyze the composition of reservoir fluids inline in the near wellbore zone, see, e.g., Coates et al. [44] or Kenyon [129]. Likewise, several methods are developed that are restricted to the measurement of the average velocity.

**NMR flow imaging**

NMR imaging has the advantage that it maps the complete flow field within complex and even opaque systems with an adequate spatial resolution. Imaging techniques are of particular interest to the chemical engineering community, because they can be used to quantify transport mechanisms, such as dispersion, diffusion and flow, for dynamic processes. Especially in case of non-steady multiphase flows, characterized by relatively fast moving bounderies, imaging can improve the investigation of the different flowrates. Almost all NMR techniques recently developed for multiphase flow measurements are imaging techniques, see for instance, the review papers by Caprihan and Fukushima [39], Elkins and Alley [60], Fukushima [70], Gladden and Sederman [81, 82], Maneval et al. [165] and Pope and Yao [202]. Unfortunately, for velocity profile determination NMR imaging has a low time resolution as drawback.

In conventional imaging methods, many scans are needed to encode the complete two-dimensional space information. This results in long imaging times of several seconds per image, unsuited for multiphase flow measurements. Their dynamic system demands a high temporal resolution. Over the last years, fast imaging techniques have been developed that cover the entire k-space, all relevant data points of an image, in one scan, such as echo-planar imaging (EPI) [167], or in a fraction of the scans used traditionally [92]. The improved temporal resolution has initiated the development of ultrafast NMR imaging techniques, i.e. Kose [137, 138], that map the velocity field in a short time compared to the velocity fluctuations.
In case of large measurement domains, like large pipe diameters, it is desirable to use a high image resolution. Measurements by Markl et al. [169] and Elkins et al. [61] illustrate the negative effect this has on the time resolution. Even though they use an innovative fast imaging technique that measures at once all velocity triplets in a three-dimensional volume, the total measurement time is very long because of the large number of pixels adressed. Therefore, their 4D-MRV method is only suited for mean velocity determination in steady state or periodic flow.
Li et al. [157] and Galvosas and Callaghan [72] both take advantage of the cylindrical symmetry to succesfully measure rapidly flowing liquids with a Reynolds number up to 9,400 or velocities on the order of 1 m/s. They decrease the acquisition time substantially by mapping a projection of the velocity vector over a single line of 128 pixels. The restrictions imposed by this one-dimensional approach are nevertheless too tight for flowmetering purposes, because the average multiphase flow has no rotational symmetry.
In recent studies, Sederman et al. [224, 225] reduce the measurement time further by acquiring a series of two-dimensional images following a single r.f. excitation. Inbetween two pulse sequences the image repetition delay is still long to allow fluid washout within the imaging coil or rebuilding of the magnetization. However, the number of necessary recycle times is reduced to a minimum by taking as many images as possible within one pulse sequence. With a SEMI-RARE sequence [224] they collect images of a bubble train at 72 ms time intervals from which the liquid flowrate is obtained by tracing the trailing edge of the liquid slug. Fronttracking through the image intensity is therefore too slow for typical multiphase flow velocities in the petroleum industry. On the contrary GERVAIS [225], an EPI-based velocity phase encoding technique, opens up new perspectives. They can decrease the repetition time

between successive images of a single velocity component to 20 ms. Particularly because the velocity map is directly obtained from the NMR signal without requiring image analysis afterwards.
Despite the substantial improvement in the temporal resolution, the above-mentioned methods are still too slow for resolving the rapid multiphase flow fluctuations. The latest trend in phase encoded NMR velocimetry focuses therefore on strong reduction of the image acquisition time by means of advanced signal processing. Jung et al. [123] use parallel imaging that combines the signal of multiple receiver coils to construct a single image. Drawback of this technique is, however, the costs of the additional hardware. Holland et al. [104] have made a lot of progress with the implementation of compressed sensing. With this nonlinear image reconstruction method, they are able to recover the velocity image from only 30% of the data points that are traditionally thought necessary. Integration hereof in the ultrafast flowmapping sequences may ultimately lead to a feasible imaging flowmetering technology that is suitable for large flowrates.

**Ongoing Developments on NMR flowmeter systems**

Several patents have been issued that describe the use of NMR to analyze two- or multiphase flows. The current market is dominated by Southwest Research Industry [131–135] and a cooperation between Spinlock SRL, Shell Oil Company, and KROHNE AG [96–100, 170, 212–215, 246]. Applied scientific research aimed at product development of an NMR multiphase flowmeter for the oil and gas industry is ongoing at John's group at the University of Western Autralia [68, 186–188, 262] and Xiao's group at the China University of Petroleum-Beijing [54, 55, 158, 229]. Generally they combine independent measurements of the fraction with a velocity measurement technique to determine the flowrate. Since usually only the average flowrates are required, practically all actual NMR flow measurement methods determine only the properties of a bulk of fluid in the detection coil.
The least advanced flowmeter designs assume that all phases have the same uniform velocity. Regarding real time applications in oil production, special consideration should be given to the fact that gas tends to flow at higher speeds than the liquid components. To rectify the velocity difference, King et al. [134, 135] equip one of their flowmeter designs with an adequate mixer upstream of the NMR sensors. Almost all other patented devices assume a mean velocity for all liquid components, i.e. water and crude oil [16, 134, 214]. The gas flowrate measurements are performed separately, if required.
Flowmeters or water-cut meters, developed on behalf of oil production facilities, often combine an NMR with an Electron Spin Resonance (ESR) sensor to determine the flow-fractions [16, 133–135]. ESR is comparable with NMR, but senses unpaired electrons, which are present in most crude oils. Because water and gas do not produce ESR signals, the ESR signal amplitude is only proportional to the amount of oil in the cross-section of the pipe. Thus by using ESR to sense the oil in multiphase flow, a separate and direct measurement of the crude oil fraction can be obtained. Once also the gas fraction is known from the NMR measurement, the remainder of the fluid can be assumed to be water.
An alternative magnetic resonance technique used to determine a specific fraction with high accuracy suppresses the signal from the other fractions in which there is no interest. In order

to study the mixing efficiency of a Liquid Jet in Cross Flow device used for liquid sampling in custody transfer, Lakshmanan et al. [148] apply the CHESS imaging sequence to generate one- and two-dimensional profiles of the water-cut in an oil-water flow, provided the flow is not very turbulent, by suppressing the oil signal.
King et al. [134, 135] also suggest various integrated solutions of instruments for measuring the complete set of flow fraction, flow velocity and flowrate measurements for multiphase fluids containing gas, oil, water or a combination thereof. One design comprises a mixer-venturi pair for measuring the total velocity of the mixture and an NMR and ESR sensor for measuring the flow fractions. An alternative design comprises an ESR sensor, providing the fraction and velocity of the oil component, and a $\gamma$-ray densiometer from which output the other fractional constituents are calculated. Hogendoorn et al. [96, 97] have also patented two integrated systems that combine an NMR sensor with an ECT sensor in one case and with a venturi tube in the other with the aim of increasing the measurement accuracy in the flowrate of the gas phase.

In the following sections we present an overview of the state of the art in NMR flowmetering, classified by their velocity measurement principle.

### 1.4.1 Time-Of-Flight Method

The first commercial NMR flowmeters, brought on the market by the Badger Meter Manufacturing Company [76, 77, 252], are based on the Time-Of-Flight method developed by Morse and Singer [179, 233]. In this tagging technique, illustated in Figure 1.7(a), a fluid volume is first tagged by maximizing or resetting the magnetization in the direction of the detector's sensitive plane. Next the arrival of this tagged volume is registered through a signal change in the detection coil downstream of the tagging coil. The time-of-flight in which the tagged volume traverses between both coils is a measure for the average flow velocity. Later on, King et al. [133] have improved the accuracy of the arrival time determination and with that also of the flowmeter by shortening the length of the tagged and detected volumes with slice-selection. However, the plug flow assumption is a major drawback of this technique. Consequently these flowmeters are only suited for high flowrate measurements of single-phase flows or homogeneously mixed multiphase flows, i.e. without phase slip.
Several authors adjusted the Time-Of-Flight method to circumvent the no-slip constraint. Libove and Singer [159] propose an alternative Time-Of-Flight method, which determines the streamwise velocity distribution with a spin-echo sequence. The two pulses, which create the echo, are applied at different positions along the production line. With each successive repetition, the gap width between the pulsed sections is gradually increased. As a result, the signal only originates from the fluid fraction that bridges the gap within the delay time between the pulses. The signal intensity is then a measure for the flowrate. Instead of a uniform tag, Jeong et al. [120] use a tagged grid through the cross-section of the pipe. In a series of images they study the grid deformation from which a qualitative map of the average flow velocity is obtained. However, both methods are inconvenient for flowmetering systems. Because of the substantial amount of repetitions, they are time-consuming and above all require steady-state or periodic flows.

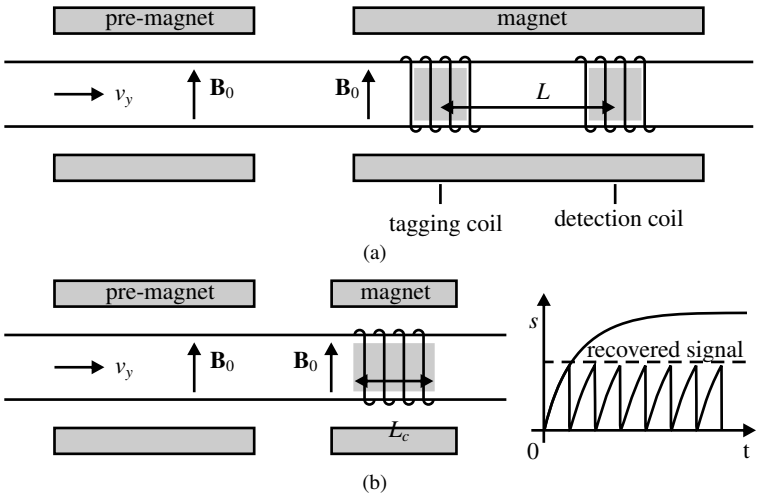


**Figure 1.7**: Two types of the Time-Of-Flight method exist, which are especially suitable for the determination of average flowrates. (a) In the tagging technique, tagging and detection occurs in separate coils at mutual distance $L$. (b) In the suppression technique the flowrate is calculated from renewed buildup of the magnetization or from the fresh spins that move inbetween two pulses into the coil.

Figure 1.7(b) illustrates another group of Time-Of-Flight methods that is able to determine the flowrate with a single coil, which is favorable for instrumentation costs. Their working principle is based on subsequent destruction of the magnetization with 90° pulses, whereafter the recovery of the magnetization by renewed buildup [153] and inflow of fresh spins in the coil [134] is monitored. The initial amplitude of this signal relative to that of the sensor full with fresh fluid indicates the flowrate.

Using this principle, Lew and Schlatter [154, 155] provide a flowmeter that measures the flowrate only of the organic portion in a flow of mixtures made of aqueous, organic and gaseous components. Specifically this is the flowrate of the phase with the smallest longitudinal relaxation time. The pulse interval is chosen so short that only the magnetization of the organic component recovers. Gas and water will no longer contribute to the NMR signal. Because of this manner in which the phase of interest is distinguished, the Time-Of-Flight method is known as Suppression Technique. Also Martin et al. [170] differentiate various two-phase fluids by their longitudinal relaxation times, except the comparable pulse trains are applied on two instead of one coil. Why these methods are developed to be used within the petroleum industry is unclear, since they are suitable only for slow-flowing media. The ability to discriminate flowing from static fluid meets on the other hand an important need in medical diagnostics.

Higher flowrates are no problem for the flowmeter introduced by King et al. [134], as it is based on influx instead of renewed buildup of magnetization. Depending on which of the

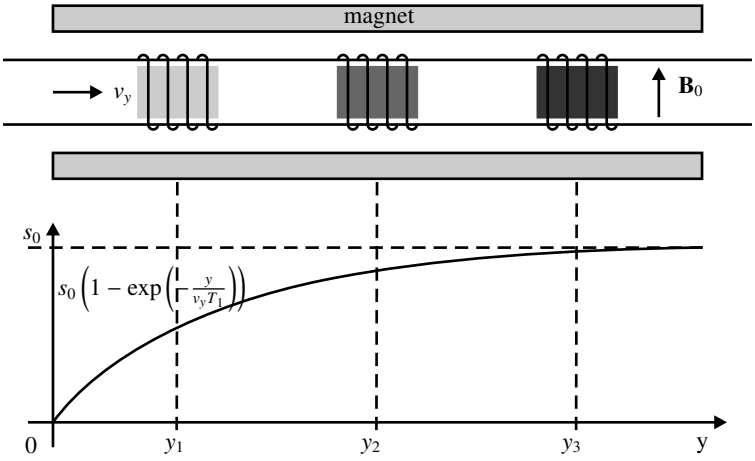


**Figure 1.8**: The Rapid Passage Method studies the exponential gain of magnetization that a volume of fresh spins experiences when it starts to move in an external magnetic field $\mathbf{B_0}$.

proposed techniques are uses, the total or individual flowrates of hydrocarbon fluids can be measured.

### 1.4.2 Rapid Passage Method

The Rapid Passage Method primarily uses the longitudinal relaxation principle in NMR to distinguish between the different components in a multiphase flow. Moreover, the method is applied for flow velocity determination.
Outside the presence of an external magnetic field the macroscopic magnetization of a fluid element is zero. When the element moves into the magnetic field of the flowmeter, the nuclei align themselves along the field direction resulting in a net magnetization of the material. The process describing at which rate the nuclei reach equilibrium magnetization, $s_0$, is called longitudinal relaxation. The flowrate determines, through the residence time in the magnetic field, the developed magnetization at the time of detection in an r.f. probe as sketched in Figure 1.8. Vice versa, the intensity of the NMR signal can be used to determine the average velocity of a single-phase fluid, provided the longitudinal relaxation time is known beforehand [163]. In this thesis we develop this technique further, enabling average liquid flowrate measurements in a two-phase gas-liquid flow.

The standard technique regarding discrimination of multiphase flow fractions is the comparison of the signal strength with the corresponding reference value for a full pipe. Except at high pressures, the proton density of gas is low compared to that of the liquid. This makes direct measurement of the gas fraction difficult. Typically, the liquid fraction is measured and the remainder assumed to be gas. Furthermore, it is customary to assume that any fluid phase possesses the same flow velocity, while only the gas phase flows at a higher velocity

[16, 134, 135].
To avoid problems associated with relaxation time effects in interpreting results from flowing fluids, Lynch and Segel [163] only operate in the thermal equilibrium range to determine the void fraction. King et al. [131, 134, 135] also prefer this approach, which is independent of the flow velocity. Alternatively, if the velocity is known from either the NMR sensor or from some other source, their flowmeter designs compensate the non-equilibrium NMR signal for the effect of velocity changes on its amplitude. Bayer [15, 16] even makes specific use of the incomplete polarization by distinguishing the different multiphase components based on their longitudinal relaxation process. With an array of NMR sensors, one per detectable component, the flowmeter reconstructs the individual fractions and flowrates from the multi-exponential gain of magnetization along the pipeline.
A new type of NMR multiphase flowmeter that uses the Earth's magnetic field for detection is being developed at the University of Western Australia [68]. The flowmeter consists of a mobile pre-polarization magnet, whose distance from the downstream detection coil can be manipulated to provide the desired $T_1$ contrast. With its comparatively low weight and smaller dimensions, this low-field design offers a lower cost system with improved portability. Recently, O'Neill et al. have demonstrated an improvement of the measuring principle, which is now able to determine the velocity distribution of the liquid phase from a model fit of the entire course of a free induction decay signal in single-phase flow [186] and air-water stratified and slug flow [187]. Due to the rapid decay between polarization and detection, the technique is unfortunately not particulary suitable for viscous liquids such as oil with a short longitudinal relaxation time. With an adjustment to the pulse sequence and data analysis, the method is extended to investigate the flowrates of two-phase oil-water mixtures [188]. An important improvement is the longitudinal relaxation time distribution which can now be measured under flow conditions together with the velocity distribution. The method is incapable of handling water-in-oil emulsions, but shows good performance for stratified flow regimes with mixing, dispersion of oil-in-water and water, and oil-in-water emulsions. To be applicable to dynamic flow conditions, the new pulse sequence's measuring time of 20 – 60 minutes will have to be strongly reduced.

There is one major drawback associated with the Rapid Passage Method. The accuracy of the method is directly dependent on the longitudinal relaxation times of the individual components. Implying that the composition of the multiphase flow must be known at all times.

### 1.4.3 Efflux Method

Under flow conditions spins, originally excited by a 90° pulse, will leave the r.f. coil with the flow velocity. The efflux method utilizes the time in which the induced signal of these tagged spins diminishes, the efflux time, to determine the flow velocity. In other words, the average fluid velocity is related to the passage time of fluid molecules in a single coil. In case of high flowrates there is no need to correct the signal evaluation for transverse relaxation, since the efflux time is much smaller than the transverse relaxation time. As shown in Figure 1.9(a), there exists a linear relation between the intensity of the NMR signal and the elapsed time. The quotient between the slope and origin ordinate is directly proportional to the mean

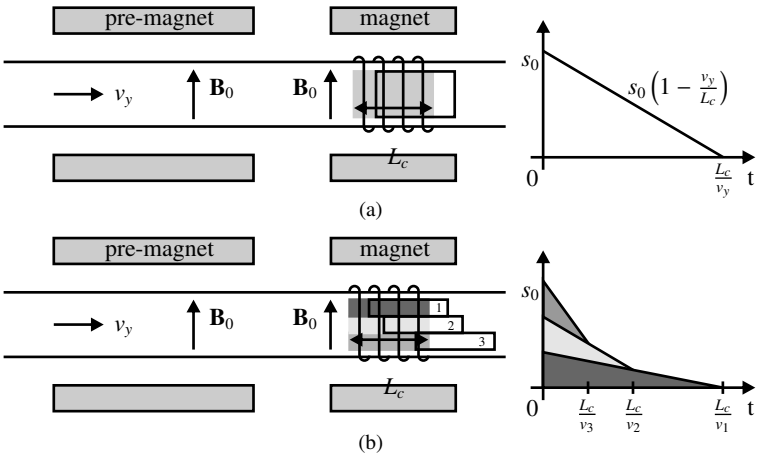


**Figure 1.9**: In the efflux method, the mean flow velocity is derived from the decaying signal intensity resulting from spins moving out of the selected slice in the r.f. coil with effective length $L_c$. (a) Regarding plug flow, the slope is a direct measure of the flow velocity. (b) In the case of a distribution of velocities, the efflux curve is analyzed in terms of a set of iso-velocity curves.

velocity of the fluid, the proportionality constant being equal to the reciprocal of the effective length of the r.f. coil.

In the predecessor of the current efflux flowmeters, Bergmann and Knüttel [20] made use of simple free induction decay signals. However, their decay is so fast that the range of flowrates in which relaxation effects can be ignored is very limited. Since the effective transverse relaxation time can be several orders smaller than the actual one, Krüger et al. [143, 144] improved the efflux method succesfully by applying Carr-Purcell-Meiboom-Gill (CPMG) pulse sequences instead. This has the additional advantage over the Time-Of-Flight influx method that magnetization of fresh spins entering the r.f. coil during the pulse sequence will not contribute to the NMR signal, thereby biasing the measurements.

In a real flow there are different local velocities over the cross-section of the pipe. When the efflux curve is analyzed in terms of a set of iso-velocity curves, see Figure 1.9(b), their respective amplitudes form the velocity probability density function. Due to the low pressure in typical hydrocarbon production lines, only the liquid phases, i.e. oil and water, are observable with NMR. If the velocity probability density function shows distinct maxima at certain different velocities, Bergmann and Knüttel [20] calculate the average velocities of the different fluids with their corresponding amplitudes from these distinct parts of the distribution. For the sake of convenience the different liquid phases are otherwise supposed to have the same mean velocity. Starting from this idea, Krüger [142] suggests NMR-spectroscopy to determine the liquid phase fractions through the chemical shift. However, in the case of

large-scale flowmeters, it is in practice almost impossible to meet the homogeneity of the permanent magnetic field required. Pusiol [214] developed therefore a feasible technique using variable pre-polarization stages to obtain the mean velocity and proportions of oil and water in a heterogeneous three-phase blend. Osán et al. [191] published preliminary experimental results of this method under single-phase turbulent flow conditions. KROHNE [24, 101–103] has further improved this concept for simultaneous three-phase flow measurements in cooperation with Shell and launched the first industrialized version of this magnetic resonance multiphase flowmeter in 2015 under the brand name M-PHASE 5000. This commercial NMR multiphase flowmeter operates at a $^1$H resonance frequency of 8.5 MHz using Halbach magnets with an operational window for the liquid velocity of 0.5 – 3 m s$^{-1}$. The magnet system consists of two different sections for polarization and detection. The liquid bulk velocities are obtained from the effective signal decay of the measured CPMG spin-echo train. To determine the phase fractions, the pre-polarization length can be varied by selectively rotating the inner ring 180 degrees relative to the outer ring in 1 or 2 of the 3 identical pre-magnetization, two-ring Halbach magnets. Detecting at a fixed position from the entrance of the flowmeter prevents the measurements from being biased by level effects. Gradient coils are also integrated into the probe head, which allow the application of a permanent vertical gradient to produce a one-dimensional velocity profile using frequency encoding, enabling the measurement of velocity slip between the flowing liquid phases. This image capability is further exploited to determine the gas phase and gas velocity. The flowmeter has been successfully tested in commercial flow loops [101, 102] and field tests [103] for a large dynamic range of flow conditions. The latest improvement of the flowmeter concerns the implementation of a broadband excitation constant-gradient low flip angle CPMG-sequence, which allows the use of a stronger field gradient for an improved spatial resolution [245].

The NMR multiphase flowmeter currently developed by the China University of Petroleum-Beijing is closely related to Krohne's M-PHASE 5000. This flowmeter, which evolved from their well-logging fluid analyzer, also uses a CPMG-based efflux method in an arrangement of Halbach magnets for high flow velocity measurements. However, the field strength in the polarization zone is slightly higher here than in the detection zone in order to achieve rapid polarization and a dual antenna structure is used [229]. For the determination of the relaxation times, the flowmeter can rely on their experience with the fluid analysis in well logging [158]. The disadvantage of the flowmetering principle is that it is based on two measurement modes: the flow is interrupted on a regular basis to determine the phase fractions under static conditions, after which the flowrates are measured in flowing state [54, 55]. This implies that the flow is considered to be very stable in composition, which is not very realistic. Also, continuously halting the flow is highly undesirable for the continuous monitoring of oil and gas production.

### 1.4.4 Phase Encoding of Velocity

Phase encoding is based on manipulation of the spin precession such that the effect of flow on the NMR signal is simply a coherent shifting in phase. Most common are Pulsed Gradient Spin Echo (PGSE) like methods, which study the phase shift in the transverse plane as illus-

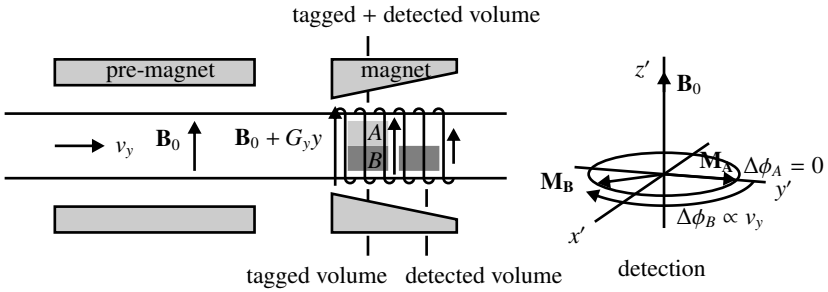


**Figure 1.10**: PGSE-like phase encoding techniques are gradient methods that manipulate the phase of the magnetization to provide the flowrate. The coherent phase shift $\Delta\phi$, which can be measured with quadrature detection, is directly proportional to the streamwise velocity.

trated in Figure 1.10. The application of a field gradient in the streamwise direction, whether pulsed or permanent, gives rise to a velocity related change in the precession frequency of the spins. Special pulse sequences of regular and refocussing r.f. pulses translate this rate of change into a phase shift of the NMR signal, proportional to the streamwise velocity. These gradient methods, among which the rheometer by Maneval et al. [166] or the two-phase air-water flowmetering procedure by Leblond et al. [150], are best known for their directional sensitivity and independence on the $T_1$ and $T_2$ relaxation times. For an elaborate description of the PGSE method is referred to section 3.2.

Less accepted is the single-phase flowmetering method invented by Wollin [260], which actually combines the Time-Of-Flight method with phase encoding. Contrary to the phase encoding method mentioned above, no gradients are required for the flow measurement itself. As depicted in Figure 1.11, a continuous r.f. field nutates the developed magnetization into the lateral plane. The nutation angle is proportional to the dwell time of the spins within this field. It can be detected through the voltage the magnetization component parallel to the $\mathbf{B_0}$-field induces into the birdcage receiver coil, whose area vector points in the same direction. Adjusting the strength of the $\mathbf{B_1}$-field to obtain a specified signal magnetization yields the mean streamwise velocity of the flow. If the device is provided with phase modulating coils that vary the $\mathbf{B_0}$-field periodically, the technique can also be used in order to map non-uniform velocity profiles. This technology is able to extract the magnetization signals corresponding to all slices from a single NMR signal, acquired in presence of this time-varying gradient, which is an important advantage for real time flow measurements. On the other hand, the flow measuring principle is very sensitive to set-up parameters as $\mathbf{B_1}$-field strength and coil lengths. The method is in principle independent of the relaxation times, but the spins must retain significant coherence during their transit through the volume defined by the receiver coil. Although not using r.f. pulses and pulsed gradients saves huge costs on amplifier and control circuits, the PGSE like phase encoding methods have a better performance.

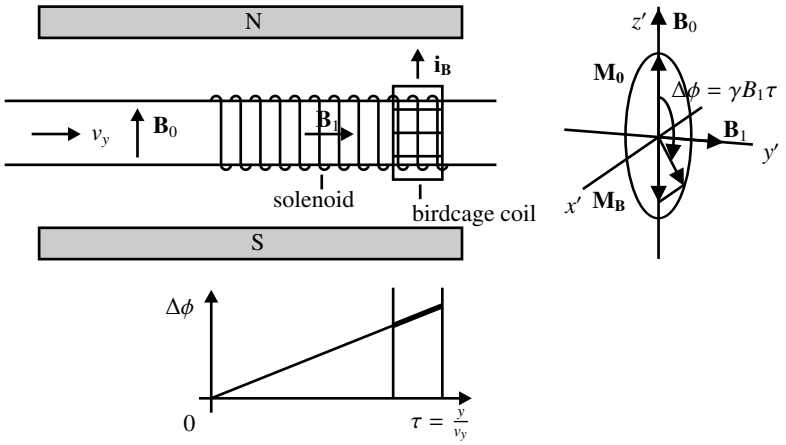


**Figure 1.11**: The flow measuring method after Wollin [260] is based on the residence time $\tau$ of the spins in a continuous $\mathbf{B_1}$-field. The amplitude of the NMR signal, received by the birdcage coil at the end of the solenoid, decreases with the cosinus of nutation angle $\Delta\phi$.

### 1.4.5 Frequency Encoding of Velocity

Frequency Encoding of Velocity after King and Riewerts [132] is another gradient technique. It utilizes the frequency shift of the NMR signal that goes together with the movement of a tagged fluid segment in the direction of a fixed linear magnetic field gradient compared to that of the signal occuring if the magnetic field had a constant intensity throughout the flow space. As illustrated in Figure 1.12, the frequency of the magnetic resonance signal emitted by the nuclei changes proportional to the magnetic field intensity. The time rate of change of the emitted NMR frequency signal is therefore a linear function of the flow velocity. This technique provides a measure of the flow velocity by means of a selective Hahn spin-echo sequence, thereby acquiring a frequency dependent signal in the same coil in which the fluid segment is tagged before. The frequency shift is obtained by contrasting the frequency of the NMR signal with that of a no-flow reference signal.
Equivalent to the efflux method, the technique measures a distribution of velocities in case the velocity is not uniform across the pipe. The amount of material flowing at each velocity is represented by the amplitudes of the detected frequency spectrum. If the multiphase flow spectrum shows distinct maxima, the separation between the spectral components permits the signal of the faster flowing gas to be separated from the signal of the slower flowing liquid. The average gas and liquid velocity is thereupon calculated from the signal amplitudes of the corresponding parts of the spectrum. For gradient field measurements, stratified or annular flow are preferable and the flowmeter may contain means for enhancing these types of flow [134].

Drawback of gradient methods are the costs of the field gradient amplifiers and control units. This is, however, compensated by many advantages. Frequency encoding is not only inde-

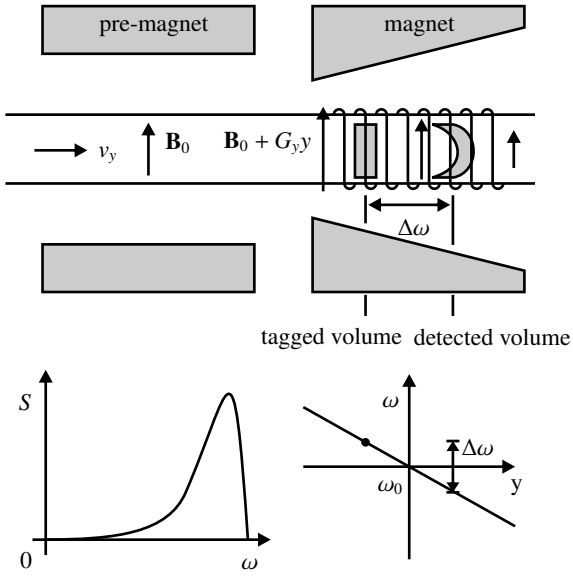


**Figure 1.12**: Frequency encoding introduces a tagged fluid segment to a relatively high linear fixed field gradient $G_y$. Based on the travelled distance, the NMR signal experiences a frequency shift $\Delta\omega$, which is proportional to the flow velocity. The frequency spectrum $S(\Delta\omega)$ is indicative for the velocitity distribution in the pipe.

pendent of the characteristic $T_1$ and $T_2$ relaxation times, but also of the fill factor and density of the fluids. The only requirement is that the volume of the material is sufficient given the signal requirement to overcome noise, which is supported by a deliberate choice of the gradient strength. On the one hand a high gradient field involves a high frequency resolution, but enhances the divergence of the NMR signal on the other hand.

## 1.5 Objective

The aim of the research presented in this thesis is the development of measurement concepts for an inline, full-bore, nuclear magnetic resonance based multiphase flowmeter intended for the petroleum industry in order to replace offshore separators. As is common, the flowrates will be derived indirectly from the product between the phase fractions and their average velocities, which are each determined separately. Three factors that make multiphase flowmetering so difficult are the existence of flow patterns, their required development length to stabilize after a disturbane and the presence of phase slip.

NMR is insensitive to the orientation of the fluids within the pipe and therefore does not impose any restrictions on the orientation used when installing the flowmeter. The developed flowmetering principles, however, use a flow regime dependent model to reconstruct the flowrates from the NMR signal. An essential part of the research is to understand and evaluate how the non-uniformities in both space and time affect the reconstruction. For this purpose it is beneficial that there are no strong transients present in the flow. This can be achieved with a sufficiently long straight pipe section upstream of the flowmeter. From a practical point of view, the research in this work is therefore limited to horizontal flow.

One of the main difficulties encountered in multiphase flowmetering is phase slip, the velocity difference that exists between the different phases. The lighter gas tends to flow at higher velocities than the liquid components. Because the heavier water and oil have a much smaller density difference, their phase slip will be correspondingly small in flow patterns in which the liquids are not homogeneously mixed. Many manufacturers therefore assume that oil and water have the same velocity. In this study we build on this approach. We limit the flowmeter design at this stage to a method for determining the average liquid flowrate of horizontal two-phase gas-liquid flows. This also allows us to circumvent for the moment the extra level of complexity that the liquid-liquid mixing patterns of the three-phase oil-water-gas flows add to the already complex nature of two-phase gas-liquid flows. In future, we want to distinguish the oil and water fractions based on their $T_1$ relaxation times by placing several NMR probes across the pipeline. The functional model of the flowmeter is verified with experiments in an air-water flowloop under typical multiphase flow conditions. This is achieved by evaluating the signal-processing for steady-state, pseudo steady-state and quasi-static, fully-developed intermittent multiphase flow regimes. The focus will first be on understanding the effect of a non-uniform streamwise velocity profile in stratified flow. Here, we will also consider the implications of regular, small-amplitude two-dimensional interfacial waves. Next, for elongated bubble and slug flow regimes, we will study how the phase-pattern and in particular phase

slip in the medium, associated with the presence of the slugs, will affect the reconstruction of the liquid flowrate. After all, slug flow is the most encountered flow regime in oil field operations [5, 48].

To which extent the flow field has to be resolved with an improved spatial resolution by NMR imaging remains questionable. Although this might improve the flowmeter accuracy, the additional information makes the postprocessing complex and slow, while it is superfluous for the average flowrate determination. The NMR flowmetering methods described in this thesis determine, therefore, only the properties of the bulk of the fluid in the detection coil. That is to say, without spatial resolution.
Regarding the determination of the liquid velocity, two measurement methods with fundamentally different working principles are investigated. The developed rapid passage technique 'T1RRT' uses the plain signal intensity, while the implemented gradient technique 'PGSE' derives the liquid velocity directly from the phase of the detected NMR signal. In order to determine the liquid holdup from the signal intensity, both proposed flowmetering concepts employ, analogous to the rapid passage technique, a model based on the relationship between the built-up longitudinal magnetization and the residence time in the polarizing magnetic field of the flowmeter as is standard practice when the signal intensity has not reached the thermal equilibrium state.

The strength and weaknesses of each method and the applicability and limitations of the methodology are discussed. Particular attention will be paid to the instrument's rangeability in relation to the fluid specific longitudinal relaxation time. In this context, tests are performed on static samples to analyze how well the composition of oil-water mixtures can be characterized.

Currently there is no international standard for the level of accuracy that multiphase flowmeters must meet. Depending on the area of application, the accuracy requirements generally used as a guide are: a relative error in the total liquid flowrate of 5 – 10% for reservoir management and well testing, 2 – 5% for production allocation and 0.25 – 1% for fiscal metering; a relative error in the gas flowrate of less than 5% and an absolute error in the water-cut measurements of less than 2% [64, 234, 242, 243]. In order to assess the performance of the developed flowmeter concepts, the following sources of errors and uncertainties are investigated:

1. Due to the no-slip condition at the wall and the presence of phase slip in the case of multiphase flow, the fluid flowing in the pipe will not have a uniform velocity profile. It is important to investigate under which circumstances the plug flow model used by the flowmeter is valid and when it needs to be adjusted.

2. The unsteady nature of multiphase flow is another challenging aspect of multiphase flowmetering. Since the key flow parameters such as the gas volume fraction and the local flow velocities can fluctuate very fast, it is essential that the measurement frequency is high enough to capture their time scales. Moreover, the flow structures

associated with the different flow regimes require different procedures to determine the average flowrate from the raw data.

3. A large part of the measurement uncertainty is inherent with the multiphase flowmeter technology. Because the velocity serves as an input for the model used to determine the fluid fractions, it is necessary to identify to what extent its uncertainty propagates in that of the liquid holdup. Other relevant factors are related to the choice to keep the size of the designed flowmeter as small as possible. Oil companies prefer a flowmeter with a small footprint as offshore space is expensive. A compact device is an industry priority. Great importance is attached to a limited length and weight of commercialized multiphase flowmeters. However, the decision to make the bore of the flowmeter just slightly larger than the pipe's outer diameter is at the expense of the homogeneity of both the pulsed r.f. field and the gradient fields. It also leads to an increase in eddy currents, which in turn disturb the time characteristics of the gradient fields. It is therefore necessary to investigate the impact of this compromise on the 90 and 180 degrees pulse lengths and the PGSE measurement method in general. The permanent magnetic field that is already present over a considerable distance before the actual start of the flowmeter is a final technical aspect which should be looked at.

The following issues fall outside the scope of this project:

1. In this study, we have only looked at the effect of regular interfacial waves on the NMR flow measurements. However, unstable waves can be of particular importance for the large-amplitude or pebbly stratified flow and annular flow regimes. It is also important to investigate the impact of these waves on the uncertainty determination of the time-averaged flowrate by considering the ratio between the dominant wavelength and the coil length.

2. In practice, multiphase flow patterns are not steady-state, but continuously evolve depending on the process conditions and fluid properties. The final flowmeter design should be able to recognize the flow regime by the raw data characteristics in order to determine the flowrate for transient flows with sufficient accuracy. Related to this, the performance of the measurement principles should be examined in the case of abrupt regime changes, such as the intermittent appearance of slugs in the transition from stratified to slug flow.

3. The NMR flowmeter must be regularly calibrated to determine in particular the longitudinal relaxation time of the flow components. The standard pulse sequences are performed under static conditions, so it must be considered how this procedure can be embedded in real time applications in the oil production with, for-example, a bypass. One can also investigate whether the NMR measurement methods for well-logging of flowing samples as e.g. developed by Masak et al. [171] can be adjusted for higher flowrates. The question remains how much the reservoir fluid properties change over time, especially when the production streams of individual wells or production facilities are commingled. In any event, the flowmeter must be supplied with pressure and

temperature sensors, ensuring that the required NMR parameters can be continuously adapted to the circumstances with the help of a PVT model.

4. Internally, all kinds of deposits such as scale, asphaltenes and wax can build up in the flowmeter, which will create erroneous measurements [5]. The full-bore design of the flowmeter has the advantage that it enables common flow assurance practices to remove the blockages.

## 1.6 Outline

This thesis is structured as follows.
Chapter 2 gives a general introduction to nuclear magnetic resonance, the basic pulse sequences and a detailed description of the NMR multiphase flowmeter system.
In chapter 3 the working principle of the two different NMR methods used to determine the liquid flowrate in a gas-liquid two-phase flow will be presented.
The flow configurations and instrumentation to validate the NMR measurements are considered in chapter 4.
In chapter 5 the results of preliminary tests on static dummies with different oil-water compositions are discussed in order to investigate how accurately the key NMR parameters, such as the pulse lengths and relaxation times, required for the measurement concepts presented in chapter 3 can be determined.
In chapter 6, the accuracy and performance of the T1RRT and the PGSE method are compared for experiments on single-phase laminar and turbulent flow with the aim of studying the factors that influence the first step in which the average streamwise velocity is determined. In addition, the significance that can be attributed to the non-polarizing magnetic field in the entry area of the flowmeter has been examined and a proposal is made to compensate for its effect in the postprocessing.
Chapter 7 provides the results of the T1RRT method applied to co-current stratified gas-liquid flow. Since the shape of the velocity profile changes substantially with the type of waves present on the interface, the extent to which the method is able to determine the liquid flowrate through the use of the plug flow model has been studied. Also discussed are the inaccuracies caused by the measurement conditions and how the probe design has been improved with a strip-shield, which tackles the adverse effect that lossy samples have on the probe efficiency.
The T1RRT method, which was limited to space independent flow profiles, is adapted to the slug flow pattern in chapter 8 with a central role for the unit-cell concept. The implementation of a k-means clustering algorithm makes it possible to determine the average velocity and liquid holdup for the film and slug sections and then combine them into an average flowrate. Furthermore, the technical limitations and possibilities of the adjusted flowmeter principle are evaluated.
Finally, chapter 9 summarizes the main conclusions of the thesis and provides suggestions for future work.

# Chapter 2

# Nuclear Magnetic Resonance

Nuclear Magnetic Resonance, NMR, is a non-invasive measurement technique with as greatest strength the ability to distinguish between different states of matter and different chemical species. Dependent on the equipment and the measurement method, a wide range of length- and time-scales can be measured. NMR spectroscopy studies the chemical and physical environment of molecular structures and their dynamics at the ångström-scale. On the other hand, NMR is used to investigate macroscopic phenomena like the structure of materials or body tissue or to quantify transport mechanisms such as diffusion, dispersion and flow for dynamic processes. The measurement techniques for these applications can be divided into two categories: (i) imaging, in which spatially resolved maps of the spin densities in objects are obtained with a resolution of $10^{-5}$ to $10^{-2}$ m and (ii) methods that determine only the properties of a bulk of material without spatial resolution.

For velocity profile determination, NMR imaging has as drawback a low time-resolution. NMR flow imaging experiments are able to probe velocities in the range of $10^{-6}$ to 1 m $s^{-1}$ [80]. This is on the low side for the applications of this kind of flowmeter, which is aimed at the oil production industry. Besides, imaging techniques require complex algorithms to derive the average flowrate from the snap-shots. Since usually only the average flowrates are required, the theory in this thesis is limited to the last mentioned type of NMR methods: the ones that determine the properties of a bulk of fluid in the detection coil.

This chapter briefly summarizes the basic principles of NMR. For a more comprehensive treatment of the fundamentals of NMR, the reader is referred to the standard textbooks by Callaghan [37], Farrar and Becker [66], Levitt [152] and Hore [106].

## 2.1 Basic Principles of NMR

When an atomic nucleus has spin angular momentum as well as nuclear magnetic moment, NMR can be used to ‘spy’ on the internal structure of an object without disturbing it. To this

end, NMR uses the resonant absorption of radio frequency, r.f., radiation by nuclei exposed to a magnetic field.

### 2.1.1 The Origin of Magnetic Resonance

One of the fundamental postulates of quantum mechanics states that the total angular momentum of an isolated particle is said to be quantized. The elementary particles carry an intrinsic angular momentum, known as spin, which appears as element of a set of stable states with discrete magnitudes

$$S_{tot} = \sqrt{I(I+1)}\hbar, \tag{2.1}$$

where the nuclear spin quantum number $I$ takes values $I = 0, \frac{1}{2}, 1, \frac{3}{2}, 2...$ and $\hbar$ is the Planck's constant divided by $2\pi$.

Because of the Heisenberg uncertainty principle, no two components of an angular momentum can be known simultaneously with complete precision. Only the component of the angular momentum in the z-direction is known precise and is given by

$$S_z = m_I\hbar. \tag{2.2}$$

The values of the x- and y-components of the angular momentum are indefinite, but they are on average equal to zero [59]. The azimuthal spin quantum $m_I$ may have one of the following values

$$m_I = I, I-1, ..., -I. \tag{2.3}$$

Spin angular momentum and magnetic moment, $\boldsymbol{\mu}$, are directly proportional to each other

$$\boldsymbol{\mu} = \gamma\mathbf{S} \tag{2.4}$$

with a proportionality constant $\gamma$, known as gyromagnetic ratio. When $\gamma$ is positive, the magnetic moment is parallel to the spin and when $\gamma$ is negative they are antiparallel. Hence the magnetic moment of the nucleus may lie in $2I + 1$ different orientations relative to the z-axis with an angle determined by $m_I$. The properties of some relevant elements are given in table 2.1.

If a strong magnetic field $\mathbf{B}$ is applied, the quantization axis z is no longer arbitrary, but coincides with the field direction. The magnetic moment of a nucleus will start to interact and the $2I + 1$ orientations of the spin get different magnetic energies

$$E_{m_I} = -\boldsymbol{\mu}\cdot\mathbf{B} = -\gamma m_I\hbar B_z. \tag{2.5}$$

that are equally spaced with an energy gap $\gamma\hbar B_z$. According to the NMR selection rule, transitions of nuclei are only allowed between adjacent energy levels: $\Delta m_I = \pm 1$. This gives for the resonance condition

$$\Delta E = \gamma\hbar B_z = h\nu_L, \tag{2.6}$$

**Table 2.1**: Nuclear spin quantum numbers, gyromagnetic ratios and natural abundances of some commonly occuring isotopes in water, air, oil, natural gas and oil field brines after Hore [106] and Kaye and Laby [126].

| nuclide | $I$ | $\frac{\gamma}{2\pi}$ [MHz T$^{-1}$] | natural abundance [%] |
|---|---|---|---|
| $^{1}$H | $\frac{1}{2}$ | 42.57 | 99.985 |
| $^{2}$H | 1 | 6.54 | 0.015 |
| $^{12}$C | 0 | - | 98.892 |
| $^{13}$C | $\frac{1}{2}$ | 10.71 | 1.108 |
| $^{14}$N | 1 | 3.07 | 99.63 |
| $^{15}$N | $\frac{1}{2}$ | -4.31 | 0.37 |
| $^{16}$O | 0 | - | 99.963 |
| $^{17}$O | $\frac{5}{2}$ | -5.78 | 0.037 |
| $^{23}$Na | $\frac{3}{2}$ | 11.26 | 100 |
| $^{24}$Mg | 0 | - | 78.8 |
| $^{25}$Mg | $\frac{5}{2}$ | -2.61 | 10.13 |
| $^{32}$S | 0 | - | 95.0 |
| $^{33}$S | $\frac{3}{2}$ | 3.27 | 0.76 |
| $^{35}$Cl | $\frac{3}{2}$ | 4.17 | 75.53 |
| $^{37}$Cl | $\frac{3}{2}$ | 3.47 | 24.47 |
| $^{39}$K | $\frac{3}{2}$ | 1.99 | 93.10 |
| $^{41}$K | $\frac{3}{2}$ | -1.09 | 6.88 |
| $^{40}$Ca | 0 | - | 96.9 |
| $^{43}$Ca | $\frac{7}{2}$ | -2.87 | 0.15 |
| $^{79}$Br | $\frac{3}{2}$ | 10.67 | 50.54 |
| $^{81}$Br | $\frac{3}{2}$ | 11.50 | 49.46 |

where $\nu_L$ is the resonance frequency of the electromagnetic radiation. Every allowed transition requires the same amount of energy. When the spins are exposed to electromagnetic radiation at the resonance frequency, they are forced to flip from a lower energy state to a higher energy state. This manipulation of the direction of the magnetic moment forms the basic principle of NMR.

In absence of a magnetic field, all magnetic moments are degenerate: they all have the same energy. A collection of magnetic spins is equally distributed among their $2I + 1$ possible levels and their magnetic moments are lying at random angles on the cones around the z-axis. The magnetization of the sample, its net magnetic moment per unit volume, is zero.

In case of hydrogen, a spin-$\frac{1}{2}$ particle, the nucleus has just two permitted orientations with corresponding energy levels (see Figure 2.1(a)):

$$E_{-\frac{1}{2}} = \frac{1}{2}\gamma\hbar B_z \tag{2.7a}$$

$$E_{\frac{1}{2}} = -\frac{1}{2}\gamma\hbar B_z. \tag{2.7b}$$

Since the gyromagnetic ratio of $^1$H is positive, it is energetically beneficient for a nuclear spin to point in the same direction as the magnetic field. To this end, a sample will contain slightly more nuclei with a magnetic moment parallel to the magnetic field, $N_+$, than with a magnetic moment antiparallel to the magnetic field, $N_-$. The ratio of the population over the two energy levels is according to the Boltzmann distribution

$$\frac{N_+}{N_-} = e^{-\Delta E/kT}, \tag{2.8}$$

where $k$ is the Boltzmann constant and $T$ the temperature. This means that the magnetic field has induced a net magnetization $M_0$ in the z-direction, which is a measure for the maximum value of the probed NMR signal. Under ordinary circumstances the magnetic energy, $\Delta E$, is much smaller than the thermal energy, $kT$. After expanding the exponentials it is obtained that the magnetization

$$M_0 = \mu_z \frac{N_+ - N_-}{N_+ + N_-} \approx \mu_z \frac{\gamma\hbar B_z}{2kT}. \tag{2.9}$$

in thermal equilibrium with a magnetic field $B_z$ is proportional to the strength of the latter. However, NMR signals are rather weak. Nuclear magnetic moments are about 2000 times weaker than the electron spin magnetic moment [9]. Consequently strong magnetic fields have to be used to optimize the signals. Figure 2.1(b) illustrates how a net magnetic moment is induced by a magnetic field in the z-direction.

Some common nuclei, notably $^{12}$C and $^{16}$O, have no angular momentum ($I = 0$), no magnetic moment and consequently no NMR signal. The developed flowmeter is, in view of its application in the oil-industry, based on hydrogen that is NMR-active and ample available in oil, water as well as in natural gas. Besides, the gyromagnetic ratio of hygrogen is one of the highest, which turns out favorably for the signal strength.

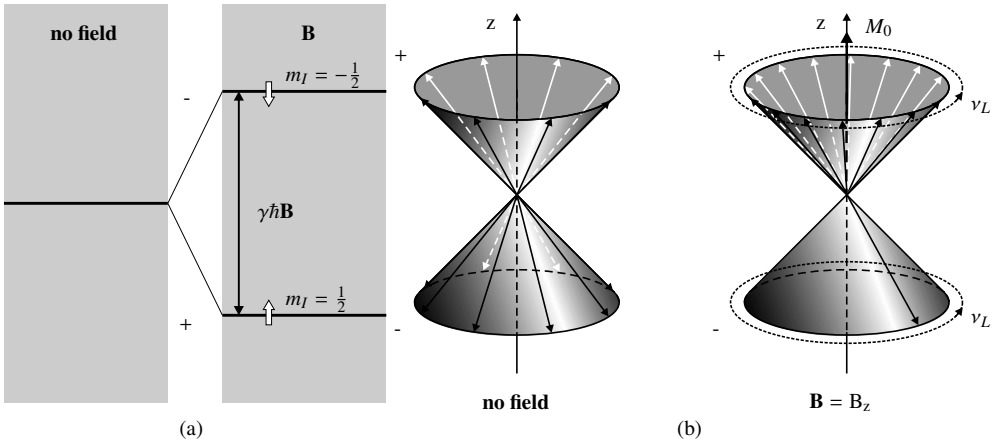


**Figure 2.1**: (a) Energy levels for hydrogen ($I = \frac{1}{2}$) in a magnetic field **B**. Resonance occurs when the energy gap between the levels matches with the energy of the photons in the electromagnetic field. (b) In absence of a magnetic field there are equal numbers of + and - spins at random angles around the z-axis and the resultant of their magnetic moments is zero. When a magnetic field is applied, there are slightly more + than - spins. As a result, there is a net magnetization $M_0$ along the z-axis.

### 2.1.2 Larmor Precession

It is shown by classical mechanics that a magnetic field **B** applied to a collection of nuclei, exerts a torque on their magnetic moment **M**. By equating the torque to the rate of change in the macroscopic angular momentum $\frac{\mathbf{M}}{\gamma}$, is obtained

$$\frac{\mathrm{d}\mathbf{M}}{\mathrm{d}t} = \gamma\mathbf{M} \times \mathbf{B}. \tag{2.10}$$

The solution of equation 2.10 shows that the tip of the magnetization vector moves with a constant angular velocity on a cone around the direction of the field while keeping a constant angle $\theta$ between the spin magnetic moment and the field as illustrated in Figure 2.2. For a magnetic field with magnitude $B_0$ the angular frequency of this precession is the Larmor frequency

$$\omega_0 = -\gamma B_0, \tag{2.11}$$

which is the angular equivalent of the frequency $\nu_L$ (Eq. 2.6), necessary to excite the spins to an adjacent energy level in the quantum mechanical treatment.

### 2.1.3 Pulsed NMR

Pulsed NMR uses a comparably weak oscillating magnetic field of amplitude $B_1$, applied transverse to a set of nuclear spins in a permanent longitudinal magnetic field $B_0\mathbf{i}_z$, to ma-

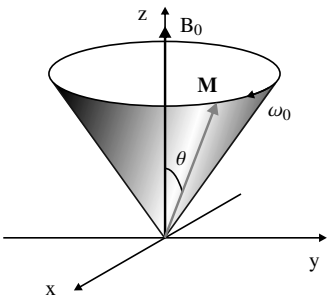


**Figure 2.2**: Precession at the Larmor frequency $\omega_0$ of the magnetization vector **M** on a cone keeping constant angle $\theta$ between the spin magnetic moment and the magnetic field.

nipulate the orientation of the magnetization vector. The coil of an electronic LC-oscillator generates a linearly polarized oscillating magnetic field $2B_1 \cos(\omega t)$ as depicted in Figure 2.3. It can be decomposed into a clockwise and a counter-clockwise rotating circularly polarized component, each of amplitude $B_1$. When the spins posses a positive gyromagnetic ratio, the clockwise component, $B_1\cos(\omega t) - iB_1\sin(\omega t)$, rotates in the same sense as the nuclear spin precession and is responsible for the resonance excitation if $\boldsymbol{\omega}$ equals the Larmor frequency $\boldsymbol{\omega}_0$. The counter-clockwise component can be ignored provided $B_1 \ll B_0$.

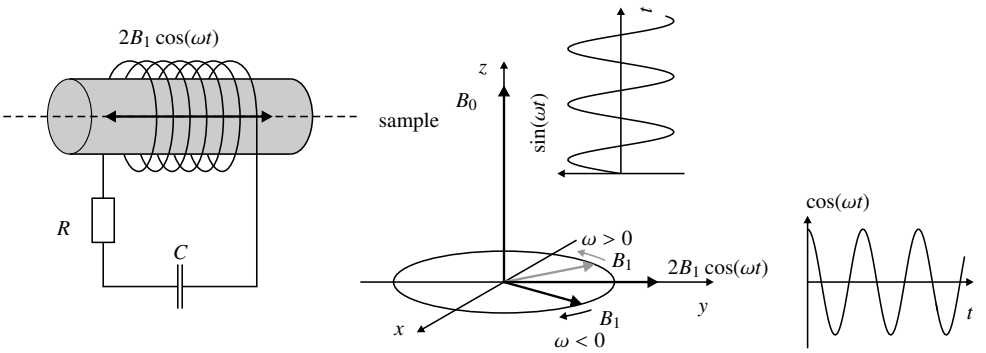


**Figure 2.3**: The coil of an electronic oscillator generates a linearly polarized, oscillating traverse r.f. field that can be represented as two counter-rotating circularly polarized fields.

It is convenient to study the effect of the oscillating magnetic field on the magnetization vector, i.e. the solution of equation 2.10, in a rotating frame of reference (x',y',z') with the same angular velocity $\boldsymbol{\omega}$ as the $B_1$-field. After applying the rotational operator

$$\left(\frac{\mathrm{d}}{\mathrm{d}t}\right)_{\mathrm{lab}} = \left(\frac{\mathrm{d}}{\mathrm{d}t}\right)_{\mathrm{rot}} + \boldsymbol{\omega}\times \tag{2.12}$$

on equation 2.10, the variation of the magnetization vector becomes:

$$\left(\frac{\mathrm{d}\mathbf{M}}{\mathrm{d}t}\right)_{\mathrm{rot}} = \gamma\mathbf{M} \times \left(\mathbf{B} + \frac{\boldsymbol{\omega}}{\gamma}\right). \tag{2.13}$$

In the rotating frame the magnetization vector precesses no longer around $\mathbf{B}$ as in the laboratory frame (x,y,z), but around the effective field $\mathbf{B}_{\mathrm{eff}} = \mathbf{B} + \frac{\omega}{\gamma}$ instead. For an r.f. field $\mathbf{B}_1$ applied on-resonance, inserting $\boldsymbol{\omega} = \boldsymbol{\omega}_0$ immediately shows that the effective longitudinal field in the rotating frame is equal to zero while $\mathbf{B}_1$ is the resulting time-independent field. The magnetization vector precesses simultaneously about the longitudinal field $\mathbf{B}_0$ at $\boldsymbol{\omega}_0$ and about the oscillating field $\mathbf{B}_1$ at $\boldsymbol{\omega}_1 = -\gamma\mathbf{B}_1$. $\mathbf{B}_1$ is, with a strength on the order of $10^{-5}$ – $10^{-4}$ T, typically a factor $10^4$ weaker than $\mathbf{B}_0$. Hence, the angular frequency at which the precession about the oscillating field occurs is for proton NMR typically in the low kHz range. In Figure 2.4(a) and 2.4(b) the reorientation of the magnetization vector is sketched in the laboratory and rotating frame of reference respectively. The derivation of the equations that describe the precessional motion in Figure 2.4(a) is presented in appendix A. A short burst of resonant r.f. field, known in NMR as the r.f. pulse, is hence a powerful means to redirect the magnetization in a controlled way. If $\mathbf{B}_1$ is turned on for a time $\Delta t_p$, the magnetization will rotate by an angle $\omega_1 \Delta t_p$ about $\mathbf{B}_1$. The most common pulses are the 90° and the 180° pulse, named after the angle over which they rotate the magnetization. Once the nuclear moments have been turned into an angle with the constant field, they will continue to precess around it and likewise cause a nuclear induction that still occurs when the driving pulse has already disappeared. This induced NMR signal, due to the magnetization component precessing in the x'y'-plane and appearing immediately after a pulse, is called a Free Induction Decay (FID).

When the circular frequency $\boldsymbol{\omega}$ of the r.f. field is in the neighborhood of the resonance frequency, $|\omega - \omega_0| \ll |\omega_0|$, an off-resonance precession will appear as illustrated in Figure 2.4(c). This off-resonant behavior is of importance in NMR imaging because of its role in selective excitation. The effective field $\mathbf{B}_{\mathrm{eff}}$ has an angle

$$\theta = \arctan\left(\frac{B_1}{B_0 + \frac{\omega}{\gamma}}\right) \tag{2.14}$$

with respect to the longitudinal field $\mathbf{B}_0$. As soon as $B_0$ is appreciably larger than the resonant field, $\frac{\omega}{\gamma}$, the angle is so small that an r.f. pulse no longer rotates the magnetic moment away from the z-axis. This implies that these spins are not selected by NMR.
In NMR pulse sequences, rapid changes of the r.f. pulse phase are used to freely manipulate the direction of the rotation of the magnetization vector in the rotating frame of reference. The direction of these discontinuous phase jumps is indicated with a subscript under the magnitude of the angle through which $\mathbf{M}$ is rotated by the pulse as given in Figure 2.5. It is common to define the phase of the first pulse as positive x'-axis.

### 2.1.4 The Bloch Equations

In section 2.1.2 the equation of motion for the magnetization vector is derived for ideal conditions. It is assumed that the changes in the orientation of each spin are solely due to the

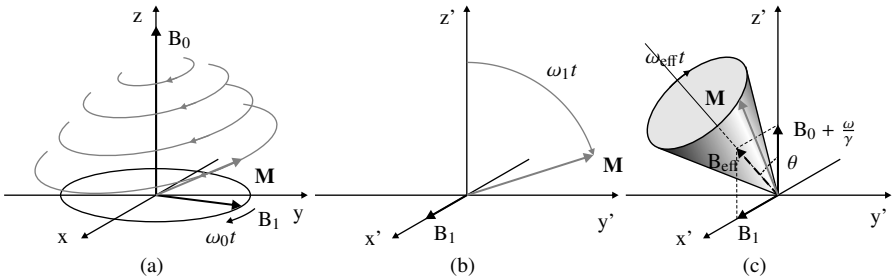


**Figure 2.4**: (a) On-resonance rotation of the magnetization vector in the laboratory frame of reference and (b) in the frame of reference rotating at Larmor frequency $\omega_0$. (c) An off-resonance applied r.f. pulse causes a precession of the magnetization vector on a cone around the effective magnetic field $B_{\text{eff}}$ in the coordinate system rotating at $\omega$.

| transmitter phase | axis applied field |
|---|---|
| 0° | +x' |
| 90° | +y' |
| 180° | -x' |
| 270° | -y' |

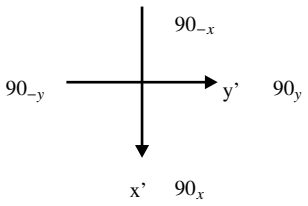


**Figure 2.5**: Definition of the transmitter phase with respect to the rotating frame of reference x'y' for e.g. a 90°-pulse.

presence of external magnetic fields that are uniform troughout the sample. Because almost all nuclear particles are magnetic and due to thermal agitation, the magnetic field experienced by the individual nuclear spins will differ slightly from spin to spin. The macroscopic magnetic moment is consequently not constant, but decreases slowly in magnitude. A process that is described by two relaxation parameters.

#### 2.1.4.1 Longitudinal relaxation time $T_1$

The equilibrium magnetization, $\mathbf{M}_0$, as derived in section 2.1.1, doesn't establish itself immediately upon application of a polarizing magnetic field $\mathbf{B}_z$. The initial isotropic distribution of spin polarizations in absence of a magnetic field (see Figure 2.1(b)), which makes no contribution to the magnetic moment of the material, only gradually breaks down when energy from the spins is transferred to the surroundings. Thermal agitation is responsible for the energy transfer and consequently for the development of a macroscopic magnetic moment. Molecules are full of magnetic particles. Each individual spin, therefore, experiences a local magnetic field, which is the sum of the external static field and a very small microscopic field that rapidly fluctuates in time with arbitraty orientation. The spins wander around between different precession cones and because of the finite temperature of the environment this motion is anisotropic: the spins are stimulated to change their orientation from - to + or vice versa to their energetically beneficient state. If at any time $\mathbf{M}_z \neq \mathbf{M}_0$, the thermal equilibrium will be re-established exponentially with a characteristic time constant $T_1$, the longitudinal relaxation time:

$$\frac{\mathrm{d}M_z}{\mathrm{d}t} = -\frac{M_z - M_0}{T_1}. \tag{2.15}$$

The relaxation time constant of this reversible process depends on the nucleus and the sample, including the temperature and viscosity if the sample is a gas or liquid. At room temperature, the value of $T_1$ is typically in the range of milliseconds to 10 s [37, 152].

#### 2.1.4.2 Transverse relaxation time $T_2$

The rapid fluctuations in the magnitude of the local magnetic fields also result in a slow decay of the macroscopic magnetization component precessing in the x'y'-plane. Due to the local difference in the precession frequency, the nuclear magnetic moments get out of phase with each other. The change in $M_x$ and $M_y$ by this loss of synchronization has an exponential character

$$\frac{\mathrm{d}M_i}{\mathrm{d}t} = -\frac{M_i}{T_2} \quad \text{for} \quad i = x, y \tag{2.16}$$

where time constant $T_2$ is the transverse relaxation time of this irreversible process. Contrary to the longitudinal relaxation process, the internuclear interactions responsible for the transverse relaxation process, leave the total spin energy unchanged. In general, $T_2 \leq T_1$. For small molecules in liquids, $T_2$ is typically of the same order of magnitude as $T_1$, i.e. several seconds. In other circumstances, such as for large molecules in liquids, or for solids, $T_2$ may

be as short as milliseconds [152]. The nuclei in a real system experience small differences in chemical environment due to magnetic field inhomogeneities. This leads to a broadening of the spectrum of resonance frequencies by no more than a few Hz. As a result, signal dephasing will take place with an effective time constant $T_2^*$, which is usually much smaller than $T_2$. The relation between them is given by

$$\frac{1}{T_2^*} = \frac{1}{T_2} + \gamma \Delta B_0, \tag{2.17}$$

where $\Delta B_0$ represents the inhomogeneity of the static magnetic field. In contrast to the irreversible coherence loss due to transverse relaxation ($T_2$), the dephasing due to magnetic field inhomogeneities is reversible.

#### 2.1.4.3 The Bloch Equations

If equation 2.10 is extended with three damping terms for the effects of the longitudinal and transverse relaxation, given by equation 2.15 and 2.16, the Bloch equations [27] are obtained that fully describe the rate of change in the macroscopic magnetic moment.

$$\frac{\mathrm{d}M_x}{\mathrm{d}t} - \gamma \left( M_y B_z - M_z B_y \right) + \frac{1}{T_2} M_x = 0 \tag{2.18a}$$

$$\frac{\mathrm{d}M_y}{\mathrm{d}t} - \gamma \left( M_x B_x - M_x B_z \right) + \frac{1}{T_2} M_y = 0 \tag{2.18b}$$

$$\frac{\mathrm{d}M_z}{\mathrm{d}t} - \gamma \left( M_x B_y - M_y B_x \right) + \frac{1}{T_1} M_z = \frac{1}{T_1} M_0 \tag{2.18c}$$

For an isotropic medium it is justified to use the same $T_2$ time for both the x and y direction.

## 2.2 The NMR system

The NMR multiphase flowmeter system, operating at a $^1$H resonance frequency of 14.1 MHz, is developed and build by Oxford Instruments in agreement with the conceptual design by KROHNE. It comprises a permanent magnet system, a MARAN-ultra DRX2 NMR electronic unit and two probe heads that contain both the r.f. coils and the shim/gradient coils. The r.f. coils used in this work are a modification of the original Oxford Instrument coils. Rhode [217] discusses in his PhD thesis the reason for the choice of this coil design.
First, the design of the NMR flowmeter prototype is described. Next, the practical theory about the functioning of the different components of the NMR system, illustrated in the block-diagram of Figure 2.6, and the most important processor operations are explained. For a comprehensive description of NMR instrumentation is referred to the textbooks by Chen and Hoult [43] and Levitt [152].

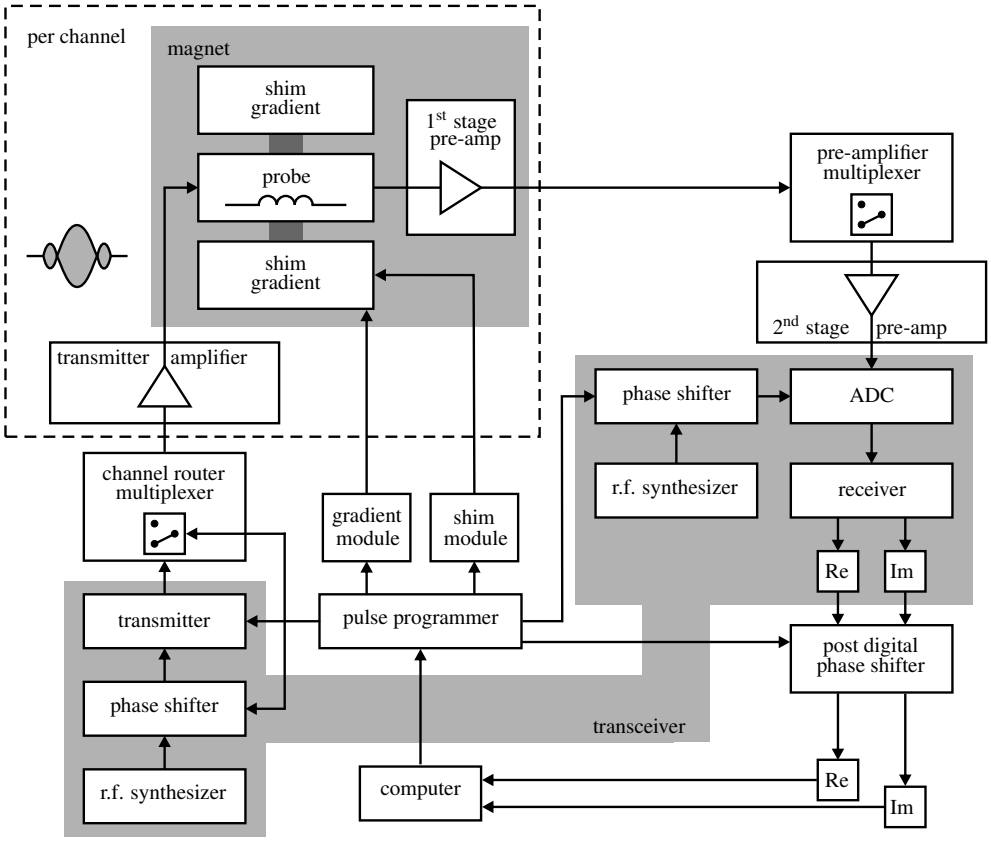


**Figure 2.6**: Block diagram of the NMR system electronics. The flowmeter consists of two measurement probes that each have their own control channel, shim/gadient coils and resonant circuitry.

### 2.2.1 The NMR Multiphase Flowmeter System Design

The laboratory prototype of the flowmeter, illustrated in Figure 2.7, consists of a 3 m long H-configuration permanent NdFeB rare earth magnet with a uniform field strength $\mathbf{B}_0$ of 0.331 T at 20°C that is used for both polarization and detection. Two r.f. probes are mounted respectively 0.5 and 2.5 m from the magnet entrance. This symmetric arrangement theoretically allows the flowrate determination of bi-directional flows. These distances are chosen such that the difference in fluid prepolarization can be used for determining the phase fractions, the so-called $T_1$ contrast. The polarizing field strength corresponds to a Larmor frequency of 14.1 MHz for hydrogen protons. The magnet is constructed by bolting 3 segments together, which are each 1 m long. The side sections of the magnet have a homogeneity better than 100 ppm at the position of the r.f. coil. With the shimming coils (see section 2.2.5), mounted on the magnet pole faces around the r.f. probes, this homogeneity is even improved to less than 30 ppm. The purpose of the magnet's middle section is to keep the magnetic moments polarized in the direction of the magnetic field, while moving between the two probes. Here, a lower homogeneity of 5‰ is sufficient. The probe heads have a bore of 112 mm, which allows a pipe with a maximum of 100 mm inner diameter to be put through. As measuring coil, the r.f. probes use a 12 cm long trifilar coil of 4 turns and 12 cm diameter. One of the two tested flowmetering principles works with a uniform polarizing magnetic field. For the other, the shimming plates are provided with a gradient coil that can generate a pulsed magnetic field gradient $\mathbf{G}_y$ in the streamwise direction on top of the permanent $\mathbf{B}_0$-field. The maximum magnetic field gradient strength is specified as 42 mT m$^{-1}$ for the first and 43 mT m$^{-1}$ for the second measurement section.

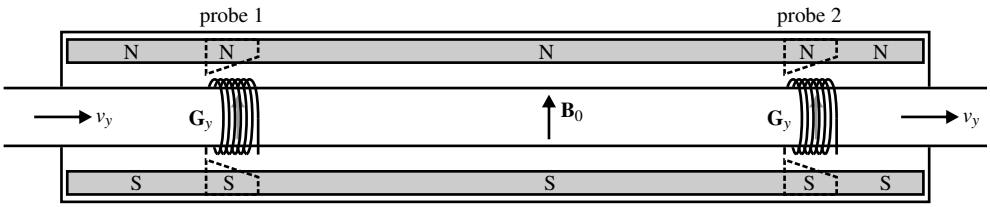


**Figure 2.7**: Schematic drawing of the NMR multiphase flowmeter. The fluid passes the magnet from left to right with average velocity $v_y$. The apparatus is made up of a permanent NdFeB rare earth magnet with a uniform field strength $\mathbf{B}_0$ of 0.331 T that polarizes the spin magnetic moments of the nuclei and two r.f. coils that detect the NMR signals. Pulsed gradient coils, which can provide a linear magnetic field gradient $G_y$ on top of the permanent $B_0$-field, are also incorporated for one of the two flowmetering principles tested.

### 2.2.2 Transmitter

The transmitter produces the exitation pulses of field strength $\mathbf{B}_1$ that rotates the magnetization from the z-direction of the magnetic field $\mathbf{B}_0$ into the traverse plane of the rotating frame of reference. With the transmitter multiplexer the shape $a(t)$ and phase shift $\psi(t)$ are controlled as specified by the pulse programmer [196]. In case the pulse programmer specifies

a nonzero transmitter phase $\phi$, as defined in Figure 2.5, the phase shifter shifts the signal no longer over phase $\psi(t)$, which defines the shape of the pulse, but over the sum of both phases instead [195]. Afterwards, the transmitter modulates the r.f. current at the required frequency $\omega_r$ and scales it to the correct amplitude. A block diagram of the transmitter operation is given in Figure 2.8.

The excitation pulse contains a frequency distribution, determined by the pulse width and shape function, around the carrier frequency $\omega_r$. In *selective excitation* this bandwidth is used to excite only those spins with a Larmor fequency within this specific region of the NMR spectrum. When in the $\mathbf{B}_0$-field a magnetic field gradient of sufficient strength is present to spread the Larmor frequencies of the spins to a width greater than the excitation bandwidth, a selective r.f. pulse may be used to excite only those spins within a specified layer of the sample. For this reason, *slice selection* is at the basis of most NMR imaging sequences.

A measure for the bandwidth of the excitation pulse can be obtained by means of a Fourier transform of the excitation pulse. A remark has to be made that this approximation is only convenient for small flip angles [108]. The Fourier transform of a rectangular pulse is a sinc function (see Figure 2.9(a)), where the majority of the excitation appears close to the carrier frequency $\omega_r$, but spins with frequencies in the side lobes are excited as well [190]. Non-selective broadband rectangular pulses are referred to as *hard pulses*, because of their short pulse width $2T$ and large $\mathbf{B}_1$-magnitude. Vice versa a sinc pulse in the time domain has a rectangular Fourier transform, as illustrated in Figure 2.9(b) and is, to this end, a suitable selective pulse. On account of their small $\mathbf{B}_1$-magnitude, the class of narrowband selective pulses is referred to as *soft pulses*.

### 2.2.3 R.F. Probe

The function of the r.f. probe, illustrated in Figure 2.10, is twofold. First its r.f. electronic circuit generates, during the pulse, the oscillating magnetic $\mathbf{B}_1$-field that irradiates the sample present in the bore of the coil. It is important that the geometry of the coil is such that the oscillating magnetic field is predominantly perpendicular to the main magnetic $\mathbf{B}_0$-field. After the r.f. pulse is terminated, the probe detects the precessing magnetization through the electrical currents that are generated in the coil and transmits the signal to the receiver.
The oscillator, comprising the parallel LC-circuit, forms the main part of the r.f. probe. As measurement coil a 12 cm long trifilar coil of 4 turns and 12 cm diameter is used (see Figure 2.12(a)) with an inductance of circa 2 $\mu$H. This has the advantage that the induction of the coil is equal to that of a general four turn solenoid of the same length [180], while the homogeneity of the pulsed $\mathbf{B}_1$-field is improved. With the variable capacitor, $C_t$, it is possible to *tune* the resonance frequency of the circuit

$$\omega_{osc} = \frac{1}{\sqrt{L(C + C_t)}}. \tag{2.19}$$

For the purpose of enhancing the currents in the coil by electromagnetic resonance, the res-

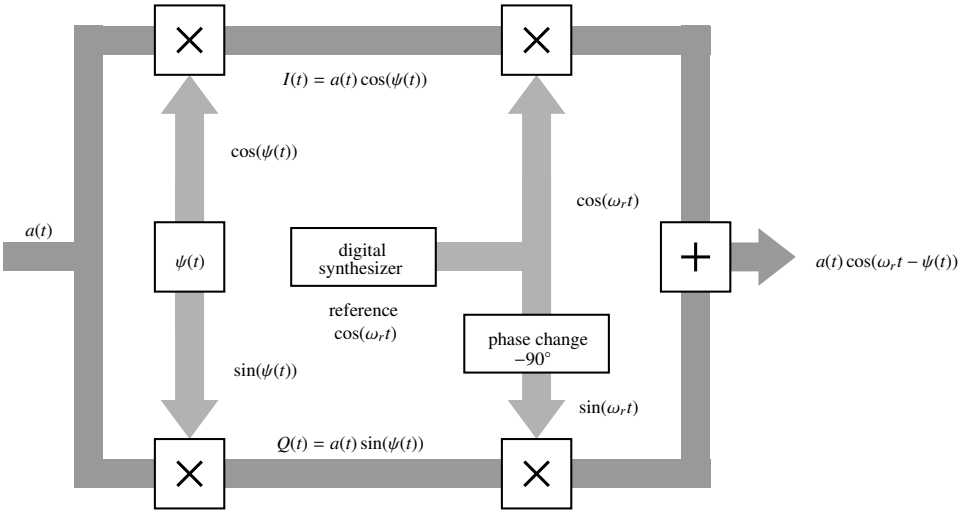


**Figure 2.8**: Block diagram of the transmitter operation. The transmitter multiplexer controls the amplitude of the output pulse via user defined amplitude $a(t)$ and phase $\psi(t)$ lists, provided by the pulse programmer [196]. In the four quadrant multipliers, the amplitude channels $I$ and $Q$ are modulated with a carrier wave of frequency $\omega_r$, generated by the digital synthesizer. After vector summation of their outputs in a combiner, a composite r.f. pulse is obtained with the required phase and shape [193].

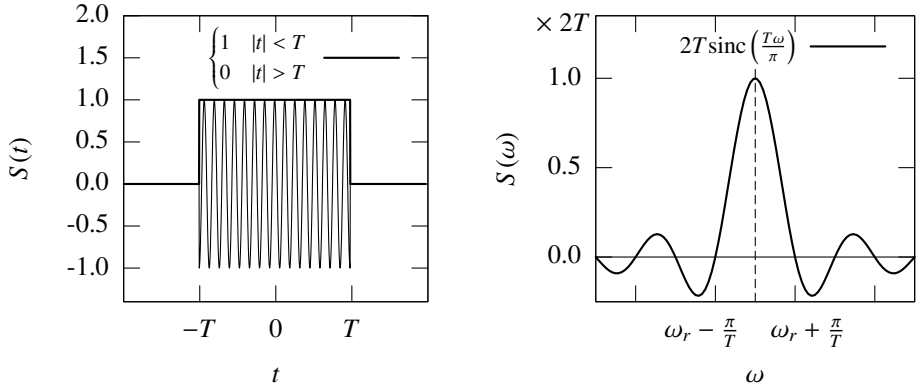


(a) The broadband excitation spectrum of a rectangular or hard pulse has a sinc shape.

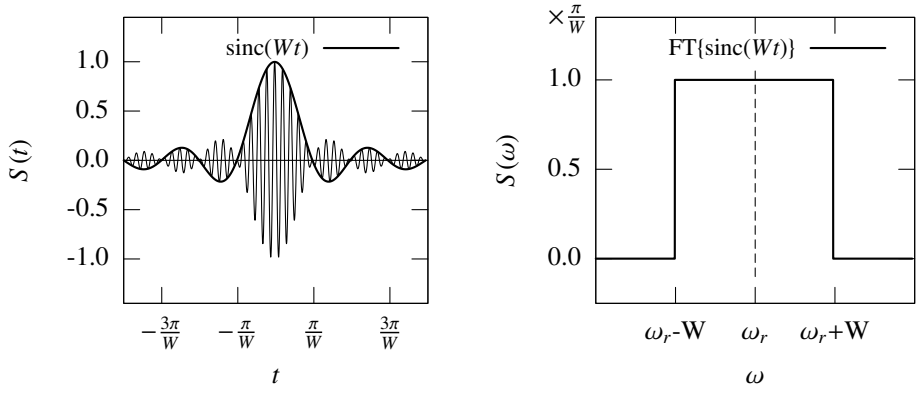


(b) A sinc-pulse, belonging to the soft pulse class, has a rectangular narrow-band excitation spectrum.

**Figure 2.9**: A measure for the bandwidth of the excitation pulse can be obtained by means of a Fourier transform of the excitation pulse. The user defined amplitude of the pulse is modulated on a carrier wave with frequency $\omega_r$.

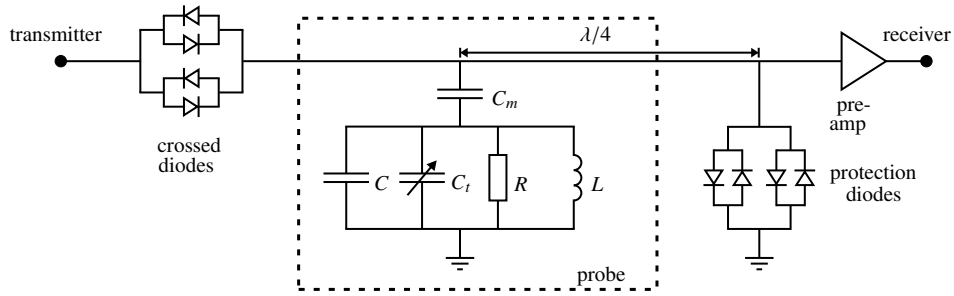


**Figure 2.10**: Original Oxford Instruments circuit design of the r.f. probe [194]. The oscillating circuit consists of a capacitor $C$ = 10 [pF], a variable tuning capacitor $C_t$ = 5-75 [pF], a matching capacitor $C_m$ = 20 [pF] and a measurement coil $L \approx 2$ [$\mu$H]. To protect the sensitive receiver circuitry from the strong r.f. pulse and eliminate noise on the detected weak NMR signal, the probe electronics is provided with two sets of crossed diode pairs.

onance frequency has to be set close to the frequency of the carrier wave. During the pulse the carrier frequency is $\omega_r$, which approaches Larmor frequency $\omega_0$, the carrier frequency of the signal during detection. To allow tuning of the circuit, the NMR system is equipped with a wobble facility. The wobble technique excites all frequencies within a predefined bandwidth, symmetric around $\omega_r$, simultaneously and produces a reflection power spectrum of the probe response [194]. As Figure 2.11(a) demonstrates, tuning the circuit ensures that the power transfer with maximum efficiency or with the least reflection, takes place at the Larmor frequency. Operation of the system under off-resonance conditions in relation to tuning has, consequently, two negative effects: it causes both an increase in the pulse length and a reduction of the signal-to-noise ratio.

With the *matching* capacitor $C_m$, the output impedance of the transmitter is matched to the impedance of the probe circuit to ensure that the r.f. power is transmitted to the probe circuit with maximum efficiency. In the used probe design, $C_m$ has a fixed value. However, with a variable capacitor, the signals could be optimized by adjusting the probe, so that the power reflection of the transmitted signal with frequency $\omega_r$ is as low as possible (see Figure 2.11(b)).
In the flowmeter application, the properties of the sample change continuously. Because the variations in composition, viscosity and temperature affect the electrical properties of the tuned circuit, it is necessary to adjust the value of $C_t$ (and of $C_m$ if possible) over time. Above all, temperature affects tuning as well, via the changes in the field strength of the permanent magnet it causes.

The design of the probe electronics is hampered by the transceiver that has to be connected to both pulsing and receiving electronics. During the transmit part of the pulse sequence the receiver amplifiers must be protected from the high source voltage, while it is desirable to eliminate noise from the pulser electronics during the receiving part. This is solved by means

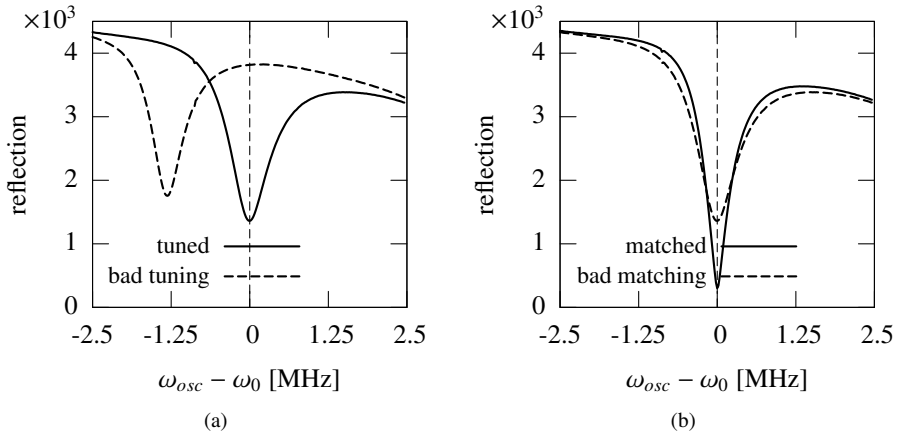


**Figure 2.11**: Reflection power spectrum, obtained with the wobble facility of the NMR system in arbitrary RINMR units. The resonant circuit is (a) tuned when the power transfer with maximum efficiency takes place at the transmitter frequency $\omega_r$ and (b) matched when the reflection coefficient is set as low as possible.

of crossed diode bridges that act like switches which are closed for large voltages, but are open for small signals [161, 162]. The set of crossed diodes in series with the output of the transmitter prevents noise of the transmitter circuit propagating to the pre-amplifier while the transmitter is switched-off in the receiving phase. In this way the transmitter cannot interfere with the induced voltage of the weak NMR signal.
The protection of the sensitive receiver circuitry during the r.f. pulse is formed by a $\lambda/4$-coaxial cable in combination with a second set of crossed diodes linking the input of the receivers pre-amplifier to earth. Since crossed diode pairs are conducting for strong signals, the r.f. pulse will enter the probe circuit but cannot pass to the receiver, because its input is shorted. After the large excitation pulse has passed, the crossed diode pairs act as open circuits that disconnect the transmitter from the probe circuit but leave a clear path to the amplifier.

### 2.2.4 Receiver

The receiver consists of the same r.f. coil as is used for the excitation. After the ringdown period, the NMR signals is detected, amplified and converted to a digital signal. The latter is analyzed using quadrature detection, to determine the direction of the Larmor precession and allow phase sensitive detection. For an extensive explanaition of quadrature detection is referred to section 2.2.6.

### 2.2.5 Shimming and Gradient Module

The sensor is equipped with electronic shimming coils to improve the homogeneity of the static magnetic field at the probe position by counteracting the irregularities in the permanent magnetic field. In a pair of 5 mm thick resin plates, mounted around the probe head, as illustrated in Figure 2.12(b), five oddly shaped coils are enclosed in a circular zone of 370 mm diameter. Each pair of identical coils forms an electromagnet that generates a different type of magnetic field gradient, i.e. $Z^0$, Z, $Z^2$, X and Y, of which the strength is controlled by manually adjusting the current. In this notation, the letter implies the direction and the superscript the order of the gradient in the static $\mathbf{B}_0$-field. Only the first four mentioned gradients comprise the series of shimming gradients, which make up the shimming module. The Y-gradient, the linear gradient in the streamwise direction, forms the gradient module. It is controlled with the pulse programmer and can be applied to perform phase encoding or to select slices in imaging experiments.

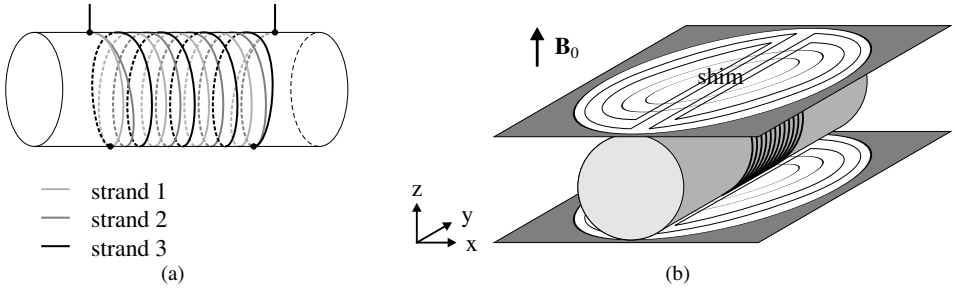


**Figure 2.12**: (a) The measurement coil of the r.f. probe is a 12 cm long trifilar coil of 12 cm diameter: the wire is split into three parallel coils of four turns enclosing the same core. This has the advantage that the induction of the coil is equal to that of a general four turn solenoid of the same length, while the homogeneity of the pulsed $\mathbf{B}_1$-field is improved. (b) The shimming/gradient plates are mounted on both sides of the r.f. probe. Each pair of identical coils in both plates acts as Helmholtz coil that generates a magnetic field gradient.

Shimming is an iterative procedure in which usually the settings of the shimming currents are searched, which optimize a quality parameter. For this system the quality is determined by the shape of the FID signal and its Fourier spectrum that should approach a perfect exponential decay and a symmetrical smooth lineshape, respectively. In this manner the inhomogeneity of the magnet is reduced to less than 30 ppm, corresponding to an inaccuracy of 423 Hz in the spectrum given the used 14.1 MHz system. A drawback of this method is the lacking of prior knowledge about the present gradients, since the observed NMR signal results from the integrated signal of all spins in the sample. An additional difficulty is that higher order shims interact with other shims, such that a bad setting of one shim control prevents finding the correct setting of another shim and results in a false optimum [199]. For example the second order gradient in the z-direction, $Z^2$, is a function of as well the z-, x- as y-direction

and interacts, therefore, with both Z and X shim. For a detailed description of the expanded equations of the generated magnetic field is referred to the manual by Miner and Conover [175].
The sketched problems make the optimisation of the static $\mathbf{B}_0$-field an iterative and time-consuming process. To this end, gradient shimming, a technique based on spatial encoding, has been implemented that uses gradient echoes to map the spatial variations in the magnetic field. Contrary to nonlocalized NMR measurements, this Fieldmap method [33], which will be discussed in section 2.3.7, allows the maximization of the homogeneity in a few iterations.

### 2.2.6 Quadrature Detection

After the magnetization is rotated into the transverse plane by an r.f. pulse, its precession induces a linearly polarized voltage $A(t)\cos(\omega_0 t + \phi)$ in the receiver coil, where function $A(t)$ describes the DC amplitude envelope of the signal in time. Because the frequency of the oscillating signal with 14 MHz is far too high to be easily recorded with a computer, heterodyning is applied to reduce the frequency. With a digital synthesizer in the transceiver, the required sinusoidal reference signal is generated at the same frequency $\omega_r$, approximately the Larmor frequency, as the current that has induced the pulsed $\mathbf{B}_1$-field in the coil [193]. After mixing-down the signal in a phase-sensitive detector, the resultant comprises two sinusoidals oscillating at the sum and difference frequency respectively. Finally the ultra-high frequency component is filtered out with a set of low-pass filters so the signal with reduced frequency, $\Omega = \omega_0 - \omega_r$, can be stored in a computer for data acquisition. In fact, the signal has undergone a transformation from the laboratory frame of reference to the rotating frame of reference as defined in section 2.1.3.

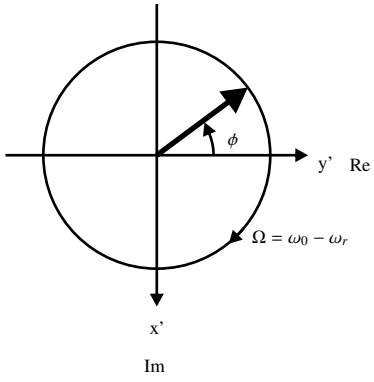


**Figure 2.13**: Convention of the rotating frame of reference. Be aware of the unusual orientation of the imaginary-axis in the complex plane, resulting from the projection of the three-dimensional vectors on the x'y'-plane.

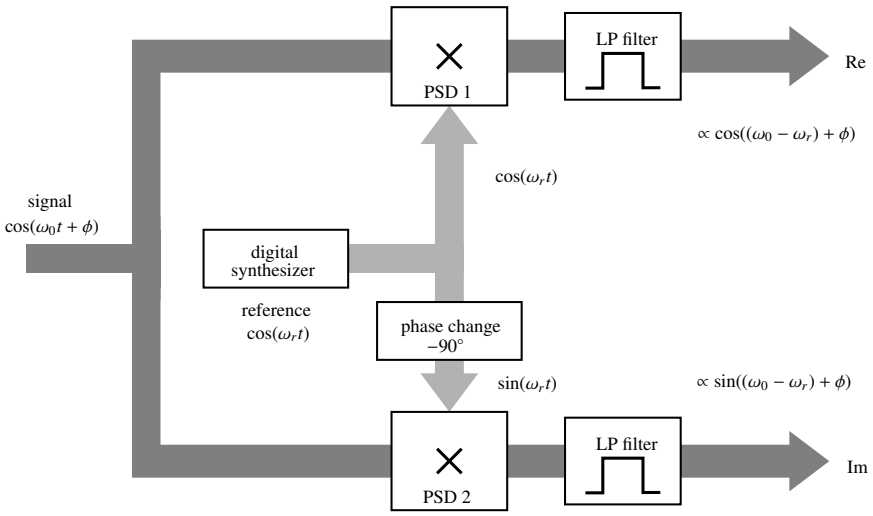


**Figure 2.14**: Block diagram for quadrature phase sensitive detection after Chen and Hoult [43]. The signal is mixed in two phase-sensitive detectors, PSD, with a reference signal from the digital synthesizer and afterwards filtered by a set of low-pass filters.

The phase-detected signal still is a linearly polarized signal that is directional ambiguous. For NMR spectroscopy and other NMR measurement principles relying on the phase of the signal with respect to the rotating frame of reference it is, however, important to know the direction of the precession. In quadrature detection a means is found to obtain the desired circularly polarized signal. As Figure 2.14 illustrates, two phase-sensitive detections are performed simultaneously, but the phase of the second reference signal is permanently 90° out of phase. In accordance with the convention of the complex plane represented in Figure 2.13, this results in two in-phase quadrature output signals:

$$s_{\mathrm{Re}}(t) = s_0 A(t) \cos(\Omega t + \phi) \tag{2.20a}$$

$$s_{\mathrm{Im}}(t) = -s_0 A(t) \sin(\Omega t + \phi). \tag{2.20b}$$

These are proportional to the orthogonal phases of the magnetization, $\mathbf{M}_{x'}$ and $\mathbf{M}_{y'}$, and together describe the precession of the magnetization vector in the rotating frame:

$$s(t) = s_{\mathrm{Re}}(t) + i s_{\mathrm{Im}}(t) = s_0 A(t) \exp(-i\Omega t) \exp(-i\phi). \tag{2.21}$$

Depending on the sign of the difference frequency, the precession is either forward or backward or does neither if the signal is on resonance ($\Omega = 0$). Thus the ambiguity concerning equal difference frequencies of opposite sign is removed.

The two quadrature signals are named after the contribution they make to the Fourier transformed signal [1]

$$S(\omega) = \int s(t) \exp(-i\omega t) \mathrm{dt} = S_{\mathrm{Re}}(\omega) - iS_{\mathrm{Im}}(\omega). \tag{2.22}$$

For a zero absolute receiver phase $\phi$, the cosine signal, representing the magnetization along the y'-axis in the rotating frame, is even and solely contributes to the real part of the spectrum, $S_{\mathrm{Re}}(\omega)$. The sine signal, representing the magnetization along the x'-axis, on the other hand is odd and solely contributes to the imaginary part of the spectrum $S_{\mathrm{Im}}(\omega)$. When the absolute receiver phase is unequal to zero, the spectrum can be restored afterwards in the postprocessing software to the 'correct phase' by multiplying by $\exp(i\phi)$.

### 2.2.7 Phase Cycling

The phase of an NMR signal depends on the phase of the transmitted r.f. pulse and the receiver. In the phase cycling technique, an NMR experiment is repeated several times, while the phases of the transmitter and receiver are systematically swapped. This is done in such a way that the desired signals add up and the unwanted signals cancel out in the final data sum. By using the appropriate phase cycling scheme it is possible to improve the signal-to-noise ratio via coherent noise cancellation [37], to orthonormalize the signal for phase and amplitude irregularities [111] or to eliminate spurious echoes due to pulse amplitude errors [264].

With the CYCLOPS phase cycling routine of Hoult and Richards [111] both the noise on the NMR signal following a 90°-pulse is reduced and the channels containing the real and imaginary data of the signal are orthonormalized. In one phase cycle, the r.f. pulse and receiver phase are rotated in four steps of 90° over the phase plane as given by table 2.2. In Figure 2.15(a) is illustrated how the receiver phase, indicated with the black dot, advances with the r.f. pulse. Since it always has the same position relative to the magnetization vector, both phase sensitive detectors observe four times the same component of the NMR signal. The NMR signal is, however, inverted with each 180° phase shift while the systematic noise from the receiver and the computer is not. Substraction of the detected signals therefore enhances the signal strength and eliminates the systematic noise.

In fact, one of the phase sensitive receivers often has a different gain and a small phase shift $\Delta$ (exaggerated in Figure2.15(a)) with respect to the reference axis due to delays in the hardware. The vector representation of the signal addition in Figure 2.15(b) shows that the sum of the signals after two phase cycle steps is corrected for this inaccuracy in the phase settings of the receiver and is orthonormal again. Nevertheless, all four steps of the measurement sequence have to be executed to make use of its noise reducing qualities.

Instead of changing the receiver phase in steps of 90°, the phase cycling procedure is performed by a smart routing procedure in the data acquisition software. The advancing receiver

[1] See for this unusual notation the convention of the complex plane in Figure 2.13. Please note that the RINMR software follows the standard definition of a complex plane with the positive Im-axis in the opposite direction.

phase is mimicked by successive addition and substraction of the incoming signals in the x'- and y'-direction according to the signs given in table 2.2. As a result, all increments of the real and imaginary signals are stored in the orthonormal channel A and B respectively.

**Table 2.2**: Routing procedure for CYCLOPS phase cycling used by the data acquisition software. It stores the real and imaginary signals in channels A and B respectively. $M_{x'}$ and $M_{y'}$ are the amplitudes of the signal along the x'- and y'-axis in the frame of reference rotating at the reference frequency $\omega_r$.

| transmitter phase | receiver phase | increment computer store A | increment computer store B |
|---|---|---|---|
| 0° | 0° | $+M_{y'}$ | $+M_{x'}$ |
| 90° | 90° | $-M_{x'}$ | $+M_{y'}$ |
| 180° | 180° | $-M_{y'}$ | $-M_{x'}$ |
| 270° | 270° | $+M_{x'}$ | $-M_{y'}$ |

## 2.3 Basic Measurement-Sequences

The basic principle behind NMR is resonant absorption of r.f. radiation by nuclei exposed to a magnetic field. Pulse programming in Oxford Instruments RINMR software allows various experiments, but the induced NMR signals can always be reduced to an FID or echo. In this section the NMR pulse sequences are described that can be used for setting up the NMR system or the determination of material properties. Moreover, they serve as building blocks for the implemented pulse sequences for multiphase flowmetering.

### 2.3.1 Free Induction Decay

When a short r.f. pulse, applied at resonance condition, rotates a magnetization vector from a state along the z-axis of the permanent $\mathbf{B_0}$-field whether or not fully in the transverse x'y'-plane, the tip of the vector will remain precessing in its transverse plane after terminating the pulse. Immediately following the pulse, the individual nuclear magnetic moments still precess united along the permanent magnetic field. But they quickly get out of sync due to the $T_2$-effect, described in section 2.1.4.2. From equation 2.16 it is found that the shape of the transverse magnetization

$$M_{xy}(t) = M_{xy}(0) \exp\left(-\frac{t}{T_2}\right) \tag{2.23}$$

decays exponentially with time constant $T_2$. Since this precession occurs in absence of an applied r.f.-field, the electromagnetic field induced in the detection coil by the magnetization component $M_{xy}$ is called Free Induction Decay (FID). A 90°-pulse, as depicted in Figure 2.16, gives maximum signal response, while an FID is absent after a 180°-pulse. Since the

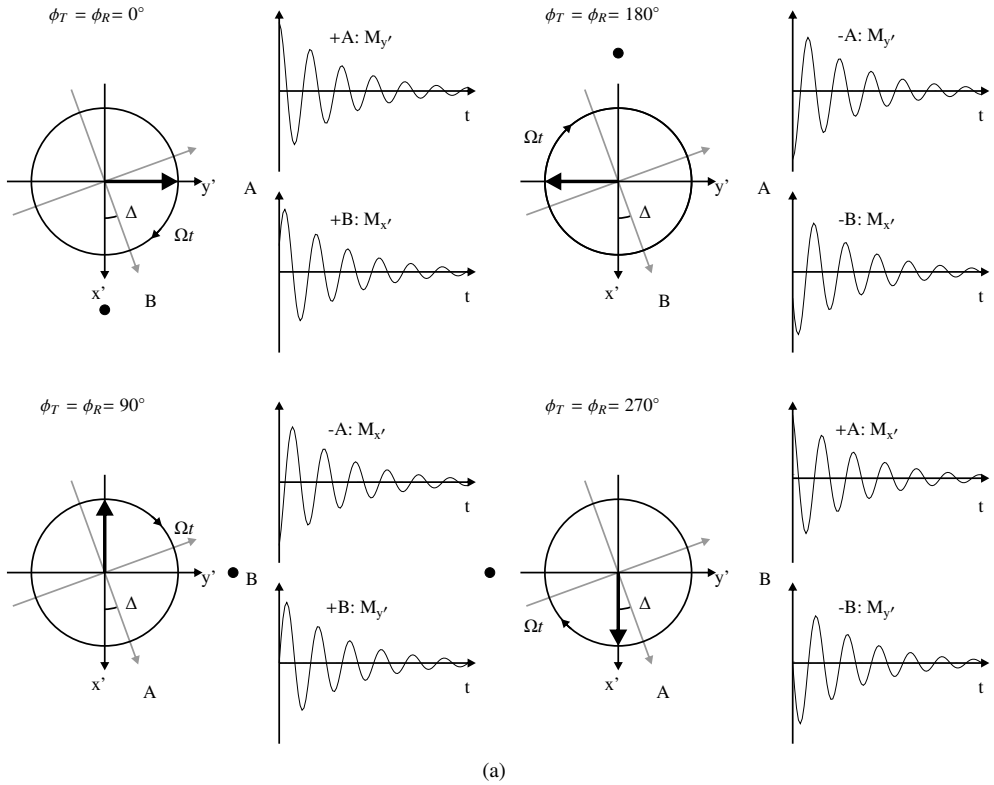


(a)

**Figure 2.15**: CYCLOPS method of phase cycling. (a) Precession of the magnetization vectors $M_{x'}$ and $M_{y'}$ at frequency $\boldsymbol{\Omega} = \boldsymbol{\omega}_0 - \boldsymbol{\omega}_r$ in the rotating frame of reference x'y', where $\boldsymbol{\Omega}$ is assumed to be negative. The big arrow represents the initial position of the magnetization vector after the 90°-pulse and the black dot the position of the receiver phase. The receivers are shown as having phase settings not precisely in quadrature.

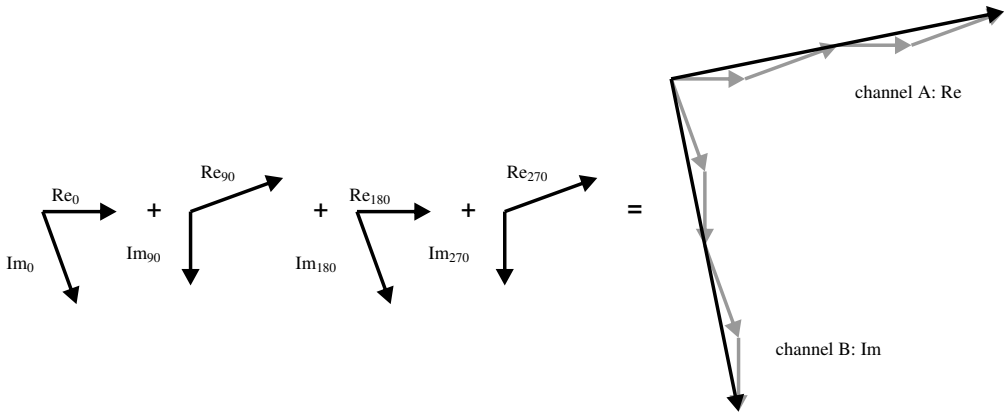


(b)

**Figure 2.15**: (continued) (b) Vector representation of the successive addition and substraction of the real and imaginary incoming signals for two receivers with different gains and phase settings not precisely in quadrature. The subscript indicates the phase of the transmitter. The vector sum shows that the resulting data in channel A and B has matched amplitudes and is orthonomal to first order.

FID occurs on its own after a single pulse, it is the simplest NMR signal that reveals information about the sample.

Nevertheless inhomogeneities in the permanent magnetic field let the individual nuclear magnetic moments phase out faster, because of the divergence in the local Larmor frequencies they are causing. So in practice the NMR signal decays with a transverse relaxation time $T_2^* << T_2$ [28, 29, 88]. Based on convention, the symbol $T_2$ is only used to specify the transverse relaxation time when the field is sufficient homogeneous. Otherwise $T_2^*$ is used.

A measure for the enhanced decay of the FID by field inhomogeneities can also be deduced from the absorption spectrum. It is convenient to assume that this spectrum of a damped oscillator has a Lorenzian distribution

$$S_{Re}(\omega) = \frac{T_2}{1 + {T_2}^2(\omega - \omega_0)^2} \tag{2.24}$$

with a Full-Width-Half-Maximum linewidth $\Delta\omega = 1/T_2$ [28, 37]. Figure 2.17 illustrates that the resonance spectrum by accidental inhomogeneities in the supposedly uniform $\mathbf{B}_0$-field is broad and low contrary to the narrow and high spectrum for a homogeneous field.

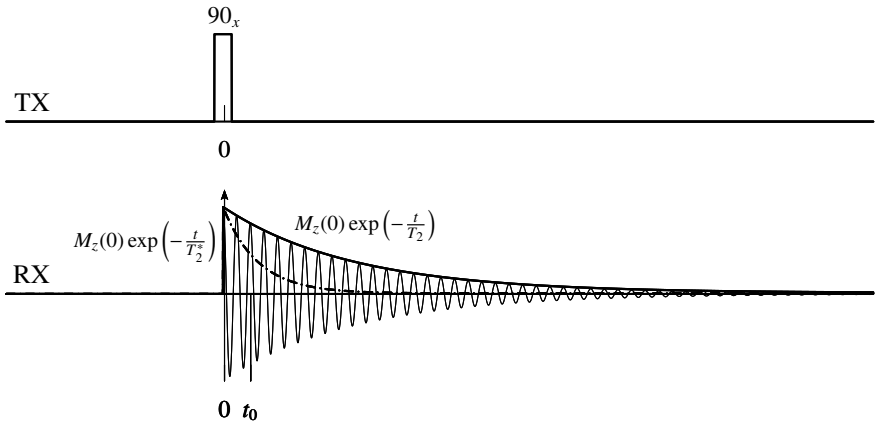


**Figure 2.16**: Diagram of the transmitter (TX) and receiver (RX) channels for an FID following a single 90°-pulse. It is assumed that the magnetization vector is initially directed along the z-axis. The decay of the FID in a homogeneous $\mathbf{B}_0$-field (continuous line) can be attributed to the time dependent local field by the magnetic particles in the sample and has a transverse relaxation time $T_2$. The dot-dashed line represents the FID in an inhomogeneous permanent magnetic field, where $T_2^*$ is the transverse time constant due to both invariant and time dependent local magnetic fields.

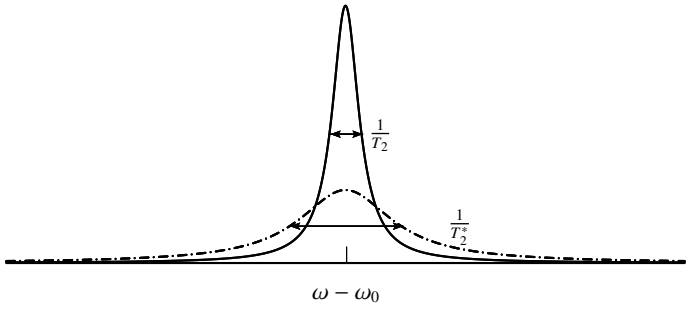


**Figure 2.17**: Absorption spectrum, $S_{Re}(\omega)$ of an FID. The continuous line represents the spectrum of a homogeneous $\mathbf{B}_0$-field that is narrow and high with linewidth $\Delta\omega = 1/T_2$. The dot-dashed line shows the broad and low spectrum for an inhomogeneous permanent field with linewidth $\Delta\omega = 1/T_2^*$.

### 2.3.2 Spin Echo

In practice the determination of the transverse relaxation time, $T_2$, from an FID is impossible due to the faster loss of phase coherence by field inhomogeneities as mentioned before. Hahn [87] proposed a pulse sequence that reverses this loss of phase coherence in the obtained NMR signal. It consists of two r.f. pulses separated by a time interval $\tau$ (see Figure 2.18). After the 90°-pulse along the x'-axis, the various pairs of magnetic moments will precess at offset frequency $|\Delta\omega|$ in the x'y'-plane but rotate in opposite direction, maintaining a symmetry about the y'-axis. In a time $T_2$ the magnetic moments attain an isotropic distribution over the transverse plane and interfere destructively with one and another. If this decaying signal is acquired, one observes the NMR signal of an FID. When instead after a time delay, $\tau$, a 180°-degrees pulse is applied along the y'-axis, the faster and slower precessing magnetic moments interchange position and start to rephase towards the positive y'-axis. To make sure that the precessing magnetic moments maintain their phase memory, it is of importance that $\tau$ is chosen smaller than $T_2$. The magnetic moments start to interfere constructively and refocus again at time $2\tau$, under assumption that the nuclei did not move relative to the $\mathbf{B}_0$-field they experienced during dephasing. The spontaneous nuclear induction signal, which is observed when the resulting phase of the individual macroscopic magnetic moments coincide is known as spin echo.

In the method for $T_2$ determination as proposed by Hahn, the pulse sequence is sequentially applied to a sample in thermal equilibrium with the permanent magnetic $\mathbf{B}_0$-field with each time a different time delay $\tau$. In the ideal situation in absence of diffusion, dispersion and flow, it is obtained from the Bloch equations that the amplitude of a spin echo is modulated according to

$$M_y(2\tau) = M_0 \exp\left(-\frac{2\tau}{T_2}\right). \tag{2.25}$$

In reality, the dermination of $T_2$ from this exponentially decaying function will be disturbed due to the attenuation of the echo amplitude by the above effects.

To suppress diffusion in the determination of $T_2$ it is recommended to use a CPMG-sequence, which will be discussed in section 2.3.5. The spin echo nevertheless is of great value in numerous NMR experiments for spectroscopy, imaging or the direct measurement of flow velocities.

### 2.3.3 Methods for correctly setting the pulse flip angle

Correctly setting the r.f. transmit power levels to achieve the desired r.f. pulse flip angle is very important in NMR for the accurate determination of e.g. $T_1$ and $T_2$. Frequent calibration of the pulse width is required, as it is affected by many parameters including probe design, whether the probe is tuned, spectrometer configuration and what nucleus is being observed. For a simple rectangular hard pulse the r.f. flip angle, $\alpha$, is equal to the gyromagnetic ratio $\gamma$ times the pulse amplitude $B_1$ times the pulse length $\Delta t_p$. For the Oxford Instruments DRX

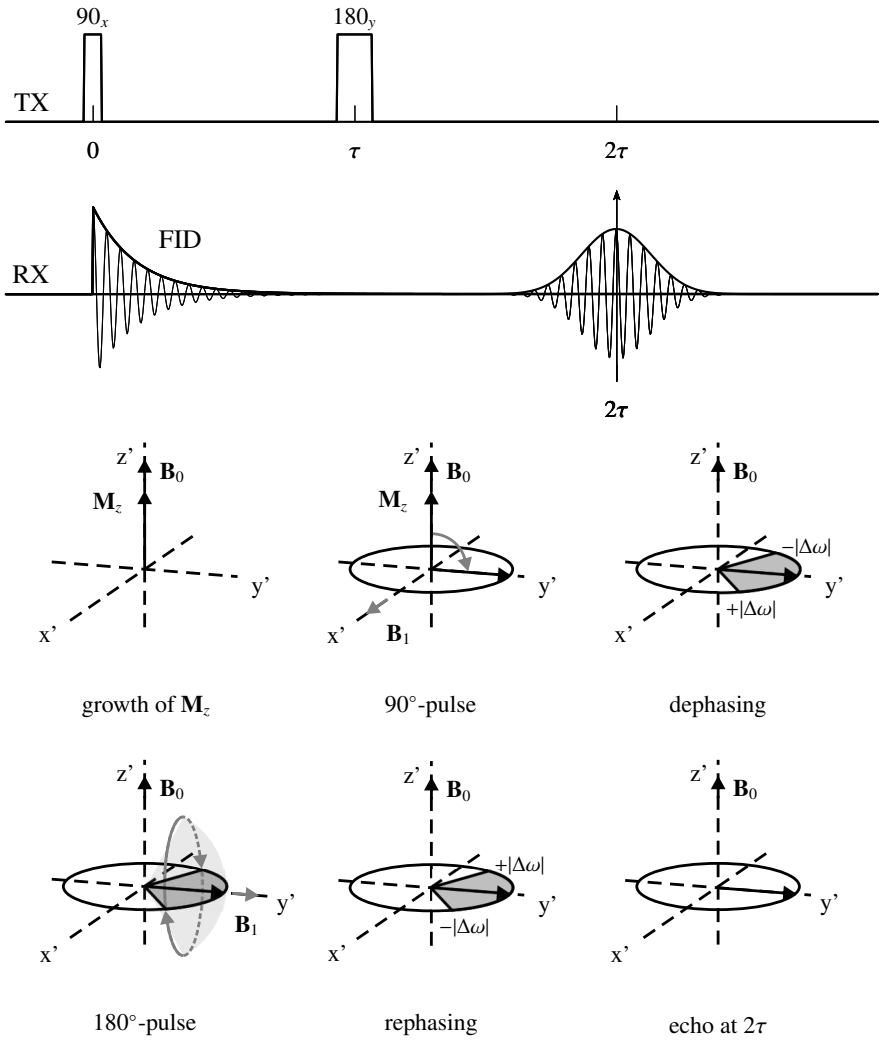


**Figure 2.18**: Hahn spin echo pulse sequence showing the manipulation of the magnetization in a frame of reference rotating at $\omega_0$. After a $90_x$-pulse, the individual magnetic moments start to dephase in the x'y'-plane. With a $180_y$-pulse after a time interval $\tau$ the dephasing due to field inhomogeneities is inverted so that perfect refocussing occurs at time $2\tau$.

console, it can be set by the adjustment of the pulse duration parameters (P90, P180 or P1-P5) or the r.f. pulse amplitude parameter (RFA0). Care should be taken that not too much amplification is applied via RFA0, since the r.f. power of a clipped r.f. pulse is not properly tranferred to the sample [192]. Therefore the pulse angles of hard pulses are set via a routine that adapts the pulse length, while the pulse amplification is kept constant. For soft pulses, on the contrary, the pulse length determines the bandwidth of the pulse. For this reason, the pulse length is kept contant, while the pulse amplitude is varied until the desired flip angle is found.
Just like the transmitter amplifier can be saturated by making the pulse amplitude too high, the same can happen to the receiver amplifier when the receiver gain (RG) is set too high. The accuracy of the NMR measurments depends largely on the receiver gain, because the resolution of the acquired data can be controlled with this parameter.

In general there are two types of experiments to obtain the pulse width of a 90° pulse. If the order of magnitude of the pulse width is known in advance, delay-pulse-acquire experiments like ALPHA3 can be fast. The second method, in which an experiment is run in a single array over a wide range of pulse durations, such as AUTOP90, has the benefit that the trend of the curve indicates deficiencies of the system [128].

#### 2.3.3.1 AUTOP90 routine for hard pulses

The RINMR program is provided with an AUTOP90 routine to set-up the true pulse length of a hard 90° pulse. In the routine, a batch of FID experiments is performed for a number of different pulse lengths ranging from 0° to 180° and the initial amplitude of each NMR signal is calculated. The repetition delay is at least $5T_1$ to allow the spins to return to thermal-equilibrium before the pulse is applied. The magnitude of the NMR signal as function of the pulse length is described by $M_0 \sin(\alpha)$, so that the correct pulse length settings for the 180° (P180) pulse is obtained from the minimum initial amplitude of the FIDs. Given the linear relation between pulse flip angle and pulse duration, the pulse duration of the 90° (P90) pulse is calculated as one half of the 180° pulse duration [196].

Keifer [128] suggests to extend the range over which the pulse width is run to 450°. Deviations from the expected sinusoidal response allow the user to evaluate the sample and spectrometer operation on nine different aspects. Four of the aspects, also noticeable in the reduced array over only 180°, are often applicable to the multiphase flowmeter configuration. The main problem is the large diameter of the sample in comparison with the r.f. coil diameter. Appendix B shows that this results in a very inhomogeneous r.f. field in which the center of the sample will always experience a stronger r.f. field than the sample at the ends of the r.f. coil. The null at 180° is the weighted average of the more than 180° excitation at the center and less than 180° excitation at the ends of the r.f. coil. This averaging effect is even stronger for the 90° pulse. It is represented in a 90° pulse width larger than half of the 180° pulse width. The 180° pulse width is on its turn larger than half of the 360° pulse width. Since the second symptom of r.f. inhomogeneity is a smooth albeit decaying curve, the ratio of the 450° to the 90° pulse width shows to which extent $B_1$ is inhomogeneous. Depending on the

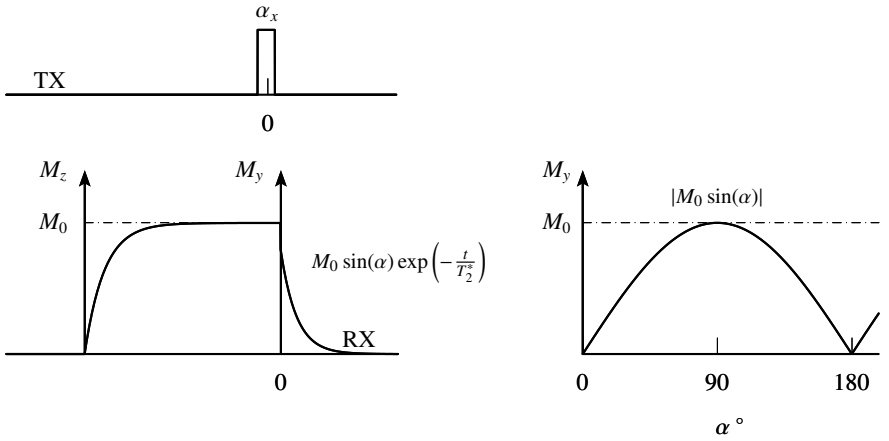


**Figure 2.19**: AUTOP90 pulse sequence showing the evaluation of the magnetization. The pulse length, $\Delta t_p$, is varied in a series of FID experiments, while the r.f. pulse amplitude, RFA0, is kept constant. Because the flip angle, $\alpha$ of a rectangular pulse is a linear function of the pulse length, the correct settings of the 90° and 180° pulse can be derived from a plot of the magnitude of the NMR signal as function of the pulse length.

probe design, the typical value ranges from as low as 50% to as high as 98%. On account of the use of samples bigger than the sensitive region of the r.f. coil, lead pickup intensifies the artifact that different parts of the sample experience measurably different field strengths.
Furthermore the system suffers from off-resonance effects due to inhomogeneities in the $B_0$ field. A 180° pulse around $B_{\text{eff}}$ leaves a residual dispersion signal in the xy plane and the null is lost. Because the bandwidth of a low-power pulse decreases, the effect becomes more pronounced as the r.f. field stength decreases.
Finally, a relaxation delay shorter than $5T_1$ will provide a skewed sinusoidal. The 180° and 360° nulls are still usable. However, the maximum signal of the 90° pulse will shift to smaller pulse widths, while the maximum of the 270° pulse will shift to larger pulse width. The more severe the $T_1$ abuse, the larger the shift will be.

#### 2.3.3.2 ALPHA3 method

A disadvantage of the general accepted methods in which the NMR signal of an AUTOP90 or $\alpha - 2\alpha$ sequence is peaked, is the relative broad maximum around the desired 90° flip angle. In search of more sensitive methods, stimulated echo pulse sequences are frequently used, such as the $\alpha - 2\alpha - \alpha$ method [177]. This method, however, does not take into account that the rise and fall times for r.f. pulses of different length are not necessarily the same. Perman et al. [200] got around this problem with the ALPHA3 method that has the same underlying stimulated echo principle. It consists of three identical pulses of flip angle, $\alpha$, as illustrated in Figure 2.20. The first and second pulse are separated by a time interval $\tau_1$ and the second and

third pulse by a time interval $\tau_2$. Hahn [87] demonstrated that such an r.f. train can create up to five distinct echoes if $2\tau_1 < \tau_2 < T_2$. Following the same reasoning as for the occurance of an echo after the Hahn spin echo sequence in section 2.3.2, a primary spin echo is formed at a time $\tau_1$ after the second r.f. pulse. With the second r.f. pulse, part of the $M_y$ component is stored into the longitudinal polarization along the z-axis. In this state only $T_1$ relaxation will occur and the dephasing during $\tau_1$ will be preserved [37]. When this magnetization component is brought back into the transverse plane by the third r.f. pulse, rephasing leads to a stimulated echo at time $2\tau_1 + \tau_2$. The last r.f. pulse generates as well three additional spin echoes. The third and fourth spin echoes are essentially primary echoes corresponding to the FIDs due to the second and first pulse respectively. The second spin echo is an imaging echo of the primary spin echo, whose magnetic moment de- and rephases a second time.

The ALPHA3 stimulated echo pulse sequence offers three possibilities of setting the correct pulse length of a 90° pulse. The first method is peaking the amplitude of the stimulated echo, $A_{ste}$, which is proportional to $\sin^3(\alpha)$. Secondly $\alpha$ can be calculated from the ratio

$$\frac{A_{ste}}{A_{pe}} = 2\cos^2(\alpha/2) \tag{2.26}$$

of the amplitudes of the stimulated echo to the primary echo, $A_{pe}$. It has as advantage that $\alpha$ can be calculated immediately after each iteration. This gives an indication in the right direction of adjusting $\Delta t_p$, which speeds up the total calibration procedure. Unfortunately the maxima of both functions around the desired 90° flip angle are rather broad with a corresponding low sensitivity. To this end, Perman et al. [200] proposed to study the amplitude of the third spin echo, $A_{3se}$ instead. For $\tau_1 \ll T_1$ this amplitude is described by

$$A_{3se} \propto M_0 \cos(\alpha)\sin(\alpha)\sin^2(\alpha/2), \tag{2.27}$$

which exhibits a sharp minimum for both 90° and 180° pulses. However, this improved accuracy is in practice reduced by the residual dispersion signal around the null, so that the AUTOP90 method, involving FID experiments, is preferred.

The same routine can be used to determine the soft-pulse settings as well, but in that case the strength of the pulse is varied instead of the pulse duration, since the latter would change the bandwidth. Above all, a background gradient should be applied for selective pulses.

### 2.3.4 The $T_1$ longitudinal relaxation time

Inversion recovery [254] is used for the measurement of the longitudinal relaxation time. A time interval of at least $5T_1$ makes sure that the magnetization of the sample reached at least 99% of the equilibrium magnetization before it is subjected to the actual pulse sequence. The pulse sequence, shown in Figure 2.21, starts with a 180° pulse that inverts the magnetization vector. Because of longitudinal relaxation, the z-component, $M_z$, begins to recover to thermal equilibrium. With a 90° applied at various times $\tau$, the remaining longitudinal magnetization

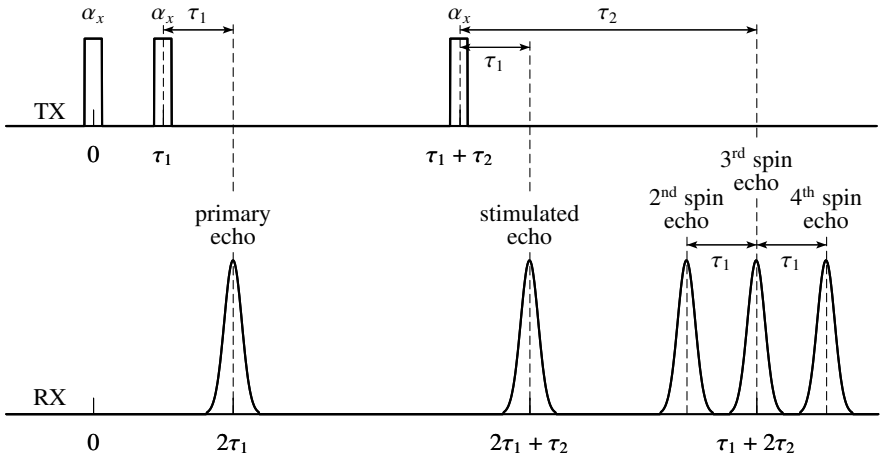


**Figure 2.20**: Stimulated echo pulse sequence for nonselective waveforms. Application of three r.f. pulses creates two FIDs (not shown) after the first two pulses and up to five distinct echoes. A primary echo at $\tau_1$ after the second pulse, a stimulated echo at $\tau_1$, a second spin echo at $\tau_2 - \tau_1$, a third spin echo at $\tau_2$, and a fourth spin echo at $\tau_2 + \tau_1$ after the third r.f. pulse [200].

is flipped into the x'y'-plane. The initial amplitude of the generated FID is described by the solution of Bloch equation 2.15:

$$M_y(\tau) = M_0 \left(1 - 2\exp\left(-\frac{\tau}{T_1}\right)\right). \tag{2.28}$$

The $T_1$ relaxation time is obtained from a fit of the FID amplitudes with this function.
When the $T_1$ time is more or less known beforehand, it can be determined much faster with the null method after Carr and Purcell [42]. This method uses the inversion recovery pulse sequence as well, but $\tau$ is only varied over a range in which the amplitude of the FID is expected to become zero. $T_1$ may be calculated directly from time delay $\tau_0$, corresponding to this FID, by using the relation $\tau_0 = T_1 \ln(2)$.

### 2.3.5 The $T_2$ transverse relaxation time

Self-diffusion in liquids limits the precision of the determination of long $T_2$, a characteristic property for low viscous fluids, with the method proposed by Hahn [87]. Also the measurement itself takes a long time, because a minimum repetition time of $5T_1$ is required to regain a longitudinal magnetization of at least 99% of the thermal equilibrium magnetization before the next spin echo is generated. Carr and Purcell [42] therefore developed a pulse sequence that takes the inhomogeneities in $\mathbf{B}_0$ into account, but saves time and can eliminate the reduction of the amplitude of an echo due to self-diffusion. Meiboom and Gill [173] optimized this

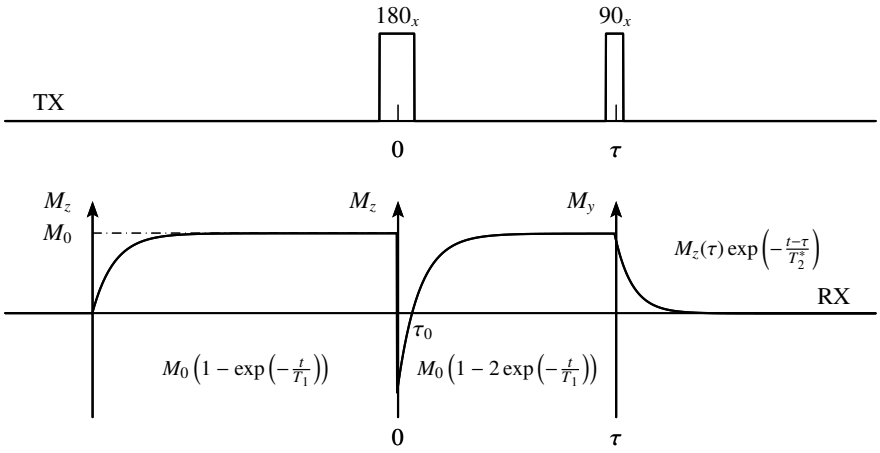


**Figure 2.21**: Diagram of the inversion recovery pulse sequence. a 180°-pulse inverts the magnetization that is initially in thermal equilibrium with the $\mathbf{B}_0$-field. Next the recovery in time of the maximum disturbed magnetization, $M_z = -M_0$, towards thermal equilibrium is observed by means of an FID, generated by the 90°-pulse at $t = \tau$.

sequence later on, so that a small deviation from the exact 180° pulse can no longer cause a cummulative error in the result.

In this CPMG-method, a single 90°-pulse is used to obtain the envelope of the spin echo amplitudes without requiring that the longitudinal magnetization returns to its thermal equilibrium. This is achieved by starting the pulse sequence with a Hahn spin echo sequence. At $t = 0$ a 90°-pulse along the x'-axis flippes the longitudinal magnetization into the x'y'-plane, followed by a 180°-pulse along the y'-axis at $t = \tau$ that causes a spin echo at $t = 2\tau$. Henceforth the individual magnetic moments will fan out again, and the echo decays in the same way as it is formed. If next a second 180°-pulse is applied along the y'-axis at $t = 3\tau$, the individual magnetic moments recluster again at $\tau$ time units after this pulse and an echo is formed at $t = 4\tau$. When this process of applying 180°-pulses along the y'-direction is continued throughout the natural lifetime of the nuclear signal, N echoes of decreasing amplitude are formed. Because each 180°-pulse reverses the direction of the precessing motion, the phase change by diffusion on the $n^{th}$ echo is reduced by a factor $n^2$ with respect to the measurement of the same echo with Hahn's method [42]. This implies that the decay caused by diffusion can be eliminated as long as N is made large enough. The $T_2$ relaxation time can be obtained from the envelope of the echoes that decays exponentially with

$$M_y(t) = M_0 \exp\left(-\frac{t}{T_2}\right), \tag{2.29}$$

as illustrated in Figure 2.22.

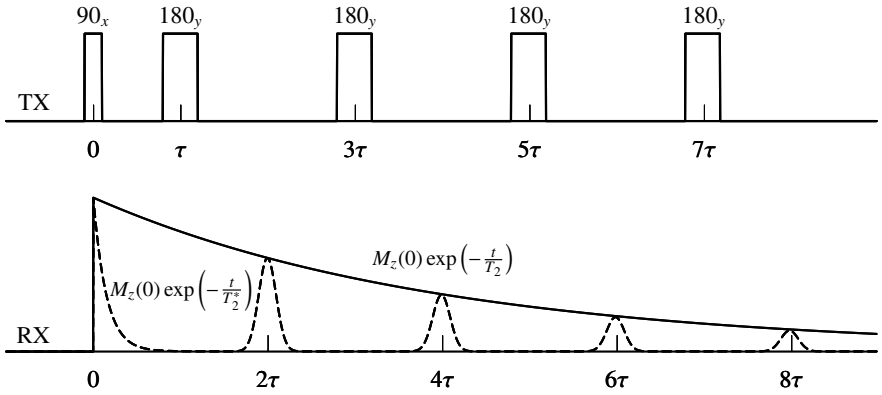


**Figure 2.22**: Diagram of the CPMG pulse sequence. A single 90°-pulse is used to obtain the envelope of the spin echo amplitudes without requiring that the longitudinal magnetization returns to its equilibrium. This is accomplished by initiating the measurement at $t = 0$ with a 90°-pulse, followed by a series of 180°-pulses. The time interval between the successive 180°-pulses is twice the time interval, $\tau$, between the 90°- and the first 180°-pulse, so that echoes occur midway between the 180°-pulse. The envelope of the succesive echoes decays exponentially with time constant $T_2$.

### 2.3.6 Effect of Pulsed Field Gradients

Each flowmeter probe is equipped with a pulsed field gradient (PFG) in either the y-direction (streamwise direction) or the x-direction of the laboratory frame, between which can be switched manually. With this field gradient a linearly varying field across the sample space can be applied on purpose in addition to the much larger polarizing field $\mathbf{B}_0$. Since the pulsed field, $\mathbf{G} \cdot \mathbf{x}$, is parallel to $\mathbf{B}_0$, there is a linear relation between Larmor frequency

$$\omega(\mathbf{x}) = -\gamma B_0 - \gamma \mathbf{G} \cdot \mathbf{x} \tag{2.30}$$

and the position in the direction of the field gradient $\mathbf{G}$. The notation for a field gradient in the x- and y-direction is $G_x$ and $G_y$. Because of the unique local dependence of the Larmor frequency on space, pulsed field gradients form the basis of imaging (to which slice selection mentioned in section 2.2.2 belongs), as well as NMR techniques aimed at the determination of parameters related to the movement of spins such as self-diffusion coefficients or flow velocities. The procedures that make use of pulse field gradients can be subdivided into two categories. Depending on the instant at which the pulsed field gradients are applied in the pulse sequence, their working principle is based on the distinction in local Larmor frequency or on the local phase shifts.

Slice selection is an application belonging to the first category of frequency based methods. It uses the gradient field during r.f. excitation to select a plane through the sample with a band limited pulse. In frequency encoding, a gradient field is likewise turned on during acquisition. The result of this read gradient is an NMR spectrum in which the resonance frequency

is proportional to the position of the spin in the direction of the gradient. The amplitude of the spectrum is proportional to the number of spins in a plane perpendicular to the direction of the gradient.

In measurement methods based on local phase shifts, the pulsed field gradient is turned on one or multiple times between r.f. excitation and acquisition to give the transverse magnetization vector a specific phase angle. While the field gradient pulse is applied, each transverse magnetization along the direction of the field gradient has its own Larmor frequency. If the pulsed field gradient is turned off, all spins experience again the same Larmor frequency, because the magnetic field returns to its original magnitude $B_0$. The phase angle $\phi$ of the transverse magnetization with the rotating coordinate system, on the contrary, is not identical. Dependent on the situation, in specific if the spins are stagnant or move in the direction of the field gradient, the phase shift is a measure for the location of the spins (phase encoding in imaging) or for the diffusion-coefficient or macroscopic velocity of the medium (see section 3.2). Pulsed field gradients can also be used to visualize permanent field inhomogeneities such as the Fieldmap procedure described in section 2.3.7.

The locally enhanced dephasing due to the application of field gradients is a major problem in NMR measurements, since it results in a fast disappearance of the signal [127]. Hoult [107] proposed to refocus the transverse magnetization vectors in slice selection experiments such that all spins are in phase in the middle of the formed echo. This procedure is also effective in other PFG methods that do not concern phase encoding and in which the gradient is turned on for a longer period. It should be noted that a rectangular slice selective field gradient is only effective during one half of the pulse. There are two ways to reverse the gradient dephasing: (i) With a gradient in the same direction of opposite sign, a gradient echo (GE) is formed with maximum amplitude at the moment that the spins get into phase. (ii) With a gradient in the same direction of the same sign preceded by a hard 180° pulse at time delay $\tau$ after the excitation pulse, a standard spin echo (SE) is produced at time $2\tau$. Contrary to the spin echo, the signal strength of the gradient echo is not compensated for attenuation by inhomogeneities in the $\mathbf{B}_0$-field and decays with $T_2^*$. On the other hand the gradient echo pulse sequence takes less time, since any excitation pulse can be used to obtain an echo. In Figure 2.23 both methods are compared for selective and nonselective excitation pulses.

#### 2.3.6.1 Phase unwrapping

The phase of an NMR signal, $s_n = s(n\delta)$ consisting of N consecutive values with sampling interval $\delta$, is defined as the angle between the magnetization vector and the axis of the rotating frame of reference along the cosine modulated signal component, $s_{\mathrm{Re}}(n\delta)$. Naturally the local resultant phase shift, $\phi$, is determined via the inverse tangens of the quadrature detected orthogonal components of the NMR signal in frequency space [2]

$$\phi = \mathrm{ARG}[S(e^{i\omega_k})] = \arctan\left(-\frac{S_{\mathrm{Im}}(e^{i\omega_k})}{S_{\mathrm{Re}}(e^{i\omega_k})}\right), \tag{2.31}$$

[2] See for this unusual notation the convention of the complex plane in Figure 2.13. Please note that the RINMR software follows the standard definition of a complex plane with the positive Im-axis in the opposite direction.

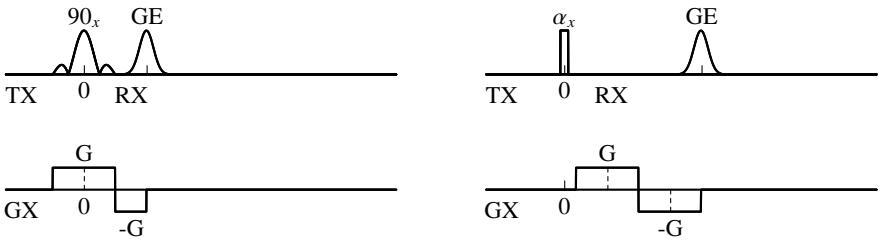


(a) gradient echo formation

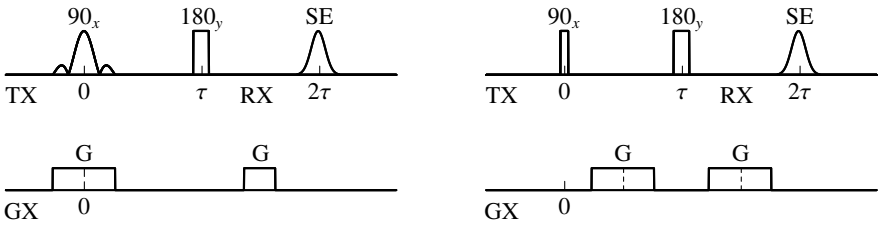


(b) spin echo formation

**Figure 2.23**: Overview of the simplest pulse-sequences to produce either gradient or spin echoes in combination with pulsed field gradients. In the left column, the sequence is given for a selective excitation pulse. Because a rectangular selective gradient is only effective during one half of the pulse, the transverse magnetization vectors are refocused with a gradient that lasts half as long as the initial gradient. For a nonselective excitation pulse both gradients have the same duration, as the right column illustrates.

where the step size of angular frequency, $\omega_k = 2\pi k/N\delta$ with $k = -\frac{N}{2}, ..., \frac{N}{2}$, is determined by the fast Fourier transform (FFT) of the NMR signal. A problem arises when the phase exceeds the boundaries $-\pi$ and $\pi$ of the phase plane, revealed by discontinuities in the phase diagram (see Figure 2.25(a)). The procedure to correct the obtained phase by removing the discontinuities is called phase unwrapping [141, 244].

The unwrapping procedure initially computes the difference between the principle values of the phase at adjacent frequencies $\omega_{k-1}$ and $\omega_k$. Whenever this difference is larger than a threshold value of $\pi$, the program ascertains a discontinuity at frequency $\omega_k$. Henceforth integer multiples of $2\pi$ are added to the principle value of the phase till the phase estimates become arbitrarily close to permissible phase values:

$$\mathrm{ARG}[S(e^{i\omega_k})] = \{\mathrm{ARG}[S(e^{i\omega_k})]\}_{\mathrm{mod}\,2\pi} \qquad \forall\omega_k \in \Omega. \tag{2.32}$$

Whenever the phase sampling is fine enough, unwrapping will yield a continuous phase diagram. Unfortunately it is not possible to estimate a priori how large the number of samples N should be to accurately unwrap the phase. Especially the limited selection of sample interval $\delta$ to choose from, limits the accuracy of phase measurements with the DRX console.

### 2.3.7 Fieldmap

Fieldmap [33] is a gradient shimming procedure that maps the spatial inhomogeneities in the permanent magnetic field. As the local field variations indicate which shim increments are needed to minimize field inhomogeneities, the field homogeneity can be maximized in very few iterations. This is a considerable reduction in time required for shimming. If all three spatial encoding gradients are available, a full three dimensional image of the inhomogeneities in the $\mathbf{B}_0$-field at the sample can be measured [33, 203]. Because the flowmeter's NMR system is equipped with merely one pulsed gradient per probe head, only the one-dimensional procedure for optimization of the shims, regarding gradient corrections in the y-direction, is considered.

The one-dimensional Fieldmap procedure, depicted in Figure 2.24, determines the static field deviations of the nominal value $\mathbf{B}_0$ as function of y, $B_i(y)$. It consists of two sequentially applied gradient echo pulse sequences. With a linear read gradient, $G_y^{re\phi}$, the spatial y-coordinate is encoded during acquisition and read out as frequency component

$$\Delta\omega(y) = \omega(y) - \omega_0 = -\gamma G_y^{re\phi} y \tag{2.33}$$

with respect to the r.f. carrier frequency $\omega_0$ at the isocenter, $(x, y, z) = (0, 0, 0)$, of the magnet. The magnitude of the Fourier transformed NMR signal is the one-dimensional projection image of the spin density in the corresponding xz-plane perpendicular to the y-axis. From the resolution of the FFT is derived that the spatial resolution is equal to

$$\Delta y = \frac{2\pi}{N\delta\gamma|G_y^{re\phi}|}, \tag{2.34}$$

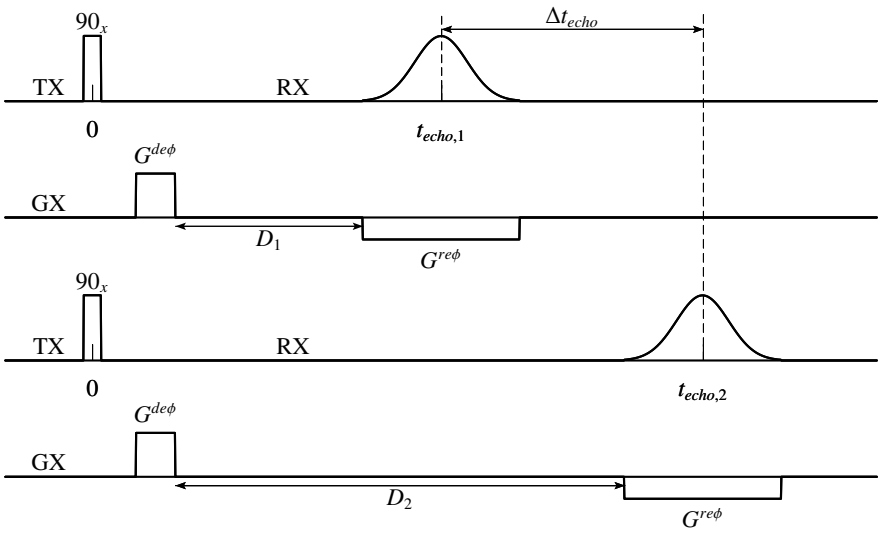


**Figure 2.24**: Diagram of the Fieldmap pulse sequence. By means of two sequencially applied gradient echo sequences with a different delay between the gradient pulses, an image of the permanent field inhomogeneity, $B_i(y)$, is reconstructed.

when the acquisition window consists of N data points at sampling interval $\delta$. As follows from equation 2.30, the actual local frequency offset is defined by the sum of the field due to the imposed gradient and the field inhomogeneity. Accurate encoding requires, to this end, that the imposed read gradient is much stronger than the existing field gradient due to field inhomogeneities.

Fieldmap determines the permanent field inhomogeneities based on the full phase information available in the NMR signal. Because phase is quite sensitive to field inhomogeneities, a frequency encoded FID gives insufficient accuracy and a gradient echo is used instead. A spin echo cannot be used, on account of its nature to rephase field inhomogeneities. Following the excitation pulse, the transverse magnetization is first dephased with a rectangular gradient pulse of amplitude $G_y^{de\phi}$. A time delay $D$ later, the transverse magnetization is rephased again with a gradient pulse, $G_y^{re\phi}$ of opposite sign, which is left on after complete rephasing to generate a frequency encoded signal. If the time integral of both echo pulses equals zero at time $t_{echo}$, the gradient echo reaches its maximum amplitude. At this moment, the phase evolution caused by the imaging gradients is undone. However, the evolution of the phase caused by the field inhomogeneity, $B_i(y)$, is additive to the phase evolution caused by the imaging gradients itself. In this way, the phase of the NMR signal at $t_{echo}$, neglecting the

duration of acquisition, will only depend on the resonance frequency offset $\Delta\omega_i(y)$:

$$\begin{aligned}\phi(y, t_{echo}) = &\quad \Delta\omega_i(y)t_{echo} + \phi_0(y) \\ = &- \gamma B_i(y)t_{echo} + \phi_0(y),\end{aligned} \tag{2.35}$$

where $\phi_0(y)$ is the unknown phase offset resulting from experimental conditions. It can be eliminated by taking the phase difference of two identical experiments performed with different echo times.

$$\begin{aligned}\Delta\phi(y, \Delta t_{echo}) = &\quad \phi(y, t_{echo,2}) - \phi(y, t_{echo,1}) \\ = &- \gamma B_i(y)\Delta t_{echo}.\end{aligned} \tag{2.36}$$

From rewriting this equation, the image of the field inhomogeneities in the y-direction is found to be

$$B_i(y) = -\frac{\Delta\phi(y, \Delta t_{echo})}{\gamma\Delta t_{echo}}. \tag{2.37}$$

Figure 2.25 shows this one dimensional fieldmap procedure for different values of the $Z^2$ shim, which also produces quadratic variations of field strength in the x and y-direction [175]. With $G_y^{de\phi} = -12.8$ mT m$^{-1}$, $G_y^{re\phi} = 6.4$ mT m$^{-1}$ and an acquisition window of N = 2048 data points at sampling interval $\delta = 1$ $\mu$s, gradient echoes are obtained for $D_1 = 200$ $\mu$s and $D_2 = 2000$ $\mu$s. Even for the short echo times, the phase spectrum is wrapped (see Figure 2.25(a)). After unwrapping, phase jumps of one or multiple times $2\pi$ are still observed in the unwrapped phase and the phase difference, illustrated in Figure 2.25(b) and 2.25(d). The field inhomogeneities in the permanent field are so strong that the phase difference between two adjacent frequencies can exceed the threshold value of $\pi$. As a result of the strong gradient present in the permanent field in proportion to the read gradient $G_y^{re\phi}$, spatial encoding is not accurate either. Nevertheless, this is no big deal for shimming where an indication of the trend is already a major help in speeding up the procedure. To this end, the signal is additionally manually unwrapped presuming a monotonic decreasing phase as shown in Figure 2.25(c). This results into smooth phase difference spectra (Figure 2.25(e)). How the convex parabola shape of the mapped field developes to concave while increasing the value of $Z^2$ on the potentiometer is illustrated in Figure 2.25(f).

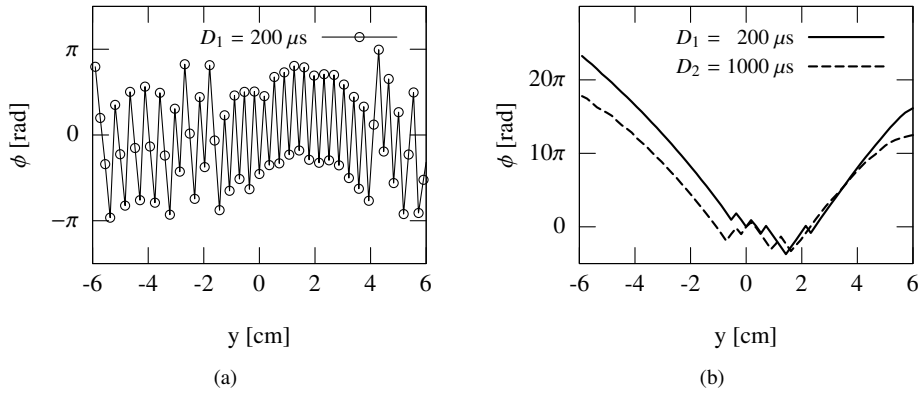


**Figure 2.25**: Intermediate stages of the Fieldmap procedure while changing the $Z^2$ shim. The transverse magnetization is dephased with $G_y^{de\phi} = -12.8$ mT m$^{-1}$ and acquired in 2048 data points at sampling interval $\delta = 1$ $\mu$s, while frequency encoding gradient $G_y^{re\phi} = 6.4$ mT m$^{-1}$ is turned on. When the phase (a), calculated from the spectrum of the gradient echo, is unwrapped (b) there are still discontinuities present.

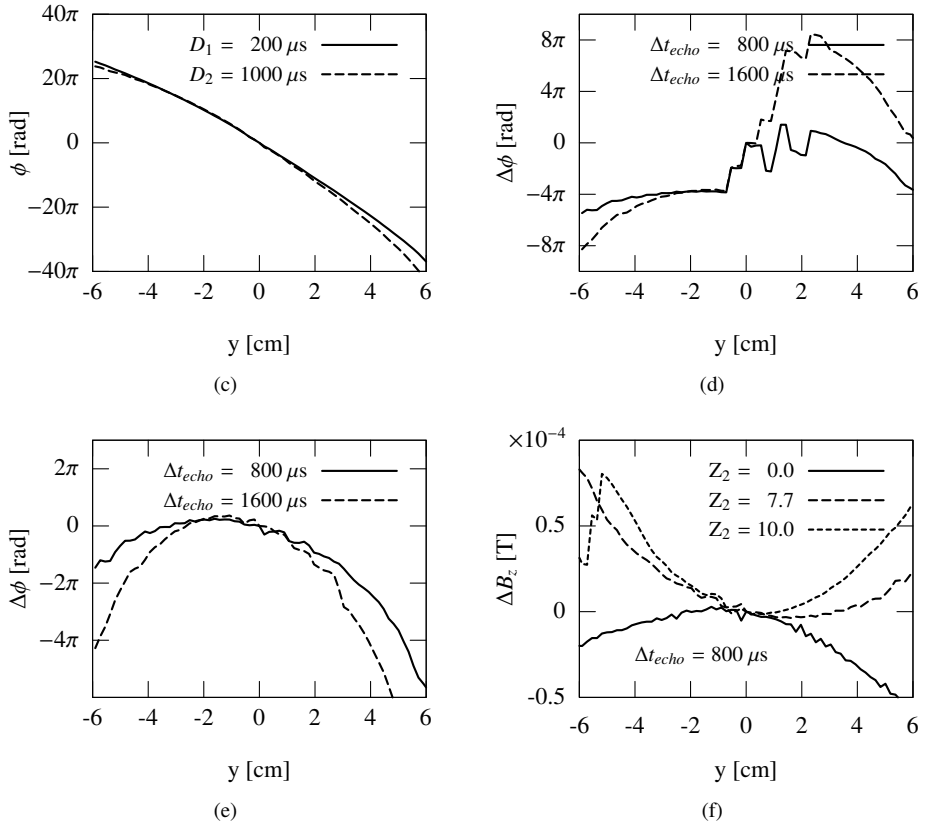


**Figure 2.25**: (continued) These staircases with steps of multples of $2\pi$ are also observed in the phase difference (d) between $D_1 = 200\ \mu$s and $D_2 = 1000\ \mu$s or $2000\ \mu$s respectively. An additional manual correction on the unwrapping, presuming a monotonic decreasing phase, gives the expected phase spectrum (c) and continous phase difference (e). The field inhomogeneity $B_i$ (f) derived from the manual corrected phase difference is a parabola that turns from convex into concave for an increased value of the $Z^2$ potentiometer.

# Chapter 3

# Measurement Methods for the NMR Flowmeter

This chapter describes the working principle of the two NMR methods used in this research to determine the liquid flowrate in a gas-liquid two-phase flow. The $T_1$ Relaxation Residence Time method (section 3.1) is a Rapid Passage method that works with a polarizing magnet of uniform field strength, while the PGSE method (section 3.2) is a velocity Phase Encoding technique that emloys pulsed field gradients. Both methods only use the cumulative signal of the liquid volume enclosed by the r.f. coil. Furthermore it is assumed that the proton density of the gas phase is so low, that the NMR signal fully originates from the liquid phase.
Also no imaging techniques that solve the velocity field two-dimensionally were applied. Besides the fact that imaging pulse sequences take longer, the comprehensive analysis to obtain the average flowrate from the snap-shots increases the processing time considerably, such that real-time flow measurements become unfeasible. After all, only the average flow velocity is usually of interest to this flowmeter application. Regarding the implemented methods to determine the liquid flowrate, the time resolution of the $T_1$ Relaxation Residence Time method is much better than that of the PGSE method. The former, on the other hand, depends on many calibration parameters, like the $T_1$ and $T_2$ relaxation times, that are on their turn a function of temperature, pressure and viscosity. The use of pulsed field gradients makes the PGSE method unsensitive to this.

## 3.1 $T_1$ Relaxation Residence Time Method

Practically all suggested NMR multiphase flowmeters with applications in the oil or nuclear industry work with a plain homogeneous polarizing magnet and do not rely on (pulsed) field gradients. The methods employed for the determination of the liquid velocity can be classified into three types that all have their own limitations.

The first commercially available NMR flowmeter, produced by Badger Meter Manufacturing [76, 77] and later improved with slice selection by King et al. [133], obtains the flowrate with a Time-of-Flight technique from the pulse frequency of the NMR signal in a detector coil downstream of a continuously tagging coil. This method has as main advantage that the measurement accuracy only depends on the precision at which the tagged liquid arrives at the detector coil. However, the accuracy is poor for low velocities and is affected as well by non-uniform velocity profiles that 'smear out' the tag. Furthermore the $T_1$ has to be within a suitable range: no adequate polarization is obtained if $T_1$ is too large, while the meter loses linearity if $T_1$ is too small. Beause of the availability of sufficient cheaper alternative single-phase flowmeters, it was not cost-effective to keep this type of NMR flowmeter on the market.

Among others, Lew's suppression method [154] belongs to a different group of Time-of-Flight techniques. They first destroy the magnetization with a 90° pulse to derive the flowrate subsequently from the rebuild magnetization [154] or the inflow of fresh spins [134, 153] in the same r.f. coil. In the form described, these methods are only suitable for low velocity flows. Solvent suppression techniques, known from NMR spectroscopy, involving the use of differences in the chemical shift and the $T_1$ relaxation time to suppress the signal from one molecular species can handle high velocity flows, such as the water-cut measurements by Lakshmanan et al. [148]. A disadvantage of the advanced suppression methods is the strong magnetic field required for the narrow-band selective excitation pulses, while electromagnets are unsuitable for the harsh and hard-to-reach environment for which the multiphase flowmeters are developed.

Other flowmeters [143, 144, 214] use an Efflux method in which the flow velocity is determined from the decrease of the CPMG signal by the outflow of net magnetization. The signal analysis applied by Krüger et al. [143, 144] has the important advantage that the fit of the full CPMG signal with iso-velocity efflux curves additionaly provides the velocity distribution. Because of the long response time, this method is too slow to get meaningful readings for a pulsating multiphase flow and is unfortunately only of use for pseudo stationary flow. To avoid this problem Pusiol [214] suggests a method based on the initial linear part of the CPMG signal where the directional coefficient of the fit is a measure for the average flow velocity. However, the velocity has to be high enough to determine the directional coefficient at required precision. Also, because non-uniform velocity profiles affect the signal linearity. This results in a bulky flowmeter, since adequate magnetization is only obtained when the polarizing magnet is sufficiently long.

Finally, a few flowmeters implement Rapid Passage methods. They measure the gain of magnetization the nuclei obtain in the time spent in the polarizing magnetic field. For flow measurements it is therefore important that, at the moment of detection, thermal equilibrium is not reached and that the magnetization is not manipulated by previous measurements. Lynch and Segel [163] have introduced a technique to measure the flowrate of relatively high single-phase flows. Morris et al. [178] claim an extension of this method, which is suitable for the relatively low single-phase flowrates. In several patents [16, 134] Rapid Passage is used for holdup determination and combined with alternative (NMR) techniques that provide

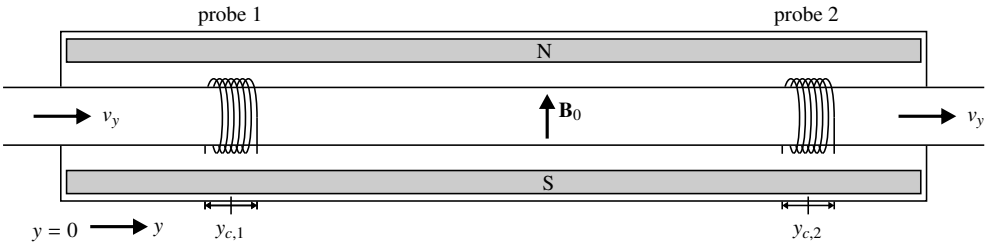


**Figure 3.1**: Schematic drawing of the NMR multiphase flowmeter. The fluid passes the magnet from left to right with average velocity $v_y$. The apparatus is made up of a permanent NdFeB rare earth magnet with an uniform field strength $\mathbf{B}_0$ of 0.331 T in the z-direction that polarizes the spin magnetic moments of the nuclei and two 12 cm long r.f. coils that detect the NMR signals. The probes are situated on $y_{c,1} = 0.5$ m and $y_{c,2} = 2.5$ m from the start of the magnet.

the average flow velocity. We have developed a new Rapid Passage technique that enables liquid velocity measurements of a gas-liquid two-phase flow in a flowmeter equiped with two r.f. coils. It has the advantage that it keeps the response time confined by using only initial FID amplitudes, such that precision is less affected by pulsating flows. Also the holdup determination via the signal strength is not as sensitive to velocity effects as in the previously mentioned methods, provided a calibration curve is used that is corrected for the velocity distribution.

In the $T_1$ Relaxation Residence Time method (T1RRT), outlined before in our paper [50], the NMR multiphase flowmeter uses pulsed NMR in combination with longitudinal relaxation to determine the average streamwise velocity of a bulk of fluid in a gas-liquid flow. The used set-up is schematically shown in Figure 3.1. It makes use of a polarizing magnet of uniform field strength. When the nuclear spins of the fluid enter the permanent magnet, they start to polarize in the direction of the magnetic field $\mathbf{B}_0$. The longitudinal relaxation proces that describes how the bulk magnetization vector $\mathbf{M}_z$ of the disturbed spin system returns to its equilibrium magnetization $\mathbf{M}_0$ is given by equation 2.15:

$$\frac{\mathrm{d}M_z}{\mathrm{d}t} = -\frac{M_z - M_0}{T_1} \tag{3.1}$$

with solution

$$M_z(t) = M_0\left(1 - \exp\left(-\frac{t}{T_1}\right)\right) + M_z(0)\exp\left(-\frac{t}{T_1}\right). \tag{3.2}$$

The material dependent longitudinal relaxation time $T_1$ indicates how fast the thermal equilibrium is obtained. Since the nuclei of the fresh fluid, entering the flowmeter from left ($y = 0$), were not influenced by the magnetic field before, their initial magnetization $\mathbf{M}_z(0)$ is zero and equation 3.2 reduces to

$$M_z(t) = M_0\left(1 - \exp\left(-\frac{t}{T_1}\right)\right), \tag{3.3}$$

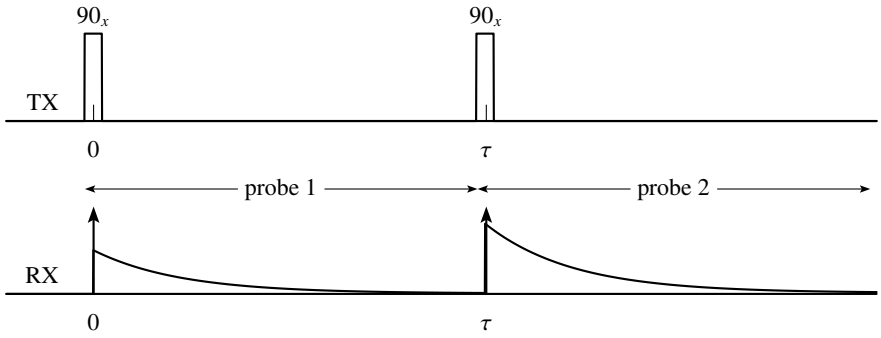


**Figure 3.2**: Diagram of the $T_1$ Relaxation Residence Time Method. To avoid cross-coupling between the probes, the NMR system electronics initially turns off probe 2, while it measures with probe 1. During the r.f. router switching time of 32 $\mu$s, immediately upon acquisition, it turns probe 1 off and starts measuring with probe 2. Within a loop the sequence is repeated a predefined relaxation delay after ending probe's 2 acquisition window.

where $t$ is the residence time of a fluid element in the $\mathbf{B}_0$-field. The residence time is proportional to the inverse of the streamwise velocity $v_y$. To begin with, an ideal plug flow is assumed for simplicity. This means that the velocity is constant over the full cross-section of the pipe and equation 3.3 can be written as

$$M_z(y) = M_0\left(1 - \exp\left(-\frac{y}{v_y T_1}\right)\right). \tag{3.4}$$

The detection of the total longitudinal magnetic moment of the nuclear spins in the fluid enclosed by each coil at two steamwise postions forms the basis of this flowmeter. To this end the r.f. coils, which have a double function, are first pulsed in order to reorient the magnetization vector over 90°. Thereafter, the r.f. coils are turned off and work as receiver coils that measure the FID. This FID is proportional to the total longitudinal magnetic moment of the spins, just before the pulse. The pulse diagram in Figure 3.2 shows how the probes are successively addressed to prevent the probes from cross-coupling, which biases the results. The length of the coil causes a gradient in the residence time in the measured volume, which implies also a gradient in the $\mathbf{M}_z$ values. The initial intensity of the detected NMR signal is therefore proportional to

$$\begin{aligned} s_y &= \frac{\pi}{4} {D_p}^2 \int_{y_c - L_c/2}^{y_c + L_c/2} s_z(y)\,\mathrm{d}y \\ &= \frac{\pi}{4} {D_p}^2 s_0 \left(L_c - v_y T_1 \exp\left(-\frac{y_c - L_c/2}{v_y T_1}\right)\left[1 - \exp\left(-\frac{L_c}{v_y T_1}\right)\right]\right), \end{aligned} \tag{3.5}$$

where $L_c$ is the length of the coil, $y_c$ the position of the center of the coil and $s_0$ the intensity of the NMR signal corresponding to thermal equilibrium magnetization $M_0$. As long as the

intensity of all FIDs are determined at a similar length of time from the 90° pulse, it is unnecessary to extrapolate the FID to its initial intensity. Alternatively, the area below the Fourier transformed FID can be used, which is common in spectroscopy. In principle it is even possible to use Hahn spin echoes instead of FIDs.
From the ratio of the initial intensity in the second coil, $s_{y,2}$, with respect to its value at the first coil, $s_{y,1}$, the streamwise velocity of the fluid is obtained. As shown in Figure 3.3(c), this ratio given by

$$\frac{s_{y,2}}{s_{y,1}} = \frac{1 - \frac{v_y T_1}{L_c} \exp\left(-\frac{y_{c,2} - L_c/2}{v_y T_1}\right)\left(1 - \exp\left(-\frac{L_c}{v_y T_1}\right)\right)}{1 - \frac{v_y T_1}{L_c} \exp\left(-\frac{y_{c,1} - L_c/2}{v_y T_1}\right)\left(1 - \exp\left(-\frac{L_c}{v_y T_1}\right)\right)} \tag{3.6}$$

has for each velocity a unique value under the condition that the $T_1$ relaxation is known and the magnetization has not reached the equilibrium state in both coils. By comparing the measured signal ratio with this curve, the velocity $v_y$ is obtained.
In case of single-phase flow, where the streamwise velocity is the only unknown, a flowmeter equiped with a single r.f. coil will do. Following Lynch and Segel [163], the velocity is obtained from a comparison of the signal intensity with the monotonically decaying function of velocity 3.5, illustrated in Figure 3.3(a) and 3.3(b).

Unlike plug flow, real flow situations have a non-uniform velocity profile. Therefore a discrete distribution of $N_v$ velocities $v_y[i]$ is used in the evaluation of the measurement technique. In this case the right hand side of equation 3.6 becomes

$$\frac{s_{y,2}}{s_{y,1}} = \frac{\sum_{i=1}^{N_v} 1 - \frac{v_y[i] T_1}{L_c} \exp\left(-\frac{y_{c,2} - L_c/2}{v_y[i] T_1}\right)\left(1 - \exp\left(-\frac{L_c}{v_y[i] T_1}\right)\right)}{\sum_{i=1}^{N_v} 1 - \frac{v_y[i] T_1}{L_c} \exp\left(-\frac{y_{c,1} - L_c/2}{v_y[i] T_1}\right)\left(1 - \exp\left(-\frac{L_c}{v_y[i] T_1}\right)\right)}. \tag{3.7}$$

The summation over the discrete velocities has, however, no effect on the trend of the intensity ratio curve and Figure 3.3(c), adapted for the velocity profile, can still be used. There is still a one-to-one relation between the average liquid velocity and the fraction of the NMR signals in both probes.

The NMR flowmeter for gas-liquid flow uses the property that gas at low pressure is normally not observable by NMR because it contains a too small number of nuclear spins. Given that the intensity of the NMR signal is proportional to the amount of nuclear spins enclosed by the coil, the liquid holdup $\alpha_L$ can be derived from the ratio between the signal intensities for multiphase flow, $s_y$, and the expected signal for single-phase flow, $s_{100\%L}$, at the same velocity $v_y$ according to

$$s_y = \alpha_L s_{100\%L}. \tag{3.8}$$

The underlying idea of the flowmeter is an equal time average of the liquid holdup in both r.f. coils. When the detected signals are analyzed in the same way as for single-phase flow, the holdup terms in the nominator and denominator of equation 3.6 cancel out and Figure 3.3(c)

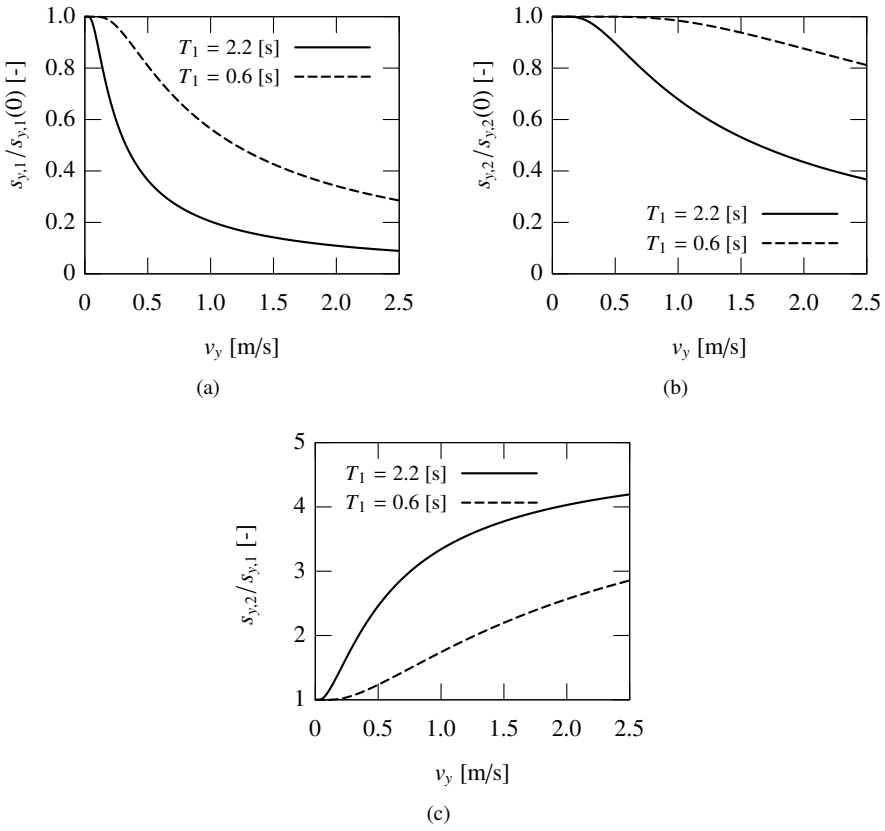


**Figure 3.3**: Variation of the NMR signal intensity in (a) probe 1 at $y_{c,1} = 0.5$ m and (b) probe 2 at $y_{c,2} = 2.5$ m with uniform flow velocity for a single-phase liquid system. (c) Ratio of the intensity of the NMR signal in the second probe $s_{y,2}$ with respect to the signal in the first probe $s_{y,1}$, which is a measure for the ensemble average of the streamwise velocity $v_y$.

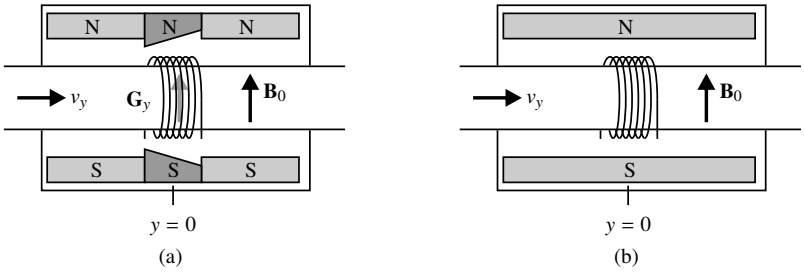


**Figure 3.4**: (a) During the gradient pulse a linear gradient $\mathbf{G}_y$ in the streamwise direction is superposed on the (b) uniform polarizing magnetic field $\mathbf{B}_0$, such that the total field strength at $y = 0$, the center of the coil, equals $\mathbf{B}_0$.

can be used again to determine the average velocity $v_y$ of the liquid phase. With the average liquid velocity and equation 3.8 the liquid holdup can be calculated. The total liquid flowrate follows than immedeately from

$$q_L = \frac{\pi}{4} D_p^2 \alpha_L v_y. \tag{3.9}$$

The technique used has one major drawback. When the magnetization is measured with a 90° pulse, the build-up of the longitudinal magnetization $\mathbf{M}_z$ has been reset to zero at pulse time $t_p$. The amplitude of the longitudinal magnetization is therefore no longer determined by the residence time in the magnet, but by the time since the last 90° pulse. Equation 3.3 should be rewritten as follows:

$$M_z(t) = M_0 \left(1 - \exp\left(-\frac{t - t_p}{T_1}\right)\right). \tag{3.10}$$

If the distance travelled by the fluid volume, $v_y \Delta t$, in time interval $\Delta t$ between two measurement pulses, is smaller than the length of the coils, the amplitude of the NMR signal is partly influenced by the previous pulse. A similar effect is observed when fluid detected in the second probe is subjected to a pulse in the first probe. Consequently, equation 3.6 can no longer be used for this situation. To obtain a signal ratio curve like Figure 3.3(c) in which the effect of the pulses is taken into account, numerical analysis is used. This shows that the fluid velocity limits the size of the time-interval between successive pulses or, in other words, the repetition rate of the sequence. That is, in this direct measurement method in which each T1RRT-sequence results in a snapshot of the flow velocity. Morris et al. [178] expose the flowing fluid intentionally, more than once, to the pulsed field. However, the flowrate has to be stable for this kind of 'influx method' that involves several repetitions at different $\Delta t$.

## 3.2 Pulsed Gradient Spin Echo Method

The use of pulsed field gradients, introduced in section 2.3.6, is a well known technique to determine fluid motion. Because of their similarity regarding spin displacement, these meth-

ods, among which the pulsed gradient spin echo method (PGSE), predominantly originate from techniques for measuring self-diffusion constants [210]. The working principle is based on the proportionality of the Larmor frequency

$$\omega_0(y) = -\gamma \mathbf{B}_0 - \gamma \mathbf{g}_y y, \tag{3.11}$$

to the streamwise position in presence of a linear field gradient $\mathbf{g}_y$ in the y-direction, which in the ideal case is identical to $\mathbf{G}_y$, as shown in Figure 3.4. On its trajectory through the gradient field, a spin experiences along the preferred direction of the gradient a continuously changing angular frequency, which is expressed in a phase shift of the transverse magnetization. In order to prevent unnecessary loss of signal through phase incoherence by the gradient Carr and Purcell [42] developed a method that makes use of spin echoes (see section 2.3.2). However, in this predecessor of the PGSE method a steady gradient is applied, which limits the maximum meaningful gradient strength substantially. During the pulses, the r.f. magnetic field must be large compared with the field variation across the sample. Besides, the bandwidth of the detection system must increase with an increasing gradient. Above all, the decay time of the acquired echo in presence of a field gradient is shorter than the decay time in a uniform field. It results in a narrow echo that is difficult to measure. McCall et al. [172] suggested therefore to use high gradient pulses between the r.f. pulses: i.e. the gradient is considerably reduced during the times at which the pulses are being applied and also at the time of the echo. This method, called PGSE, was initially used by Stejskal and Tanner [237] and Groß and Kosfeld [86] to determine self-diffusion constants. Following Packer [197], Hayward et al. [91] and Leblond et al. [150] the PGSE method is used here to study flow. Nevertheless PGSE is not qualified for all types of flow. A sufficient degree of coherence is required, which is found in laminar flow or on the short time scales of moderate turbulent flow. Randomness on the large time scales of high Reynolds turbulent flow will bias the results.

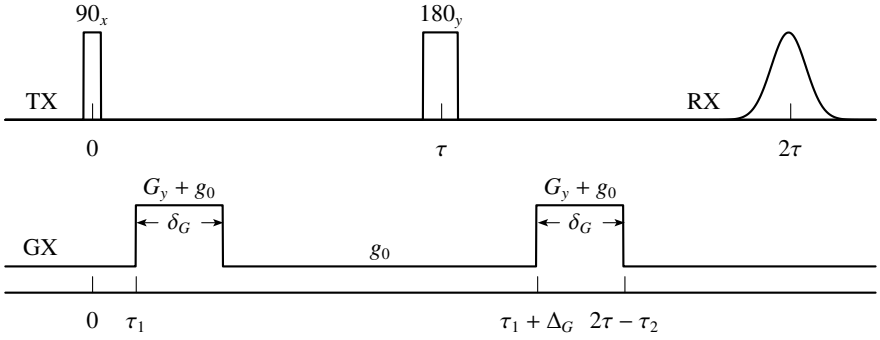


**Figure 3.5**: Diagram of the Pulsed Field Spin Echo pulse sequence. The FID signal that occurs immediately after the 90° pulse is not shown.

A pulse diagram of the PGSE sequence is illustrated in Figure 3.5. In this extensive spin echo sequence, the nuclei are subjected to a steady gradient $g_0$, which is, for at least a part, due to

the inhomogeneities in the permanent field. On a time delay $\tau_1$ after the 90° pulse a second gradient $G_y$ is turned on for a time $\delta_G$. A time $\Delta_G$ later an identical gradient pulse is applied once again between the 180° pulse and the echo. This second gradient pulse ends a time $\tau_2$ before the spin echo.

Under assumption of $\mathbf{B} = \mathbf{B}_0$ at the center of the probe ($y = 0$), a spin at position $y$ will gain a phase $\phi$ relative to a spin at the center of the probe at a rate

$$\frac{\mathrm{d}\phi}{\mathrm{d}t} = -\gamma g_y y \tag{3.12}$$

with respect to a frame of reference rotating at frequency $\omega_0 = \gamma B_0$ about the static field in absence of the gradients. The total field gradient $g_y$ equals in absence of and at the time of the pulsed gradient $g_0$ and $g_0 + G_y$, respectively. If a nucleus moves with a constant velocity $v_y$ in the positive y-direction, its position in time as a function of its initial position, $y_0$ at $t = 0$, is given by

$$y(t) = y_0 + v_y t. \tag{3.13}$$

The phase shift of the transverse magnetization is obtained by integrating equation 3.12 towards time:

$$\Delta\phi(t) = -\int \gamma g_y y(t)\,\mathrm{d}t \tag{3.14}$$

Substitution of equation 3.13 shows that the phase of the NMR signal will have both position- and flow-dependent contributions. Since the position-dependent phase shift is canceled out by the $180^\circ_y$ refocussing pulse, which mirrors the magnetization along the x-axis on account of its phase shift of 90° with the $90^\circ_x$ pulse, the analysis is limited to the flow-dependent phase shift

$$\Delta\phi(t) = -\int \gamma g_y v_y t\,\mathrm{d}t. \tag{3.15}$$

Because of the refocussing effect of the $180^\circ_y$ pulse, the total phase shift of the spin echo is evaluated in two parts that are separated by the 180° pulse. Furthermore it is assumed that the r.f. pulses have a negligible length. In the first period from $t = 0$ to $t = \tau$, the transverse magnetization gains a phase angle of

$$\begin{aligned}\Delta\phi_{0\to\tau} &= -\int_0^{\tau} \gamma g_0 v_y t\,\mathrm{d}t - \int_{\tau_1}^{\tau_1+\delta_G} \gamma G_y v_y t\,\mathrm{d}t \\ &= -\frac{1}{2}\gamma g_0 v_y \tau^2 - \frac{1}{2}\gamma G_y v_y \left(2\tau_1\delta_G + {\delta_G}^2\right).\end{aligned} \tag{3.16}$$

During the second period from $t = \tau$ to $t = 2\tau$, the transverse magnetization gains a phase

angle of

$$\begin{aligned}\Delta\phi_{\tau\to 2\tau} &= -\int_{\tau}^{2\tau} \gamma g_0 v_y t \,\mathrm{d}t - \int_{\tau_1+\Delta_G}^{\tau_1+\Delta_G+\delta_G} \gamma G_y v_y t \,\mathrm{d}t \\ &= -\frac{3}{2}\gamma g_0 v_y \tau^2 - \frac{1}{2}\gamma G_y v_y \left(2\tau_1\delta_G + 2\Delta_G\delta_G + {\delta_G}^2\right). \end{aligned} \tag{3.17}$$

Subsequently, the net gain of phase at the time of the echo

$$\Delta\phi_{2\tau} = -\Delta\phi_{0\to\tau} + \Delta\phi_{\tau\to 2\tau} = -\gamma g_0 v_y \tau^2 - \gamma G_y v_y \Delta_G \delta_G, \tag{3.18}$$

is found from the sum of both phase angles, in which $\Delta\phi_{0\to\tau}$ is negated on account of the 180° refocussing pulse. This implies that all nuclei, independent of their position, obtain the same phase shift. The effect of flow on the transverse magnetization is simply a coherent shifting in phase.

Diffusional motion, for which the PGSE sequence was originally intended, has in addition to flow an effect on the NMR signal. On account of the random path the nuclei cover in the direction of the present gradient field, their transverse magnetization develops a phase shift with respect to $-\gamma B_0 t$, the cumulative phase in absence of the field gradient. Contrary to the phase shift due to flow, the phase shift due to diffusion varies randomly across the ensemble and so causes dephasing. Callaghan [37] uses a probability model, which describes the diffusion of nuclei as a succession of random hops. Using the central limit theorem, the ensemble averaged phase shift by diffusion is then approximated with a Gaussian distribution to calculate the attenuation of the echo $\overline{\exp(i\Delta\phi)}$. For nuclei with a self-diffusion constant $D$ it is found that the ratio of the echo peak amplitude ($t = 2\tau$) at gradient $G_y$ to that at zero gradient is given by

$$\begin{aligned}\frac{s(2\tau, G_y)}{s(2\tau, 0)} = \exp\Bigg( -\gamma^2 D \Bigg[ {G_y}^2 {\delta_G}^2 \left(\Delta_G - \frac{\delta_G}{3}\right) - \frac{2}{3}{g_0}^2\tau^3 \\ - G_y g_0 \delta_G \left({\tau_1}^2 + {\tau_2}^2 + \delta_G(\tau_1+\tau_2) + \frac{2}{3}{\delta_G}^2 - 2\tau^2\right)\Bigg]\Bigg). \end{aligned} \tag{3.19}$$

The proportionality of the exponent towards $D$ makes the ratio of echo amplitudes the standard method in determining self-diffusion constant $D$.

Equation 3.18 and 3.19 demonstrate that flow and diffusion have a fundamentally different effect on the transverse magnetization. Whereas the phase memory of the nuclei in case of coherent motion by flow is conservative, it is dissipative in case of diffusion. Assuming that the effects of diffusion and flow are independent, their combined effect on the fraction of the

echo amplitude at time $2\tau$ may be described by

$$\begin{aligned}\frac{s(2\tau, G_y)}{s(2\tau, 0)} = \exp\Bigg( &- \gamma^2 D\Bigg[{G_y}^2{\delta_G}^2\left(\Delta_G - \frac{\delta_G}{3}\right) - \frac{2}{3}{g_0}^2\tau^3 \\ &- G_y g_0 \delta_G\left({\tau_1}^2 + {\tau_2}^2 + \delta_G(\tau_1 + \tau_2) + \frac{2}{3}{\delta_G}^2 - 2\tau^2\right)\Bigg]\Bigg) \\ &\exp\left(\mathrm{i}\gamma G_y \delta_G \Delta_G v_y + \mathrm{i}\gamma g_0 \tau^2 v_y\right),\end{aligned} \tag{3.20}$$

in which the attenuation is caused by diffusion, while flow is responsible for the phase shift. This equation reduces to

$$\frac{s(2\tau, G_y)}{s(2\tau, 0)} = \exp\left( - \gamma^2 D {G_y}^2 {\delta_G}^2\left(\Delta_G - \frac{\delta_G}{3}\right)\right)\exp\left(\mathrm{i}\gamma G_y \delta_G \Delta_G v_y\right) \tag{3.21}$$

if thanks to shimming the constant field gradient $g_0$, the natural field gradient in $\mathbf{B}_0$, is small. The different nature of the two effects thus allows the flow to be studied independent of diffusion. Provided diffusion does not completely dephase the nuclei before acquisition, the velocity $v_y$ can be determined from the difference in phase shift between an echo at $t = 2\tau$ without and in presence of pulsed gradient $G_y$. The use of this difference in phase shift has the additional advantage that the phase shift by the constant gradient $\gamma g_0 \tau^2 v_y$ cancels out. When the real and imaginary component of the spin echo are determined by means of quadrature detection (see section 2.2.6) the phase is calculated with [1]

$$\phi = \arctan\left(-\frac{s_{\mathrm{Im}}(2\tau)}{s_{\mathrm{Re}}(2\tau)}\right). \tag{3.22}$$

According to the definition of the r.f. pulse phases, the real and imaginary direction correspond to the x- and y-axis of the rotating frame of reference. Investigation of $s(2\tau)$ as a function of $G_y$, $\Delta_G$ or $\delta_G$ in a series of PGSE measurements is therefore a simple experimental method of obtaining velocity

$$v_y = -\frac{\Delta\phi}{\gamma G_y \Delta_G \delta_G}, \tag{3.23}$$

which is not critically dependent upon problems of obtaining a very homogeneous $\mathbf{B}_0$ [91]. Although the accuracy increases if more echoes are used, it is required that the velocity is constant in the time between the first excitation pulse and the readout of the last spin echo. The PGSE method is therefore unsuited to study flows with rapid velocity fluctutations.

Like in the $T_1$ Relaxation Residence Time method, the liquid holdup is determined by means of the intensity of the NMR signal, which is proportional to the amount of nuclear spins enclosed by the sensitive volume of the coil. The flowmeter routine also uses the property that gas in a gas-liquid flow at low pressure is normally not observable by NMR due to a too small

[1] See for this unusual notation the convention of the complex plane in Figure 2.13. Please note that the RINMR software follows the standard definition of a complex plane with the positive Im-axis in the opposite direction.

number of nuclear spins present. In order to obtain the liquid holdup of multiphase flow, the intensity of the signal peak, $s$, is compared to a reference signal representing a 100% sample of the same component, $s_{100\%L}$, at the same fluid velocity $v_y$ and pulsed gradient strength $G_y$:

$$\alpha_L = \frac{s(2\tau, v_y, G_y)}{s_{100\%L}(2\tau, v_y, G_y)}. \tag{3.24}$$

Preferably spin echoes measured in absence of pulsed field gradients are used, since the gradient causes additional attenuation that goes with noise. The total liquid flowrate

$$q_L = \frac{\pi}{4} D_p^2 \alpha_L v_y \tag{3.25}$$

follows immediately from the product between the liquid holdup and the liquid velocity.

It should be mentioned that the theory derived so far uses plug flow as starting point. Real-life pipe flows require an investigation into the validity of the technique for non-uniform flow profiles. In the first place, the gain of phase because of flow, as described by equation 3.18, is not necessarily coherent. Starting from the velocity probability function, Leblond et al. [150] show that the phase shift of the echo is unaffected by a laminar flow profile and is still proportional to the average velocity $\overline{v_y}$. The phase shift of the echo in case of turbulent flow is, on the other hand, no longer a simple linear function of the flowrate. By means of numerical calculations on a turbulent flow profile, approximated with the power law [223], they show that

$$\frac{\Delta\phi_{2\tau} + \gamma G_y \overline{v_y} \Delta_G \delta_G}{\Delta\phi_{2\tau}} \ll 1 \quad \text{if} \quad \Delta\phi_{2\tau} > -\frac{\pi}{2}. \tag{3.26}$$

As a result, the parameters $G_y$, $\Delta_G$ and $\delta_G$ should be selected such that $\Delta\phi_{2\tau} > -\frac{\pi}{2}$.
Secondly, self-diffusion in the radial direction leads, on account of the large velocity gradients that exist in laminar or developed turbulent flow, to an extra dephasing of nuclear magnetization. Hayward et al. [91] modeled this additional diffusion process in the direction of flow with an effective diffusion, which is a function of the velocity gradient and the self-diffusion constant. They showed that this effect may be neglected in general, since even normal diffusion effects may be neglected in most cases.
Finally, random turbulent velocity fluctuations in the direction of the gradient cause dephasing that results, like diffusion, in an additional attenuation of the echo. Dependent on the choice of $\Delta_G$ and $\tau$ with respect to the time scale of the turbulence, it is even possible to determine the turbulent intensity or turbulent diffusion from the signal strength of the echo [75]. Although the turbulent intensity has no significant influence on the PGSE average velocity measurements, it can affect the accuracy of the holdup determination considerably if $s_{100\%L}$ is not corrected.
The ensemble averaged phase shift of non-uniform flow is nevertheless a measure for the average velocity, as long as the rules mentioned above are observed.

Later on, the PGSE method for flow measurement has been replaced by advanced gradient methods that reduce the influence of diffusion [74, 91, 197] or the loss of coherence by any

spatial non-uniform velocity profile [40]. Our research is however limited to the naive PGSE method, since this study aims at testing the flowmeter for a simple method by which the average flow velocity is directly obtained from the NMR signal. This means independent of a model that requires recalibration for changing NMR parameters like the relaxation times. With regard to multiphase flowmeting, there are disadvantages to the PGSE method compared to the T1RRT method. It is inconvenient that the pulsed field gradients require power, the implementation is more complex and because of the series of scans the method is not suitable for non-periodic dynamic flow conditions.

# Chapter 4

# Flow Configuration and Instrumentation

Three different flow loops are used to study various possibilities of the NMR multiphase flowmeter prototype. NMR imposes substantial restrictions on the material of the pipe inside the flowmeter. It has to be nonmagnetic to prevent that the pipe itself will produce NMR emission. Because the material may neither be electrically conducting, which shields the fluid against the field of the r.f. coil, all flow loops are made of PVC.
To isolate effects, a small adjustable single-phase flow loop is used. See section 4.2 and 4.3 for its two forms. More realistic flow patterns are mimicked with the air-water two-phase flow loop described in section 4.4. First the multiphase flow algorithm is tested for relatively uncomplicated stratified flows. Furthermore, extensive testing is performed with naturally intermittent slug flows. Also the measurement principles of the conductivity techniques by which comparitive measurements are carried out have been described in detail.

## 4.1 NMR multiphase flowmeter

A detailed description of the NMR multiphase flowmeter system is given in section 2.2. The flowmeter consists of a 3 m long rare earth magnet with a uniform field strength $\mathbf{B_0}$ of 0.331 T at 20 °C that polarizes the spin magnetic moments of the nuclei. Two trifilar r.f. coils of 4 turns (12 cm long, 12 cm i.d.) surround the pipe at 0.5 and 2.5 m downstream of the magnet entry. Their function is twofold. First they are used as transmitter to excite the enclosed liquid spins. Thereafter the coils work as receiver in order to detect the resulting NMR signal. The r.f. coils are controlled with an Oxford Instruments MARAN-ultra DRX2 spectrometer, operating at a proton frequency corresponding to $\mathbf{B_0}$ of 14.1 MHz. In the NMR regions of the magnet the field homogeneity is optimized to less than 30 ppm using a shim unit. For performing PGSE measurements a pulsed field gradient in the streamwise y-direction with a nominal value $G_y$ = 42 mT m$^{-1}$ is produced using the Y-shim control. The maximum outer diameter of pipes that fit within the air gap in the polarizing magnet is 11 cm.

## 4.2 Small Laminar Flow Loop

As there is an analytical solution for the velocity profile of laminar flow, there should be a good agreement between the measurements and simulations. This makes it a perfect test to study the performance of the NMR flowmeter. To meet the requirements of the T1RRT method, there is a special flow set-up designed which ensures that the average velocity is not too small while a sufficient signal to noise ratio is achieved. The flow loop, shown in Figure 4.2, consists of a 120 m long pipe bundle that is spiralwise folded through the NMR flowmeter, occupying a cross-sectional area of 5.3 cm diameter. In this manner the flowrate and velocity distribution is the same in all pipes. Each of the twelve pipes of 9.85 mm i.d. has an entrance length of at least 75 $D_p$ before the liquid reaches the first NMR probe. The flowrate is electronically controlled using three Grundfos Magna 40-120 F circulator pumps in series and measured with the integrated system of a KROHNE Altoflux 4080K electromagnetic flowmeter having a range of 0 – 1.200 $m^3h^{-1}$ and a KROHNE IFC 090 signal converter. By means of a 510 Ω resistor the current output of the IFC 090 is converted into a voltage. Connected to an analogue input of a LabJack UE9 data acquisition card the voltage is continuously recorded on a PC from which the flowrate is retrieved later on. The sampling frequency can be set in the driving DAQ Factory Express 5.78 software (© 2008 Azeotech). Frictional heating of the liquid is reduced by means of a copper cooling coil (5 m long, 1 cm o.d. tube) that is installed in the buffer-tank and connected to the cold-water supply.

## 4.3 Small Turbulent Flow Loop

In favor of a compact flowmeter design the homogeneity of the r.f. and gradient field have been sacrificed. Both fields have only a high homogeneity in the central region of the r.f. coil. This has in particular a direct effect on the accuracy of techniques like PGSE that study the phase shift of refocussed NMR signals in presence of gradient fields. To exclude the influence, the small set-up is equipped with a 5 m long pipe of 34 mm i.d. centered in the core of the probes (see Figure 4.1). A turbulent single-phase flow can develop over 70 $D_p$ before the first NMR probe is reached. The flow is circulated with a single electronically controlled Grundfos Magna 40-120 F circulator pump. The flowrate is measured using the integrated system of a KROHNE IFM 4080 electromagnetic flowmeter with a range of 0 – 21.000 $m^3h^{-1}$ and a KROHNE IFC 090 signal converter.

## 4.4 Large Two-phase Flow Loop

Multiphase flowpatterns are characterized by non-uniformities in time as well as in space. In order to study the performance of the NMR flowmeter under these technically difficult circumstances, a horizontal two-phase air-water flow loop is constructed that operates at atmospheric conditions. Also experiments on single-phase turbulent flow can be performed in this facility. With an internal diameter of 98.6 mm the dimension of the pipe is representative for real applications in the petroleum industry. The flowloop, illustrated in Figure 4.3, is

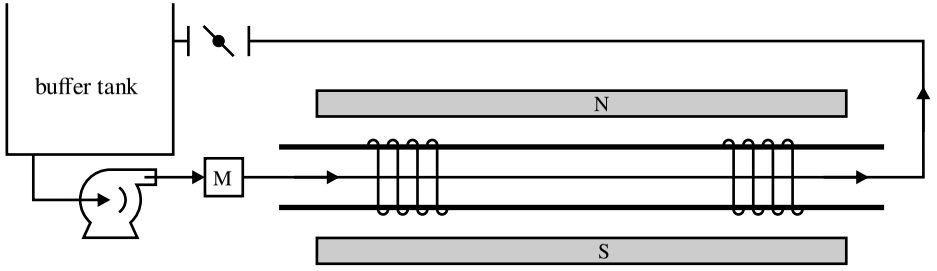


**Figure 4.1:** Sketch of the small flow loop with 34 mm inner diameter pipe.

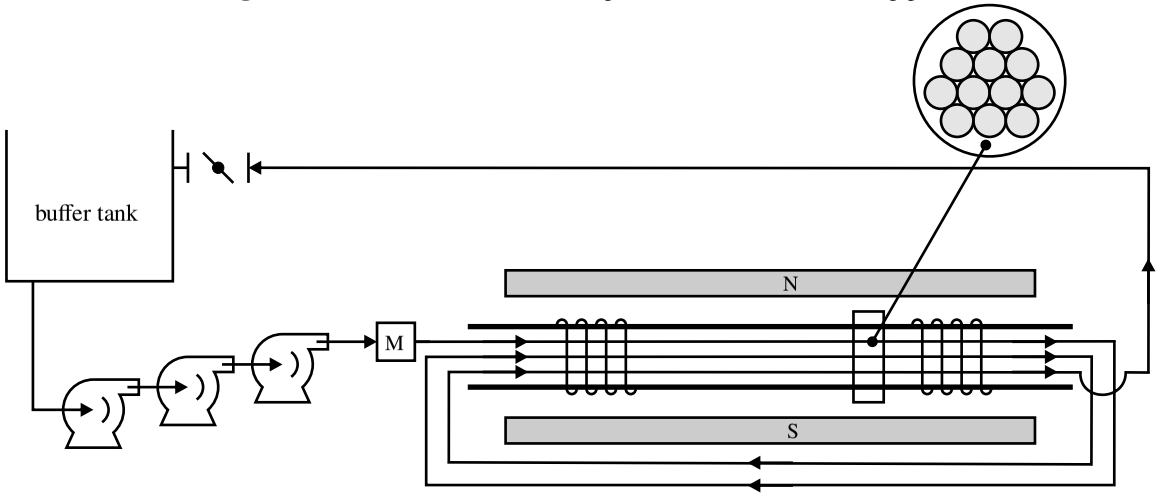


**Figure 4.2**: Schematic drawing of the laminar flow loop. A 120 m long pipe system is spiralwise folded through the NMR flowmeter. The detailed graph of the cross section of the NMR flowmeter shows how the 12 pipes cross its inner volume.

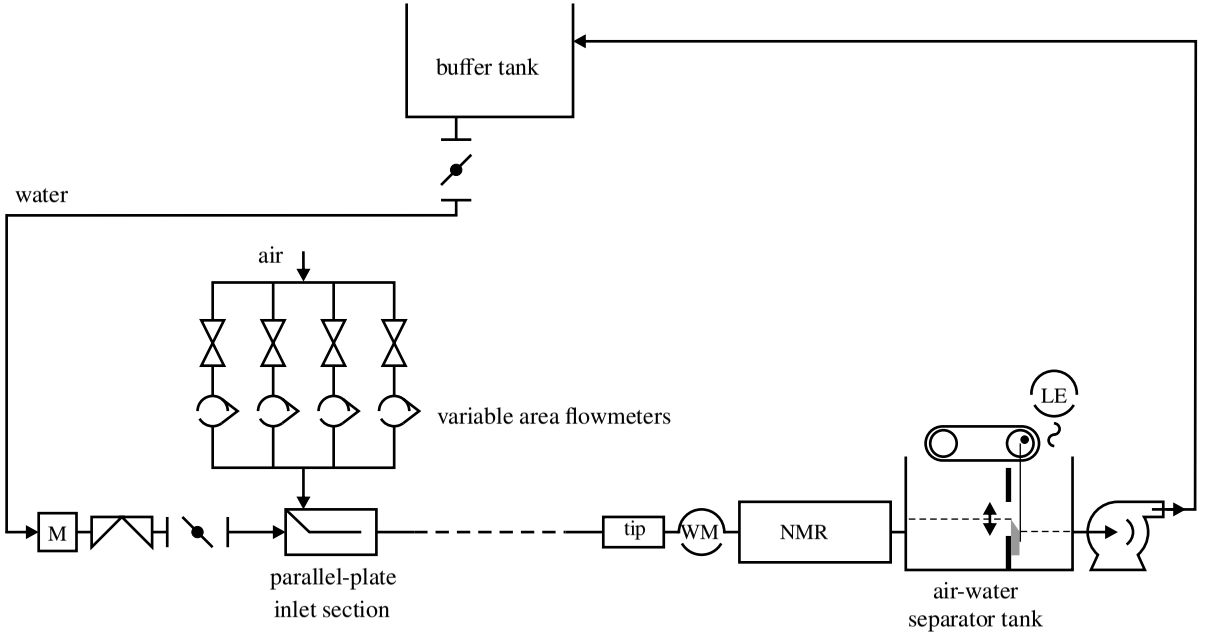


**Figure 4.3**: Schematic drawing of the large air-water two-phase flow loop with 98.6 mm i.d. pipe. The butterfly valves are installed to close the system in case of power failure (top valve) and easy drainage of the pipe (bottom valve).

gravity driven with a height difference of about 5 m between the water level in the buffer tank and the horizontal supply pipe. A Lowara Hydrovar 3.4 centrifugal pump coupled to an MJK Shuttle Ultrasonic Sensor 200570 controls the water level in the air-water separator tank by pumping tapwater back into the buffer tank. To guarantee a constant water height in case of a stratified flow, a level tank (see section 4.4.1) is integrated in the air-water separator tank.
At the beginning of the horizontal pipe, the superficial water velocity is adjusted with a diaphragm valve and measured with the integrated system of a KROHNE Optiflux 2300C electromagnetic flowmeter and a KROHNE IFC300 signal converter. The flowrate of air is set using one of the four valves corresponding to the Kytölä variable area flowmeters (0.07 – 0.19, 0.1 – 0.6, 0.2 – 0.7 and 0.3 – 6.0 $m^3$ air $min^{-1}$), which were calibrated with a rotary gas meter. The pipe has an entrance length of 32 m, corresponding to 320 $D_p$. The development of stratified and slug flow is accelerated with a parallel-plate inlet section. By injecting air from the top of the pipe parallel to the water, the flow enters the pipeline stratified with layers according to their density.
To validate the NMR flow measurements on two-phase flow, the instantaneous holdup and the speed and length of observed slugs must be measured. The height of the stratified liquid layer and the local holdup in slug flow are measured with a wiremesh sensor, described in section 4.4.2, that is placed 1.01 m upstream of the NMR flowmeter. The velocity of the bubbles and length of the elementary slug structures is determined with a dual tip-sensor on the basis of the time the slug needs to cross the sensor. See section 4.4.3 for a detailed description of this sensor located 5 m upstream of the NMR flowmeter.
The signals of all probes are recorded simultaneously. With exception of the NMR flowmeter, the total control is done from a DAQ Factory Express 5.78 program (© 2008 Azeotech) driving two LabJack data acquisition cards. These cards also act as AD converters. The signals from the tip-sensor are recorded using two analogue input channels of the LabJack U12. Its +5V line is used to trigger the wiremesh measurement. The flowmeter is continuously monitored using an analogue input channel of a LabJack UE9. To this end, the current output of the IFC300 is converted into a voltage by means of a 470 Ω resistor. Preceding the slug flow measurements, a single bubble is sent through the pipe to synchronize the time traces of the wiremesh, tip-sensor and NMR flowmeter.

### 4.4.1 Level Tank

With a distance of 1.5 m the outlet of the pipe in the air-water separator tank is very close to the second probe of the NMR flowmeter. In case of stratified flow, outflow effects occur in the NMR flowmeter. The flow is not strong enough to keep the water in the two NMR probes at the same level. These outflow effects are corrected with the level tank, integrated in the big separator tank (see Figure 4.4). The water level in this inner overflow tank can be adjusted precisely with the grey PVC plate. Through chain driving it can move up and down in front of the gap in the inner tank, which is at the height of the pipes outlet. A uniform flowpattern in the two NMR probes is guaranteed by leveling the holdup in front and behind the NMR flowmeter.

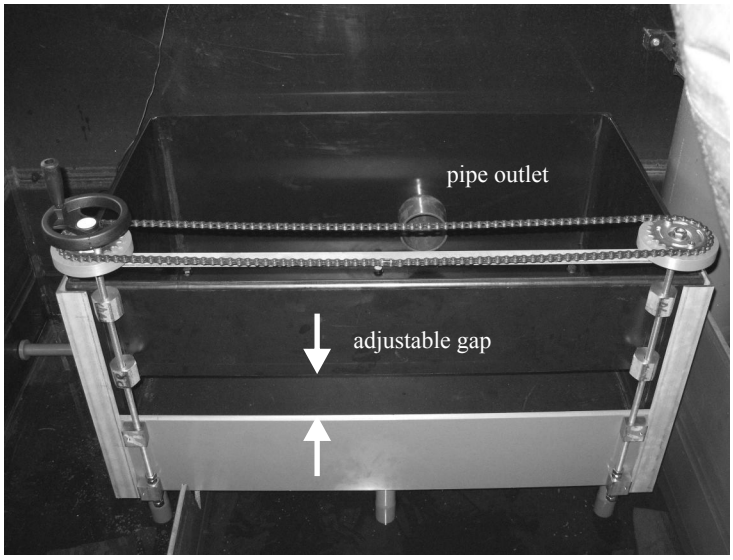


**Figure 4.4:** Level tank integrated in the air-water separator tank.

### 4.4.2 Wiremesh technique

The flow loop has a wiremesh of 98.6 mm inner diameter incorporated, which allows high-speed visualisations of transient holdups in two-phase air-water flows as reference for reliability tests of the developed NMR flowmeter. It is based on the measurement of the local instantaneous conductivity of the fluid. The sensor, manifactured by Research Center Rossendorf (FZR), is a variant of the wiremesh described in Prasser et al. [205]. It consists of two planes of electrode grids placed on a distance of 1.5 mm in the flow direction that each have 32 stainless steel electrodes of 0.125 mm diameter. The wires of the two grids are at an angle of 90°, making a mesh of 1024 sensitive points as illustrated in Figure 4.5. Their equal distribution over the cross-section results in an electrode pitch of 3 mm, which corresponds to a high spatial resolution.

One plane of electrodes is used as transmitter, the other as receiver. During a measurement cycle, a voltage pulse is supplied to the transmitter electrodes in successive order. If a conducting phase is present in the crossing-point between a selected transmitter and receiver wire, the pulse arrives at the receiver electrode. Figure 4.6 schematically shows the evaluation of this analogue current signal by the SGITT100 data acquisition unit. All receiver electrodes detect the signal at their crossing-point with the excited transmitter electrode at the same time. With pre- and main operational amplifiers the currents are transformed into voltages that are sampled by individual sample and hold circuits. Their amplifications are digitally adjusted to the conductivity of the fluid during calibration. Finally, the signals are

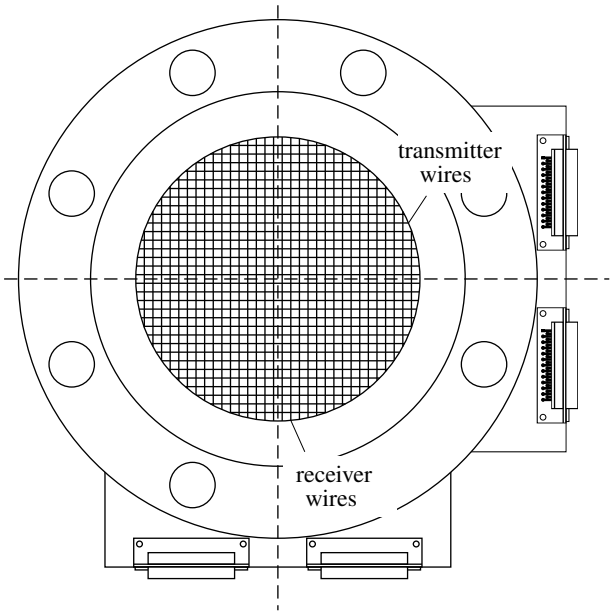


**Figure 4.5:** Wiremesh sensor with 32 x 32 sensitive points.

digitized by an AD converter and for each receiver electrode recorded by a data acquisition computer. The raw data, reflecting the conductivity in the vicinity of the related sensitive point, is stored in 12 bit format, i.e. integer numbers between 0 and 4095. Repeating this procedure for all transmitter electrodes provides a complete two-dimensional matrix of the conductivity in the pipes cross-section at the particular time of measurement.

The method is sensitive to blurring by cross-talk. Unintended driving potential differences between non-activated transmitter and receiver electrodes or neighboring receiver electrodes lead to parasitic currents. For suppressing this additional contribution to the acquired signal, both the outputs of the transmitter drivers and the receiving inputs were designed with an impedance significantly lower than the impedance of the conducting fluid. It keeps the electrical potential zero over the entire cross-section except for the measurement point. Richter et al. [218] define the measurement volume therefore as a cubic cell of the size of one mesh (3 x 3 x 1.5 mm) centered at the electrodes crossing-point. Comparisons with high-speed camera images show that this assumption is wrong. The presence of a bubble is also detected in two surrounding cells of the interface. Electrical potential simulations by Smeets [235] show that the actual measurement volume rather has a diamond shape. In the direction of the transmitter wire the measurement volume has indeed approximately the size of a grid cell centered at the cross point of interest as suggested by Richter et al. [218]. However, in the direction of the receiver wire the volume is about four electrode pitches long. So there are

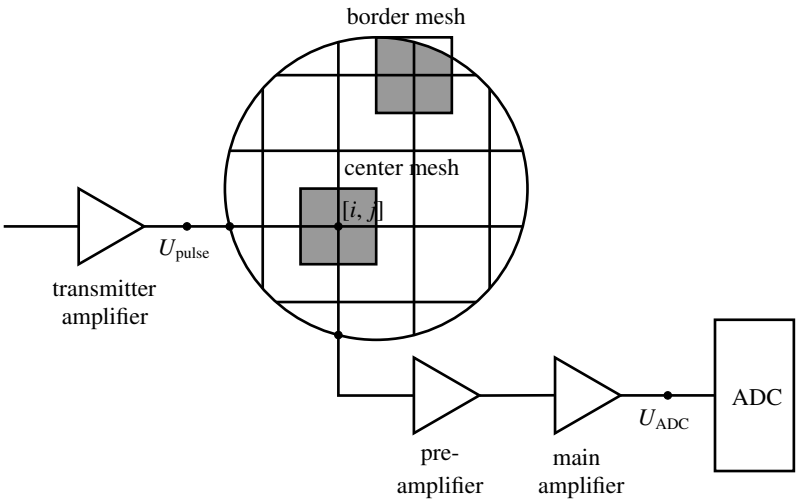


**Figure 4.6**: Sketch of the connection diagram of the wiremesh. Actually all electrodes are connected to individual operational amplifiers. The transmitter amplifiers are preceded by a voltage supply that activates the transmitter electodes in successive order with a multiplex circuit. Inbetween the main amplifier and ADC card, a sample-and-hold circuit makes sure that the simultaneously arriving signals of the receiver electrodes are separately recorded.

overlapping measurement volumes but also unsensed 'dead zones'. This can have a major impact on the estimation of bubble volumes based on the interface position. In this study we are only interested in the total holdup as validation of the NMR flowmeter data and not in the internal structure of the two-phase flow. Because the inaccuracy is marginal for this purpose, we use an algorithm starting from cubic measurement volumes to convert the wiremesh signals to liquid holdups.

The measurements presented here are obtained with the 'continuous working mode' of the wiremesh, in which the data is directly written to the PC harddisk. Although the measurement frequency is limited to 1 kHz by the interface between the data acquisition unit and PC, the duration of the measurements is, contrary to the 'high-speed-mode', practically unlimited. The wiremesh produces a sequence of two-dimensional matrices of the local instantaneous conductivity in grid points, defined by the crossing-point of transmitter wire $i$ and receiver wire $j$. In case of gas-water two-phase flow, local liquid fractions

$$\alpha_{L\ i,j}[k] = \frac{U_{i,j}[k] - < U^G_{i,j} >}{< U^W_{i,j} > - < U^G_{i,j} >} \tag{4.1}$$

are calculated assuming a linear dependency between the gas fraction and strength of the wiremesh signal $U_{i,j}$. For this, the measured values are related to calibration values of the time-averaged signals obtained for pure water, $< U^W_{i,j} >$, or pure gas, $< U^G_{i,j} >$ [207]. Index $k$

is the number of the instantaneous holdup distribution in the time sequence that denotes the current time $t = {}^{k}/_{f_m}$ for measurement frequency $f_m$.
In the particular case of an air-water flow, the liquid phase is slightly conducting while the gas phase is practically an ideal insulator [208]. Equation 4.1 reduces therefore to

$$\alpha_{L\ i,j}[k] = \frac{U_{i,j}[k]}{< U^W_{i,j} >}, \tag{4.2}$$

implying that a calibration value is only required for the pipe completely filled with water. During a calibration procedure prior to each series of measurements, the temperature dependent matrix $< U^W_{i,j} >$ is determined. The total water fraction is obtained by relating the number of crossing-points occupied with water to the total number of crossing points. Because not all grid cells have the same volume, the total liquid holdup should be calculated as weighted average of all local holdup values $\alpha_{L\ i,j}$ within the cross-section

$$< \alpha_L[k] >= \frac{\sum_{i,j} w_{i,j}\ \alpha_{L\ i,j}[k]}{\sum_{i,j} w_{i,j}}. \tag{4.3}$$

As illustrated in Figure 4.6, all center meshes that are completely enclosed by the pipe have a weight coefficient $w_{i,j} = 1$. Elements which are completely outside the cross-section of the pipe obtain weight coefficients equal to zero. Following Prasser et al. [207], all other meshes near the wall have a value between 0 and 1, related to the part of the mesh that is inside the pipe. These values are determined based on goniometric calculations.

For a comprehensive overview of the measurement accuracy is referred to the review papers by Velasco Peña and Rodriguez [253] and Shaban and Tavoularis [226]. Prasser et al. [209] showed by comparison to reference measurements with ultrafast X-ray tomography that the absolute error on the total average holdup over the cross-section is 0.01 for regimes with small bubbles of around one electrode pitch in size. For medium-size Taylor bubbles of around 3 – 4 electrode pitches, they have found that the overestimation of the average cross-sectional liquid holdup is less than 0.04. As a result of the significant bubble fragmentation by the wiremesh, the sensor tends to underestimate the gas fraction in larger bubbles. High speed camera observations by Prasser et al. [206] demonstrate the appearance of water films in the wakes of the first wiremesh plane, that establish a certain electrical contact with the second plane also at those crossing-points, where plain gas should be detected. In the case of large bubbles with a diameter of 10 electrode pitches or more, the water can completely drain from the gap between the electrode layers and the gas fraction reaches 100%. De Salve et al. [53] compared wiremesh measurements of the average void fraction in horizontal air-water flow with the quick closing valve method. The wiremesh sensor underestimates the void fraction in the case of stratified and (pseudo)slug flow with a gas holdup between 0.5 and 0.8 and overestimates the values for gas holdups below 0.15. At very high void fractions when the flow becomes annular, a good agreement between the two methods is found. The absolute overestimation of the liquid holdup in the two-phase flow measurements in this work seems to be close to the 0.04 as mentioned above for the validation study by Prasser et al. [209] on medium-size Taylor bubbles.

Moreover, the intrusive nature of the wiremesh is no cause for concern. With growing bubble size the process of recombination and coalescence of fragments becomes more and more effective and the initial shape of the bubble is better restored. In air-water systems at room temperature, the distortion effect vanishes at liquid velocities greater than 0.2 m $s^{-1}$, which is about the lower bound of the flow regimes studied [208].

### 4.4.3 Dual Tip-Sensor for Bubble Detection

To verify the NMR measurements of a horizontal air-water slug flow, knowledge of the local flow properties is required. The dual tip-sensor enables measurements of the characteristic bubble velocity, $v_B$, and the lengths of the elementary slug structures along the pipe, i.e. the length of the elongated bubble, $L_B$, and of the liquid slug, $L_S$. Complemented by the wiremesh data of the total cross-sectional phase fractions, a good approximation for the local liquid velocity in the film and slug region is found using the slug unit-cell model, described in section 8.1. It is not possible to measure the liquid velocity directly with the sensors implemented, because water has a continuous phase in contrast to the air.
Due to the experimental difficulties associated with the intermittent nature of slug flow, literature about measurements of the local velocity field is very limited. Especially the axial asymmetry of the internal flow structure in the horizontal configuration and the absence of a quasi-fully-developed equilibrium condition complicate them even more. Kvernvold et al. [146] use a combination of Laser Doppler Velocimetry and optical two-phase probes to measure the axial velocity distribution throughout a slug flow unit. Sharma et al. [227] and Lewis et al. [156] investigate the local velocity profile development by simultaneously using two hot-film anemometers. In both single-point methods, the measured profile is an average over several similar slug units. These attempts demonstrate that convincing experimental techniques for in-situ instantaneous slug velocity measurements have not been developed yet.

The measurement principle of the tip-sensor, proposed by Neal and Bankoff [181], is based on the difference in resisitivity between water and air. The sensor, illustrated in Figure 4.7, is made up of a platinum electrode tip at the top of the pipe, which is 0.45 mm in diameter and sticks 1 – 2 mm into the interior of the pipe. At right angles across a circular stainless-steel plate electrode of 3 cm diameter is glued to the bottom of the pipe and connected in series with an external resistor, $R_{ext}$, of 13 kΩ. At the tip a voltage is applied with the +5V internal power supply of a LabJack U12 connector block and the plate is grounded through the external resistor. The voltage across the external resistor, $U_s$, in the voltage-divider circuit is acquired with an analogue input terminal of the LabJack U12 that is controlled using DAQFactory Express 5.78 (© 2008 Azeotech). The sampling rate is set to 500 Hz.
When the conducting water forms a closed circuit between the tip and plate electrodes, a voltage of constant amplitude is detected. If the tip becomes completely surrounded by air, an almost perfect insulator, the circuit is open. Although the detected voltage drops to a lower level, it will not equal zero due to the voltage-dependent input bias current of the LabJack combined with a high source impedance [147]. Thus the sensor only identifies the phase, which is instantaneously present at the location of the sensitive tip. Bubbles in the lower part of the pipe are not observed by the probe. The tip alternatingly piercing the nose of a slug or

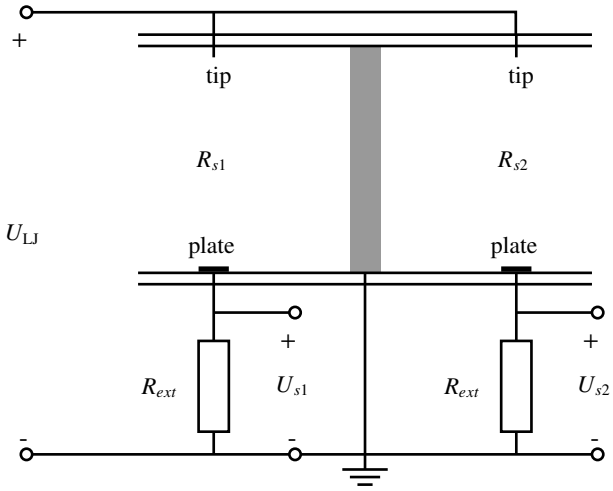


**Figure 4.7**: Sketch of the tipsensor's electrical circuit. A voltage $U_{\mathrm{LJ}} = 5$ V is applied to a series circuit of the tip- and plate electrodes and an external resistor $R_{ext} = 13$ kΩ with the internal power supply of a LabJack U12. The grey strip represents the grounded steal flange that decouples the electrical circuits of the two tip sensors. The voltages across the external resistors, $U_{s1}$ and $U_{s2}$ respectively, are acquired with two analogue input terminals of the LabJack data connector block.

bubble will form a two-level square wave of irregular frequency. To simplify processing, this analogue signal is digitized by indicating a bubble by 0, while indicating the liquid phase by 1. This is achieved by setting a threshold value of 0.8 V.

Individual bubbles are represented in the signal as periods in which the tip is covered by the gas phase. Their chord-length can be derived from the time that the signal equals zero. For this, information about the velocity is necessary. It may be obtained by applying a dual tip-sensor and evaluating the time-of-flight from the first to the second sensitive tip. Two sensors are placed at a mutual distance $\Delta y_{tip}$ of 48.7 cm. This distance ensures that signals of the same bubble are matched while keeping a sufficient resolution in the time-of-flight. To avoid cross-talk, both probes are decoupled with a 3.5 cm wide steel flange in the middle that is connected to ground. Since the velocity of a bubble can only be determined by the velocity of its interface, it is assumed that this velocity is representative for the entire structure.

The typical slug structure makes a proper identification of the bubble-to-slug phase change difficult. Especially in the front of a slug many bubbles are dispersed. When such a small gas bubble is encountered by the tip, the signal exhibits a small drop immedeately followed by a sharp increase. Only the nose of the bubble is well defined. We assume that the length of bubbles and slugs is stable during their displacement between the tips, as well as towards the NMR flowmeter; the rate of liquid picked up from the preceding film equals the rate of liquid

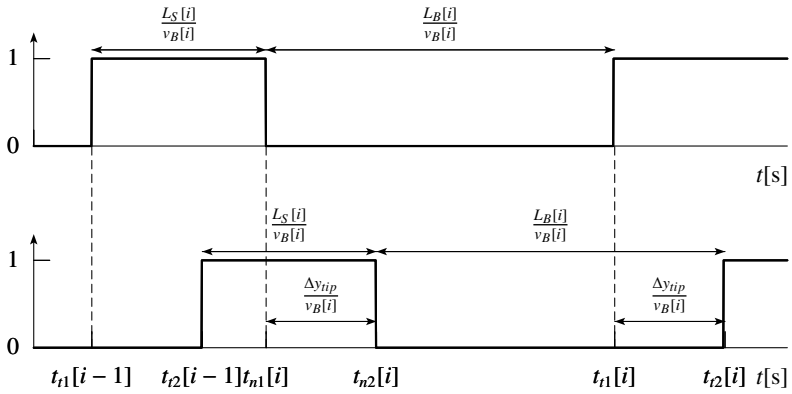


**Figure 4.8**: Timing of a typical slug flow signal acquired with the dual tip-sensor. The top graph corresponds to the signal of the first (upsteam) sensor and the bottom graph corresponds to the second (downstream) sensor. $t_n$ and $t_t$ refer to the time at which the nose and tail interface of a bubble contact the tip electrode.

shed the rear of the slug. The translational velocity of a gas bubble

$$v_B[i] = \frac{\Delta y_{tip}}{t_{n2}[i] - t_{n1}[i]}, \tag{4.4}$$

can be calculated from the difference in arrival time of the bubble's nose, $t_n$, at the individual tip-sensors, shown in Figure 4.8. The chord-length of the gas bubbles, $L_B$, and liquid slugs, $L_S$, can be derived by multiplying each respective time-of-flight with the bubble velocity:

$$L_B[i] = v_B[i]\,(t_t[i] - t_n[i])\,, \tag{4.5a}$$

$$L_S[i] = v_B[i]\,(t_n[i] - t_t[i-1])\,, \tag{4.5b}$$

where $t_t$ is the arrival time of the tail of the bubble at a tip-sensor. Implying that the velocity of the gas-liquid interfaces of slug $i$ are similar to that of the propelling gas bubble $i$. Of course, the dispersed bubbles in the slug will bias the length a bit. However, since the structures are much longer than $\Delta y_{tip}$, this effect is much smaller than the contribution it would have if the bubble velocity would be calculated by means of the arrival time of the tail of the bubble. Details about the postprocessing procedure can be found in section 8.3.1.

By studying the propagation of errors, the accuracy of the tip-sensor detection has been estimated for the observed slug flow regimes with bubble velocities in the range $2 - 3$ m s$^{-1}$. The relative error in the bubble velocity $v_B$ is found to be 2% and mainly determined by its time-of-flight from the first to the second sensor. Also the relative error in the chord-length of a bubble, $L_B$, is estimated on 2% [249]. The largest contributions originate from the number of samples in the structure and the uncertainty in $t_t$. Because the length of liquid slugs is generally shorter than that of gas bubbles, the dispersed small bubbles in the slug are expected to

have more impact on the slug length. This is in agreement with the estimated relative error of 6% on the chord-length $L_S$ of the slug.

# Chapter 5

# NMR Parameter Determination of Static Dummies

Reservoir fluids, consisting of brine water, natural gas and light, medium and heavy hydrocarbons, cover a wide range of compositions. Moreover, the longitudinal and transverse relaxation times change considerably with viscosity, temperature, pressure and the presence of paramagnetic ions. This means that, the accuracy of the flowmeter depends strongly on the ability to determine the NMR parameters of the reservoir fluids and to quantify their composition on the fly. Especially the holdups are important as the flowrates are directly proportional to them.

In this chapter preliminary tests on static dummies are used to investigate how accurate the multiphase flowmeter can determine the 90° pulse length, both relaxation times and the composition of oil-water mixtures. Because most calibration pulse sequences require that both the magnetization initially reaches the equilibrium state and that the composition has to stay constant, the use of static dummies is comparable to the real flowmeter process. Since extending the polarizing magnet is not satisfactory, the fluid stream has to be interrupted or a representative sample has to be measured in a bypass.

## 5.1 Pulse length calibration

Usually the length of a 90° hard pulse is determined with the AUTOP90 routine, described in section 2.3.3.1, which sets it to half of the pulse length at which the null of the 180° pulse is found. As an alternative the ALPHA3 method, described in section 2.3.3.2, can be used, which is faster in obtaining the 90° pulse length. However, the curve of the AUTOP90 signal against the pulse length provides a lot of information about shortcomings of the system configuration. Therefore the AUTOP90 results are first analyzed accordingly in section 5.1.1. Next, both pulse length calibration methods are compared in section 5.1.2.

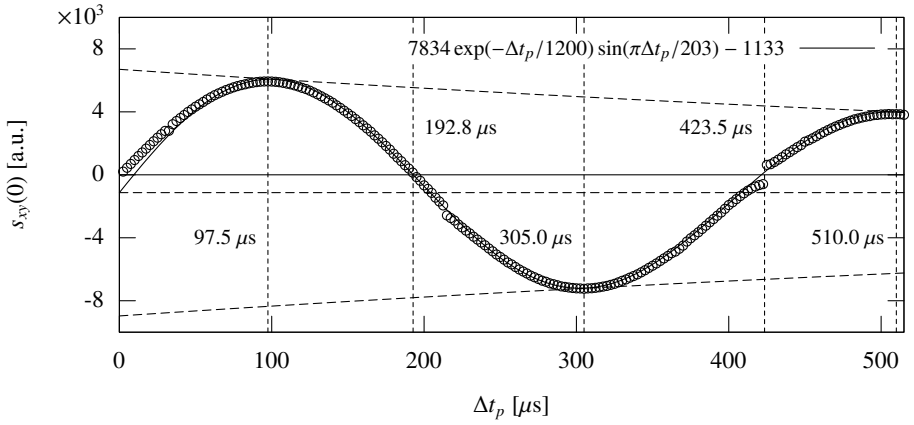


**Figure 5.1**: AUTOP90 for flip angles ranging from 0° to 450° in a 12 cm long trifilar coil of 4 turns with a diameter of 12 cm. The sample is a 9.86 cm diameter pipe, fully filled with tapwater at room temperature, which is much longer than the sensitive region of the coil.

### 5.1.1 AUTOP90 as indicator of the NMR system quality

The AUTOP90 nutation experiment is once repeated for flip angles ranging from 0° to 450° after Keifer [128], because of the additional information it gives about the sample and coil configuration. From the evaluation of the curve, depicted in Figure 5.1, we can point out three aspects that contribute to measurement inaccuracies: inhomogeneous $B_0$ and $B_1$ magnetic fields and lead pickup due to samples that extend the sensitive region of the r.f. coil considerably. These will be shortly discussed here.

Especially the 180° pulse suffers from distortions prohibiting the observation of a real null signal. The null gets lost due to the off-resonance effect by inhomogeneities in the $B_0$-field, which leaves a residual dispersion signal in the xy-plane. However decreasing the inhomogeneities by better shimming of the $B_0$-field is difficult, since all positions have a different weight in the total NMR signal.

Determination of the correct pulse length is further hampered by the inhomogeneous distribution of the r.f. $B_1$-field, which is illustrated in Figure B.2 of Appendix B. It is assumed that the reorientation of the magnetization is forced by the axial field $B_y$ alone. To this end it is important that the radial field $B_r$ is small with respect to the axial field. In general this is the case, except on the edges of the current sheet, where $B_r$ is infinite by definition. The inhomogeneous distribution of the $B_y$ field has as problem that it results in a wide variation of flip angles. On top of that the contribution to the NMR signal is location dependent because of the reciprocity principle [109, 112]. It states that the magnetization in a point will contribute to the induced voltage in the coil with an amplitude corresponding to the magnetic field produced at that point if a current were to flow in the coil. Thus each pulse length corresponds to

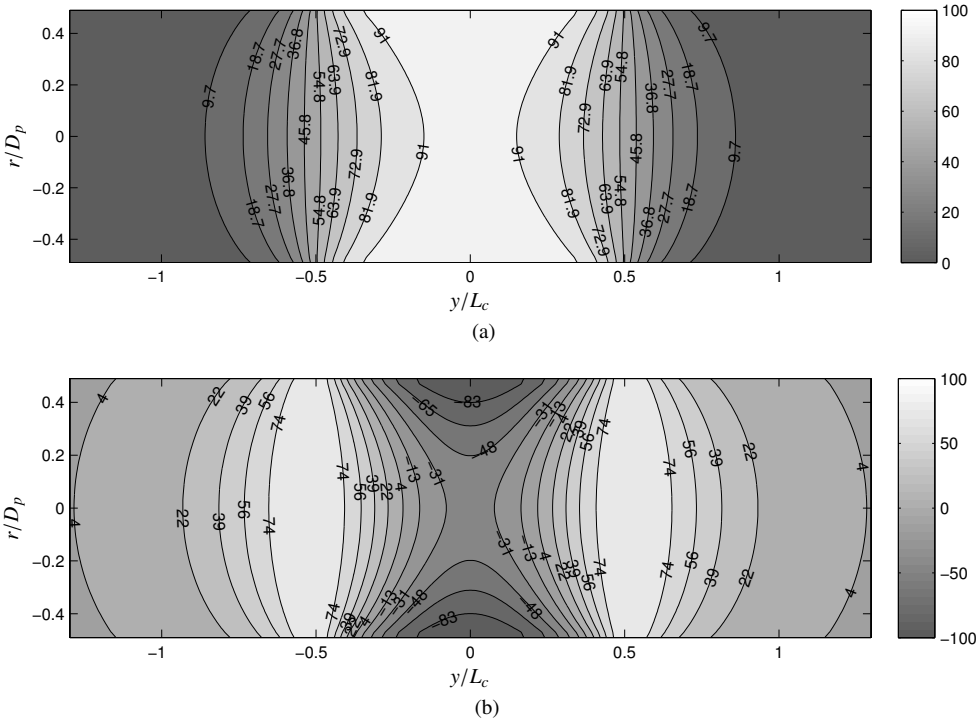


**Figure 5.2**: Starting from the reciprocity principle, the contribution to the induced NMR signal as percentage of its maximum value is simulated for a 31.2 cm long cylindrical sample of 9.86 cm diameter according to equation B.12. In a 12 cm long trifilar coil of 4 turns and 12 cm diameter, the sample is previously exposed to (a) a 90° and (b) a 180° pulse. It was assumed that the 90° pulse corresponds to the average field strength $\overline{B}_y$ of the volume of the sample enclosed by the coil.

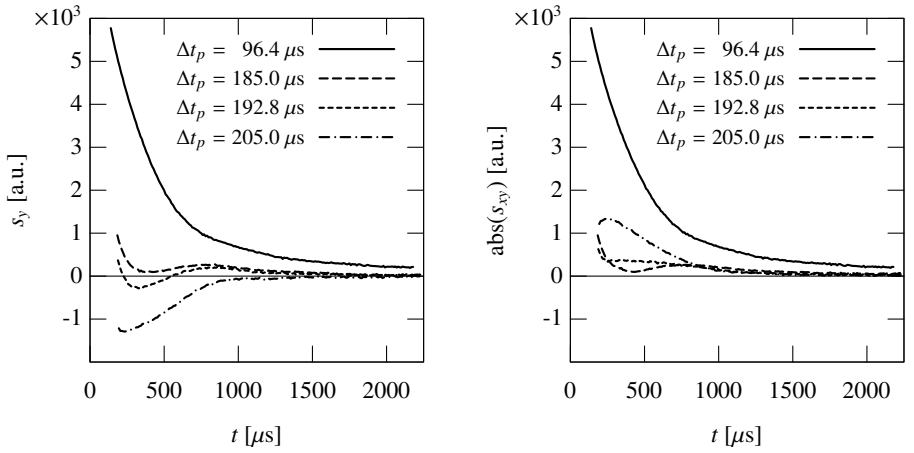


**Figure 5.3**: The real component of the FID signal $s_y(t)$ for a single nutation experiment of the AUTOP90 routine shows that the amplitude of the FID around the 180° pulse is a weighted average of a negative contribution by spins at the center and a positive contribution by spins at the ends of the coil. The pulse lengths can be derived from the initial amplitude of the absolute FID signal abs($s_{xy}(t)$), which also takes the dispersive $s_x(t)$ signal into account.

the weighted average of flip angles belonging to the magnetic moments within the sensitive volume of the probe. As shown in Figure 5.2(b), the null at a 180° pulse is the weighted average of the more than 180° excitation at the center, resulting in a negative signal contribution, and the less than 180° excitation at the ends of the r.f. coil. Contrary to this, in case of a 90° pulse, all magnetic moments in the sensitive volume of the coil contribute with the same sign to the NMR signal (see Figure 5.2(a)). The pulse length is primarily determined by the regions within the coil with flip angles in the proximity of the 90° pulse: namely the zone adjacent to the coil surface with larger flip angles and the zone at the center of the coil with smaller flip angles. Because of this more important role of averaging, the 90° pulse length obtained from the first signal maximum is, with its 97.5 $\mu$s, larger than half of the 180° pulse length obtained from the minimum signal at 192.8 $\mu$s.
It is clearly visible from the $s_y(t)$ component in Figure 5.3 that the FID amplitude is a weighted average. As shimming primarily corrects the region with the strongest signal strength, the center of the coil has a better homogeneity and the exponential decay of the FID has a larger $T_2^*$ than the region with a lower $B_1$ near the coil ends. For pulse lengths around the 180° pulse all spins contribute equally to the intial FID amplitude, with the contribution by the center zone of the coil dominating in the time evolved signal. This trend vanishes in the absolute FID signal used by AUTOP90, which also takes the dispersive $s_x(t)$ signal into account, however, the obtained pulse lengths are unaffected.

A second indication for the inhomogeneous r.f. field is the sinusoidal but exponential decaying curve of the signal strength as function of the pulse width. Keifer [128] reports that

typical values for a 450°/90° ratio range from as low as 50% to as high as 98% depending upon the probe design. With a ratio of 71% for signal strength of the 450° to the 90° pulse, the 12 cm diameter r.f. coil has an average homogeneity for a sample of 9.86 cm diameter. A substantial part of the inhomogeneity in the flowmeter application is caused by lead pickup on account of the samples extending the sensitive region of the r.f. coil considerably.

Inhomogeneity of the pulsed field is especially an issue for the used type of coil with a short length in comparison to its diameter and a sample that almost completely fills the core of the coil. At positions near the center of the coil ($y \approx 0$) the axial field strength changes rapidly from the coil axis to the wall, like it does for a single circular filament. The radial variations in the axial field decrease for an increasing coil length until the field becomes homogeneous for an infinite coil. It seems obvious to make the coil length-to-diameter ratio as large as possible. Designing NMR coils is however complex matter that does not only concern the field homogeneity. The length of the coil is mainly limited by the wavelength $\lambda = c/\nu_L$ of the current induced in the coil operating in the receiver mode, where the speed of light $c = 3 \cdot 10^8$ m s$^{-1}$. If the conductor is too long, the $B_1$-field at the center of the coil will contain multiple phases and the resultant field will be rather small. Chen and Hoult [43] therefore recommend that the length of the conductor never exceeds $\lambda/20$. A condition too tight for the used trifilar coil of 4 turns, which conductors have a length of $\lambda/14$. Guiding charts for a certain coil design that also take all other factors like skin and proximity effects into account, can help to select the optimum number of turns, optimum conductor spacing and optimum conductor cross-section at a given frequency. If the optimal coil length is rather short, a better field homogeneity can be obtained by giving the sample a considerably smaller diameter than the coil diameter. During the design of the flowmeter, it was chosen to have a small ratio of the coil-to-sample diameter, in view of its application in the oil industry. The rare earth permanent magnet, which determines the actual size of the apparatus, makes the system very bulky when a larger ratio is used combined with pipes that have a diameter of a number of inches. For the benefit of obtaining a compact flowmeter, the air gap is reduced at the cost of the homogeneity of the pulsed magnetic field.

### 5.1.2 Comparison of AUTOP90 with ALPHA3

The significance of the inhomogeneous $B_1$-field is studied by determining the pulse length of a 90° hard pulse for cylindrical PVC containers of different dimensions that are filled with tapwater at room temperature and centered in the bore of the measurement probe. The results of both the AUTOP90 and ALPHA3 routine are given in table 5.1 for samples with a diameter of 4.44 or 9.86 cm and a length of 1.6, 5.7 or 29.6 cm. Because it is difficult to vary time intervals between successive pulses and the acquisition in the RINMR software, it should be noted that the ALPHA3 measurements are performed in two parts. To this end, the primary echo is measured with a modified HAHN pulse sequence in which both pulses have the same length and phase. Thereupon the four other echoes are acquired with the ALPHA3 pulse sequence.

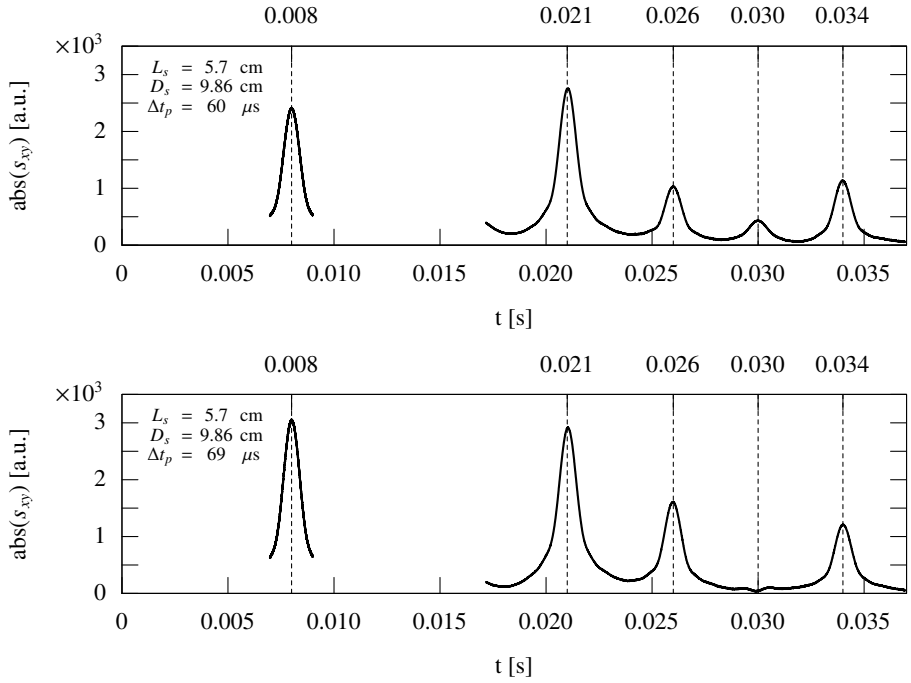


**Figure 5.4**: ALPHA3 signal acquired at time interval settings $\tau_1 = 4000\ \mu$s and $\tau_2 = 13000\ \mu$s for 5.7 cm long cylindrical containers with a diameter of 9.86 cm that are filled with tapwater at room temperature. The second plot shows how the pulse width minimizes the third spin echo.

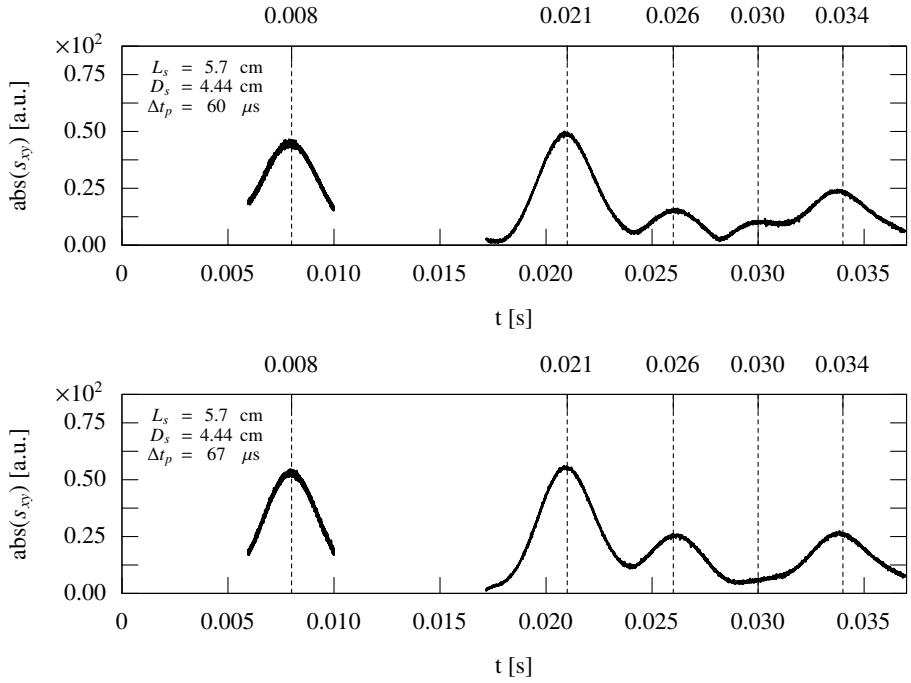


**Figure 5.4**: (continued) ALPHA3 results under identical experimental settings as in the previous two plots, but with a sample diameter of 4.44 cm. The second plot shows again how the pulse width minimizes the third spin echo.

**Table 5.1**: Pulse lengths corresponding to a 90° hard pulse for cylindrical containers of different dimensions that are filled with tapwater at room temperature and are centered in the bore of the 12 cm long tuned r.f. probe. The time intervals between the pulses in the ALPHA3 routine are set at $\tau_1 = 4000\ \mu$s and $\tau_2 = 13000\ \mu$s. The results of the ALPHA3 routine are analyzed in the three possible manners: $P90_{ste/pe}$ from the ratio of the stimulated to the primary echo amplitude by means of equation 2.26, $P90_{ste}$ by peaking the amplitude of the stimulated echo and $P90_{3se}$ by searching fro the minimum of the third stimulated echo.

| | | AUTOP90 | ALPHA3 | | |
|---|---|---|---|---|---|
| length [cm] | diameter [cm] | P90 [$\mu$s] | $P90_{ste/pe}$ [$\mu$s] | $P90_{ste}$ [$\mu$s] | $P90_{3se}$ [$\mu$s] |
| 1.6 | 4.44 | 68.0 | 63.8 | 66 | 66 |
| 1.6 | 9.86 | 64.8 | 63.6 | 68 | 66 |
| 5.7 | 4.44 | 70.4 | 72.0 | 68 | 67 |
| 5.7 | 9.86 | 66.4 | 66.7 | 66 | 69 |
| 29.6 | 4.44 | 69.6 | 68.0 | 70 | 72 |
| 29.6 | 9.86 | 65.6 | 68.0 | 72 | 71 |

As the simulations of the pulsed field in Figure B.2 of appendix B illustrate, the field is weaker at the center of the coil and stronger near the coil surface. The pulse length is therefore expected to be longer near the center of the pipe than adjacent to the pipe wall. Both the pulse lengths obtained with AUTOP90 and with the ratio of the stimulated to the primary echo, $P90_{ste/pe}$, display this trend: the small diameter samples have a longer pulse length than the large diameter ones. This in contrast to the pulse lengths obtained from the amplitudes of the stimulated echo, $P90_{ste}$, and the third spin echo, $P90_{3se}$, where this trend is lacking. It suggests that the residual dispersion signal biases the amplitudes of the echoes and that the third pulse enhances this effect. Figure 5.4 shows how residual dispersion hampers the determination of the 90° pulse length from the third spin echo of the ALPHA3 routine. The minimum of the 9.98 cm diameter sample is made up from a broad echo with a smaller flip angle and a narrow echo with a larger flip angle. In the case of the 4.44 cm diameter sample, there is always a residual signal left and the echo amplitude never gets zero.
Another characteristic of the r.f. field is that the $B_y$-component becomes weaker towards the coil ends. To this end the 90° pulse length is expected to increase when the length of the sample is extended. However the zone outside the coil hardly contributes to the determination of the right pulse length, as Figure 5.2(a) illustrates. It only gives an offset, while the magnetization within the sensitive volume of the probe is dominating the NMR signal. The length of this sensitive volume is estimated in table 5.2 from the signal strengths of different samples with the same diameter. This is a reasonable approach, since the signal strength in a volume is proportional to the number of protons present. It is assumed that the 5.7 cm long sample represents the signal homogeneity within the r.f. probe best. The sensitive length of the probe is now determined as the length at which the signal strength of the 29.6 cm long

**Table 5.2**: Maximum signal strength of the FID and all five ALPHA3 echoes, obtained with hard 90° pulses, for cylindrical containers filled with tapwater at room temperature. The signal strength has an uncertainty of 10 arbitrary units. The pulse widths in the FID and ALPHA3 pulse-sequence are set resepectively at the P90 and $P90_{3se}$ values, which are given in table 5.1. The length of the sensitive volume is estimated from the ratio of the signals of the 29.6 and 5.7 cm long samples and has an uncertainty of 0.5 cm.

| | | abs($s_{xy}$) [a.u.] | | | sensitive length |
|---|---|---|---|---|---|
| | length = | 1.6 cm | 5.7 cm | 29.6 cm | probe [cm] |
| diameter = 4.44 cm | FID | 356.3 | 1224.4 | 1904.4 | 8.9 |
| | primary echo | 157 | 538 | 595 | 6.3 |
| | stimulated echo | 150 | 556 | 596 | 6.1 |
| | $2^{nd}$ spin echo | 73 | 258 | 355 | 7.8 |
| | $3^{rd}$ spin echo | 16 | 62 | 94 | - |
| | $4^{th}$ spin echo | 76 | 265 | 277 | - |
| diameter = 9.86 cm | FID | 1762.3 | 5783.6 | 9961.3 | 9.8 |
| | primary echo | 906 | 3057 | 5738 | 10.7 |
| | stimulated echo | 860 | 2924 | 5381 | 10.5 |
| | $2^{nd}$ spin echo | 445 | 1610 | 2559 | 9.1 |
| | $3^{rd}$ spin echo | 45 | 47 | 180 | - |
| | $4^{th}$ spin echo | 445 | 1213 | 948 | - |

sample, which extends the coil, corresponds to the length-to-signal ratio of the 5.7 cm long sample. Since the fourth spin echo of the 29.6 cm long samples exhibits a dip in the center due to the flip angle inhomogeneity, it is ignored in the calculations. The results prove that the sensitive volume of the coil is roughly similar to the volume bound by the coil domain. However for a small diameter sample the sensitive volume is slightly smaller because the r.f. field contribution is smaller. This is due to the fact that in a relatively larger volume the decline starts at a lower axial position. As expected there is a minimum difference in the 90° pulse lengths of the 5.7 and 29.6 cm long samples that are obtained in the 12 cm long r.f. coil. The difference in the pulse lengths determined with the four different methods can be mainly attributed to the different weighting factors that the methods have for deviations in the flip angle of the desired 90°.
Because of the incoherence in the pulse lengths obtained with ALPHA3 and the fact that the main multiphase flowmetering routine only uses FID experiments, the AUTOP90 routine is preferred for the determination of P90. Above all the obtained P90 are all within the same range.

## 5.2 Determination of the $T_1$ and $T_2$ relaxation times

The reliability of the NMR multiphase flowmeter depends to a large extent on the accuracy at which the $T_1$ and $T_2$ relaxation times are measured. On the one hand, the flowmeter principle of the '$T_1$ Relaxation Residence Time Method' is directly based on the individual $T_1$ times of all mixture components. On the other hand one of the two relaxation times is necessary to classify the composition of the multiphase mixture. Together with the substance dependent hydrogen density, obtained from a predefined calibration file, this allows the quantification of the volume fraction of each component. Above all during the flowmeter operation, the relaxation times have to be measured repeatedly, because they are closely correlated with viscosity and are affected by both temperature and pressure [2, 19, 232]. Exactly these properties differ widely at reservoir conditions. The temperature and pressure cover a range of 15 - 150 °C and 1 - 545 atm between surface and subsurface conditions [17].
Quantification of the composition of reservoir fluids is not easy, because of its complex nature consisting of brine water, natural gas and light, medium and heavy hydrocarbons. The $T_1$ and $T_2$ relaxation times of water and oil are closest and sometimes even overlap. It is important to stress that both flowmetering principles developed here are severely hampered if there is a lack of contrast between the $T_1$ relaxation times of water and light oils or condensates. A limitation for which there is no simple solution. To this end, we test in this section if it is possible at all to compute the individual relaxation times unambiguously for samples of oil and tapwater mixtures.

### 5.2.1 Determination of the longitudinal relaxation time

The longitudinal relaxation time $T_1$ has been determined with the inversion recovery sequence, described in section 2.3.4, for a number of samples consisting of an oil-water mix-

ture and their single-phase components, a method demonstrated earlier by Abouelwafa and Kendall [1] for various oil-water samples. In case of a pure sample the intensity of the NMR signal, $s_{xy}(\tau)$, is analogous to equation 2.28 given by

$$s_{xy}(\tau) = -s_{xy}(0)\left(1 - 2\exp\left(-\frac{\tau}{T_1}\right)\right), \tag{5.1}$$

where $\tau$ is the time delay between the 180° and the 90° pulse in which the longitudinal magnetization can recover towards the equilibrium state. Whereas in a mixture the individual $T_1$ relaxation times of both components play a part in the NMR response, since oil and water are immiscible. The NMR signal is described by a multiexponential curve, whose sum is composed of as many functions 5.1 as the number of components in the mixture:

$$s_{xy}(\tau) = -\sum_{i=1}^{n} s_{xy_i}(0)\left(1 - 2\exp\left(-\frac{\tau}{T_{1i}}\right)\right). \tag{5.2}$$

The initial amplitude $\sum s_{xy_i}(0)$ of the signal is a measure for the total hydrogen density of the sample. Unnecessary inaccuracies due to the measurement method are avoided by setting the repetition delay on at least $5T_1$, so that equilibrium is reached before the 180° pulse inverts the longitudinal magnetization. For an improved accuracy the inversion recovery sequence is performed with logarithmically spread $\tau$.
Estimates of the $T_1$ relaxation times and the initial signal intensities $s_{xy}(0)$ are obtained by fitting the data with a nonlinear least squares fit. For this purpose the trust-region optimization algorithm with weighted robust regression and 95% confidence bounds in cftool, Matlab's curve fitting toolbox, has been used. The data of the pure samples is fitted with a single exponential function

$$f(\tau) = c_1(1 - 2\exp(-c_2\tau) + c_3), \tag{5.3}$$

while for the data of the two-component mixtures a bi-exponential function

$$f(\tau) = c_1(1 - 2\exp(-c_2\tau) + c_3) + c_4(1 - 2\exp(-c_5\tau)) \tag{5.4}$$

is used. In these equations the parameters $c_1$ and $c_4$ are indirect estimates of the amount of hydrogen present in the sensitive volume of the coil. The parameters $c_2$ and $c_5$ are estimates for the inverse of the $T_1$ relaxation time and $c_1c_3$ is a signal offset. However care should be taken since the nonlinear fit method is very sensitive to the starting values of the estimators. The starting values of ($c_1$, $c_2$, $c_3$) in the single exponential fit are set to ($-s_{xy}(\tau[1])$, 0.9, 0.0) with a lower limit of (0.0, 0.0, $-\infty$). The starting values of ($c_1$, $c_2$, $c_3$, $c_4$, $c_5$) in the bi-exponential fit are set to ($-0.9s_{xy}(\tau[1])$, 0.9, 0.0, $-0.1s_{xy}(\tau[1])$, 0.9) with a lower limit of (0.0, 0.0, $-\infty$, 0.0, 0.0). The term $\tau[1]$ refers to the smallest time delay at which an experiment of the inversion recovery sequence is performed. For fits with functions consisting of more than two exponentials, the nonlinear least squares method has difficulties to obtain convergence. In practice, when mixtures are composed of multiple components, it is therefore better to determine the $T_1$-distibution in a different way: e.g. with the mapping process used in NUMAR's MRIL logging tool [44] to determine the $T_2$-distibution. The mapping process

assumes that the relaxation time distribution consists of N discrete relaxation times $T_{1i}$ with corresponding signal intensities $s_{xy_i}(0)$. After pre-setting the $T_{1i}$'s within the expected range, the multiexponential model of equation 5.2 is used to form for each time delay step $\tau$ a linear equation of the unknown $s_{xy_i}(0)$. The best method to estimate the $T_1$-distribution is inverting this linear system of equations with an iterative method that takes care of the constraint that the signal intensities $s_{xy_i}$ must be greater than or equal to zero. However, for the simple tests represented in this section the exponential nonlinear fit will do.

The capability of the NMR apparatus to discriminate between the different components in an oil-water mixture is tested on two sets of samples. The first set consists of samples of tapwater, Euroshopper sunflower oil, and their mixtures with a proportion of 33:67 and 50:50, respectively. In addition to the measurements with this medium oil, tests are performed with a heavy marine residual fuel oil (MRFO) to get a feeling for the measurement uncertainty over the full spectrum of oils that are found in the field. Accordingly, the second set of samples consists of a mixture of tapwater and Argos residual fuel oil, characterized by a kinematic viscosity of 380 $mm^2 \cdot s^{-1}$ at 50 °C, with a proportion of 50:50 and both unmixed components. The liquids of 'set 1' are enclosed in $1\frac{1}{2}$ liter plastic bottles with a diameter of 8.5 cm, while 265 ml of the liquids of 'set 2' is enclosed in glass jars with a diameter of 7.1 cm. All measurements are carried out at room temperature. For the samples that contain water, $\tau$ is raised from 0.01 to 12.5 s in 40 logarithmic steps. Like MRFO, the dynamic viscosity of sunflower oil is with approximately 75 mPa · s at room temperature much higher than that of water. Simpson and Carr [232] have found that the $T_1$ relaxation time at constant temperature is inversely proportionate to the dynamic viscosity. Regarding the oil samples, $\tau$ is therefore raised from 0.001 to 0.5 s in 20 logarithmic steps. The results of the inversion recovery experiments and their exponential fits are shown in Figure 5.5 and 5.6. In table 5.3 a total overview of all obtained relaxation curves is given.

Following the work by Simpson and Carr [232], the $T_1$ relaxation time of 2.642 s for tapwater in 'set 1' resembles pretty well with the 2.95 s they obtained at 20 °C. An explanation for the shorter value is found in dissolved oxygen that reduces the $T_1$ value on account of its paramagnetism.
The relaxation curve of the sunflower oil sample is noticeably non-exponential. This is as expected, since sunflower oil is no pure fat, but composed by saturated, monounsaturated and polyunsaturated fat, which each have their own relaxation time. However, it is still possible to represent the relaxation curve within the accuracy of the data by the sum of two exponentials with a $T_1$ of 49 ms and 153 ms, respectively. Brown [32] reports the same behavior for many crude oil samples, where the relaxation curve due to a distribution of $T_1$ relaxation times cannot be distinguished from a curve composed of two distinct exponentials. Since the difference between the short and long relaxation time is not that big, the average relaxation rate of the pure sunflower sample is determined with the single exponential fit too. The average $T_1$ of 94 ms can be attributed to the inital values of the experimental data. A striking result is the initial signal intensity, which is for the single exponential fit 10% lower than for the bi-exponential fit. This source of inaccuracy is caused by the absence of the relaxation curve with the short $T_1$ of 49 ms, which is initially very steep.

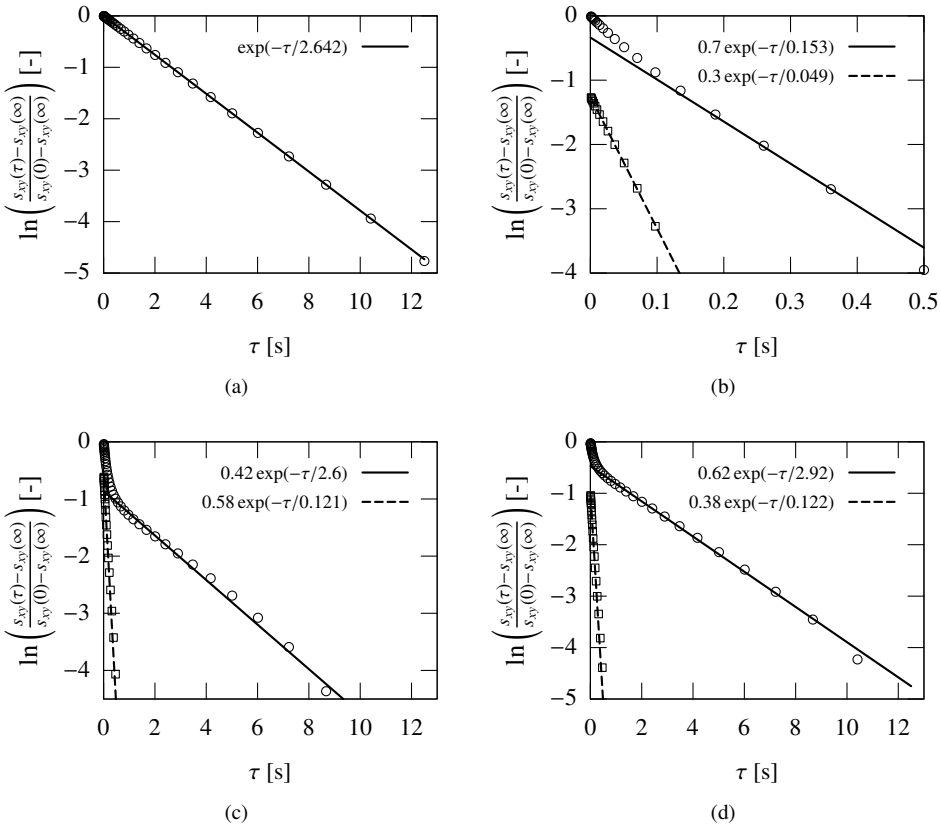


**Figure 5.5**: $T_1$ relaxation curve of (a) tapwater, (b) Euroshopper sunflower oil and their mixtures in the proportion of (c) 33:67 and (d) 50:50, respectively. In case of two well-separated relaxation rates, the solid line is the fit of the component with the longest $T_1$ relaxation time. The squared data points show the difference between the dotted experimental data and the solid line. The dashed line is the fit of these squared data points and represents the component with the shortest $T_1$ relaxation time.

**Table 5.3**: Inversion recovery curves, $f(\tau)$, and the relative errors in the estimates of the intial signal strength, $s_{xy}(0)$, and the $T_1$ relaxation time that are based on the 95 % confidence interval of the fit. The composition of the mixtures is specified in volume percent. As sunflower oil and MRFO are in fact compound substances, both the single and the bi-exponential fit are used to analyze the data of their pure samples. The first exponental term of the bi-exponential fit matches with the full curve in Fig. 5.5 and 5.6, whereas the second exponential term matches with the dashed curve.

| | | $f(\tau)$ $\times 10^3$ [a.u.] | $\frac{\mathrm{u}(s_{xy_i}(0))}{s_{xy_i}(0)}$ [%] | $\frac{\mathrm{u}(T_{1i})}{T_{1i}}$ [%] |
|---|---|---|---|---|
| | tapwater | $6.130(1-2\exp(-\tau/2.642))+0.048$ | 0.05 | 0.2 |
| | sunflower oil | $4.97(1-2\exp(-\tau/0.094))-0.67$ | 1 | 4 |
| | | $3.9(1-2\exp(-\tau/0.153))+$ | 5 | 5 |
| | | $1.6(1-2\exp(-\tau/0.049))-0.2$ | $0.1\cdot 10^2$ | 8 |
| | 33% tapwater | $2.37(1-2\exp(-\tau/2.6))+$ | 3 | 8 |
| | 67% sunflower oil | $3.23(1-2\exp(-\tau/0.121))+0.09$ | 2 | 6 |
| set 1 | 50% tapwater | $3.59(1-2\exp(-\tau/2.92))+0.07+$ | 1 | 4 |
| | 50% sunflower oil | $2.17(1-2\exp(-\tau/0.122))$ | 2 | 6 |
| | tapwater | $3.445(1-2\exp(-\tau/2.290))+0.125$ | 0.1 | 0.3 |
| | MRFO | $2.39(1-2\exp(-\tau/0.0333))+0.2$ | 1 | 4 |
| | | $2.04(1-2\exp(-\tau/0.0395))+$ | 4 | 3 |
| | | $0.40(1-2\exp(-\tau/0.016))+0.18$ | $0.2\cdot 10^2$ | $0.1\cdot 10^2$ |
| | 50% tapwater | $1.772(1-2\exp(-\tau/3.05))+$ | 0.3 | 0.7 |
| set 2 | 50% MRFO | $1.061(1-2\exp(-\tau/0.0368))+0.233$ | 0.7 | 1 |

For both sunflower oil-tapwater mixtures it is very well possible to derive the individual relaxation times of the components. Though the $T_1$ of the sunflower oil turns out to be larger than the average value of the pure sample. Principally this is caused by the coarser delay time intervals, which have on top of that a logarithmic distribution. Also the larger longitudinal relaxation time of the present tapwater can bias the fitted $T_1$ of sunflower oil upwards. Noteworthy too is the $T_1$ obtained for the tapwater components: in the 33:67 tapwater-sunflower oil mixture, the value of 2.6 s is in full agreement with the $T_1$ of the pure tapwater sample, while the value of 2.92 s in the 50:50 mixture is too long. This is a consequence of the nonlinear fit procedure, which has difficulties in distinguishing the separate curves if they are not obviously present. The tapwater curve describes the tail of the relaxation curve and the sunflower oil curve dominates in the initial part. There is an apparent transition between both regions in the 33:67 mixture. On the contrary they merge smoothly in the 50:50 mixture, so that this fit becomes more uncertain. However, the inaccuracy of the relaxation time value might originate as well from a temperature increase. In general the relative uncertainty of the $T_1$ values is around 10% when multiple components are involved.

The results of 'set 2' with the marine residual fuel oil can be explained similarly to 'set 1'. Even though the $T_1$ obtained for the pure tapwater sample is with 2.290 s shorter, it is comparable with Simpson's results since the temperature is a good 2 °C lower.
Contrary to sunflower oil, a single exponential curve with a $T_1$ of 33.3 ms describes the relaxation curve of MRFO well, because the component with a $T_1$ of 16 ms contributes to a lesser degree to the total signal. The initial signal intensity of the average relaxation curve can be used to quantify the liquid mixture composition.
For the 50:50 tapwater - MRFO mixture the same interpretation holds as for the 50:50 tapwater-sunflower oil mixture. Again the overprediction of MRFO's $T_1$ can be assigned to the coarser distribution of delay time intervals, while inaccuracies in the nonlinear fit procedure underlie the overprediction of the $T_1$ of tapwater. Despite the lower uncertainty that is estimated from the 95% confidence bounds of the fit, the relative uncertainty of the derived $T_1$ values in the mixture is for this reason around 10%.

Because the intensity of the NMR signal of each fluid is related to its volume fraction, it can be used to determine the quantities of different fluids. In practice, water has the strongest signal intensity due to its high hydrogen density, but many reservoir fluids have a hydrogen density sufficiently close to that of water [136]. It is therefore common in well-logging to express the hydrogen density of a material relative to that of pure water at the same pressure and temperature by the hydrogen index

$$\mathrm{HI} = \frac{s_{xy_i}(0)}{s_{100\%_w}(0)} \tag{5.5}$$

which scales the initial signal intensity of the liquid, $s_{xy_i}(0)$, with that of pure tapwater with the same sensitive volume, $s_{100\%_w}(0)$. If tapwater, sunflower oil and MRFO have an equal hydrogen density, the factor in front of the exponential terms in Figure 5.5 and 5.6 quantifies the tapwater-oil ratio. As shown in table 5.3, sunflower oil has, unfortunately, a 20% lower hydrogen density than tapwater because of its unsaturated hydrocarbons. The hydrogen den-

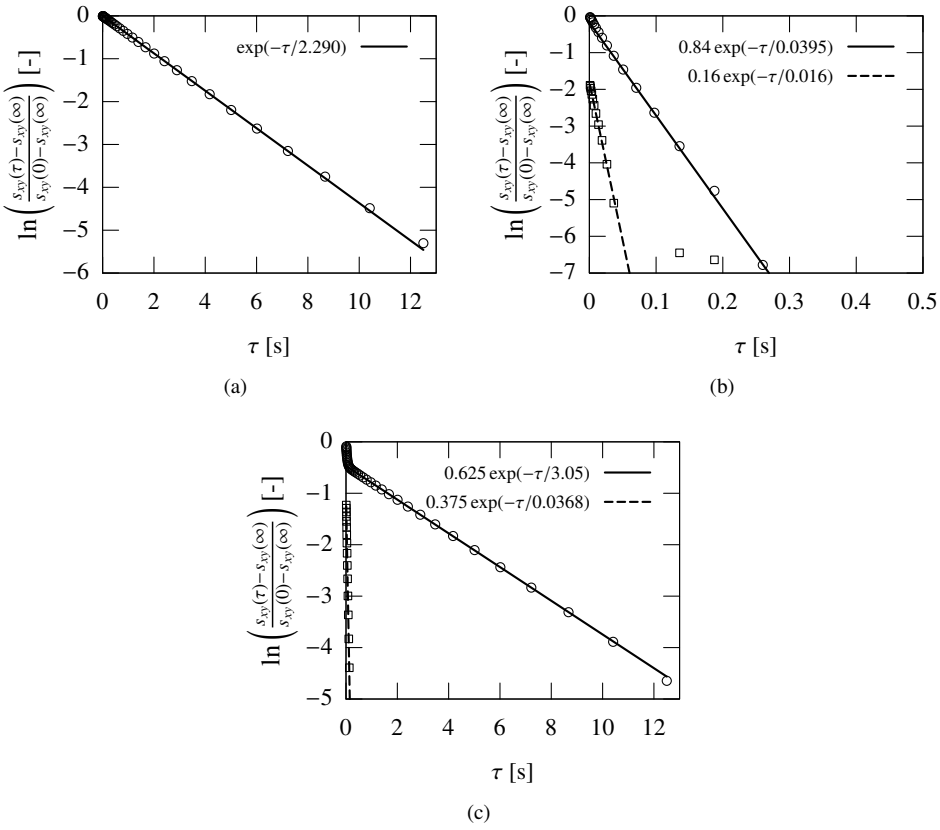


**Figure 5.6**: $T_1$ relaxation curve of (a) tapwater, (b) Argos marine residual fuel oil and (c) their mixture in the proportion of 50:50. In case of two well-separated relaxation rates, the solid line is the fit of the component with the longest $T_1$ relaxation time. The squared data points show the difference between the dotted experimental data and the solid line. The dashed line is the fit of these squared data points and represents the component with the shortest $T_1$ relaxation time.

sity of MRFO is even reduced with 30%. Kleinberg and Vinegar [136] mention that this is primarily caused by components in the oil that relax faster than 1 ms. This implies that a hydrogen correction is necessary to determine the holdups. To this end, the mixture components are first discriminated on the basis of their $T_1$ relaxation time. Next, the corrected holdups are determined from the ratio of the initial amplitude of a component to the corresponding initial amplitude of the pure sample:

$$\alpha_i = \frac{s_{xy_i}(0)}{s_{100\%i}(0)} \tag{5.6}$$

with the restriction that $\sum \alpha_i = 1$. In the holdup calculations for both data sets, the initial amplitude of the oil sample is estimated with the single exponential model. In this manner the real tapwater-sunflower oil mixture of 33:67 and 50:50, respectively, is estimated by a ratio of 39:65 and 59:44. For the 50:50 tapwater-MRFO mixture a ratio of 51:44 is obtained. Because of a measurement uncertainty of 6%, the sum of the distibutions is unequal to 100%. The systematic overprediction of the tapwater component and underprediction of the oil component is mainly caused by the uncertainty in the $T_1$ value of the oil component to which the nonlinear fit procedure is very sensitive. The tapwater component will increase if a too small $T_1$ is estimated for oil. Another source of systematic errors in the holdup of oil is the discrepancy between the initial amplitude modelled with a single and bi-exponential fit.

### 5.2.2 Determination of the transverse relaxation time

The transverse relaxation time, $T_2$, has been determined with the CPMG pulse sequence, described in section 2.3.5, for the same two sets of tapwater-oil samples that are used in the previous section to investigate the accuracy of the inversion recovery method in the determination of the longitudinal relaxation time. Following equation 2.29, the envelope of the NMR signal, $s_{xy}(t)$, of a pure sample is described by

$$s_{xy}(t) = s_{xy}(0) \exp\left(-\frac{t}{T_2}\right), \tag{5.7}$$

whereby the signal intensity is acquired from the maximum amplitude of the echo at every discrete time step, $t = 2N\tau$. Because each fluid keeps its own $T_{2i}$, the NMR response of immiscible fluids can be modelled with a multiexponential function

$$s_{xy}(t) = \sum_{i=1}^{n} s_{xy_i}(0) \exp\left(-\frac{t}{T_{2i}}\right), \tag{5.8}$$

which consists of as many functions as the number of components present. Like in equation 5.2, the initial amplitude $\sum s_{xy_i}(0)$ of the function is a measure for the total hydrogen density of the sample. The accuracy of the model improves if more echoes are used with a smaller delay time $\tau$. However, the number of scans is bound to the maximum size of the acquisition window of the RINMR software, which can only store a limited amount of data. To obtain the

**Table 5.4**: CPMG curves, $f(t)$, and their relative errors in the estimates of the initial signal strength, $s_{xy}(0)$, and the $T_2$ relaxation time that are based on the 95% confidence interval of the fit. The composition of the mixtures is specified in volume percent. The bi-exponential fit of the 50:50 tapwater-MRFO mixture is only given for $\tau = 0.375$ ms.

| | | $f(t)$ $\times 10^3$ [a.u.] | $\frac{\mathrm{u}(s_{xy_i}(0))}{s_{xy_i}(0)}$ [%] | $\frac{\mathrm{u}(T_{2i})}{T_{2i}}$ [%] |
|---|---|---|---|---|
| set 1 | tapwater | $7.34\exp(-t/1.852)$ | 0.5 | 0.9 |
| | sunflower oil | $6.12\exp(-t/0.123)$ | 0.3 | 3 |
| | | $4.55\exp(-t/0.0636)+$ | 2 | 2 |
| | | $2.30\exp(-t/0.229)$ | 4 | 2 |
| | 33% tapwater | $2.30\exp(-t/2.06)+$ | 0.9 | 2 |
| | 66% sunflower oil | $4.18\exp(-t/0.108)$ | 1 | 2 |
| | 50% tapwater | $4.09\exp(-t/2.165)+$ | 0.4 | 0.6 |
| | 50% sunflower oil | $2.69\exp(-t/0.111)$ | 1 | 3 |
| set 2 | tapwater | $3.464\exp(-t/1.704)$ | 0.3 | 0.5 |
| | MRFO | $1.86\exp(-t/0.0038)$ | 0.8 | 8 |
| | | $0.42\exp(-t/0.010)+$ | 3 | $0.2 \cdot 10^2$ |
| | | $1.76\exp(-t/0.0023)$ | 0.6 | $0.1 \cdot 10^2$ |
| | 50% tapwater | $1.875\exp(-t/2.55)+$ | 0.1 | 3 |
| | 50% MRFO | $0.970\exp(-t/0.00311)$ | $0.2 \cdot 10^2$ | 3 |

$T_2$-spectrum of liquids with multicomponent characteristics, the inverse Laplace transform is now commonly used [114].

A nonlinear least squares fit of the CPMG data provides estimates of the $T_2$ relaxation times and the initial signal intensities $s_{xy}(0)$. To this end, the data has been fitted by means of cftool, Matlab's curve fitting toolbox. By applying the trust-region optimization algorithm with weighted robust regression and 95% confidence bounds, the data of the pure samples is fitted with a single exponential function

$$f(t) = c_1 \exp(-c_2 t), \tag{5.9}$$

while for the data of the two-component mixtures a bi-exponential function

$$f(t) = c_1 \exp(-c_2 t) + c_3 \exp(-c_4 t) \tag{5.10}$$

is used. The parameters $c_1$ and $c_3$ are indirect estimates of the amount of hydrogen present in the sensitive volume of the coil, whereas parameters $c_2$ and $c_4$ are estimates of the inverse of the $T_2$ relaxation time. This model is just like the more complex model of equation 5.3 and 5.4 very sensitive to the initial values of the estimator, although to a lesser extent. The starting values of ($c_1$, $c_2$) in the single exponential fit are set to ($s_{xy}(2\tau)$, 0.9) with a lower limit of (0.0, 0.0). The starting values of ($c_1$, $c_2$, $c_3$, $c_4$) in the bi-exponential fit are set to ($0.7 s_{xy}(2\tau)$, 0.9, $0.3 s_{xy}(2\tau)$, 0.9) with a lower limit of (0.0, 0.0, 0.0, 0.0). Fitting CPMG data is more robust than fitting inversion recovery data, but in case of higher order exponentials it is again better to use a mapping process that solves a linear set of equations.

Figure 5.7 and 5.8 successively show the results of the CPMG experiments for 'set 1', consisting of tapwater and sunflower oil, and for 'set 2', consisting of tapwater and MRFO. The CPMG sequence of the experiments in 'set 1' consists of $N$ is 256 echoes with a time delay $\tau$ of 5 ms. The experiments in 'set 2' are all carried out with different settings. In the pure tapwater case, $N$ is set to 512 and $\tau$ is set to 5 ms. In the pure MRFO case, $N$ is set to 32 and $\tau$ is set to 0.5 ms. The 50:50 tapwater-MRFO case is measured twice, both using a CPMG sequence of 256 echoes: once with a $\tau$ of 0.375 ms and once with a $\tau$ of 0.750 ms. For a total overview of all obtained relaxation curves is referred to table 5.4. A comparison of the latter with table 5.3 shows that $s_{xy}(0)$, obtained from the CPMG data, is in general larger than $s_{xy}(0)$, obtained from the inversion recovery data. This is an effect of the way in which the signal intensity is derived from the raw NMR data: the CPMG sequence really takes the maximum amplitude of each echo, whereas the inversion recovery sequence omits extrapolation of the FID amplitude to its initial value right after the 90° pulse.
The nonlinear least squares method fits the model of equation 5.9 or 5.10 without much difficulty to the CPMG results. In contrast, large differences exist between the $T_2$ values obtained for the pure and mixture samples. Especially tapwater, whose $T_2$ is found to be far below 2 s in case of a pure sample and well over 2 s in case of a mixture. It is, on the one hand, not unlikely that the difference is due to non-optimized shimming. On the other hand, mutual effects play a more important part than in the inversion recovery fits: for all mixtures a longer $T_2$ is found for the tapwater component and a smaller $T_2$ for the oil component. However, the $T_2$

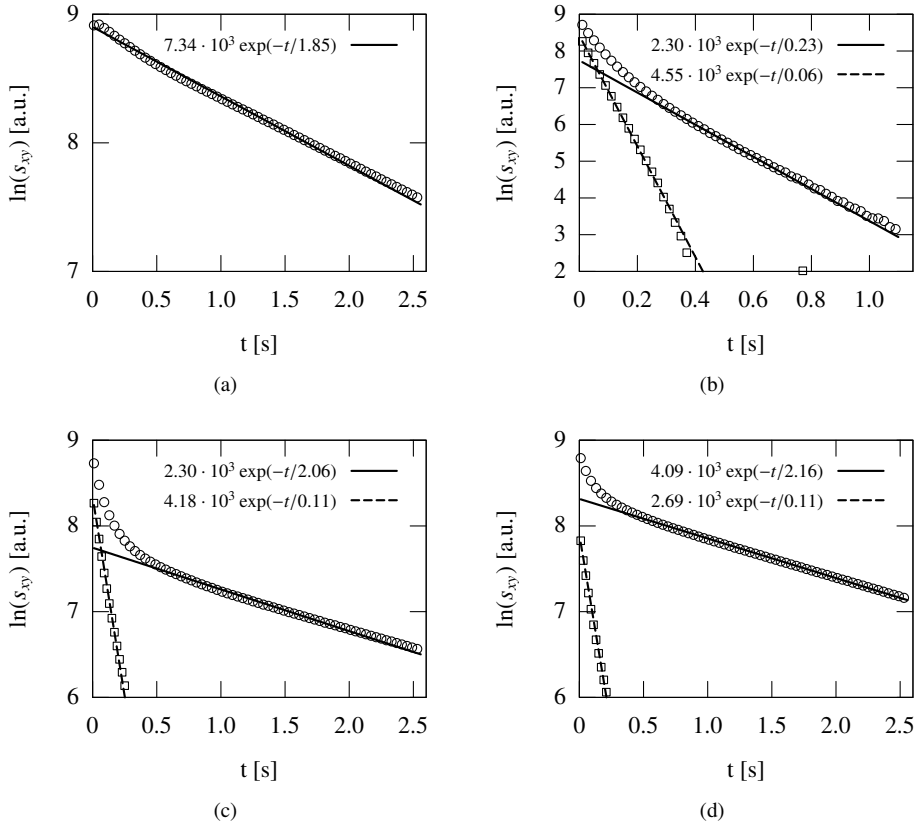


**Figure 5.7**: $T_2$ relaxation curve resulting from a CPMG pulse sequence of 256 echoes and $\tau$ = 5 ms of (a) tapwater, (b) Euroshopper sunflower oil and their mixtures in the proportion of (c) 33:67 and (d) 50:50, respectively. In case of two well-separated relaxation rates, the solid line is the fit of the component with the longest $T_2$ relaxation time. The squared data points show the difference between the dotted experimental data and the solid line. The dashed line is the fit of these squared data points and represents the component with the shortest $T_2$.

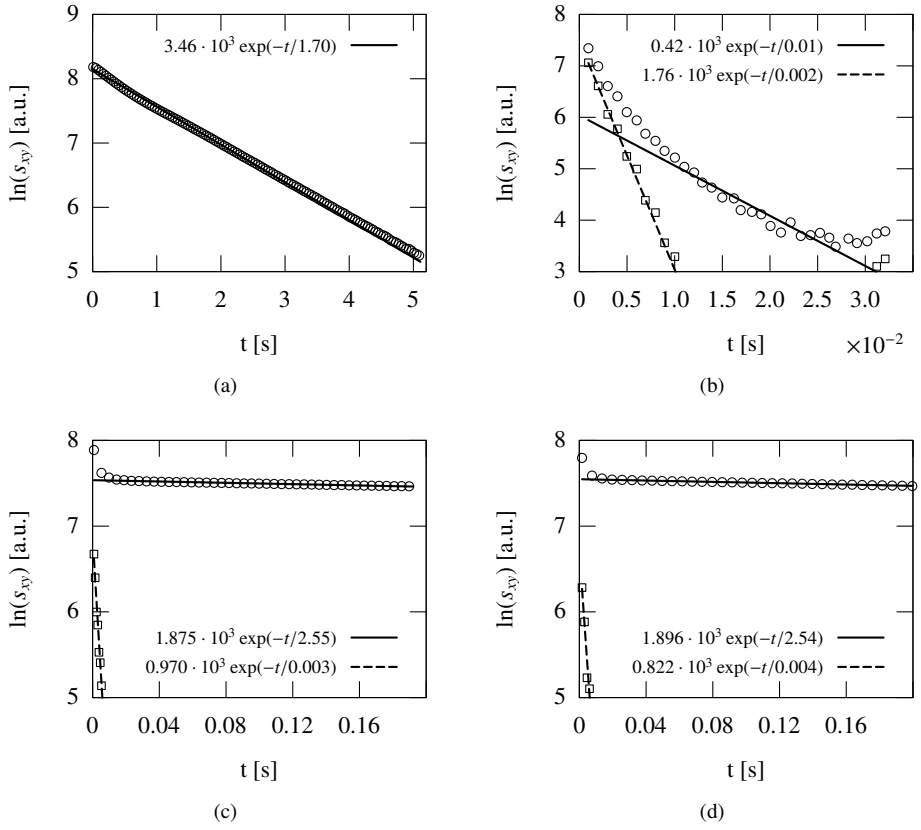


**Figure 5.8**: $T_2$ relaxation curve resulting from a CPMG pulse sequence of (a) tapwater (512 echoes, $\tau$ = 5 ms), (b) Argos marine residual fuel oil (32 echoes, $\tau$ = 0.5 ms) and (c,d) their mixtures in the proportion of 50:50 (256 echoes, $\tau$ = 0.375 ms and $\tau$ = 0.750 ms respectively). In case of two well-separated relaxation rates, the solid line is the fit of the component with the longest $T_2$ relaxation time. The squared data points show the difference between the dotted experimental data and the solid line. The dashed line is the fit of these squared data points and represents the component with the shortest $T_2$.

relaxation times are, according to the NMR rule for bulk fluids, on the whole smaller or equal than their $T_1$ relaxation times. It seems that the deviations originate in the bi-exponential model with which the CPMG data of the mixture has been fitted. Both sunflower oil and MRFO are now better described with a bi-exponential than a single exponential model, as Figure 5.7(b) and 5.8(b) illustrate. Nevertheless, the CPMG data of the mixtures is approximated with a bi-exponential instead of a triexponential function, such that the two relaxation times are both averages. Also the distribution of delay time $\tau$ can contribute to the difference in $T_2$ values. The relaxation curve of a two-component mixture consists in fact of two parts: the tail of the curve is fully described by the component with the largest $T_2$, while the contribution of the component with the shortest $T_2$ is only visible in the initial part of the curve. In contrast to the inversion recovery data, the CPMG data points are regulary spread with an interval of $2\tau$. Since fewer data points significantly contribute to the fit of the oil component, the accuracy decreases correspondingly. And erratic results for the $T_2$ of oil propagate via the least squares fit into erratic results for the $T_2$ of water. Therefore it is important that the value of $\tau$ is chosen in pursuance of the smallest expected $T_2$, such that enough data points lie in the nonuniform part of the CPMG curve. A large $\tau$ changes the lower limit of the range of $T_2$ that can be detected with the CPMG routine. The number of 180° pulses sets the maximum $T_2$ that can be measured.
Furthermore, the exact $T_2$ value has no influence on the accuracy of the flowmeter, provided the $T_2$ of all liquids is sufficiently long to be detected by the NMR probe. Although we have to investigate the influence of the uncertainty in $T_2$ on the values of the initial signal strength per component. Depending on the hydrogen density, the holdup of the individual components can be calculated again with equation 5.5 or 5.6. From table 5.4 it turns out that the hydrogen density of sunflower oil is as well 20% lower than water, whereas that of MRFO even reduced with 40%. The holdup has to be calculated again with equation 5.6 that is corrected for the hydrogen density. In the holdup calculations of both data sets, the initial amplitude of the NMR signal, $s_{xy}(0)$, is estimated with the single exponential model. In this way, the real tapwater-sunflower oil mixture of 33:67 and 50:50, respectively, is estimated by a ratio of 32:68 and 56:44. For the 50:50 tapwater-MRFO mixture a ratio of 54:52 is obtained. To test the effect of the $T_2$ fluctuations, the data is fitted in combination with the values obtained for the pure samples. This leads to an estimation of the uncertainty in the holdup of 5%. Just better than the uncertainty of the holdups as derived with the inversion recovery method, but much higher than estimated from the 95% confidence interval of the fit. This can be attributed to the fact that it is easier to fit a set of exponents without offset constraints.

## 5.3 Conclusions

Static dummies are used to investigate several essential phases of the flowmeter routine concerning the determination of NMR parameters. Related to their purpose in a multiphase flowmeter application, we can conclude the following:
Many inaccuracies in the measurements are due to the inhomogeneity of the pulsed magnetic field, among which the incoherence in the pulse lengths obtained with ALPHA3. Because the '$T_1$ Relaxation Residence Time Method', the main multiphase flowmeter routine, only

uses FID experiments, we prefer the AUTOP90 routine for the determination of P90. Despite the long duration of AUTOP90, the number of recalibrations is limited since P90 has a very stable value.

The inversion recovery sequence in combination with a multiexponential curve fit model is able to determine the $T_1$ over the full range of oil viscosities. With a nonlinear least squares fit the highest accuracy is obtained for the pure tapwater samples with an uncertainty of 0.5%. In contrast, for oil blends and mixtures the uncertainty is 10%. It is particularly difficult to discriminate mixtures if their $T_1$ values are close to each other, because the nonlinear fit will still converge even when signal contributions are assigned to other phases. Nonlinear fits with more than two exponentials do not converge. In that case, there should be switched to mapping in which a linear system of equations is solved for a predefined range of $T_1$. There are signs that the method works slightly better for an unequal distribution of significant mixed fractions than for almost equal fractions. However, when the ratio is highly unbalanced and one phase is in excess, it is expected that determination of the insignificant component will be very difficult. The holdups are estimated from the initial amplitudes of the phases with the values of the pure samples as reference. The inaccuracy is with 6% substantial and directly related to the accuracy of the $T_1$ value and initial amplitude of the oil component. They cause a systematic overprediction of the tapwater component and underprediction of the oil component.

The accuracy of the $T_2$ relaxation time as determined from the CPMG data is unsufficient when a nonlinear least squares fit with a bi-exponential model is used. Although the fit converges better than for the inversion recovery data, the relaxation time values of the pure and mixture samples easily deviate 20%. It can be attributed to the mutual exchange of signal contributions by the different components in the fit routine. As $\tau$ and the number of echoes determine the range of detectable $T_2$, using wrong settings can bias the results as well. Mapping is again the alternative for nonlinear fits of more than two exponential terms, since these do not converge either. In spite of the big error in the $T_2$ values, the holdup has an uncertainty of only 5%. Furthermore, the estimated volume fractions deviate less from the real values than with the inversion recovery data. It is therefore recommended to use CPMG data for the determination of the reservoir fluid composition.

The difference between the $T_1$ and $T_2$ relaxation times is in practice smaller and the distribution more complex. Moreover, at low pressures air does not contribute to the NMR signal where natural gas does. More sophisticated methods are required to determine the reservoir fluid composition: e.g. the '$T_1$ Relaxation Contrast' or 'Diffusivity Contrast' methods, which are used in NMR logging applications [44, 129, 168]. The obtained distribution can then be used as input parameter in the determination of the relevant $T_1$ relaxation times with the inversion recovery sequence.

The biggest advantage of the CPMG sequence over the inversion recovery sequence is the higher speed at which the fluid composition is determined. In the CPMG sequence the liquid magnetization has to reach the equilibrium state only once before the first pulse is applied.

In the inversion recovery sequence this is required for any pulse cycle anew. An additional drawback of the equilibrium restriction is the fact that both sequences can be applied under static conditions only.

The short $T_1$ of MRFO shows that the current flowmeter design is unsuited to measure flowrates of high viscous fluids with the $T_1$ Relaxation Residence Time Method, since thermal equilibrium is reached before the liquid enters the first probe. Several empirical functions of viscosity and temperature for the $T_1$ and $T_2$ relaxation times of crude oil, water and natural gas (see e.g. Coates et al. [44], Hirasaki et al. [95], Mardon et al. [168] and Winkler et al. [259]) can be helpful in designing a new apparatus that concentrates on a specific application. Besides this, they can serve as guidelines in controlling the two different delay times $\tau$ and the number of echoes provided the composition of reservoir fluids is roughly known.

# Chapter 6

# T1RRT and PGSE Measurements on Single-Phase Flow

Developing a flowmeter based on NMR requires a sound measurement method. Here, we examine if it matters whether T1RRT or PGSE is applied. Referring to the schematic diagram in Figure 6.1, the methods are each grounded on different NMR principles. T1RRT is a rapid passage technique, which looks at the plain magnetization envelope of the NMR signal. The signal intensity is a measure for the residence time of the fluid in a polarizing magnetic field and, as such, of the flow velocity. On the other hand, PGSE is a gradient technique that uses quadrature detection to derive the flow velocity from the phase of the NMR signal.

Apart from the experimental conditions, there are many factors that can influence the performance of the NMR multiphase flowmeter. Measuring the flowrate of multiphase flow is significantly more complex than of single-phase flow. As explained in chapter 3, both measurement methods actually derive the liquid flowrate in two stages. Successively, the flow velocity and liquid holdup are determined from the NMR signal, whereafter the total liquid flowrate is computed by taking their product. In order to get a clear sense for the quality of the velocity detection procedures, the single-phase flow regime is investigated first.

The first part of this chapter is a continuation of the research on the T1RRT method, presented in Daalmans et al. [50]. Since the technique does not provide information on the spatial velocity distribution, experiments on single-phase flow are very important. The plug flow assumption, commonly used in the flowmeter industry for analyzing the NMR signals, introduces systematic errors due to the presence of no-slip at the wall or phase slip in the case of multiphase flow. A comparison of numerical simulations with experimental results for laminar and turbulent single-phase flow is used to give an indication of the accuracy and performance of the flowmeter. Especially the laminar flow measurements are a perfect test, because its well known parabolic flow profile should give a good agreement between the measurements and simulations. Furthermore, the influence of the non-uniform polarizing magnetic field in the entry area of the flowmeter is investigated.

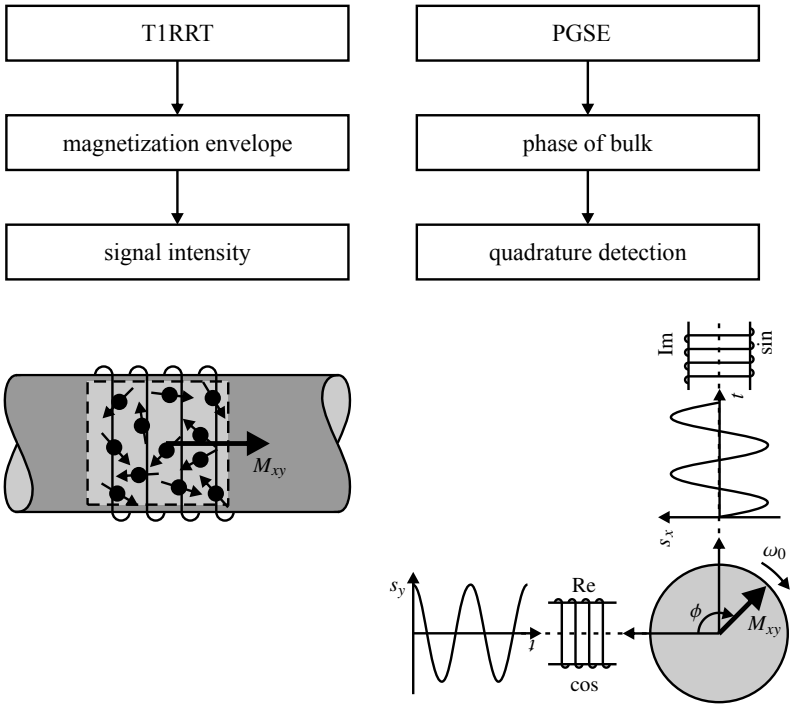


**Figure 6.1:** Comparison of the measurement principles of the T1RRT and PGSE methods.

In the second part of this chapter, the PGSE method is evaluated under the same flow conditions as the T1RRT experiments. PGSE has the great advantage that the phase shift is a weighted average of the flow velocity if the velocity probability distribution is symmetric around the average velocity [41]. A condition that is both applicable to plug and laminar flow. When it comes to turbulent flow, the relationship deviates from linear due to the higher order moments of velocity fluctuations [248]. Also much attention is paid to the technical difficulties in the production of well-calibrated gradient fields. The effect of eddy-currents on the results is discussed, along with the applicability and limitations of the measurement algorithm.

To conclude, the circumstances are addressed under which T1RRT and PGSE perform best by comparing their advantages and disadvantages.

## 6.1 Flow Configuration

Designing a configuration for the single-phase flow measurements at room temperature is complicated by the diverse requirements of the two NMR flowmetering methods studied. In the T1RRT method the NMR signal may not reach the equilibrium magnetization, while the PGSE method performs best with the strongest possible signal, but is much more sensitive to inhomogeneities in the magnetic fields. Given the limitations imposed by the dimensions and fixed positions of the r.f. probes at 0.5 and 2.5 m inside the NMR flowmeter, see section 4.1, three different flow loops are constructed that each serve a specific purpose.
The laminar flow loop is designed to serve in particular the T1RRT measurements. It was difficult to select a Newtonian fluid with the right balance between viscosity and related $T_1$ for which the signal detected by the first r.f. probe has not reached thermal equilibrium. Only then are the different velocities distinguished by a unique signal strength. When changing the concentration of an aqueous glycerol solution, the $T_1$ is not proportional to the viscosity, but changes only 100-fold by a 1000-fold change in the dynamic viscosity [28]. We take advantage of this property using a 60.6% vol. glycerol solution, which has a $T_1$ of approximately 350 ms. The chemical composition is crosschecked on the material properties of a sample at 22.5 °C. The density of 1154 kg m$^{-3}$ and, measured with an AR–G2 rheometer, dynamic viscosity of 15.2 mPa s are in good agreement with the values found in literature [30, 118]. Therefore, we will use these reference tables to correct the fluid properties for the temperature in the calculations of the Reynolds number. To obtain laminar flow with an average flow velocity of 0.2 – 1.0 m s$^{-1}$, the measurements are performed in a pipe of 9.85 mm inner diameter. A tube bundle of twelve of these pipes is spiralwise folded through the NMR flowmeter. This ensures that the flowrate and velocity distribution is the same in all pipes, whereas the increased occupied cross-sectional area optimizes the signal-to-noise ratio.
All measurements on turbulent pipe flow are performed with tap water. Without the strict upper limit on the Reynolds number, a perfect fluid for testing the T1RRT method with its $T_1$ of about 2.5 s. First of all, measurements are carried out in a facility with a pipe of 98.6 mm inner diameter, the size on which the NMR flowmeter design is based, which also serves as

two-phase flow loop. In order to study the influence of the inhomogeneous r.f. and gradient fields in the area around the probe head, which particularly affect the phase shift in the PGSE measurements, another small turbulent flow loop with a reduced inner pipe diameter of 34 mm has been built. A detailed description of the flow configurations is found in chapter 4.

## 6.2 $T_1$ Relaxation Residence Time Method

The T1RRT-method is a typical rapid passage technique, which uses the degree of longitudinal magnetization build-up during the residence time of the liquid in a polarizing magnetic field for measuring the average fluid velocity. It is also the material dependent longitudinal relaxation time $T_1$, which determines the phase-distinctiveness of the method in the case of multiphase flows.

### 6.2.1 Measurement Method

For the details of the T1RRT-method is referred to section 3.1. Here the essentials for the signal analysis are briefly repeated.

The basis of this flowmeter principle is formed by the pair-wise detection of an FID at two different streamwise positions. Their intensity is associated to the longitudinal magnetic moment of the nuclear spins in the fluid enclosed by the r.f. coil, just before the pulse. Depending on the initial magnetization, $\mathbf{M}_z(0)$, and the residence time, $t$, of a fluid element in magnetic field $\mathbf{B}_0$, the bulk magnetization vector, $\mathbf{M}_z$, will return in accordance with

$$M_z(t) = M_0\left(1 - \exp\left(-\frac{t}{T_1}\right)\right) + M_z(0)\exp\left(-\frac{t}{T_1}\right) \tag{6.1}$$

to its equilibrium magnetization $\mathbf{M}_0$. To avoid interactions, the repetition delay of the pulse sequence is set longer than the transit time of the fluid through the NMR flowmeter. When fresh fluid, i.e. initial magnetization zero, enters the uniform polarizing field of the flowmeter at $y = 0$, Eq. 6.1 reduces to

$$M_z(y, v_y) = M_0\left(1 - \exp\left(-\frac{y}{v_y T_1}\right)\right), \tag{6.2}$$

in which the residence time is replaced by the fraction of the streamwise position and velocity. The initial intensity of the FID following the 90° pulse,

$$s_y(v_y) = \frac{\pi}{4} {D_p}^2 s_0\left(L_c - v_y T_1 \exp\left(-\frac{y_c - L_c/2}{v_y T_1}\right)\left[1 - \exp\left(-\frac{L_c}{v_y T_1}\right)\right]\right), \tag{6.3}$$

is proportional to the integral of $M_z(y, v_y)$ over the coil length $L_c$, where $s_0$ is the intensity of the NMR signal corresponding to thermal equilibrium magnetization $M_0$. Nevertheless, the

signal processing works equally well with the intensity at a later instant, provided $s_0$ is corrected for the transverse relaxation. In the postprocessing software the integral is numerically solved

$$s_y(v_y) = \frac{\pi}{4} {D_p}^2 \frac{L_c}{N_y} s_0 \sum_{j=1}^{N_y} 1 - \exp\left( - \frac{y_c + L_c \left(2j - 1 - N_y\right)/2N_y}{v_y T_1} \right), \tag{6.4}$$

where the streamwise probe domain is divided into $N_y$ equidistant cells. If the r.f.coil is short, $s_y$ can be approximated with

$$s_y(v_y) \approx \frac{\pi}{4} {D_p}^2 L_c s_0 \left(1 - \exp\left( - \frac{y_c}{v_y T_1} \right)\right). \tag{6.5}$$

Equation 6.2 is almost linear over the length of a short r.f. coil, which results in an average of the longitudinal magnetization that is practically equal to its center value.

In order to determine the flowrate, the flowmeter makes use of a reference curve of the fraction between the signal intensities in the second and first r.f. coil. This fraction

$$\frac{s_{y,2}}{s_{y,1}}(\bar{v}_y) = \frac{\sum_{i=1}^{N_v} \sum_{j=1}^{N_y} 1 - \exp\left( - \frac{y_{c,2} + L_c \left(2j - 1 - N_y\right)/2N_y}{v_y[i] T_1} \right)}{\sum_{i=1}^{N_v} \sum_{j=1}^{N_y} 1 - \exp\left( - \frac{y_{c,1} + L_c \left(2j - 1 - N_y\right)/2N_y}{v_y[i] T_1} \right)} \tag{6.6}$$

is unique for the average flow velocity, as long as the magnetization in the first probe has not reached the equilibrium state. Equation 6.6 is evaluated over the velocity range of interest, whereafter the average streamwise velocity is obtained by consulting the curve for the fraction of the measured amplitude readings. The shape of the function depends principally on the actual $T_1$ relaxation time, but also on the velocity profile, which is, for this purpose, discretized as described in the next section. Contrary to two-phase flow, single-phase flow has a known liquid holdup. Therefore, it is also possible to resolve the velocity, being the only unknown, in a similar way with the signal of a single probe.

### 6.2.2 Average velocity field

Due to the nonlinear nature of the magnetization build-up, slow velocities contribute more to the total longitudinal magnetization $\mathbf{M}_z$ than the high velocities. Especially for flows with large slip between the phases or no slip at the wall, errors in the measured liquid flowrate are introduced when plug flow ($\forall i \in 1 \,..\, N_v\colon\ v_y[i] = \bar{v}_y$) is assumed in the algorithm of equation 6.6. Therefore, in the evaluation of the performance of the flowmeter, the measurement data are compared with simulations based on better representations of the flow pattern. For single-phase laminar flow the parabolic velocity profile

$$v_y(r) = 2\bar{v}_y \left(1 - \frac{4r^2}{D_p^2}\right) \tag{6.7}$$

**Table 6.1**: Exponent $n$ of power law Eq. 6.8, which is a simple representation of the average velocity distribution in single-phase turbulent pipe flow, in terms of the Reynolds number, $\mathrm{Re} = \bar{v}_y D_p/\nu$, for experiments carried out by Nikuradse [182].

| $n$ | 6 | 6.6 | 7 | 8.5 | 9.8 | 10 |
|---|---|---|---|---|---|---|
| Re | $4 \cdot 10^3$ | $9 \cdot 10^3$ | $4.3 \cdot 10^4$ | $3.96 \cdot 10^5$ | $1.536 \cdot 10^6$ | $3.240 \cdot 10^6$ |

is implemented, while the simulations of single-phase turbulent flow are based on the power law velocity profile

$$v_y(r) = v_y(0)\left(1 - \frac{2r}{D_p}\right)^{\frac{1}{n}}, \tag{6.8}$$

an empirical equation derived by Nikuradse [182, 223]. The value of the exponent $n$ depends on the ratio of the average to the maximum velocity

$$\frac{\bar{v}_y}{v_y(0)} = \frac{2n^2}{(n+1)(2n+1)}, \tag{6.9}$$

which varies slightly with the Reynolds number, as given in table 6.1. It increases from $n = 6$ at $\mathrm{Re} = 4 \cdot 10^3$ to $n = 7$ at $\mathrm{Re} = 1 \cdot 10^5$ and to $n = 10$ at the highest $\mathrm{Re} = 3.24 \cdot 10^5$ that Nikuradse investigated. In the simulations, the velocity profile is discretized into $N_v = 100$ concentric rings with an identical surface $\pi {D_p}^2/4N_v$. The average velocity $v_y[i]$ of each ring is determined by integrating respectively equation 6.7 or 6.8 over its surface.

### 6.2.3 Signal Processing

In a set of measurements, the NMR signal is obtained for different velocities including the equilibrium magnetization $s_0$ in each probe. It is measured at zero velocity, while the proton spins of the fluid remain at least a period of $5T_1$ in the polarizing magnetic field.
As equation 6.3 – 6.5 demonstrate, the strength of the NMR signal depends directly on the magnitude of the longitudinal relaxation time. For accurate velocity measurements with the NMR flowmeter, it is necessary to know the correct value of the $T_1$ relaxation time that belongs to the particular NMR signal. Before and after the total set T1RRT-measurements, the longitudinal relaxation time is therefore determined with the inversion recovery pulse sequence $180° - \tau - 90°$, see section 2.3.4, at zero velocity. Using the average of both $T_1$ values, $N_y = 120$ and $N_v = 100$, the reference curve of the flowmeter is calculated by means of Eq. 6.6 over an average velocity range of 0 – 3 m s$^{-1}$ with a resolution of 1 mm s$^{-1}$. Only for the study towards the applicability of the plug flow model, $N_v = 1$ is used.

Each flow measurement consists of $N_s$, respectively 10 and 30, consecutive acquired T1RRT sequences. The time average $v_{\mathrm{NMR}}$ is then calculated from the 10 – 30 velocities, determined for the sequences. Many factors contribute to the measurement accuracy of the flowmeter.

The experiment is designed such that setup errors are not significant: i.e. the measuring frequency is so low that the fluid in the r.f. coil is either completely replaced or can re-obtain equilibrium magnetization $M_0$. By using the average $T_1$ value, errors due to temperature fluctuations are also minor. The other factors can be distinguished in those related to the actual flow measurement or to the reference measurement at $v_y = 0$. Both mainly suffer from the fluctuating signal strength $s_y$ along the series of FIDs, which is only to a very limited extent influenced by phase errors as a result of the omitted phase cycling. As a result, repeatability is the largest contributor to the total accuracy. Accordingly, the uncertainty of the flow measurement is calculated corresponding to the 95 percent confidence level of the series' standard deviation, $\sigma(v_{\mathrm{NMR}})$,

$$u(\bar{v}_{\mathrm{NMR}}) = \frac{t_{\mathrm{ST}\ 0.025}(N_s - 1)\ \sigma(v_{\mathrm{NMR}})}{\sqrt{N_s}}, \tag{6.10}$$

where $t_{\mathrm{ST}\ 0.025}(N_s - 1)$ is the Student's t distribution for $N_s - 1$ degrees of freedom and the true standard deviation is estimated by the sample standard deviation

$$\sigma(v_{\mathrm{NMR}}) = \sqrt{\frac{1}{N_s - 1}\sum_i (v_{\mathrm{NMR}}[i] - v_{\mathrm{NMR}})^2}. \tag{6.11}$$

Prior to each repetition of the two FID experiments, subsequently carried out in the two probes, a relaxation delay of at least 5 $T_1$ is applied. This will prevent that previous pulses influence the amplitude of the NMR signal, as the 90° pulse resets the build-up of longitudinal magnetization $\mathbf{M}_z$. It is not really neccessary, but the steady flow conditions lend themselves well to such an exceptionally long delay. Besides, it ensures that systematic errors by the non-uniform velocity distribution can be excluded.
Because only the start of the FID is of interest, acquisition is limited to 128 points a dwell time of 1 $\mu$s apart, following a dead time of 92 $\mu$s. For comparison, the signal amplitude is quantified in two ways: (i) the initial strength at time zero, the center of the r.f pulse, by a linear least squares fit of the first 64 data points, and (ii) the average strength of the first 20 data points. All signals are normalized with the $s_0$, corresponding to the r.f. probe and method of data analysis, after which the flow velocity is determined for each pair of FIDs. The fit, which was thought as method to improve the accuracy of the flow measurements, turned out to be very sensitive to the riples on the FID signal. However, with 64 points the standard deviation is reduced to the level obtained with the average signal of method ii.

A big pro for the T1RRT method is its robustness regarding the NMR settings. Even an improper pulse length has a minor effect on the accuracy. The 90°-pulse is chosen for its maximum signal yield, but a different pulse length functions just as well, provided this is consistently used. Errors are mainly introduced by assumptions in the calculations of the reference curve. It is obvious that the method is sensitive to the $T_1$ relaxation time, on which the measurement principle is based. In practice, a comprehensive database, which links the $T_1$ to the temperature and composition of the fluid, can overcome this difficulty. Of a more fundamental nature is the error that is introduced when the permanent magnetic field is not conform the uniform block-shape we presumed. Together with a strategy to control the error, this problem will be addressed in the next section.

### 6.2.4 Non-uniform permanent field near the magnet entrance

As a result of the continuity property of magnetic field lines, the permanent magnetic field present does not satisfy the presumed rectangular shape, but starts already centimeters in front of the physical entrance of the magnet to grow gradually towards the inner magnet's field strength $\mathbf{B}_0$. The equilibrium magnetization $M_0$, which is according to equation 2.9 directly proportional to the magnetic field strength of the polarizing magnet, will therefore become a function of the spins position along the streamwise y-axis. Because the T1RRT-method is based on the rate at which the magnetization builds-up, deviations from a uniform permanent magnetic field are directly affecting the accuracy of measurement results calculated with equation 6.2. Therefore also the macroscopic magnetization $M_z(0)$ that has been built-up in a plug of fluid before entering the magnet, the last term in equation 6.1, should be taken into account.

To investigate the influence, the permanent magnetic field is first mapped with a Hall-sensor (Magnet-Physik HS-TGB5-104005) for a FH 55 magnetic field strength meter (Magnet-Physik 2000550) and the aid of a 3D traversing system. The measuring range in the y-direction extends from 25 cm in front to 43 cm within the magnet. Every centimeter, the cross sectional field is determined in 31 points that span the area between x = -1 – +5 cm and z = -5 – +5 cm at a grid resolution of 2 cm with some extra points on the main axes. In Figure 6.3 these points are denoted with dots. To get an impression of the entire field, we make use of the symmetry in the set-up by completing the remaining cross sectional area with the measured field strength values that are mirrored along the z-axis. In Figure 6.3, these points are marked with open circles.
Figure 6.2 shows some typical traces of the permanent magnetic field strength along the streamwise y-direction. It is clear that the initial polarizing field is far from uniform. Moreover, the first 20 cm inside the magnet are very inhomogeneous with strong peaks near the edges of the magnet blocks (x = 0, y = 6, z = ±5 cm). Only hereafter, the uniform field strength $\mathbf{B}_0$ of 0.334 T is reached. Because of its temperature dependence, the permanent magnetic field strength is slightly higher than the the nominal value of 0.331 T at 20 °C, mentioned in section 2.2.1 [45].

With Lagrangian simulations of the steady-state magnetization, in principle similar to Sudmeier et al. [239], we will analyze to which extent the measurement results are influenced by the non-uniform field. In order to track the history of the changing thermal equilibrium magnetization, experienced by a sample of fluid, it is necessary to divide the distance over which the magnetic field is present until detection in a fixed number of cells $N_B$. For convenience, we use cells with a length $\Delta y$ of 1 cm, corresponding to the measurement resolution of the magnetic field in the streamwise direction. Plug flow assumed, the use of equidistant cells has the additional advantage that the residence time

$$\Delta t = \frac{\Delta y}{v_y} \tag{6.12}$$

is the same in each cell. With the Hall-probe we observe the polarizing field for the first time at 25 cm in front of the magnet. Starting here with the lower bound of the first cell, $N_B$ is 75

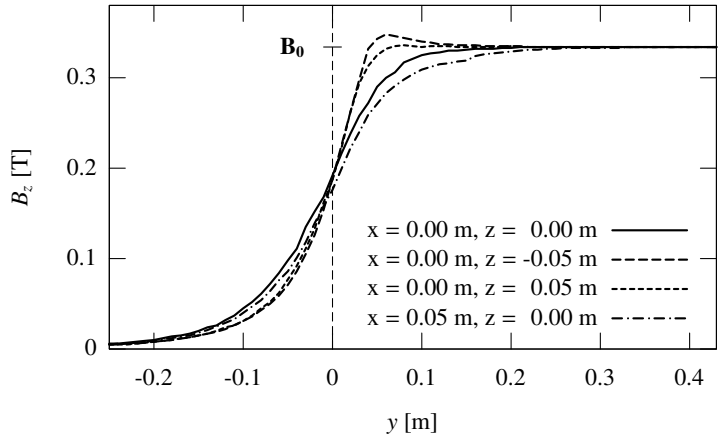


**Figure 6.2**: Hall-sensor measurements of the permanent polarizing $B_z$-field on several traces along the streamwise y-axis. $\mathbf{B}_0$ represents the level of the uniform field strength at the center of the magnet.

and 275 for, respectively, the first and second r.f. probe.

Considering magnetization $M_z[i-1]$ entering cell $i$, equation 6.1 is discretized to calculate the magnetization at the cell's end after a residence time $i\Delta t$ in the polarizing field

$$\mathbf{M}_z[i] = \mathbf{M}_0[i]\left(1 - \exp\left(-\frac{\Delta y}{v_y T_1}\right)\right) + \mathbf{M}_z[i-1]\exp\left(-\frac{\Delta y}{v_y T_1}\right), \tag{6.13}$$

where $M_0[i]$, the magnetization in thermal equilibrium with magnetic field $B_z[i]$, is supposed to stay at the constant level as determined for the lower bound of the cell. For the initial magnetization of fresh fluid entering the first cell at $y = -0.25$ m, $M_z[0] = 0$.

It remains to be seen whether the data processing should be corrected for the shape of the magnetic field. The length $y_c + \Delta l$ to which the actual field is equivalent, if uniform, is found from a comparison of the simulated magnetization attained when the sample leaves the last cell $N_B$ with the analytical expression of equation 6.2:

$$\mathbf{M}_z[N_B] = \mathbf{M}_0\left(1 - \exp\left(-\frac{y_c + \Delta l}{v_y T_1}\right)\right). \tag{6.14}$$

Because the magnetization is best distinguished at the first r.f. probe, all calculations are performed for this sensor at $y_c = 0.50$ m. Figure 6.3 shows the distribution of the added length of the replacement magnetic field

$$\Delta l = -v_y T_1 \ln\left(1 - \frac{M_z[N_B]}{M_0}\right) - y_c. \tag{6.15}$$

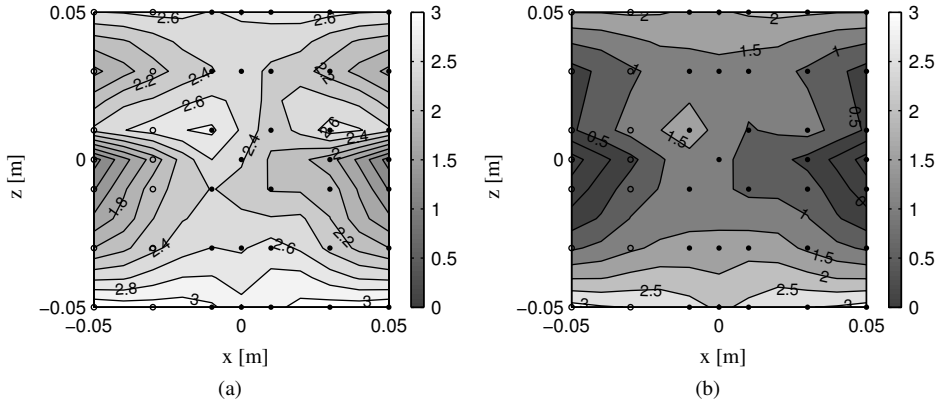


**Figure 6.3**: Simulation results of the added length $\Delta l$ [cm] by the non-uniform permanent magnetic field for plug flow at $v_y = 0.5$ m s$^{-1}$ and a) $T_1 = 2.5$ s or b) $T_1 = 0.35$ s. The closed dots are real measured grid points, while the open circles are their reflections by assuming symmetry with respect to both the x- and z-axis.

over the cross-section of the flowmeter for $T_1$ is 2.50 s and 0.35 s, typical for the water and 65 vol% glycerol-water solution that are used in the experiments. Implementation of the average added length as a correction factor prevents the postprocessing software from becoming unnecessarily complicated since it allows to keep on using the simplified uniform field model. At velocity $v_y = 0.5$ m s$^{-1}$, a considerable lower $\Delta l$ is obtained for glycerol-water than for water. However, when we look in Figure 6.4(a) at the average added length $\overline{\Delta l}$ as function of the flow velocity, both curves finally reach the same asymptotic value of 2.57 cm. Figure 6.4(b) shows the results of a similar study for the laminar flow profile. As in section 6.2.2, the parabolic velocity profile is first discretized into $N_v = 100$ concentric rings with an identical surface area $\pi {D_p}^2/4N_v$, whereafter equation 6.13 is summed over the velocity distribution:

$$\mathbf{M}_z[i] = \frac{1}{N_v}\sum_{j=1}^{N_v}\mathbf{M}_0[i]\left(1-\exp\left(-\frac{\Delta y}{v_y[j]T_1}\right)\right)+\mathbf{M}_z[i-1]\exp\left(-\frac{\Delta y}{v_y[j]T_1}\right). \tag{6.16}$$

To avoid that we have to deal with the spatial dependence of velocity and magnetic field, only the average magnetic field strength in the xz-cross section is used. The analytical solution of equation 6.15 is no longer valid for the determination of the added field length. Instead, the right side of equation 6.14 is calculated numerically for the discretized laminar profile as a function of $\Delta l$ between 0 and 10 cm with a resolution of 1 mm. The average added length is obtained from a comparison of $\mathbf{M}_z[N_B]$ with this curve, analogous to the flow measurements by means of calibration curve 3.7. Again, $\overline{\Delta l}$ eventually reaches an asymptotic value of 2.57 cm, although this takes considerably longer because of the more flattened shape of the curves.

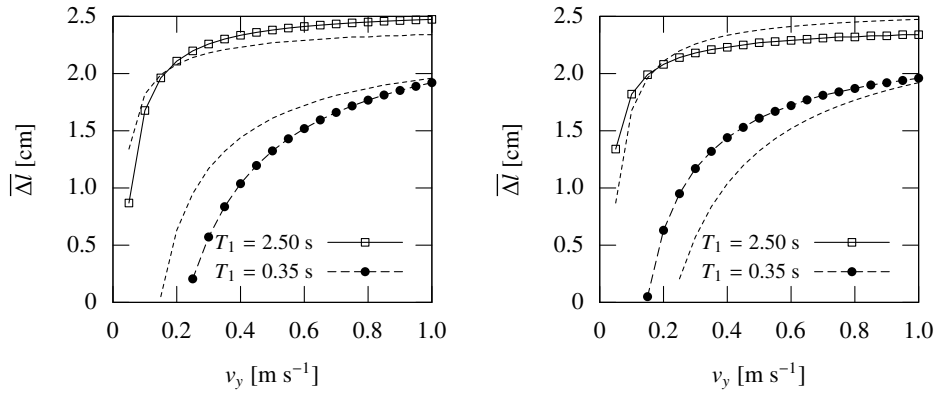


(a) plug flow (b) laminar flow

**Figure 6.4**: Added length of the non-uniform permanent magnetic field for a) plug flow and b) laminar flow, averaged over the full 5x5 cm cross-sectional area of Figure 6.3. The asymptote that all $\overline{\Delta l}$ approach is 2.57 cm. For reference purposes, the results for a) laminar and b) plug flow are plotted with dashed lines in the graphs of the other flow profile.

At last, the sensitivity of the T1RRT-method towards postprocessing the NMR signal with an incorrect added length $\Delta l_{\text{ref}}$ instead of the actual added length $\Delta l$ is studied. Based on the NMR signal of a single probe, this causes, in the case of plug flow, an error

$$\delta v_y = v_y \frac{\Delta l_{\text{ref}} - \Delta l}{y_c + \Delta l} \tag{6.17}$$

in the velocity reading. Three situations are examined: i.e. (i) $\Delta l_{\text{ref}} = 0$ cm, corresponding to a perfectly uniform magnetic field, (ii) the added length belonging to the median velocity $v_y = 0.5$ m s$^{-1}$ of the analyzed range and (iii) the asymptote $\Delta l_{\text{ref}} = 2.57$ cm. Figure 6.5 makes clear that the non-uniformity of the magnetic field should be taken into account, as the measurement error for $\Delta l_{\text{ref}} = 0$ cm rapidly increases for higher flow velocities. Because of the small nearly constant error, we advise to correct with the asymptotic value. However, this cannot remove its clear dependence on $T_1$. For the more viscous glycerol-water solution the error is a few mm s$^{-1}$ larger than for water.
The lower sensitivity of the second probe to changes in the magnetization, the signal is closer to equilibrium than in the first probe, results in a smaller error. This is somewhat misleading, since the measurements by the second probe are, for the same reason, generally less accurate.

## 6.2.5 Results and Discussion T1RRT

### 6.2.5.1 Laminar flow measurements

Because laminar flow has a well known parabolic velocity profile, it should give a good agreement between the measurements and simulations. This makes it a perfect test to study the

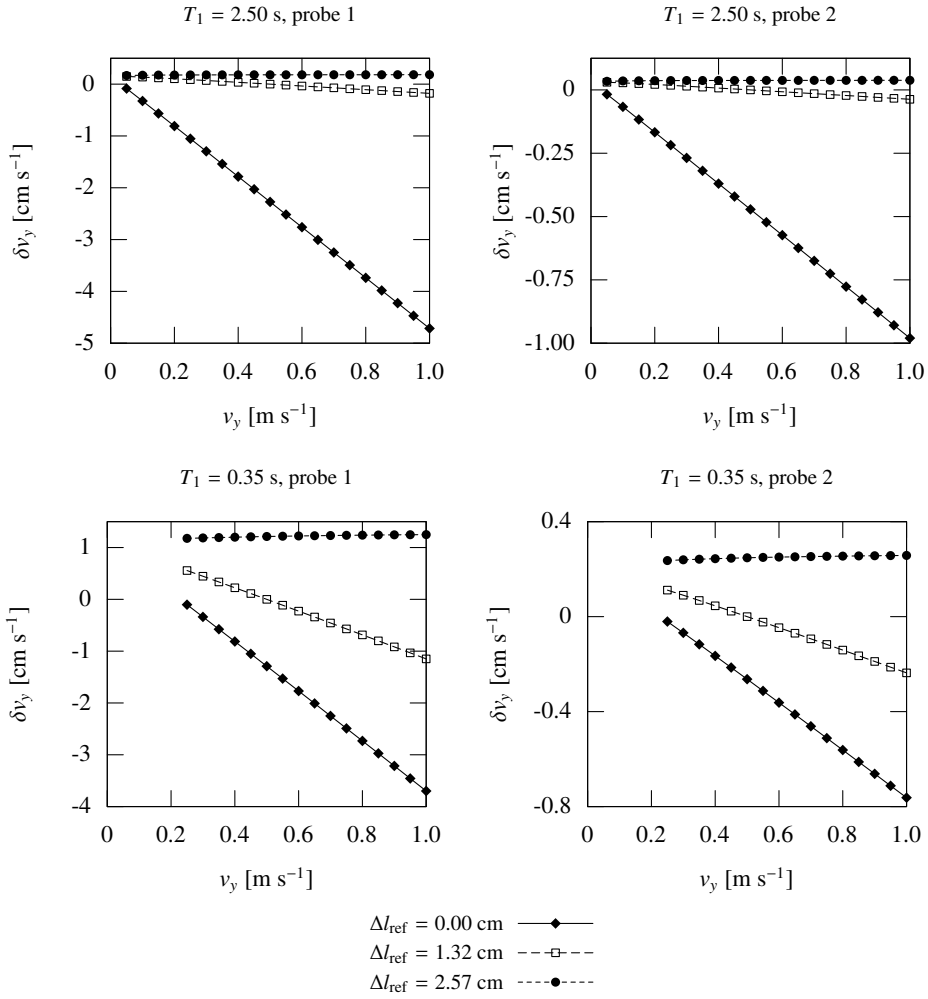


**Figure 6.5**: The error $\delta v_y$, which is made when the velocity measured with a single r.f. probe is evaluated with an incorrect added length $\Delta l_{\mathrm{ref}}$ of the non-uniform magnetic field, assuming plug flow.

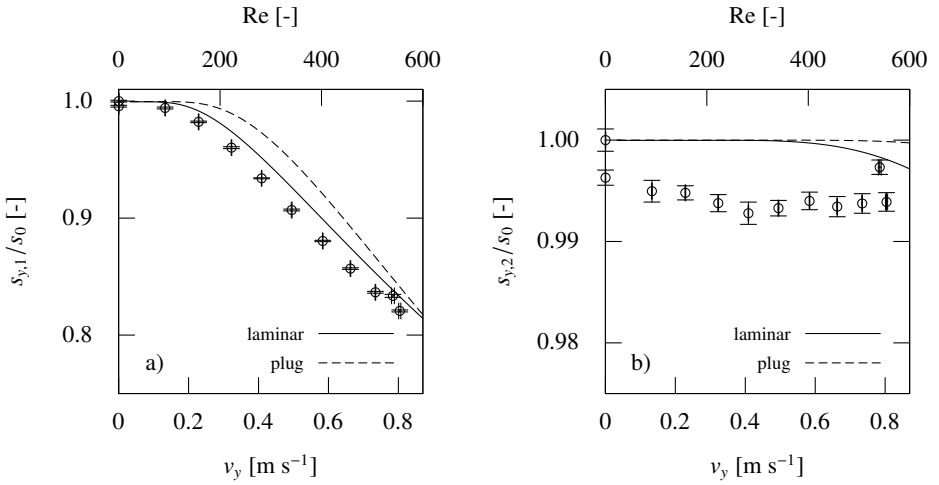


**Figure 6.6**: Comparison of the (∘) measured NMR signal intensity with simulation results ($T_1$ = 0.354 s, $\overline{\Delta l}$ = 2.57 cm) for the laminar flow model of equation 6.7 and plug flow in the (a) 1st and (b) 2nd r.f. probe.

performance of the NMR flowmeter. The measurements are carried out at 20.7 °C, where the 60.6% vol. glycerol-water solution has a dynamic viscosity of 16.5 mPa s and density of 1155 kg m$^{-3}$. The $T_1$ relaxation time is, on average, 0.354 s. Each flow measurement consists of 30 consecutive acquired T1RRT sequences.
Unless mentioned, the data in the Figures is processed according to the second method, which takes the average strength of the first 20 data points in the FID as signal amplitude reading. Figure 6.6(a) and 6.6(b) show the variation of the NMR signal normalized with the equilibrium magnetization measured in the 1st and 2nd coil, respectively, as function of the average fluid velocity. The solid line represents the expected signal intensity for the laminar flow pattern of equation 6.7. The dashed line gives the NMR signal when plug flow is assumed. In both simulations, the added length by the non-uniform polarizing magnetic field $\overline{\Delta l}$, is approximated with the asymptotic value of 2.57 cm as determined in section 6.2.4. It demonstrates that the flowrate reconstruction scheme based on plug flow ($\forall i, v_y[i] = \bar{v}_y$) is unsuited for the evaluation of laminar flow, where the flow profile is non-uniform.

The liquid holdup of single-phase flow is by definition equal to one. To this end, only one unknown, the average liquid velocity, has to be measured with the NMR flowmeter. Because the signal intensity curve $s_y(v_y)$ has also a unique value for each average velocity, the value of the NMR signal obtained with a single r.f. probe is in principle enough to determine the liquid flowrate. Since there are two r.f. probes available in the NMR multiphase flowmeter, this enables us to determine simultaneously the average fluid velocity for single-phase flow in

three different ways: (i) from the NMR signal in the 1st r.f. probe, (ii) from the NMR signal in the 2nd r.f. probe, and (iii) from the ratio of the NMR signals in both r.f. probes. However, for accurate velocity measurements, the slope of the separate intensity curves, or its ratio, should be large enough to distinguish different velocities. This applies to the first detection coil, where the slope of the intensity curve is large enough for average velocities larger than 0.24 m $s^{-1}$. As Figure 6.6(b) demonstrates, we cannot use the second probe for the velocity determination in this particular velocity range. The residence time of the fluid is much larger than the spin-lattice relaxation time ($t \gg T_1$) and the total magnetic moment of the proton spins is consequently near thermal equilibrium. Due to the almost uniform intensity distribution curve in combination with the measurement inaccuracy, different velocities cannot be distinguished.

In Figure 6.7(a) the ratio of the signal intensities measured in both r.f. probes is presented. Because the strength of the NMR signal measured in the 2nd r.f. probe is almost uniform, this curve is, in fact, the inverse of the signal measured in the 1st r.f. probe, plotted in Figure 6.6(a). Consequently, it is expected that the average velocities, determined with the flowmeter, will be the same for the evaluation algorithm based on the NMR signal of the 1st r.f. probe and the algorithm based on the ratio of the NMR signal in both coils. Besides, Figure 6.7(a) makes again clear that the flowmeter algorithm based on plug flow introduces systematic errors. It overpredicts the velocity for low flowrates, while it underestimates the flow for high flowrates as the plug and laminar curve intersect just after the displayed $v_y$-range.

Figure 6.6(a) and 6.7(a) show that the measured data clearly deviates from the simulations. On the steep slope, the simulated curve is parallel to the data. As a result, the measured velocity is sytematically overestimated in the postprocessing. Contrary to our presumption in Daalmans et al. [50], this is not caused by the use of a wrong $T_1$ relaxation time. The difference is due to the non-uniformity of the permanent magnetic field, which we simulate with an artificial extra length $\overline{\Delta l}$ of the uniform magnet. Instead of using an added length that is corrected for the velocity and $T_1$, we use the asymptotic value of 2.57 cm as recommend in section 6.2.4. Based on the study for plug flow in the same section, we expect the velocity to be overestimated with about 1.2 cm $s^{-1}$. The real offset is found from the fit of $v_{\mathrm{NMR}}$, the velocity obtained with the NMR flowmeter, versus $v_y$, the velocity measured with a calibrated electromagnetic flowmeter in Figure 6.7(b). With 3.7 cm $s^{-1}$, the overprediction is constant but larger than expected. Most likely, the difference is related to the space-dependent inhomogeneity of the permanent magnetic field transverse to the flow direction, which is ignored in the investigation of $\overline{\Delta l}$. Furthermore, it is enhanced by the non-uniformity of the laminar flow profile. To a lesser degree, the repeatability plays a part. This is demonstrated by Figure 6.7(c) in which the directional bias error, the difference between the measured and reference velocity, is shown. Under steady flow conditions, a substantial variation is observed in the signal strength of the series consecutively acquired FIDs. For the flowrates with a sufficient signal-fraction resolution ($v_y > 0.24$ m $s^{-1}$), the interval of the measurement uncertainty calculated with Eq. 6.10, is with 1 cm $s^{-1}$ almost 25% of the average velocity bias error. However, since the velocity offset is a systematic error, the flowmeter readings could, in principle, be corrected by the calibration value of the bias for the $T_1$ in question.

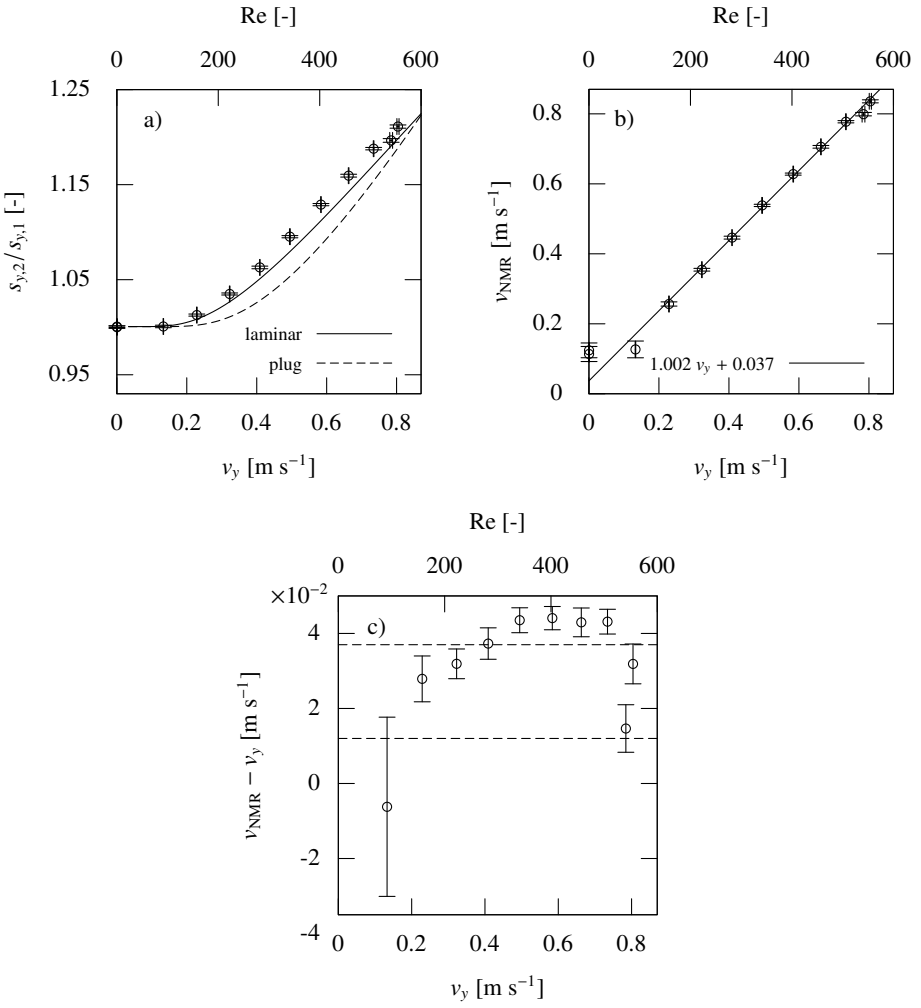


**Figure 6.7**: (a) Ratio of the signal intensity in the 2nd r.f. coil with respect to the 1st r.f. coil as a function of the fluid velocity. In the flowmeter reconstruction algorithm, the curve of the laminar flow simulations ($T_1$ = 0.354 s, $\overline{\Delta l}$ = 2.57 cm, $N_v$ = 100, $N_y$ = 120) is consulted to determine the flow velocity ($v_{\mathrm{NMR}}$). (b) A comparison of the NMR velocity with reference velocity $v_y$ gives an indication of the linearity and (c) their difference that of the directional bias error. The dashed construction lines are located at 1.2 and 3.7 cm s$^{-1}$.

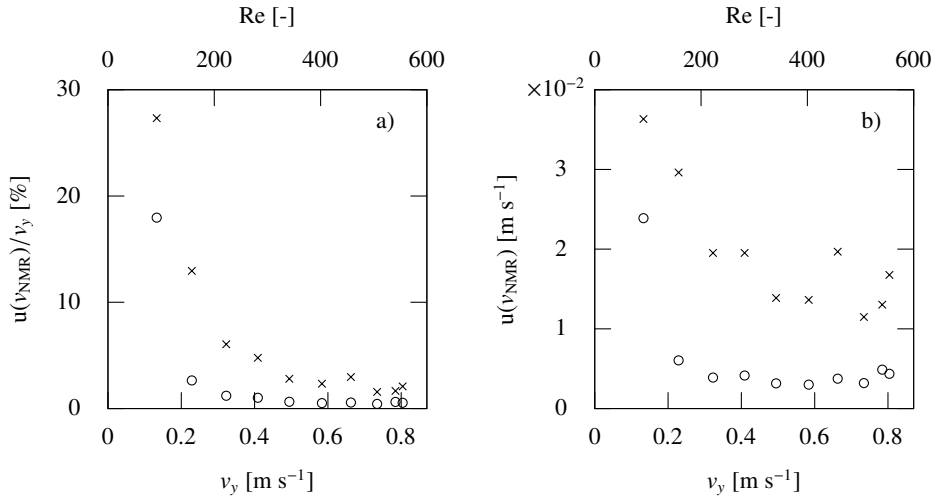


**Figure 6.8**: (a) Relative and (b) absolute uncertainty with 95% confidence level of the laminar flow measurements based on 2 methods of quantifying FID signal amplitude $s_y$: (×) the initial signal strength by extrapolating the linear least squares fit of the first 64 points towards time zero, the center of the r.f. pulse, and (∘) the average strength of the first 20 data points.

In order to study the linearity of the flowmeter, the velocity measured with NMR is plotted in Figure 6.7(b) as a function of the reference values obtained with a calibrated electromagnetic flowmeter. The T1RRT method achieves with +0.2% of the flowrate a very good linearity. This confirms that it is justified to replace the effect of the inhomogeneous entry area of the magnet with an extra length of 2.57 cm, equivalent to a uniform field. Usage of an incorrect polarization length would result in a wrong slope of the signal-fraction curve and, as such, in a poor linearity of the flowmeter.

At last, we investigate how well the data reflects the actual flowrate. To this end, both the relative and absolute measurement uncertainty are depicted in, respectively, Figure 6.8(a) and (b). For comparison, both methods of quantifying the signal amplitude of the FIDs are plotted. Crosses denote postprocessing with the initial signal strength at time zero, which is obtained from a linear least squared fit of the first 64 data points. Circles denote the data processed as average signal strength of the first 20 data points. It is obvious that the fit results in a reduced measurement accuracy. The extrapolation exaggerates the ripples on the FID signal and the fitting method should, therefore, not be used. Further analysis is again limited to the second method, based on the average FID signal.
From the graphs also appears that the accuracy of the flowrate is directly related to the gradient of the signal-fraction curve 6.6. From $v_y = 0.46$ m s$^{-1}$, corresponding to a gradient of

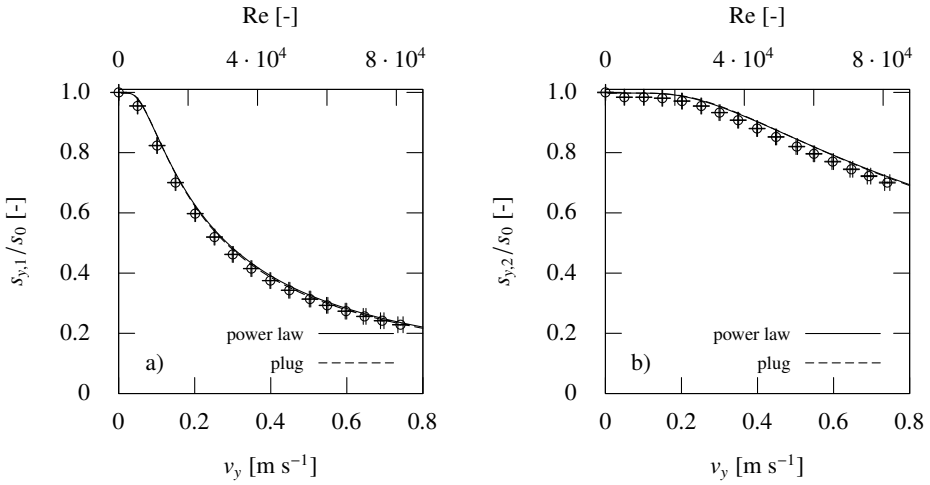


**Figure 6.9**: Comparison of the (∘) measured NMR signal intensity in the 98.6 mm i.d. pipe with simulation results ($T_1$ = 2.69 s, $\overline{\Delta l}$ = 2.57 cm) for the turbulent 'power law' flow model of equation 6.8 and plug flow in the (a) 1st and (b) 2nd r.f. probe.

0.37 s m$^{-1}$, the absolute uncertainty reaches a constant level of 4 mm s$^{-1}$ for the displayed flowrange. This means, as Figure 6.8(a) shows, that the flowmeter exhibits 0.6 percent of rate performance with 95% confidence level. Actually, there is a slight improvement of the performance with the flowrate, because the slope of the signal-fraction curve is practically constant.

#### 6.2.5.2 Turbulent flow measurements

To study the effect of non-uniformities in time, experiments on single-phase turbulent flow with normal tap water are carried out at room temperature in two horizontal pipelines, respectively of 98.6 and 34 mm inner diameter.

#### 98.6 mm i.d. pipe

The pipe with an inner diameter of 98.6 mm and an entrance length of 320 $D_p$ approaches the aimed application of the NMR flowmeter in the oil industry best. The $T_1$ relaxation time, as measured with the inversion recovery pulse sequence, is on average 2.69 s. In a measurement series, the T1RRT pulse-sequence is repeated 30 times. Unless mentioned, we present again only the data processed according to the second method, which uses the average strength of the first 20 data points in the FID as amplitude reading. Also the inhomogeneous area of the polarizing magnet $\mathbf{B}_0$ is again replaced by an added length $\overline{\Delta l}$ of 2.57 cm.

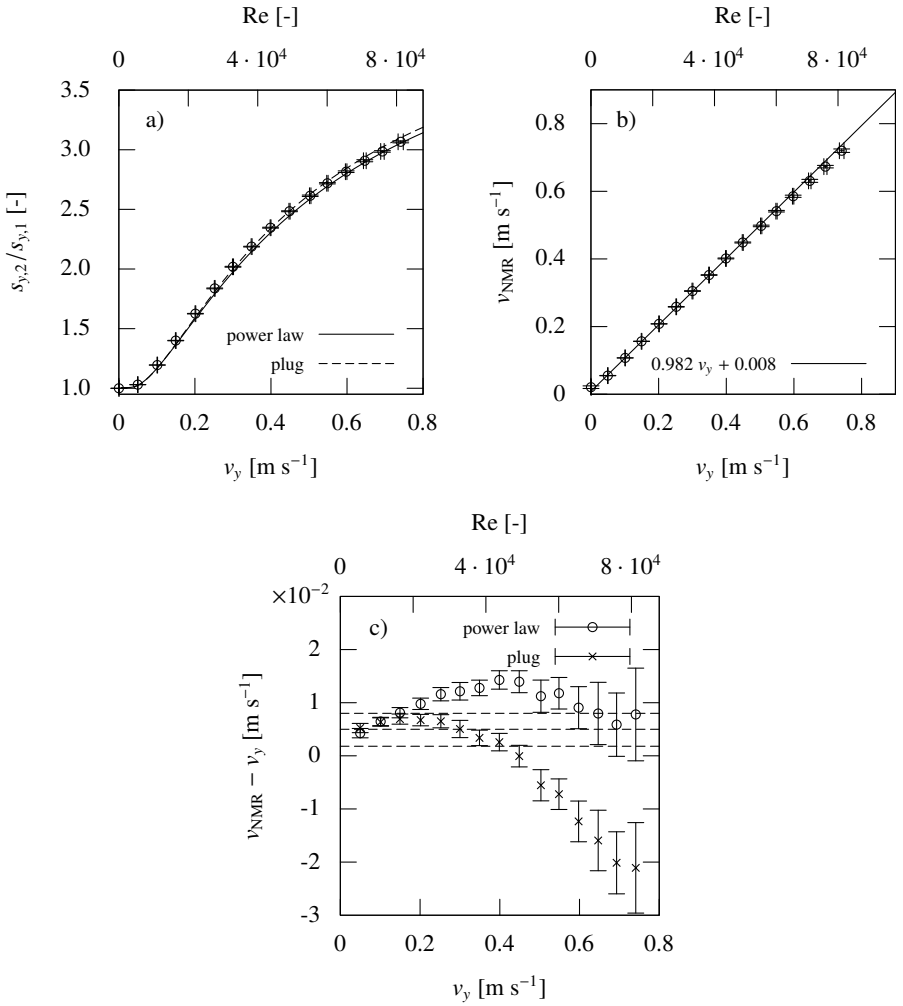


**Figure 6.10**: (a) Ratio of the intensity in the 2nd r.f. coil with respect to the 1st r.f. coil as a function of the velocity. The NMR velocity, $v_{\mathrm{NMR}}$, is reconstructed by consulting the simulated curve ($T_1$ = 2.69 s, $\overline{\Delta l}$ = 2.57 cm, $N_y$ = 200) for both plug flow ($N_v$ = 1) and the power law velocity profile ($N_v$ = 100, $n$ = 7). (b) A comparison of the plug flow based NMR velocity with reference velocity $v_y$ gives an indication of the linearity. For the power law model, the fit reads $v_{\mathrm{NMR}} = 1.020 v_y + 0.005$ m s$^{-1}$. (c) The directional bias error with construction lines at 0.18, 0.5 and 0.8 cm s$^{-1}$.

In Figure 6.9 the results of the normalized NMR signal against the fluid velocity are given. The slope of the intensity curve in the second coil is, contrary to the laminar flow experiments, large enough to be used for velocity determination. Only for velocities below 0.3 m s$^{-1}$ larger inaccuracies can be expected in the velocity that is obtained with the NMR flowmeter. The trend of the measured data agrees well with the simulation results for both plug flow and the power law velocity profile of equation 6.8 with $n$ set to 7. Despite the actual Reynolds number dependence of $n$ as given in table 6.1, this is a very defensible choice. The $1/7$-th-power velocity distribution law is related to Blasius's law of friction for smooth pipes of circular cross-section, which is valid for Reynolds numbers, $\mathrm{Re} = \bar{v}_y D_p/\nu$, between 4000 and 100,000 [223]. All data points fall within this range. As the simulations nearly coincide, the flowmeter can now use, contrary to laminar flow, the much simpler plug flow model.
However, the measured data has in both coils a small negative offset compared to the simulated intensity curves. Both using the asymptote for the added length of the $\mathbf{B}_0$-field and the efflux of magnetization between the r.f. pulse and acquisition have only a minor contribution. The NMR signal loss is mainly caused by turbulence, which leads to increased dephasing in the presence of the weak magnetic field gradients in the poorly shimmed zones in the vicinity of the pipe wall. For an estimation of the theoretical signal loss, one could develop a model, similar to those for echo amplitudes in a CPMG sequence by e.g. Gao and Gore [73] or Kuethe and Gao [145], which takes both turbulent diffusivity and the turbulence intensity, $\overline{v'^2}$, in the direction of the gradient into account. Nevertheless, the signal loss hardly leads to errors, when the velocity is determined from the ratio of the signal intensities. The effect cancels itself out, as the signal multiplier is almost equal for both r.f. probes. Figure 6.10(a) shows indeed a good agreement between the measurements and simulations.

Unlike the individual signal intensities, a small difference can be noticed between the power law and plug flow simulations of the signal ratio in Figure 6.10(a). At higher flowrates, the plug flow model will result in velocities about 3% lower than the power law model. The flowmeter readings appear midway between the two curves. This also follows from the linear fits of the NMR velocity in Figure 6.10(b) and its caption, giving a linearity of -2% and +2% of the flowrate for processing with, respectively, the plug and power law model.

With upper bounds at 2 cm s$^{-1}$, the absolute velocity bias is again many times larger than the error $\delta v_y$, expected for using the asymptote of the added length by the non-uniform magnetic field and estimated with Eq. 6.17 to be 0.2 cm s$^{-1}$. It is clear from Figure 6.10(c) that the behaviour is quite different for both methods of modeling $v_y$. The power law model causes a systematic overprediction of the velocity, which becomes insignificant towards repeatability with increasing flowrate. The velocity bias by the plug flow model has a similar start, but is followed by a negative growth for average velocities above the inflection point of the signal-fraction reference curve at $v_y = 0.17$ m s$^{-1}$. We can explain the trend with the different weight every velocity in the turbulent profile has, owing to the non-linearity of function 3.6. Because of the upward curvature for average velocities below the inflection point, the high velocities contribute relatively more to the signal fraction and the plug flow algorithm will overestimate the average velocity. Above the inflection point, the function curves downward. There, the weighting factor is larger for low velocities, so the average streamwise velocity will

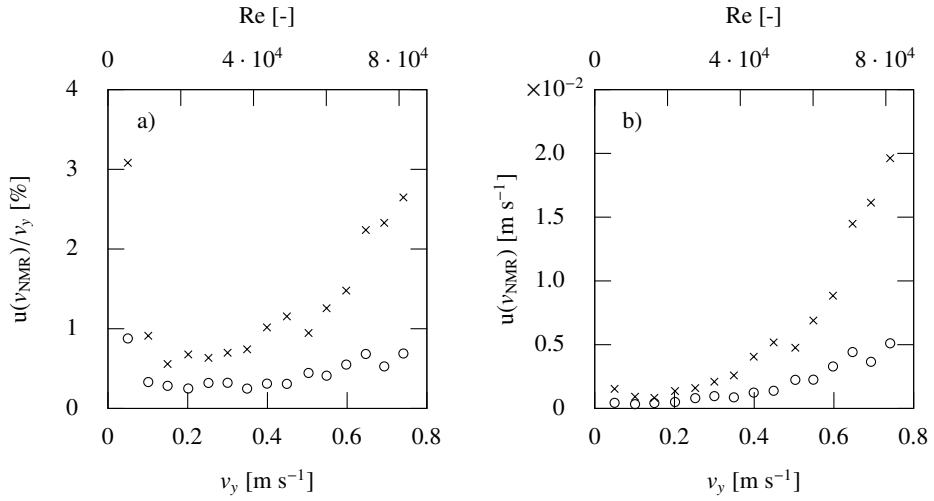


**Figure 6.11**: (a) Relative and (b) absolute uncertainty with 95% confidence level of the plug flow based turbulent flow measurements in the 98.6 mm i.d. pipe based on 2 methods of quantifying FID signal amplitude $s_y$: (×) the initial signal strength by extrapolating the linear least squares fit of the first 64 points towards time zero, the center of the r.f. pulse, and (∘) the average strength of the first 20 data points.

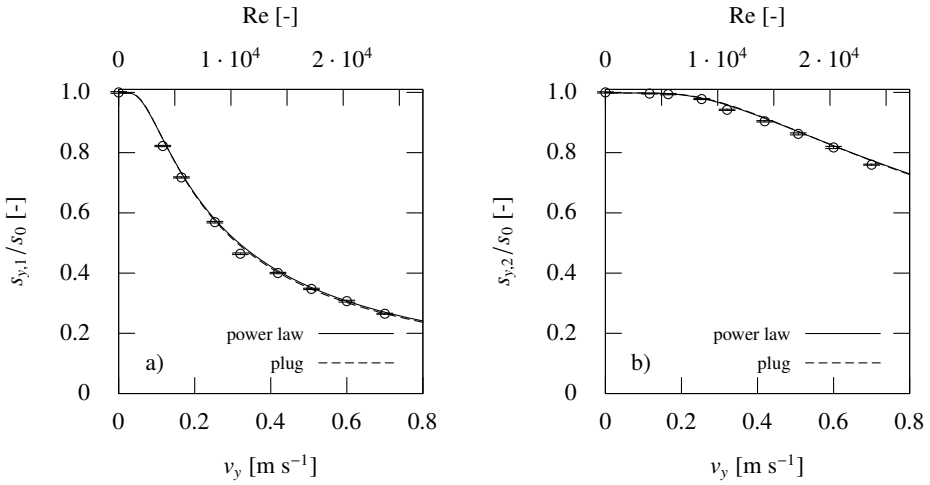


**Figure 6.12**: Comparison of the (∘) measured NMR signal intensity in the 34 mm i.d. pipe with simulation results ($T_1$ = 2.43 s, $\overline{\Delta l}$ = 2.57 cm) for the turbulent 'power law' flow model of equation 6.8 and plug flow in the (a) 1st and (b) 2nd r.f. probe.

be underestimated by the plug flow model. However, we expect the growth of the velocity bias eventually to come to a halt. As the time-averaged velocity profile flattens with increasing Reynolds number, the approximation by the plug flow model gets better. Besides, only for velocities above 0.6 m s$^{-1}$ the plug flow model performs worse than the power law model.

The uncertainty owing to repeatability is directly dependent on the slope of the signal-fraction curve. In Figure 6.11(a) and (b) we show, respectively, the relative and absolute uncertainty calculated using Eq. 6.10. As we saw before in the laminar flow measurements, the post-processing method that determines the amplitude of the FID by fitting its first 64 data points (crosses) has a poor performance in comparison with the method that takes the average of the first 20 data points (circles) and should not be used. Disregarding the velocity bias, the repeatability exhibits then 0.7% of rate performance with the flowrate.

### 34 mm i.d. pipe

For a comparative study on the influence of the field inhomogeneity, the turbulent measurements are also performed in a pipe with 34 mm i.d. and an entrance length of 70 $D_p$. The $T_1$ relaxation time, as measured with the inversion recovery pulse sequence, is on average 2.43 s. Contrary to the previous cases, the T1RRT pulse sequence is repeated only 10 times in each measurement series. Without notice, the signal strength is again processed as average of the first 20 data points of each FID. Also the inhomogeneous entry area of the magnet is again modeled with an added length $\overline{\Delta l}$ of 2.57 cm.

The normalised signals, detected from the individual probes, show in Figure 6.12 a comparable behaviour with the turbulent measurements in the 98.6 mm i.d. pipe. However, the difference between the measurements and simulations has decreased. This supports our hypothesis that the negative offset is due to turbulence in presence of parasitic magnetic field gradients. Because of the smaller pipe diameter, the homogeneity of the magnetic field strongly improves, whereas the lower turbulence intensity, the Reynolds number is a factor three less, causes less dephasing as well.

Due to the decreased accuracy, inherent to the lower number of T1RRT-sequence repetitions, both simulated curves in Figure 6.13(a) lie almost completely within the uncertainty interval of the measured ratio between the signal intensities. Accordingly, we expect the velocities obtained with the NMR flowmeter to approximate the reference velocities by the electromagnetic flowmeter. With a linearity of -0.3%, the comparison of the measured data with the power law model has indeed an excellent agreement. For processing with the plug flow model, we find in Figure 6.13(b) a linearity of -4% of the flowrate. As demonstrated in Figure 6.13(c), the directional bias error is of the same size as for the turbulent flow in the bigger pipe. An indication that the bias error is caused by the model of the velocity profile and not by the inhomogeneity of the magnetic field.

The relative and absolute measurement uncertainty are respectively shown in Figure 6.14(a) and (b). In comparison with the values for the 98.6 mm i.d. pipe in Figure 6.11(a) and (b), the measurement uncertainty by the use of only 10 instead of 30 repetitions doubles. In accordance with the difference in the multiplier of equation 6.10, the flowmeter achieves indeed a repeatability of 1.4 percent rate performance with 95% confidence level. Hence, the standard deviation of the series FIDs already converges at 10 measurements to a fixed value.

### 6.2.6 Conclusion T1RRT

Experiments on laminar and turbulent flow over a velocity range of 0 to 0.8 m $s^{-1}$ demonstrate that the T1RRT-sequence is an appropriate flowmetering principle for single-phase flow. The flowmeter achieves a very good linearity, as long as the non-uniform shape of the polarizing magnetic $B_0$-field is taken into account. With Lagrangian simulations of the magnetization build-up in the fluid, based on Hall-sensor measurements of the magnet's entrance area, we have shown that the premise of a perfectly uniform field produces a velocity bias that increases with the flowrate. Usage of an incorrect polarization length results in a wrong inclination of the signal-fraction reference curve. The actual field deviation is best processed as an added length, equivalent to its asymptote when having a uniform magnetic field strength. This has two advantages: (i) the asymptote is universal for all velocity distributions, and (ii) the velocity dependence is removed, since correcting the polarization length with the asymptote results in a small, but constant, positive velocity bias. However, this cannot remove the $T_1$-dependence of the velocity bias. The offset is larger for shorter $T_1$.
Considering the measurement uncertainty, the signal amplitude should be determined from

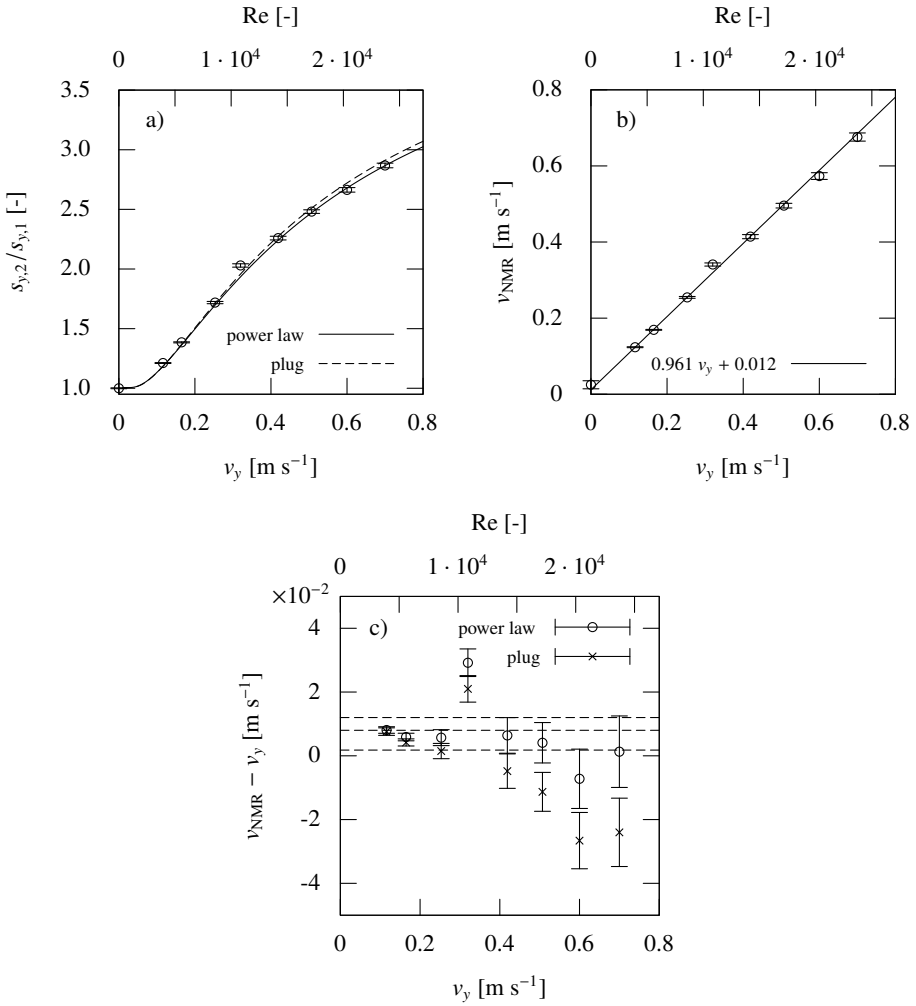


**Figure 6.13**: (a) Ratio of the intensity in the 2nd r.f. coil with respect to the 1st r.f. coil as a function of the velocity. The NMR velocity, $v_{NMR}$, is reconstructed by consulting the simulated curve ($T_1$ = 2.43 s, $\overline{\Delta l}$ = 2.57 cm, $N_y$ = 200) for both plug flow ($N_v$ = 1) and the power law velocity profile ($N_v$ = 100, $n$ = 7). (b) A comparison of the plug flow based NMR velocity with reference velocity $v_y$ gives an indication of the linearity. For the power law model, the fit reads $v_{NMR} = 0.997 v_y + 0.008$ m s$^{-1}$. (c) The directional bias error with construction lines at 0.18, 0.8 and 1.2 cm s$^{-1}$.

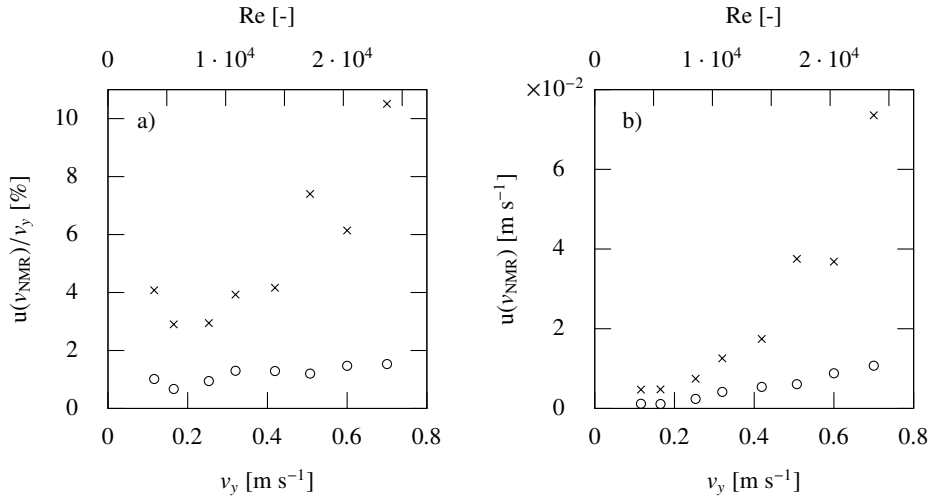


**Figure 6.14**: (a) Relative and (b) absolute uncertainty with 95% confidence level of the plug flow based turbulent flow measurements in the 34 mm i.d. pipe based on 2 methods of quantifying FID signal amplitude $s_y$: (×) the initial signal strength by extrapolating the linear least squares fit of the first 64 points towards time zero, the center of the r.f. pulse, and (∘) the average strength of the first 20 data points.

the average strength of, at least, the first 20 data points of the FID. A linear least squares fit of the first data points is unsuited for obtaining the signal strength, as the fit amplifies the ripples on the FID signal.

The plug flow algorithm cannot be used for the evaluation of laminar flow, because it introduces systematic errors. For turbulent flow, the much simpler plug flow approach can be fairly used. There, the simulations for plug flow and the power law profile nearly coincide. Though the linearity of the measurements shows that the power law profile has a slightly better performance.

Unlike the constant velocity bias of about 4 cm $s^{-1}$ in the laminar measurements, the error varies in the case of turbulent pipe flow between -2 and 2 cm $s^{-1}$. Turbulent measurements at two different pipe diameters demonstrate that this total directional bias error is due to the flow model used in processing the NMR signals and not to the inhomogeneity of the magnetic field. Because of the different weight every velocity has in the bulk magnetization of the fluid, the readings analyzed with the plug flow model deviate from the reference velocity. The better the flow profile is modeled, the more constant the velocity bias is, which would allow for a simple correction afterwards.

To obtain a maximum measurement resolution, it is important that the range of the flowmeter falls within the steepest part of the signal-fraction curve. Thermal equilibrium of the NMR signal must be avoided at all times. Neither may the signal become weak with respect to the noise. The flowmeter design should, thus, match the position of the r.f. coils on the $T_1$ of the fluids to be measured. This is crucial for the accuracy of the flowmeter, as also the uncertainty by the repeatability scales similarly with the slope of the reference curve. Using 10 instead of 30 T1RRT repetitions per flow measurement doubles the repeatability from 0.7 to 1.4 percent rate performance with 95% confidence level.

When the method is applied to single-phase flow, it is, in principle, sufficient to use only a single r.f. coil. This is true in the case of laminar flow. For the short $T_1$ of the glycerol-water mixture, the signal in the $2^{nd}$ r.f. coil is so close to thermal equilibrium that essentially only the signal of the $1^{st}$ probe can be used for the flow measurements.
However, turbulence causes a small negative offset to the signal amplitude, owing to increased dephasing by weak magnetic field gradients. These are present in the poorly shimmed zones near the pipe wall. If it comes to single-phase flow, the signal loss hardly leads to errors when the velocity is determined from the ratio of the signal intensities. The effect cancels itself out as the signal multiplier is almost equal in both r.f. probes. Therefore, analysis based on the ratio of the signal intensities should be preferred.

Because the T1RRT-method is highly sensitive to the $T_1$-time, it is important to know its correct value. Since the $T_1$-time depends on the dynamic viscosity and temperature of the substance to be measured, this might have consequences for the application of the apparatus in the oil industry, where the flow composition can change continuously.

## 6.3 Pulsed Gradient Spin Echo Method

The PGSE method is in contrast to the T1RRT method not based on the magnitude, but on the phase of the NMR signal. This has the main advantage that a calibration curve is, in principle, not required for the determination of the liquid's streamwise velocity $v_y$.

For comparison purposes the gradient method is tested on the same laminar and turbulent flow configurations as the T1RRT method discussed above. All measurements are performed in the second r.f. coil of the NMR flowmeter to ascertain an acceptable signal-to-noise ratio, i.e., the magnetization has developed sufficiently.

### 6.3.1 Measurement Principle

The measurement principle of the PGSE method is discussed at length in section 3.2. It uses an extended spin echo sequence in which two identical gradient pulses $G_y$ of duration $\delta_G$ are applied between both the 90° and 180° r.f. pulses and between the 180° r.f. pulse and the echo. When the natural field gradient in $\mathbf{B}_0$ is insignificant, the transverse magnetization gains, following equation 3.18, at time $2\tau$ of the echo a net phase angle

$$\Delta\phi_{2\tau} = -\gamma G_y v_y \Delta_G \delta_G, \tag{6.18}$$

where $\Delta_G$ is the time interval between the gradient pulses. By increasing step-by-step either $G_y$, $\Delta_G$ or $\delta_G$ in a series of PGSE measurements, the average velocity $v_y$ is calculated by linear regression of the phase shift as a function of this variable. To correct for the phase of the transmitter's digital synthesizer, we make use of phase referencing. Every first PGSE measurement is carried out as regular spin echo sequence without gradient pulses, whereafter

$$\Delta\phi_{2\tau}(G_y) = \phi_{2\tau}(G_y) - \phi_{2\tau}(0) \tag{6.19}$$

is calculated from the difference in phase between the echo in presence of and without pulsed gradients. Moreover, the phase shift is at the same time automatically adjusted for any potential contribution from the natural field gradient $g_0$. In this work two methods are studied, one in which $G_y$ and one in which $\delta_G$ is altered. They are referred as PGSEG and PGSET respectively. To assure unambiguous velocity measurements, the parameters are selected such that phase shift $|\Delta\phi_{2\tau}(G_y)|$ at maximum velocity never exceeds $\pi$.

### 6.3.2 Signal Processing

The data points in the inset of Figure 6.15 show the phase of typical quadrature detected spin echoes, as computed using equation 3.22. To remove the noise, the phase signal is smoothed with Gaussian kernel $h[k]$ with standard deviation 9.0 and length 21 [256]. In the main Figure we schematically show the procedure of determining phase shift $\Delta\hat{\phi}_{2\tau}$ from the resulting curves of the filter operation

$$\hat{\phi}[n] = \frac{\sum_{k=-10}^{10} h[k]\phi[n+k]}{\sum_{k=-10}^{10} h[k]}. \tag{6.20}$$

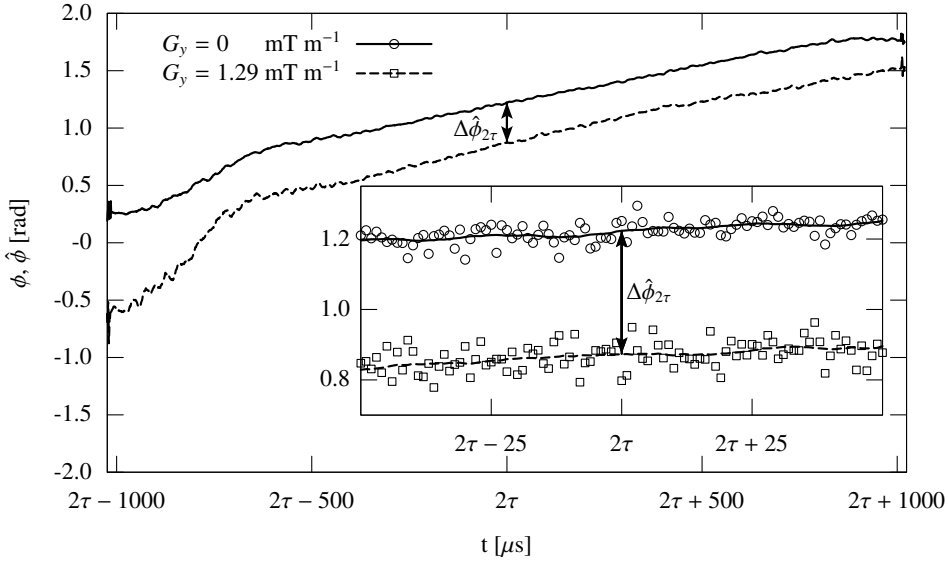


**Figure 6.15**: Filtered phase $\hat{\phi}$ of typical PGSEG experiments in the small turbulent flowloop for a velocity $v_y$ = 0.27 m s$^{-1}$ without and in presence of pulsed gradients $G_y$ = 1.29 mT m$^{-1}$. The inset part shows a good agreement between the filtered (lines) and the raw phase $\phi$ (data points) of the signals.

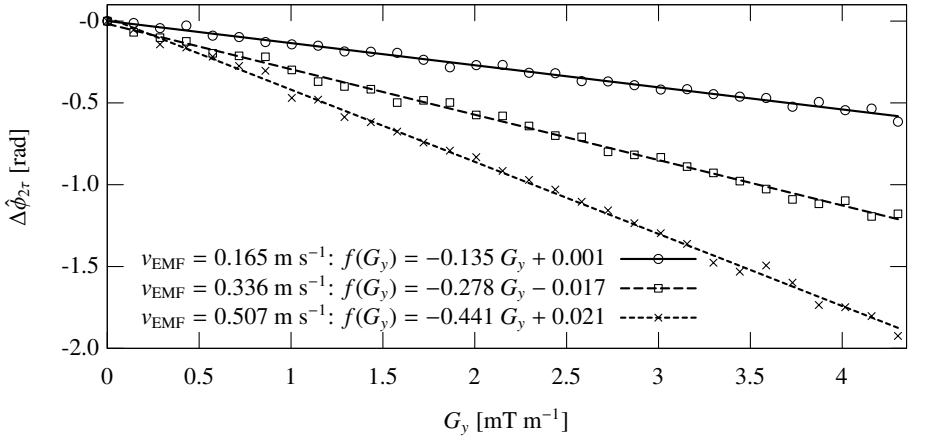


**Figure 6.16**: Phase shift of PGSEG-experiments in the small turbulent flowloop (34 mm i.d.) as function of gradient strength $G_y$ for three different velocities

Figure 6.16 investigates for three different velocities the phase shift $\Delta\hat{\phi}_{2\tau}$ of all echoes in a PGSEG measurement-sequence as function of the gradient strength $G_y$. As far as PGSET experiments are concerned, the phase can be plotted similarly as a function of $\delta_G$. In accordance with the expectations, the data points lie neatly on a straight line. Depending on the measurement method, one of the least square linear fits

$$f(G_y) = c_1 G_y + c_2 \tag{6.21a}$$

$$f(\delta_G) = c_1 \delta_G + c_2 \tag{6.21b}$$

is used to obtain the average flow velocity from directional coefficient $c_1$. Referring to equation 6.18, $c_1$ is a measure for $-\gamma\Delta_G\delta_G v_y$ and $-\gamma G_y\Delta_G v_y$ respectively. This is confirmed by the Figure, where the slope increases proportional to the velocity. Offset $c_2$ mainly originates from the uniform magnetic field produced by eddy-currents and inhomogeneous gradient effects associated with a different flow velocity.

The absolute measurement uncertainty of the PGSE velocity measurements is mainly determined by the random uncertainty at the 95 percent confidence level

$$u(v_{\mathrm{NMR}}) = t_{\mathrm{ST}\ 0.025}(N-1)\ \sigma(v_{\mathrm{NMR}}), \tag{6.22}$$

where $t_{\mathrm{ST}\ 0.025}(N-1)$ is the Student's t distribution for $N-1$ degrees of freedom and

$$\sigma(v_{\mathrm{NMR}}) = \frac{1}{\gamma\Delta_G\delta_G}\sqrt{\frac{1}{N-1}\sum_{i=1}^{N}\left(\frac{\Delta\hat{\phi}_{2\tau}[i]-f[i]}{G_y[i]}\right)^2} \tag{6.23}$$

is determined from the standard deviation of the slope of the fit, assuming true gradient strength values. Unfortunately the design of the flowmeter causes systematic (bias) errors, as we will explain in the next section. Also the bias-error range, corresponding to this directional bias error, negatively contributes to the measurement uncertainty. However, after correcting the readings for this directional bias, the bias-error range given by the standard deviation of the mean of the set of readings $\pm u(v_{\mathrm{NMR}})/\sqrt{N}$ is small compared to the random uncertainty. And even negligible if a large number of data points ($N > 5$) is used [13, 174], as is the case in the measurements presented. In other words, the measurement uncertainty at a given velocity can be set equal to the random uncertainty.

### 6.3.3 Experimental Aspects of Errors by the Flowmeter Design

There are many technical problems involved in gradient production that can bias PGSE measurements. Price [211] gives a comprehensive survey of all aspects to be reckoned with. Here, we only address the two factors that are relevant to the used NMR flowmeter.

#### 6.3.3.1 Inhomogeneous gradient field

Ideally all of the sample is subject to exactly the same linear gradient along the y-direction. In reality, the volume of high gradient linearity is very small, owing to space constraints the

compact flowmeter design imposes on the dimensions of the gradient modules placed inside the bore of the magnet. See section 2.2.5. The typical separation of a pair of circular Helmholtz coils is half the diameter, though a slightly larger separation would optimize the field uniformity [220]. However in the flowmeter configuration, the distance between the resin plates, which contain the gradient coils in a circular zone of 37 cm, is only 14 cm. Reason enough to examine the way in which the linear gradient $G_y$ is generated.

Figure 6.17 shows the x-ray used to visualize all five coils in the opaque shimming/gradient plate. To determine in this crisscross of lines the area corresponding to the linear gradient, we make use of the heat an active coil dissipates. Black thermochromic paper, which is stuck on the plate, brightens while sensing a temperature between 27 and 31 °C by changing color from red to blue. Figure 6.18(a) shows the pattern that appears when the $G_y$ gradient coil is directly connected to a current supply. It gives the impression that the linear gradient field is formed by two kidney-shaped Helmholtz pairs of opposite polarity, which have the highest wire density near the discoloration. Peaks in the field are expected in the center of the cells around the blind rivets at a radius of 11 cm. This indicates a narrow linear zone from where the isolines of gradient field $B_{\text{grad}}$ quickly fan out in circular direction.

For a better understanding, the gradient field is also visualized using a Hall-sensor (Magnet-Physik HS-TGB5-104005) for the FH55 magnetic field strength meter. With a 3D traversing system the probe is accurately moved within the probe head area. Because the coil is installed within the magnet, the gradient field measurements have to be corrected for the relatively strong permanent $\mathbf{B}_0$-field. The measurements are performed at a gradient pulse of maximum strength and duration of 5 seconds that anticipates on the response time of the sensor. Owing to the long pulse width, the values of the measured field strength may be compared to get an overall picture, but are not representative for the actual gradient pulse in the PGSE experiments with a typical duration in the range of 0 – 2 ms. The induced heat changes the gradient coil resistance and consequently the amplitude of the gradient pulse. Moreover, the effect of the eddy-currents will have died away.

First the length is analyzed over which a linear gradient is produced by the gradient plate. Figure 6.19 shows the measured field strength, $B_{\text{grad}}$, on a trace along the axis of the r.f. coil and one parallel thereof at a 3 cm vertical offset. In agreement with the thermochromic paper results, the strongest field appears at 11 cm distance from the coil center. The linear zone is situated within a radius of 7 cm around the center of the gradient plate. This means that the entire sensitive volume of the r.f. coil is indeed present within this area. However, a linear fit of the data belonging to the points present within the r.f. coil of 12 cm length shows that the gradient has no uniform strength. Closer to the pipe wall third order effects start to occur. As expected, the observed gradient of 60 mT m$^{-1}$ is for the reasons mentioned above stronger than the 42 mT m$^{-1}$ specified by Oxford Instruments.

Likewise, local inhomogeneities are studied by mapping the cross sectional gradient field in xz-planes at $y = -1.2$ cm and $y = -4.2$ cm. In the profiles shown in Figure 6.20, the closed dots are real measured grid points. Assuming symmetry, we have supplied missing

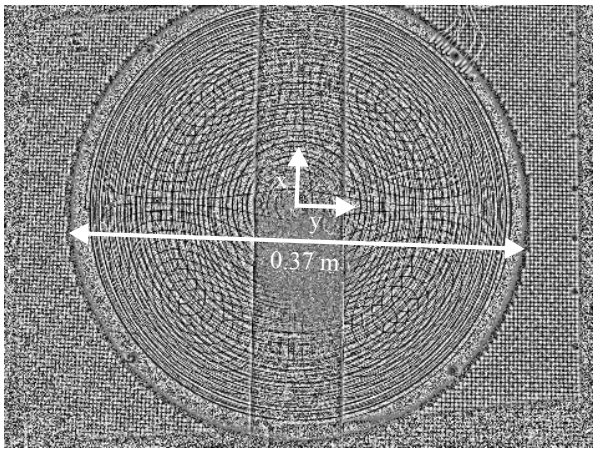


**Figure 6.17**: X-ray image of the plate in which five coils of the shimming and gradient Helmholtz pairs are enclosed in a circular zone of 370 mm diameter. The gray spot is an artefact of the camera's flash, but the pattern of the wires continues as mirrored version of the upper half of the plate.

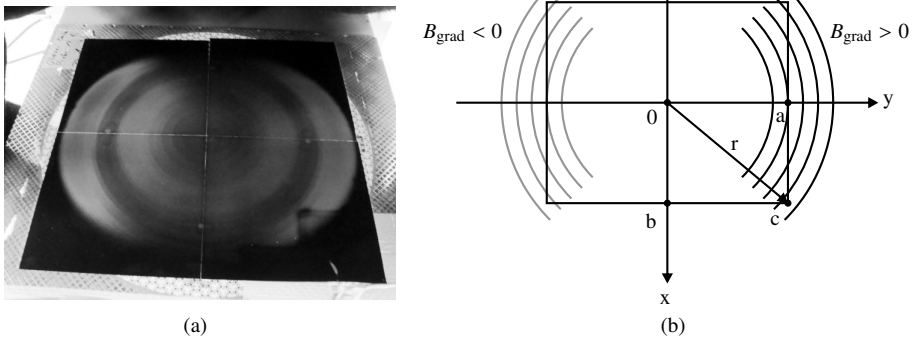


**Figure 6.18**: (a) Photo of the pattern appearing on the thermochromic paper, which is stuck on the shimming/gradient plate, when heated by the $G_y$ gradient. The originally black paper brightens if a temperature of 27 °C is exceeded. The discoloration suggests that the gradient is generated by two kidney-shaped Helmholtz pairs of opposite polarity. (b) Model to explain the increase in $G_y$ with radius r. Each line represents an iso-value of $B_{grad}$. Due to the circular structure towards the edges of the gradient field, the field experienced in c will be stronger than in a. Because the two fields of opposite polarity counterbalance each other along the x-axis with a zero field strength as result, the linear gradient over line segment bc is stronger than over 0a.

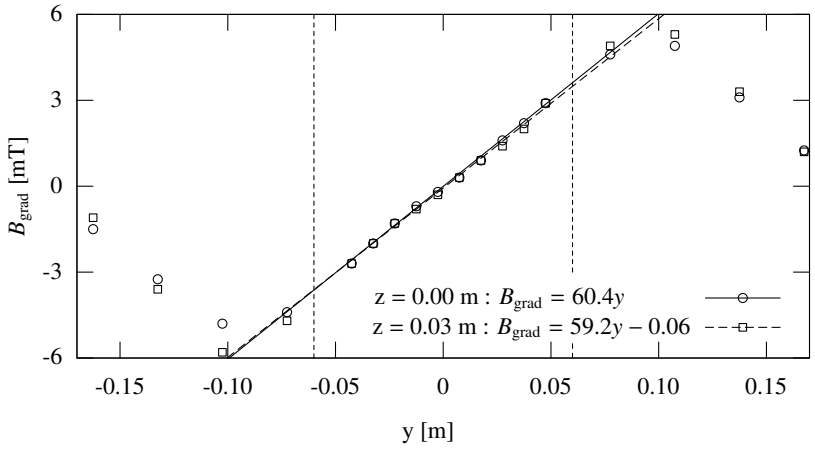


**Figure 6.19**: Hall-sensor measurements of gradient $G_y$ at maximum strength on a trace along the axis of the r.f. coil and parallel thereof at a 3 cm vertical offset. The linear fit of the data within the sensitive area of the r.f. coil ($-6$ cm $\leq y \leq 6$ cm) shows that the gradient strength decreases towards the gradient coils.

grid points with data mirrored in the x- and z-axis to give the interpolated field a natural appearance. These are denoted by the open circles. The physical dimensions of the probe prevent from measuring closer to the edge of the sample area.
From the saddle shape it becomes immediately clear that we are dealing with a very inhomogeneous gradient field. $G_y$ is strongly weakened in the vicinity of the gradient coil. Furthermore, we observe in all other directions the trend that $G_y$ increases with the radius. The latter can be explained by the circular structure towards the edges of the gradient field. As sketched in Figure 6.18(b), $B_{\text{grad}}$ is for constant y stronger at position c than at position a. Thus the gradient will be stronger over line segment bc than over 0a. Only in a small linear zone of about 3 x 3 cm, the gradient is sort of uniform. This poor uniformity has major consequences on the accuracy of the PGSE measurements. The phase shift, supposed to be proportional to the flow velocity, is not only an ensemble average of the gradient distribution that is sensed by the sample. The signal-to-noise ratio will also drop as a result of the enhanced effect diffusion has.

#### 6.3.3.2 Eddy-Currents

Another common problem in pulsed gradient measurements are eddy-currents that result from time-varying magnetic fluxes. They are induced by the rapid rise and fall of strong gradient pulses in nearby conducting surfaces, such as the probehead housing and shimming coils. As described by the Faraday-Neumann-Lenz law, the eddy-currents generate exponentially decaying magnetic fields, $B_{ec}$, that oppose the change in the magnetic flux. Their field strength is directly proportional to the flux variation over time, but attenuates rapidly with increasing

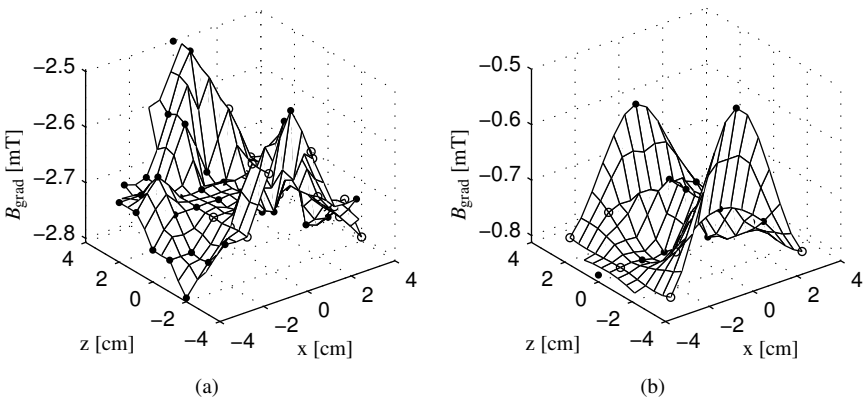


**Figure 6.20**: Interpolated Hall-sensor measurements of the cross sectional gradient field in xz-planes at a) $y = -4.2$ cm and b) $y = -1.2$ cm for $G_y$ set at maximum strength. The closed dots are real measured grid points, while the open circles are their reflections by assuming symmetry with respect to both the x- and z-axis.

distance [211]. Moreover, the field persist long after the gradient pulse has been switched off. Its time constant depends also on the geometry of the magnet system. The eddy-currents originating from closer metal surfaces decay faster than those from other conducting parts further away [41]. So, the integral effect

$$B_{ec}(\mathbf{r}, t) = \Delta B_0(t) + \Delta \mathbf{g}(\mathbf{r}, t) \cdot \mathbf{r} \tag{6.24}$$

is a time- and space-dependent offset of the uniform $B_0$-field and an additional linear gradient field, of which only the $g_y$-component affects the PGSE measurements. Higher order terms are not considered, since their disturbance is only minor. In practice, there are two ways in which eddy-currents can cause problems [79, 211]:

1. If the eddy-current tail from the first gradient pulse extends into the second $\tau$-period, illustrated in Figure 6.21, there is a mismatch in the total field gradient experienced during this first and second transverse evolution periods. Even if a spin has not moved in the direction of the gradient during the pulse-sequence, there will be a residual phase shift. As a result, the maximum echo amplitude will shift in time, while the amplitude at $t = 2\tau$ will be additionally attenuated.

2. When gradient pulses have a long tail, which is still present during acquisition, the eddy-currents may distort the time evaluation of the spin echo. Owing to the broadened spectrum, especially experiments using space encoding are biased. Except for off-resonance, the effect on the current PGSE measurements is limited.

To investigate the effect the first problem has on the estimation of the velocity by means of the PGSE method, we evaluate, analogous to section 3.2, the net gain of phase by the eddy-current induced field at the time of the echo. Following Jezzard et al. [121], the magnetic

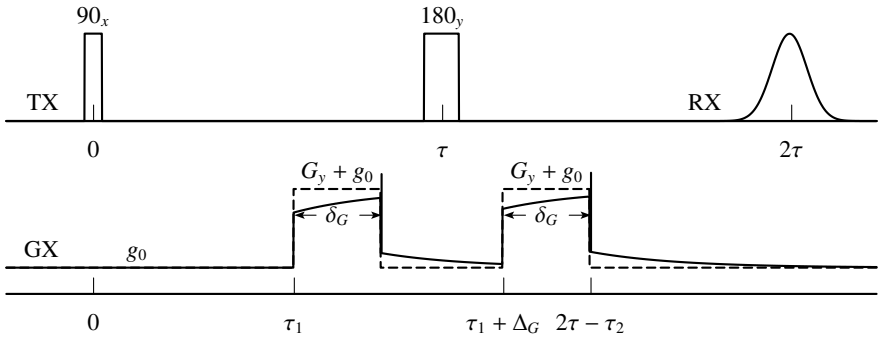


**Figure 6.21**: Diagram of the Pulsed Field Spin Echo pulse sequence with the exaggerated effect of the eddy-currents in the linear gradient field. As a result, the gradient pulses are not perfectly rectangular and an exponentially decaying field persists after termination of the pulse. For the sake of clarity, the FID signal that occurs immediately after the 90° pulse is not shown.

field produced by eddy-currents is represented by a sum of exponentially decaying fields of the form

$$B_{ec}(y,t) = \sum_i k_0^i \exp\left(-\frac{t}{\tau_i}\right) G_y + k_1^i \exp\left(-\frac{t}{\tau_i}\right) G_y y, \tag{6.25}$$

where $\tau_i$ is their time constant and where the magnitude of $k_0^i$ and $k_1^i$ is proportional to amplitude $G_y$, duration $\delta_G$ and separation $\Delta_G$ of the gradient pulses. Thus, we assume that the strength of the gradient is linearly related to the current. For the sake of convenience, we also assume that the eddy-currents are time-dependent but spatially invariant. The range of the summation index i depends on the number of conducting structures in the probe head. Closely related to our formulation is the eddy-current model by Jehenson et al. [119]. Just as the multiple L-R series circuits in this model are inductively coupled to the pulsed gradient coil, the conducting structures of the probe head can be regarded as electrical circuits, mutually coupled both with the gradient coil and with the other eddy-current circuits. Because the current induced in a single circuit, in turn, induces currents in the other eddy-current circuits, as many terms need to be included in the summation as there are mutual couplings. However, three $\tau_i$-terms are usually enough to specify the eddy-currents with excellent accuracy [251]. Typical values for time constant $\tau_i$ are 1, 10 and 100 ms. For most modern magnets the ratio $k_1$ between the eddy-current and the pulsed gradient amplitude is of the order 0.05 or less [121].

The residual phase of the detected signal at $t = 2\tau$ is determined by the field history of the induced eddy-current fields, given in table 6.2. Integration of the time-dependent Larmor

frequency shows that the uniform term results in a bulk shift

$$\begin{aligned}\Delta\phi^i_{2\tau} = {} & 2\gamma k^i_0 G_y \tau_i \left(\exp\left(-\frac{\tau-\tau_1}{\tau_i}\right) - \exp\left(-\frac{\tau-\tau_1-\delta_G}{\tau_i}\right)\right) \\ & -\gamma k^i_0 G_y \tau_i \left(\exp\left(-\frac{2\tau-\tau_1}{\tau_i}\right) - \exp\left(-\frac{2\tau-\tau_1-\delta_G}{\tau_i}\right) + \right. \\ & \left. \exp\left(-\frac{2\tau-\tau_1-\Delta_G}{\tau_i}\right) - \exp\left(-\frac{2\tau-\tau_1-\Delta_G-\delta_G}{\tau_i}\right)\right),\end{aligned} \tag{6.26}$$

which appears as a constant offset in the detected velocity that phase-referencing with the signal without pulsed gradients cannot remove. The linear gradient term in the y-direction acts similar as the gradient pulses by which it has been induced, although also cross-terms originating from $g_x$- and $g_z$-gradient coils often have a significant contribution. Its presence causes a phase shift

$$\begin{aligned}\Delta\phi^i_{2\tau} = {} & 2\gamma k^i_1 G_y v_y \left(\tau\tau_i + {\tau_i}^2\right)\left(\exp\left(-\frac{\tau-\tau_1}{\tau_i}\right) - \exp\left(-\frac{\tau-\tau_1-\delta_G}{\tau_i}\right)\right) \\ & -\gamma k^i_1 G_y v_y \left(2\tau\tau_i + {\tau_i}^2\right)\left(\exp\left(-\frac{2\tau-\tau_1}{\tau_i}\right) - \exp\left(-\frac{2\tau-\tau_1-\delta_G}{\tau_i}\right) + \right. \\ & \left. \exp\left(-\frac{2\tau-\tau_1-\Delta_G}{\tau_i}\right) - \exp\left(-\frac{2\tau-\tau_1-\Delta_G-\delta_G}{\tau_i}\right)\right),\end{aligned} \tag{6.27}$$

which is, as expected, proportional to the flow velocity $v_y$. This means that the strength of the gradient is in fact artificially decreased. Referring to equation 6.18, the total gain of phase of the detected signal at $t = 2\tau$ by the applied field gradient pulses and eddy-currents is given by

$$\Delta\phi_{2\tau} = -\gamma G_y \Delta_G \delta_G \left(v_y - \sum_i k^i_1 v_y \, \mathrm{f}_1\left(\delta_G, \Delta_G, \tau, \tau_1, \tau_i\right) + k^i_0 \, \mathrm{f}_2\left(\delta_G, \Delta_G, \tau, \tau_1, \tau_i\right)\right), \tag{6.28}$$

where the functions $\mathrm{f}_1$ and $\mathrm{f}_2$ can be derived from equation 6.26 and 6.27.

Because both $G_y$ and $\delta_G$ but especially $\tau$, $\tau_1$ and $\Delta_G$ influence the extent to which eddy-currents introduce errors in the estimation of the flow velocity, the size of these errors must be re-evaluated for each new setting. During postprocessing, the velocity is calculated using a proportionality constant and offset that have been corrected accordingly.
Apart from that, several methods are developed that reduce the eddy-current effect [211]. Hardware solutions are very easy in use, but often unfeasible owing to the high costs of shielded gradient coils or the use of very small samples in wide-bore magnets. The software solutions are inexpensive, but usually experimentally complicated and time-consuming because their trial-and-error approach involves many iterations. The most primitive methods cancel the mismatch in the time integral of the gradient pulses by adjusting their relative duration or strength. More effective are the methods that make use of long eddy-current settling periods. With pulse sequences, like stimulated echo PFG [240] or longitudinal eddy-current

**Table 6.2**: Strength of the time-dependent eddy-current field for the PGSE sequence in which eddy currents generated by the first $G_y$-gradient pulse have not totally decayed by the time of application of the 180° pulse. The complete expression of $\mathbf{B}_{ec}(y,t)$ is given by equation 6.25.

| subinterval time t | total eddy-current field |
|---|---|
| 0 to $\tau_1$ | 0 |
| $\tau_1$ to $\tau_1+\delta_G$ | $-\mathbf{B}_{ec}(y,t-\tau_1)$ |
| $\tau_1+\delta_G$ to $\tau_1+\Delta_G$ | $-\mathbf{B}_{ec}(y,t-\tau_1)+\mathbf{B}_{ec}(y,t-\tau_1-\delta_G)$ |
| $\tau_1+\Delta_G$ to $\tau_1+\Delta_G+\delta_G$ | $-\mathbf{B}_{ec}(y,t-\tau_1)+\mathbf{B}_{ec}(y,t-\tau_1-\delta_G)-\mathbf{B}_{ec}(y,t-\tau_1-\Delta_G)$ |
| $\tau_1+\Delta_G+\delta_G$ to $2\tau$ | $-\mathbf{B}_{ec}(y,t-\tau_1)+\mathbf{B}_{ec}(y,t-\tau_1-\delta_G)-\mathbf{B}_{ec}(y,t-\tau_1-\Delta_G)+\mathbf{B}_{ec}(y,t-\tau_1-\Delta_G-\delta_G)$ |

delay PFG [79], either following gradient pulses or acquisition are delayed until the eddy-currents have dissipated. However, these long waiting periods have a significant signal loss as drawback. The pre-emphasis technique manages to circumvent this problem, though it can only partly compensate for the eddy-current fields as a consequence of the gradient's spatial dependence. With sophisticated drivers, the current input of the gradient coils is shaped in such a way as to produce almost rectangular gradient pulses: i.e. the leading- and trailing edges of the current pulse are overdriven to self-compensate for induced eddy-currents [119, 251]. Other methods minimize the effect of the eddy-currents with advanced bipolar gradient pulse sequences [258]. Their working principle is based on self-compensation by transient responses of opposite sign, which result from pairs of sign-inverted but otherwise identical pulsed field gradients. Unlike the other solutions, this method remains free from time-consuming adjustments and requires no additional hardware. Finally, postprocessing is commonly used to correct the signal afterwards for eddy-current effects via e.g. phase referencing [41]. As described above, we will limit ourselves here to an indication of the systematic error in the flow velocity that can be attributed to the eddy-currents.

### 6.3.4 Results and Discussion PGSE

Given the experimental difficulties in generating ideal gradient pulses, the critical parameter for the flowmeter's performance is the actual value of $G_y$. Because of the high degree of nonuniformity in combination with different overall pipe diameters (9.85, 34 and 98.6 mm), the only proper calibration of the gradient strength would be the laborious method of mapping the local resonance frequency using a small sample. Instead we adjust the gradient value supplied by Oxford Instruments such that a 1:1 slope of the NMR- versus the known EMF-velocity for a range of single-phase flowrates is found. All subsequent signals obtained under the same conditions can be postprocessed with the effective gradient strength $G_{y,\max}$ and velocity offset $\Delta\nu_{\mathrm{NMR}}$ that result from the linear regression of this calibration series. In this way, the determination of the velocity out of directional coefficient $c_1$ in Eq. 6.21 is automatically corrected for the phase shift by eddy-currents, described in Eq. 6.27. Note that both the gradient value and velocity offset are strictly related to the pipe diameter and pulse sequence settings.

#### 6.3.4.1 PGSEG

Analogous to the T1RRT measurements, it is for PGSE measurements on laminar flow also benficial to measure at high flowrates, where the same phase resolution is obtained at weaker gradient pulses. Therefore the measurements in the laminar flow loop of section 4.2 are performed over an average velocity range of 0 – 0.8 m $s^{-1}$ with the same 60.6% vol. glycerol-water solution as used for the T1RRT measurements at a temperature of 21.5 – 22 °C. The dynamic viscosity and density of the mixture are 15.8 mPa s and 1157 kg $m^{-3}$, respectively. Because of the short transverse relaxation time $T_2$ = 318 ms, typical for more viscous fluids, the measurements are performed at $\tau$ = 3000 $\mu$s. Figure 6.22 shows the results of the PGSEG measurement sequences at $\delta_G$ = 400 $\mu$s, $\Delta_G$ = 3045 $\mu$s and $\tau_1$ = 1570 $\mu$s, in which $G_y$ is increased from 0 to 5.70% of the maximum gradient strength in 7 steps of 0.815%. The repetition delay is set at 4 s, which gives the fluid magnetization enough time to reach thermal equilibrium before the next spin echo experiment in the sequence is performed. At $G_{y,\max}$ = 39.5 mT $m^{-1}$, the obtained NMR-velocity varies in a one-to-one ratio with the reference EMF-velocity, measured with the electromagnetic flowmeter.

Turbulent flow measurements are more complex than those on laminar flow, due to signal loss as a result of the velocity fluctuations in presence of gradient magnetic fields. The measurement principle of several PGSE related techniques to measure the normal Reynolds stresses or turbulent intensity [52, 60, 145] is therefore based on the ratio of the signal amplitude obtained with and without gradient pulses. To resolve the turbulent time scales, the right timing is crucial. Because we are only interested in the average velocity, the timing is of minor importance. However, for an adequate signal-to-noise ratio, turbulence should be factored into the selection of NMR parameters. A good base for estimating its influence is the turbulent diffusivity, which reduces the signal amplitude analogous to fluid specific diffusion coefficient $D$ in equation 3.20.
The performance of the method for a turbulent velocity profile is studied with tapwater of room temperature in both the small flow loop of 34 mm i.d. (see section 4.3), giving the highest overall field homogeneity, and the large two-phase flow loop of 98.6 mm i.d. (see section 4.4). Because the relatively low viscosity of water results in a higher transverse relaxation time, $T_2$ = 1816 ms, these measurements are performed at $\tau$ = 8000 $\mu$s. Again it has been decided to place the gradient pulses with a duration of 400 $\mu$s in the middle of the $\tau$-periods. The differences in $\Delta_G$ and $\tau_1$ arise from the different durations of 90°- and 180°-pulses for the different sample sizes. The strength of the gradient pulse $G_y$ is increased from 0 to 9.16% of the maximum gradient strength in 30 steps of 0.305%. Because of the slower longitudinal relaxation process of water, this time the repetition delay is set at 30 s. Figure 6.23 shows the mean velocity obtained with the NMR flowmeter plotted versus the EMF-velocity with a range of 0 – 0.8 m $s^{-1}$. For the 34 mm and 98.6 mm i.d. pipes, a one-to-one proportionality with the EMF-velocity is found at a $G_{y,\max}$ of 47.0 mT $m^{-1}$ and 57.7 mT $m^{-1}$, respectively.

As expected, $G_{y,\max}$ exhibits large variations that can be attributed to the inhomogeneous field gradient. The increase of the gradient with the pipe diameter is best reflected in the values found for the turbulent measurements, since these are obtained under similar measurement

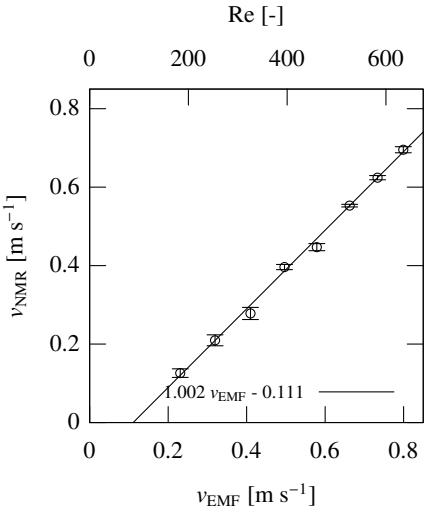


**Figure 6.22**: Comparison of the velocity obtained with the PGSEG measurement sequence ($v_{NMR}$), using $\tau$ = 3000 $\mu$s, $\tau_1$ = 1570 $\mu$s, $\delta_G$ = 400 $\mu$s, $\Delta_G$ = 3045 $\mu$s and $G_{y,max}$ = 39.5 mT m$^{-1}$, in the 9.85 mm i.d. laminar flow loop with the velocity measured with a calibrated flowmeter ($v_{EMF}$).

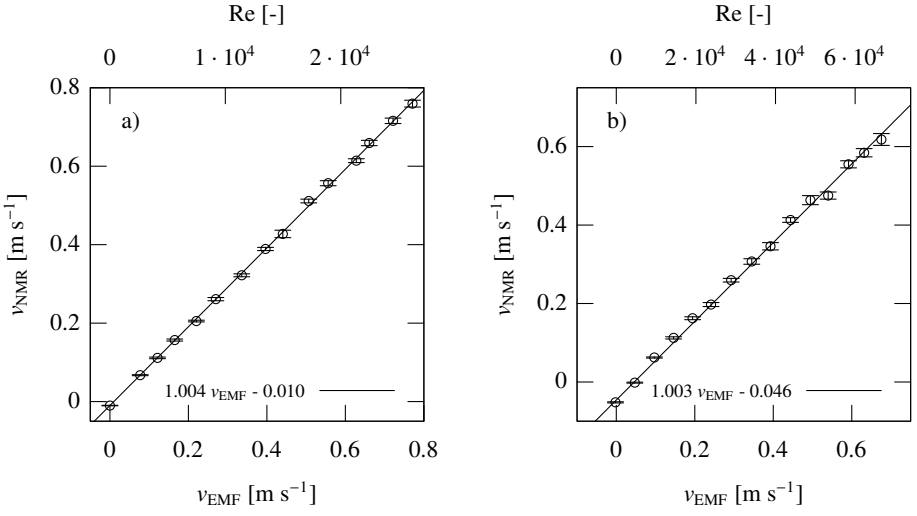


**Figure 6.23**: Comparison of the mean velocity obtained with the PGSEG measurement sequence ($v_{NMR}$) with the velocity obtained with the velocity measured with a calibrated flowmeter ($v_{EMF}$) of turbulent flow in a) the small flow loop of 34 mm i.d. at $\tau$ = 8000 $\mu$s, $\tau_1$ = 4074 $\mu$s, $\delta_G$ = 400 $\mu$s, $\Delta_G$ = 8054 $\mu$s and $G_{y,max}$ = 47.0 mT m$^{-1}$ and in b) the large two-phase flow loop of 98.6 mm i.d. at $\tau$ = 8000 $\mu$s, $\tau_1$ = 4084 $\mu$s, $\delta_G$ = 400 $\mu$s, $\Delta_G$ = 8064 $\mu$s and $G_{y,max}$ = 57.7 mT m$^{-1}$.

**Table 6.3**: Estimation of the effect the used PGSEG-settings have on the eddy-current contributions in the velocity measurements, using equation 6.28. Both the eddy-current amplitude factors $k_0^i$ and $k_1^i$ are supposed to be the same for all i. For time constants $\tau_i$ and ratio $k_1$ between the eddy-current and pulsed gradient amplitude, we use the typical values mentioned by Jezzard et al. [121]: i.e. $\tau_i$ = 1, 10 and 100 ms and $k_1 = 0.05$.

| | $k_0 \mathrm{f}_2(\delta_G, \Delta_G, \tau, \tau_1, \tau_i)$ | $k_1 v_y \mathrm{f}_1(\delta_G, \Delta_G, \tau, \tau_1, \tau_i)$ | effective gradient strength |
|---|---|---|---|
| laminar flow | 171 $k_0$ | 1.47 $k_1 v_y$ | 0.93 $G_y$ |
| turbulent flow | 59 $k_0$ | 1.01 $k_1 v_y$ | 0.95 $G_y$ |

conditions. However, the calculated maximum gradient strengths are not the actual values. They are biased by the flow dependent phase shift due to eddy-currents, given by equation 6.27.

The impact of eddy-currents is evident from the magnitudes of the zero ordinates of the curve fits through the data points. The average velocity is systematically underestimated by the NMR flowmeter. In the turbulent cases with 34 mm and 98.6 mm i.d. the directional bias error $\Delta v_{\mathrm{NMR}}$ is -1.0 and -4.6 cm s$^{-1}$, respectively, and in the laminar case even -11.1 cm s$^{-1}$. The enhanced offset in the laminar measurements is caused by the shorter transverse evolution periods $\tau$ after the gradient pulses. A rough estimation is given by factor $\mathrm{f}_2$ in table 6.3, where we have summed equation 6.28 over the typical values 1, 10 and 100 ms of time constant $\tau_i$ and suppose all $k_0^i$ are identical. Ignoring the cross-terms originating from the $g_x$- and $g_z$-gradient coils, the residual bulk shift for the laminar measurements is three times larger as derived for the turbulent measurements. However, $\tau_i$ and $k_0$ are not necessarily the same for all three diameters. Closer to the conducting surfaces in which they are generated, the eddy-currents will be stronger and last longer. The actual phase shift will, therefore, be comparatively larger in the 98.6 mm pipe. Moreover, the estimation is not corrected for the artifical lowering of $G_{y,\mathrm{max}}$ through eddy-currents. The eddy-currents reduce the effective gradient strength significantly, such that the value in the laminar experiments drops below 42 mT m$^{-1}$ specified by Oxford Instruments. If we assume the typical $k_1$ of 5% in the second column of table 6.3, for the effective gradient strength indeed 5 – 7% lower values are found. For a fair comparison of the measured velocity offset, we actually should increase the estimated $\mathrm{f}_2$-value with the inverse of this gradient proportionality factor.
Because of unfamiliarity with eddy-currents we decided to use centered gradient pulses. From the above it is clear that this was a bad choice. In particular for more viscous fluids, where the rapid signal decay requires a small transverse evolution period $\tau$. To reduce the interference of eddy-currents, it is recommended to maximize the waiting period after the first gradient pulse in order that the gradient falls zero before the 180°-pulse is applied. Oxford Instruments [194] advises, as a rough guide, an interval of 100 $\mu$s after the 90°-pulse and of at least 2 ms prior to the 180°-pulse. For heavy oil, as the marine residual fuel oil (MRFO) studied in chapter 5, with a $T_2$ of a few ms or less, there is nothing else we can do but postprocessing to correct for eddy-currents. Optionally, longitudinal eddy-current delay

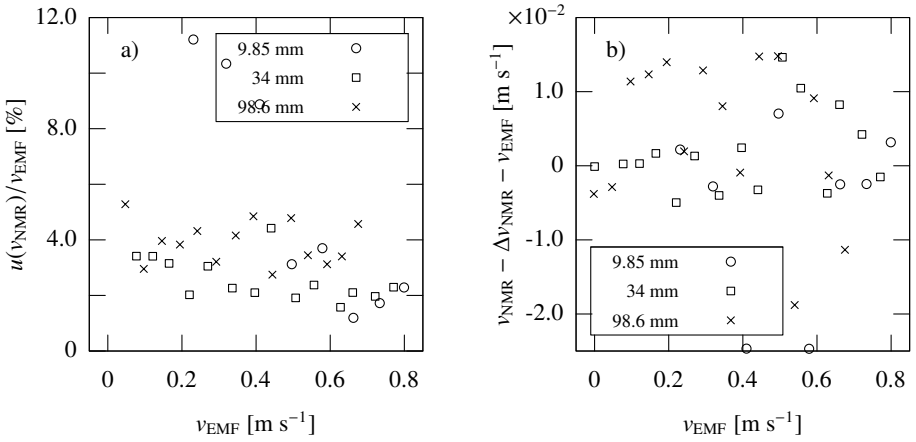


**Figure 6.24**: a) Relative measurement uncertainty of the PGSEG velocity measurements and b) the absolute measurement error resulting after substracting reference velocity $v_{EMF}$ from the measured average NMR velocity $v_{NMR}$, which is corrected for the directional bias mainly due to eddy-current effects by substracting the actual velocity offset $\Delta v_{NMR}$.

PFG [79] can be considered to avoid a deteriorated signal quality by the presence of eddy-currents during acquisition. In very viscous liquids, however, the influence of eddy-currents is best reduced by equipping the spectrometer with pre-emphasis facilities. Especially since pulsed field gradient techniques are able to measure the flowrate in case of short $T_1$ relaxation times, in contrast to the T1RRT method.

Once the flowmeter is calibrated for the actual $G_{y,max}$ and velocity offset $\Delta v_{NMR}$, the velocity can be reconstructed accurately. In particular because the method is not sensitive to temperature fluctuations. This is supported by the measurement errors given in Figure 6.24. Not only the measurement uncertainty calculated with equation 6.23 for a 95% confidence level is, apart from three outliers in the case of laminar flow, between 2 and 5% of the true velocity. Also the difference between the NMR velocity, which is corrected for offset $\Delta v_{NMR}$, and the reference velocity $v_{EMF}$ is always less than 2 cm s$^{-1}$. Entirely according to the expectations, the PGSEG-method is most accurate for the 34 mm pipe, where the flow is experiencing the most homogeneous magnetic fields. Despite the strong field inhomogeneities, the method performs surprisingly well in the 98.6 mm pipe.

The laminar measurements are mainly affected by the low measurement resolution, causing a 20% larger uncertainty range than in the turbulent measurements. However, it is quite easy to improve the measurement uncertainty by basing the PGSE measurement series on sufficient echoes. For 30 readings or more, the 95% confidence interval is narrowest. Especially for large $\tau$, such a long series has the disadvantage that the flow is supposed to be constant for

a considerable amount of time. A good compromise is a series of 20 echoes. Compared to a series of 10 echoes the uncertainty is only 2% poorer instead of 10% with respect to the 30-echoes series, while the measurement time is also much shorter.
Moreover, the echoes experience phase and envelope instabilities that increase when the gradient pulses become larger. To which degree varies from series to series and concerns in particular the three measurements with outliers in the uncertainty. It is difficult to indicate the direct source. At a gradient strength of 3.26% of the maximum field gradient and beyond, the maximum echo intensity shifts noticeably in time. This effect is related to a mismatch between the gradient pulses, mainly caused by the presence of eddy-currents as mentioned above in section 6.3.3.2, problem 1 [113]. The imbalance between the effective gradient pulses in the dephasing and rephasing periods of the echo formation has the result that we determine at $t = 2\tau$ the phase of an incoherent signal. The laminar measurements are more sensitive, since the influence of eddy currents is enhanced by the much shorter time delay $\tau$ in combination with the choice of centered gradient pulses.
Since the gradient channel, unlike the r.f. channel, is not actively en- and disabled by the spectrometer, it is also likely that spurious gradient currents have been stimulated by the r.f. pulses or by other pickup on the sensing resistor of the current supply [38]. The latter explanation is supported by the significant differences in echo deformation for the various measurement series. Also the fact that the sample extends outside the linear gradient field is not conductive to the quality of the measurements. An improvement on this point can be made relatively easy, replacing the hard 90° r.f pulse by a slice selecting one.

Considering the many disturbing factors, it is remarkable how robust the PGSEG method is. All measured mean velocities respond linearly to changes in the reference velocity and after the bias correction they agree very well with the reference values. For the laminar measurements a comparable accuracy to the turbulent measurements is expected, provided an equal number of gradient steps is used.

#### 6.3.4.2 PGSET

To examine whether varying the pulse duration $\delta_G$ functions equally well as varying gradient strength $G_y$, we have tested the PGSET method in the 34 mm i.d. pipe under similar circumstances as those in the PGSEG measurements: i.e. with tapwater of room temperature. The time delay $\tau$ is again set at 8000 $\mu$s, while the gradient strength $G_y$ is this time fixed at 3.05% of the maximum gradient strength. With $\tau_1$ is 4074 $\mu$s and $\Delta_G$ is 8054 $\mu$s, both gradient pulses start almost halfway each $\tau$-interval. During a PGSET series, the pulse duration $\delta_G$ is stepwise increased with 200 $\mu$s from 0 to 1200 $\mu$s. This means that the influence of eddy-currents will rise substantially with each step, because of the bad choice for centered gradient pulses. Figure 6.25 shows the measured mean velocity versus the reference velocity of the electromagnetic flowmeter with a range of 0 – 0.8 m s$^{-1}$.
At a maximum gradient strength $G_{y,\max} = 44.7$ mT m$^{-1}$, the determined NMR velocity exhibits a one-to-one proportionality with the reference velocity. This is more than 2 mT m$^{-1}$ below the value we have found for the PGSEG method in the same setup, also at $\tau = 8000\,\mu$s. The difference seems to be caused by the gradient fall time, which is not necessarily identical

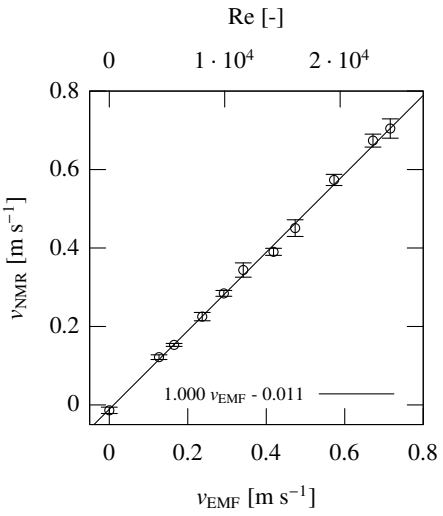


**Figure 6.25**: Comparison of the velocity obtained with the PGSET measurement sequence ($v_{\mathrm{NMR}}$), using $\tau = 8000\ \mu$s, $\tau_1 = 4074\ \mu$s, $\Delta_G = 8054\ \mu$s and $G_y = 1.36$ mT m$^{-1}$ for $G_{y,\mathrm{max}} = 44.7$ mT m$^{-1}$, in the 34 mm i.d. turbulent flow loop with the velocity measured with a calibrated flowmeter ($v_{\mathrm{NMR}}$).

for gradient pulses of different length. Illustrated in Figure 6.26, the gradient pulses are not rectangular but have finite rise and fall times. Only when they last long enough, the rise and fall times are identical for each pulse. Although we have checked with a Hall-sensor if the top of gradient pulses with $\delta_G = 400\ \mu$s is flat on an oscilloscope, we have the impression that the pulses approach but do not reach their maximum amplitude. This means that the fall time, dominated by eddy-currents, still increases with the pulse length. The gradient field in the PGSEG measurements will disappear faster than in the PGSET measurements with $\delta_G > 400\ \mu$s [194], such that larger time constants $\tau_i$ should be used in the model estimating the effects of the eddy-currents on the PGSET measurements. With increasing $\tau_i$ the influence of eddy-currents increases and leads, in turn, to a lower effective gradient strength. Because of the high sensitivity to in particular the middle-long existing eddy-currents of order $10^4\ \mu$s, the obtained gradient decrease seems reasonable.

In addition, this effect is somewhat enhanced by the way in which the phase shift resulting from eddy-current induced linear gradient fields (see Eq. 6.27) influences the data processing. Since this phase shift is linear in $G_y$ but nonlinear in $\delta_G$, the artificial lowering of the gradient strength is, contrary to the PGSEG measurements, no longer constant during the entire measurement series. Table 6.4 illustrates the tendency of the $f_1$-term and, as a consequence, the effective gradient strength to decrease with $\delta_G$. In the model we use for the time constants $\tau_i$ of the eddy-current fields again the typical values mentioned by Jezzard et al. [121]. Only the $f_1$ value at $\delta_G = 400\ \mu$s corresponds exactly to that in the PGSEG measurements. Due to the larger weight of data with $\delta_G > 400\ \mu$s, the average effective gradient in the PGSET

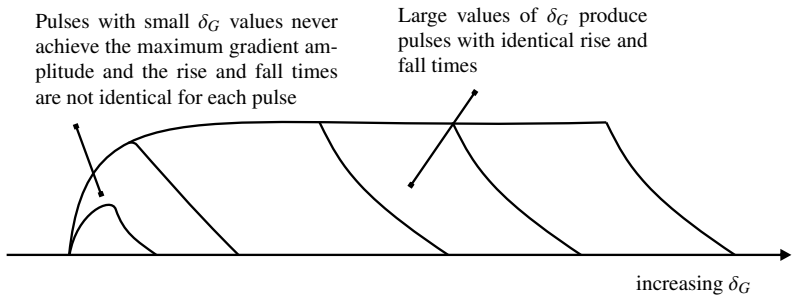


**Figure 6.26**: Effect of increasing gradient pulse duration $\delta_G$ on the shape of imperfect gradient pulses after Oxford Instruments [194]. Very short pulses are significantly less ideal than the long-lasting, because the rise and fall times constitute a larger proportion of the total gradient pulse duration.

measurements will be a little lower than in the PGSEG measurements once the pulse have identical rise and fall times.

Figure 6.27 shows the errors corresponding to the PGSET measurements. Comparable to the laminar PGSEG measurements, the measurement uncertainty $u(v_{\mathrm{NMR}})$ is in general large owing to the larger $t_{\mathrm{ST}}$ caused by only 7 echoes per measurement sequence. Again a few measurement series were corrupted by deformed echoes. Due to their lower signal-to-noise ratio, the phase shifts of the echoes with the largerst two $\delta_G$s of 1000 and 1200 $\mu$s are especially affected. These series are characterized by a very large relative error of approximately 12%. The other series with a relative error of 6% measure almost up to the PGSEG-measurements. Surprisingly enough, the mean velocity is hardly affected by the big uncertainties of the directional coefficient estimator $c_1$. The difference of only 2 cm s$^{-1}$ between the NMR velocity, corrected for an offset $\Delta v_{\mathrm{NMR}}$ of -1.1 cm s$^{-1}$, and the reference velocity implies a very good performance.
Nevertheless it is recommended to optimize the results by increasing the number of echoes per series to 20 or more. To avoid the increasing influence of eddy-currents with a reduced time delay between the end of the gradient pulse and acquisition, one should rather choose for an improved measurement resolution with a smaller stepsize of pulse duration $\delta_G$. Additional research into the fall time of the gradient pulses used is required for a proper selection of the maximum pulse duration. Because a clear trend has been observed that strong gradient pulses quickly introduce noise in the NMR signal - probably due to the more pronounced field inhomogeneities - the gradient strength is best kept as low as possible. In general, it is favorable to aim for a maximum phase shift $\Delta\phi_{2\tau}$ of $\pi/2$ rad by combining weak gradient pulses with the longest duration as possible for only slightly disturbed echoes.

### 6.3.5 Conclusion PGSE

In this preliminary study of the applicability of the PGSE method for multiphase flowmetering is shown that it is possible to determine, independent of the velocity profile, the average streamwise velocity of single-phase flow with high accuracy. After correction for eddy-

**Table 6.4**: Estimation of the effect the used PGSET-settings have on the eddy-current contributions in the velocity measurements in the 34 mm i.d. pipe, using equation 6.28. Again we assume that the eddy-current amplitude factors $k_0^i$ and $k_1^i$ are the same for all i. For time constants $\tau_i$ and ratio $k_1$ between the eddy-current and pulsed gradient amplitude, we use the typical values mentioned by Jezzard et al. [121]: i.e. $\tau_i$ = 1, 10 and 100 ms and $k_1$ = 0.05.

| $\delta_G$ [$\mu$s] | $k_0 \mathrm{f}_2(\delta_G, \Delta_G, \tau, \tau_1, \tau_i)$ | $k_1 v_y \mathrm{f}_1(\delta_G, \Delta_G, \tau, \tau_1, \tau_i)$ | effective gradient strength |
|---|---|---|---|
| 0 | 0.0 $k_0$ | 0.000 $k_1 v_y$ | 1.00 $G_y$ |
| 200 | 57.9 $k_0$ | -1.008 $k_1 v_y$ | 0.95 $G_y$ |
| 400 | 58.6 $k_0$ | -1.010 $k_1 v_y$ | 0.95 $G_y$ |
| 600 | 59.4 $k_0$ | -1.013 $k_1 v_y$ | 0.95 $G_y$ |
| 800 | 60.3 $k_0$ | -1.015 $k_1 v_y$ | 0.95 $G_y$ |
| 1000 | 61.2 $k_0$ | -1.018 $k_1 v_y$ | 0.95 $G_y$ |
| 1200 | 62.2 $k_0$ | -1.020 $k_1 v_y$ | 0.95 $G_y$ |
| turbulent flow | (60 ± 2) $k_0$ | (−1.014 ± 0.005) $k_1 v_y$ | 0.95 $G_y$ |

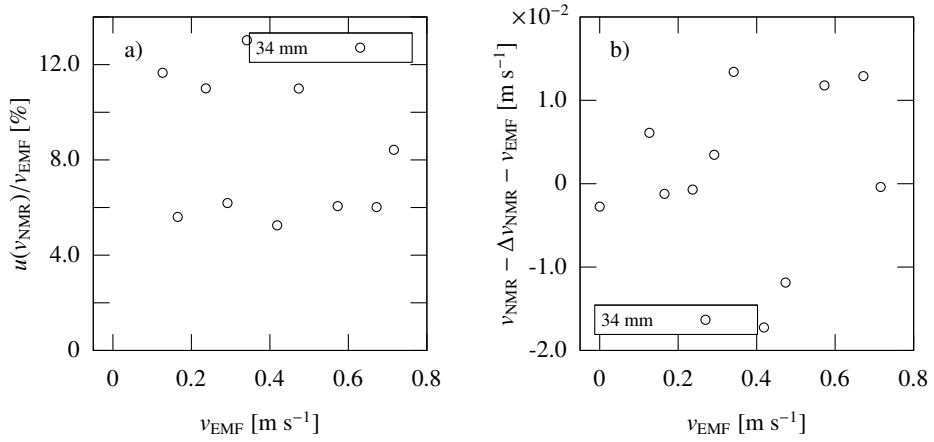


**Figure 6.27**: a) Relative measurement uncertainty of the PGSET velocity measurements and b) the absolute measurement error resulting after substracting reference velocity $v_{EMF}$ from the measured average NMR velocity $v_{NMR}$, which is corrected for the directional bias mainly due to eddy-current effects by substracting the actual velocity offset $\Delta v_{NMR}$.

current related directional bias, all measurements over a velocity range of 0 – 0.8 m $s^{-1}$ show a difference of less than 2 cm $s^{-1}$ with the reference velocity. In the case of turbulence, signal loss resulting from turbulent diffusivity in presence of gradient magnetic fields should be taken into account. The big advantage of PGSE is the fact that the equipment does not need to be recalibrated repeatedly for slightly modified fluid properties due to temperature variations or a different composition. The method is also suitable for more viscous liquids.
Due to sub-optimal conditions, a consequence of the design of the flowmeter and ill-chosen settings, the claim that a single calibration of the gradient strength is sufficient for PGSE measurements does not hold. There was no opportunity to repeat the measurements under better conditions, because of the late stage in which the problems were discovered. The net phase gain of the echo is strongly affected by eddy-currents and the partly associated gradient field inhomogeneities. We have proven the existence of these error sources with, respectively, a model-based calculation and Hall-sensor measurements. The inhomogeneous gradient field makes that its strength increases with the diameter of the pipe. Slice-selection is suggested to reduce the area in the streamwise direction with a non-linear gradient to a minimum. A factor that we have underestimated are eddy-currents, which are a major problem in pulsed field gradient NMR. Depending on the pipe diameter and pulse sequence settings, the eddy-currents cause (i) a systematic overestimation of the effective gradient strength and (ii) a velocity offset. The effect increases with the diameter of the pipe or decreasing $\tau$. An algorithm has been proposed to correct the velocity calculation during the general postprocessing of the NMR signal once the real $G_{y,\max}$ and $\Delta\nu_{\mathrm{NMR}}$ are accurately reconstructed. When a selection of only a few $\tau$-values is enough to cover the whole $T_2$-range, the number of calibration constants is limited. To minimize the bias by eddy-currents, it is important that the gradient pulses succeed the r.f. pulses on the shortest waiting period possible. Centered gradient pulses are a bad idea. To avoid interference we recommend to investigate the fall-time of the aimed gradient pulse prior to the measurements. In the case of very small $\tau$, required for more viscous liquids, the influence by eddy-currents cannot be prevented and the effect has to be removed as far as possible during the postprocessing of the signal.
To achieve reliable results with a relative uncertainty of 5% or less, a series of at least 20 echoes is recommended. The poorer reliability as a result of the lower measurement resolution and unintended extra large influence of eddy-currents in the PGSET measurements makes it impossible to give preference to either varying the strength (PGSEG) or the duration of the gradient pulses (PGSET). However, we can conclude that stronger and longer gradient pulses rapidly lead to more noise in the NMR signal and as such should be avoided.

## 6.4 Comparison studies

At last, we compare the strengths and weaknesses of the T1RRT and PGSE method as flowmetering principle for single-phase flow. The results of this comparison are summarized in table 6.5.

T1RRT is unsuited to determine the velocity of very viscous fluids with a short $T_1$ relaxation time. If it is already possible to discriminate the NMR signal from the equilibrium

**Table 6.5**: Comparison of the strengths and weaknesses in the application of the T1RRT and PGSE method to single-phase flow measurements.

| | T1RRT | PGSE |
|---|---|---|
| velocity measurement | | |
| short $T_1$ | × | ✓ |
| long $T_1$ | ✓ | ✓ |
| measurement time | ✓ | × |
| essential parameters | $y_{c,1}$, $y_{c,2}$, $T_1$ | P90, P180, $G_y$, $\tau$, $\delta_G$, $\Delta_G$, $\tau_1$ |
| no. of r.f. probes | 1, 2 | 1 |

state, a large measurement uncertainty is the result. PGSE is a good alternative under these conditions. For longer $T_1$ relaxation times, both methods are applicable. Especially the long measurement time is a negative aspect for PGSE. Because many sequence repetitions are necessary, the flow must be very stable. Although with a lower accuracy, T1RRT can determine the flowrate already from a single cycle and is therefore more suitable for fluctuating flow regimes.

A major drawback of T1RRT is the strong dependence of the calibration curves, which describe the relation between the flow velocity and the measured signal, on the flow profile and the $T_1$ relaxation time of the fluid to be measured. Particularly the relaxation time varies considerably with temperature, viscosity and substance, introducing a high degree of uncertainty in the analysis of the NMR signal, so that comparatively large measurement errors may arise. In industrial applications continuous monitoring of $T_1$ is, therefore, highly recommended. Moreover, the $T_1$ relaxation time plays a second decisive role on the performance of the flowmeter through the selection criteria for the coil positions.

For PGSE, the small changes in the $T_1$ and $T_2$ relaxation times are no problem, so frequent recalibration of the equipment is not required. However, this method is severely hampered by the technical difficulties to produce a well-calibrated magnetic field gradient. Its poor uniformity does not only directly affect the phase shift, but also reduces the signal-to-noise ratio. In addition, the presence of eddy-currents gives rise to a velocity offset and an artificial lowering of the effective gradient strength. Since the extent depends on the timing of the gradient pulses in the sequence, the acquisition parameters should be chosen with great care. The absence of a working model to correct the NMR signal for eddy-currents, demands a comprehensive calibration of the effective gradient strength $G_{\mathrm{y,max}}$ and velocity offset $\Delta v_{\mathrm{NMR}}$ for all settings, which can be selected. On the other hand, the use of only one instead of, preferably, two or more r.f. probes in the case of T1RRT saves quite some electronics.

Because the ability of high frequent measurements is essential for a multiphase flowmeter,

we will focus in the next two chapters on the application of the T1RRT method to stratified and slug flow. When the inhomogeneous polarizing field in the entrance area is integrated in the reference curve, T1RRT is a very robust method, which is much less sensitive to hardware imperfections and pulse settings than PGSE.

# Chapter 7

# T1RRT Measurements on Horizontal Stratified Flow

As a first step in the development of an NMR multiphase flowmeter, the T1RRT method is applied to co-current stratified air-water flow. Because of its fully separated phases, it is the least complex two-phase flow regime that, if developed, has a certain degree of time independence. However, the flowmeter used is not particularly suitable for this flow regime, because it is actually designed for higher fluid velocities.

In the past, Lynch and Segel [163] have successfully determined the void fraction of a vertical air-water flow with a similar rapid passage technique based on continuous wave NMR. By using only one r.f. coil, their measuring principle is unsuited for determining the liquid velocity. If the NMR signal has not reached thermal equilibrium, they need an external velocity measurement to work out the void fraction.

Stratified flow is subdivided into several sub-regimes named after the interfacial flow pattern. For a fixed superficial liquid velocity, the interface will be smooth in the case of low gas velocities. At higher gas velocities, small waves occur. When the gas velocity increases even further, they change into large waves via a number of intermediate stages. Despite the great resemblance, the shape of the velocity profile changes substantially with the different subregimes. It is studied to which extent the T1RRT method is able to determine the flowrate of the liquid phase starting from a plug flow model. How well the flowmeter handles the poorer signal-to-noise ratio due to the lower filling factor of the probes is another topic of interest.

In the description of the flow configuration, much attention is paid to technical problems encountered with the instrumentation. Based on a literature study, it is investigated what the best strategy is to deal with the overestimation of the liquid holdup by the wiremesh sensor. Furthermore, the detrimental effect that lossy samples have on the probe efficiency is discussed along with the successful application of strip-shields to reduce this problem. This

is very important because the volume of liquid present in the r.f. coils changes constantly during two-phase flow measurements.

In the analysis of the quality of the flow measurements, an attempt was made to give an overview of all the factors that contribute to the measurement uncertainty. In this regard, both the model on which the signal processing is based and the inaccuracies caused by the measurement conditions are examined. Finally a sensitivity study is presented of the T1RRT measurement algorithm with respect to what we consider as the most dominant sources of systematic errors.

## 7.1 Measurement Principle

In the T1RRT measurement technique, the liquid flowrate of a two-phase gas-liquid flow is determined through the paired detection of an FID at two different streamwise positions. The basic assumption here is that the proton density of a low-pressure gas phase is normally so low that it does not contribute to the NMR signal. As explained in detail in section 3.1, we relate the extent to which the longitudinal magnetization has built up to the average residence time, $y/v_y$, of the liquid in the uniform polarizing magnetic field, $\mathbf{B}_0$. To avoid interactions, a low repetition rate of the pulse sequence is selected, which ensures that only fresh liquid with initial magnetization zero is measured.

The intensity of an NMR signal is proportional to the amount of nuclear spins enclosed by the r.f. coil. Following Lynch and Segel [163], we assume that there are insufficient nuclear spins available in the gas phase to effectively contribute to the NMR signal. Hence, the signal strength for a gas-liquid flow can be written as the product

$$s_y(v_y) = \alpha_L s_{100\%L}(v_y) \tag{7.1}$$

of the liquid holdup, $\alpha_L$, and the expected signal strength for single-phase flow at the same bulk velocity, $s_{100\%L}(v_y)$.

The NMR signal analysis is made insensitive to variations in the $T_1$ relaxation time of the liquid phase by scaling the streamwise velocity as

$$v_y^* = \frac{v_y\, T_1}{y_{c,1} + \overline{\Delta l}}, \tag{7.2}$$

where $y_{c,1}$ is the streamwise position of the center of the first r.f. coil and $\overline{\Delta l}$ the asymptotic value of the added length by the non-uniform polarizing magnetic field as defined in section 6.2.4. On substituting this expression in Eq. 3.5, which is generalized for gas-liquid flow, the initial intensity of the FID following a 90° pulse is given by

$$s_y(v_y^*, \alpha_L) = \alpha_L \frac{\pi}{4} D_p^2 L_c s_0 \left(1 - \frac{v_y^*\,(y_{c,1} + \overline{\Delta l})}{L_c} \exp\left(-\frac{y_c + \overline{\Delta l} - L_c/2}{v_y^*(y_{c,1} + \overline{\Delta l})}\right)\left[1 - \exp\left(-\frac{L_c}{v_y^*(y_{c,1} + \overline{\Delta l})}\right)\right]\right), \tag{7.3}$$

where $L_c$ is the length of the coil and $s_0$ the intensity of the NMR signal corresponding to the thermal equilibrium magnetization $M_0$. Like in section 6.2.1, this function is numerically solved in the postprocessing software using

$$s_y(v_y^*, \alpha_L) = \alpha_L \frac{\pi}{4} D_p^2 L_c s_0 \frac{1}{N_y} \sum_{j=1}^{N_y} 1 - \exp\left( - \frac{y_c + \overline{\Delta l} + L_c(2j - 1 - N_y)/2N_y}{v_y^*(y_{c,1} + \overline{\Delta l})} \right) \tag{7.4}$$

in which the probe domain is divided into $N_y$ equidistant cells. If the r.f coil is short, $s_y$ is approximately equal to

$$s_y(v_y^*, \alpha_L) \approx \alpha_L \frac{\pi}{4} D_p^2 L_c s_0 \left( 1 - \exp\left( - \frac{y_c + \overline{\Delta l}}{v_y^*(y_{c,1} + \overline{\Delta l})} \right) \right), \tag{7.5}$$

the signal strength associated with the gained longitudinal magnetization at the center of the coil.

In contrast to single-phase flow, there are two stages required to measure the liquid flowrate in a gas-liquid two-phase flow. Starting from the idea that the liquid holdup has an equal time average in both r.f. coils, the dimensionless liquid bulk velocity is first determined by comparing the fraction of the detected signal intensities in the second and first r.f. coil for each FID pair with the reference curve

$$\frac{s_{y,2}}{s_{y,1}}(v_y^*) = \frac{\sum_{j=1}^{N_y} 1 - \exp\left( - \frac{y_{c,2} + \overline{\Delta l} + L_c(2j-1-N_y)/2N_y}{v_y^*(y_{c,1} + \overline{\Delta l})} \right)}{\sum_{j=1}^{N_y} 1 - \exp\left( - \frac{y_{c,1} + \overline{\Delta l} + L_c(2j-1-N_y)/2N_y}{v_y^*(y_{c,1} + \overline{\Delta l})} \right)}. \tag{7.6}$$

As the holdup terms in the nominator and denominator cancel each other out, the same reference curve can be used as for the single-phase flow measurements, see Eq. 3.6. The signal fraction is an injective function of the bulk velocity, as long as the magnetization in the first probe has not reached the equilibrium state. Actually the reference curve should be adjusted for the shape of the velocity profile. This is complicated. The velocity profile of the stratified liquid phase changes shape with the shear stress and the type of waves at the interface [12, 25, 26, 238]. Because it is demonstrated in chapter 6 that a plug flow model is sufficiently accurate for turbulent single-phase flowmetering, we stick in the present analysis to the same approach.

Second, the liquid holdup is resolved from the non-dimensional equivalent of Eq. 7.1, where the expected signal strength for a fully-filled pipe is defined by Eqs. 7.3 and 7.4 for $\alpha_L = 1$. Using the liquid bulk velocity as input parameter has the disadvantage that errors in the velocity will propagate in the holdup.

Once the bulk velocity and liquid holdup are known, the total liquid flowrate is finally calculated as

$$q_L = \frac{\pi}{4} D_p^2 \alpha_L v_y. \tag{7.7}$$

## 7.2 Flow Configuration and Instrumentation

The experiments on horizontal co-current stratified pipe flow are performed in a two-phase air-water flow loop with an internal diameter of 98.6 mm. The facility operates at room temperature and at ambient pressure. Compressed air and tap water are fed into the pipe through a parallel-plate inlet section, located 320 $D_p$ upstream of the NMR flowmeter in order to obtain a fully-developed stratified flow. The superficial liquid velocity, $v_{SL}$, is measured by means of a KROHNE Optiflux 2300C electromagnetic flowmeter with a standard uncertainty of ± 0.2% + 1 mm $s^{-1}$ of the measured value. The gas flowrate is measured by means of four different variable area flowmeters for the different ranges: 0.07 – 0.19 $m^3$ air $min^{-1}$ (Kytölä HV3KC), 0.1 – 0.6 $m^3$ air $min^{-1}$ (Kytölä HV4DC), 0.2 – 0.7 $m^3$ air $min^{-1}$ (Kytölä HV4FC) and 0.3 - 6.0 $m^3$ air $min^{-1}$ (Kytölä HT4FC), with a standard uncertainty of ± 5% of the full scale value. This translates into a standard uncertainty of the superficial gas velocity, $v_{SG}$, of ± 0.02 m $s^{-1}$, ± 0.06 m $s^{-1}$, ± 0.08 m $s^{-1}$ and ± 0.6 m $s^{-1}$ respectively. The two r.f. probes are at fixed positions of 0.5 and 2.5 m inside the NMR flowmeter. Reference measurement of the liquid holdup are carried out with a 32x32 wiremesh sensor that is placed 1.01 m upstream of the NMR flowmeter. As the outlet of the pipe is only 1.5 m downstream of the second r.f. probe, the flow is not strong enough to keep a constant water level within the NMR flowmeter. For this purpose, the air-water separator tank is equipped with an inner overflow tank by which the liquid holdup can be leveled with an adjustable baffle. More details about the flow loop can be found in section 4.4.
Two issues regarding the accuracy of the NMR two-phase flow measurements need further attention and will be discussed in the remainder of this section. First, systematic errors in the wiremesh measurements are assessed that hamper the validation of the NMR measurements. Second, two-phase flow behaves as a lossy dielectric that detunes the r.f. probe. Due to electromagnetic interactions, there is no longer a linear relationship between the strength of the NMR signal and the amount of protons in the r.f. coil. In section 7.2.2 is addressed how this effect is reduced with the help of a strip-shield, even though it can not prevent the necessity of a calibration curve to determine the liquid holdup.

### 7.2.1 Method to deal with measurement uncertainties of the wiremesh

Although Shaban and Tavoularis [226] report in their review paper that a fair agreement has been found between the wiremesh sensor and other void fraction measurement methods for stratified flow in horizontal channels, a clear systematic overestimation of the liquid holdup is observed in the present study. This will bias the validation of the NMR measurements, as the liquid holdup is an input parameter for the calculation of $v_{BL}$, the liquid bulk velocity.
The measurement volumes of the wiremesh sensor are not the cubic cells that are used in the postprocessing, like discussed in section 4.4.2. From simulations of the potential field of a $3 \times 3$ wire configuration, Smeets [235] concludes that the actual measurement volume is a rhombic pyramid, i.e. with a diamond shaped base. The measurement volume has indeed the size of a grid cell in the direction of the transmitter wire, but the volume is about four electrode pitches long in the direction of the receiver wire. As a result, measurement volumes partly overlap and other areas of the cross-section are not sensed at all. What this implies for

the determination of the area-averaged liquid holdup in a center mesh grid cell that is fully enclosed by the pipe is pictured in Fig. 7.1. The subvolumes adjacent to the receiver wire have a four times higher weight in the total holdup calculation as the outermost subvolumes. The natural orientation of the wiremesh sensor is a very unfortunate choice for applications in a horizontal pipe, because the receiver wires are in the vertical direction. Water is also detected in the two grid nodes above the actual water level of a stratified flow, which hampers the identification of the interface. However, the effect on the area-averaged liquid holdup is rather limited as the cells below the interface compensate this surplus of water with an equal amount of air. The presence of water bridges in the wake of the first plane of electrodes in the mesh cells just above the water surface may well be a possible explanation for the detection of a too high liquid fraction. By means of high-speed camera observations, Prasser et al. [206] have demonstrated the existence of these liquid films, which do not drain fast enough and maintain electrical contact between the transmitter and receiver wire, for medium size bubbles crossing the wiremesh sensor in vertical pipe flow. It is not unlikely that the same phenomenon occurs in horizontal stratified flow due to a combination of small-amplitude waves with a relatively weak airflow. In this respect, it does not help that the area surrounding the receiver wire makes an extra heavy contribution to the measured conductivity. For future validation studies of horizontal stratified flow, it is recommended to rotate the wiremesh sensor over 90 degrees. The longest diagonal of the a-symmetric measurement volume is then parallel to the water surface, thereby reducing the bias in the holdup measurements.

Many studies try to improve the accuracy of the wiremesh sensor by applying a threshold in addition to the weighting coefficient approach. In general, all this research focuses on the identification of a sharp interface between the liquid and the gas phase. Smeets [235] was the first one, who introduced a threshold in order to determine the local void fraction in bubbly flow. Roitberg et al. [219] and De Salve et al. [53] adopt this idea to define the instantaneous boundaries of the gas-liquid interface and the void fraction chordal profile in stratified and (pseudo)slug flow. Also the refined reconstruction algorithm by Schleicher et al. [222] makes use of thresholds to recognize the gas-liquid interface for stratified-flow under low liquid loadings. In absence of a theoretical basis, the choice of the threshold-value is arbitrary and requires prior knowledge of the sensor's geometry and the flow pattern, as sensitivity studies show [222, 235]. It is possible to compute the cross-sectional liquid holdup in stratified flows from the filling level of the wiremesh columns, assuming no bubble entrainment. Considering the unknown uncertainties of this method, it has been decided to leave the threshold concept and to estimate the systematic errors that the wiremesh introduces in the reference measurements of the bulk velocities instead.

Because the wiremesh sensor overestimates the liquid holdup with $\delta\alpha_L$, a too low liquid bulk velocity and a too high gas bulk velocity are calculated from their respective superficial velocities. The bias is estimated by taking a second order Taylor series expansion around $\delta\alpha_L = 0$ on the functions

$$v_{\mathrm{BL}}(\delta\alpha_L) = \frac{v_{\mathrm{SL}}}{\alpha_{\mathrm{L,WM}} - \delta\alpha_L} \tag{7.8a}$$

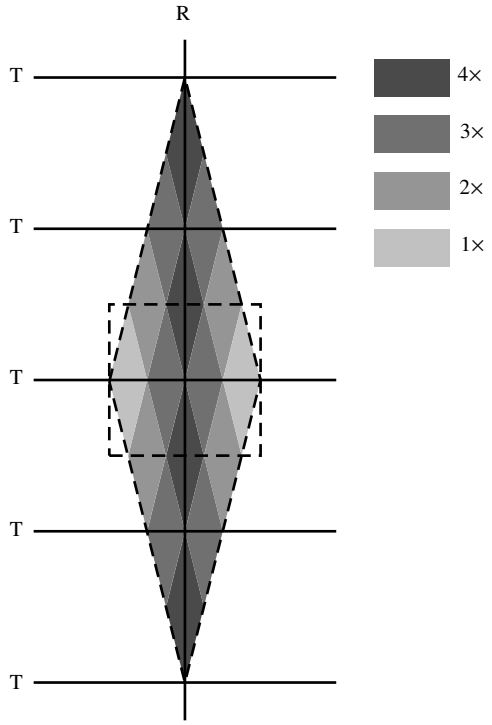


**Figure 7.1**: View from above of the linearized measurement volume in the inner domain of the pipe along with the total weight the subvolumes have on the determination of the area-averaged liquid holdup due to overlapping measurement volumes. The white areas within the usually assumed square measurement volume are the undetectable dead zones.

$$v_{\mathrm{BG}}(\delta\alpha_L) = \frac{v_{\mathrm{SG}}}{1 - \alpha_{\mathrm{L,WM}} + \delta\alpha_L}, \tag{7.8b}$$

where the true liquid holdup is expressed by $\alpha_{\mathrm{L,WM}} - \delta\alpha_L$. Accordingly, the systematic error in the liquid bulk and the gas bulk velocity can be approximated by

$$\delta v_{\mathrm{BL}} = \frac{v_{\mathrm{SL}}}{\alpha^2_{\mathrm{L,WM}}}\delta\alpha_L + \frac{v_{\mathrm{SL}}}{\alpha^3_{\mathrm{L,WM}}}\delta\alpha_L^2 \tag{7.9a}$$

$$\delta v_{\mathrm{BG}} = -\frac{v_{\mathrm{SG}}}{(1 - \alpha_{\mathrm{L,WM}})^2}\delta\alpha_L + \frac{v_{\mathrm{SG}}}{(1 - \alpha_{\mathrm{L,WM}})^3}\delta\alpha_L^2. \tag{7.9b}$$

Prasser et al. [209] have found in a validation study by ultrafast X-ray tomography on Taylor bubbles in vertical flow that the average cross-sectional liquid holdup values measured by the wiremesh sensor are maximum $\delta\alpha_L = 0.04$ too high. This value also appears to be useful as an approximation for the calculation of the error bars in the current stratified flow situation.

### 7.2.2 Strip-shield to reduce effects of lossy samples on the signal strength

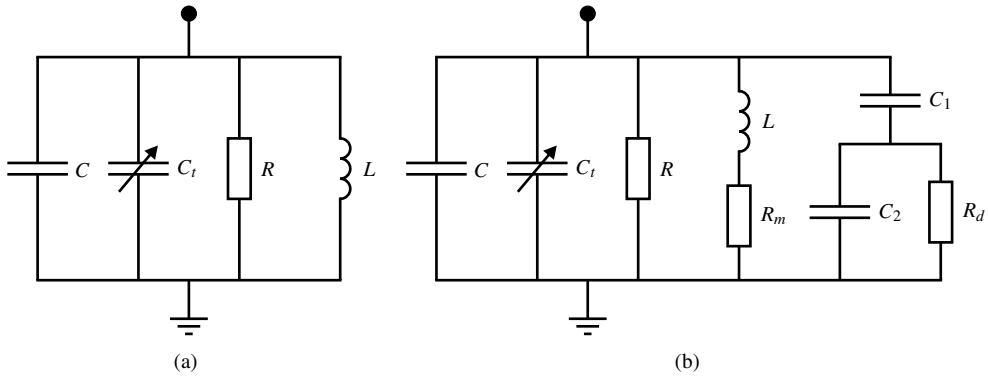


**Figure 7.2**: Representation of the probe circuit in Figure 2.10 (a) without and (b) with a lossy sample placed into the r.f. coil, where capacitor $C = 10$ pF, variable tuning capacitor $C_t = 5 - 75$ pF, resistor $R = 10$ kΩ and the inductance of the measurement coil $L \approx 2\ \mu$H.

As addressed in section 2.2.3, electrical properties of the sample affect the tuning and matching characteristics of the r.f. probes circuit. In presence of an alternating field, conducting samples give rise to radio frequency losses, which reduce the signal-to-noise ratio of the measurements. While Hoult and Richards [112] assume that the noise originates solely from the resistance of the coil, Hoult and Lauterbur [110] demonstrate that noise is also associated with dielectric and magnetic losses in the sample.

Magnetic losses are a direct result of the conductivity $\sigma_s$ of the sample. The electromotive force (emf), generated in the vicinity of the r.f. coil by the alternating $\mathbf{B}_1$-field, induces currents within a conducting sample that dissipate power. Gadian and Robinson [71] show that this power dissipation in a cylindrical sample of length $L_s$ and diameter $D_s$ can be expressed as an effective resistance

$$R_m = \frac{\pi\omega_0{}^2\mu_0{}^2 n_c{}^2 D_s{}^4 L_s \sigma_s}{128\left(D_c{}^2 + L_s{}^2\right)} \tag{7.10}$$

in series with the receiving solenoidal coil of diameter $D_c$ and $n_c$ ($\gg 1$) number of turns. Because of the fourth-order dependence on the sample diameter, the magnetic losses will increase when bigger samples are used.

Contrary to magnetic losses, which can be calculated from the geometry of the coil and the sample, dielectric losses can not. They depend on the actual way in which alternating current flows in the conducting coil [43]. The skin effect makes that ac current only flows in a thin skin on the surface of the wire. However, in the case of a solenoid, there are more conductors

– the turns – in close proximity. Each of them generates a changing magnetic field, which is, indirectly, again the source of the r.f. pulse's power loss. It influences, via the induced emf, the flow of current through all nearby conductors. The resulting redistribution of charge on the coil's surface causes a voltage difference between the turns of the coil. This conservative electrostatic field within the air and dielectric sample near the coil can be modeled with a distributed capacity between the two ends of the coil.
Most biological samples are very lossy dielectrics, which are heated in the presence of this alternating field [43]. The dielectric loss, the dissipation gives rise to, is equivalent to adding a resistance

$$R_{d,s} = \tau {\omega_0}^3 L^2 C_d \tag{7.11}$$

in series with the coil, where $\tau$ is the loss factor of the sample, $L$ the inductance and $C_d$ the distributed capacity of the coil [241]. For an isolated single-layer solenoid, Terman [241] reports that the distributed capacity is approximately proportional to the diameter of the coil, decreases slowly with increasing length and is largely independent of the number of turns. Hoult and Lauterbur [110] estimate a capacitance of typically 2 pF per centimeter diameter for this solenoid geometry. The actual distributed capacity will be larger, because the sample is a dielectric. Metal objects within a distance from the coil of the size of its dimensions, such as the shielding, the shimming and the gradient coils, also increase the distributed capacity.
Equation 7.11 describes the dielectric resistance when the r.f. coil is located within the dielectric. The actual sample is insulated from the r.f. coil by the pipe material. As the air gap between the PVC coil former and the pipe is practically lossless, it is convenient to convert the series connection of $R_{d,s}$ into the equivalent electronic circuit with the dielectric resistance parallel to the r.f. coil. Generally $\omega_0 L \gg R_{d,s}$, by which the parallel dielectric resistance, $R_d$, can be simplified to

$$R_d = \frac{(\omega_0 L)^2}{R_{d,s}}. \tag{7.12}$$

Substitution of Eq. 7.11 gives

$$R_d = (\tau \omega_0 C_d)^{-1}. \tag{7.13}$$

Figure 7.2(b) shows the adjustments that the presence of a lossy sample makes to the resonance circuit of the r.f. probe in Fig. 7.2(a). Following Gadian and Robinson [71], $C_1$ is the lossless capacitance from coil to sample, and $C_2$ and $R_d$ now represent the lossy sample. Associated, there is a second way in which the signal-to-noise ratio is adversely affected by the dielectric loss. As the resonance frequency of a parallel RLC-circuit is given by

$$\omega_{\text{osc}} = \frac{1}{\sqrt{LC}}, \tag{7.14}$$

the introduced capacity will detune the r.f. probe. Together with the additional relation between the dielectric resistance and the specific conductivity of the dielectric,

$$\frac{1}{R_d} = \frac{\sigma_s C_2}{\epsilon_0 \epsilon_r}, \tag{7.15}$$

where $\epsilon_0$ is the vacuum permittivity and $\epsilon_r$ the relative permittivity, Gadian and Robinson [71] conclude from straightforward calculations that the resonance frequency of the r.f. probe decreases as the conductivity of the sample increases. The reduction in frequency in changing from a sample of zero conductivity to one of infinite conductivity is

$$\Delta\omega_0 = \omega_0 \left( \left( \frac{C_1}{C + C_t} + 1 \right)^{-1/2} - \left( \frac{1}{C + C_t} \frac{C_1 C_2}{C_1 + C_2} + 1 \right)^{-1/2} \right), \tag{7.16}$$

where

$$\omega_0 = \frac{1}{\sqrt{L\,(C + C_t)}} \tag{7.17}$$

is the resonance frequency of the r.f. probe in absence of a lossy sample. As a matter of fact, the total capacitance of a dielectric-filled capacitor increases rapidly with the diameter of the sample. This, in particular, is a serious problem for this flowmeter design, since the gap between the coil and the sample of about 1 cm is, for lack of space, rather small. Detuning of the r.f. probe will be the most distinctive consequence of lossy samples and not the dissipation. This is in agreement with the reflection power spectrum in Figure 7.3(a) of wobble measurements on 29.6 cm long cylindrical containers of 98.6 mm diameter, the static dummies discussed before in chapter 5, either filled with air (insulator; $\sigma_s = 0$) or with water. With a reduction of more than 0.4 MHz in the resonance frequency, the probe is very susceptible to loading by a water sample. At both frequencies where one of the samples has its resonance frequency, there is a big difference in the reflected and, hence, also in the absorbed power between one phase compared to the other. However, the continuous operation in multiphase flow measurements excludes frequent re-tuning of the r.f. probe. Usually the probe is tuned once to a full pipe, whereafter the NMR signal is monitored over a longer period. The liquid holdup is, consequently, no longer a linear function of the NMR signal strength, but is underestimated if Eq. 7.1 is used. Ergo, reducing the parasitic capacitance $C_2$, which is experienced by the dielectric sample, is an important issue as far as multiphase flowmetering is concerned.

Various Faraday shields have been suggested, which screen the sample from the conservative electrostatic field that is associated to the distributed capacity, but still maintain a significant $B_1$-field. Although the presence of a shield causes, on account of the capacitance they introduce, a similar but fixed detuning as by bringing a liquid sample into the coil [43], this shift in the resonance frequency is easily corrected with the tuning capacitor $C_t$. Park et al. [198] show with numerical simulations that the geometry of the shield can largely determine its efficiency. Both strip-shields [71, 261] and loop-gap shields [140] significantly reduce the conservative electrostatic field. However, Park et al. [198] have found that the loop-gap shield, in contrast to the strip-shield, has a serious effect on the magnitude and homogeneity of the $B_1$-field. The passive conductors prevent the field lines from passing through the sample by carrying a charge density distribution opposing the conservative electromagnetic field. Since the arrangement of strips parallel to the coil ensures that they cannot carry any significant current in the circumferential direction, the strip-shield has only a a minor effect on the $B_1$-field of the solenoid. For that reason, we have implemented strip-shields between the r.f. coils and the pipeline that goes through the NMR flowmeter.

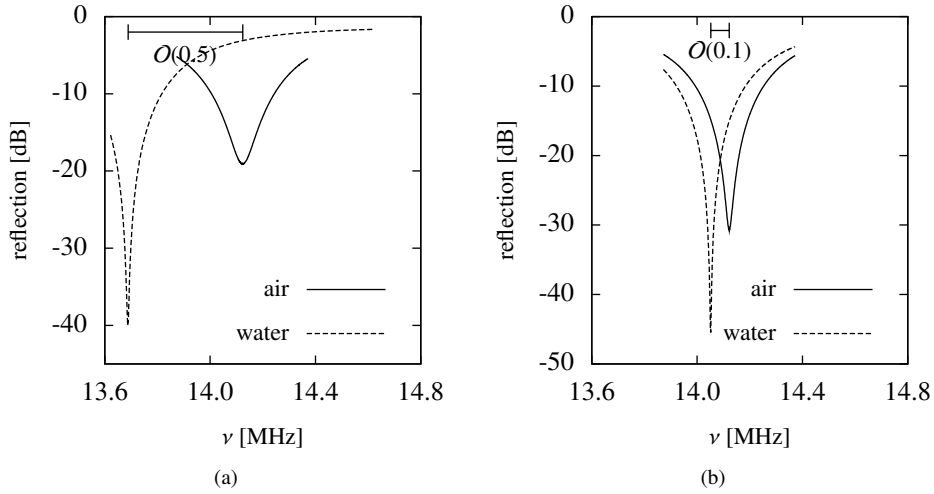


**Figure 7.3**: Reflection power spectrum, obtained with the Bode100 Vector Network Analyzer (Omicron Electronics, Ser. no. CK193C) connected to the wobble facility of the NMR system, (a) without and (b) with a strip-shield inserted between the coil and the sample. The samples are 29.6 cm long cylindrical containers of 98.6 mm inner diameter, which are either filled with air or with tap water at room temperature.

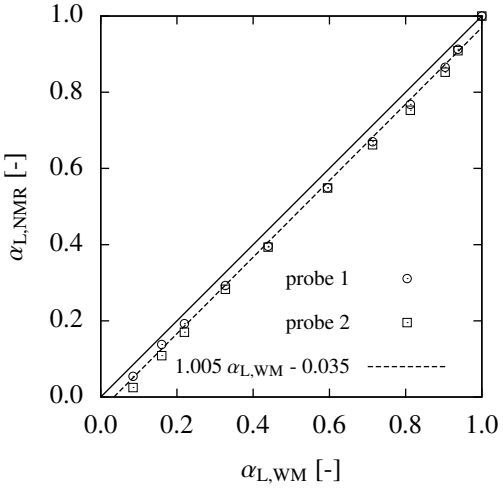


**Figure 7.4**: Calibration curve for the liquid holdup, $\alpha_{\mathrm{L,NMR}}$, in the T1RRT measurements carried out in the large two-phase flow loop. The wiremesh is operated at 800 Hz, taking the time average of 48000 samples as standard for the real liquid holdup $\alpha_{\mathrm{L,WM}}$.

The strip-shields consist of PVC coil formers of 112 mm inner diameter on the inside of which thin self-adhesive copper strips are taped with their long axis parallel to the axis of the solenoid coil. The rectangular strips are about 35 cm long, 10 mm wide and are equally spaced along the circumference with a distance of 10 mm between them [217]. The strips are neither grounded nor connected to each other through annular strips. This is very important, since the discontinuity of the screen prevents eddy-currents to flow [43]. As pointed out in section 6.3.3.2, the eddy-currents induce a magnetic field counteracting the magnetic fields that go together with both the transmitting and receiving function of the r.f. probe. This attenuation of the resultant field is obviously problematic for the performance of the NMR probe.

Figure 7.3(b) shows a substantial improvement of the strip-shield on the detuning. As a result, the difference in reflected power between the two samples at either of their resonance frequencies has decreased to an acceptable level. Also the matching gets significantly better for both samples. However, the strip-shield cannot completely remove the signal loss, caused by the inability to retune the probes repeatedly for changing holdups. To that end, a calibration curve is still required that links the measured holdup, $\alpha_{L,NMR}$, to the real holdup.
For the T1RRT measurements in this thesis, the calibration curve is given by Figure 7.4, where the wiremesh provides the standard for the real holdup $\alpha_{L,WM}$. The measurements are carried out under static conditions, leveling the height of the stratified liquid layer in front of the wiremesh and behind the NMR flowmeter with the level tank, described in section 4.4.1. The single-shot T1RRT measurements are again processed using the average signal strength of the first 20 data points of the FID, a dwell time of 1 $\mu$s apart. The real liquid holdup is the time average of 48,000 wiremesh scans, simultaneously detected at 800 Hz. At practically all gas fractions, there is a constant negative offset of 0.035 with respect to the real liquid holdup. Only if the pipe is almost full or empty, the attenuation must be determined through interpolation.

## 7.3 Signal Processing

In a set of measurements, the NMR signal is obtained for different combinations of the superficial liquid and superficial gas velocity. The signal amplitude is quantified as the average strength of the first 20 data points of the FID, a dwell time of 1 $\mu s$ apart, which in chapter 6 turned out to be the best method. One of the measurements of the set involves determining $s_0$, the signal intensity of the NMR signal corresponding to the thermal equilibrium magnetization $M_0$, in each probe. While the probes are completely filled with water at zero velocity, the spins of the water remain for this purpose at least $5T_1$ in the polarizing magnetic field. Knowledge of the $T_1$ relaxation time is essential for the accuracy of the flow measurements based on the T1RRT method. Therefore, each set of measurements is preceded and followed by determining the $T_1$ with the inversion recovery pulse sequence, see section 2.3.4, at zero velocity. In order to reduce the influence of the temperature, the mean of both $T_1$ relaxation times is used in the signal processing.

Using this mean $T_1$, $N_y = 120$, $L_c = 12$ cm and $\overline{\Delta l} = 2.57$ cm, the reference curve expressed by Eq. 7.6 is calculated for an absolute velocity range of 0 – 3 m s$^{-1}$ with a resolution of 1 mm s$^{-1}$. The conversion factor for the $v_y^*$ range is about 4.5. Along with this reference curve for the determination of $v^*_{\mathrm{NMR}}$, the curve describing the signal strength $s_{100\%L}(v_y)$ in the second r.f. probe is calculated by means of Eq. 7.4 for the same conditions with $\alpha_L = 1$. After the determination of $v^*_{\mathrm{NMR}}$, the value of $s_{100\%L}(v_{\mathrm{NMR}})$ is used as an input parameter to calculate $\alpha_{\mathrm{NMR,2}}$ with Eq. 7.1. As discussed in section 7.2.2, a second calibration curve between $\alpha_{\mathrm{NMR,2}}$ and $\alpha_{\mathrm{L,WM}}$ is required, which corrects the obtained liquid holdup for the loss due to detuning. To this end, the data points in Fig. 7.4 have been piecewise interpolated with a resolution of 0.001.

Each flow measurement consists of $N_s$, respectively 30 ($v_{\mathrm{SL}} = 0.05$ and 0.15 m s$^{-1}$) and 60 ($v_{\mathrm{SL}} = 0.10$ m s$^{-1}$) consecutively acquired T1RRT sequences. All signals are normalized with the $s_0$ corresponding to the r.f. probe.

Under a quasi-steady state approximation, the average NMR velocity is first determined from the individual velocities obtained for each pair of FIDs. The measurement frequency is intentionally kept very low. Applying a delay of at least $5T_1$ between each repetition of the T1RRT sequence prevents previous pulses from influencing the amplitude of the NMR signal. This allows the water in the probe to be either completely replaced or to regain thermal equilibrium magnetization. Although the method works in theory with all pulse lengths, the choice for 90° pulses maximizes the signal yield. The T1RRT method is particularly sensitive to assumptions in the calculation of the reference curves. By using the mean $T_1$, temperature effects are of secondary importance. In practice this can be overcome by a database that relates the $T_1$ to the composition and temperature of the fluid. The expanded uncertainty of the mean velocity is accordingly calculated corresponding to the 95 percent confidence level of the series' standard deviation, $\sigma(v_{\mathrm{NMR}})$,

$$U(\bar{v}_{\mathrm{NMR}}) = \frac{t_{\mathrm{ST}\ 0.025}(N_s - 1)\ \sigma(v_{\mathrm{NMR}})}{\sqrt{N_s}}, \tag{7.18}$$

where $t_{\mathrm{ST}\ 0.025}(N_s - 1)$ is the Student's t distribution for $N_s - 1$ degrees of freedom and the true standard deviation is estimated by the sample standard deviation

$$\sigma(v_{\mathrm{NMR}}) = \sqrt{\frac{1}{N_s - 1}\sum_i (v_{\mathrm{NMR}}[i] - \bar{v}_{\mathrm{NMR}})^2}. \tag{7.19}$$

In order to evaluate the expanded uncertainty of the dimensionless velocity, an expression for its combined standard uncertainty

$$u(\bar{v}^*_{\mathrm{NMR}}) = |\bar{v}^*_{\mathrm{NMR}}| \sqrt{\left(\frac{u(\bar{v}_{\mathrm{NMR}})}{\bar{v}_{\mathrm{NMR}}}\right)^2 + \left(\frac{u(T_1)}{T_1}\right)^2 + \left(\frac{u(y_{c,1})}{y_{c,1} + \overline{\Delta l}}\right)^2 + \left(\frac{u(\overline{\Delta l})}{y_{c,1} + \overline{\Delta l}}\right)^2} \tag{7.20}$$

is first derived by applying the law of propagation of uncertainty to Eq. 7.2. The effective degrees of freedom of $u(\bar{v}^*_{\mathrm{NMR}})$ are estimated by using the Welch-Satterthwaite approximation

[122]:

$$\nu(\bar{v}^*_{\mathrm{NMR}}) = \frac{u(\bar{v}^*_{\mathrm{NMR}})^4}{\bar{v}^*_{\mathrm{NMR}}{}^4 \left( \left( \frac{u(\bar{v}_{\mathrm{NMR}})}{\bar{v}_{\mathrm{NMR}}} \right)^4 \frac{1}{\nu(\bar{v}_{\mathrm{NMR}})} + \left( \frac{u(T_1)}{T_1} \right)^4 \frac{1}{\nu(T_1)} + \left( \frac{u(y_{c,1})}{y_{c,1}+\overline{\Delta l}} \right)^4 \frac{1}{\nu(y_{c,1})} + \left( \frac{u(\overline{\Delta l})}{y_{c,1}+\overline{\Delta l}} \right)^4 \frac{1}{\nu(\overline{\Delta l})} \right)}, \quad (7.21)$$

where the standard uncertainties and the corresponding degrees of freedom of $T_1$, $y_{c,1}$ and $\overline{\Delta l}$ are given in table C.1 in appendix C. If the calculated $\nu(\bar{v}^*_{\mathrm{NMR}})$ is a non-integer, its value is truncated to the next lower integer. The expanded uncertainty is then obtained by multiplying the combined standard uncertainty by a coverage factor based on the Student's t distribution for $\nu(\bar{v}^*_{\mathrm{NMR}})$ degrees of freedom

$$U(\bar{v}^*_{\mathrm{NMR}}) = t_{\mathrm{ST}\ 0.025}(\nu(\bar{v}^*_{\mathrm{NMR}}))\ u(\bar{v}^*_{\mathrm{NMR}}) \quad (7.22)$$

providing a level of confidence of approximately 95%.

The average liquid holdup is calculated along the same lines as the average NMR velocity. For each of the $N_s$ acquired FIDs in the second r.f. probe, a liquid holdup is determined. The NMR velocity corresponding to the same T1RRT sequence serves as input parameter for the calculation. Since the signal from the second r.f. probe is closer to the thermal equilibrium level, the use of this signal is preferable to that from the first r.f. probe. Not only is the signal stronger and therefore less susceptible to noise, the calculated holdup is also less affected by the velocity profile that differs from the plug flow model applied in the signal processing.
The quasi-steady state approximation is obviously only valid if the gas-liquid interface is stable. In the case that strong waves are present, the signal's standard deviation is actually mixed with the fluctuations by the wavy surface. However, the power spectral density analysis in section 7.4.1 will show that the characteristic length scales of the waves are such that 2 to 3 wavelengths fit into the 12 cm long coil. This means that the measured result is always a spatial average of the holdup. The measurements can also be regarded as instantaneous, since they take place within a time interval of less than 250 $\mu s$.

Despite the fact that uncertainties in the NMR velocity propagate into that of the holdup, it may be assumed that they fall within the margin of the series' standard deviation

$$\sigma(\alpha_{\mathrm{NMR},2}) = \sqrt{\frac{1}{N_s - 1} \sum_i (\alpha_{\mathrm{NMR},2}[i] - \bar{\alpha}_{\mathrm{NMR},2})^2}. \quad (7.23)$$

The calculation of the expanded uncertainty of the mean liquid holdup is based on the sample standard deviation with a level of confidence of 95%

$$U(\bar{\alpha}_{\mathrm{NMR},2}) = \frac{t_{\mathrm{ST}\ 0.025}(N_s - 1)\ \sigma(\alpha_{\mathrm{NMR},2})}{\sqrt{N_s}}, \quad (7.24)$$

where $t_{\mathrm{ST}\ 0.025}(N_s - 1)$ is the Student's t distribution for $N_s - 1$ degrees of freedom.

Finally, $v^*_{\mathrm{NMR}}$ is converted back into its dimensional equivalent $v_{\mathrm{NMR}}$, whereafter the liquid flowrate, $q_{\mathrm{NMR}}$ is calculated from Eq. 7.7. Neglecting the uncertainty in the pipe diameter, the combined standard uncertainty in $q_{\mathrm{NMR}}$ can be written as

$$u(q_{\mathrm{NMR}}) = |q_{\mathrm{NMR}}| \sqrt{\left(\frac{u(\bar{\alpha}_{\mathrm{NMR},2})}{\bar{\alpha}_{\mathrm{NMR},2}}\right)^2 + \left(\frac{u(\bar{v}_{\mathrm{NMR}})}{\bar{v}_{\mathrm{NMR}}}\right)^2}. \tag{7.25}$$

The effective degrees of freedom of $u(q_{\mathrm{NMR}})$ required for the calculation of the expanded uncertainty with a confidence level of 95% 

$$U(q_{\mathrm{NMR}}) = t_{\mathrm{ST}\ 0.025}(\nu(q_{\mathrm{NMR}}))u(q_{\mathrm{NMR}}) \tag{7.26}$$

are estimated with the Welch-Satterthwaite formula at

$$\nu(q_{\mathrm{NMR}}) = \frac{u(q_{\mathrm{NMR}})^4}{\frac{{q_{\mathrm{NMR}}}^4}{N_s - 1}\left(\left(\frac{u(\bar{\alpha}_{\mathrm{NMR},2})}{\bar{\alpha}_{\mathrm{NMR},2}}\right)^4 + \left(\frac{u(\bar{v}_{\mathrm{NMR}})}{\bar{v}_{\mathrm{NMR}}}\right)^4\right)}. \tag{7.27}$$

The main disadvantage of the T1RRT method for two-phase flow measurements is the reinforcing effect due to the two-stage system of the signal processing. When the NMR velocity is overestimated, the NMR signal will be scaled with a too small $s_{100\%L}(v_{\mathrm{NMR}})$, so the liquid holdup is also overestimated. Both contribute to a too high flowrate. Likewise an underestimation of the NMR velocity provides a too big reference signal strength $s_{100\%L}(v_{\mathrm{NMR}})$, resulting in an underestimation of the holdup. This results in an extra low flowrate.

For a full overview of all the involved uncertainties, including those in the reference measurements, and their derivations is referred to appendix C.1.

## 7.4 Results and Discussion

### 7.4.1 Experimental Matrix

The experiments are carried out for 24 different combinations of the superficial liquid and superficial gas velocity. In each set of measurements, the superficial liquid velocity is kept fixed at 0.05, 0.10 or 0.15 m s$^{-1}$, while the superficial gas velocity is varied in the range from 0.15 to 2.7 m s$^{-1}$.

To determine which sub-regime the flow case belongs to, the power spectral density (PSD) of the liquid level fluctuations is analyzed. Because different wave structures have typical frequencies, wavelengths and amplitudes, this is an approved method to discriminate the flow cases from each other on objective terms. The transitions between the flow patterns are characterized by the appearance and disappearance of peaks in the frequency spectrum.
Ayati et al. [12], Shi and Kocamustafaogullari [228] and Strand [238] applied the spectral

method to the liquid level time records of parallel-wire conductance probes in pipe flow. Fernandino and Ytrehus [67] have shown that the method is also successful when the spectrum is computed from LDV measurements of the vertical velocity just below the interface in a squared channel flow. In the present study, the characterization of the interfacial flow patterns is based on the wiremesh signal, measured 310 $D_p$ downstream of the inlet section.
In the series with a superficial liquid velocity of 0.05 and 0.15 m s$^{-1}$, the liquid holdup is acquired during 100 s at a sampling frequency of 800 Hz. In the series with a superficial liquid velocity of 0.10 m s$^{-1}$, the liquid holdup is acquired during 1000 s at a sampling frequency of 500 Hz. Each series of measurements is preceded by a calibration measurement of the nodal wiremesh signal strength under static pure water conditions. Under the assumption of a uniform water level, the average liquid height in the entire cross-section, $h_L$, is derived from the total liquid holdup.
As explained in appendix D, the interfacial wave power spectrum is calculated through Welch's periodogram averaging method combined with 50% overlapping Hamming windows. The sample length of the liquid height signal of the measurement series at $v_{\mathrm{SL}} = 0.10$ m s$^{-1}$ is truncated to 102,400 elements, such that all PSDs can be estimated with 99 Hamming windows of 2 – 4 s in length. From the comprehensive analysis in section D.3 can be concluded that all flow cases belong either to the stratified smooth or the stratified wavy regime with regular 2D small amplitude waves.

Figure 7.5 shows the experimental conditions in a flow map compared to the transitions obtained by Strand [238] for a 10 cm i.d. pipe and by Andritsos and Hanratty [6] for a 9.53 cm i.d. pipe. The results are in good agreement with those of Strand, whereas the visual observations by Andritsos and Hanratty notice the initiation of small amplitude 2D waves at considerably lower gas velocities. As addressed by Fernandino and Ytrehus [67] this is a limitation of the spectral method. Light reflections from the liquid surface reveal the presence of the first disturbances that appear with increasing gas velocity. Although they may already be considered waves, their amplitude is so low that the spectrum shows no difference with the stratified smooth case.

A summary of the experimental flow conditions is given in table 7.1. In the calculation of the actual Reynolds numbers for the liquid and the gas phase

$$\mathrm{Re}_L = \frac{\rho_L v_{\mathrm{BL}} D_{hL}}{\mu_L} \quad \text{and} \quad \mathrm{Re}_G = \frac{\rho_G v_{\mathrm{BG}} D_{hG}}{\mu_G} \tag{7.28}$$

the hydraulic diameters used are as defined by Agrawal et al. [4]

$$D_{hL} = \frac{4A_L}{P_L} \quad \text{and} \quad D_{hG} = \frac{4A_G}{P_i + P_G}, \tag{7.29}$$

where $A_L$ and $A_G$ are the cross-sectional areas occupied by liquid and gas, $P_L$ and $P_G$ the wetted perimeters of the liquid and the gas phase and $P_i$ the width of the gas-liquid interface (see Fig. 7.6). With the criterion $\mathrm{Re}_L > 5500$ proposed by Lioumbas et al. [160], all measured flow cases have a turbulent liquid layer. Considering the experience with single-phase turbulent NMR flow measurements, the expectation is that a plug flow model gives sufficiently

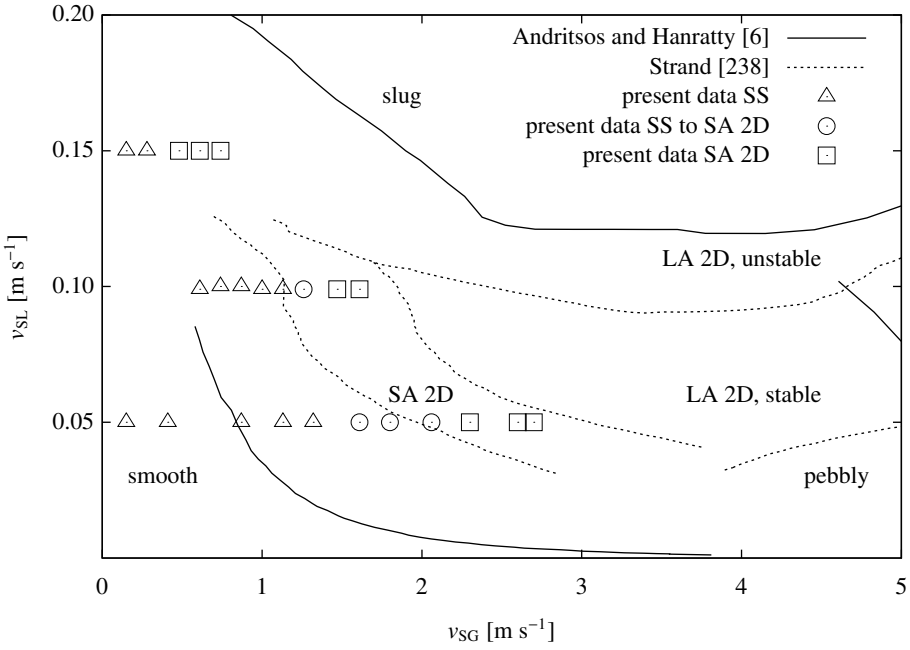


**Figure 7.5**: Comparison of the experimental conditions with the flow map for horizontal air-water two-phase flow from Strand [238] for 10 cm i.d. pipes and the empirical map from Andritsos and Hanratty [6] for 9.53 cm i.d. pipes (SS: stratified smooth; SA: small amplitude; LA: large amplitude; 2D: two-dimensional waves).

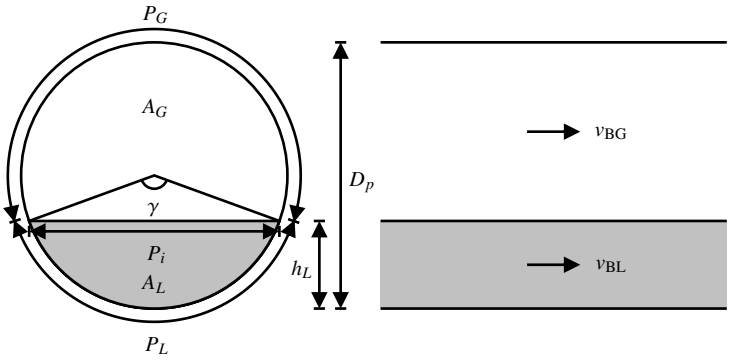


**Figure 7.6:** Definition of the parameters for the evaluation of horizontal stratified gas-liquid flow.

**Table 7.1:** Summary of the experimental flow conditions.

| $v_{SL}$ | $v_{SG}$ | $v_{BL}$ | $v_{BG}$ | $Re_L$ | $Re_G$ | $\bar{\alpha}_{L,WM}$ | $\bar{h}_{L,WM}$ | $D_{hL}$ | $D_{hG}$ |
|---|---|---|---|---|---|---|---|---|---|
| [m s$^{-1}$] | | | | $\times 10^3$ [-] | | [-] | | [mm] | |
| 0.050 | 0.15 | 0.072 | 0.50 | 9.1 | 1.3 | 0.70 | 65 | 114 | 43 |
| 0.050 | 0.41 | 0.072 | 1.3 | 9.1 | 3.7 | 0.69 | 64 | 114 | 43 |
| 0.050 | 0.87 | 0.092 | 1.9 | 10.5 | 6.9 | 0.55 | 53 | 103 | 56 |
| 0.050 | 1.13 | 0.102 | 2.2 | 11.0 | 8.6 | 0.49 | 49 | 98 | 61 |
| 0.050 | 1.32 | 0.11 | 2.5 | 11.2 | 10.0 | 0.47 | 47 | 96 | 62 |
| 0.050 | 1.61 | 0.13 | 2.6 | 12.6 | 11.6 | 0.38 | 40 | 85 | 70 |
| 0.050 | 1.8 | 0.14 | 2.8 | 12.8 | 12.8 | 0.35 | 38 | 82 | 72 |
| 0.050 | 2.1 | 0.15 | 3.1 | 13.2 | 14.8 | 0.33 | 36 | 79 | 74 |
| 0.050 | 2.3 | 0.16 | 3.3 | 13.6 | 16.1 | 0.31 | 35 | 77 | 75 |
| 0.050 | 2.6 | 0.16 | 3.8 | 13.5 | 18.2 | 0.32 | 35 | 77 | 75 |
| 0.050 | 2.7 | 0.16 | 3.9 | 13.7 | 19 | 0.31 | 34 | 76 | 76 |
| 0.099 | 0.61 | 0.15 | 1.8 | 14.6 | 5.5 | 0.66 | 62 | 112 | 46 |
| 0.100 | 0.74 | 0.16 | 2.0 | 15.0 | 6.5 | 0.63 | 60 | 110 | 49 |
| 0.100 | 0.87 | 0.17 | 2.1 | 15.6 | 7.4 | 0.59 | 56 | 107 | 53 |
| 0.099 | 1.00 | 0.17 | 2.4 | 15.6 | 8.5 | 0.59 | 56 | 106 | 53 |
| 0.099 | 1.13 | 0.18 | 2.5 | 16.1 | 9.4 | 0.55 | 54 | 104 | 56 |
| 0.099 | 1.26 | 0.19 | 2.7 | 16.5 | 10.3 | 0.53 | 51 | 101 | 58 |
| 0.099 | 1.47 | 0.19 | 3.1 | 16.3 | 12.0 | 0.53 | 52 | 101 | 58 |
| 0.099 | 1.61 | 0.19 | 3.3 | 16.7 | 13.0 | 0.51 | 50 | 99 | 60 |
| 0.150 | 0.15 | 0.20 | 0.62 | 25.1 | 1.4 | 0.76 | 70 | 117 | 37 |
| 0.150 | 0.28 | 0.20 | 1.2 | 25.1 | 2.7 | 0.76 | 70 | 117 | 36 |
| 0.150 | 0.48 | 0.23 | 1.4 | 27.7 | 4.1 | 0.66 | 62 | 112 | 47 |
| 0.150 | 0.61 | 0.23 | 1.7 | 27.9 | 5.2 | 0.65 | 61 | 111 | 47 |
| 0.150 | 0.74 | 0.26 | 1.8 | 29.5 | 6.1 | 0.59 | 56 | 106 | 53 |

**Table 7.2**: Measurement conditions, where the number in parenthesis is the standard uncertainty $u$ expressed in the unit of the quoted result.

| $v_{SL}$ | 0.05 m s$^{-1}$ | 0.10 m s$^{-1}$ | 0.15 m s$^{-1}$ |
|---|---|---|---|
| $\bar{T}_L$ | 25 (1) °C | 15 (1) °C | 24 (1) °C |
| $\bar{T}_G$ | 26 (1) °C | 19 (1) °C | 26 (1) °C |
| $\mu_L$ | 0.90 (0.02) mPa s | 1.16 (0.03) mPa s | 0.92 (0.02) mPa s |
| $\mu_G$ | 1.85 (0.01) $\cdot 10^{-2}$ mPa s | 1.82 (0.01) $\cdot 10^{-2}$ mPa s | 1.85 (0.01) $\cdot 10^{-2}$ mPa s |
| $\rho_L$ | 997.1 (0.3) kg m$^{-3}$ | 999.1 (0.2) kg m$^{-3}$ | 997.3 (0.3) kg m$^{-3}$ |
| $\rho_G$ | 1.181 (0.004) kg m$^{-3}$ | 1.209 (0.004) kg m$^{-3}$ | 1.181 (0.004) kg m$^{-3}$ |
| $T_1$ | 2.69 (0.01) s | 2.26 (0.01) s | 2.64 (0.01) s |
| $N_s$ | 30 | 60 | 30 |

accurate values. Nevertheless, some restraint is required. Ayati et al. [12] demonstrate that, due to wave dynamics, the axial velocity profile is very sensitive to changes in the wave structures at the transition from stratified smooth to stratified wavy flow. The lack of knowledge about the prevalent flow pattern makes it difficult to implement a working velocity distribution model in the signal processing of the flowmeter. In section 7.4.3.2 is investigated to what extent the shape change of the axial velocity profile influences the NMR flow measurements.

Whether the quasi-steady state approximation is valid for the stratified wavy cases is examined by estimating the wavelength with $\lambda = v_{BL}/f_p$ from the peak frequency obtained with the spectral analysis in appendix D. The dominant small-amplitude 2D waves have a wavelength in the range of 5 – 7 cm. So the signal strength of the FID is an spatial average of the 2 – 3 $\lambda$ that fit in the 12 cm long coil. We can therefore assume that the waves do not influence the value of the uncertainty determined on the basis of the standard deviation. Especially when the flowrate is evaluated as a long-time average by basing it on repeated measurements.

### 7.4.2 Flowmeter Performance Evaluation

The measurements are carried out at the conditions listed in table 7.2. Both the water and the air temperature fluctuate at most 1 °C around their average over the series of measurements at a fixed superficial liquid velocity. The $T_1$ relaxation time is on average 2.69 s ($v_{SL}$ = 0.05 m s$^{-1}$), 2.26 s ($v_{SL}$ = 0.10 m s$^{-1}$) and 2.64 s ($v_{SL}$ = 0.15 m s$^{-1}$).

Figure 7.7 shows the ratio of the signal intensities measured in both coils. Almost all data points follow the trend of the plug flow algorithm used by the flowmeter. A small underestimation of the measured signal fraction by the model is expected because of the approximation of the non-uniform polarizing magnetic field with the asymptotic added length value of 2.57 cm. Because of the huge systematic error in the reference measurements of the liquid holdup, the flowmeter curve falls in most cases even within the error bars. Obviously the 3 stratified wavy cases with a dimensionless liquid bulk velocity of about 0.8 are outliers. This seems to

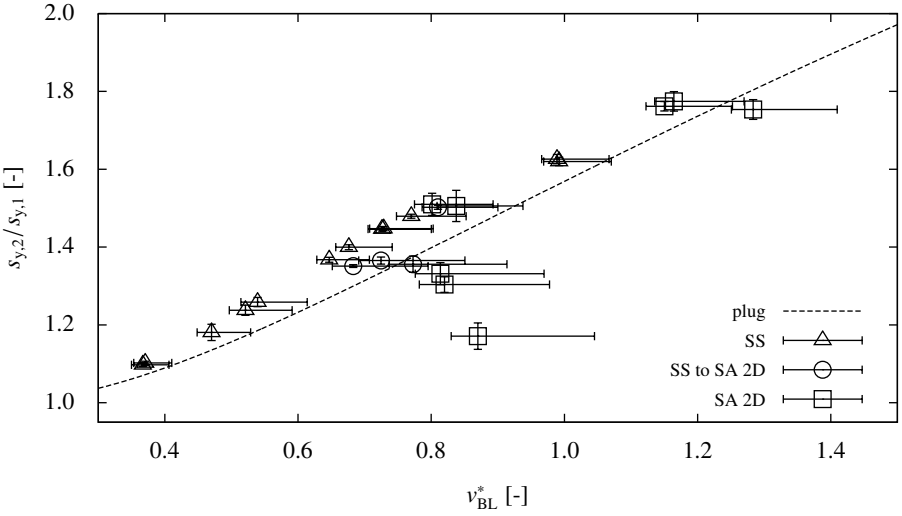


**Figure 7.7**: Ratio of the signal intensity in the 2nd r.f. coil with respect to the 1st r.f. coil as a function of the dimensionless liquid bulk velocity. In the flowmeter reconstruction algorithm, the curve of the plug flow simulations of Eq. 7.6 ($\overline{\Delta l}$ = 2.57 cm, $N_y$ = 120 ) is consulted to determine the dimensionless flow velocity $v^*_{\mathrm{NMR}}$.

be due to the existence of a water level gradient. Under the lowest liquid holdup conditions ($\alpha_{\mathrm{L,WM}} \approx 0.3$), it was difficult to maintain a constant water level within the NMR flowmeter. An issue that will be further discussed in section 7.4.3.1.

In Figure 7.8(a) the linearity of the flowmeter is studied by plotting the NMR velocity against the liquid bulk velocity. A linear least squares fit of the data points without the 3 stratified wavy outliers gives a linearity of -4%. When the expanded uncertainty is included in the fit, a linearity of +1% is found. Better reference measurements are needed in order to be able to draw quantitative conclusions.
The data is more scattered than in the case of single-phase flow. This is not very surprising since the flowmeter operates in the range with liquid bulk velocities below 0.3 m $s^{-1}$ of which in section 6.2.5.2 has been found that the NMR signal in the second probe is close to the thermal equilibrium. Larger inaccuracies in the velocity can be expected, because it is effectively only determined by the signal measured by the first probe.
Although the data processing is corrected for the inhomogeneity of the initial polarizing magnetic field, the implemented value of $\overline{\Delta l}$ is derived in section 6.2.4 for a completely filled pipe. Figure 6.3(a) shows the spatial distribution of the added length in the xz-cross-section of the coil. The added length is larger in the vicinity of the magnets and the average value for stratified flow measurements is hence smaller than the 2.57 cm used. This will cause an additional overestimation of the velocity on top of the estimated 0.2 cm $s^{-1}$ for the use of the asymptotic

value of $\overline{\Delta l}$. Because the liquid holdup differs from case to case, this can explain the slight curvature in the results.

Between the two fits a big difference is found in the offset of the NMR velocity. In Figure 7.8(b) we will examine the directional bias error further. The absolute velocity overestimation by the flowmeter is fairly constant around 2 cm $s^{-1}$. The accuracy of the flowmeter is probably better due to the large uncertainty introduced by the reference measurements. If we take the systematic error in the liquid bulk velocity $\delta v_{BL}$ into account, the directional bias error is rather 1 cm $s^{-1}$, which is comparable to the value found for the turbulent single-phase flow measurements in the 98.6 mm i.d. pipe in the $v_y$ range of 0.05 – 0.30 m $s^{-1}$.

In Figure 7.9(a) and (b) we show respectively the relative and absolute expanded uncertainty in the NMR velocity using Eq. 7.22. Although the T1RRT pulse sequence has been repeated 60 times in some of the measurements ($v_{SL}$ = 0.10 m $s^{-1}$) and only 30 times in the remainder, the difference in coverage factor has no clear effect on the uncertainty. The absolute uncertainty is in the range of 0.1 – 1.2 cm $s^{-1}$. If we leave out the 3 outliers, the upper limit is only 0.6 cm $s^{-1}$ and the flowmeter achieves a repeatability of 1 – 3 percent rate performance with 95% confidence level. Provided Eq. 7.9a approaches the estimated systematic error in the liquid bulk velocity well, at least half of the directional bias error can be attributed to the repeatability. Since the flowmeter is actually designed for higher liquid velocities where the signal in the second probe is not in thermal equilibrium, this is not a bad result at all.

A large part of the measurement errors is caused by the model on which the flowmeter is based. The main cause seems to be the presumption of an equal water level in both r.f. coils. A condition that could not be realized with sufficient accuracy with the used flow loop. There seems to be a weak gradient in the water level. The sensitivity study in section 7.4.3.1 will show that an elevation angle of 0.075° under the prevailing flow conditions leads to a velocity offset of 1 – 3 cm $s^{-1}$. Other less dominant factors are the use of an incorrect added length for the non-homogeneous $B_0$-field and the velocity distribution that actually differs from plug flow and that is also very sensitive to changes in the interfacial structure. Only their influence on the modeled signal in the first r.f. coil is important here, because the signal in the second r.f. coil is almost in thermal equilibrium.

In the second step of the two-phase flow measurements, the liquid holdup is determined. As is apparent from Figure 7.10(a), there is little to comment on the linearity of the obtained liquid holdup. The directional bias error in the liquid holdup is given in Figure 7.10(b). Almost all measured holdups are too low, even after correction for the systematic overestimation by the wiremesh sensor. Underestimation of the liquid holdup is a general problem of the T1RRT measurement method. This has manifested itself before in the single-phase flow results in Figure 6.9 where the measured signal strengths are below the expected curve. The signal loss hardly leads to errors in the velocity measurements. When the velocity is determined from the ratio of the signal intensities, the effect cancels itself out as the multiplication factor is almost equal for both coils. It is remarkable, given the bias error in the velocity measurements, that the measurement series with $v_{SL}$ = 0.05 m $s^{-1}$ best approximates the expected holdup. This

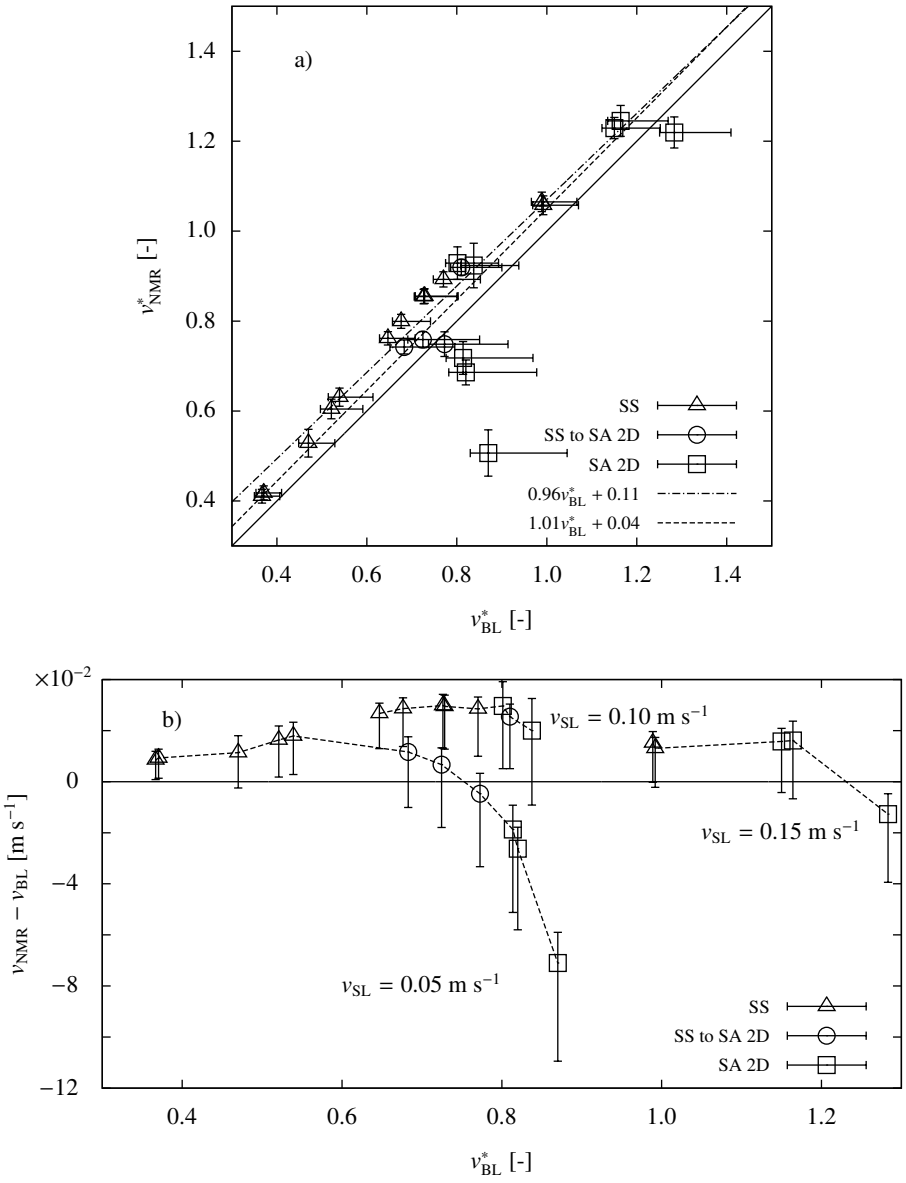


**Figure 7.8**: (a) A comparison of the NMR velocity with the liquid bulk velocity gives an indication of the linearity. Omitting the 3 outlying SA 2D data points for $v_{SL}$ = 0.05 m s$^{-1}$, the dashed line is the fit that takes the error bars into account, while the dash-dotted line is the fit of the data points solely. (b) The difference between the two velocities is an indication of the directional bias error. The data points belonging to the same series of measurements are connected with a dashed line.

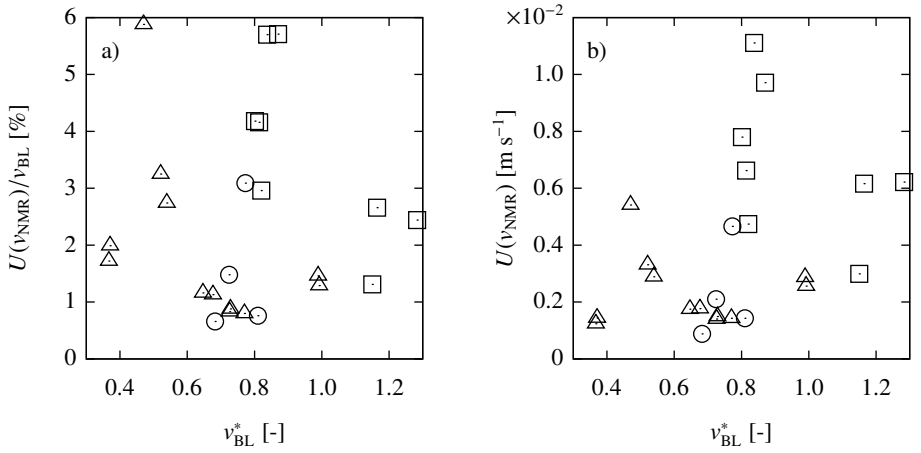


**Figure 7.9**: (a) Relative and (b) absolute expanded uncertainty in the NMR velocity with 95% confidence level, where △ is the SS, ○ the transitional SS to SA 2D and □ the SA 2D flow regime.

may be due to the fact that the signal measured by the second probe has virtually reached the thermal equilibrium state. Neither the reinforcement effect nor $B_0$-inhomogeneities combined with changes in the velocity distribution will therefore affect the holdup determination. A condition that Lynch and Segel [163] intentionally aim for to avoid problems with relaxation time effects in their comparable void fraction measurement method of two-phase flows.

The presence of a weak gradient in the water level can explain both the over- and underestimation of the liquid holdup in the measurement series with a $v_{SL}$ of 0.05 and 0.15 m s$^{-1}$. The T1RRT method is very sensitive to such a gradient if the r.f. coils are far apart as in the configuration used. The measurement series at $v_{SL} = 0.10$ m s$^{-1}$ does not meet the conditions, because a too high velocity is found at a too low liquid holdup.

There are a number of possible sources for the NMR signal loss: i.e. detuning and dematching of the r.f. probe by lossy samples, lead pickup and turbulent diffusivity in the presence of magnetic field gradients.
Despite the fact that the efficiency of the probe has been greatly improved by applying a strip-shield between the coil and the sample, the tuning and matching characteristics are still significantly affected when the amount of liquid in the sensitive volume of the coil changes. The resonance frequency of the NMR system is tuned for a completely water-filled pipe. The lower the liquid holdup, the stronger the detuning of the probe becomes. The pulse length increases due to the off-resonance condition of the $B_1$-field, causing the magnetization vector to be rotated through an angle of less than 90 degrees. This results in less transverse magnetization and less signal. Moreover, the signal-to-noise ratio decreases as a result of both the detuning and the dematching of the probe. Apparently the calibration curve for the liquid

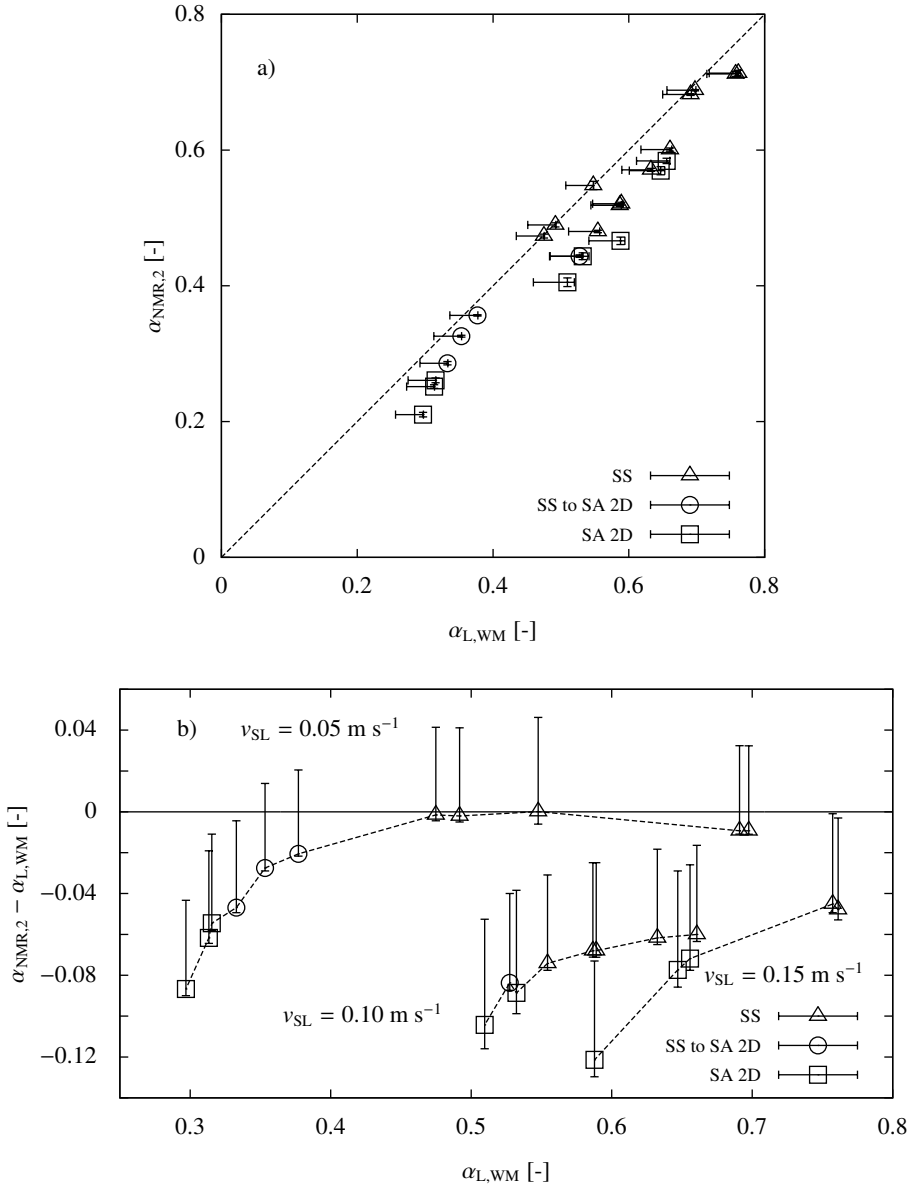


**Figure 7.10**: (a) A comparison of the liquid holdup detected with the 2nd r.f. probe with the reference value measured with the wiremesh sensor gives an indication of the linearity and (b) their difference that of the directional bias error. The data points belonging to the same series of measurements are connected with a dashed line.

holdup does not compensate enough under flowing conditions. It can be concluded that this may be regarded as the main cause of the too low signal intensities in leveled stratified flow measurements.
Lead pickup by the inhomogeneity in the pulsed $B_1$-field due to samples that extend the sensitive region of the r.f. coil considerably can be excluded as a cause. The calibration curve for the liquid holdup, see Figure 7.4, should correct for this. Because the calibration curve is obtained under static conditions, it does not correct for the holdup overestimation of 0.04 by water adhering to the wiremesh sensor.
As previously suggested in chapter 6, it is logical to assume that turbulence is also a source of signal loss in the stratified flow measurements. Turbulent diffusion leads in the presence of magnetic field gradients to increased dephasing [73, 145]. Although the T1RRT method does not use gradients, weak field gradients are present in the poorly shimmed zones in the vicinity of the pipe wall. Furthermore, there is an enhancement of the turbulence intensity near the interface due to waves. To investigate the proportion of turbulent diffusion with respect to molecular self-diffusion, the turbulent diffusivity is calculated as $\overline{v_y'^2}\tau$, where $v_y'$ is the streamwise fluctuating velocity component and $\tau$ the travel time of about 250 $\mu$s between r.f. pulse and FID detection. Ayati et al. [12] measured with PIV in a 10 cm pipe for the stratified smooth subcase ($v_{SL}$ = 0.08 m s$^{-1}$, $v_{SG}$ = 1.09 m s$^{-1}$) an average $v_y'$ of 3 cm s$^{-1}$ and for the subcase of stratified wavy flow with regular 2D waves of 6 cm s$^{-1}$. With this turbulent diffusivities of $2 \cdot 10^{-7}$ m$^2$ s$^{-1}$ and $9 \cdot 10^{-7}$ m$^2$ s$^{-1}$ respectively are found. This is $O(10^2)$ higher than the self-diffusion coefficient of water, which is at 20 °C about $2 \cdot 10^{-9}$ m$^2$ s$^{-1}$ [18, 105]. The signal intensity associated with the thermal equilibrium magnetization is determined under static conditions. Because molecular self-diffusion effects are small, the NMR signal will hardly be affected by the gradient fields present. As a result, the turbulent stratified flow measurements are scaled with a too high $s_0$. An extra large underestimation can be expected for stratified wavy measurements. Most likely, the shimming of the static magnetic field at the probe position has been worse in the measurement series at $v_{SL}$ = 0.10 m s$^{-1}$.

The relative and absolute expanded uncertainty in the liquid holdup measurements with 95% confidence level are shown in Figure 7.11(a) and (b). Repeatability is excellent with a relative expanded uncertainty of up to 1.2%. Basing the measurement on more than 30 repetitions of the T1RRT pulse sequence is certainly not necessary. Figure 7.11(b) demonstrates that there is no correlation between the magnitude of the absolute uncertainty and the presence or absence of waves.

Figure 7.12(a) gives the directional bias error between the obtained flowrates and the reference measurements by the electromagnetic flowmeter. Because of systematic errors in the execution of the measurements, the flowmeter in the current configuration is unsuitable for accurately measuring stratified flow. A very small gradient in the liquid leads to large measurement uncertainties. Extending the measuring system with one extra r.f. probe could solve this problem. As far as the random effects are concerned, the flowmeter is as accurate as the velocity determination. In Eq. 7.25 the relative measurement uncertainty in the liquid holdup is negligible compared to that in the velocity. A comparison of Figure 7.12(b) with Figure 7.8(a) confirms this.

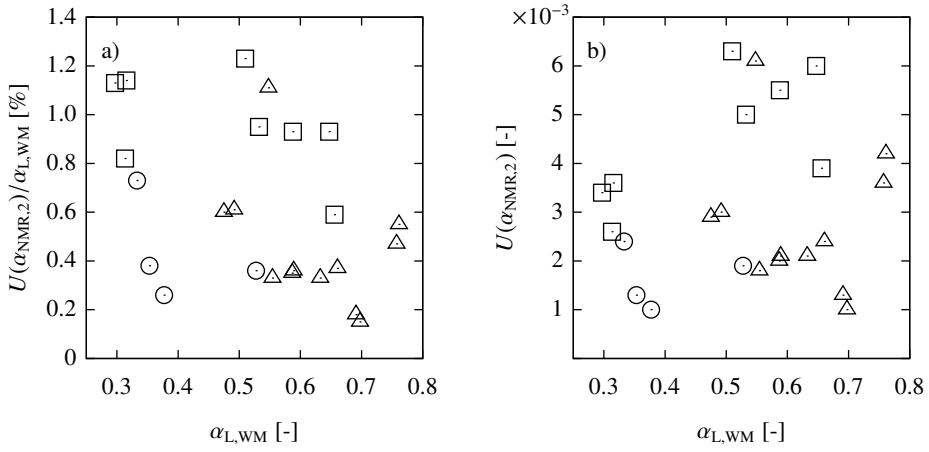


**Figure 7.11**: (a) Relative and (b) absolute uncertainty of the liquid holdup with 95% confidence level, where △ is the SS, ○ the transitional SS to SA 2D and □ the SA 2D flow regime.

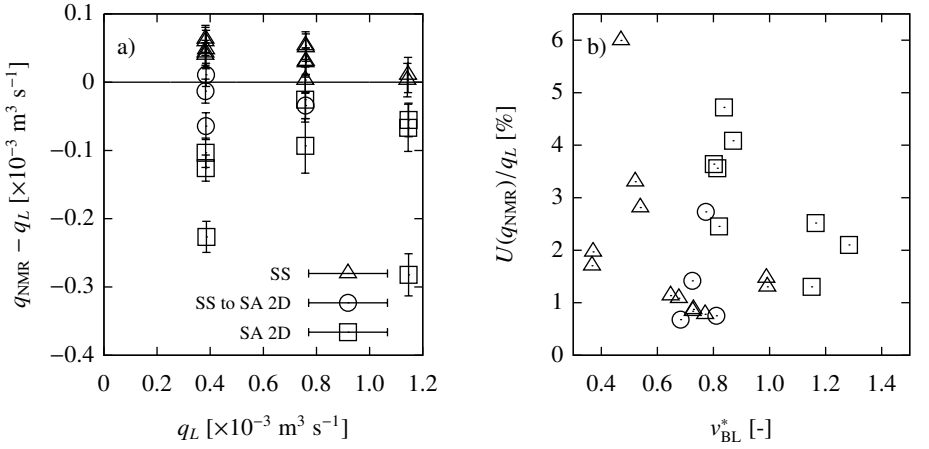


**Figure 7.12**: (a) Difference between the flowrate detected with the NMR flowmeter and the reference value measured with the electromagnetic flowmeter. (b) Relative uncertainty of the flowrate with 95% confidence level.

### 7.4.3 Sources of Systematic Errors in the Execution

As pointed out in the analysis of the results, there are two possible causes for the introduction of systematic errors in the measurements, both of which contribute to the directional bias error in the velocity and the liquid holdup.

#### 7.4.3.1 Gradient in the water level

One of the causes of systematic errors in the flow measurements is the presence of a weak gradient in the water level. Despite the fact that the air-water separator tank is equipped with a level tank, it is not possible to level the water within the NMR flowmeter manually with sufficient precision. The presence of waves makes this even harder. Because the distance between the wiremesh sensor, where the reference measurements are made, and the second r.f. coil is 3.51 m, an elevation angle of only 0.075° already causes a level difference of ±4.6 mm.
In a sensitivity study, the effect of the presence of the gradient on the accuracy of the velocity and holdup determination based on a uniform water level is modeled here. The applicable liquid holdup range 0.3 – 0.8 is divided into equal steps of 0.01. In the case of an elevation angle $\beta$, the liquid level in the r.f. coils is described by

$$h_{L,i} = h_{L,\mathrm{WM}} + \tan(\beta)\,(y_{c,i} - y_{\mathrm{WM}})\,, \qquad i = 1,2 \tag{7.30}$$

where $h_{L,\mathrm{WM}}$ is the water level in the wiremesh sensor. For small angles it can be assumed that the relationship between the local liquid holdup and the streamwise position is also linear:

$$\alpha_L(y) = \alpha_{\mathrm{L,WM}} + C_\beta\,(y - y_{\mathrm{WM}}) \qquad \text{with} \qquad C_\beta = \frac{\alpha_{L,2} - \alpha_{\mathrm{L,WM}}}{y_{c,2} - y_{\mathrm{WM}}}. \tag{7.31}$$

The liquid holdup follows from

$$\alpha_L = \frac{\gamma - \sin(\gamma)}{2\pi} \tag{7.32}$$

if the top angle $\gamma$, see Fig. 7.6, is defined as

$$\gamma = 4\arcsin\left(\sqrt{\frac{h_L}{D_p}}\right). \tag{7.33}$$

With plug flow assumed, the dimensionless residence time, $t/T_1$, in the polarizing magnetic field is given by

$$\begin{aligned} t^*(\beta) &= \int_{-\overline{\Delta l}}^{y_c} \frac{\mathrm{d}y}{v_y\left(y_{c,1} + \overline{\Delta l}\right)} = \int_{-\overline{\Delta l}}^{y_c} \frac{\alpha_L \mathrm{d}y}{v^*_{\mathrm{SL}}\left(y_{c,1} + \overline{\Delta l}\right)} \\ &= \frac{\alpha_{\mathrm{L,WM}}\left(y_c + \overline{\Delta l}\right)}{v^*_{\mathrm{SL}}\left(y_{c,1} + \overline{\Delta l}\right)} + \frac{C_\beta}{v^*_{\mathrm{SL}}\left(y_{c,1} + \overline{\Delta l}\right)}\left(\frac{1}{2}\left(y_c^2 - \overline{\Delta l}^2\right) - y_{\mathrm{WM}}\left(y_c + \overline{\Delta l}\right)\right), \end{aligned} \tag{7.34}$$

where in the calculation of the local bulk velocity Eq. 7.31 for the liquid holdup is used. The first term is the contribution to the residence time by leveled stratified flow, while the second term is the contribution by the liquid level gradient. The residence time is longer than for leveled flow if the water level ascends ($\beta > 0$) and shorter if the water level descends ($\beta < 0$). On substituting $y_c[j] = y_c + \overline{\Delta l} + L_c(2j - 1 - N_y)/2N_y$ for the position within the coil, the expected normalized signal strength of the FID can, similar to Eq. 7.4, be written as

$$s^*_{y,i}(\beta) = \frac{s_{y,i}}{s_{y,0}}(\beta) = \sum_{j=1}^{N_y} \alpha_{L,i}[j]\,(1 - \exp(-t^*_i[j]))\,, \qquad i = 1, 2. \tag{7.35}$$

In the flowmeter, the liquid bulk velocity $v^*_{\mathrm{NMR}}$ is determined by comparing $s^*_{y,2}/s^*_{y,1}(\beta)$ with the reference curve of Eq. 7.6.

The systematic error in the velocity introduced by the gradient in the water level is equal to

$$dv^* = v^*_{\mathrm{NMR}}(\beta) - \frac{v^*_{\mathrm{SL}}}{\alpha_{\mathrm{L,WM}}}. \tag{7.36}$$

For $\beta < 0$, the residence time decreases as a result of which the signal strength is lower than expected for leveled flow. At the same time, the signal strength decreases due to the lower number of nuclear spins present in the coil. Effectively, $s^*_{y,2}$ decreases more than $s^*_{y,1}$, causing $s^*_{y,2}/s^*_{y,1}(\beta)$ to be lower than the expected signal fraction for leveled flow at the prevailing liquid bulk velocity. As a result, the velocity is systematically underestimated by the flowmeter algorithm. Conversely, the velocity is systematically overestimated for $\beta > 0$. This is a counter-intuitive result, inasmuch as the liquid bulk velocity increases with a descending and decreases with an ascending liquid level.

The systematic error made by the flowmeter in the determination of the liquid holdup

$$d\alpha_{L,2}(\beta, dv^*) = \frac{s^*_{y,2}(\beta)}{s_{100\%L}(v^*_{\mathrm{BL}} + dv^*)} - \alpha_{\mathrm{L,WM}} \tag{7.37}$$

is a combination of the gradient that is present and the reinforcing effect due to the two-stage system of the signal processing. Applying Eq. 7.1, the NMR signal is scaled with the signal for a completely filled pipe at the biased velocity $v^*_{\mathrm{NMR}} = v^*_{\mathrm{BL}} + dv^*$. Because it is imposed in the signal processing, the acquired liquid holdup in both r.f. coils will be the same, so will $d\alpha_{L,1}(\beta, dv^*)$. The error in the velocity determination has hardly any effect on the holdup determination by the second r.f probe, because the signal is almost in thermal equilibrium under the current conditions. In the first r.f. coil, the velocity underestimation at $\beta < 0$ causes a too high reference signal $s_{100\%L}$, as a result of which a too low holdup is found. Owing to the velocity overestimation at $\beta > 0$, the reference signal $s_{100\%L}$ is too low so that the holdup in the first r.f. coil is overestimated.

The left column in Figure 7.13 shows the modeled systematic errors in the velocity for elevation angles of −0.075°, −0.050°, −0.025°, 0.025°, 0.050°, and 0.075° and the measurement

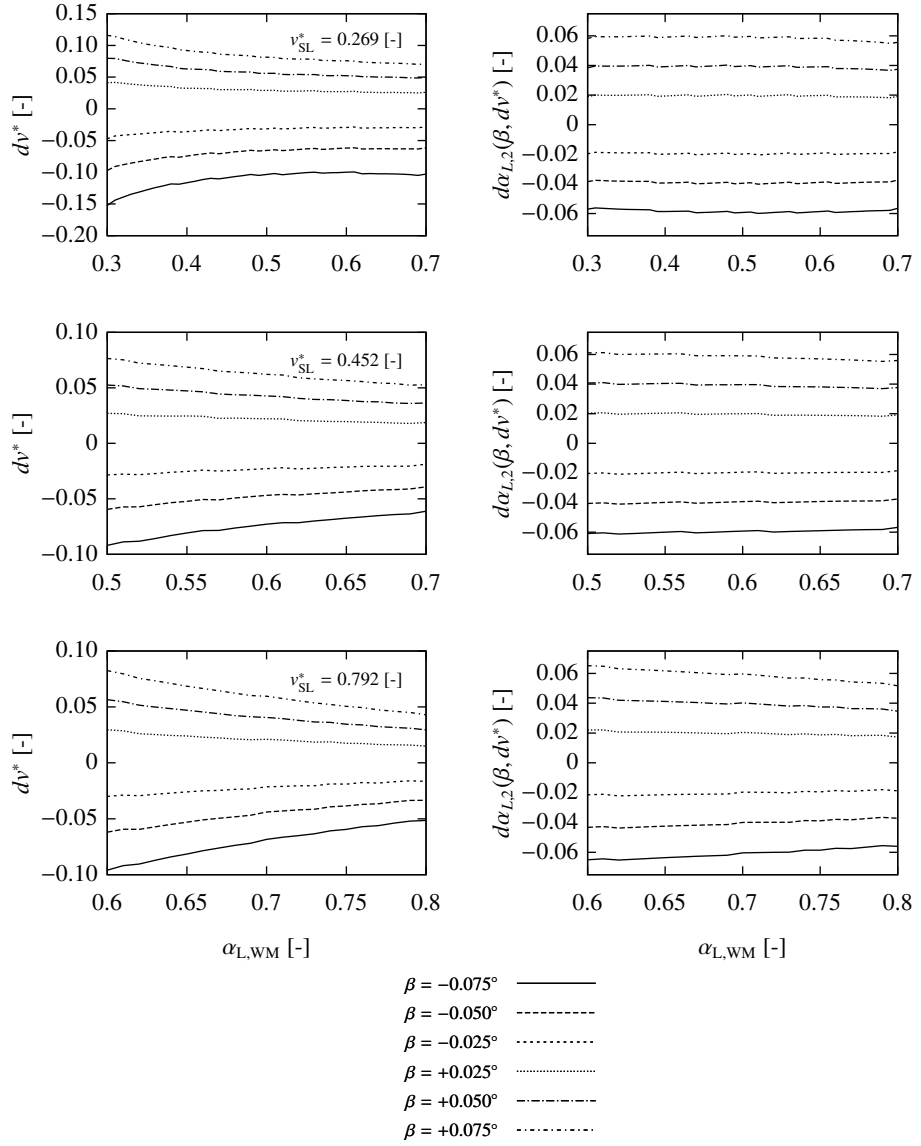


**Figure 7.13**: Sensitivity study to the systematic errors in the velocity and liquid holdup determination of stratified flow when there exists a gradient with elevation angle $\beta$ in the water level for the measurement series at (top) $v_{SL}$ = 0.05 m s$^{-1}$, (middle) $v_{SL}$ = 0.10 m s$^{-1}$, and (bottom) $v_{SL}$ = 0.15 m s$^{-1}$.

conditions described in this chapter. The right column depicts the expected corresponding systematic errors in the liquid holdup determination. This confirms the suspicion that there was a descending water level with an elevation angle of $-0.075°$ to $-0.025°$ in the stratified wavy measurements belonging to the measurement series with a superficial liquid velocity of 0.05 and 0.15 m s$^{-1}$. The lower the liquid holdup, the greater the systematic error introduced by the gradient in the velocity determination with the algorithm based on leveled stratified flow.

#### 7.4.3.2 Effect of the streamwise velocity profile

In reality, the streamwise velocity profile in the liquid phase does not meet the plug flow model that is assumed in the signal processing. Just like the moving wall does in a Couette flow, the liquid is pulled to a higher velocity at the free surface due to the drag exerted by the faster moving gas. However, in the presence of waves, the velocity profile undergoes a considerable transformation. The turbulence intensity near the interface is enhanced by the fluctuations the waves superimpose on the turbulent fluctuations. Momentum transfer, driven by the anisotropy of the turbulence, redistributes the streamwise velocity both in the vertical and the horizontal direction.

Strand [238] and Ayati et al. [12] investigated how different interfacial wave patterns influence the velocity distribution. To this end, Strand conducted LDA measurements of the mean streamwise velocity and the RMS value of its velocity fluctuations for a whole range of stratified sub-regimes in a 10 cm i.d. pipe. Ayati et al. [11, 12] used PIV to study the impact of the transition from stratified smooth to stratified wavy flow in a 10 cm i.d. pipe.

To examine what the deviation from plug flow means for the accuracy of our measurands, we use the data bank of Strand [238] to construct an artificial two-dimensional velocity field for stratified smooth flow and the stratified regime with regular 2D waves. The Fortran code with which the $N_v \times N_v$ velocity matrix $v_y[i, j]$ is calculated is given in appendix E.

Because the velocity profiles normalised with the average velocity have about the same shape, all simulated cases will be scaled accordingly with the constructed template.

The turbulent stratified smooth velocity profile, see Figure 7.14 (a), is based on fits of Strand's data for the case with $v_{SL} = 0.10$ m s$^{-1}$ and $v_{SG} = 1.2$ m s$^{-1}$. Power law equations are used to approximate the streamwise velocity both in the vertical and the horizontal direction. In fact, the velocity is slightly increased in a small zone close to the interface. Its contribution is insignificant thereby being disregarded. The derivation of the functions can be found in appendix E.

Strand reports that the transition from stratified smooth to stratified wavy flow at $v_{SL} = 0.10$ m s$^{-1}$ takes place when the superficial gas velocity is increased from 1.2 to 1.7 m s$^{-1}$. This is in agreement with the observations made by Ayati et al. [12]. The vertical velocity profile attains an S-shape, which is typical for the stratified flow regime with regular 2D waves. Due

to secondary flow in the cross-section, the maximum velocity along a horizontal chord at $r_z = -20$ mm moves from the center to halfway between center and wall. It has the shape of a camel back, as is demonstrated by the velocity field in Figure 7.14 (b). This is the result of the interpolation of Strand's data for the case with $v_{SL} = 0.10$ m s$^{-1}$ and $v_{SG} = 1.7$ m s$^{-1}$.

In accordance with Eq. 7.4, the signal corrected for the velocity profile is modeled by

$$s_{y,i}(\bar{v}_y^*) = \frac{\pi}{4} D_p^2 \frac{L_c}{N_y} \frac{1}{\sum_{i=1}^{N_v} \sum_{j=1}^{N_v} w[i,j]} s_0 \cdot \sum_{i=1}^{N_v} \sum_{j=1}^{NzhL} \sum_{k=1}^{N_y} w[i,j] \left( 1 - \exp\left( - \frac{y_{c,i} + \overline{\Delta l} + L_c(2k - 1 - N_y)/2N_y}{v_y^*[i,j](y_{c,1} + \overline{\Delta l})} \right) \right), \quad (7.38)$$

where $w[i, j]$ is the weight coefficient with a value between 0 and 1 related to the part of the grid cell that is inside the pipe and $NzhL$ is the j-index of the cell containing the water level. In this study Eq. 7.38 is evaluated ($N_y = 120$, $L_c = 12$ cm, $\overline{\Delta l} = 2.57$ cm, $N_v = 32$) for the nondimensionalised liquid bulk velocity range of 0.04 – 1.5 with a resolution of 0.0005. The signals are processed as described in section 7.3. This means that the NMR velocity is determined by comparing the fraction of the signal intensity in both r.f. coils with the reference curve of Eq. 7.6 used by the flowmeter. The liquid holdup is found by scaling the modeled signal strength for the second r.f. probe with $s_{100\%L}(v_{NMR})$.

Figure 7.15 (a) and (b) respectively show the velocity bias $dv^*$ and liquid holdup bias $d\alpha_{L,2}$ for turbulent stratified smooth regimes, which are approximately introduced by the flowmeter with the plug flow assumption. In the experiments described in this chapter, $v_{BL}^*$ is between 0.37 and 1, while the liquid holdup is between 0.5 and 0.8. In this range a very small velocity underestimation of around 0.5 cm s$^{-1}$ is expected. The reinforcement effect hardly affects the obtained liquid holdup. Only at higher velocities does it play a role.

For the modeled stratified wavy regime, $dv^*$ and $d\alpha_{L,2}$ are depicted in Figure 7.16 (a) and (b) respectively. Measurements were made with $v_{BL}^*$ between 0.82 and 1.16 and a liquid holdup between 0.3 and 0.7. In this range, a velocity underestimation of 0.5 – 1 cm s$^{-1}$ is expected. Because the signal in the second r.f. probe is virtually in thermal equilibrium, the bias in the holdup determination is again not worth mentioning.

A part of the directional bias error in the velocity determination can thus be explained by the use of the plug flow model in the signal analysis. There is no noticeable effect on the holdup determination.

## 7.5 Conclusions

With experiments it has been shown that the flowmeter in the current configuration, is not precise enough for the measurement of stratified flow at low bulk velocities. As far as the repeatability is concerned, the flowmeter is as accurate as the velocity determination.

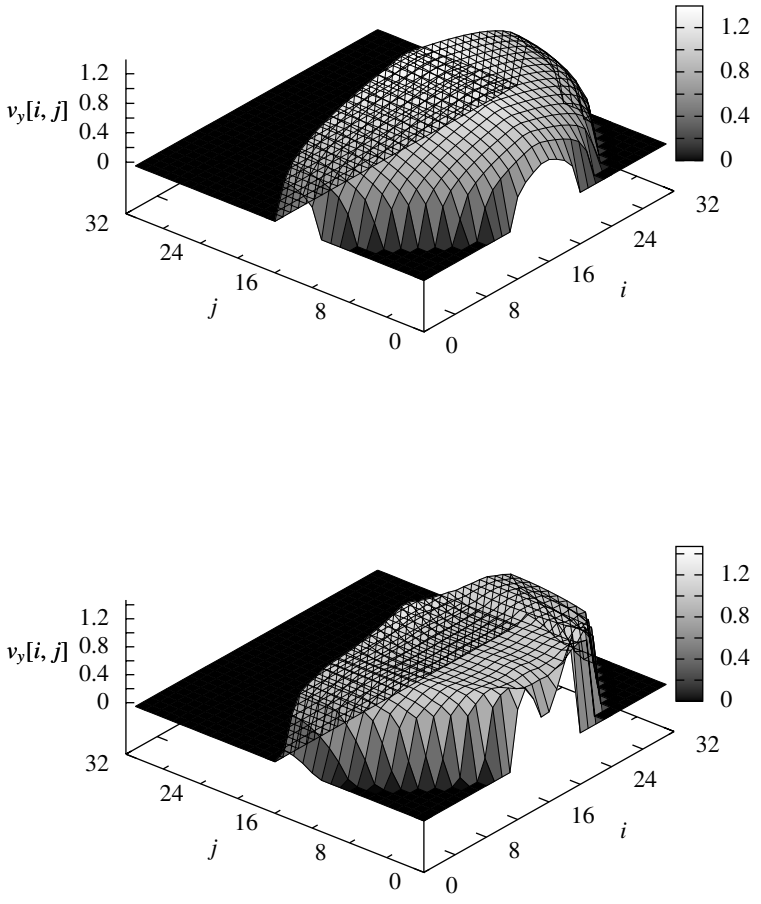


**Figure 7.14**: Typical artificial streamwise velocity profile of the liquid phase used to model (top) turbulent stratified smooth flow and (bottom) stratified flow with regular 2D waves at $\alpha_L = 0.5$.

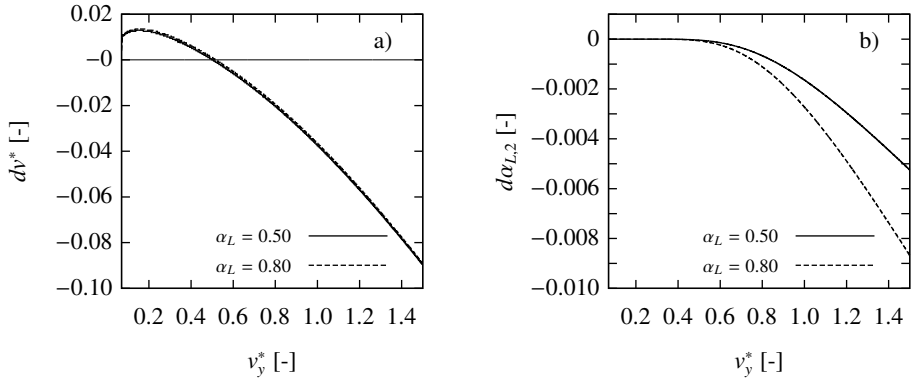


**Figure 7.15**: Expected directional bias error in (a) the NMR velocity and (b) the liquid holdup in the case of turbulent stratified smooth flow when the flowmeter processes the modeled signals ($N_v$ = 32) according to a plug flow model.

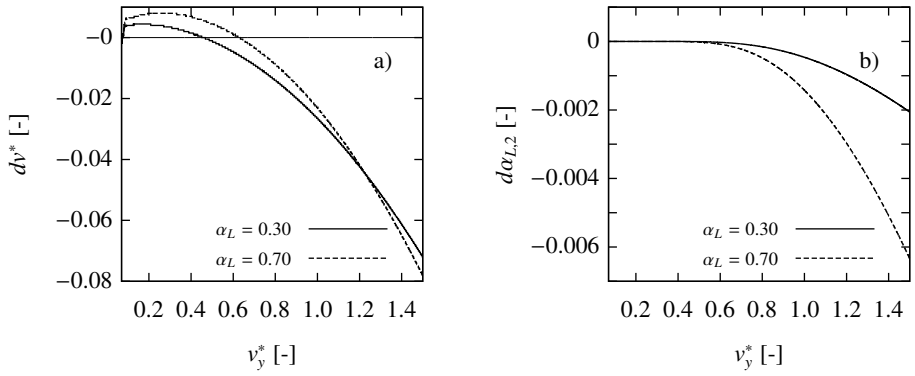


**Figure 7.16**: Expected directional bias error in (a) the NMR velocity and (b) the liquid holdup in the case of stratified wavy flow with regular 2D waves when the flowmeter processes the modeled signals ($N_v$ = 32) according to a plug flow model.

Because the distance between the two r.f. coils is too large for the flow range, the signal has almost reached thermal equilibrium in the second coil. Effectively, the velocity is therefore only determined on the basis of the signal in the first coil, which makes the measurement less accurate due to systematic errors. Unintentionally, the virtually equilibrium signal in the second probe is favorable for the holdup determination. The reinforcing effect, the weakness of the T1RRT method, can be excluded as a source of systematic errors. Measurement errors in the NMR velocity do not influence the holdup calculation. The determination of the liquid velocity and the liquid holdup can be seen as independent components in the flowrate determination.

The assumption of a constant liquid level is found to be the source of large measurement errors. With a sensitivity study it has been shown that a weak gradient of only 0.075° in the water level can cause a velocity bias up to 3 cm $s^{-1}$ and a holdup bias of 0.06. Also this effect is directly related to the large distance between the coils. Since small gradients are not unlikely in practical applications, it is recommended to equip the flowmeter with an additional third coil so that the algorithm can be adjusted for the existence of a gradient in the liquid level.

A large uncertainty in the reference measurement of the liquid holdup with the wiremesh sensor makes it difficult to validate the performance of the flowmeter.

The flowmeter achieves a reasonable linearity in the velocity measurements. The absolute uncertainty owing to repeatability is with 0.6 cm $s^{-1}$ slightly worse than in the single-phase flow measurements with the same flow range. Furthermore, it gives the impression that a measurement based on 30 repetitions of the T1RRT pulse sequence is sufficient for a reliable result. The expanded uncertainty is insufficient to explain the velocity bias. If we take the systematic error in the reference liquid bulk velocity into account, the directional bias error is closer to 1 cm $s^{-1}$, which is comparable with the value found for the single-phase flow measurements within the same velocity range. A gradient in the water level, the deviation from a plug flow velocity distribution and the spatial dependence of the added length by the non-uniform polarizing magnetic field may be the reason for this error. The velocity measurements for the stratified smooth cases are very good. The spatial dependence of the velocity profile does not seem to play too big a role. For the stratified wavy cases this cannot be said with certainty as it was found that the velocity bias $dv^*$ increases with the liquid bulk velocity. However, not much can be done about the significant change of the velocity distribution in the presence of waves, due to a lack of knowledge about the prevailing flow pattern.

Underestimation of the liquid holdup is a general problem of the T1RRT measurement method. For the two-phase measurements, especially the dielectric losses by the organic material of which most samples consist are a major problem. Despite the fact that the tuning and matching characteristics with changing filling factor of the probe are significantly improved by the application of a strip-shield between the coil and the sample, this still leads to losses in the signal intensity. In the current configuration we are spatially limited. Otherwise, increasing the distance between the sample and the coil could further improve the probe efficiency. With

a relative expanded uncertainty of up to 1.2%, the repeatability of the holdup is excellent. The directional bias error in the liquid holdup is large due to various systematic errors. In addition to the sensitivity to a weak gradient in the liquid level, turbulent diffusion also causes a small negative offset of the signal amplitude.

# Chapter 8

# T1RRT Measurements on Horizontal Slug Flow

Elongated bubble and slug flow are perhaps the most complex multiphase flow patterns to determine the flowrates of the individual phases. Intermittent flow patterns are not only time- but also space-dependent. For proper flow measurements, the T1RRT method as applied to the stratified flow measurements in chapter 7, must therefore be adapted to the slug flow pattern.

Most experimental studies of slug flow focus on determining the phase and velocity distribution in detail with the aim of improving understanding of the physical transport phenomena involved. Simple techniques apply interface tracking on the signals obtained with conductance [47, 247] and optical probes [21, 250] or on high-speed camera images [84, 176] to determine the in-situ velocity in the slug. Direct measurement of the film and slug velocities is, however, impossible as the liquid forms a continuum. The quality of these measurement methods relies therefore heavily, as Kouba et al. [139] explain, on the flow-pattern dependent model used.
Techniques used to measure the axial velocity profile in the liquid phase include: LDV [146], photochromic dye activation [125], hot-film anemometry [156, 227], PIV [83, 130] and PIV LIF [231]. For multiphase flowmetering, these methods are generally too time consuming whereas only the global parameters are of interest. NMR is, in this sense, considered as a measurement technique with potential [243].

At the moment, only a few studies are known that conduct NMR/MRI research on slug flow in macroscale systems. Barberon and Leblond [14] measure the probability distribution of the axial liquid velocity and liquid fraction of isolated rising Taylor bubbles by means of PFGSE. The measuring time of 10 hours is nevertheless very long and moreover requires a periodic flow pattern.
Reyes, Jr. et al. [216] use a FLASH variant to measure the liquid volumetric flux distribution and the void fraction in cross-sectional slices of slug flow in a horizontal air-water system.

However, in order to obtain the local liquid volumetric flux, they need to relate the results to the externally measured total volumetric liquid flowrate. Though, in this scaling they have made a minor mistake by presuming the local flowrate to be space and time independent. The flowmeter technique of O'Neill et al. [187], which also uses low field NMR, is closely related to the T1RRT method from this dissertation. With a single r.f. probe, they manage to derive the relevant liquid velocity probability distribution from a fit of the entire FID. Just like in the present work, the measuring frequency is in the range of 0.5 - 2 Hz. In the liquid volumetric flowrates based on time averaged FIDs, a mean absolute error of 6% is found. That the velocity distribution can also be determined for each FID obtained by single acquisition is a positive aspect of this method, which is highly desirable for measuring intermittent flow regimes. Although performance is now slightly worse due to the reduced signal-to-noise ratio and the flowrates tend to be underestimated in the case of slug flow, a mean absolute error of only 10% is found in the average liquid volumetric ratio of all scans.

In this study, the unit-cell concept introduced by Wallis [255] will be used in developing an adjusted flowmeter principle for the T1RRT measurements and in deriving expressions for the reference measurements of the film and slug velocity with a dual tip-sensor. Following the first mechanistic model developed by Dukler and Hubbard [58] to predict the slug flow characteristics such as local holdup, velocity and pressure drop, the unit-cell concept still lies at the heart of the improved models developed over the years. Fabre and Liné [63], Fabre [62] and Dukler and Fabre [57] present comprehensive reviews of the proposed models, which generally differ on small points in the closure laws. Because the local liquid holdups in the film and slug and the translational bubble velocity, obtained via external measurements, serve as input, it is unnecessary to derive a complete model here.

## 8.1 The Unit-Cell Model

The slug flow is assumed to be quasi-static and fully-developed. This means that the slugs have a stable length while traveling along the pipe and that the probability distributions of both the slug and the bubble length are narrow. It is not important that the slug flow is regular; i.e. every bubble, respectively every slug, must have the same length. As long as the slug flow is averaged over a reasonable amount of time, statistically, the same model is obtained [62]. The flow characteristics can be described on the basis of an individual bubble. This typical unit-cell, shown in figure 8.1, consists of an elongated bubble of length $L_B$ and a liquid slug of length $L_S$ in which small bubbles are dispersed. The gas and liquid phase in the bubble section are completely separated. The average liquid holdups in the film and slug regions are respectively $\alpha_{\mathrm{LF}}$ and $\alpha_{\mathrm{LS}}$. Since the T1RRT flowmeter principle will not take into account the actual bullet-shape of the elongated bubble (indicated by the dashed line), the same assumption of a uniform stratified film is made in deriving a model for the tip-sensor measurements.
The elongated bubble propagates along the pipe at a translational velocity $v_B$. By examining the fluid dynamics in a frame of reference moving at the bubble velocity, the gas-liquid interfaces will look as if stagnant and the unsteady problem is simplified to a steady one.

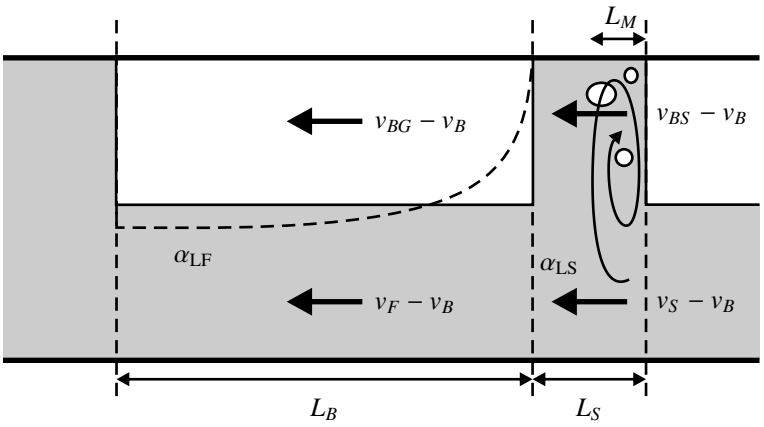


**Figure 8.1**: Ideal slug unit-cell in the frame of reference moving at the translational bubble velocity $v_B$.

As the bubble travels at a higher velocity than the average slug velocity, $v_S$, liquid is shed at the rear of the slug and, to meet the stable slug length criterion, picked up at the same rate from the preceding film. In the film region, the liquid flows the slowest of the entire elementary slug cell at an average velocity $v_F$. The liquid entering the film rapidly decelerates under the influence of wall and interfacial shear to a stable velocity. When the liquid from the film enters the front of the next slug, it needs a mixing length, $L_M$, to accelerate to the velocity of the liquid in the slug. Dukler and Hubbard [58] estimate the mixing length based on the 'velocity head' $v_H$ at [230]

$$L_M = 0.3 v_H = 0.3 \frac{(v_S - v_F)^2}{2g}. \tag{8.1}$$

Because dispersed bubbles get trapped in the mixing vortex, an increased void fraction is observed at the leading edge of the slug. The amount of entrained air in the liquid slug increases with the superficial gas velocity [93]. Owing to the liquid shedding process, the velocity in the elongated bubbles, $v_{BG}$, is usually slightly less than $v_B$. Given that the streamwise velocity of the dispersed bubbles, $v_{BS}$, does not differ much from $v_S$, no slip is assumed between the liquid phase and the entrained bubbles in the slug.

In order to obtain expressions for the average velocity of the liquid phase in the film and the slug in terms of the parameters to be measured, a mass balance is applied to the control volume of the elongated bubble section in the frame moving at the translational bubble velocity $v_B$. Supposing that the flow is also incompressible, conservation of mass in the liquid phase is given by

$$\alpha_{\mathrm{LS}}(v_S - v_B) = \alpha_{\mathrm{LF}}(v_F - v_B), \tag{8.2}$$

where the left-hand and the right-hand side of the equation represent the volumetric liquid flux shed from and picked up by the liquid slug. This equation can be rearranged to give a relation for the average film velocity

$$v_F = v_S \frac{\alpha_{\mathrm{LS}}}{\alpha_{\mathrm{LF}}} - v_B \left( \frac{\alpha_{\mathrm{LS}}}{\alpha_{\mathrm{LF}}} - 1 \right). \tag{8.3}$$

Based on the entire unit-cell, the superficial liquid and gas velocities are by definition:

$$v_{\mathrm{SL}} = \alpha_{\mathrm{LF}} v_F \frac{L_B}{L_B + L_S} + \alpha_{\mathrm{LS}} v_S \frac{L_S}{L_B + L_S} \tag{8.4}$$

and

$$v_{\mathrm{SG}} = (1 - \alpha_{\mathrm{LF}}) v_B \frac{L_B}{L_B + L_S} + (1 - \alpha_{\mathrm{LS}}) v_{BS} \frac{L_S}{L_B + L_S}. \tag{8.5}$$

Substitution of Eq. 8.3 into Eq. 8.4 yields the demanded equation for the average slug velocity,

$$v_S = \frac{v_{\mathrm{SL}}}{\alpha_{\mathrm{LS}}} + \left( 1 - \frac{\alpha_{\mathrm{LF}}}{\alpha_{\mathrm{LS}}} \right) v_B \frac{L_B}{L_B + L_S}. \tag{8.6}$$

As a result, the derived equation for the average film velocity can be rewritten as

$$v_F = \frac{v_{\mathrm{SL}}}{\alpha_{\mathrm{LF}}} - \left( \frac{\alpha_{\mathrm{LS}}}{\alpha_{\mathrm{LF}}} - 1 \right) v_B \frac{L_S}{L_B + L_S}. \tag{8.7}$$

## 8.2 T1RRT Measurement Principle for Slug Flow

As has been discussed at length in section 3.1, the measurement principle of the T1RRT method is based on the extent to which longitudinal magnetization is built up in the liquid phase as a function of its residence time in the permanent magnetic field of the flowmeter. The liquid flowrate of a two-phase gas-liquid flow is determined through the paired detection of an FID at two streamwise positions, provided that the flow meets the same on-site conditions. This is a problem in the case of slug flow, where a slug can be present in the first r.f. coil and an elongated bubble in the second r.f. coil, or vice versa. The method developed for stratified flow, presented in section 7.1, is therefore not one-to-one applicable. By using cluster analysis to identify the different levels in the time series of the initial FID intensity corresponding to the different sections in the unit-cell model, the T1RRT method has been made suitable for slug flow measurements. However, only the time-averaged liquid flowrate can be determined.

The second property that the measurement method uses when applied to gas-liquid flow is that the intensity of an NMR signal is proportional to the amount of nuclear spins enclosed

by the coil. The number of nuclear spins present in a low-pressure gas is generally considered insufficient to contribute effectively to the NMR signal. As given by Eq. 6.4, which is generalized for gas-liquid flow, the initial intensity of the FID following a 90° pulse in r.f. coil $i$ with its center at streamwise position $y_{c,i}$ can hence be written as

$$s_{y,i}(v_y, \alpha_L) = \alpha_L \frac{\pi}{4} D_p^2 \frac{L_c}{N_y} s_0 \sum_{j=1}^{N_y} 1 - \exp\left( - \frac{y_{c,i} + \overline{\Delta l} + L_c(2j - 1 - N_y)/2N_y}{v_y T_1} \right), \tag{8.8}$$

where $\alpha_L$ is the liquid holdup and the remainder of the right-hand term, previously defined as $s_{100\%L}(v_y)$, the expected signal strength for single-phase flow at the same bulk velocity $v_y$. Furthermore, $L_c$ is the length of the coil, $N_y$ the number of cells in which the streamwise probe domain is divided, $s_0$ the intensity of the NMR signal corresponding to the equilibrium magnetization $M_0$ and $\overline{\Delta l}$ the asymptotic value of the added length by the non-uniform polarizing magnetic field as defined in section 6.2.4.

The differences in the local liquid holdup ($\alpha_{\mathrm{LF}} < \alpha_{\mathrm{LS}}$) and the local velocity ($v_F < v_S$) result in a low signal level for the liquid film sections and a somewhat higher level for the liquid slug sections. In addition, there is a third, even higher level that corresponds to the mixing zone at the front of the slug. The liquid picked up by the slug has a longer residence time in the $\mathbf{B}_0$-field than the rest of the slug, because it initially travels through the flowmeter at the film velocity $v_F$.
By determining the average for each of the three distinct levels, the average velocity and average liquid holdup for the film and slug sections can be obtained, analogous to the method on which the stratified flow signals are analyzed in chapter 7. The liquid flowrate is calculated from these components as a weighted sum according to the unit-cell model.

With the k-means method [256], the series of measured values $s_{y,i}[k]$ of the $N_s$ consecutively acquired T1RRT sequences, is partitioned per probe $i$ into 3 cluster groups: $j = 1$, film; $j = 2$, slug; and $j = 3$, mixing zone. This is an iterative clustering method that minimizes the variance about the $j$ centroids. The procedure consists of 3 steps:

1. Positioning the prototypes of the cluster means at

$$\begin{aligned} m_{i1} &= \min(s_{y,i}) \\ m_{i2} &= (\min(s_{y,i}) + \max(s_{y,i}))/2 \\ m_{i3} &= \max(s_{y,i}) \end{aligned}$$

2. Assigning the objects to the group whose prototype is closest based on the Euclidian distance $|s_{y,i}[k] - m_{ij}|$.

3. Calculation of the new mean of cluster $j$ according to

$$m_{ij} = \frac{1}{N_{c,ij}} \sum_{k=1}^{N_s} b_{jk} s_{y,i}[k], \tag{8.9}$$

where

$$b_{jk} = \begin{cases} 1, & \text{if } s_{y,i}[k] \in \text{group } j \\ 0, & \text{otherwise} \end{cases} \tag{8.10}$$

is the cluster group indicator and

$$N_{c,ij} = \sum_{k=1}^{N_s} b_{jk} \tag{8.11}$$

the number of objects in each cluster. The within-group standard deviation for group $j$ is

$$\sigma(m_{ij}) = \sqrt{\frac{1}{N_{c,ij} - 1} \sum_{k=1}^{N_s} b_{jk} \left( s_{y,i}[k] - m_{ij} \right)^2}. \tag{8.12}$$

The process is terminated if the difference between the new and the previous mean of each group is less than $0.001(\max(s_{y,i}) - \min(s_{y,i}))$. Otherwise, the assignment and update steps 2 and 3 are repeated, using the new mean of the clusters as new prototype positions. An example of a slug flow measurement processed with clustering is shown in Fig. 8.2.

Now that the mean signal levels for the film and slug sections are known, they can be processed using the same two stages as are required to determine the liquid flowrate of a time-independent two-phase gas-liquid flow, as discussed in section 7.1. Assuming that the average holdup of respectively the film and slug section is in both r.f. coils the same, the velocities $v_{\text{NMR,F}}$ and $v_{\text{NMR,S}}$ are first determined by comparing the fraction of the signal levels found with clustering in the second and first r.f. coil, i.e. $m_{21}/m_{11}$ and $m_{22}/m_{12}$, with the numerically computed reference curve

$$\frac{s_{y,2}}{s_{y,1}}(v_y) = \frac{\sum_{j=1}^{N_y} 1 - \exp\left( -\frac{y_{c,2} + \overline{\Delta l} + L_c(2j - 1 - N_y)/2N_y}{v_y T_1} \right)}{\sum_{j=1}^{N_y} 1 - \exp\left( -\frac{y_{c,1} + \overline{\Delta l} + L_c(2j - 1 - N_y)/2N_y}{v_y T_1} \right)}. \tag{8.13}$$

The signal fraction is an injective function of the bulk velocity, as long as the magnetization in the first probe has not reached the equilibrium state. So it is assumed that the elementary slug sections have a fixed uniform velocity over the distance traveled within the flowmeter. The shape of the velocity profile or gradients in the residence time due to the liquid shedding and pickup phenomenon is not taken into account.

In the second stage the liquid holdups, $\alpha_{\text{NMR,F}}$ and $\alpha_{\text{NMR,S}}$, are resolved from Eq. 8.8 by scaling the obtained mean value of the film and slug clusters with the expected signal strength for a single-phase flow at the relevant bulk velocity. The signal belonging to the second r.f. probe is used because of the better signal resolution.

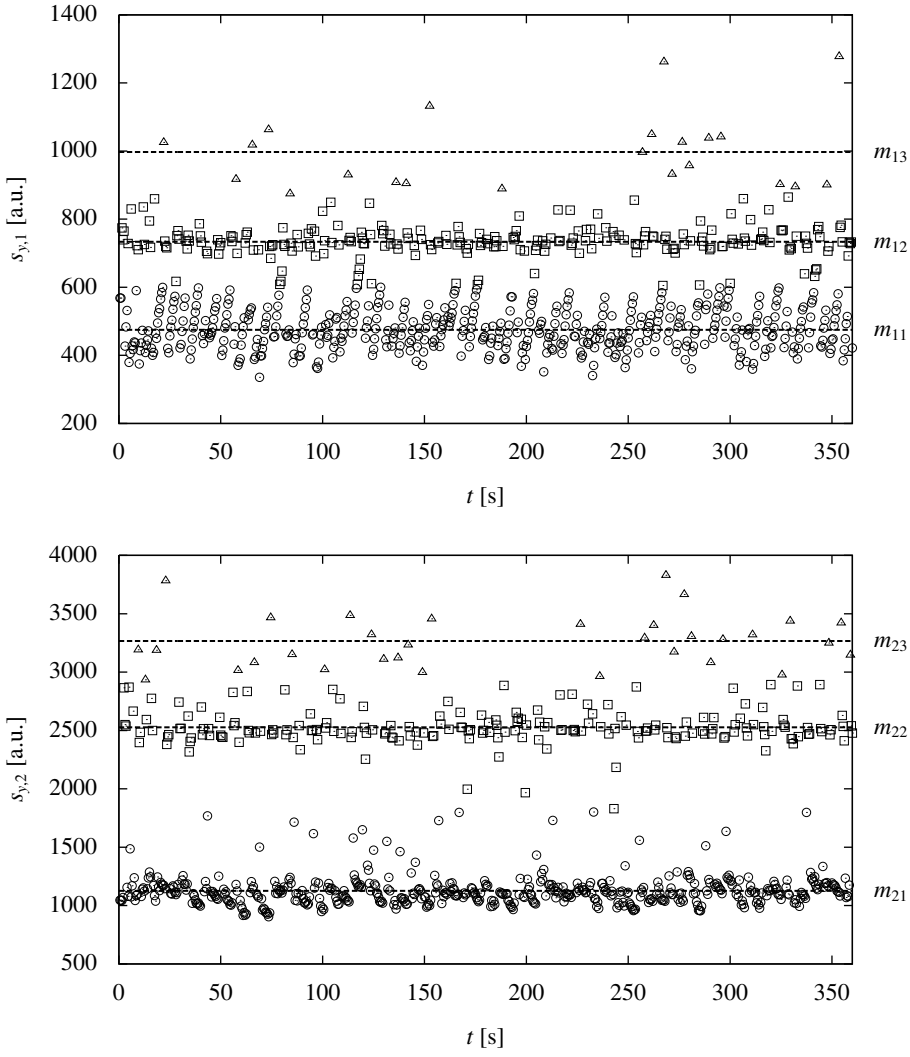


**Figure 8.2**: Clusters for typical time series of the initial FID intensity acquired at a repetition delay RD = 0.5 [s], $v_{SL}$ = 0.7 [m s$^{-1}$], and $v_{SG}$ = 1.04 [m s$^{-1}$] in the (top) 1$^{st}$ r.f. coil, where $s_{y,1}(0,1) = 5803$ and in the (bottom) 2$^{nd}$ r.f. coil, where $s_{y,2}(0,1) = 5451$.

Finally, the unit-cell model is adopted again to determine the liquid flowrate. The number of objects in each cluster can be used to calculate the average bubble fraction

$$\frac{L_B}{L_B + L_S} = \frac{N_{c,i1}}{N_s} \tag{8.14}$$

and the average slug fraction

$$\frac{L_S}{L_B + L_S} = \frac{N_{c,i2} + N_{c,i3}}{N_s}. \tag{8.15}$$

The total liquid flowrate follows from the weighted sum of the liquid flowrate in the film and the slug sections:

$$q_{\mathrm{NMR}} = \frac{\pi}{4} D_p^2 \left( \alpha_{\mathrm{NMR,F2}} v_{\mathrm{NMR,F}} \frac{N_{c,21}}{N_s} + \alpha_{\mathrm{NMR,S2}} v_{\mathrm{NMR,S}} \frac{N_{c,22} + N_{c,23}}{N_s} \right). \tag{8.16}$$

Similarly, the expression for the superficial liquid velocity is given by

$$v_{\mathrm{NMR}} = \alpha_{\mathrm{NMR,F2}} v_{\mathrm{NMR,F}} \frac{N_{c,21}}{N_s} + \alpha_{\mathrm{NMR,S2}} v_{\mathrm{NMR,S}} \frac{N_{c,22} + N_{c,23}}{N_s} \tag{8.17}$$

and that for the average liquid holdup by

$$\alpha_{\mathrm{NMR,2}} = \alpha_{\mathrm{NMR,F2}} \frac{N_{c,21}}{N_s} + \alpha_{\mathrm{NMR,S2}} \frac{N_{c,22} + N_{c,23}}{N_s}. \tag{8.18}$$

The T1RRT method has the disadvantage that the 90° pulse resets the buildup of longitudinal magnetization. To avoid interactions, a very low repetition rate of the pulse sequence should be selected, which ensures that only fresh liquid is measured. Technically this is not feasible in the case of slug flow. The upper limit, determined by $v_F$, is a measuring frequency where the liquid is never pulsed more than once in the same coil. It is unlikely that a reset in the first probe will strongly affect the mean value of the signal in the second probe. Because the flowrate determination is actually an ensemble average over multiple slug units, the chances are small that the pulse sequence period always fits exactly in the time-of-flight between the two probes.

Another critical remark must be made about the position of the probes. As a longer residence time in the polarizing magnetic field results in a stronger NMR signal, this is an opposing factor in the distinctive character of the low film level compared to the higher slug level. If the probe is not mounted far enough inside the flowmeter, the clusters can easily coincide. An important design criterion is therefore to ensure that the holdup is the dominant term that determines the difference between the film and slug signals, and not the residence time.

## 8.3 Flow Configuration and Instrumentation

Experiments on air-water slug flow are carried out at room temperature and ambient pressure in a horizontal pipe of 98.6 mm internal diameter and about 36 m in length. To accelerate the development of a stable slug flow, compressed air and tap water are introduced in the pipe through a parallel-plate inlet section, 270 $D_p$ upstream of the first (dual tip-)sensor. Model predictions of the distribution and evolution of slug lengths along horizontal pipelines by Cook and Behnia [47] show that the actual development length for intermittent flow is about 500 – 600 diameters. Despite the fact that this condition is not met, the slugs in the measurements presented here have reached the minimum stable slug length, which Cook and Behnia have found to be close to 10 diameters in length.
The superficial liquid velocity, $v_{SL}$, is measured with a KROHNE Optiflux 2300C electromagnetic flowmeter with a standard uncertainty of ±0.2% + 1 mm $s^{-1}$ of the measured value. The output signal of the KROHNE IFC300 flow converter, used in combination with the flowmeter, is recorded at a sampling rate of 2 Hz. The gas flowrate is measured with a Kytölä HV4FC variable area flowmeter for the range 0.2 – 0.7 $m^3$ air $min^{-1}$ with a standard uncertainty of ±5% of the full scale value. This corresponds with a standard uncertainty of the superficial gas velocity, $v_{SG}$, of ±0.08 m $s^{-1}$. The two r.f. probes are located at 0.5 and 2.5 m inside the NMR flowmeter. The pipe discharges 1.5 m downstream of the second r.f. probe in an air-water separator tank.
In order to validate the NMR measurements, the flow facility is equipped with a 32x32 wiremesh sensor that measures the cross-sectional liquid holdup 1.01 m upstream of the NMR flowmeter. The systematic overestimation of the liquid holdup by the wiremesh sensor is extensively discussed in section 7.2.1. Quantifying the in-situ liquid velocity in the film and slug regions is more difficult, as this can only be done indirectly from the bubble velocity. The bubble velocity is determined with a conductance-based dual tip-sensor, the tips of which are located at 5.007 and 4.52 m upstream of the NMR flowmeter. The quality of the velocity validation is therefore as good as the selected unit-cell model that is used in conjunction with the measurements. In addition, the tip-sensor is used for determining the chord-lengths of the bubble and liquid slug zones. Both the wiremesh and the tip-sensor data are recorded at a sampling rate, $f_m$, of 500 Hz. Fig. 8.3 illustrates the sequence of steps that make up the processing of the tip-sensor and wiremesh signals, which will be discussed below. Full details of the large two-phase flow loop can be found in section 4.4.

### 8.3.1 Signal Processing of the Tip-Sensor Data

The tip-sensor detects the instantaneous phase that is present at the sensitive tip located at the top of the pipe. If the pipe is completely filled with water, the electrical circuit is closed and a maximum voltage is detected. If the tip is surrounded by air, the electrical circuit is open and the voltage drops to a lower level. To facilitate the detection of the air-water interfaces, the analogue signal is first binarized by applying a threshold of 0.8 V. Bubbles are indicated by 0, while the liquid phase is indicated by 1.

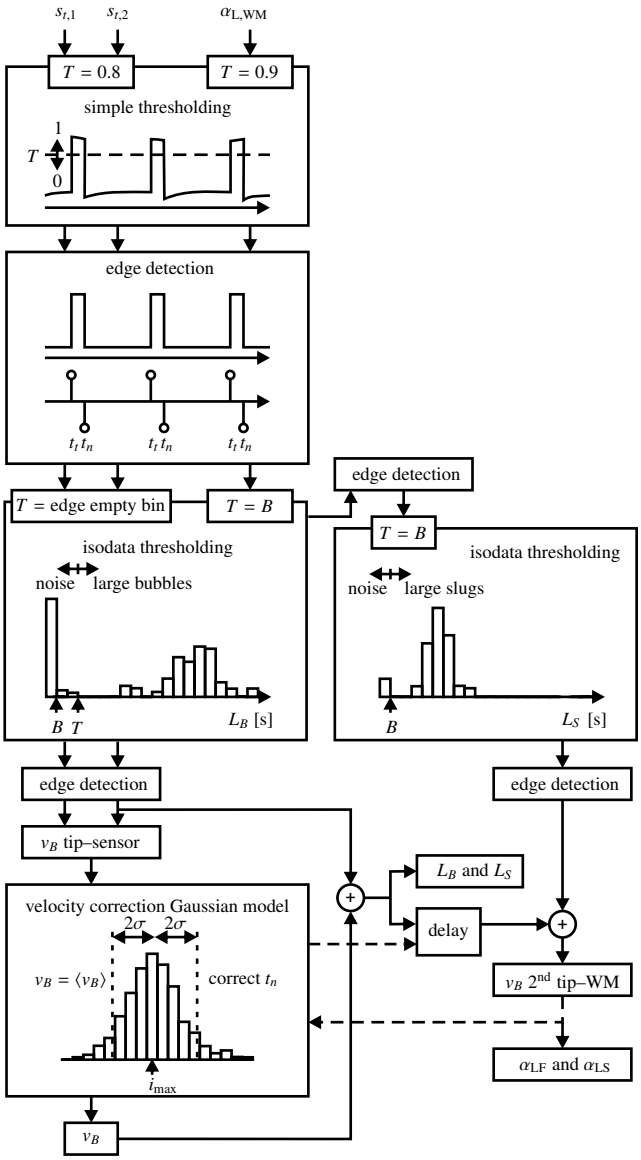


**Figure 8.3:** Schematic of the used tip-sensor and wiremesh signal processing.

Next the position of the air-water interfaces is found by means of a simple gradient-based edge detection method [34, 263]. Taking the first derivative of the signal, $s_t$, by computing the difference in signal strength between two consecutive time steps

$$Rs[i] = s_t[i] - s_t[i-1], \qquad i \in \{2, ..., N_t\} \tag{8.19}$$

allows the identification of the bubble's nose and tail from the negative minima and positive maxima as

$$Rs[i] = \begin{cases} -1, & \text{phase change water into air:} \quad t_n = i/f_t \\ 0, & \text{no change} \\ 1, & \text{phase change air into water:} \quad t_t = i/f_t. \end{cases} \tag{8.20}$$

The problem is that the detection of the elementary slug units is affected by noise due to the small dispersed bubbles in the liquid slugs, see Fig. 8.4(b). Bertola and Cafaro [22] report that the characteristic dimension of these bubbles is about 100 times smaller than that of the large gas pockets. By analyzing the bubble time length histogram, the data can be split into small and large bubbles with isodata thresholding [35]. The histogram is constructed for a number of bins equal to the square-root of the sum of phase changes in the tip-sensor signal,

$$N_i = \sum_{i=2}^{N_t} |Rs[i]|, \tag{8.21}$$

taking the smallest value of the two, with a uniform width in the range of 0 up to the largest observed bubble time length, $\max(t_t - t_n)$. Since there is a clear separation between the distributions and the small bubbles are all in the first contiguous bins, the threshold is selected as the lower limit of the first empty bin of the histogram. Undesirable dispersed bubbles with a size smaller than the larger of the two thresholds, one for each tip-sensor, are filtered out of the signal, as shown in Fig.8.4(c). After that the arrival time of the nose, $t_n$, and tail, $t_t$, of the bubbles is determined again using the edge detection procedure described above.

Only the nose of the bubble is well defined. Identification of the tail of the bubble is difficult because of the high level of aeration in the mixing zone at the front of the slug. For that reason, front tracking is used to calculate the translational velocity of a gas bubble as

$$v_B[i] = \frac{\Delta y_{tip}}{t_{n2}[i] - t_{n1}[i]}, \tag{8.22}$$

where the distance between the two tip-sensors, $\Delta y_{tip}$, is 48.7 cm.
There is a difference up to 2% in the number of bubbles detected in the first and second tip signal. These are the few smaller bubbles that are not suppressed in either signal with the automated isodata filtering. Because the nose of a bubble at the second tip is paired with the last preceding nose of a bubble at the first tip, the obtained bubble velocity will be biased in those cases. In oder to correct for this, the bubble velocity is assumed to have a normal distribution, which is one of the main findings in the statistical slug flow characterization by

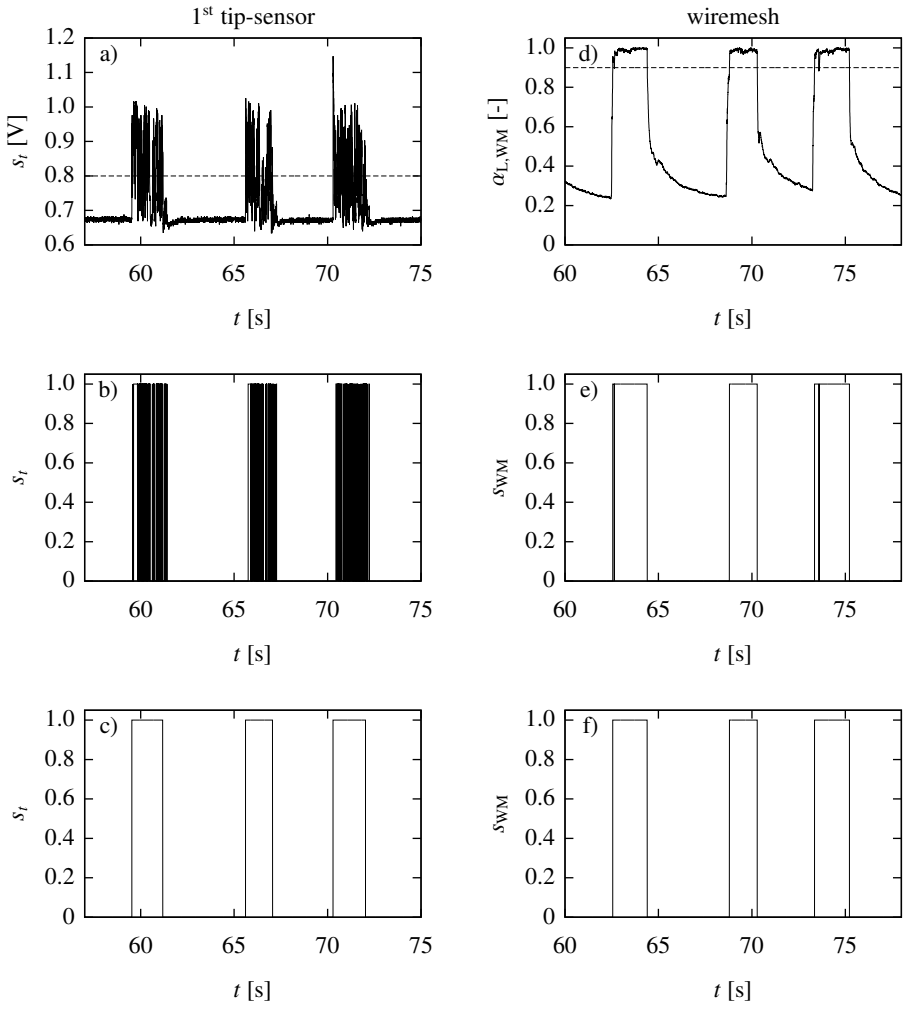


**Figure 8.4**: Signal processing procedure for the air-water interface detection in respectively the first tip-sensor and the wiremesh signal, where $f_t$ = 500 Hz, $v_{SL}$ = 0.70 m s$^{-1}$, and $v_{SG}$ = 1.04 m s$^{-1}$: (a, d) time trace of the raw signal, (b, e) converted into a binary signal with simple thresholding, and (c, f) after filtering out the dispersed bubbles in the liquid slug by means of isodata thresholding.

Nydal et al. [183]. All velocity values that deviate more than $2\sigma$ from the mean are considered erroneous. The standard deviation is estimated from the velocity distribution by iteratively fitting a Gaussian till the standard deviation changes less than 1% of the mode bubble velocity. The parametric density estimation method [256] involves the following steps:

1. Construction of the bubble velocity histogram with 50 equally sized bins in the range from 0 to 3 times the mixing velocity, $v_{\text{mix}}$, given by $v_{\text{SL}} + v_{\text{SG}}$.

2. Using the mode bubble velocity, $3(i_{\max} - \frac{1}{2})v_{\text{mix}}/50$, as an initial guess for both the mean velocity and its standard deviation, where $i_{\max}$ is the corresponding bin number of the histogram.

3. Calculation of the mean bubble velocity and standard deviation for the $N_b$ bubbles in the second tip signal, the velocity of which is in the range of the $i$ bins on both sides of $i_{\max}$: i.e. the bins from $i_{\max} - i$ to $i_{\max} + i$. In the first iteration only one adjacent bin on each side of $i_{\max}$ is considered. The mean bubble velocity is obtained from

$$\langle v_B \rangle = \frac{1}{N_{bG}} \sum_{j=1}^{N_b} b_j v_B[j], \tag{8.23}$$

where

$$b_j = \begin{cases} 1, & \text{if} \quad 3(i_{\max} - i - 1)v_{\text{mix}}/50 \le v_B[j] \le 3(i_{\max} + i)v_{\text{mix}}/50 \\ 0, & \text{otherwise} \end{cases} \tag{8.24}$$

indicates the presence of the bubble in the considered velocity range, while the total number of bubbles in this range is given by

$$N_{bG} = \sum_{j=1}^{N_b} b_j. \tag{8.25}$$

The associated standard deviation is defined as

$$\sigma(\langle v_B \rangle) = \sqrt{\frac{1}{N_{bG}} \sum_{j=1}^{N_b} (v_B[j] - \langle v_B \rangle)^2}. \tag{8.26}$$

The procedure is terminated if the difference between the new and previous estimate of the standard deviation is less than 1% of $3(i_{\max} - \frac{1}{2})v_{\text{mix}}/50$. Otherwise, the range over which the mean and standard deviation are calculated in step 3 is extended with a pair of bins by incrementing $i$ with 1 until one of the edges of the histogram's velocity range is reached.
If $v_B[i] > \langle v_B \rangle + 2\sigma(\langle v_B \rangle)$, $v_B[i]$ is recalculated by searching for the next preceding nose and its matching tail encountered by the first tip sensor. If $v_B[i] < \langle v_B \rangle - 2\sigma(\langle v_B \rangle)$, $v_B[i]$ is set to the mean velocity $\langle v_B \rangle$ without correcting the arrival times of the bubble at the first tip sensor.

After that the propagation velocity of the bubbles is used to compute the chord-length of the bubbles and the slugs:

$$L_B[i] = v_B[i]\,(t_t[i] - t_n[i])\,, \tag{8.27a}$$

$$L_S[i] = \frac{v_B[i] + v_B[i-1]}{2}\,(t_n[i] - t_t[i-1]) \tag{8.27b}$$

Contrary to Eq. 4.5b, the absolute slug length is calculated based on the average velocity of the preceding and subsequent bubble to compensate for the velocity fluctuations.

### 8.3.2 Signal Processing of the Wiremesh Data

The local liquid holdup in the film and slug regions serve as input parameters for the film and slug velocity calculations with the unit-cell model. Each set of typically 12 flow measurements is preceded by a 15-minute calibration measurement at 500 Hz of the nodal wiremesh signal strength under static pure water conditions. See section 4.4.2 for more details about the postprocessing used to determine the time series of the area-averaged liquid holdup. To distinguish the gas from the liquid phase, the analogue wiremesh signal is first binarized by applying a threshold of 0.9. Whenever $\alpha_{\mathrm{L,WM}}$ exceeds the threshold, the slug region is indicated by 1. If not, the bubble region is indicated by 0. Next the air-water interfaces are located by means of the edge detection procedure used above in the signal processing of the tip-sensor data. Occasionally the binarization threshold is too high and segmentation of the slugs takes place, see Fig.8.4(d) and 8.4(e). The time length of these bubbles is a lot smaller compared to the tip-sensor measurements. All bubbles fall within the first bin of the histogram, as defined for the bubble time length in the tip-sensor signal. Its bin width is therefore chosen as threshold to remove the dispersed bubbles with isodata filtering from the slug signal. The false liquid slugs with a time length shorter than the bin width are similarly filtered out. Subsequently, the air-water interfaces are redefined.

In order to determine the liquid holdups associated with the bubbles measured by the second tip-sensor, the time shift relative to the wiremesh signal should be known. Like in the velocity measurements with the tip-sensor, the time-of-flight concept is used to correlate the arrival time of the nose of the bubbles. As the wiremesh sensor is triggered a time $\tau_{t,\mathrm{WM}}$ before the data acquisition with the tip-sensor starts, the bubble is expected to arrive at the wiremesh with a delay,

$$\frac{\Delta y_{t2,\mathrm{WM}}}{\langle v_B \rangle} + \tau_{t,\mathrm{WM}}, \tag{8.28}$$

where $\Delta y_{t2,\mathrm{WM}}$ is the distance between the second tip-sensor and the wiremesh sensor of 3.51 m and $\langle v_B \rangle$ the average bubble velocity given by Eq. 8.22. The fixed time delay is used to prevent bubbles from being combined multiple times with the same bubble in the wiremesh signal. This can not be completely avoided. With isodata filtering, undesired segmentation can be effectively removed from the wiremesh signal. However, in 20% of the measured cases, in particular those with modest dispersion, up to 3% too few bubbles are filtered out

of the tip signal. Because the trigger delay is slightly different in each measurement, it has to be improved iteratively until the average Gaussian translational bubble velocity, calculated as in section 8.3.1 for $\Delta y_{f2,\mathrm{WM}}$ , equals $\langle v_B \rangle$. The index of the nose of bubble $i$ with the closest arrival time is then denoted by $j_{n,\mathrm{WM}}[i]$ and that of the corresponding tail by $j_{t,\mathrm{WM}}[i]$.

Finally, the liquid holdup in the film and slug regions associated with the bubbles in the second tip-signal is calculated as follows:

$$\alpha_{\mathrm{LF}}[i] = \frac{1}{j_{t,\mathrm{WM}}[i] - j_{n,\mathrm{WM}}[i]} \sum_{j=j_{n,\mathrm{WM}}[i]}^{j_{t,\mathrm{WM}}[i]-1} \alpha_{\mathrm{L,WM}}[j] \qquad i \in \{1, ..., N_b\} \tag{8.29}$$

$$\alpha_{\mathrm{LS}}[i] = \frac{1}{j_{n,\mathrm{WM}}[i] - j_{t,\mathrm{WM}}[i-1]} \sum_{j=j_{t,\mathrm{WM}}[i-1]}^{j_{n,\mathrm{WM}}[i]-1} \alpha_{\mathrm{L,WM}}[j] \qquad i \in \{1, ..., N_b\}. \tag{8.30}$$

If successive bubbles in the tip-signal are correlated multiple times with the same bubble in the wiremesh signal, the calculation of the liquid holdup can not be performed since $j_{t,\mathrm{WM}}[i-1] > j_{t,\mathrm{WM}}[i]$ for each following bubble. It is then assumed that $\alpha_{\mathrm{LS}}[i]$ is the same as $\alpha_{\mathrm{LS}}[i-1]$. This will not introduce major errors because the liquid holdup in the slugs, unlike in the films, is very constant.

### 8.3.3 Film and slug velocity analysis

In order to obtain reliable results with a low measurement frequency, the NMR flowmeter principle is based on the determination of time averaged velocities and holdups in the different regions of the slug unit-cell. Knowledge of the time dependent flow properties is therefore not required in the reference measurements either. The ensemble average of the film and slug velocity will be evaluated for the number of slug units detected at the second tip-sensor. However, the measured film velocity is unreliable in up to 3% of the measured bubbles. In these cases, the bubble length is 3 to 5 times shorter than the average bubble length, while the slug length is incidentally twice as long. Normally the slug fraction is around 0.2. Because it is now up to a factor 4 larger, negative film velocities are found with Eq. 8.7. These data points are not taken into account when calculating the ensemble averages and their unbiased standard deviations.

The systematic overestimation of the area-averaged liquid holdup by the wiremesh sensor with $\delta\alpha_L$ introduces a negative bias in the calculated film and slug velocity. Similar to section 7.2.1, the systematic error is estimated by taking a second order Taylor series expansion around $\delta\alpha_L = 0$ on Eq. 8.6 and 8.7, where the true liquid holdup in respectively the slug and film region is expressed by $\alpha_{\mathrm{LS,WM}} - \delta\alpha_L$ and $\alpha_{\mathrm{LF,WM}} - \delta\alpha_L$. Hence, the systematic error in

the slug and film velocity can be approximated by

$$\begin{aligned}\delta v_S &= \left(\frac{\delta\alpha_L}{\alpha_{\mathrm{LS,WM}}} + \frac{{\delta\alpha_L}^2}{\alpha^2_{\mathrm{LS,WM}}}\right) v_S \\ &= \left(\frac{\delta\alpha_L}{\alpha_{\mathrm{LS,WM}}} + \frac{{\delta\alpha_L}^2}{\alpha^2_{\mathrm{LS,WM}}}\right)\left(\frac{v_{\mathrm{SL}}}{\alpha_{\mathrm{LS,WM}}} + \left(1 - \frac{\alpha_{\mathrm{LF,WM}}}{\alpha_{\mathrm{LS,WM}}}\right) v_B \frac{L_B}{L_B + L_S}\right)\end{aligned} \tag{8.31}$$

$$\begin{aligned}\delta v_F &= \left(\frac{\delta\alpha_L}{\alpha_{\mathrm{LF,WM}}} + \frac{{\delta\alpha_L}^2}{\alpha^2_{\mathrm{LF,WM}}}\right) v_F \\ &= \left(\frac{\delta\alpha_L}{\alpha_{\mathrm{LF,WM}}} + \frac{{\delta\alpha_L}^2}{\alpha^2_{\mathrm{LF,WM}}}\right)\left(\frac{v_{\mathrm{SL}}}{\alpha_{\mathrm{LF,WM}}} - \left(\frac{\alpha_{\mathrm{LS,WM}}}{\alpha_{\mathrm{LF,WM}}} - 1\right) v_B \frac{L_S}{L_B + L_S}\right).\end{aligned} \tag{8.32}$$

Based on the study by Prasser et al. [209] the overestimate $\delta\alpha_L$ is, as in chapter 7, supposed to be 0.04 in the error bar calculation.

## 8.4 T1RRT Signal Processing

Flow measurements consist of a series of $N_s$ repetitions of the T1RRT pulse sequence. The initial FID intensities are quantified as the average of the first 20 data points, a dwell time of 1 $\mu$s apart, which turned out to be the method with the best performance in chapter 6.
Before and after each set of typically 12 flow measurements, the $T_1$ relaxation time of water is determined with the inversion recovery pulse sequence set out in section 2.3.4 for a fully water-filled pipe at zero velocity. To reduce the influence of the temperature to which the measurement method is very sensitive, the mean $T_1$ value is used in the analysis of the results. Both the water and air temperature fluctuate at most 1 °C around their average over the set of flow measurements. Under similar static conditions, a T1RRT measurement with a repetition delay, RD, of at least $5T_1$ is also carried out prior to the flow measurements in order to obtain $s_0$, the signal intensity of the NMR signal corresponding to the thermal equilibrium magnetization $M_0$, in each probe. Because the gain factor of both r.f. probes is not identical, the NMR signals are normalized with the corresponding signal strength for a fully water-filled pipe at zero velocity, $s_{y,i}(0,1)$, before the signal fractions for the film and slug section

$$\left.\frac{s_{y,2}}{s_{y,1}}\right|_F = \frac{m_{21}}{m_{11}}\frac{s_{y,1}(0,1)}{s_{y,2}(0,1)} \qquad \text{and} \qquad \left.\frac{s_{y,2}}{s_{y,1}}\right|_S = \frac{m_{22}}{m_{12}}\frac{s_{y,1}(0,1)}{s_{y,2}(0,1)}. \tag{8.33}$$

are processed.

The reference curve required to determine the average film and slug velocity, given by Eq. 8.13, is calculated using the mean $T_1$, $N_y = 120$, $L_c = 12$ cm and $\overline{\Delta l} = 2.57$ cm for an absolute velocity range of 0 – 5 m s$^{-1}$ with a resolution of 1 mm s$^{-1}$. In the same way, the reference curve describing the expected signal strength $s_{y,2}(v_y, 1)$ for a single-phase flow in the second r.f probe is calculated from Eq. 8.8 with $\alpha_L = 1$. Once $v_{\mathrm{NMR,F}}$ and $v_{\mathrm{NMR,S}}$ are known, the section-specific liquid holdup can be derived from the fraction between the mean signal level

of the cluster group, i.e. $m_{21}$ and $m_{22}$, and $s_{y,2}(v_{\mathrm{NMR}}, 1)$ for the region concerned. The liquid holdups thus obtained are corrected with the calibration curve depicted in Fig. 7.4 for the losses by detuning of the r.f. probe when operating in two-phase flow regimes as has been addressed in section 7.2.2. The calibration data is for this purpose piecewise interpolated with a resolution of 0.001.

Since slug flow is characterized by a wide distribution of bubble and slug lengths, the film velocity in particular has a small but significant range for a given $v_{\mathrm{SL}}$ and $v_{\mathrm{SG}}$. Because of this stochastic behaviour, it is assumed that the measurement uncertainty is mainly determined by the random distribution of the measurement points around the cluster means, $m_{ij}$. The reference curve describing the fraction of the signal level in the first and second r.f. coil is not linear in velocity. In order to obtain an estimate for the standard uncertainty in $v_{\mathrm{NMR,F}}$ and $v_{\mathrm{NMR,S}}$ , the standard uncertainty in the signal fraction is therefore converted with this curve in the corresponding velocity interval around the measured value. The combined standard uncertainty in the signal fractions for the film and the slug section is derived as follows:

$$u\left(\left.\frac{s_{y,2}}{s_{y,1}}\right|_F\right) = \left|\frac{m_{21}}{m_{11}}\frac{s_{y,1}(0,1)}{s_{y,2}(0,1)}\right|\left(\frac{1}{N_{c,11}}\left(\frac{\sigma(m_{11})}{m_{11}}\right)^2 + \frac{1}{N_{c,21}}\left(\frac{\sigma(m_{21})}{m_{21}}\right)^2 + \frac{1}{N_s}\left(\frac{\sigma(s_{y,1}(0,1))}{s_{y,1}(0,1)}\right)^2 + \frac{1}{N_s}\left(\frac{\sigma(s_{y,2}(0,1))}{s_{y,2}(0,1)}\right)^2\right)^{1/2} \tag{8.34}$$

$$u\left(\left.\frac{s_{y,2}}{s_{y,1}}\right|_S\right) = \left|\frac{m_{22}}{m_{12}}\frac{s_{y,1}(0,1)}{s_{y,2}(0,1)}\right|\left(\frac{1}{N_{c,12}}\left(\frac{\sigma(m_{12})}{m_{12}}\right)^2 + \frac{1}{N_{c,22}}\left(\frac{\sigma(m_{22})}{m_{22}}\right)^2 + \frac{1}{N_s}\left(\frac{\sigma(s_{y,1}(0,1))}{s_{y,1}(0,1)}\right)^2 + \frac{1}{N_s}\left(\frac{\sigma(s_{y,2}(0,1))}{s_{y,2}(0,1)}\right)^2\right)^{1/2} \tag{8.35}$$

by applying the law of propagation of uncertainty to Eq. 8.33, while using the standard uncertainty of the mean in $m_{ij}$ and $s_{y,i}(0,1)$. The 'low bound' velocity obtained for the signal fraction minus its standard uncertainty is denoted by lb and the 'upper bound' velocity obtained for the signal fraction plus its standard uncertainty by ub. The maximum difference with the measured NMR velocity is considered to be a measure of the standard uncertainty in the film and slug velocity:

$$u(v_{\mathrm{NMR,F}}) = \max(v_{\mathrm{NMR,F}} - \mathrm{lb}(v_{\mathrm{NMR,F}}), \mathrm{ub}(v_{\mathrm{NMR,F}}) - v_{\mathrm{NMR,F}}) \tag{8.36}$$

$$u(v_{\mathrm{NMR,S}}) = \max(v_{\mathrm{NMR,S}} - \mathrm{lb}(v_{\mathrm{NMR,S}}), \mathrm{ub}(v_{\mathrm{NMR,S}}) - v_{\mathrm{NMR,S}}). \tag{8.37}$$

Velocities will be normalized according to Eq. 7.2 in the results section 8.6, so that the $T_1$ relaxation time of the liquid phase, which varies between measurements, can be ruled out as a factor in the performance evaluation of the measurement method. The conversion factor between the absolute and dimensionless velocity is about 4.5.

A disadvantage of the T1RRT method for two-phase flow measurements is that uncertainties in the velocity propagate in the liquid holdup due to the two-stage system of signal processing.

However, it is believed that they fall within the margin of the standard deviation of the cluster average. The combined standard uncertainty in the liquid film and slug holdup are defined as

$$u(\alpha_{\mathrm{NMR,F2}}) = \sqrt{{\alpha_{\mathrm{NMR,F2}}}^2 \left( \frac{1}{N_{c,21}} \left( \frac{\sigma(m_{21})}{m_{21}} \right)^2 + \frac{2}{N_s} \left( \frac{\sigma(s_{y,2}(0,1))}{s_{y,2}(0,1)} \right)^2 \right)} \tag{8.38}$$

$$u(\alpha_{\mathrm{NMR,S2}}) = \sqrt{{\alpha_{\mathrm{NMR,S2}}}^2 \left( \frac{1}{N_{c,22}} \left( \frac{\sigma(m_{22})}{m_{22}} \right)^2 + \frac{2}{N_s} \left( \frac{\sigma(s_{y,2}(0,1))}{s_{y,2}(0,1)} \right)^2 \right)}, \tag{8.39}$$

where the contribution of both the normalization and the reference curve value is taken into account by the factor 2.

When the uncertainties in the number of points per cluster are assumed to be negligible relative to the other terms, the combined standard uncertainty in the superficial NMR velocity can be written as

$$\begin{aligned} u(v_{\mathrm{NMR}}) = \Bigg( & \left( \alpha_{\mathrm{NMR,F2}} \frac{N_{c,21}}{N_s} \right)^2 u(v_{\mathrm{NMR,F}})^2 + \left( \alpha_{\mathrm{NMR,S2}} \frac{N_{c,22} + N_{c,23}}{N_s} \right)^2 u(v_{\mathrm{NMR,S}})^2 \\ & + \left( v_{\mathrm{NMR,F}} \frac{N_{c,21}}{N_s} \right)^2 u(\alpha_{\mathrm{NMR,F2}})^2 + \left( v_{\mathrm{NMR,S}} \frac{N_{c,22} + N_{c,23}}{N_s} \right)^2 u(\alpha_{\mathrm{NMR,S2}})^2 \Bigg)^{1/2}. \end{aligned} \tag{8.40}$$

Assuming an underlying normal distribution, the expanded uncertainty for a 95% confidence level is given by

$$U(v_{\mathrm{NMR}}) = 1.96 u(v_{\mathrm{NMR}}). \tag{8.41}$$

In the calculation of the combined standard uncertainty in the average liquid holdup,

$$u(\alpha_{\mathrm{NMR,2}}) = \sqrt{\left( \frac{N_{c,21}}{N_s} \right)^2 u(\alpha_{\mathrm{NMR,F2}})^2 + \left( \frac{N_{c,22} + N_{c,23}}{N_s} \right)^2 u(\alpha_{\mathrm{NMR,S2}})^2}, \tag{8.42}$$

the contributions of the uncertainties in the number of points per cluster are as well ignored. With a coverage factor based on a normal distribution, the expanded uncertainty for a 95% confidence level can be expressed by

$$U(\alpha_{\mathrm{NMR,2}}) = 1.96 u(\alpha_{\mathrm{NMR,2}}). \tag{8.43}$$

Omitting the uncertainty in $D_p$, which is small compared to the uncertainty in the superficial liquid velocity, the standard uncertainty and the expanded uncertainty providing a level of confidence of 95% in the liquid flowrate are calculated according to

$$u(q_{\mathrm{NMR}}) = \frac{\pi}{4} D_p^2 u(v_{\mathrm{NMR}}) \tag{8.44}$$

$$U(q_{\mathrm{NMR}}) = \frac{\pi}{4} D_p^2 U(v_{\mathrm{NMR}}). \tag{8.45}$$

For a full overview of all the involved uncertainties, including those in the reference measurements and their derivations is referred to appendix C.2.

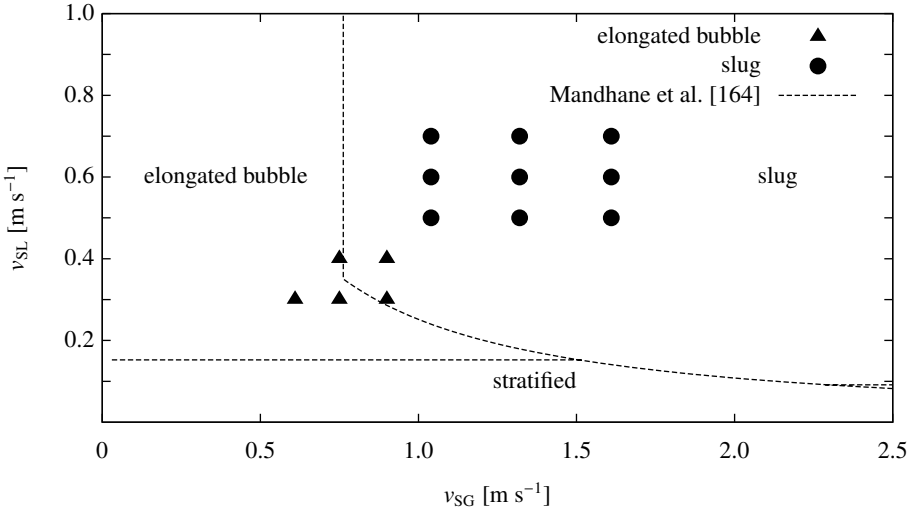


**Figure 8.5**: Comparison of the experimental conditions with the Mandhane et al. [164] flow map for horizontal air-water two-phase pipe flow.

## 8.5 Experimental Matrix

The experiments are carried out for 14 different combinations of the superficial liquid and gas velocity. Elongated bubble flow is found in 5 of the cases in which the superficial liquid velocity is 0.3 or 0.4 m s$^{-1}$, whereas the superficial gas velocity ranges from 0.6 to 0.9 m s$^{-1}$. Slug flow is found in the other cases, where the superficial liquid velocity is 0.5, 0.6 or 0.7 m s$^{-1}$ and the superficial gas velocity is varied between 1.0, 1.3 and 1.6 m s$^{-1}$. Figure 8.5 shows the experimental conditions plotted in the Mandhane et al. [164] flow map. Taking into account that the regimes gradually change into one another, the transition from elongated bubble to slug flow is in good agreement with the flow map predictions.

The measurements are repeated for each flow case with different repetition delays of the T1RRT pulse sequence: namely, 0.5 and 1 s (elongated bubble flow); 0.5, 0.6, 0.7, 0.8, 0.9 and 1 s (slug flow). Shorter repetition delays increase the possibility of exposing the liquid in the film to an r.f. pulse in the same coil more than once. The signals are recorded during 15 minutes, except in the cases where $v_{SL} = 0.7$ m s$^{-1}$. In those cases the capacity of the centrifugal pump is insufficient to pump the water fast enough back into the buffer tank. To prevent the raising water level from obstructing the free discharge into the air-water separator tank, the measurement duration is then limited to 6 minutes. This means that each flow measurement consists of $N_s = 360$ to 1800 consecutively acquired T1RRT sequences.
The number of slugs that are observed in the experiments increases with the superficial liquid velocity. Each elongated bubble experiment at $v_{SL} = 0.3$ m s$^{-1}$ (case 1 – 3) involves approx-

imately 50 slugs and at $v_{SL} = 0.4$ m s$^{-1}$ (case 4 – 5) approximately 90 slugs. In each slug flow experiments at $v_{SL} = 0.5$ m s$^{-1}$ (case 6 – 8) approximately 170, while at $v_{SL} = 0.6$ m s$^{-1}$ (case 9 – 11) approximately 240 slugs are observed. Because of the shorter measurement duration, the slug experiments at $v_{SL} = 0.7$ m s$^{-1}$ (case 12 – 14) only involve approximately 130 slugs.

Results of the validation measurements are listed in Table 8.1. The threshold used in the isodata filtering of the tip-signal is on average 1.7 s in case 1 and gradually decreases with the mixture velocity to 0.3 s in case 14. The associated absolute bubble length, in the range of 1 – 2.5 m, is an order of magnitude larger than the size of the dispersed bubbles. Since the value is at least a factor of two smaller than the chord-length of the slugs, it is unnecessary to optimize the threshold selection algorithm through the choice for smaller bin widths in the histogram.
Based on the unit-cell model, it is expected that the slug velocity in the case of slugs with a low void fraction is approximately equal to the mixing velocity. The table shows that the slug velocities calculated with Eq. 8.6 are all 0.1 – 0.2 m s$^{-1}$ lower. This can be partly attributed to the systematic overestimation of the liquid holdup by the wiremesh sensor. With Eq. 8.31, the systematic underestimation is expected to be about 4% of $v_S$. The relatively large measurement uncertainty in the superficial gas velocity, $u(v_{SG}) = 0.08$ m s$^{-1}$, is also of influence. In future work, it is recommended to use more precise flowmeters than variable area flowmeters.
Due to the unstable nature of slug flow, the standard deviation of the main slug parameters is substantial. However, it should not be confused with the measurement error since the measurements of the mean parameters are much more accurate. For want of a better alternative, the standard deviation is nevertheless used to give an indication of the uncertainty window in which the NMR results are expected.

## 8.6 Flowmeter Performance Evaluation

The fact that the T1RTT measurements at different repetition delays offer repetitive results, supports the validity of the presumption in section 8.2 that the longitudinal magnetization of the fluid measured by the second r.f. coil is usually not reset by an earlier r.f. pulse in the first coil.

### 8.6.1 Clustering

Figure 8.6 shows a comparison between the mean bubble fraction for the T1RRT measurements at a repetition delay of 1 s, computed with Eq. 8.14, and the validation measurements with the tip-sensor where the chord-length of the bubbles and slugs is computed with Eq. 8.27a and 8.27b. While the values for the second NMR probe correspond well with those for the tip-sensor, the graph demonstrates that the cluster algorithm does not work well for the first probe signal. As the flowmeter was not designed for the current flow conditions, the signal levels between the film and slug section are so close together that points belonging to

**Table 8.1**: Summary of the experimental flow conditions, where the number following the plus/minus sign is the value of the standard deviation expressed in the unit of the quoted result. The standard uncertainties in the superficial velocities and the $T_1$ relaxation time are $u(v_{SL}) = 0.001$ m s$^{-1}$, $u(v_{SG}) = 0.08$ m s$^{-1}$ and $u(T_1) = 0.01$ s, respectively. The T1RRT measurements referred to by case 'a' are performed at a repetition delay of 0.5 and 1 s, while those referred to by case 'b' are performed at a repetition delay of 0.5, 0.6, 0.7, 0.8, 0.9 and 1 s.

| case | $v_{SL}$ | $v_{SG}$ | $\alpha_{LF}$ | $\alpha_{LS}$ | $v_B$ | $v_F$ | $v_S$ | $L_B$ | $L_S$ | $T_1$ |
|---|---|---|---|---|---|---|---|---|---|---|
| | [m s$^{-1}$] | | [-] | | [m s$^{-1}$] | | | [m] | | [s] |
| 1 | 0.301 | 0.61 | 0.54 ± 0.01 | 0.99 ± 0.001 | 1.34 ± 0.06 | 0.32 ± 0.03 | 0.78 ± 0.05 | 21 ± 2 | 5.6 ± 0.7 | 2.36 |
| 2 | 0.301 | 0.75 | 0.51 ± 0.01 | 0.99 ± 0.001 | 1.46 ± 0.09 | 0.34 ± 0.04 | 0.88 ± 0.06 | 25 ± 3 | 5.6 ± 0.9 | 2.36 |
| 3 | 0.300 | 0.90 | 0.47 ± 0.02 | 0.99 ± 0.001 | 1.5 ± 0.1 | 0.36 ± 0.04 | 0.95 ± 0.08 | 28 ± 4 | 5.6 ± 0.7 | 2.35 |
| 4 | 0.399 | 0.75 | 0.55 ± 0.03 | 0.99 ± 0.009 | 1.5 ± 0.1 | 0.5 ± 0.2 | 0.9 ± 0.1 | 13 ± 5 | 3 ± 2 | 2.35 |
| 5 | 0.399 | 0.90 | 0.51 ± 0.04 | 0.99 ± 0.005 | 1.6 ± 0.3 | 0.5 ± 0.2 | 1.0 ± 0.2 | 15 ± 6 | 4 ± 1 | 2.27 |
| 6a | 0.500 | 1.04 | 0.41 ± 0.06 | 0.98 ± 0.005 | 1.9 ± 0.2 | 0.6 ± 0.3 | 1.4 ± 0.2 | 9 ± 5 | 2.4 ± 0.6 | 2.33 |
| 6b | 0.501 | 1.04 | 0.40 ± 0.07 | 0.98 ± 0.005 | 1.9 ± 0.2 | 0.6 ± 0.3 | 1.4 ± 0.3 | 9 ± 5 | 2.4 ± 0.6 | 2.25 |
| 7a | 0.500 | 1.32 | 0.32 ± 0.05 | 0.98 ± 0.009 | 2.1 ± 0.2 | 0.8 ± 0.4 | 1.7 ± 0.3 | 11 ± 4 | 3 ± 1 | 2.36 |
| 7b | 0.501 | 1.32 | 0.32 ± 0.05 | 0.98 ± 0.004 | 2.1 ± 0.2 | 0.8 ± 0.4 | 1.6 ± 0.3 | 11 ± 4 | 3 ± 1 | 2.23 |
| 8a | 0.500 | 1.61 | 0.28 ± 0.04 | 0.97 ± 0.007 | 2.4 ± 0.2 | 0.9 ± 0.4 | 2.0 ± 0.3 | 13 ± 5 | 2.3 ± 0.9 | 2.36 |
| 8b | 0.500 | 1.61 | 0.28 ± 0.04 | 0.97 ± 0.008 | 2.4 ± 0.2 | 0.9 ± 0.4 | 1.9 ± 0.3 | 12 ± 4 | 2.3 ± 0.9 | 2.23 |
| 9a | 0.600 | 1.04 | 0.38 ± 0.04 | 0.98 ± 0.007 | 2.0 ± 0.1 | 0.8 ± 0.3 | 1.5 ± 0.2 | 6 ± 2 | 2.0 ± 0.9 | 2.39 |
| 9b | 0.599 | 1.04 | 0.38 ± 0.06 | 0.98 ± 0.007 | 2.0 ± 0.2 | 0.8 ± 0.4 | 1.5 ± 0.2 | 7 ± 3 | 2 ± 1 | 2.25 |
| 10a | 0.600 | 1.32 | 0.33 ± 0.03 | 0.98 ± 0.006 | 2.3 ± 0.2 | 0.9 ± 0.4 | 1.8 ± 0.2 | 7 ± 2 | 1.9 ± 0.8 | 2.39 |
| 10b | 0.597 | 1.32 | 0.33 ± 0.03 | 0.98 ± 0.006 | 2.3 ± 0.2 | 0.9 ± 0.4 | 1.8 ± 0.2 | 7 ± 3 | 1.8 ± 0.8 | 2.25 |
| 11a | 0.597 | 1.61 | 0.30 ± 0.05 | 0.95 ± 0.01 | 2.5 ± 0.2 | 1.1 ± 0.5 | 2.1 ± 0.3 | 9 ± 4 | 1.9 ± 0.8 | 2.42 |
| 11b | 0.594 | 1.61 | 0.30 ± 0.04 | 0.96 ± 0.01 | 2.6 ± 0.2 | 1.1 ± 0.5 | 2.1 ± 0.3 | 9 ± 4 | 1.9 ± 0.8 | 2.27 |
| 12a | 0.695 | 1.04 | 0.37 ± 0.06 | 0.99 ± 0.007 | 2.2 ± 0.2 | 0.9 ± 0.5 | 1.7 ± 0.3 | 7 ± 3 | 3 ± 1 | 2.42 |
| 12b | 0.697 | 1.04 | 0.37 ± 0.05 | 0.99 ± 0.003 | 2.1 ± 0.2 | 0.9 ± 0.4 | 1.6 ± 0.3 | 7 ± 3 | 3 ± 1 | 2.27 |
| 13a | 0.698 | 1.32 | 0.33 ± 0.05 | 0.97 ± 0.006 | 2.3 ± 0.2 | 1.0 ± 0.5 | 1.9 ± 0.3 | 7 ± 3 | 2.2 ± 0.8 | 2.37 |
| 13b | 0.692 | 1.32 | 0.33 ± 0.03 | 0.97 ± 0.005 | 2.4 ± 0.2 | 1.0 ± 0.4 | 2.0 ± 0.2 | 6 ± 2 | 1.9 ± 0.7 | 2.27 |
| 14a | 0.698 | 1.61 | 0.31 ± 0.03 | 0.95 ± 0.007 | 2.8 ± 0.2 | 1.2 ± 0.4 | 2.2 ± 0.3 | 7 ± 2 | 1.8 ± 0.6 | 2.37 |
| 14b | 0.695 | 1.61 | 0.31 ± 0.03 | 0.95 ± 0.007 | 2.7 ± 0.2 | 1.2 ± 0.4 | 2.2 ± 0.2 | 7 ± 2 | 1.8 ± 0.6 | 2.27 |

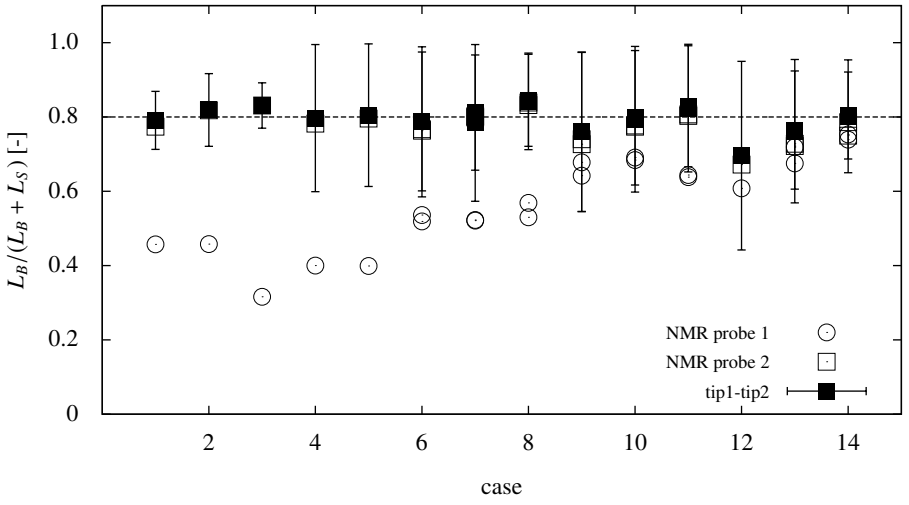


**Figure 8.6:** Mean bubble fraction for T1RRT measurements at a repetition delay RD = 1.0 s.

the film section are assigned to the slug section. When the velocity difference between the film and the slug sections increases for the higher case numbers, the cluster algorithm has a better performance. From case 9 on, the values measured by the first probe fall within the $\pm 2\sigma$ window, indicated by the error bars, which serves as a measure for the statistical distribution of the bubble fraction. The reliability of the other measurements may be questioned.

The following could serve as a guideline to be able to distinguish between the levels of the film and the main slug cluster:

$$m_{i1} < m_{i2} - \sigma(m_{i1}) - \sigma(m_{i2}). \tag{8.46}$$

The position of the r.f. coils comes very precisely to meet this condition. The initial intensity of the FID is the product of the liquid holdup and the longitudinal magnetization built up in the polarizing magnetic field, see Eq. 8.8. Intrinsic to slug flow is a slug section with a high velocity and a liquid holdup of about 1, while the film section has a low velocity and a much lower liquid holdup. Because the signal intensity is the product of a low magnetization and a large liquid holdup of comparable magnitude in the slug section and vice versa in the film section, whether the holdup is the determining factor for the signal difference between the sections depends on the coil position in relation to the $T_1$. This means that the first r.f. coil must be placed further into the flowmeter, given that the magnetization buildup is an exponential function of the residence time in the polarizing magnetic field. For the flow cases 1 – 8, the signal difference becomes significant if the first coil were located at approximately 1.5 m from the flowmeter entrance. However, being able to discriminate between the cluster levels comes at the expense of the velocity resolution of the flowmeter.

### 8.6.2 Velocity Determination

In Figure 8.7 the ratio of the signal intensity in the second r.f. coil to that in the first r.f. coil is shown for all measured cases. Measurements of the same flow case at different repetition delays of the T1RRT pulse sequence are organized into small groups. Both the data points of the elongated bubble's film and slug section follow the trend of the reference curve of Eq. 8.13, which is used by the flowmeter to determine the flow velocity, albeit with a small shift. The data points for the slug section of the slug flow measurements are evenly distributed around the curve. A too low, almost uniform signal fraction is observed for the data points of the slug flow's film section. Given the current configuration, the T1RRT measurement method is thus unable to determine the film velocity under slug flow conditions. Apart from the slug velocity in the slug flow regime, all velocities are systematically underestimated in the postprocessing.
This is also demonstrated by Figure 8.8[1] in which the directional bias error, the difference between the measured and reference velocity, is shown. The underprediction of the NMR film velocity shows a linear decrease with the film velocity from the reference measurements. In the slug velocity, no clear trend in the velocity bias can be observed. Because $v_F$ and $v_S$ are systematically underestimated owing to the overestimation of the liquid holdup by the wiremesh sensor, as given by Eq. 8.32 and 8.31, the directional bias error in the film velocity will even be up to 0.16 m s$^{-1}$ larger. On the slug velocity measurements, a correction for $\delta v_S$ is beneficial in the majority of cases. As will be elaborated on in the next section, the directional bias error is the result of the liquid pickup and shedding mechanisms that take place in the liquid slugs. This makes that the residence time is not single-valued over the slug and film section as is assumed in the cluster algorithm. Due to the wide distribution of film and slug velocities, inherent to the chaotic nature of slug flow, the standard deviation of the reference measurements gives little information about the quality of the NMR measurements. All data points fall within the margin, but a deviation of 0.5 m s$^{-1}$ on a velocity of 1 m s$^{-1}$ is by far too high.

The relative expanded uncertainty in the NMR film and the slug velocity measurements with 95% confidence level are shown in Figure 8.9(a) and (b). The repeatability of the film velocity measurements with a maximum relative uncertainty of 3% is better than the 6% found for the stratified flow measurements, which are comparable in terms of flow profile. The slug flow is stable enough to determine the signal levels with the cluster algorithm. For the slug velocity measurements, the flowmeter operates in the velocity range for which it was not designed. As can be concluded from Fig. 8.7, the gradient of the signal-fraction curve is too low to get reliable measurement results: a small difference in the signal ratio results in a large difference in the bulk velocity. Although the standard deviation in $v_{\mathrm{NMR,F}}$ is of the same order as that in $v_{\mathrm{NMR,S}}$, the relative uncertainty in the slug velocity increases to an unacceptable 30%. Given the good repeatability, it is however believed that the T1RRT method can be applied to slug flow provided the systematic errors introduced by the liquid pickup and shedding processes are resolved.

[1] The error bars are a measure for the statistical distribution of the film and slug velocities and not for the uncertainty in the velocity bias.

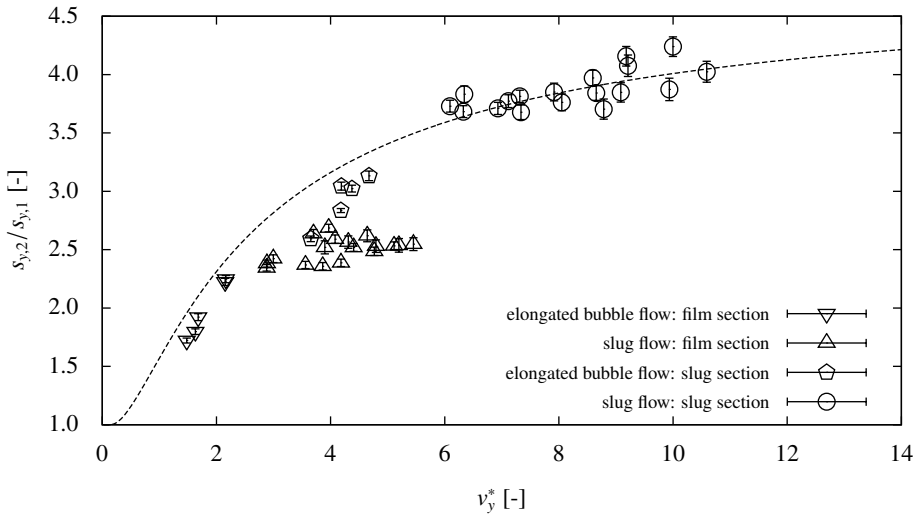


**Figure 8.7**: Ratio of the signal intensity in the 2nd r.f. coil with respect to the 1st r.f. coil for respectively the film and slug section as a function of their dimensionless liquid bulk velocity. The reference curve of Eq. 8.13 ($\overline{\Delta l}$ = 2.47 cm, $N_y$ = 120), which is consulted in the flowmeter reconstruction algorithm in order to determine the flow velocity $v^*_{\mathrm{NMR}}$, is adjusted to the dimensionless velocity defined by Eq. 7.2.

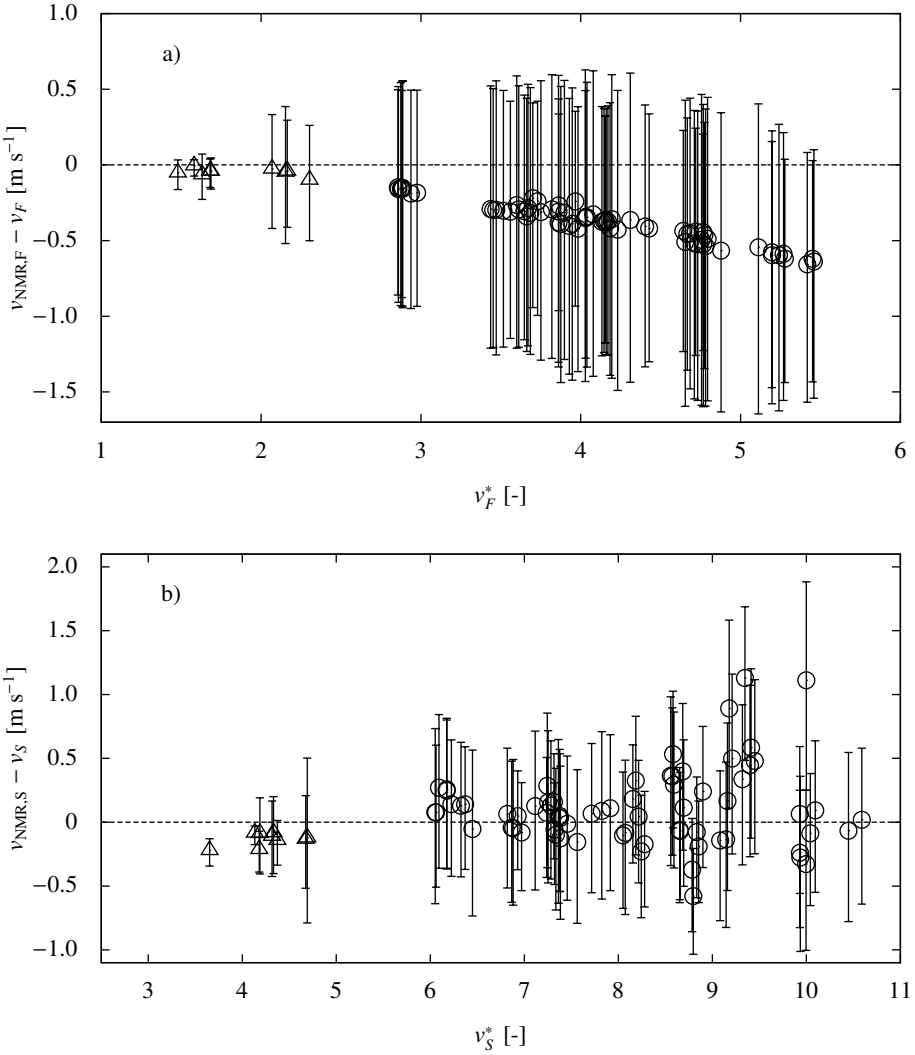


**Figure 8.8**: The difference of a) the NMR film velocity and b) the NMR slug velocity with respect to the reference measurements with the tip-sensor is an indication of the directional bias error. The elongated bubble regime is marked by △ and the slug flow regime by ○.

### 8.6.3 Systematic errors by the pickup and shedding processes

Due to the pickup and shedding processes, the residence time in the polarizing magnetic field of the flowmeter does not have a uniform value in each of the slug sections as presumed in

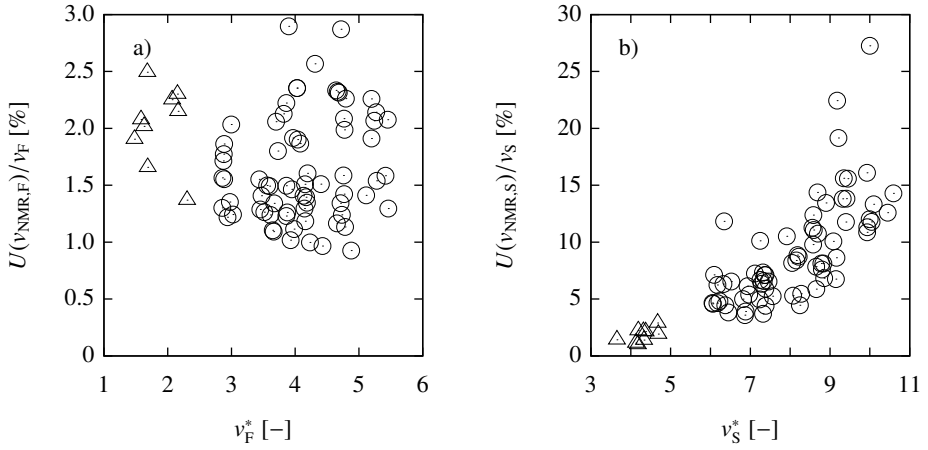


**Figure 8.9**: Relative expanded uncertainty with 95% confidence level in a) the NMR film velocity and b) the NMR slug velocity, where △ is the elongated bubble and ○ the slug flow regime.

the T1RRT measurement principle presented in section 8.2. The liquid picked up by the slug from the preceding film has a longer residence time in the polarizing magnetic field than the liquid in the rest of the slug section:

$$\tau_{S,i} = \frac{y_{c,i} + \overline{\Delta l}}{v_S}. \tag{8.47}$$

Conversely, the liquid shed at the rear of the slug has a shorter residence time in the magnetic field than the liquid in the rest of the film section:

$$\tau_{F,i} = \frac{y_{c,i} + \overline{\Delta l}}{v_F}. \tag{8.48}$$

A simple model is proposed in an attempt to understand which systematic errors are introduced by these gradients in the residence time. Assuming that the velocity of the liquid picked up from the film accelerates instantaneously to the slug velocity, there exists a linear gradient in the residence time over a distance

$$L_{sp,i} = \frac{y_{c,i} + \overline{\Delta l}}{v_B}(v_S - v_B) \tag{8.49}$$

from the front of the slug as illustrated in the left-hand column of Fig. 8.10. Referring to table 8.2, the mixing length it takes for the fluid to accelerate to the slug velocity, calculated with Eq. 8.1, is indeed small compared to $L_{sp,i}$. If it is similarly assumed that the liquid shed from

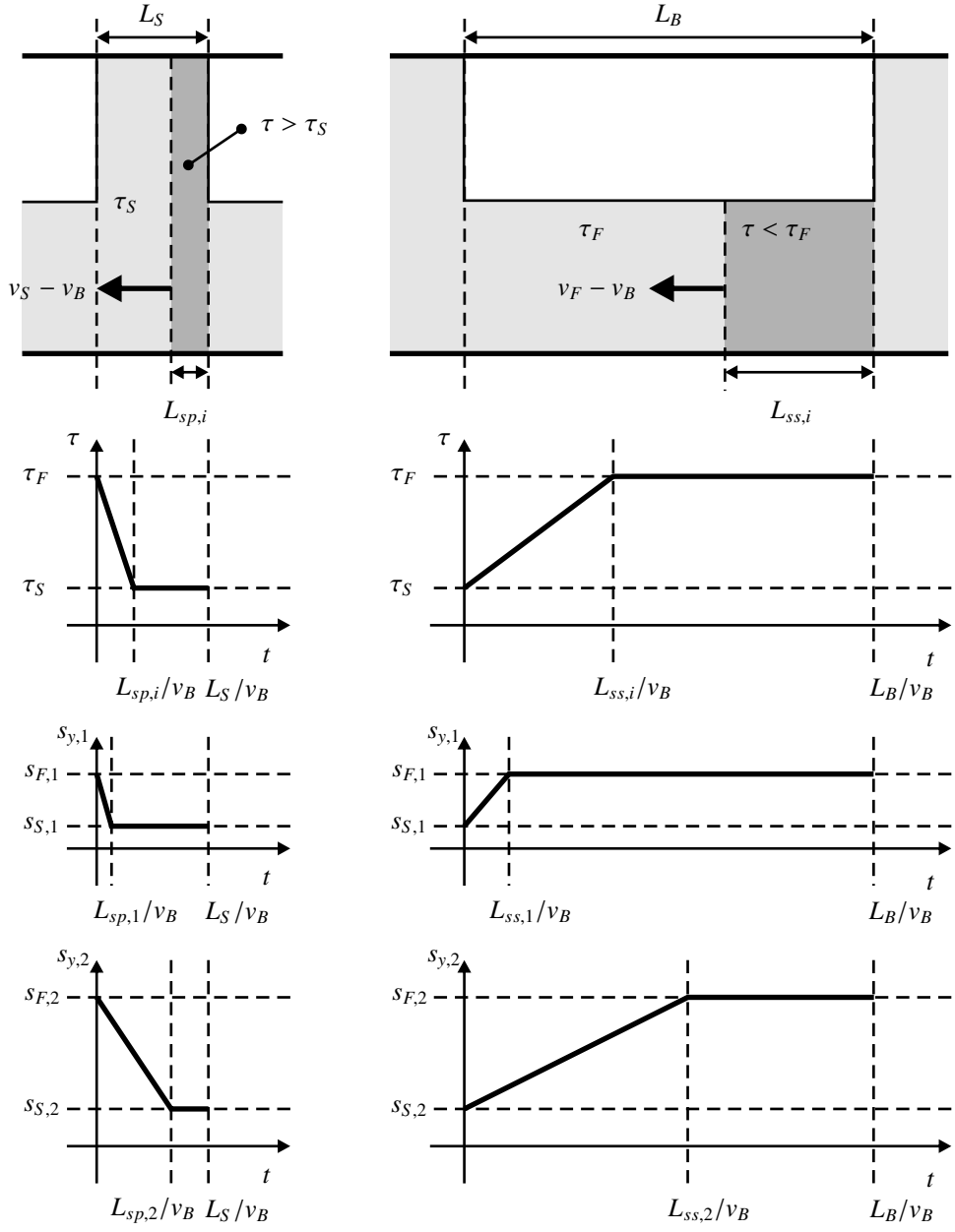


**Figure 8.10**: Simple model for estimating the influence of the liquid pickup at the front of the slug (left) and the liquid shedding at the rear of the slug (right) on the time-dependent residence time in the permanent magnetic field and the signal levels measured by the first and second NMR coil.

the slug instantaneously slows down to the film velocity, a linear gradient in the residence time exists over a distance

$$L_{ss,i} = \frac{y_{c,i} + \overline{\Delta l}}{v_B}(v_F - v_B) \tag{8.50}$$

from the rear of the slug, see the right-hand column of Fig. 8.10. Since $L_{sp,i} < L_S$ and $L_{ss,i} < L_B$, there is no need to take a longer history into account in the calculation of the residence time than one preceding film or slug section.

In the area where liquid pickup controls the residence time, the magnetization will be higher than expected based on the average slug velocity. Though the magnetization is an exponential function of the residence time, the NMR time signal is approximated by a linear function. The average signal level for the entire slug section can then be written as

$$s_{sp,i} = \frac{\alpha_{\mathrm{LS}}}{L_S}\left(s_{S,i}(L_S - L_{sp,i}) + \frac{1}{2}(s_{S,i} + s_{F,i})L_{sp,i}\right), \tag{8.51}$$

where $s_{S,i}$ and $s_{F,i}$ are the signal strengths for $\tau_{S,i}$ and $\tau_{F,i}$ if the pipe is completely filled with water. Because $L_{sp,1}$ is only a few percent of $L_S$ and only little magnetization has been built up, the first probe signal is hardly affected by pickup. The increased fraction of the signal levels can be fully attributed to the higher second probe signal, $s_{sp,2}$. As the signal processing with reference curve Eq. 8.13 takes no account of the pickup effect, the measured average slug velocity is overestimated. It should be noted that the use of the third cluster, intended for the mixing zone, is effective against the introduction of systematic errors by the pickup process. Most of the data points in question are assigned to this third cluster, as is clear from Fig. 8.2. This makes $m_{i2}$ a fairly reliable estimate of the expected signal level for $v_S$. The velocity bias, $\delta v_{S,sp} = v_{\mathrm{NMR,S}} - v_S$, is therefore much smaller than predicted in table 8.2.

In the area where the residence time is controlled by liquid shedding, the magnetization will be lower than expected on the basis of the average film velocity. If the NMR time signal is approximated by a linear function of the residence time, the average signal level for the entire bubble section becomes

$$s_{ss,i} = \frac{\alpha_{\mathrm{LF}}}{L_B}\left(s_{F,i}(L_B - L_{ss,i}) + \frac{1}{2}(s_{S,i} + s_{F,i})L_{ss,i}\right). \tag{8.52}$$

Figure 8.2 demonstrates the validity of this assumption. The data points associated with the film section in the first probe signal display a linear relation with time.
Also the influence of liquid shedding on the first probe signal is insignificant. The decrease in the fraction of the signal levels as observed in Figure 8.7 is entirely due to the lower second probe signal, $s_{ss,2}$. Because of shedding, too low velocities will be found with the reference curve given by Eq. 8.13. As can be seen from table 8.2, the predicted velocity bias, $\delta v_{F,ss} = v_{\mathrm{NMR,F}} - v_F$, for the elongated bubble regime is with 1 cm s$^{-1}$ not bad. In the slug regime, however, the underestimation of the velocity increases with the relative velocity between the bubble and the film to $-0.10$ m s$^{-1}$ for case 14. Despite the difference with the

**Table 8.2:** Analysis of the systematic errors by the shedding and pickup processes for $T_1 = 2.4$ s according to the simple model of Fig. 8.10.

| case | $v_B$ | $v_F$ | $v_S$ | $L_B$ | $L_S$ | $L_M$ | $L_{ss,1}$ | $L_{ss,2}$ | $L_{sp,1}$ | $L_{sp,2}$ | $\delta v_{F,ss}$ | $\delta v_{S,sp}$ | $\alpha_{\mathrm{LF}}$ | $\alpha_{\mathrm{LS}}$ | $\delta\alpha_{\mathrm{LF},ss}$ | $\delta\alpha_{\mathrm{LS},sp}$ |
|---|---|---|---|---|---|---|---|---|---|---|---|---|---|---|---|---|
| | | [m s$^{-1}$] | | | | | [m] | | | | [m s$^{-1}$] | | | | [-] | |
| 1 | 1.34 | 0.32 | 0.78 | 21 | 5.6 | 0.00 | 0.40 | 1.92 | 0.22 | 1.06 | -0.01 | 0.01 | 0.54 | 0.99 | -0.01 | 0.04 |
| 2 | 1.46 | 0.34 | 0.88 | 25 | 5.6 | 0.00 | 0.40 | 1.94 | 0.21 | 1.00 | -0.01 | 0.03 | 0.51 | 0.99 | -0.01 | 0.05 |
| 3 | 1.5 | 0.36 | 0.95 | 28 | 5.6 | 0.01 | 0.40 | 1.93 | 0.19 | 0.93 | 0.00 | 0.04 | 0.47 | 0.99 | -0.01 | 0.06 |
| 4 | 1.5 | 0.5 | 0.9 | 13 | 3 | 0.00 | 0.36 | 1.74 | 0.20 | 0.98 | -0.01 | 0.06 | 0.55 | 0.99 | -0.01 | 0.08 |
| 5 | 1.6 | 0.5 | 1.0 | 15 | 4 | 0.00 | 0.36 | 1.75 | 0.19 | 0.93 | -0.01 | 0.09 | 0.51 | 0.99 | -0.01 | 0.10 |
| 6 | 1.9 | 0.6 | 1.4 | 9 | 2.4 | 0.01 | 0.35 | 1.69 | 0.15 | 0.73 | -0.03 | 0.29 | 0.40 | 0.98 | -0.02 | 0.23 |
| 7 | 2.1 | 0.8 | 1.7 | 11 | 3 | 0.01 | 0.33 | 1.57 | 0.11 | 0.55 | -0.03 | 0.33 | 0.32 | 0.98 | -0.01 | 0.20 |
| 8 | 2.4 | 0.9 | 2.0 | 12 | 2.3 | 0.02 | 0.33 | 1.60 | 0.10 | 0.49 | -0.05 | 0.60 | 0.28 | 0.97 | -0.01 | 0.31 |
| 9 | 2.0 | 0.8 | 1.5 | 7 | 2.2 | 0.01 | 0.31 | 1.48 | 0.12 | 0.59 | -0.05 | 0.31 | 0.38 | 0.98 | -0.02 | 0.21 |
| 10 | 2.3 | 0.9 | 1.8 | 7 | 1.8 | 0.01 | 0.31 | 1.51 | 0.11 | 0.52 | -0.07 | 0.59 | 0.33 | 0.98 | -0.02 | 0.33 |
| 11 | 2.6 | 1.1 | 2.1 | 9 | 1.9 | 0.02 | 0.31 | 1.48 | 0.10 | 0.49 | -0.07 | 0.74 | 0.30 | 0.95 | -0.02 | 0.35 |
| 12 | 2.2 | 0.9 | 1.6 | 7 | 3 | 0.01 | 0.31 | 1.49 | 0.12 | 0.59 | -0.06 | 0.29 | 0.37 | 0.99 | -0.03 | 0.18 |
| 13 | 2.4 | 1.0 | 1.9 | 7 | 2.0 | 0.01 | 0.29 | 1.41 | 0.09 | 0.45 | -0.08 | 0.50 | 0.33 | 0.97 | -0.03 | 0.26 |
| 14 | 2.8 | 1.2 | 2.2 | 7 | 1.8 | 0.02 | 0.30 | 1.46 | 0.10 | 0.50 | -0.10 | 1.01 | 0.31 | 0.95 | -0.03 | 0.44 |

values as they appear in Figure 8.8(a), it is clear that the velocity bias can be explained by the shedding process. Note that this model is too simple to capture the deceleration of the liquid under influence of wall and interfacial shear with sufficient accuracy.

The major disadvantage of the T1RRT method for two-phase flow is that errors in the measured velocity propagate into the holdup determination. This effect is furthermore negatively reinforced by both the liquid pickup and the liquid shedding process.
Because of the underestimation of the film velocity, the NMR signal, which is already too low due to liquid shedding, is also scaled with a too high reference signal strength for a completely water-filled pipe, resulting in an extra large underestimation of the liquid film holdup. The model calculates the bias in the liquid holdup, $\delta\alpha_{\mathrm{LF},ss} = \alpha_{\mathrm{NMR,F}} - \alpha_{\mathrm{LF}}$, to be $-0.01$ to $-0.03$ for the cases considered here. The decrease will be stronger for a larger velocity bias.
As a consequence of the overestimation of the slug velocity, the NMR signal that is already too high due to liquid pickup is scaled with a too low reference signal for a completely water-filled pipe, giving rise to an extra large overestimation of the liquid slug holdup. The values given in table 8.2 for the directional bias error estimated with the model are larger than expected, because the slug velocities correspond better with reality by using the third cluster for the mixing zone.

### 8.6.4 Liquid Holdup

During the second stage of the two-phase flow measurements, the liquid holdup is determined. The directional bias error in the average liquid film and slug holdup is given in Figure 8.11[2]. A too low value is found for the liquid holdup in the film section, even if it is corrected for the systematic overprediction by the wiremesh sensor. As explained in the previous section, this can be attributed to the liquid shedding process in the film behind the slug. However, there seems to be more going on in the elongated bubble flow measurements. Just as in the stratified flow measurements reported in chapter 7, there may exist a weak negative gradient in the water level due to outflow effects. The flow conditions in the film section are very similar to stratified flow; extremely long bubbles of 13 – 28 m and a film velocity not much higher than the liquid bulk velocity in the stratified flow measurements. Because the outlet of the pipe is only 1.5 m from the second NMR probe, it is quite possible that the flow is not powerful enough to keep the water in the two NMR probes at the same level, while the measuring principle of the T1RRT method is based on that. In the sensitivity study in section 7.4.3.1, it is demonstrated that a descending water level with an elevation angle of $-0.075°$ introduces, in addition to a negative velocity bias, a systematic error of approximately -0.06 in the liquid holdup. A comparison with the shedding process shows furthermore that both affect the measurement results in the same way.

Apart from this, two-phase flow measurements on lossy samples suffer always from some signal loss. The probe, tuned for a fully filled pipe, becomes detuned and dematched when the amount of liquid in the sensitive volume of the coil decreases. The strip-shield that is

[2]The error bars are a measure for the statistical distribution of the liquid holdup in the film and slug section and not for the uncertainty in the directional bias error of the average liquid holdup.

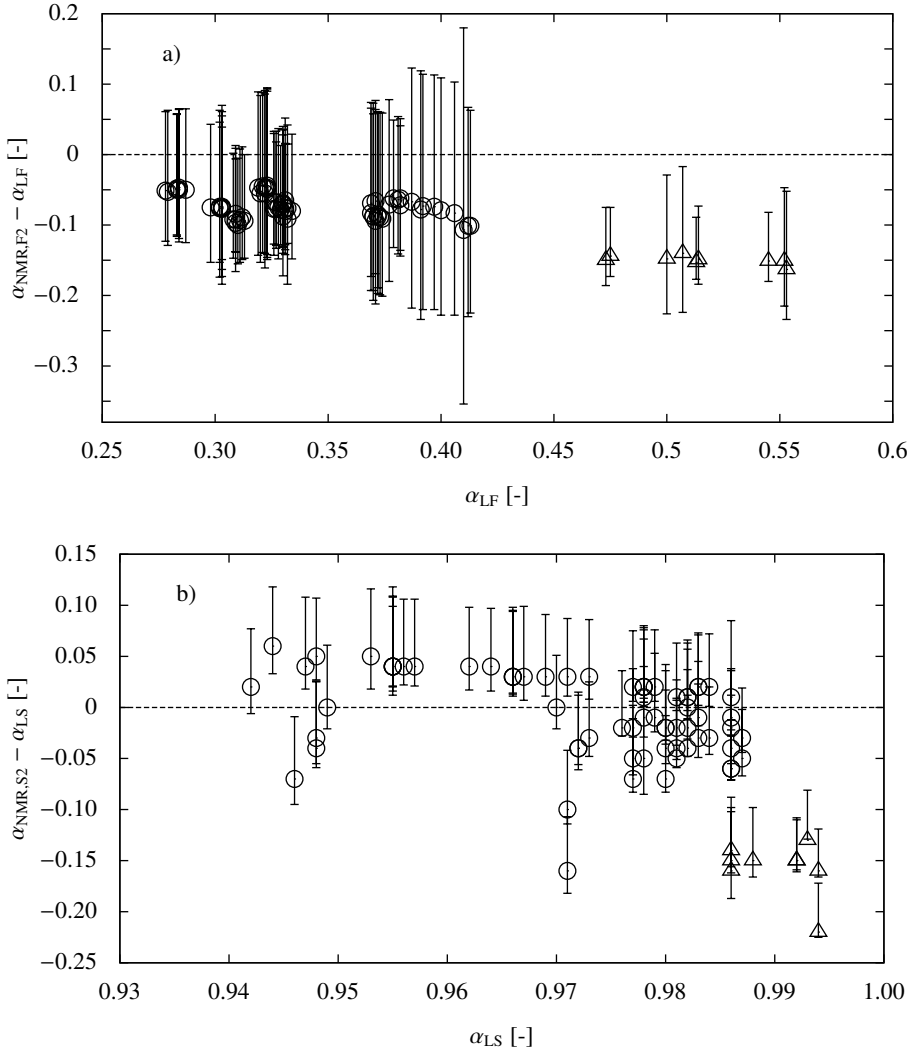


**Figure 8.11**: The difference between the liquid holdup detected with the second NMR probe and the wiremesh sensor of a) the film section and b) the slug section is an indication of the directional bias error. The elongated bubble regime is marked by △ and the slug flow regime by ○.

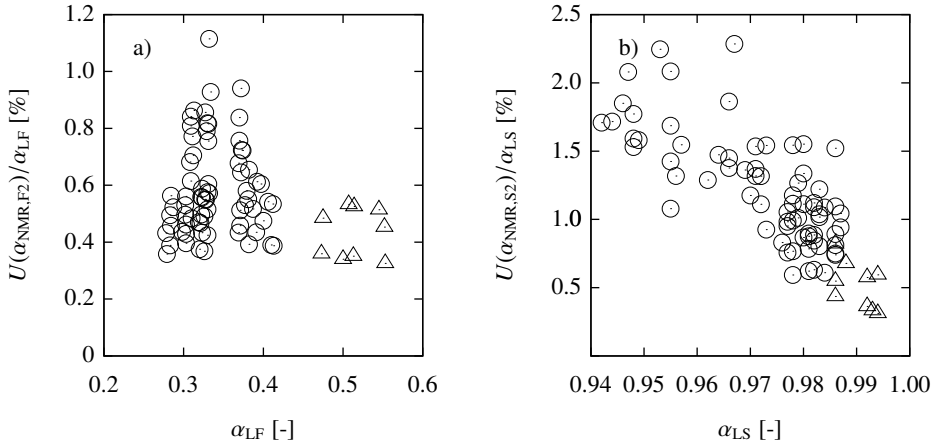


**Figure 8.12**: Relative expanded uncertainty with 95% confidence level in the liquid holdup detected by the second NMR probe of a) the film section and b) the slug section, where △ marks the elongated bubble and ○ the slug flow regime.

placed between the sample and the coil improves the efficiency of the probe significantly, but cannot completely screen the dielectric sample from its electromagnetic interaction with the resonator (see section 7.2.2). This problem does not arise in the velocity determination, as the signal loss for both probes will be comparable and therefore cancels each other out in the analysis of the signal fraction.
For the liquid holdup in the slug section, a too high value is found in most of the slug flow cases. This can be explained by the pickup process, as a result of which the NMR signal is higher than expected, since liquid from the previous film that is overrun by the slug has a longer residence time in the polarizing magnetic field than the rest of the slug section. The degree of overestimation is much smaller than predicted in table 8.10, which proves that the use of a third cluster is an effective means against the introduction of systematic errors by liquid pickup. The slug liquid holdup in the elongated bubble cases is underestimated by 0.15 as is the film liquid holdup, supporting the suspicion that the water level is descending towards the pipe outlet.

The relative expanded uncertainty in the measurements of the liquid film and slug holdup with 95% confidence level are shown in Figure 8.12(a) and (b). The repeatability of the liquid holdup in the film section is excellent with a relative expanded uncertainty of 1.2%, the same range as in the stratified flow measurements. The relative expanded uncertainty of the liquid holdup in the slug section increases with the void fraction up to 2.4%. This is obvious since the NMR signal fluctuates more due to the presence of dispersed bubbles.

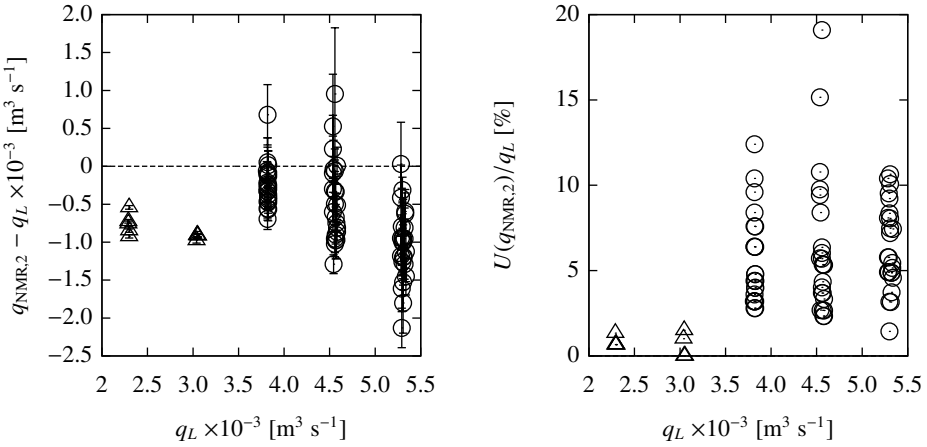


**Figure 8.13**: a) Difference between the liquid flowrate detected with the NMR flowmeter and the reference value measured with the electromagnetic flowmeter. (b) Relative expanded uncertainty with 95% confidence level of the liquid flowrate. The elongated bubble regime is indicated by △ and the slug flow regime by ○.

### 8.6.5 Liquid Flowrate

In Figure 8.13(a) the directional bias error between the obtained flowrate and the reference measurement by the electromagnetic flowmeter is shown. In order to accurately measure the liquid flowrate in the slug flow regime, the signal processing must be adjusted to take the pickup and shedding processes better into account. Because the bubble fraction makes up 80% of the unit-cell, the weighted sum with which the total liquid flowrate is calculated, Eq. 8.16, is dominated by the contribution of the liquid film. While both the liquid holdup and the velocity in the film section are underestimated, the liquid holdup and, in general, also the velocity in the slug section are overestimated. As a result, a too low total liquid flowrate is obtained.

As far as the random effects are concerned, the flowmeter is, like in the measurements on stratified flow, as accurate as the velocity determination. Because the flowmeter is not designed for the prevailing slug velocity range, the relative expanded uncertainty with 95% confidence level of the liquid flowrate is almost completely determined by the contribution from the slug velocity as is apparent from a comparison of Figure 8.13(b) with Figure 8.8(b).

## 8.7 Conclusions

In this proof of principle study, it has been demonstrated that the T1RRT method can be adapted to horizontal slug flow by using clustering to discriminate the slug section data from

the film section data, whereafter the average liquid flowrate is calculated by means of the unit-cell concept. The upper limit of the measurement frequency, determined by the film velocity, is the frequency where the liquid is never pulsed more than once in the same coil.

The measurement principle presumes incorrectly that the residence time in the polarizing magnetic field of the flowmeter has a uniform value over the film section, resulting in a systematic underprediction of the liquid flowrate. In order to reduce the influence of liquid shedding, a procedure should be developed to distinguish the zone controlled by liquid shedding from the rest of the film section. Because the flowmeter prototype is not designed for the range of slug velocities at which the experiments are performed, it is not possible to judge if the third cluster resolves the problems related to the pickup process.

As in the stratified flow measurements, it has been found that a weak gradient in the water level with an elevation angle of order $-0.1^\circ$ gives rise to large measurement errors due to the large distance between the two r.f. coils.
The cluster algorithm only works well if the position of the coils is finely tuned to the flow conditions. A design criterion is proposed that can serve as guideline to ensure that the signal levels associated with the film and slug section are sufficiently far apart. For the measurements presented here, this means that the first r.f. coil must be placed further into the flowmeter. Optionally, some cluster validation procedure could be used to identify if the clusters are really separate [256].

Because of the chaotic nature of slug flow, looking at the mean parameters is not the best way to validate the NMR measurements. The standard deviation of the film and slug velocity is too high to give information about the quality of the flowrate measurements. It is recommended to model the NMR signals based on the reference measurements and then compare that slugwise with the actual measured signals.

# Chapter 9

# Conclusions and Recommendations

## 9.1 Conclusions

Driven by the demand of the petroleum industry to continuously monitor the produced reservoir fluids, two NMR multiphase flowmeter concepts have been developed for measuring the liquid flowrate of two-phase gas-liquid flows inline and without phase separation. They derive the liquid flowrate indirectly, from the product between the average velocity and the holdup.
The two methods have a fundamentally different NMR working principle for determining the average fluid velocity. T1RRT is a rapid passage technique that examines the plain magnetization envelope of the NMR signal. It relates the residence time in the polarizing magnetic field, and therefore the velocity, to the build-up of longitudinal magnetization, which is expressed by the signal intensity. In the pulsed gradient technique, PGSE, the fluid velocity is obtained from the phase of the NMR signal. Both flowmetering concepts resolve the fractions of the fluid components in an identical manner as implemented in the T1RRT method: from the multi-exponential course of the signal intensity associated with the different polarization lengths of measurement probes at different streamwise positions.
The performance evaluation of the methods in this study is limited to the horizontal orientation of the flowmeter. Since the NMR signal intensity is independent of the orientation of the fluids in the pipe, it is expected that a vertical or inclined installation of the instrument will not influence measurements of steady-state, pseudo steady-state or quasi-static, fully-developed intermittent multiphase flows, provided that the flow model integrated in the hardware of the flowmeter is adapted to the prevailing flow pattern. The developed methods will have difficulties in measuring regimes with strong transients.

Comparing the strengths and weaknesses of the two methods, a disadvantage of the T1RRT method over the PGSE method is that the velocity and fraction determination are correlated,

causing errors in the velocity to propagate, to an increased extent, in the holdup. In the PGSE method, the average flow velocity is obtained directly from the NMR signal and does not depend on a model that requires prior knowledge of the velocity profile.
In contrast, the time resolution of the T1RRT method is much better than that of the PGSE method. A repetition delay of the pulse sequence longer than the transit time of the fluid through the NMR flowmeter has proved to be overcareful. The upper limit of the measurement frequency is close to the frequency at which the liquid is never exposed to more than one r.f. pulse in the same coil. In the current configuration, that is, depending on the lowest occurring velocity, a measurement frequency of a few Hz. Because the PGSE method requires a stable velocity over the different repetitions of the pulse sequence, the technique is less suitable for fast fluctuating multiphase flow regimes.
Another important issue is the sensitivity of both measurement principles to changes in the $T_1$ relaxation time, although in the PGSE method only the determination of the fraction and not also that of the velocity relies on $T_1$. This material specific parameter is highly dependent on the viscosity and hence of the temperature and pressure. The flowmeter must therefore continuously monitor the $T_1$ relaxation time. Unfortunately, the used inversion recovery pulse sequence can be performed under static conditions only. This is a problem in the application intended for the petroleum industry, where the production stream cannot be stopped at any desired time. Other standard pulse sequences known from well-logging work only at very low flowrates. A possibility could be to carry out the measurements in a bypass of the main production line. Alternatively, the flowmeter could use table values of $T_1$ based on the readings of external temperature and pressure sensors, which are obtained beforehand in an extensive series of calibration measurements under the prevailing conditions.

### 9.1.1 Calibration procedure of the essential NMR parameters

The calibration procedure is an essential part of the proper functioning of an NMR multiphase flowmeter. In addition to the $T_1$ relaxation time of the reservoir fluids to be measured, the 90 and 180 degrees pulse lengths must be calibrated. The accuracy of the multiphase flowmeter with regard to the calibration procedure has been evaluated using static dummies of different dimensions filled with tapwater and oil-tapwater mixtures. Static dummies represent well the conditions for the calibration measurements, since all routines tested require that the magnetization has reached the thermal equilibrium, i.e., it is fully polarized.

#### Longitudinal relaxation time

The INVREC pulse sequence in combination with a bi-exponential curve fit model is not able to determine the $T_1$ relaxation times of oil and water simultaneously, over the full range of viscosities. The difficulty comes from the fact that mineral oil is a mixture of hydrocarbons of varying molecular structure and size; it has no uniform properties, such as synthetic oil or water. Both $T_1$ of the studied sunflower oil and marine residual fuel oil actually have a distribution, which is usually broader for more viscous oils. Resolving this $T_1$ distribution with a better resolution is complicated, considering that the fit of a sum of more than two exponentials is unstable. Therefore, it is recommended to switch in the actual flowmeter application

to a mapping procedure in which a linear system of equations is solved for a predefined range of $T_1$ and which involves regularization to stabilize the solution of the ill-conditioned inverse problem.
An indication of the feasible quality of the fluid composition determination on the fly is obtained by scaling the initial amplitudes of the exponentials with the amplitude of its equally large pure counterpart, thereby correcting it for the different hydrogen densities of the components. The uncertainty is with 6% substantial and directly related to the accuracy of the $T_1$ value of the oil component to which the nonlinear fit procedure is very sensitive. An underestimated $T_1$ for the most common molecular oil component will be reflected in a systematic overprediction of the tapwater component and underprediction of the oil component. An additional source of uncertainty in the determination of the volume fraction of oil is the initial amplitude of its relaxation curve, for which a lower value is found when the distribution of $T_1$ relaxation times is estimated with a 'mean' value by a single exponential fit.

**Transverse relaxation time**

Knowing the exact value of the $T_2$ relaxation time is not essential for the developed multiphase flowmeter concepts. Only the order of magnitude is important to select an appropriate timing of the r.f. and the gradient pulses in the PGSE method. Nevertheless, the determination of the $T_1$ relaxation times of oil-water samples could benefit from the volume fractions co-determined with the $T_2$ relaxation times using the CPMG method. The estimated volume fractions deviate, with an uncertainty of only 5%, less from the real values than with the incersion recovery data. It is, therefore, recommended to use the reservoir fluid composition obtained with this technology as an input parameter in determining the relevant $T_1$ relaxation times with the INVREC pulse sequence.
The determination of the $T_2$ relaxation times from the CPMG data of oil-water samples with a bi-exponential nonlinear least squares fit, just like that of the $T_1$ relaxation times from the INVREC data, suffers from the ill-posedness of the inverse problem. Although the fit converges better than for the INVREC data, it is advisable to look for more sophisticated CPMG-based hydrocarbon-typing methods developed for well-logging such as '$T_1$ Relaxation Contrast' or 'Diffusivity Contrast' [44].

**Inhomogeneous $B_1$-field**

Many inaccuracies in the measurements are due to the inhomogeneity of the pulsed magnetic field. By making the bore of the flowmeter only slightly larger than the outer diameter of the pipe to keep the format of the flowmeter 'compact', the homogeneity of the pulsed field is sacrificed. With numerical simulations it has been shown that the axial component of $B_1$ is stronger in the zone adjacent to the coil surface and weaker in the center of the coil. Especially in the case of a small coil-to-sample diameter ratio, this results in a wide distribution of flip angles. The different weight that each zone has in the total signal intensity makes that the pulse length of a 90 degrees hard pulse, as found with the AUTOP90 routine, is a little longer than half of the 180 degrees pulse length. Because of the incoherence in the pulse lengths obtained with the faster ALPHA3 routine and the fact that the T1RRT method, the main

multiphase flowmeter principle, only uses FID experiments, the AUTO90 routine is preferred for the determination of the 90 degrees pulse. Despite the long duration of AUTOP90, the number of recalibrations is limited, since the 90 degrees pulse length has a very stable value. Furthermore, it has been demonstrated with a comparison of the signal intensity for water samples of different lengths that the sensitive volume of the coil is approximately equal to the volume bound by the coil. The zone outside of the r.f. coil hardly contributes to the determination of the right pulse length.

### 9.1.2 Rangeability

The long measurement time is a negative aspect of the PGSE method. Because many sequence repetitions are necessary for an acceptable measurement uncertainty, the flow must be very stable. This makes PGSE unsuited for measuring multiphase flow regimes with fast moving flow structures. Although with a lower accuracy, T1RRT can determine the flowrate already from a single cycle. The applicability of the T1RRT method has therefore been tested for both single-phase flow and two-phase air-water stratified and slug flow, while research into the PGSE method is limited to single-phase flow.

The design of the flowmeter operating according to the T1RRT method should match the position of the r.f. coils on the $T_1$ of the fluids to be measured. Thermal equilibrium of the NMR signal detected by the first coil should be avoided at all times. Also, the signal should not become weak with respect to the noise.
The number of r.f. coils required depends on the number of reservoir fluid components to be measured. In order to measure two-phase air-water flow, the flowmeter prototype is equipped with two r.f. coils. If the method is applied to single-phase flow, it is in principle sufficient to use only a single r.f. coil. Analysis based on the fraction between the signal intensities in the second and first r.f. coil, like in the two-phase flow application, is, nevertheless, preferred, because of its better performance if turbulence is present. For accurate velocity measurements, it is important that the range of the flowmeter falls within the steepest part of the signal-fraction curve. Not only is maximum resolution achieved by doing so, the uncertainty by repeatability is also directly related to the slope of the this curve.
The lower velocity limit is best noticeable in the laminar single-phase flow measurements with the more viscous glycerol-water mixture, because the signal in the first probe is for a lower $T_1$ only sufficiently far below the thermal equilibrium at a higher velocity. When the velocity is made dimensionless, by using the fraction of the $T_1$ relaxation time with the polarization length up to the first probe, the uncertainty due to repeatability then reaches a constant level for the studied flowrange, at a gradient $\mathrm{d}(s_{y,2}/s_{y,1})/\mathrm{d}v_y^*$ of 0.25. In the current configuration, with the first r.f. coil at 0.5 m and the second r.f. coil at 2.5 m from the magnet entrance, this corresponds to a $v_y^*$ range of 0.24 – 4.47. This implies that the range over which the flowmeter can accurately measure the bulk velocity is 0.05 – 0.94 m s$^{-1}$ for tapwater with a typical $T_1$ of 2.5 s, and 0.84 – 15.7 m s$^{-1}$ for light oils, like sunflower oil, with a typical $T_1$ of 0.15 s. For petroleum industry applications, with expected maximum superficial liquid velocities of 5 m s$^{-1}$, the designed flowmeter operates best at a $T_1$ of 0.5 s. The flowmeter design is unsuited to measure flowrates of highly viscous fluids, like marine residual fuel oil,

with the T1RRT method, since thermal equilibrium is reached before the liquid enters the first r.f coil.

For the PGSE method, it is favorable to have the signal as strong as possible, for which reason the measurements are carried out with the second probe of the flowmeter. Unlike the T1RRT method, the PGSE method is capable of measuring the velocity of more viscous liquids, with a very short $T_1$. To avoid ambiguous velocity measurements by phase wrapping, the pulse sequence parameters $\delta_G$, $\Delta_G$ and $G_y$ should preferably be selected such that phase shift $|\Delta\phi_{2\tau}|$ at maximum velocity never exceeds $\pi/2$. An upper limit on the measurable velocity range cannot be given based on this study. Measurements were made over a range of 0 – 0.8 m s$^{-1}$ without any problems. A point of attention is the attenuation caused by turbulent diffusion, in the presence of magnetic field gradients. Although the turbulent intensity has no significant influence on the average velocity measurements, it can affect the accuracy of the holdup determination considerably if the reference value of the signal strength for a fully-filled pipe, which is measured under static conditions, is not corrected.

### 9.1.3 Flowmeter performance T1RRT method

A comparison of numerical simulations with experimental results for laminar and turbulent pipe flow in the velocity range of 0 – 0.8 m s$^{-1}$ demonstrates that the T1RRT method is an appropriate flowmeter principle for single-phase flow if the following sources of errors and uncertainties are addressed. Technical aspects that need to be tackled in the same way when the T1RRT method is applied to multiphase flow.
The flowmeter achieves a very good linearity as long as the non-rectangular shape of the polarizing magnetic field is taken into account. The permanent magnetic field starts already centimeters in front of the physical entrance of the flowmeter and gradually grows stronger to the inner magnet's field strength $B_0$. With Lagrangian simulations of the magnetization build-up, based on Hall-sensor measurements of the magnet's entrance area, it has been found that the premise of a perfectly uniform field results in a velocity bias that increases with velocity. The model used by the flowmeter is best adapted for the incorrect polarization length by raising it with the distance, equivalent to the asymptote of the effective field deviation when having a uniform magnetic field strength. This has two advantages: (i) the asymptote is universal for all velocity distributions, and (ii) the velocity dependency has been removed, since the correction with the asymptote as added length leads to a small, but constant, positive velocity bias. This approach cannot remove the clear dependence of the velocity bias on the $T_1$ relaxation time. The systematic error is larger for lower $T_1$ relaxation times. The overestimation at the same average velocity is also greater for laminar than for turbulent flow due to the stronger non-uniformity of its velocity profile.

A substantial part of the inaccuracy in the flowmeter application is caused by lead pick-up on account of the samples extending the sensitive region of the r.f. coil considerably. Although the pulsed $B_1$ field weakens to the ends of the r.f. coil and it has been shown that the sensitive volume of the coil is about the size of the volume bound by the coil, protons in the area outside the coil also contribute to the measured NMR signal due to the external field. Restricting the

active volume of the coil to the central part of the coil with slice-selective excitation could prevent this. For the velocity measurements with the T1RRT method, the effects are limited as the velocity is determined from the ratio of the signal intensities measured in both coils. Because the r.f. coils are the same, the factors of volume in the signal strength cancel out. In the same way, the influence of a less homogeneous $B_0$-field than possible at the level of the measuring coils due to the non-optimal mounting of the shimming coils is also resolved.

**Single-phase flow**

The use of the plug flow model in the analysis of the NMR signals is a source of systematic errors in the evaluation of laminar flow. For turbulent flow, it is fair to use the much simpler plug flow approach. The almost coinciding simulations for plug flow and the power law profile show that the presence of no-slip at the wall is of secondary importance, though the linearity of the measurements is slightly better for the power law profile. This is good news for the flowmetering of multiphase flows. The T1RRT technique does not provide information about the velocity distribution. Because the multiphase flow regimes to be measured are ususally turbulent, it will only be necessary to investigate how to deal with the phase slip. As with turbulent single-phase flow, the no-slip at the wall will be of little influence.
The velocity bias is larger than expected for estimating the non-uniformity of the polarizing magnetic field in the entrance area of the magnet with the asymptotic equivalent of its field deviation. In the laminar measurements a constant velocity bias of about 4 cm $s^{-1}$ is found, while the error varies in the case of turbulent pipe flow between -2 and 2 cm $s^{-1}$. Turbulent measurements at two different pipe diameters show that the cause is to be found in the model of the velocity profile that is used in processing the NMR signals. Each velocity has a different weight in the signal intensity due to the exponential relationship between the residence time and the magnetization build-up. The better the flow profile is modeled, the more constant the velocity bias is, which would allow for a simple correction afterwards.
Repeatability is the largest contributor to the total accuracy. From 10 repetitions of the sequence per flow measurement, the standard deviation of the signal strength along the series of FIDs converges to a fixed value. The average of 30 T1RRT experiments results in a rate performance with 95% confidence level of 0.7% in the flowrate of single-phase flow.

**Stratified flow**

It should be noted that the assessment of the two-phase flowmeter performance is seriously hampered by the uncertainty in the validation measurements with the wiremesh sensor on acount of its systematic overestimation of the liquid volume fraction. Nevertheless, experiments have shown that the flowmeter in the current configuration and set-up is not precise enough to measure the liquid flowrate of horizontal co-current stratified air-water flow at low bulk velocities in the range of 0.07 – 0.26 m $s^{-1}$. Issues with the holdup determination are primarily responsible for this. After all, the bulk velocities are within the range for which the uncertainty due to repeatability, as found for single-phase flow, is sufficiently reliable.

Underestimation of the liquid holdup is a general problem of the T1RRT method. Especially the dielectric losses in the organic material of which most samples consist are a major problem related to the probehead design, causing loss of linearity between the NMR signal strength and the filling factor of the probe. Much of the adverse effect this has on the probe efficiency has been successfully tackled by placing strip-shields between the sample and the coils, but loss of signal intensity can not be completely prevented and is compensated for with a calibration curve.
The large distance between the two coils with which the components are distinguished from one another based on the contrast of their $T_1$ relaxation time is another factor of a technical nature that contributes to the directional bias error in both the velocity and the holdup. The assumption of a constant average water level in the flowmeter, a starting point of the measuring principle, is therefore difficult to guarantee. With a sensitivity study it has been shown that a weak gradient of only $-0.075°$ in the water level can cause a velocity bias of up to 3 cm $s^{-1}$ and a holdup bias of 0.06. When installing the flowmeter, flow disturbances, such as in- and outflow effects, must therefore be avoided as much as possible; ideally the flow is fully-developed. Since small gradients are not unlikely in practical applications, the problem could be solved by equipping the flowmeter with an additional third coil. The algorithm can then be adjusted for the existence of a gradient in the liquid level. If there is no adverse effect on the velocity range to be measured, it may also be considered to place the coils closer to each other.

Regarding the flowmeter performance with respect to the implementation of the T1RRT measuring principle, the findings suggest the following.
Because of the higher signal strength, the liquid holdup is best determined from the signal of the second r.f. coil. It has been shown that it is advantageous that the signal has virtually reached the thermal equilibrium state, since this prevents errors in the velocity from propagating in the liquid fraction.
With simulations of the artificial two-dimensional velocity profile of the liquid phase of both stratified smooth and stratified wavy flow with regular 2D waves, the shape of which changes under the influence of shear stress and the type of waves at the interface, it has been demonstrated that the velocity bias introduced by the use of a plug flow model is not too bad for the flowrange studied. A velocity underestimation of 0.5 cm $s^{-1}$ is expected for the stratified smooth sub-regime and of 0.5 – 1 cm $s^{-1}$ for the stratified wavy cases. The simulations predict only at higher bulk velocities a slight underestimation of the holdup. The reinforcing effect, the weakness of the T1RRT method, can thus be excluded as a source of systematic errors. Moreover, the flowmeter routine does not have to be adjusted for phase slip and can use the plug flow model without any problems for the stratified sub-regimes studied.

In terms of repeatability, the flowmeter is as accurate as the velocity determination. With a relative uncertainty of 1 – 6% at 95% confidence level and 30 repetitions of the T1RRT sequence, decreasing with the flowrate, the flowmeter performs worse than in the single-phase flow measurements. Most likely because the flowmeter operates in the least accurate part of its bandwidth owing to the low bulk velocity. However, the expanded uncertainty is insufficient to explain the directional bias error in the flowrate, even if a correction is applied

for the systematic error in the validation measurements with the wiremesh sensor. There is clear evidence that the presence of a gradient in the water level has a strong negative effect on the reliability of the measurements. Additional reasons for the errors are the deviation from a plug flow velocity distribution and the spatial dependence or the added length by the non-uniform polarizing magnetic field.

**Slug flow**

While stratified flow has a certain degree of time independence, that is not the case for elongated bubble and slug flow. This study was undertaken to investigate how the procedure of determining the average flowrate from the raw data should be altered to the flow structures present in slug flow. The T1RRT method is adapted to horizontal slug flow by using clustering to distinguish the slug section data from the film section data, whereafter the average liquid flowrate is calculated by means of the unit-cell concept. The cluster algorithm only works well if the position of the coils is finely tuned to the flow conditions. A design criterion is proposed that can serve as guideline to ensure that the signal levels associated with the film and slug section are sufficiently far apart. Because clustering is a statistical average technique that requires a few hundred data points, a 'shift register' can be used to calculate a new average after each cycle of the T1RRT sequence. As the flow conditions need to be stable for several minutes, only gradual regime transitions are possible.
Because the velocities in particularly the slug section have too wide a distribution for the bandwidth of the current flowmeter design, the performance of the flowmeter cannot be quantified for the circumstances studied.
It has been shown that it is particularly important that the flowmeter algorithm incorporates the liquid shedding and pickup processes that take place in slug flow. This is also an important conclusion for NMR flowmetering concepts that determine the velocity with a different NMR method, because they also use the degree of magnetization build-up during the residence time in the polarizing magnetic field to determine the fraction composition of multiphase flows. Incorrectly assuming a constant velocity during the transit time through the flowmeter results in an underestimation of the liquid holdup in the film sections and an overestimation of the liquid holdup in the slug sections. In addition, the T1RRT method overestimates the velocity in the slug sections and underestimates it in the film sections. When the presence of liquid shedding and pickup in slug flow is ignored, too low flowrates are found by the T1RRT method.

**Level of accuracy**

Based on repeatability of the flowrate for a 95% confidence level, the T1RRT metering principle meets the requirements set by the industry for reservoir management and well testing. With an upper range value of 6% for the measured flowrate of stratified flow, the method is in its current form just too inaccurate to qualify for production allocation at low bulk velocities. It should be noted that this is mainly due to the fact that the experiments were carried out in the flowmeter range with the lowest sensitivity. For higher velocities, the repeatability is also within the desired range for production allocation. However, it is unlikely that the high accuracy required for fiscal metering will be achieved by low-resolution NMR systems.

The repeatability of the liquid holdup is with 1.2% excellent for both the stratified flow measurements and the film sections in slug flow. Even in the slug sections the repeatability in the liquid holdup almost meets the upper limit of 2% in the water-cut. The relative uncertainty in the liquid holdup found for the slug sections, which increases with the gas fraction up to 2.4%, is surprisingly good considering the lower signal intensity for higher velocities, not to mention that the slug velocities are outside the flowmeter's bandwidth.
Above all, there is thus the need to improve the flowmeter model in such a way that the directional bias in the velocity and holdup measurements is reduced.

### 9.1.4 Flowmeter performance PGSE method

The preliminary study carried out here demonstrates that the PGSE method is capable of determining the average streamwise velocity of single-phase flow with a reasonable accuracy in a range of $0 - 0.8$ m s$^{-1}$, irrespective of the velocity profile. The greatest contributors to the uncertainties in the PGSE method are associated with technical problems involved in the production of the magnetic field gradient.

The poor uniformity of the gradient field due to the closely spaced gradient modules has major consequences on the accuracy of the PGSE measurements. The gradient is only approximately uniform in a small zone of about $3 \times 3 \times 3$ cm and increases in strength with the pipe diameter. Nevertheless, the linear response of the flowmeter to velocity is excellent, if the phase shift is scaled with the gradient strength obtained from calibration for the respective pipe diameter. This is, of course, no solution for future multiphase flow applications. The calibrated effective gradient strength is only valid for a certain phase distribution and the velocity profile must be fairly uniform with the flowrate. This is very unlikely in the case of multiphase flow; both because of its unsteady nature with constantly changing flow structures and the fact that the velocity profile changes under the influence of phase slip. The gradient field really has to be more homogeneous to deal with those spatial variations. Slice-selection is suggested to reduce the area in the streamwise direction with a non-linear gradient to a minimum.

Eddy-currents that generate both homogeneous and gradient fields, depending on the nearby conductive surfaces in which they are induced, are the other common source of errors in pulsed gradient measurements to be reckoned with. To minimize their bias, it is important that the gradient pulses succeed the r.f. pulses on the shortest waiting period possible. A strategy has been proposed, based on calibration against a flowmeter standard for the pipe diameter and the pulse sequence settings that can be selected to cover the desired $T_2$-range, to correct the velocity in the post-processing of the NMR signals for (i) the systematic overestimation of the effective gradient strength and (ii) the velocity offset that they cause.

When the NMR velocity is corrected for the bias by eddy currents, a maximum directional bias error of 2 cm s$^{-1}$ is found, just like in the T1RRT measurements. The relative uncertainty of $2 - 6$% for a 95% confidence level and a series of 20 echoes is a lot worse than in the single-phase flow measurements with the T1RRT method. Although an objective judgment

is not entirely possible due to the sub-optimal conditions and the ill-chosen pulse sequence settings, the performance is not good enough to meet the industry requirements, especially if the holdup is yet to be determined. Adding to this, the comparatively long measurement duration (for 20 echoes, the composition of the flow at a bulk velocity of 1 m $s^{-1}$ must remain constant for at least 2.5 s, i.e. a length of 2.5 m), which is unsuitable for intermittent flows, makes us conclude that a less sophisticated NMR measurement method, like T1RRT, is the better option as a measurement principle for a multiphase flowmeter.

## 9.2 Recommendations for future work

From a technical point of view, developments with regard to NMR hardware have progressed considerably in the last decade. Especially the introduction of Halbach magnets for use in flowmeters of this type has been a technical breakthrough. The special way in which these rare earth magnets are built-up means that stronger, homogeneous, magnets can easily be constructed that, despite the large bore-magnet size ratio, are much less bulky and heavy than the H-configuration permanent magnet used in this study [45, 89]. Beyond the fact that they are easier to handle, this is beneficial for the signal-to-noise ratio for two reasons. In the first place, the sensitivity of the meter is enhanced because the magnitude of the built-up magnetization is directly proportional to the field strength of the polarizing magnet. Secondly, the larger bore makes it possible to increase the coil-to-sample diameter ratio, which improves the homogeneity of the pulsed magnetic field and also reduces the effect of eddy-currents in pulsed gradient field experiments. Moreover, Halbach magnets have very small stray fields and can be opened and closed around the petroleum carrying pipeline without a significant force. Much can also be gained by the use of automatic tuning and matching of the probe for the changing filling factor during the course of the experiment [115]. The use of varicaps strives for a constant quality factor of the probe, which, in addition to the applied strip-shield, is a rapid way to compensate for the signal loss that might occur by detuning and dematching of the probe [51]. Technically, there are therefore no serious obstacles to the development of an NMR multiphase flowmeter.

However, a solution still has to be found for the calibration measurements of the pulse length and the $T_1$ relaxation time, which cannot be carried out on the fly with the standard pulse sequences, as these require a fully polarized signal. This is very important, because the reliability of the flowmeter depends to a large extent on the accuracy with which the $T_1$ relaxation times are measured. A relevant point is to evaluate whether the values of the $T_1$ relaxation times are precise enough to justify the determination from table values on the basis of external pressure and temperature measurements. Another option is to investigate if the technology for well-logging of flowing samples as e.g. developed by Masak et al. [171] can be adjusted for higher flowrates. Associated is the question of how much the reservoir properties change over time, and what the consequences are if multiple production streams of individual wells or production facilities are commingled.
Fortunately, no large drift was observed in the pulse length, making the calibration frequency for this purpose low. When autotuning and matching is implemented, it is expected that

the need for correcting the pulse length will decrease even further. A big advantage of the T1RRT method is, moreover, its robustness regarding the NMR settings. Even an improper pulse length has a minor effect on the accuracy.

As indicated above, the T1RRT method has more potential than the PGSE method in being a fast enough algorithm for multiphase flowmetering. The real challenge lies in making the measurement principle suitable for three-phase flows. The T1RRT method is applicable to light and medium hydrocarbons, but unfortunately a different method will have to be considered for the velocity measurement of very viscous crude oils, like marine residual fuel oil. Their $T_1$ relaxation time is so short, that the magnetization has already reached the thermal equilibrium at the first r.f. probe, even if an additional probehead is placed further upstream [94, 95, 149].

### 9.2.1 Improvements of the T1RRT measuring principle in general

Although it has been demonstrated that the plug flow approach can be adequately used in the case of the turbulent single-phase and stratified flow measured here, the numerical simulations show that the flow model is the cause of the remaining velocity bias that cannot be explained with the non-uniformity of the permanent magnetic field in the entrance area of the flowmeter. The performance of the T1RRT method would benefit if a one-dimensional velocity profile could be measured, instead of a single bulk velocity, by applying a vertical frequency encoding gradient when the signal is received. Because FIDs decay much faster under influence of a gradient field, the pulse sequence should also employ spin echoes instead, whereby, the measuring principle remains the same.

A point of concern is the limited range for the absolute velocity with the T1RRT method. To increase the operational envelope to high velocities, the magnet and, therefore, the flowmeter becomes extremely long, which means that problems due to a slight slope in the liquid level are more likely to occur. It is worth investigating whether other methods, such as the efflux method (see section 1.4.3), which also use simple pulse sequences that work best for low-resolution NMR, are not more suitable for determining the flow velocity. Efflux methods should also be better able to measure the velocity of highly viscous liquids, which is a weakness of the T1RRT method.

In addition, a way must be found to identify which flow regime is being measured, since slug flow data must be analyzed using a different method than the stratified and single-phase flow data. The variance of the signal seems to be a good measure for this, because it will be much higher for intermittent flow than for layered separated flow. Discrimination of the flow regimes based on a pressure sensor is another possibility.

In the case of slug flow, much can also be gained by improving the clustering technique that is combined with the unit-cell concept. Neglecting the liquid shedding and pickup processes causes a very large systematic bias in the flow measurements, which increases with the difference between the film and slug velocity. Particularly disadvantageous for the T1RRT method

is that the bias, which is introduced by this in the velocity, is reinforced in the liquid holdup. Even when it is decided to determine the velocity with an alternative NMR technique, it remains very important for the fraction determination to capture the liquid shedding and pickup processes properly, in the data analysis. The measured velocity is only a snapshot, while the fraction is derived from the signal intensity determined by the velocity encountered along the entire trajectory in the polarizing magnetic field. It has been shown that the extra clustering level, intended for the mixing zone in the liquid slugs, is effective against the introduction of systematic errors by the pickup process. Because the flowmeter has been operating outside its bandwidth, additional research is needed to determine whether the proposed solution is capable of filtering enough data points associated with liquid pickup from the signal. Similarly, a procedure should be developed to distinguish the zone controlled by liquid shedding from the rest of the film section. The problem may be overcome by the implementation of a fourth lower cluster level that classifies the points associated with liquid shedding.
If the extra cluster levels fail to resolve the issues, it can be investigated whether the simple unit-cell model proposed in section 8.6.3 is able to estimate the systematic bias with sufficient accuracy so that it can be corrected for afterwards. The focus should be on verifying whether the assumption of a linear gradient in the residence time over a distance $L_{sp}$ from the front of the slug and a distance $L_{ss}$ from the rear of the slug is justified. Points for improvement are the description of the velocity in the mixing zone and the deceleration of the liquid film under influence of wall and interfacial shear.

### 9.2.2 Three-phase flow application

In order to make the measurement principle applicable to three-phase flow, the typical NMR properties of the components must be exploited to differentiate the hydrocarbons from the water and the natural gas from the fluids. Water usually has medium $T_1$, $T_2$ and diffusion coefficient values. Natural gas is typified by very long $T_1$, but very short $T_2$ relaxation times and is highly diffusive. The characteristics of oil vary greatly and depend to a large extent on the viscosity. The characteristics of lighter oils are comparable to water, but $T_1$, $T_2$ and the diffusion coefficient values decrease with increasing viscosity.

As long as there is sufficient contrast between the $T_1$ relaxation times of the components, the T1RRT method can theoretically be employed for three-phase flow, by expanding the number of coils at different strategic streamwise positions in the polarizing magnetic field of the flowmeter, depending on the number of parameters to be determined. Because the NMR signals are a superposition of the signals from oil, water and natural gas, these unknown parameters can be derived by resolving the system of equations that describes the course of the signal at the different coil positions.
Besides, the recently introduced NMR flowmeters by Spinlock and KROHNE use an ingenious approach to vary the polarization length. They are able to rotate a number of segments of the pre-polarizing Halbach magnet mechanically, to change the polarization length over the course of a measurement [7, 101]. This has the advantage that measurements are always taken at the same position, so that gradients in the liquid level no longer play a role.

Because of the safety measures that have to be taken to measure with natural gas under high pressure, the feasibility study of the T1RRT method on three-phase flow is best started by determining the flowrates of oil and water in three-phase air-water-oil flow instead of in natural gas-water-oil flow. Given the experiences with the bi-exponential fits to determine the $T_1$ and $T_2$ relaxation times of oil-water mixtures in the static dummy tests with the INVREC and CPMG sequences in chapter 5, it is questionable whether the T1RRT method is accurate enough to work out the liquid velocities in three-phase flow regimes. To start with, the best approach is to look at the flow regimes in which there is no or little slip between oil and water, that is where the oil and water are well mixed. To solve the 4 unknowns (the 3 holdups and the liquid velocity) using an iterative process, the flowmeter must be expanded to a minimum of three r.f. coils. The current configuration with two measurement sections will suffice if the T1RRT method is only used to determine the composition of the stream and the velocity is obtained in a different way. Two r.f. coils are also enough for two-fluid oil-water applications.

In this work, important knowledge has been gathered about the influence of phase slip on the quality of using a plug flow model for measurements on two-phase air-water stratified and slug flow. The situation is much more complex in three-phase oil-water-air flow. In addition to slip between the gas and the compound liquid phase, slip can also occur between the oil and water phase, though to a lesser extent than between the gas and the liquid phase. The difference in velocity between the oil and the water phase is largely determined by the degree of mixing. When the liquids form a homogeneous dispersion of either 'water in oil' or 'oil in water', the slip between the oil and water will be virtually absent. Under these circumstances, in which oil and water can be treated as one liquid phase, it is expected that the conclusions regarding the use of the plug flow model for two-phase flow will also be applicable to the three-phase flow regimes with the same basic flow patterns. For the other regimes in which oil and water are more separated, the first question that needs to be answered is to which extent the phase slip between the two liquids will play a significant role in the functioning of the flowmeter making use of the plug flow model.
Related to this is the question whether the streamwise velocity of a fluid element changes in the presence of flow structures during its trajectory along the flowmeter and, if so, what the influence of this is on the fraction determination from the built-up magnetization. In chapter 8, clustering was used as a powerful tool to filter out the signals biased by those velocity changes from the determination of the average slug velocity. It is worthwhile to examine whether a similar approach is also effective for three-phase intermittent flow. Especially since slug flow is the most commonly encountered flow regime in oil field operations [5].

So far, the focus of the research has been on determining the liquid flowrates in the presence of an undetectable air phase. The ultimate goal is to simultaneously measure the flowrate of the gas phase too. The ability of the NMR flowmeter to measure natural gas has yet to be proven. Compared to the measurements of the liquid phase, there are two factors that make gas more difficult to detect: (i) due to the low hydrogen density, the signal intensity will be significantly lower than that of the liquid phase and (ii) the FID decays very fast because of the high molecular diffusivity and the very short $T_2$ relaxation time. For the latter, if the FID decays too fast in the probe's dead time, it is better to consider the use of spin echoes,

leaving the described measurement concept otherwise unchanged. The measurement method could be further improved for measurements with natural gas by taking advantage of the large difference in diffusion coefficient between the gas and the liquid, just like in the 'Diffusivity Contrast' method developed for well-logging purposes [44]. This technique suppresses the magnetization of the gas phase in one measurement with crusher gradient pulses that enhance the dephasing process. The gas contribution can be determined from the difference with the follow-up measurement in which no gradient fields are applied.

### 9.2.3 Concluding thoughts

NMR is a very promising technique for multiphase flowmeters, because, in contrast to current technologies, it is possible to determine both the individual velocities and volume fractions of the production stream with the same measuring principle. Moreover, NMR sensors do not disturb the flow, as is the case with the Venturi meters and orifice plates, which are currently widely used in the offshore industry for determining the multiphase flow velocity. Another advantage is the fact that the NMR measuring principle is not harmful to the operators, such as hold-up techniques based on radiation attenuation, like gamma densitometry, which are used in most industrial multiphase flowmeter solutions, because they can achieve a much higher accuracy than the various tomography methods, like electrical impedance tomography, and work for the full gas volume-fraction range [90].
Because the flowmeter must provide a reliable and low-maintenance operation over a circa 10 year period, due to its application in hard-to-reach areas, the method is currently restricted to low-resolution NMR with permanent magnets. Unfortunately, this means that the possibilities of NMR technology cannot yet be fully utilized. Directly determining the velocity with advanced gradient pulse sequences does not seem feasible with low-resolution NMR. It also excludes the use of spectral NMR to determine the precise composition of the liquids from the chemical shift. However, much depends on the pace at which the hardware is improved. If hardware developments continue to advance as fast as in recent years, medium-resolution NMR and thus these applications would come within the limits of what is possible. For now, the most important step of improvement seems to be the procedure of measuring the velocity.

# Bibliography


[1] M. S. A. Abouelwafa and E. J. M. Kendall, "In-situ volume fraction determination in multi-component mixtures using pulsed nuclear magnetic resonance," *Can. J. Chem. Eng.*, vol. 58, pp. 643–645, 1980.

[2] A. Abragam, *The Principles of Nuclear Magnetism*, ser. The International Series of Monographs on Physics. Oxford at the Clarendon Press, 1961.

[3] M. Açikgöz, F. França, and R. T. Lahey Jr, "An experimental study of three-phase flow regimes," *Int. J. Multiphase Flow*, vol. 18, no. 3, pp. 327–336, 1992.

[4] S. S. Agrawal, G. A. Gregory, and G. W. Govier, "An analysis of horizontal stratified two phase flow in pipes," *Can. J. Chem. Eng.*, vol. 51, pp. 280–286, 1973.

[5] American Petroleum Institute (API), Recommended Practice 86 *Measurement of Multiphase Flow*, 1st ed., September 2005.

[6] N. Andritsos and T. J. Hanratty, "Interfacial instabilities for horizontal gas-liquid flows in pipelines," *Int. J. Multiphase Flow*, vol. 5, pp. 583–603, 1987.

[7] M. Appel, J. J. Freeman, and D. Pusiol, "Robust multi-phase flow measurement using magnetic resonance technology," in *SPE Middle East Oil and Gas Show and Conference*, Manama, Bahrain, September 25–28, 2011, SPE 141565.

[8] S. Ashkuri and T. J. Hill, "Measurements of multiphase flows in crude oil production systems," *Pet. Rev.*, vol. 39, no. 466, pp. 14–16, November 1985.

[9] P. W. Atkins, *Physical Chemistry*, 6th ed. Oxford University Press, 1998.

[10] I. Atkinson, B. Theuveny, M. Berand, G. Conort, J. Groves, T. Lowe, A. McDiarmid, P. Mehdizadeh, P. Pericot, B. Pinguet, G. Smith, and K. J. Williamson, "A new horizon in multiphase flow measurement," *Oilfield Rev.*, vol. 16, no. 4, pp. 42–63, Winter 2004/2005.

[11] A. A. Ayati, J. Kolaas, A. Jensen, and G. W. Johnson, "A PIV investigation of stratified gas–liquid flow in a horizontal pipe," *Int. J. Multiphase Flow*, vol. 61, pp. 129–143, 2014.

[12] A. A. Ayati, J. Kolaas, A. Jensen, and G. W. Johnson, "Combined simultaneous two-phase piv and interface elevation experiments in stratified gas/liquid pipe flow," *Int. J. Multiphase Flow*, vol. 74, pp. 45–58, 2015.

[13] R. C. Baker, *Flow Measurement Handbook - Industrial Designs, Operating Principles, Performance, and Applications*, 1st ed. Cambridge University Press, 2000.

[14] F. Barberon and J. Leblond, "Intermittent two-phase flow study by NMR," *C. R. Acad. Sci. Paris - Series IIC - Chimie/Chemistry*, vol. 4, pp. 853–856, 2001.

[15] A. Bayer, "The use of $T_1/T_2$-relaxation effects for NMR sensors in multiphase flow," PhD thesis, Cranfield University, 1994.

[16] A. Bayer, "Method and apparatus for the determination of the individual mass flow rates of a multicomponent flow," European Patent EP0 691 526B1, Nov. 21, 2001.

[17] C. Beal, "The viscosity of air, water, natural gas, crude oil and its associated gases at oil field temperatures and pressures," *Trans. AIME*, vol. 165, pp. 94–115, 1946.

[18] C. R. Becker, L. R. Schad, and W. J. Lorenz, "Measurement of diffusion coefficients using a quick echo split NMR imaging technique," *Magn. Reson. Imaging*, vol. 12, no. 8, pp. 1167–1174, 1994.

[19] G. B. Benedek and E. M. Purcell, "Nuclear magnetic resonance in liquids under high pressure," *J. Chem. Phys.*, vol. 22, no. 12, pp. 2003–2012, 1954.

[20] W. Bergmann and B. Knüttel, "Method and apparatus for measuring the quantity of a fluid flowing through a pipe by means of nuclear magnetic spin resonance," U.S. Patent US4 110 680, Aug. 29, 1978.

[21] V. Bertola, "Slug velocity profiles in horizontal gas-liquid flow," *Exp. Fluids*, vol. 32, pp. 722–727, 2002.

[22] V. Bertola and E. Cafaro, "Slug frequency measurement techniques in horizontal gas-liquid flow," *AIAA J.*, vol. 40, no. 5, pp. 1010–1012, 2002.

[23] T. Bikmukhametov and J. Jäschke, "First principles and machine learning virtual flow metering: A literature review," *J. Petrol. Sci. Eng.*, vol. 184, no. 106487, 2020.

[24] A. M. Bilgic, J. W. Kunze, V. Stegemann, J. Hogendoorn, L. Cerioni, and M. Zoeteweij, "Multiphase flow metering with nuclear magnetic resonance," *tm – Technisches Messen*, vol. 82, no. 11, pp. 539–548, 2015.

[25] M. Birvalski, M. J. Tummers, R. Delfos, and R. A. W. M. Henkes, "PIV measurements of waves and turbulence in stratified horizontal two-phase pipe flow," *Int. J. Multiphase Flow*, vol. 62, pp. 161–173, 2014.

[26] M. Birvalski, M. J. Tummers, and R. A. W. M. Henkes, "Measurements of gravity and gravity-capillary waves in horizontal gas-liquid pipe flow using PIV in both phases," *Int. J. Multiphase Flow*, vol. 78, pp. 102–113, 2016.

[27] F. Bloch, "Nuclear induction," *Phys. Rev.*, vol. 70, no. 7-8, pp. 460 – 474, 1946.

[28] N. Bloembergen, E. M. Purcell, and R. V. Pound, "Relaxation effects in nuclear magnetic resonance absorption," *Phys. Rev*, vol. 73, no. 7, pp. 679–712, 1948.

[29] B. Blümich, *Essential NMR*. Springer, 2005.

[30] L. W. Bosart and A. O. Snoddy, "Specific gravity of glycerol," *Ind. Eng. Chem.*, vol. 20, no. 12, pp. 1377–1379, 1928.

[31] C. E. Brennen, *Fundamentals of Multiphase Flow*, 1st ed. Cambridge University Press, 2005.

[32] R. J. S. Brown, "Proton relaxation in crude oils," *Nature*, vol. 189, no. 4762, pp. 387–388, 1961.

[33] Bruker BioSpin, *Gradient Shimming Principles and Practical Aspects*, November 2005.

[34] W. Burger and M. J. Burge, *Principles of Digital Image Processing: Fundamental Techniques*, ser. Undergraduate Topics in Computer Science. Springer-Verlag London Ltd., 2009.

[35] W. Burger and M. J. Burge, *Principles of Digital Image Processing: Advanced Methods*, ser. Undergraduate Topics in Computer Science. Springer-Verlag London Ltd., 2013.

[36] E. E. Callaghan and S. H. Maslen, "The magnetic field of a finite solenoid," NASA, TN D-465, October 1960.

[37] P. T. Callaghan, *Principles of Nuclear Magnetic Resonance Microscopy*. Oxford University Press, 2004.

[38] P. T. Callaghan, K. W. Jolley, and C. M. Trotter, "Stable and accurate spin echoes in pulsed field gradient NMR," *J. Magn. Reson.*, vol. 39, pp. 525–527, 1980.

[39] A. Caprihan and E. Fukushima, "Flow measurements by NMR," *Phys. Rep.*, vol. 198, no. 4, pp. 195–235, 1990.

[40] A. Caprihan, J. G. Davis, S. A. Altobelli, and E. Fukushima, "A new method for flow velocity measurement: Frequency encoded NMR," *Magn. Reson. Med.*, vol. 3, pp. 352–362, 1986.

[41] A. Caprihan, S. A. Altobelli, and E. Benitez-Read, "Flow-velocity imaging from linear regression of phase images with techniques for reducing eddy-current effects," *J. Magn. Reson.*, vol. 90, pp. 71–89, 1990.

[42] H. Y. Carr and E. M. Purcell, "Effects of diffusion on free precession in nuclear magnetic resonance experiments," *Phys. Rev*, vol. 94, no. 3, pp. 630–638, 1954.

[43] C.-N. Chen and D. I. Hoult, *Biomedical Magnetic Resonance Technology*. Adam Hilger, 1989.

[44] G. Coates, L. Xiao, and M. Prammer, *NMR Logging Principles and Applications*. Gulf Publishing Company, 1999, Halliburton Energy Services Publication H02308.

[45] L. A. Colnago, F. D. Andrade, A. A. Souza, R. B. V. Azeredo, A. A. Lima, L. M. Cerioni, T. M. Osán, and D. J. Pusiol, "Why is inline NMR rarely used as industrial sensor? challenges and opportunities," *Chem. Eng. Technol.*, vol. 37, no. 2, pp. 191–203, 2014.

[46] J. T. Conway, "Exact solution for the magnetic fields of axisymmetric solenoids and current distributions," *IEEE Trans. Magn.*, vol. 37, no. 4, pp. 2977–2988, 2001.

[47] M. Cook and M. Behnia, "Slug length prediction in near horizontal gas–liquid intermittent flow," *Chem. Eng. Sci.*, vol. 55, pp. 2009–2018, 2000.

[48] S. Corneliussen, J–P. Couput, E. Dahl, E. Dykesteen, K–E. Frøysa, E. Malde, H. Moestue, P. O. Moksnes, L. Scheers, and H. Tunheim, *Handbook of Multiphase Flow Metering*, 2nd ed., Norwegian Society for Oil and Gas Measurement & The Norwegian Society of Chartered Technical and Scientific Professionals, March 2005.

[49] J.-P. Couput, "Subsea multiphase measurements: where we are and what's next from an oil & gas operator perspective," in *29th Int. North Sea Flow Measurement Workshop*, Tønsberg, Norway, October 25–28, 2011.

[50] A. C. L. M. Daalmans, L. M. Portela, and R. F. Mudde, "Development of a NMR multiphase flowmeter," in *Proceedings of ICMF 2007* 6$^{\text{th}}$ *International Conference on Multiphase Flow*, M. Sommerfeld, Ed., Leipzig, Germany, July 9–13, 2007, PS7 11.

[51] R. P. De Alejo, C. Garrido, P. Villa, I. Rodriquez, J. J. Vaquero, J. Ruiz-Cabello, and M. Cortijo, "Automatic tuning and matching of a small multifrequency saddle coil at 4.7 T," *Magn. Reson. Med.*, vol. 51, pp. 869–873, 2004.

[52] P. G. De Gennes, "Theory of spin echoes in a turbulent fluid," *Phys. Lett. A*, vol. 29, no. 1, pp. 20–21, 1969.

[53] M. De Salve, G. Monni, and B. Panella, "Horizontal air-water flow analysis with wire mesh sensor," *J. Phys. Conf. Ser.*, vol. 395, no. 1, 2012, 012179.

[54] F. Deng, G. Chen, M. Wang, D. Xu, S. Chen, X. Zhang, C. Xiong, J. Zhang, Q. Lei, J. Shi, R. Zhao, C. Wang, and Y. Sun, "Magnetic resonance multi-phase flowmeter & fluid analyzer," in *SPE Asia Pacific Oil & Gas Conference and Exhibition*, virtual, November 17 – 19, 2020, SPE-202208-MS.

[55] F. Deng, C. Xiong, S. Chen, G. Chen, M. Wang, H. Liu, J. Zhang, Q. Lei, G. Cao, D. Xu, Y. Tao, and L. Xiao, "A method and device for online magnetic resonance multiphase flow detection," *Pet. Explor. Dev.*, vol. 47, no. 4, pp. 855–866, 2020.

[56] W. J. Duffin, *Electricity and Magnetism*, 4th ed. McGraw-Hill, 1997.

[57] A. E. Dukler and J. Fabre, "Gas-liquid slug flow: Knots and loose ends," in *Multiphase Science and Technology. Two Phase Flow Fundamentals*, G. Hewitt, J. H. Kim, R. T. Lahey, J. M. Delhaye, and N. Zuber, Eds. Wallinford, UK: Begell House, 1994, no. 8, ch. 7.

[58] A. E. Dukler and M. G. Hubbard, "A model for gas-liquid slug flow in horizontal and near horizontal tubes," *Ind. Eng. Chem. Fundam.*, vol. 14, no. 4, pp. 337–347, 1975.

[59] R. Eisberg and R. Resnick, *Quantum Physics of Atoms, Molecules, Solids, Nuclei, and Particles*, 2nd ed. John Wiley & Sons, 1985.

[60] C. J. Elkins and M. T. Alley, "Magnetic resonance velocimetry: applications of magnetic resonance imaging in the measurement of fluid motion," *Exp. Fluids*, vol. 43, pp. 823–858, 2007.

[61] C. J. Elkins, M. Markl, N. Pelc, and J. K. Eaton, "4D magnetic resonance velocimetry for mean velocity measurements in complex turbulent flows," *Exp. Fluids*, vol. 34, pp. 494–503, 2003.

[62] J. Fabre, "Gas-liquid slug flow," in *Modelling and Experimentation in Two-Phase Flow*, ser. CISM Courses and Lectures, V. Bertola, Ed. Udine: Springer, 2003, no. 450.

[63] J. Fabre and A. Liné, "Modeling of two-phase slug flow," *Annu. Rev. Fluid Mech.*, vol. 24, pp. 21–46, 1992.

[64] G. Falcone, G. F. Hewitt, C. Alimonti, and B. Harrison, "Multiphase flow metering: Current trends and future developments," in *SPE Annual Technical Conference and Exibition*, New Orleans, Lousiana, September 30 – October 3, 2001, SPE 71474.

[65] G. Falcone, G. F. Hewitt, and C. Alimonti, *Multiphase Flow Metering, Principles and Applications*, 1st ed., ser. Developments in Petroleum Science. Elsevier, 2010, no. 54.

[66] T. C. Farrar and E. D. Becker, *Pulse and Fourier Transform NMR, Introduction to Theory and Methods*, 1st ed. Academic Press Inc., 1971.

[67] M. Fernandino and T. Ytrehus, "Determination of flow sub-regimes in stratified air-water channel flow using LDV spectra," *Int. J. Multiphase Flow*, vol. 32, pp. 436–446, 2006.

[68] E. O. Fridjonsson, P. L. Stanwix, and M. L. Johns, "Earth's field NMR flow meter: Preliminary quantitative measurements," *J. Magn. Reson.*, vol. 245, pp. 110–115, 2014.

[69] M. Fujimoto, *Physics of Classical Electromagnetism*. Springer, 2007.

[70] E. Fukushima, "Nuclear magnetic resonance as a tool to study flow," *Annu. Rev. Fluid Mech.*, vol. 31, pp. 95–123, 1999.

[71] D. G. Gadian and F. N. H. Robinson, "Radiofrequency losses in NMR experiments on electrically conducting samples," *J. Magn. Reson.*, vol. 34, pp. 449–455, 1979.

[72] P. Galvosas and P. T. Callaghan, "Fast magnetic resonance imaging and velocimetry for liquids under high flowrates," *J. Magn. Reson.*, vol. 181, pp. 119–125, 2006.

[73] J.-H. Gao and J. C. Gore, "Turbulent flow effects on NMR imaging: Measurement of turbulent intensity," *Med. Phys*, vol. 18, no. 5, pp. 1045–1051, 1991.

[74] A. N. Garroway, "Velocity measurements in flowing fluids by MNR," *J. Phys. D: Appl. Phys.*, vol. 7, no. 14, pp. L159–L163, 1974.

[75] J. C. Gatenby and J. C. Gore, "Characterization of turbulent flows by NMR measurements with pulsed gradients," *J. Magn. Reson, Ser. A*, vol. 110, pp. 26–32, 1994.

[76] W. K. Genthe, W. H. Vander Heyden, and D. H. Strobel, "NMR flowmeter employing pulsed magnetization," U.S. Patent US3 419 795, Dec. 31, 1968.

[77] W. Genthe, W. R. Vander Heyden, J. H. Bartocletti, W. S. McCormick, and H. M. Snowball, "NMR applied to flow measurement; an obstructionless, digital flowmeter," *Instrum. Technol.*, vol. 15, no. 11, pp. 53–58, 1968.

[78] S. M. Ghiaasiaan, *Two-Phase Flow, Boiling, and Condensation in Conventional and Miniature Systems*, 1st ed. Cambridge University Press, 2008.

[79] S. J. Gibbs and C. S. Johnson, Jr., "A PFG NMR experiment for accurate diffusion and flow studies in the presence of eddy currents," *J. Magn. Reson.*, vol. 93, pp. 395–402, 1991.

[80] L. F. Gladden, "Nuclear magnetic resonance in chemical engineering: Principles and applications," *Chem. Eng. Sci.*, vol. 49, no. 20, pp. 3339–3408, 1994, Review Article Number 46.

[81] L. F. Gladden and A. J. Sederman, "Recent advances in flow MRI," *J. Magn. Reson.*, vol. 229, pp. 2–11, 2013.

[82] L. F. Gladden and A. J. Sederman, "Magnetic resonance imaging and velocity mapping in chemical engineering applications," *Annu. Rev. Chem. Biomol. Eng.*, vol. 8, pp. 227–247, 2017.

[83] A. Goharzadeh and P. Rodgers, "Experimental characterization of solid particle transport by slug flow using particle image velocimetry," *J. Phys. Conference Series 147, The 6th Int. Symp. on Meas. Tech. for Multiphase Flows*, vol. 147, 2009, 012069.

[84] M. Gopal and W. P. Jepson, "The study of dynamic slug flow characteristics using digital image analysis - part i: Flow visualization," *J. Energy Res. Technol.*, vol. 120, pp. 97–101, June 1998.

[85] G. W. Govier and K. Aziz, *The Flow of Complex Mixtures in Pipes*. Van Nostrand Reinhold Company, 1972.

[86] B. Groß and R. Kosfeld, "Anwendung der Spin-Echo-Methode bei der Messung der Selbstdiffusion," *Messtechnik*, vol. 7/8, pp. 171–177, 1969.

[87] E. L. Hahn, "Spin echoes," *Phys. Rev.*, vol. 80, no. 4, pp. 580–594, 1950.

[88] E. L. Hahn, "Nuclear induction due to free larmor precession," *Phys. Rev.*, vol. 77, no. 2, pp. 297–298, 1950.

[89] K. Halbach, "Design of permanent multipole magnets with oriented rare earth cobalt material," *Nucl. Intrum. Methods*, vol. 169, pp. 1–10, 1980.

[90] L. S. Hansen, S. Pedersen, and P. Durdevic, "Multi-phase flow metering in offshore oil and gas transportation pipelines: Trends and perspectives," *Sensors*, vol. 19, no. 2184, 2019.

[91] R. J. Hayward, K. J. Packer, and D. J. Tomlinson, "Pulsed field-gradient spin echo N.M.R. studies of flow in fluids," *Mol. Phys.*, vol. 23, no. 6, pp. 1083–1102, 1972.

[92] J. Hennig, "K-space sampling techniques," *Eur. Radiol.*, vol. 9, pp. 1020–1031, 1999, Review Article.

[93] N. I. Heywood and J. F. Richardson, "Slug flow of air-water mixtures in a horizontal pipe: Determination of liquid holdup by $\gamma$-ray absorption," *Chem. Eng. Sci.*, vol. 34, pp. 17–30, 1979.

[94] G. J. Hirasaki and K. K. Mohanty, "Fluid-rock characterization and interactions in NMR well logging," Rice University, Houston, US DOE report, September 2002, chapter 2: NMR properties of reservoir fluids.

[95] G. J. Hirasaki, S. W. Lo, and Y. Zhang, "NMR properties of petroleum reservoir fluids," *Magn. Reson. Imaging*, vol. 21, pp. 269–277, 2003.

[96] C. J. Hogendoorn, "Kernmagnetisches durchflussmessferät und verfahren zum betreiben von kernmagnetischen durchflussmessgeräten," European Patent EP2 733 472B1, Jan. 1, 2020.

[97] C. J. Hogendoorn, R. R. Tromp, M. L. Zoeteweij, and O. J. P. Bousché, "Flowmeter with a measuring device implementing a tomographic measuring principle," U.S. Patent US10 151 817B2, Dec. 11, 2018.

[98] C. J. Hogendoorn, L. M. C. Cerioni, R. R. Tromp, M. L. Zoeteweij, and O. J. P. Bousché, "Method for operating a nuclear magnetic flowmeter and nuclear magnetic flowmeter," U.S. Patent US10 393 559B2, Aug. 27, 2019.

[99] C. J. Hogendoorn, R. R. Tromp, L. M. C. Cerioni, M. L. Zoeteweij, and O. J. P. Bousché, "Method for operating a nuclear magnetic flowmeter and nuclear magnetic flowmeter," U.S. Patent US10 466 086B2, Nov. 5, 2019.

[100] C. J. Hogendoorn, R. R. Tromp, M. L. Zoeteweij, J. J. Freeman, and M. Appel, "Nuclear magnetic flowmeter and method for operating nuclear magnetic flowmeters," U.S. Patent US10 234 314B2, Mar. 19, 2019.

[101] J. Hogendoorn, A. Boer, M. Appel, H. de Jong, and R. de Leeuw, "Magnetic resonance technology; a new concept for multiphase flow measurement," in *31th Int. North Sea Flow Measurement Workshop*, Tønsberg, Norway, October 22–25, 2013.

[102] J. Hogendoorn, A. Boer, M. Zoetweij, O. Bouché, R. Tromp, R. de Leeuw, P. Moeleker, M. Appel, and H. de Jong, "Magnetic resonance multiphase flow meter: Gas flow measurement principle and wide range testing results," in *32nd Int. North Sea Flow Measurement Workshop*, St. Andrews, Scotland, October 21–24, 2014.

[103] J. Hogendoorn, A. M. van der Zande, M. Zoetweij, R. Tromp, L. Cerioni, A. Boer, and R. de Leeuw, "Practical experiences obtained with the magnetic resonance multiphase flowmeter," in *33rd Int. North Sea Flow Measurement Workshop*, Tønsberg, Norway, October 20–23, 2015.

[104] D. J. Holland, D. M. Malioutov, A. Blake, and L. F. Gladden, "Reducing data acquisition times in phase-encoded velocity imaging using compressed sensing," *J. Magn. Reson.*, vol. 203, pp. 236–246, 2010.

[105] M. Holz, S. R. Heil, and A. Sacco, "Temperature-dependent self-diffusion coefficients of water and six selected molecular liquids for calibration in accurate $^1$H NMR PFG measurements," *Phys. Chem. Chem. Phys.*, vol. 2, pp. 4740–4742, 2000.

[106] P. J. Hore, *Nuclear Magnetic Resonance*, ser. Oxford Chemistry Primers. Oxford University Press, 2005, no. 32.

[107] D. I. Hoult, "Zeugmatography: A criticism of the concept of a selective pulse in the presence of a field gradient," *J. Magn. Reson.*, vol. 26, pp. 165–167, 1977.

[108] D. I. Hoult, "The solution of the Bloch equations in the presence of a varying $B_1$ field – an approach to selective pulse analysis," *J. Magn. Reson.*, vol. 35, pp. 69–86, 1979.

[109] D. I. Hoult, "The principle of reciprocity in signal strength calculations – A mathematical guide," *Concepts Magn. Reson.*, vol. 12, pp. 173–187, 2000.

[110] D. I. Hoult and P. C. Lauterbur, "The sensitivity of the zeugmatographic experiment involving human samples," *J. Magn. Reson.*, vol. 34, pp. 425–433, 1979.

[111] D. I. Hoult and R. E. Richards, "Critical factors in the design of sensitive high resolution nuclear magnetic resonance spectrometers," *Proc. R. Soc. London, Ser. A*, vol. 344, no. 1638, pp. 311–340, 1975.

[112] D. I. Hoult and R. E. Richards, "The signal-to-noise ratio of the nuclear magnetic resonance experiment," *J. Magn. Reson.*, vol. 24, pp. 71–85, 1976.

[113] M. I. Hrovat and C. G. Wade, "NMR pulsed gradient diffusion measurements. II. residual gradients and lineshape distortions," *J. Magn. Reson.*, vol. 45, pp. 67–80, 1981.

[114] M. D. Hürlimann and L. Venkataramanan, "Quantitative measurement of two-dimensional distribution functions of diffusion and relaxation in grossly inhomogeneous fields," *J. Magn. Reson.*, vol. 157, pp. 31–42, 2002.

[115] F. Hwang and D. I. Hoult, "Automatic probe tuning and matching," *Magn. Reson. Med.*, vol. 39, pp. 214–222, 1998.

[116] A. W. Jamieson, "High-performance multiphase metering: a personal perspective," *Meas. Control*, vol. 22, pp. 73–77, April 2000.

[117] A. W. Jamieson, R. G. Smeenk, and P. B. Vriezen, "Multi-phase flow measurements at production platforms," *Pet. Rev.*, vol. 39, no. 466, pp. 23–28, November 1985.

[118] L. P. N. M. Janssen and M. M. C. G. Warmoeskerken, *Transport Phenomena Data Companion*, 3rd ed. Delft University Press, 1997.

[119] P. Jehenson, M. Westphal, and N. Schuff, "Analytical method for the compensation of eddy-current effects induced by pulsed magnetic field gradients in NMR systems," *J. Magn. Reson.*, vol. 90, pp. 264–278, 1990.

[120] E.-K. Jeong, S. A. Altobelli, and E. Fukushima, "NMR imaging studies of stratified flows in a horizontal rotating cylinder," *Phys. Fluids*, vol. 6, no. 9, pp. 2901–2906, 1994.

[121] P. Jezzard, A. S. Barnett, and C. Pierpaoli, "Characterization of and correction for eddy current artifacts in echo planar diffusion imaging," *Magn. Reson. Med.*, vol. 39, pp. 801–812, 1998.

[122] Joint Committee for Guides in Metrology, *JCGM 100:2008, Evaluation of measurement data – Guide to the expression of uncertainty in measurement*, 2008.

[123] B. Jung, M. Honal, P. Ullmann, J. Hennig, and M. Markl, "Highly k-t-space-accelerated phase-contrast MRI," *Magn. Reson. Med.*, vol. 60, pp. 1169–1177, 2008.

[124] J. Kan, *Numerieke Wiskunde voor technici*, 3rd ed. Delft University Press, 2000.

[125] M. Kawaji, "Two-phase flow measurements using a photochromic dye activation technique," *Nucl. Eng. Des.*, vol. 184, pp. 379–392, 1998.

[126] G. W. C. Kaye and T. H. Laby, *Tables of Physical & Chemical Constants*, sixteenth ed. Longman, 1995.

[127] J. Keeler, R. T. Clowes, A. L. Davis, and E. D. Laue, "Pulsed-field gradients: Theory and practice," *Methods Enzymol.*, vol. 239, pp. 145–199, 1994.

[128] P. A. Keifer, "90° pulse width calibrations: How to read a pulse width array," *Concepts Magn. Reson.*, vol. 11, no. 3, pp. 165–180, 1999.

[129] W. E. Kenyon, "Petrophysical principles of application of NMR logging," *Log Anal.*, vol. 38, no. 2, pp. 21–43, 1997.

[130] T. W. Kim, T. B. Aydin, E. Pereyra, and C. Sarica, "Detailed flow field measurements and analysis in highly viscous slug flow in horizontal pipes," *Int. J. Multiphase Flow*, vol. 106, pp. 75–94, 2018.

[131] J. D. King, "Method and apparatus for measuring flow of non-homogeneous material in incompletely filled flow," U.S. Patent US4 638 251, Jan. 20, 1987.

[132] J. D. King and E. S. Riewerts, "Method and apparatus for measuring flow in a pipe or conduit," U.S. Patent US4 536 711, Aug. 20, 1985.

[133] J. D. King, E. S. Riewerts, and W. L. Pollwitz, "Method and apparatus for nuclear magnetic resonant measurement of flow velocity," U.S. Patent US4 629 987, Dec. 16, 1986.

[134] J. D. King, Q. Ni, and A. De Los Santos, "Detection of magnetized fluid flows," U.S. Patent US6 046 587, Apr. 4, 2000.

[135] J. D. King, Q. Ni, and A. De Los Santos, "Measurement of flow fractions flow velocities and flow rates of a multiphase fluid using ESR sensing," U.S. Patent US6 268 727B1, Jul. 31, 2001.

[136] R. L. Kleinberg and H. J. Vinegar, "NMR properties of reservoir fluids," *Log Anal.*, vol. 37, no. 6, pp. 20–32, 1996.

[137] K. Kose, "One-shot velocity mapping using multiple spin-echo EPI and its application to turbulent flow," *J. Magn. Reson.*, vol. 92, pp. 631–635, 1991.

[138] K. Kose, "Instantaneous flow-distribution measurements of the equilibrium turbulent region in a circular pipe using ultrafast NMR imaging," *Phys. Rev. A*, vol. 44, no. 4, pp. 2495–2504, 1991.

[139] G. E. Kouba, O. Shoham, and J. P. Brill, "A nonintrusive flowmetering method for two-phase intermittent flow in horizontal pipes," *SPE Prod. Eng.*, pp. 373–380, Nov. 1990.

[140] A. Krahn, U. Priller, L. Emsley, and F. Engelke, "Resonator with reduced sample heating and increased homogeneity for solid state NMR," *J. Magn. Reson.*, vol. 191, pp. 78–92, 2008.

[141] E. Krajník, "A simple and reliable phase unwrapping algorithm," in *Signal Processing VI Theories and Applications*, J. Vandewalle *et al.*, Eds., vol. 2, EUSIPCO. Brussels, Belgium: Elsevier, August 1992, pp. 917–919.

[142] G. J. Krüger, "Kernspinresonanzverfahren zur Bestimmung des Massenflusses der einzelnen Komponenten einer Mehrkomponentenströmung," European Patent Request EP0 496 330A2, Jul. 29, 1992.

[143] G. J. Krüger, J. Haupt, and R. Weiss, "A nuclear magnetic resonance method for the investigation of two-phase flow," in *Measuring Techniques in Gas-Liquid Two-Phase Flows*, J. M. Delhaye and G. Cognet, Eds. IUTAM Symposium 1983 Nancy, France: Springer, 1984, pp. 435–454.

[144] G. J. Krüger, A. Birke, and R. Weiss, "Nuclear magnetic resonance (NMR) two-phase mass flow measurements," *Flow Meas. Intrum.*, vol. 7, no. 1, pp. 25–37, 1996.

[145] D. O. Kuethe and J.-H. Gao, "NMR signal loss from turbulence: Models of time dependence compared with data," *Phys. Rev. E*, vol. 51, no. 4, pp. 3252–3362, 1995.

[146] O. Kvernvold, V. Vindøy, T. Søntvedt, A. Saasen, and S. Selmer-Olsen, "Velocity distribution in horizontal slug flow," *Int. J. Multiphase Flow*, vol. 10, no. 4, pp. 441–457, 1984.

[147] LabJack Corporation, *LabJack U12 User's Guide*, December 2004, revision 1.09.

[148] S. Lakshmanan, W. A. Maru, D. J. Holland, M. D. Mantle, and A. J. Sederman, "Measurement of an oil–water flow using magnetic resonance imaging," *Flow Meas. Instrum.*, vol. 53, pp. 161–171, 2017.

[149] G. A. LaTorraca, K. J. Dunn, P. R. Webber, and R. M. Carlson, "Low-field NMR determinations of the properties of heavy oils and water-in-oil emulsions," *Magn. Reson. Imaging*, vol. 16, pp. 659–662, 1998.

[150] J. Leblond, Y. Benkedda, S. Javelot, and L. Oger, "Two-phase flows by pulsed field gradient spin-echo NMR," *Meas. Sci. Technol.*, vol. 5, pp. 426–434, 1994.

[151] A. Lee, J. Sun, and W. P. Jepson, "Study of flow regime transitions of oil-water-gas mixtures in horizontal pipes," in *3rd International Offshore and Polar Engineering Conference*, Singapore, June 6 – 11 1993, pp. 159–164.

[152] M. H. Levitt, *Spin Dynamics, Basics of Nuclear Magnetic Resonance*, 2nd ed. John Wiley & Sons, 2006.

[153] H. S. Lew, "Nuclear magnetic resonance flowmeter," U.S. Patent US4 782 295, Nov. 1, 1988.

[154] H. S. Lew, "Nuclear magnetic resonance organic flowmeter," U.S. Patent US4 901 018, Feb. 13, 1990.

[155] H. S. Lew and G. L. Schlatter, "Rapid pulse NMR cut meter," U.S. Patent US4 785 245, Nov. 15, 1988.

[156] S. Lewis, W. L. Fu, and G. Kojasoy, "Internal flow structure description of slug flow-pattern in a horizontal pipe," *Int. J. Heat Mass Transfer*, vol. 45, pp. 3897–3910, 2002.

[157] T.-Q. Li, J. D. Seymour, R. L. Powell, K. L. McCarthy, L. Ödberg, and M. J. McCarthy, "Turbulent pipe flow studied by time-averaged NMR imaging: Measurements of velocity profile and turbulent intensity," *Magn. Reson. Imaging*, vol. 12, no. 6, pp. 923–934, 1994.

[158] G.-Z. Liao, W.-L. Chen, F.-R. Zong, F. Deng, H.-B. Liu, B.-S. Wu, Z. Sun, and S.-H. Luo, "NMR fluid analyzer applying to petroleum industry," *Pet. Sci.*, vol. 18, pp. 54–91, 2021.

[159] J. M. Libove and J. R. Singer, "Method for flow measurement using nuclear magnetic resonance," U.S. Patent US4 574 240, Mar. 4, 1986.

[160] J. S. Lioumbas, S. V. Parras, and A. J. Karabelas, "Co-current stratified gas-liquid downflow – influence of the liquid flow field on interfacial structure," *Int. J. Multiphase Flow*, vol. 31, pp. 869–896, 2005.

[161] G. R. Lockwood, J. W. Hunt, and F. S. Foster, "The design of protection circuitry for high-frequency ultrasound imaging systems," *IEEE Trans. Ultrason. Ferroelectr. Freq. Control*, vol. 38, no. 1, pp. 48–55, 1991.

[162] I. J. Lowe and C. E. Tarr, "A fast recovery probe and receiver for pulsed nuclear magnetic resonance spectroscopy," *J. Phys. E: Sci. Instrum. Series 2*, vol. 1, pp. 320–322, 1968.

[163] G. F. Lynch and S. L. Segel, "Direct measurement of the void fraction of a two-phase fluid by nuclear magnetic resonance," *Int. J. Heat Mass Transfer*, vol. 20, pp. 7–14, 1977.

[164] J. M. Mandhane, G. A. Gregory, and K. Aziz, "A flow pattern map for gas-liquid flow in horizontal pipes," *Int. J. Multiphase Flow*, vol. 1, pp. 537–553, 1974.

[165] J. E. Maneval, R. L. Powell, M. J. McCarthy, and K. L. McCarthy, "Magnetic resonance imaging of multiphase systems," in *Particulate Two-Phase Flow*, M. C. Roco, Ed. Butterworth-Heinemann, 1993, pp. 127–168.

[166] J. E. Maneval, K. L. McCarthy, M. J. McCarthy, and R. L. Powell, "Nuclear magnetic resonance imaging rheometer," US Patent US5 532 593, Jul. 2, 1996.

[167] P. Mansfield and I. L. Pykett, "Biological and medical imaging by NMR," *J. Magn. Reson.*, vol. 29, pp. 355–373, 1978.

[168] D. Mardon, M. G. Prammer, and G. R. Coates, "Characterization of light hydrocarbon reservoirs by gradient-NMR well logging," *Magn. Reson. Imaging*, vol. 14, pp. 769–777, 1996.

[169] M. Markl, F. P. Chan, M. T. Alley, K. L. Wedding, M. T. Draney, C. J. Elkins, D. W. Parker, R. Wicker, C. A. Taylor, R. J. Herfkens, and N. J. Pelc, "Time-resolved three-dimensional phase-contrast MRI," *J. Magn. Reson.*, vol. 17, pp. 499–506, 2003.

[170] C. Martin, D. J. Pusiol, M. E. Ramia, J. M. Garnero, and E. D. Fried, "Method and procedure to measure fluid flow and fluid fraction, and equipment used to that end," U.S. Patent US7 028 557B2, Apr. 18, 2006.

[171] P. C. Masak, J. Bouton, M. G. Prammer, S. Menger, E. Drack, B. Sun, K–J. Dunn, and M. Sullivan, "Field test results and applications of the downhole magnetic resonance fluid analyzer," in *SPWLA* 43rd *Annual Logging Symposium*, Oiso, Japan, June 2 – 5 2002, pp. 1–14.

[172] D. W. McCall, D. C. Douglass, and E. W. Anderson, "Self-diffusion studies by means of nuclear magnetic resonance spin-echo techniques," *Ber. Bunsen Ges.*, vol. 67, no. 3, pp. 336–340, 1963.

[173] S. Meiboom and D. Gill, "Modified spin-echo method for measuring nuclear relaxation times," *Rev. Sci. Instr.*, vol. 29, no. 8, pp. 688–691, 1958.

[174] R. W. Miller, *Flow Measurement Engineering Handbook*, 3rd ed. McGraw-Hill, 1996.

[175] V. W. Miner and W. W. Conover, *The Shimming of High Resolution NMR Magnets, As Told by A Couple of Nuts*, Acorn NMR Inc., 1997.

[176] A. O. Mohmmed, M. S. Nasif, H. H. Al-Kayiem, and R. W. Time, "Measurements of translational slug velocity and slug length using an image processing technique," *Flow Meas. Instrum.*, vol. 50, pp. 112–120, 2016.

[177] H. Morneburg, *Bildgebende Systeme für die medizinische Diagnostik*, 3rd ed. Publicis Corporate Publishing - Siemens AG, 1995.

[178] P. Morris, T. Moore, P. Anuzis, and K. Astley, "NMR methods for measuring fluid flow rates," U.S. Patent US7 378 845B2, May 27, 2008.

[179] O. C. Morse and J. R. Singer, "Blood velocity measurements in intact subjects," *Science*, vol. 170, pp. 440–441, 1970.

[180] H. Nagaoka, "The induction coefficients of solenoids," *Journ. Coll. Sci. Imp. Univ. Tokyo*, vol. 27, no. Art. 6, pp. 18–33, 1909.

[181] L. G. Neal and S. G. Bankoff, "A high resolution resistivity probe for determination of local void properties in gas-liquid flow," *AIChEJ*, vol. 9, pp. 490–494, 1963.

[182] J. Nikuradse, "Laws of turbulent flow in smooth pipes," NASA, TT F-10 359, October 1966.

[183] O. J. Nydal, S. Pintus, and P. Andreussi, "Statistical characterization of slug flow in horizontal pipes," *Int. J. Multiphase Flow*, vol. 18, no. 3, pp. 439–453, 1992.

[184] G. Oddie, H. Shi, L. J. Durlofsky, K. Aziz, B. Pfeffer, and J. A. Holmes, "Experimental study of two and three phase flows in large diameter inclined pipes," *Int. J. Multiphase Flow*, vol. 29, pp. 527–558, 2003.

[185] R. Oliemans, "Oil-water liquid flow rate determined from measured pressure drop and water hold-up in horizontal pipes," *J. of the Braz. Soc. of Mech. Sci & Eng., Special Issue*, vol. 33, pp. 259–264, 2011.

[186] K. T. O'Neill, E. O. Fridjonsson, P. L. Stanwix, and M. L. Johns, "Quantitative velocity distributions via nuclear magnetic resonance flow metering," *J. Magn. Reson.*, vol. 269, pp. 179–185, 2016.

[187] K. T. O'Neill, A. Klotz, P. L. Stanwix, E. O. Fridjonsson, and M. L. Johns, "Quantitative multiphase flow characterisation using an earth's field NMR flow meter," *Flow Meas. Instrum.*, vol. 58, pp. 104–111, 2017.

[188] K. T. O'Neill, L. Brancato, P. L. Stanwix, E. O. Fridjonsson, and M. L. Johns, "Two-phase oil/water flow measurement using an earth's field nuclear magnetic resonance flow meter," *Chem. Eng. Sci.*, vol. 202, pp. 222–237, 2019.

[189] A. V. Oppenheim and R. W. Schafer with J. R. Buck, *Discrete-Time Signal Processing*, second international ed. Prentice-Hall Inc., 1999.

[190] A. V. Oppenheim and A. S. Willsky, *Signals & Systems*, second international ed. Prentice-Hall Inc., 1997.

[191] T. M. Osán, J. M. Ollé, M. Carpinella, L. M. C. Cerioni, D. J. Pusiol, M. Appel, J. Freeman, and I. Espejo, "Fast measurements of average flow velocity by low-field $^{1}$H NMR," *J. Magn. Reson.*, vol. 209, pp. 116–122, 2011.

[192] Oxford Instruments Molecular Biotools Ltd., *Basic MRI with the DRX console v2.2*, April 2006.

[193] Oxford Instruments Molecular Biotools Ltd., *DRX Hardware User Manual v4.3*, April 2006.

[194] Oxford Instruments Molecular Biotools Ltd., *MARAN Ultra Non Expert User Manual v1.7*, April 2006.

[195] Oxford Instruments Molecular Biotools Ltd., *DRX Programming User Manual v4.6*, April 2006.

[196] Oxford Instruments Molecular Biotools Ltd., *RINMR Software for NMR Research and Applications User Manual v5.1*, November 2006.

[197] K. Packer, "The study of slow coherent motion by pulsed nuclear magnetic resonance," *Mol. Phys.*, vol. 17, no. 4, pp. 355–368, 1969.

[198] B. Park, T. Neuberger, A. G. Webb, D. C. Bigler, and C. M. Collins, "Faraday shields within a solenoidal coil to reduce sample heating: Numerical comparison of designs and experimental verification," *J. Magn. Reson.*, vol. 202, pp. 72–77, 2010.

[199] G. A. Pearson, "Shimming an NMR magnet," University of Iowa, Tech. Rep., December 1991.

[200] W. H. Perman, M. A. Bernstein, and J. C. Sandstrom, "A method for correctly setting the rf flip angle," *Magn. Reson. Med*, vol. 9, pp. 16–24, 1989.

[201] B. Pinguet, N. Vågen, and M. Smith, "Subsea business: Fiscal allocation, a new endeavour for a better wet gas and multiphase measurement," in *International Petroleum Technology Conference*, no. IPTC-180001-MS, Kuala Lumpur, Malaysia, December 10–12, 2014.

[202] J. M. Pope and S. Yao, "Quantitative NMR imaging of flow," *Concepts Magn. Reson.*, vol. 5, pp. 281–302, 1993.

[203] M. G. Prammer, J. C. Haselgrove, M. Shinnar, and J. S. Leigh, "A new approach to automatic shimming," *J. Magn. Reson.*, vol. 77, pp. 40–52, 1988.

[204] H.-M. Prasser and R. Häfeli, "Signal response of wire-mesh sensors to an idealized bubbly flow," *Nucl. Eng. Des.*, vol. 336, pp. 3–14, 2018.

[205] H.-M. Prasser, A. Böttger, and J. Zschau, "A new electrode-mesh tomograph for gas-liquid flows," *Flow. Meas. Instrum.*, vol. 9, pp. 111–119, 1998.

[206] H.-M. Prasser, D. Scholz, and C. Zippe, "Bubble size measurement using wire-mesh sensors," *Flow. Meas. Instrum.*, vol. 12, pp. 299–312, 2001.

[207] H.-M. Prasser, E. Krepper, and D. Lucas, "Evoluation of the two-phase flow in a vertical tube – decomposition of gas fraction profiles according to bubble size classes using wire-mesh sensor," *Int. J. Therm. Sci.*, vol. 41, pp. 17–28, 2002.

[208] H.-M. Prasser, M. Beyer, A. Böttger, H. Carl, D. Lucas, A. Schaffrath, P. Schütz, F.-P. Weiss, and J. Zschau, "Influence of the pipe diameter on the structure of the gas-liquid interface in a vertical two-phase flow," *Nucl. Technol.*, vol. 152, pp. 3–22, 2005.

[209] H.-M. Prasser, M. Misawa, and I. Tiseanu, "Comparison between wire-mesh sensor and ultra-fast x-ray tomograph for an air – water flow in a vertical pipe," *Flow Meas. Instrum.*, vol. 16, pp. 73–83, 2005.

[210] W. S. Price, "Pulsed-field gradient nuclear magnetic resonance as a tool for studying translational diffusion: Part I. Basic theory," *Concepts Magn. Reson.*, vol. 9, no. 5, pp. 299–335, 1997.

[211] W. S. Price, "Pulsed-field gradient nuclear magnetic resonance as a tool for studying translational diffusion: Part II. Experimental aspects," *Concepts Magn. Reson.*, vol. 10, no. 4, pp. 197–237, 1998.

[212] D. Pusiol, M. Carpinella, G. Albert, T. M. Osán, J. M. Ollé, J. J. Freeman, M. Appel, and I. S. E. L. Garmundi, "Method for analyzing a multi-phase fluid," U.S. Patent US8 212 557B2, Jul. 3, 2012.

[213] D. Pusiol, M. Carpinella, G. Albert, T. M. Osán, J. M. Ollé, J. J. Freeman, M. Appel, and I. S. E. L. Garmundi, "Method for analyzing a multi-phase fluid," U.S. Patent US8 441 256B2, May 14, 2013.

[214] D. J. Pusiol, "Apparatus and method for real time and real flow-rates measurements of oil and water cuts from oil production," U.S. Patent US7 719 267B2, May 18, 2010.

[215] D. J. Pusiol, M. Carpinella, G. Albert, T. Osan, J. M. Olle, J. J. Freeman, M. Appel, and I. S. L. G. Espejo, "Magnetic resonance based apparatus and method to analyze and to measure the bi-directional flow regime in a transport or a production conduit of complex fluids, in real time and real flow rate," U.S. Patent US7 872 474B2, Jan. 18, 2011.

[216] J. N. Reyes, Jr., A. Y. Lafi, and D. Saloner, "The use of MRI to quantify multi-phase flow patterns and transitions: an application to horizontal slug flow," *Nucl. Eng. Des.*, vol. 184, pp. 213–228, 1998.

[217] M. Rhode, "Multiphase flow measurement concepts based on nuclear magnetic resonance," PhD thesis, Ruhr-Universität Bochum, 2010.

[218] S. Richter, M. Aritomi, H.-M. Prasser, and R. Hampel, "Approach towards spatial phase reconstruction in transient bubbly flow using a wire-mesh sensor," *Int. J. Heat Mass Transfer*, vol. 45, pp. 1063–1075, 2002.

[219] E. Roitberg, L. Schemer, and D. Barnea, "Measurements of cross-sectional instantaneous phase distribution in gas–liquid pipe flow," *Exp. Therm Fluid Sci.*, vol. 31, pp. 867–875, 2007.

[220] M. E. Rudd and J. R. Craig, "Optimum spacing of square and circular coil pairs," *Rev. Sci. Instrum.*, vol. 39, pp. 1372–1374, 1968.

[221] L. A. M. Scheers, K. Busaldi, M. Harper, M. Halvorsen, and T. Wideroe, "Multiphase flow metering per well, can it be justified?" in *20th North Sea Flow Measurement Workshop*, St. Andrews, Scotland, October 22 – 25, 2002.

[222] E. Schleicher, T. B. Aydin, R. E. Vieira, C. F. Torres, E. Pereyra, C. Sarica, and U. Hampel, "Refined reconstruction of liquid–gas interface structures for stratified two-phase flow using wire-mesh sensor," *Flow Meas. Instrum.*, vol. 46, pp. 230–239, 2015.

[223] H. Schlichting, *Boundary-Layer Theory*, third english ed. McGraw-Hill, 1979.

[224] A. J. Sederman, M. D. Mantle, and L. F. Gladden, "Single excitation multiple image RARE (SEMI-RARE): ultra-fast imaging of static and flowing systems," *J. Magn. Reson.*, vol. 161, pp. 15–24, 2003.

[225] A. J. Sederman, M. D. Mantle, C. Buckley, and L. F. Gladden, "MRI technique for measurement of velocity vectors, acceleration, and autocorrelation functions in turbulent flow," *J. Magn. Reson.*, vol. 166, pp. 182–189, 2004.

[226] H. Shaban and S. Tavoularis, "Performance evaluation of conductivity wire-mesh sensors in vertical channels," *Flow Meas. Instrum.*, vol. 54, pp. 185–196, 2017.

[227] S. Sharma, S. Lewis, and G. Kojasoy, "Local studies in horizontal gas–liquid slug flow," *Nucl. Eng. Des.*, vol. 184, pp. 305–318, 1998.

[228] J. Shi and G. Kocamustafaogullari, "Interfacial measurements in horizontal stratified flow patterns," *Nucl. Eng. Des.*, vol. 149, pp. 81–96, 1994.

[229] J.-F. Shi, F. Deng, L.-Z. Xiao, H.-B. Liu, F.-Q. Ma, M.-Y. Wang, R.-D. Zhao, S.-W. Chen, J.-J. Zhang, and C.-M. Xiong, "A proposed NMR solution for multi-phase flow fluid detection," *Pet. Sci*, vol. 16, pp. 1148–1158, 2019.

[230] O. Shoham, *Mechanistic Modeling of Gas-Liquid Two-Phase Flow in Pipes*. Society of Petroleum Engineers (SPE), 2006.

[231] M. I. Siddiqui, S. Munir, M. R. Heikal, G. de Sercey, A. Rashid, A. Aziz, and S. D. Dass, "Simultaneous velocity measurements and the coupling effect of the liquid and gas phases in slug flow using PIV-LIF technique," *J. Visualization*, vol. 19, pp. 103–114, 2016.

[232] J. H. Simpson and H. Y. Carr, "Diffusion and nuclear spin relaxation in water," *Phys. Rev.*, vol. 111, no. 5, pp. 1201–1202, 1958.

[233] J. R. Singer, "Apparatus for measuring flow using magnetic resonance," U.S. Patent US3 191 119, Jun. 22, 1965.

[234] W. F. J. Slijkerman, A. W. Jamieson, W. J. Priddy, O. Økland, and H. Moestue, "Oil companies' needs in multiphase flow metering," in *13th North Sea Flow Measurment Workshop*, Lillehammer, Norway, October 24–26 1995, paper 23.

[235] P. T. M. Smeets, "Spatially resolved phase distributions in a vertical gas-liquid-liquid flow," Master's thesis, Delft University of Technology, 2007.

[236] P. L. Spedding, G. F. Donnelly, and J. S. Cole, "Three phase oil-water-gas horizontal co-current flow; i. experimental and regime map," *Trans IChemE, Part A, Chem. Eng. Res. Des.*, vol. 83, no. A4, pp. 401–411, 2005.

[237] E. O. Stejskal and J. E. Tanner, "Spin diffusion measurements: Spin echoes in the presence of a time-dependent field gradient," *J. Chem. Phys.*, vol. 42, no. 1, pp. 288–292, 1965.

[238] Ø. Strand, "An experimental investigation of stratified two-phase flow in horizontal pipes," PhD thesis, University of Oslo, 1993.

[239] J. L. Sudmeier, U. L. Günther, K. Albert, and W. W. Bachovchin, "Sensitivity optimization in continuous-flow FTNMR," *J. Magn. Reson., Ser. A*, vol. 118, pp. 145–156, 1996.

[240] J. E. Tanner, "Use of the stimulated echo in NMR diffusion studies," *J. Chem. Phys.*, vol. 52, no. 5, pp. 2523–2526, 1970.

[241] F. E. Terman, *Radio Engineers' Handbook*, 1st ed., ser. McGraw-Hill Electrical and Electronic Engineering Series. McGraw-Hill Book Company, Inc, 1943.

[242] R. Thorn, G. A. Johansen, and E. A. Hammer, "Recent developments in three-phase flow measurement," *Meas. Sci. Technol.*, vol. 8, pp. 691–701, 1997, review Article.

[243] R. Thorn, G. A. Johansen, and B. T. Hjertaker, "Three-phase flow measurements in the petroleum industry," *Meas. Sci. Technol.*, vol. 24, 2013, 012003, Topical Review.

[244] J. M. Tribolet, "A new phase unwrapping algorithm," *IEEE Trans. Acoust. Speech Signal Process.*, vol. 25, no. 2, pp. 170–177, 1977.

[245] R. R. Tromp and L. M. C. Cerioni, "Multiphase flow regime characterization and liquid flow measurement using low-field magnetic resonance imaging," *Molecules*, vol. 26, 2021, 3349.

[246] R. R. Tromp and M. L. Zoeteweij, "Method for operating a nuclear magnetic flowmeter," U.S. Patent US10 502 603B2, Dec. 10, 2019.

[247] P. M. Ujang, C. J. Lawrence, C. P. Hale, and G. F. Hewitt, "Slug initiation and evolution in two-phase horizontal flow," *Int. J. Multiphase Flow*, vol. 32, pp. 527–552, 2006.

[248] A. Vallatos, H. F. I. Al-Mubarak, J. M. Mullin, and W. M. Holmes, "Accuracy of phase-contrast velocimetry in sytems with skewed intravoxel velocity distributions," *J. Magn. Reson.*, vol. 296, pp. 121–129, 2018.

[249] R. M. E. van der Mijle, "Development of a long bubble detector based on a conductivity technique," Bachelor's thesis, Delft University of Technology, 2008.

[250] R. van Hout, D. Barnea, and L. Shemer, "Translational velocities of elongated bubbles in continuous slug flow," *Int. J. Multiphase Flow*, vol. 28, pp. 1333–1350, 2002.

[251] J. J. van Vaals and A. H. Bergman, "Optimization of eddy-current compensation," *J. Magn. Reson.*, vol. 90, pp. 52–70, 1990.

[252] H. Vander Heyden and J. H. Battocletti, "Phase locked NMR flowmetering system," U.S. Patent US3 551 794, Dec. 29, 1970.

[253] H. F. Velasco Peña and O. M. H. Rodriguez, "Applications of wire-mesh sensors in multiphase flows," *Flow Meas. Instrum.*, vol. 45, pp. 255–273, 2015.

[254] R. L. Vold, J. S. Waugh, M. P. Klein, and D. E. Phelps, "Measurement of spin relaxation in complex systems," *J. Chem. Phys.*, vol. 48, no. 8, pp. 3831–3832, 1968.

[255] G. B. Wallis, *One-dimensional Two-phase Flow*. McGraw-Hill, 1969.

[256] A. R. Webb, *Statistical Pattern Recognition*, 2nd ed. John Wiley & Sons Ltd., 2002.

[257] P. D. Welch, "The use of fast fourier transform for the estimation of power spectra: A method based on time averaging over short, modified periodograms," *IEEE Trans. Audio Electroacoust.*, vol. AU-15, pp. 70–73, 1967.

[258] G. Wider, V. Dötsch, and K. Wüthrich, "Self-compensating pulsed magnetic-field gradients for short recovery times," *J. Magn. Reson., Ser. A*, vol. 108, pp. 255–258, 1994.

[259] M. Winkler, J. J. Freeman, and M. Appel, "The limits of fluid property correlations used in NMR well logging: An experimental study of reservoir fluids at reservoir conditions," *Petrophysics*, vol. 46, no. 2, pp. 104–112, 2005.

[260] E. Wollin, "Magnetic resonance analyzing flow meter," U.S. Patent US6 452 390B1, Sep. 17, 2002.

[261] C. H. Wu, C. V. Grant, G. A. Cook, S. H. Park, and S. J. Opella, "A strip-shield improves the efficiency of a solenoid coil in probes for high-field solid-state NMR of lossy biological samples," *J. Magn. Reson.*, vol. 200, pp. 74–80, 2009.

[262] M. Zargar, M. L. Johns, J. M. Aljindan, M. N. Noui-Mehidi, and K. T. O'Neill, "Nuclear magnetic resonance multiphase flowmeters: Current status and future prospects," *SPE Prod. Oper.*, pp. 423–436, May 2021, SPE 205351.

[263] D. Ziou and S. Tabbone, "Edge detection techniques - an overview," *Int. J. Pattern Recognit. Image Anal.*, vol. 8, pp. 537–559, 1998.

[264] Y. Zur and S. Stokar, "A phase-cycling technique for cancelling spurious echoes in nmr imaging," *J. Magn. Reson.*, vol. 71, pp. 212–228, 1987.

# Appendix A

# Solution of the Bloch Equations in Absence of Relaxation

In absence of relaxation, the forced precession of the net nuclear magnetization, **M**, in presence of an applied magnetic field, **B**, is given by Eq. 2.10:

$$\frac{\mathrm{d}\mathbf{M}}{\mathrm{d}t} = \gamma \mathbf{M} \times \mathbf{B}. \tag{A.1}$$

Two magnetic fields act upon the NMR active nuclei: (i) in the z-direction a strong static field $B_0$ and (ii) at right angles to it, a comparatively weak r.f. field $B_1$ that oscillates at angular frequency $\omega$. Thus, as depicted in Figure A.1(a), the components of **B** are

$$B_x = B_1 \cos(\omega t), \quad B_y = -B_1 \sin(\omega t), \quad B_z = B_0. \tag{A.2}$$

Note that the sign convention of the angular frequency is opposite to that of the Larmor frequency, defined in Eq. 2.11. The resonance condition is met, when the r.f. pulse is applied at $\omega = \gamma B_0 = -\omega_0$. Combined with the expanded vector product of Eq. A.1 in terms of the components along the Cartesian axes, three equations are obtained for the time dependence of the components of **M**:

$$\frac{\mathrm{d}M_x}{\mathrm{d}t} = \gamma B_0 M_y + \gamma B_1 \sin(\omega t) M_z \tag{A.3a}$$

$$\frac{\mathrm{d}M_y}{\mathrm{d}t} = \gamma B_1 \cos(\omega t) M_z - \gamma B_0 M_x \tag{A.3b}$$

$$\frac{\mathrm{d}M_z}{\mathrm{d}t} = -\gamma B_1 \sin(\omega t) M_x - \gamma B_1 \cos(\omega t) M_y. \tag{A.3c}$$

Before being subjected to the first r.f. pulse of a sequence, the macroscopic magnetization is fully aligned with the polarizing $B_0$ field. For convenience, it is assumed that at time zero the state of thermal equilibrium, with magnetization $M_0$, actually has been established. However,

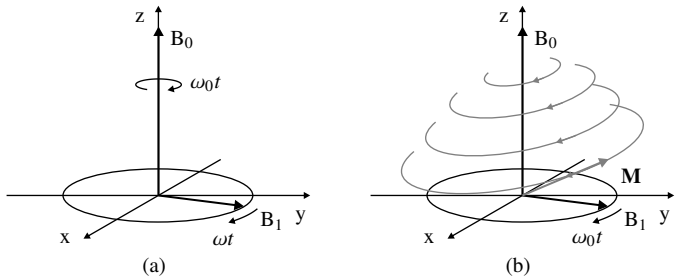


**Figure A.1**: (a) Schematic diagram of the applied magnetic fields in the laboratory frame of reference. (b) On-resonance rotation of the magnetization vector in the laboratory frame of reference .

any magnetization $M_z(0) < M_0$ will lead to a similar result. In addition, the r.f. pulse is supposed to be applied on resonance. So the initial conditions that have to be satisfied are

$$M_x(0) = 0, \quad M_y(0) = 0, \quad M_z(0) = M_0 \tag{A.4a}$$

$$\frac{\mathrm{d}M_z}{\mathrm{d}t}(0) = 0 \tag{A.4b}$$

$$\omega = \gamma B_0. \tag{A.4c}$$

**Expression for $\mathbf{M_z}$**

To obtain a solution for $M_z(t)$, equation A.3c is first differentiated towards t:

$$\begin{aligned}\frac{\mathrm{d}^2M_z}{\mathrm{d}t^2} = &-\gamma B_1 \sin(\omega t)\frac{\mathrm{d}M_x}{\mathrm{d}t} - \gamma B_1\omega\cos(\omega t)M_x \\ &-\gamma B_1 \cos(\omega t)\frac{\mathrm{d}M_y}{\mathrm{d}t} + \gamma B_1\omega\sin(\omega t)M_y.\end{aligned} \tag{A.5}$$

Substitution of Eq. A.3a and A.3b for $\mathrm{d}M_x/\mathrm{d}t$ and $\mathrm{d}M_y/\mathrm{d}t$ gives

$$\frac{\mathrm{d}^2M_z}{\mathrm{d}t^2} = \gamma B_1\cos(\omega t)\left(\gamma B_0 - \omega\right)M_x - \gamma B_1\sin(\omega t)\left(\gamma B_0 - \omega\right)M_y - (\gamma B_1)^2 M_z. \tag{A.6}$$

As the r.f. pulse is applied on resonance, i.e. $\omega = \gamma B_0$, the first two terms on the right-hand side are canceled out and

$$\frac{\mathrm{d}^2M_z}{\mathrm{d}t^2} = -(\gamma B_1)^2 M_z. \tag{A.7}$$

On substituting the general solution $M_z(t) = \alpha\mathrm{e}^{\lambda_1 t} + \beta\mathrm{e}^{\lambda_2 t}$ follows that

$$M_z(t) = \alpha\mathrm{e}^{-i\gamma B_1 t} + \beta\mathrm{e}^{i\gamma B_1 t}. \tag{A.8}$$

Evaluation of initial condition A.4b gives $\alpha = \beta$, whereafter $\alpha = {}^1/_2 M_0$ must be chosen to satisfy the first initial condition, $M_z(0) = M_0$. Hence

$$M_z(t) = M_0 \cos(\gamma B_1 t) \tag{A.9}$$

is the solution of differential equation A.7.

With this solution an additional relation between $M_x$ and $M_y$ is found upon substitution into Eq. A.3c

$$-\gamma M_0 B_1 \sin(\gamma B_1 t) = -\gamma B_1 \sin(\gamma B_0 t) M_x - \gamma B_1 \cos(\gamma B_0 t) M_y, \tag{A.10}$$

where again the resonance condition A.4c is applied. Rewriting leads to

$$M_x(t) = M_0 \frac{\sin(\gamma B_1 t)}{\sin(\gamma B_0 t)} - M_y \frac{\cos(\gamma B_0 t)}{\sin(\gamma B_0 t)} \tag{A.11}$$

or

$$M_y(t) = M_0 \frac{\sin(\gamma B_1 t)}{\cos(\gamma B_0 t)} - M_x \frac{\sin(\gamma B_0 t)}{\cos(\gamma B_0 t)}. \tag{A.12}$$

**Expression for $M_x$**

Substitution of Eq. A.9 and A.12 in Eq. A.3a gives

$$\frac{\mathrm{d}M_x}{\mathrm{d}t} + \gamma B_0 \frac{\sin(\gamma B_0 t)}{\cos(\gamma B_0 t)} M_x = \gamma B_0 \frac{\sin(\gamma B_1 t)}{\cos(\gamma B_0 t)} M_0 + \gamma B_1 \sin(\gamma B_0 t) \cos(\gamma B_1 t) M_0. \tag{A.13}$$

This nonhomogeneous differential equation is solved by means of the variation of parameter method. First, the complementary solution $M_{x,c}$ of the corresponding homogeneous equation

$$\frac{\mathrm{d}M_{x,c}}{\mathrm{d}t} + \gamma B_0 \frac{\sin(\gamma B_0 t)}{\cos(\gamma B_0 t)} M_{x,c} = 0 \tag{A.14}$$

is computed. Integration of

$$\frac{\mathrm{d}M_{x,c}}{M_{x,c}} = -\gamma \tan(\gamma B_0 t) \mathrm{d}t \tag{A.15}$$

gives

$$\ln(M_{x,c}) = \ln|\cos(\gamma B_o t)|. \tag{A.16}$$

Therefore, by taking the exponential of both sides, the integration factor

$$M_{x,c} = \cos(\gamma B_0 t) \tag{A.17}$$

is obtained. Next, the solution of initial value problem A.4a, A.13

$$M_x(t) = c(t) M_{x,c}(t) = c(t) \cos(\gamma B_0 t) \tag{A.18}$$

is found by means of the variation of parameter method. By substitution in Eq. A.13, the differential equation for $c(t)$ becomes

$$\frac{\mathrm{d}c(t)}{\mathrm{d}t} = \gamma M_0 \left( B_0 \frac{\sin(\gamma B_1 t)}{\cos^2(\gamma B_0 t)} + B_1 \tan(\gamma B_0 t) \cos(\gamma B_1 t) \right). \tag{A.19}$$

Using the chain rule in the integration of the first term on the right-hand side gives

$$\begin{aligned} c(t) = &- M_0 \int \gamma B_1 \tan(\gamma B_0 t) \cos(\gamma B_1 t) \mathrm{d}t + M_0 \left[ \sin(\gamma B_1 t) \tan(\gamma B_0 t) \right] \\ &+ M_0 \int \gamma B_1 \tan(\gamma B_0 t) \cos(\gamma B_1 t) \mathrm{d}t, \end{aligned} \tag{A.20}$$

such that

$$c(t) = M_0 \sin(\gamma B_1 t) \tan(\gamma B_0 t) \tag{A.21}$$

and finally, in combination with Eq. A.18,

$$M_x(t) = M_0 \sin(\gamma B_1 t) \sin(\gamma B_0 t). \tag{A.22}$$

**Expression for $\mathbf{M_y}$**

Substitution of Eq. A.9 and A.22 into Eq. A.3b results in

$$\frac{\mathrm{d}M_y}{\mathrm{d}t} = \gamma B_1 M_0 \cos(\gamma B_1 t) \cos(\gamma B_0 t) - \gamma B_0 M_0 \sin(\gamma B_1 t) \sin(\gamma B_0 t). \tag{A.23}$$

Making again use of the chain rule in the integration of the first term on the right-hand side gives

$$\begin{aligned} M_y(t) = &+ M_0 \int \gamma B_0 \sin(\gamma B_1 t) \sin(\gamma B_0 t) \mathrm{d}t + M_0 \left[ \sin(\gamma B_1 t) \cos(\gamma B_0 t) \right] \\ &- M_0 \int \gamma B_0 \sin(\gamma B_1 t) \sin(\gamma B_0 t) \mathrm{d}t, \end{aligned} \tag{A.24}$$

thus

$$M_y(t) = M_0 \sin(\gamma B_1 t) \cos(\gamma B_0 t). \tag{A.25}$$

When $1 - \sin^2(\gamma B_0 t)$ is replaced by $\cos^2(\gamma B_0 t)$, the same result is directly obtained from the substitution of Eq. A.22 into Eq. A.12.

**Complete solution of the Bloch equations**

Summarizing, the precessional motion of the magnetization in the laboratory frame of reference is described by

$$M_x(t) = M_0 \sin(\gamma B_1 t) \sin(\gamma B_0 t) \tag{A.26a}$$

$$M_y(t) = M_0 \sin(\gamma B_1 t) \cos(\gamma B_0 t) \tag{A.26b}$$

$$M_z(t) = M_0 \cos(\gamma B_1 t). \tag{A.26c}$$

An illustration of the spiral motion is shown in Figure A.1(b).

# Appendix B

# Magnetic Field Induced by a Finite Length Solenoid

The length $L_c$ of the trifilar coils, used as r.f. probe, is with 12 cm short with respect to its diameter of also 12 cm. This results in non parallel magnetic field lines within a large part of the volume enclosed by the coil and its direct extension. In combination with a pipe of 9.86 cm diameter, $D_p$, containing the sample and exceeding the sensitive region of the coil, the non uniform flip angles can have a strong effect on the measurement results. The derivation of the $\mathbf{B}_1$-field that is induced by a thin film finite length solenoid is given in this appendix.

A static magnetic field $\mathbf{B}$, which originates from a steady current $I$ and in absence of magnetic media satisfies the two Maxwell equations:

$$\nabla \cdot \mathbf{B} = 0 \tag{B.1a}$$

$$\nabla \times \mathbf{B} = \mu_0 \mathbf{J} \tag{B.1b}$$

that are in turn Gauss' law for magnetism and Ampères law. Here is $\mu_0$ the magnetic permeability of vacuum, which is $4\pi \cdot 10^{-7}$ H m$^{-1}$, and $\mathbf{J}$ is the current density.

Analogous to potential flow as solution of the Euler equations in fluid mechanics, the induced magnetic field can be derived from this set of equations by the introduction of a vector potential $\mathbf{A}$ such that

$$\mathbf{B} = \nabla \times \mathbf{A}. \tag{B.2}$$

The meaning of the vector potential is better understood from the integral form of equation B.2:

$$\Phi_S = \oint_C \mathbf{A} \cdot \mathrm{d}\mathbf{l}. \tag{B.3}$$

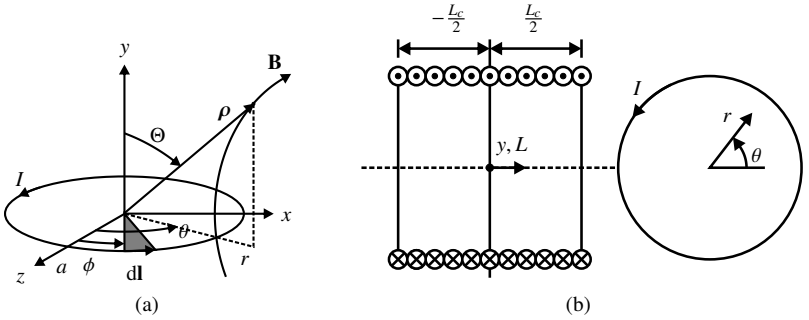


**Figure B.1**: Geometry of (a) a single filament of (b) a thin film solenoid of length $L_c$, radius $a$ and consisting of $n$ filaments per length scale. The position within the coil is expressed in cylindrical coordinates $(y, r, \theta)$. To determine the magnetic field induced by current element $I$ $\mathrm{d}\mathbf{l}$, the auxiliary spherical coordinates $(\rho, \Theta, \theta)$ are used.

It states that the line integral of the vector potential around any closed path C in the **B**-field is equal to the magnetic flux $\Phi_S$ across any surface S bounded by C. If **A** meets the additional condition $\nabla \cdot \mathbf{A} = 0$, the vector potential satisfies a Poisson equation

$$\nabla^2 \mathbf{A}(r, y) = -\mu_0 \mathbf{J}(r, y). \tag{B.4}$$

Because the solenoid in the r.f. probe is formed out of a thin electric wire, the current density can be replaced by the current $I$. Starting from Biot-Savart law, Duffin [56] proves mathematically that the vector potential due to a single circular filament with a constant current $I$ will be

$$\mathbf{A} = \frac{\mu_0}{4\pi} \oint_C \frac{I\,\mathrm{d}\mathbf{l}}{R}, \tag{B.5}$$

where $R$ is the distance from the fieldpoint to the current element. In the used axisymmetric coil geometry, sketched in Figure B.1, the torrodial component $A_\theta$ is therefore the only nonzero component of the vector potential. When the actual expression for **A** is substituted into equation B.2 suitable expressions for the axial and radial component of **B** can be obtained:

$$B_y(r, y) = \frac{1}{r}\frac{\partial}{\partial r} r A_\theta(r, y) \tag{B.6a}$$

$$B_r(r, y) = -\frac{\partial}{\partial y} A_\theta(r, y). \tag{B.6b}$$

Fujimoto [69] shows that the tangential component of **A** for a single circular filament of radius $a$ yields

$$A_\theta(r, y) = \frac{\mu_0 a I}{4\pi} \oint_C \frac{\cos(\psi)\,\mathrm{d}\psi}{\sqrt{\rho^2 + a^2 - 2\rho a \sin(\Theta)\cos(\psi)}}, \tag{B.7}$$

where $\rho$ is the distance from the field point to the center of the current filament and writing $\phi - \theta = \psi$. Hence for a solenoid made up of a series of $n$ filaments per unit length the tangential component of $\mathbf{A}$ becomes

$$A_\theta(r,y) = \frac{\mu_0 anI}{2\pi} \int_{-\frac{L_c}{2}}^{\frac{L_c}{2}} \mathrm{d}L \int_0^\pi \frac{\cos(\psi)\,\mathrm{d}\psi}{\sqrt{(y-L)^2 + r^2 + a^2 - 2ar\cos(\psi)}}. \tag{B.8}$$

The expressions for the axial and radial magnetic field are now easily obtained by differentiating this equation according to B.6a and B.6b, i.e.

$$B_y(r,y) = \frac{\mu_o anI}{2\pi} \cdot \int_0^\pi \left[ \frac{(y-L)(a - r\cos(\psi))\,\mathrm{d}\psi}{(r^2 + a^2 - 2ar\cos(\psi))\sqrt{(y-L)^2 + r^2 + a^2 - 2ar\cos(\psi)}} \right]_{-\frac{L_c}{2}}^{\frac{L_c}{2}} \tag{B.9a}$$

$$B_r(r,y) = -\frac{\mu_0 anI}{2\pi} \int_0^\pi \left[ \frac{\cos(\psi)\,\mathrm{d}\psi}{\sqrt{(y-L)^2 + r^2 + a^2 - 2ar\cos(\psi)}} \right]_{-\frac{L_c}{2}}^{\frac{L_c}{2}}. \tag{B.9b}$$

Many authors choose to express the magnetic field solution in terms of standard elliptic integrals using Bessel function identities. A result that can also be derived straightaway from Poisson equation B.4 in the torroidal direction, which has a Green's function as solution of $A_\theta$ [46]. The local field strength is henceforth calculated by means of already tabulated elliptic integral representations. In this work, the results of the magnetic field are found by numerical integration of equation set B.9, as suggested by Callaghan and Maslen [36]. As integration scheme Simpson's rule [124]

$$\int_{x_0-h}^{x_0+h} f(x)\,\mathrm{d}x = \frac{h}{3}(f_{-1} + 4f_0 + f_1) + Ch^5 \tag{B.10}$$

is used, which follows from the integration of a second order polynomial through the three function values $f_{-1} = f(x_0 - h)$, $f_0 = f(x_0)$ and $f_1 = f(x_0 + h)$.
The magnetic fields induced by a 2 A current $I$ through a 12 cm long trifilar coil of 4 turns and 12 cm diameter are mapped in Figure B.2 for the cross-section of a 9.86 cm diameter pipe. The domain has an axial and radial resolution of 0.6 mm and 2.0 mm respectively, while the integration over $\psi$ is performed using 100 integration steps $h$.

Figure B.2(a) and B.2(b) show a clear field inhomogeneity within the volume enclosed by the coil. The behavior of a single circular filament is still strongly present in the produced fields. The axial field $B_y$ at positions near the center of the coil ($y \approx 0$) changes rapidly from the coil axis to the wall. In the radial field $B_r$, zones of a higher field strength are present around the edges of the current sheet, where the radial field is infinite by definition. Because

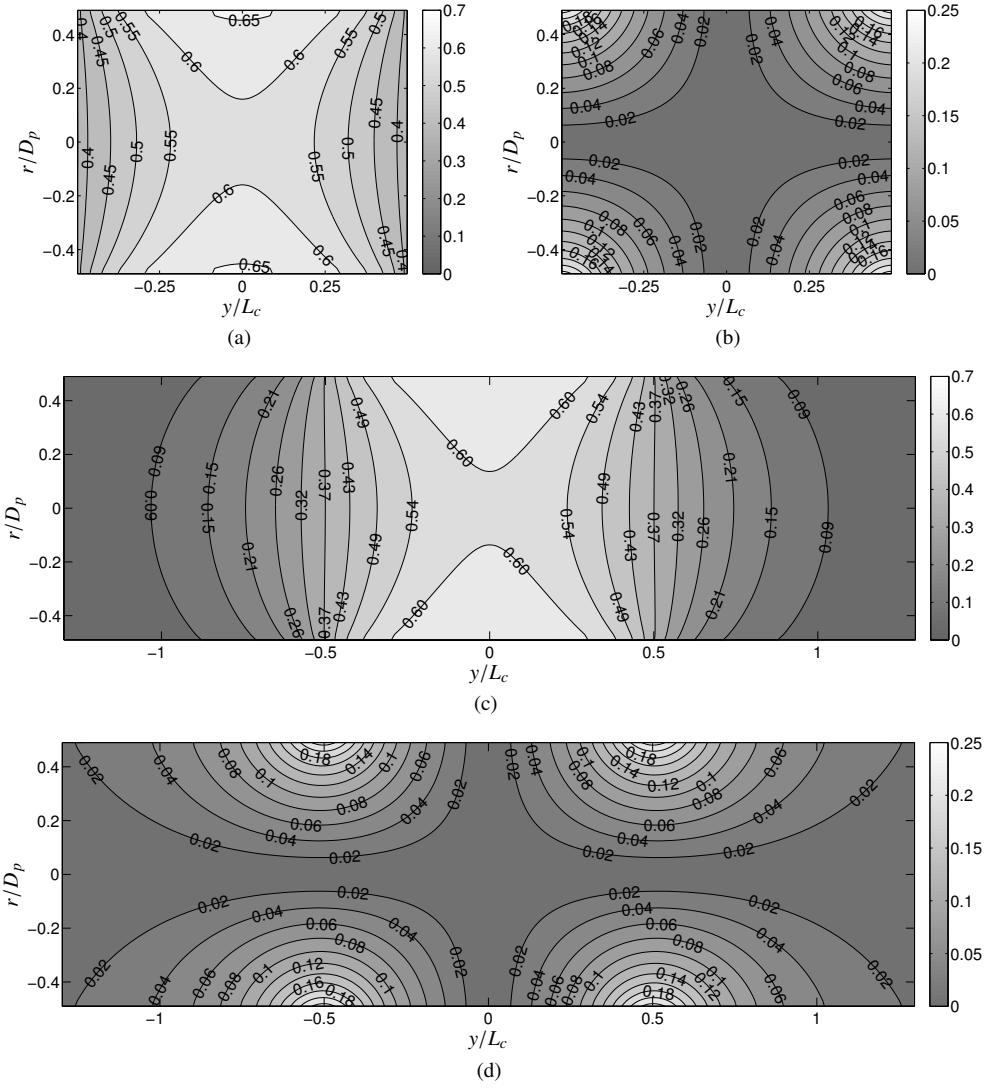


**Figure B.2**: Distribution of the magnetic field $\mathbf{B}_1$ in Gauss, produced by a 2 A current $I$ through a 12 cm long trifilar coil of 4 turns and 12 cm diameter. The (a, c) axial $B_y$-field and (b, d) radial $B_r$-field are mapped for the cross-section of a 9.86 cm diameter pipe with a length of 12 and 31.2 cm, respectively.

especially in these regions the radial field is large in proportion to the axial field, the effective field $B_{\text{eff}}$ does not point into the desired axial direction but 2 to 25° outwards. Though in 85% of the volume enclosed by the coil, the deviation is less than 15°. This provides an axial contribution of at least 97% of the effective field strength, which is sufficient. However, the sensitive region of the coil does not stop at its edges. As shown in Figure B.2(c) and B.2(d), the field in the volume adjacent to the coil is still so strong that an r.f. pulse will excite the spins present.
Because of the principle of reciprocity [109, 112], the magnetization in a point will contribute to the induced voltage in the coil with an amplitude corresponding to the magnetic field produced at that point if a current were to flow in the coil. Thus we can estimate the pulse length at small pulse angles, provided the full sensitive region of the coil is known.

In the AUTOP90 method, see section 2.3.3.1, the pulse length of a 90° pulse is obtained by maximizing the amplitude of an FID

$$\xi = -\frac{\partial}{\partial t}(\mathbf{B}_1 \cdot \mathbf{M}), \tag{B.11}$$

where $\mathbf{B}_1$ is the field produced by the current at the position of the magnetization $\mathbf{M}$. The field is principally pointing in the axial direction, so the contribution of a small volume $\Delta V$ to the induced field follows

$$\Delta\xi \propto B_y(r,\theta)\, M_0 \cos(\alpha(r,\theta) - 90°)\, \Delta V\, \omega_0 \cos(\omega_0 t). \tag{B.12}$$

If $\overline{B}_y$ is the average field strength that corresponds to the obtained pulse length for a 90° pulse, the position dependent flip angle, using a linear approximation, is given by

$$\alpha(r,\theta) = 90° \frac{B_y(r,\theta)}{\overline{B}_y}. \tag{B.13}$$

The $B_y$-term in equation B.12 only limits the volume that effectively contributes to the average flip angle. It is a weighting factor that is, unlike the magnetization component in the y-directon $M_y$, independent of the pulse length. The magnetization within the coil is, due to the field distribution, more important for the signal strength than the magnetization outside the coil. Furthermore the magnetization outside the coil is much weaker. As the magnetization $M_y$ in the outer region hardly changes with the pulse length if the 90° flip angle is approached, it only contributes with an offset in the signal strength, but does not change the value of the optimal 90° pulse length. This means that the average field strength $\overline{B}_y$ of the current geometry is in essence set by the mean induced field within the coil domain.

When studying the influence of different regions in the pipe on the induced NMR signal, it is assumed for convenience that the mean produced $B_y$-field within the pipe element enclosed by the coil is a measure for the 90° pulse length. The result will deviate a little from reality, as the real effective volume follows the contour lines of the axial magnetic field and damping factors are not taken into account. In Figure B.3(a) the distribution of the flip angle $\alpha$ is mapped for a 31.2 cm long pipe segment (2.6 $L_c$). In a large region near the coil surface the

magnetization is rotated over more than 90°, which results in an axial magnetization less than the equilibrium magnetization (see Figure B.3(b)). To which extent each position contributes to the induced NMR signal is mapped in Figure B.3(c), in which the values are represented as percentage of the maximum local signal contribution. It shows that the main signal contribution originates indeed from the pipe volume enclosed by the coil, while liquid at more than 0.35 $L_c$ outside the coil does not contribute any more.

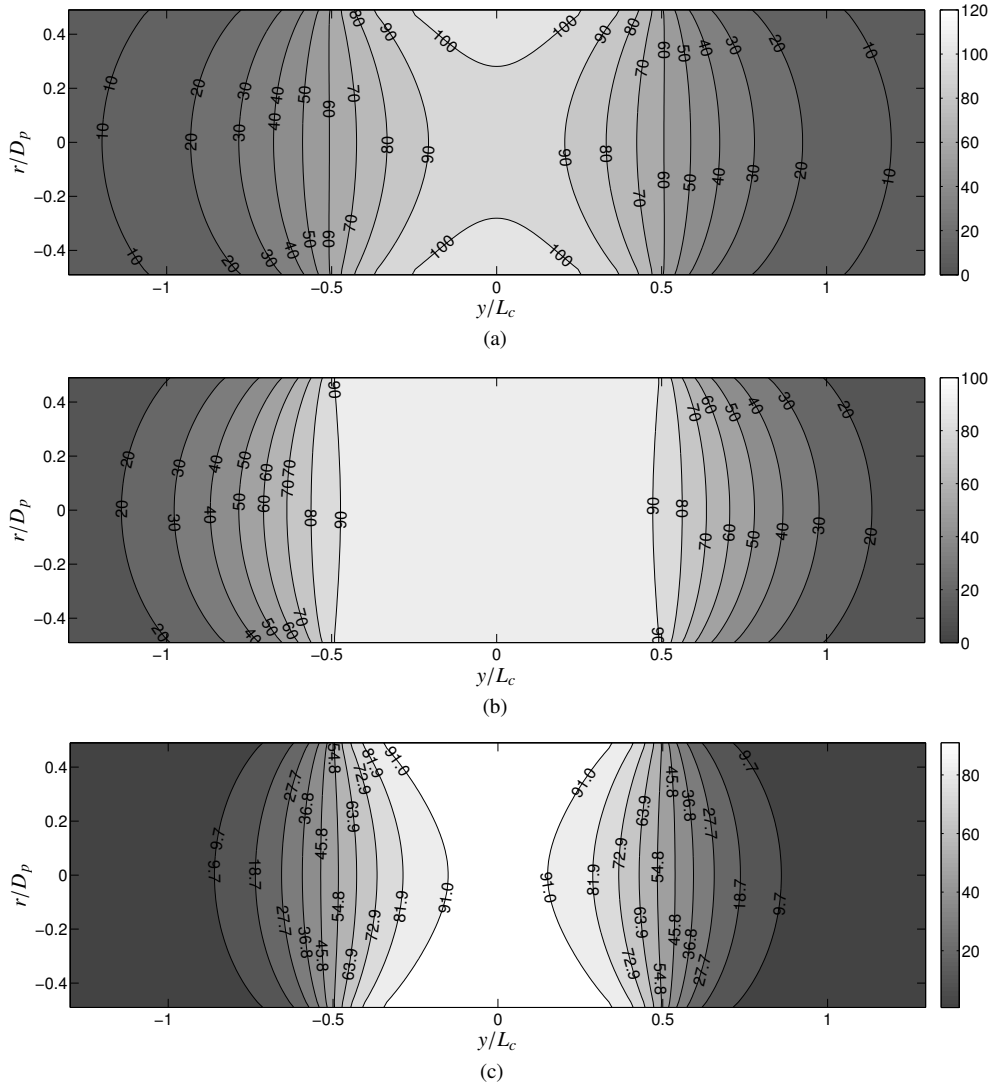


**Figure B.3**: The induced NMR signal in a 12 cm long trifilar coil of 4 turns and 12 cm diameter is modelled for a sample, enclosed in a 31.2 cm long pipe of 9.86 cm diameter, being previously exposed to a hard 90° pulse at a 2 A current. The mean axial field $\overline{B}_y$ of the volume of the sample enclosed by the coil is 0.554 G. Starting from $\overline{B}_y$ as measure for the 90° pulse length, the distribution of (a) the flip angle, (b) the resulting percentage of equilibrium magnetization in the axial direction and (c) the contribution to the induced NMR signal as percentage of its maximum value are calculated.

# Appendix C

# Uncertainties

In this appendix a summary of the expressions of the uncertainties in the two-phase flow measurements is given, processed according to the methods defined in the 'Guide to the expression of uncertainties in measurements' (GUM) [122].

Standard uncertainties, $u(x_i)$, of measurands that result from a series of observations are determined with the statistical analysis of a Type A evaluation. For the standard uncertainties of other measurands the Type B evaluation is used. Combined standard uncertainties are calculated by means of propagation of uncertainty.

The expanded uncertainty, $U(x_i)$, for a 95% confidence level is obtained by multiplying the standard uncertainty by a coverage factor, $t_{\mathrm{ST}\ 0.025}(\nu(x_i))$, which is the value of the Student's t distribution for $\nu(x_i)$ degrees of freedom. Each method of evaluation has its own rule to assign the degrees of freedom to the standard uncertainty. In the case of a Type A evaluation, the degrees of freedom are equal to the number of observations minus 1. For a Type B evaluation, the degrees of freedom are defined from the relative uncertainty of the standard uncertainty

$$\nu(x_i) \approx \frac{1}{2}\left(\frac{\Delta u(x_i)}{u(x_i)}\right)^{-2}, \tag{C.1}$$

whose value is obtained by scientific judgment of the experimentalist. The effective degrees of freedom in the combined uncertainty are obtained from the Welch-Satterthwaite formula

$$\nu_{\mathrm{eff}}(y) = \frac{u_c^4(y)}{\sum_{i=1}^{N} \frac{u_i^4(y)}{\nu_i}} \quad \text{with} \quad \nu_{\mathrm{eff}} \leq \sum_{i=1}^{N} \nu_i. \tag{C.2}$$

## C.1 Uncertainties in the stratified flow measurements

**NMR velocity**

average

$$\bar{v}_{\mathrm{NMR}} = \frac{1}{N_S} \sum_{i=1}^{N_s} v_{\mathrm{NMR}}[i] \tag{C.3}$$

experimental standard deviation

$$\sigma(v_{\mathrm{NMR}}) = \sqrt{\frac{1}{N_s - 1} \sum_{i=1}^{N_s} (v_{\mathrm{NMR}}[i] - \bar{v}_{\mathrm{NMR}})^2} \tag{C.4}$$

experimental standard deviation of the mean

$$u(\bar{v}_{\mathrm{NMR}}) = \frac{\sigma(v_{\mathrm{NMR}})}{\sqrt{N_s}} \tag{C.5}$$

expanded uncertainty

$$U(\bar{v}_{\mathrm{NMR}}) = t_{\mathrm{ST}\ 0.025}(N_s - 1)u(\bar{v}_{\mathrm{NMR}}) \tag{C.6}$$

**NMR liquid holdup**

average

$$\bar{\alpha}_{\mathrm{NMR},2} = \frac{1}{N_s} \sum_{i=1}^{N_s} \alpha_{\mathrm{NMR},2}[i] \tag{C.7}$$

experimental standard deviation

$$\sigma(\alpha_{\mathrm{NMR},2}) = \sqrt{\frac{1}{N_s - 1} \sum_{i=1}^{N_s} (\alpha_{\mathrm{NMR},2}[i] - \bar{\alpha}_{\mathrm{NMR},2})^2} \tag{C.8}$$

experimental standard deviation of the mean

$$u(\bar{\alpha}_{\mathrm{NMR},2}) = \frac{\sigma(\alpha_{\mathrm{NMR},2})}{\sqrt{N_s}} \tag{C.9}$$

expanded uncertainty

$$U(\bar{\alpha}_{\mathrm{NMR},2}) = t_{\mathrm{ST}\ 0.025}(N_s - 1)u(\bar{\alpha}_{\mathrm{NMR},2}) \tag{C.10}$$

**NMR signal fraction**

average

$$\frac{\bar{s}_{y,2}}{s_{y,1}} = \frac{1}{N_s}\sum_{i=1}^{N_s}\frac{s_{y,2}[i]}{s_{y,1}[i]} \tag{C.11}$$

experimental standard deviation

$$\sigma\left(\frac{s_{y,2}}{s_{y,1}}\right) = \sqrt{\frac{1}{N_s-1}\left(\frac{s_{y,2}[i]}{s_{y,1}[i]} - \frac{\bar{s}_{y,2}}{s_{y,1}}\right)^2} \tag{C.12}$$

experimental standard deviation of the mean

$$u\left(\frac{\bar{s}_{y,2}}{s_{y,1}}\right) = \frac{1}{\sqrt{N_s}}\sigma\left(\frac{s_{y,2}}{s_{y,1}}\right) \tag{C.13}$$

expanded uncertainty

$$U\left(\frac{\bar{s}_{y,2}}{s_{y,1}}\right) = t_{\mathrm{ST}\ 0.025}(N_s-1)u\left(\frac{\bar{s}_{y,2}}{s_{y,1}}\right) \tag{C.14}$$

**dimensionless NMR velocity**

combined standard uncertainty

$$u(\bar{v}^*_{\mathrm{NMR}}) = |\bar{v}^*_{\mathrm{NMR}}|\sqrt{\left(\frac{u(\bar{v}_{\mathrm{NMR}})}{\bar{v}_{\mathrm{NMR}}}\right)^2 + \left(\frac{u(T_1)}{T_1}\right)^2 + \left(\frac{u(y_{c,1})}{y_{c,1}+\overline{\Delta l}}\right)^2 + \left(\frac{u(\overline{\Delta l})}{y_{c,1}+\overline{\Delta l}}\right)^2} \tag{C.15}$$

effective degrees of freedom

$$\nu(\bar{v}^*_{\mathrm{NMR}}) = \frac{u(\bar{v}^*_{\mathrm{NMR}})^4}{\bar{v}^{*\,4}_{\mathrm{NMR}}\left(\left(\frac{u(\bar{v}_{\mathrm{NMR}})}{\bar{v}_{\mathrm{NMR}}}\right)^4\frac{1}{\nu(\bar{v}_{\mathrm{NMR}})} + \left(\frac{u(T_1)}{T_1}\right)^4\frac{1}{\nu(T_1)} + \left(\frac{u(y_{c,1})}{y_{c,1}+\overline{\Delta l}}\right)^4\frac{1}{\nu(y_{c,1})} + \left(\frac{u(\overline{\Delta l})}{y_{c,1}+\overline{\Delta l}}\right)^4\frac{1}{\nu(\overline{\Delta l})}\right)} \tag{C.16}$$

expanded uncertainty

$$U(\bar{v}^*_{\mathrm{NMR}}) = t_{\mathrm{ST}\ 0.025}(\nu(\bar{v}^*_{\mathrm{NMR}}))u(\bar{v}^*_{\mathrm{NMR}}) \tag{C.17}$$

**NMR liquid flowrate**

Omitting the uncertainty in $D_p$, which is small compared to the other terms.
combined standard uncertainty

$$u(q_{\mathrm{NMR}}) = |q_{\mathrm{NMR}}|\sqrt{\left(\frac{u(\bar{\alpha}_{\mathrm{NMR},2})}{\bar{\alpha}_{\mathrm{NMR},2}}\right)^2 + \left(\frac{u(\bar{v}_{\mathrm{NMR}})}{\bar{v}_{\mathrm{NMR}}}\right)^2} \tag{C.18}$$

**Table C.1**: Standard uncertainty and the corresponding degrees of freedom for the stratified flow measurements described in chapter 7. When the degrees of freedom are obtained with Eq. C.1 for a Type B evaluation, the assumed relative uncertainty is given.

| $v_{SL}$ | 0.05 m s$^{-1}$ | 0.10 m s$^{-1}$ | 0.15 m s$^{-1}$ | assumed reliability |
|---|---|---|---|---|
| $u(T_1)$ | 0.01 s | 0.01 s | 0.01 s | |
| $\nu(T_1)$ | 39 | 39 | 39 | |
| $u(y_{c,1})$ | 0.001 m | 0.001 m | 0.001 m | |
| $\nu(y_{c,1})$ | 8 | 8 | 8 | $u(y_{c,1})$ to 25% |
| $u(\overline{\Delta l})$ | 0.003 m | 0.003 m | 0.003 m | |
| $\nu(\overline{\Delta l})$ | 2 | 2 | 2 | $u(\overline{\Delta l})$ to 50% |
| $u(\mu_L)$ | $2 \cdot 10^{-5}$ Pa s | $3 \cdot 10^{-5}$ Pa s | $2 \cdot 10^{-5}$ Pa s | |
| $u(\rho_L)$ | 0.3 kg m$^{-3}$ | 0.2 kg m$^{-3}$ | 0.3 kg m$^{-3}$ | |
| $u(\mu_G)$ | $1 \cdot 10^{-7}$ Pa s | $1 \cdot 10^{-7}$ Pa s | $1 \cdot 10^{-7}$ Pa s | |
| $u(\rho_G)$ | 0.004 kg m$^{-3}$ | 0.004 kg m$^{-3}$ | 0.004 kg m$^{-3}$ | |
| $\nu(v_{SL,r})$ | 449 | 1,799 | 449 | |
| $\nu(v_{SL,s})$ | 50 | 50 | 50 | $u_s(v_{SL})$ to 10% |
| $\nu(\alpha_{L,WM})$ | 79,999 | 499,999 | 79,999 | |

effective degrees of freedom

$$\nu(q_{NMR}) = \frac{u(q_{NMR})^4}{\frac{{q_{NMR}}^4}{N_s-1}\left(\left(\frac{u(\bar{\alpha}_{NMR,2})}{\bar{\alpha}_{NMR,2}}\right)^4 + \left(\frac{u(\bar{v}_{NMR})}{\bar{v}_{NMR}}\right)^4\right)}. \tag{C.19}$$

expanded uncertainty

$$U(q_{NMR}) = t_{ST\ 0.025}(\nu(q_{NMR}))u(q_{NMR}) \tag{C.20}$$

**superficial liquid velocity Krohne Optiflux 2300 C**

systematic standard uncertainty

$$u_s(v_{SL}) = 0.002 v_{SL} + 0.001 \text{ m s}^{-1} \tag{C.21}$$

random experimental standard deviation of the mean

$$u_r(\bar{v}_{SL}) = \frac{1}{\sqrt{N_{LJ}}}\sqrt{\frac{1}{N_{LJ}-1}\sum_{i=1}^{N_{LJ}}(v_{SL}[i] - \bar{v}_{SL})^2} \tag{C.22}$$

combined standard uncertainty

$$u(\bar{v}_{\mathrm{SL}}) = \sqrt{u_s(\bar{v}_{\mathrm{SL}})^2 + u_r(\bar{v}_{\mathrm{SL}})^2} \tag{C.23}$$

effective degrees of freedom

$$\nu(\bar{v}_{\mathrm{SL}}) = \frac{u(\bar{v}_{\mathrm{SL}})^4}{\frac{u_s(\bar{v}_{\mathrm{SL}})^4}{\nu(\bar{v}_{\mathrm{SL,s}})} + \frac{u_r(\bar{v}_{\mathrm{SL}})^4}{\nu(\bar{v}_{\mathrm{SL,r}})}}, \tag{C.24}$$

where $\nu(\bar{v}_{\mathrm{SL,s}})$ is determined with Eq. C.1 and $\nu(\bar{v}_{\mathrm{SL,r}}) = N_{LJ} - 1$.
expanded uncertainty

$$U(\bar{v}_{\mathrm{SL}}) = t_{\mathrm{ST}\ 0.025}(\nu(\bar{v}_{\mathrm{SL}}))u(\bar{v}_{\mathrm{SL}}) \tag{C.25}$$

**liquid holdup wiremesh sensor**

systematic overestimation liquid holdup

$$\delta\alpha_L = 0.04 \tag{C.26}$$

random standard uncertainty

$$u(\alpha_{\mathrm{L,WM}}) = \sqrt{\frac{1}{N_{\mathrm{WM}} - 1}\sum_{i=1}^{N_{\mathrm{WM}}}(\alpha_{\mathrm{L,WM}}[i] - \bar{\alpha}_{\mathrm{L,WM}})^2} \tag{C.27}$$

expanded uncertainty

$$U(\alpha_{\mathrm{L,WM}}) = 2u(\alpha_{\mathrm{L,WM}}) \tag{C.28}$$

The asymmetric error bars are defined by the interval from $\bar{\alpha}_{\mathrm{L,WM}} - U(\alpha_{\mathrm{L,WM}}) - \delta\alpha_L$ to $\bar{\alpha}_{\mathrm{L,WM}} + U(\alpha_{\mathrm{L,WM}})$.

**liquid bulk velocity**

combined standard uncertainty:

$$u(v_{\mathrm{BL}}) = |v_{\mathrm{BL}}|\sqrt{\left(\frac{u(\bar{v}_{\mathrm{SL}})}{\bar{v}_{\mathrm{SL}}}\right)^2 + \left(\frac{u(\alpha_{\mathrm{L,WM}})}{\alpha_{\mathrm{L,WM}}}\right)^2} \tag{C.29}$$

effective degrees of freedom

$$\nu(v_{\mathrm{BL}}) = \frac{u(v_{\mathrm{BL}})^4}{{v_{\mathrm{BL}}}^4\left(\left(\frac{u(\bar{v}_{\mathrm{SL}})}{\bar{v}_{\mathrm{SL}}}\right)^4\frac{1}{\nu(\bar{v}_{\mathrm{SL}})} + \left(\frac{u(\alpha_{\mathrm{L,WM}})}{\alpha_{L,WM}}\right)^4\frac{1}{N_{\mathrm{WM}}-1}\right)} \tag{C.30}$$

expanded uncertainty

$$U(v_{\mathrm{BL}}) = t_{\mathrm{ST}\ 0.025}(\nu(v_{\mathrm{BL}}))u(v_{\mathrm{BL}}) \tag{C.31}$$

The asymmetric error bars are defined by the interval from $v_{\mathrm{BL}} - U(v_{\mathrm{BL}})$ to $v_{\mathrm{BL}} + U(v_{\mathrm{BL}}) + \delta v_{\mathrm{BL}}$, where $\delta v_{\mathrm{BL}}$ is defined in Eq. 7.9a.

**dimensionless liquid bulk velocity**

combined standard uncertainty

$$u(v^*_{\mathrm{BL}}) = |v^*_{\mathrm{BL}}| \sqrt{\left(\frac{u(v_{\mathrm{BL}})}{v_{\mathrm{BL}}}\right)^2 + \left(\frac{u(T_1)}{T_1}\right)^2 + \left(\frac{u(y_{c,1})}{y_{c,1}+\overline{\Delta l}}\right)^2 + \left(\frac{u(\overline{\Delta l})}{y_{c,1}+\overline{\Delta l}}\right)^2} \tag{C.32}$$

effective degrees of freedom

$$\nu(v^*_{\mathrm{BL}}) = \frac{u(v^*_{\mathrm{BL}})^4}{{v^*_{\mathrm{BL}}}^4 \left(\left(\frac{u(v_{\mathrm{BL}})}{v_{\mathrm{BL}}}\right)^4 \frac{1}{\nu(v_{\mathrm{BL}})} + \left(\frac{u(T_1)}{T_1}\right)^4 \frac{1}{\nu(T_1)} + \left(\frac{u(y_{c,1})}{y_{c,1}+\overline{\Delta l}}\right)^4 \frac{1}{\nu(y_{c,1})} + \left(\frac{u(\overline{\Delta l})}{y_{c,1}+\overline{\Delta l}}\right)^4 \frac{1}{\nu(\overline{\Delta l})}\right)} \tag{C.33}$$

expanded uncertainty

$$U(v^*_{\mathrm{BL}}) = t_{\mathrm{ST}\ 0.025}(\nu(v_{\mathrm{BL}}))u(v^*_{\mathrm{BL}}) \tag{C.34}$$

The asymmetric error bars are defined by the interval from $v^*_{\mathrm{BL}} - U(v^*_{\mathrm{BL}})$ to $v^*_{\mathrm{BL}} + U(v^*_{\mathrm{BL}}) + \delta v^*_{\mathrm{BL}}$.

**liquid flowrate**

Omitting the uncertainty in $D_p$, which is small compared to the relative uncertainty in $\bar{v}_{\mathrm{SL}}$.
combined standard uncertainty

$$u(q_L) = |q_L| \left|\frac{u(\bar{v}_{\mathrm{SL}})}{\bar{v}_{\mathrm{SL}}}\right| \tag{C.35}$$

effective degrees of freedom

$$\nu(q_L) = \nu(\bar{v}_{\mathrm{SL}}) \tag{C.36}$$

expanded uncertainty

$$U(q_L) = t_{\mathrm{ST}\ 0.025}(\nu(q_L))u(q_L) \tag{C.37}$$

**directional bias error $\bar{\mathbf{v}}_{\mathrm{NMR}} - \mathbf{v}_{\mathrm{BL}}$**

combined standard uncertainty

$$u(\bar{v}_{\mathrm{NMR}} - v_{\mathrm{BL}}) = \sqrt{u(\bar{v}_{\mathrm{NMR}})^2 + u(v_{\mathrm{BL}})^2} \tag{C.38}$$

effective degrees of freedom

$$\nu(\bar{v}_{\mathrm{NMR}} - v_{\mathrm{BL}}) = \frac{u(\bar{v}_{\mathrm{NMR}} - v_{\mathrm{BL}})^4}{\frac{u(\bar{v}_{\mathrm{NMR}})^4}{\nu(\bar{v}_{\mathrm{NMR}})} + \frac{u(v_{\mathrm{BL}})^4}{\nu(v_{\mathrm{BL}})}} \tag{C.39}$$

expanded uncertainty

$$U(\bar{v}_{\mathrm{NMR}} - v_{\mathrm{BL}}) = t_{\mathrm{ST}\ 0.025}(\nu(\bar{v}_{\mathrm{NMR}} - v_{\mathrm{BL}}))u(\bar{v}_{\mathrm{NMR}} - v_{\mathrm{BL}}) \tag{C.40}$$

The asymmetric error bars are defined by the interval from $v_{\mathrm{NMR}} - v_{\mathrm{BL}} - U(v_{\mathrm{NMR}} - v_{\mathrm{BL}}) - \delta v_{\mathrm{BL}}$ to $v_{\mathrm{NMR}} - v_{\mathrm{BL}} + U(v_{\mathrm{NMR}} - v_{\mathrm{BL}})$.

**directional bias error** $\bar{\alpha}_{\mathrm{NMR},2} - \alpha_{\mathrm{L,WM}}$

combined standard uncertainty

$$u(\bar{\alpha}_{\mathrm{NMR},2} - \alpha_{\mathrm{L,WM}}) = \sqrt{u(\bar{\alpha}_{\mathrm{NMR},2})^2 + u(\alpha_{\mathrm{L,WM}})^2} \tag{C.41}$$

effective degrees of freedom

$$\nu(\bar{\alpha}_{\mathrm{NMR},2} - \alpha_{\mathrm{L,WM}}) = \frac{u(\bar{\alpha}_{\mathrm{NMR},2} - \alpha_{\mathrm{L,WM}})^4}{\frac{u(\bar{\alpha}_{\mathrm{NMR},2})^4}{\nu(\bar{\alpha}_{\mathrm{NMR},2})} + \frac{u(\alpha_{\mathrm{L,WM}})^4}{\nu(\alpha_{\mathrm{L,WM}})}} \tag{C.42}$$

expanded uncertainty

$$U(\bar{\alpha}_{\mathrm{NMR},2} - \alpha_{\mathrm{L,WM}}) = t_{\mathrm{ST}\ 0.025}(\nu(\bar{\alpha}_{\mathrm{NMR},2} - \alpha_{\mathrm{L,WM}}))u(\bar{\alpha}_{\mathrm{NMR},2} - \alpha_{\mathrm{L,WM}}) \tag{C.43}$$

The asymmetric error bars are defined by the interval from $\bar{\alpha}_{\mathrm{NMR},2} - \bar{\alpha}_{\mathrm{L,WM}} - U(\bar{\alpha}_{\mathrm{NMR},2} - \alpha_{\mathrm{L,WM}})$ to $\bar{\alpha}_{\mathrm{NMR},2} - \bar{\alpha}_{\mathrm{L,WM}} + U(\bar{\alpha}_{\mathrm{NMR},2} - \alpha_{\mathrm{L,WM}}) + \delta\alpha_L$.

## C.2 Uncertainties in the slug flow measurements

**NMR signal fraction film region**

combined standard uncertainty

$$\begin{aligned} u\left(\left.\frac{s_{y,2}}{s_{y,1}}\right|_F\right) = \left|\frac{m_{21}}{m_{11}}\frac{s_{y,1}(0,1)}{s_{y,2}(0,1)}\right| \Bigg( & \frac{1}{N_{c,11}}\left(\frac{\sigma(m_{11})}{m_{11}}\right)^2 + \frac{1}{N_{c,21}}\left(\frac{\sigma(m_{21})}{m_{21}}\right)^2 \\ & + \frac{1}{N_s}\left(\frac{\sigma(s_{y,1}(0,1))}{s_{y,1}(0,1)}\right)^2 + \frac{1}{N_s}\left(\frac{\sigma(s_{y,2}(0,1))}{s_{y,2}(0,1)}\right)^2 \Bigg)^{1/2} \end{aligned} \tag{C.44}$$

using the standard deviation of the mean in $m_{11}$, $m_{21}$, $s_{y,1}(0,1)$ and $s_{y,2}(0,1)$.
expanded uncertainty

$$U\left(\left.\frac{s_{y,2}}{s_{y,1}}\right|_F\right) = 1.96u\left(\left.\frac{s_{y,2}}{s_{y,1}}\right|_F\right) \tag{C.45}$$

**NMR signal fraction slug region**

combined standard uncertainty

$$\begin{aligned} u\left(\left.\frac{s_{y,2}}{s_{y,1}}\right|_S\right) = \left|\frac{m_{22}}{m_{12}}\frac{s_{y,1}(0,1)}{s_{y,2}(0,1)}\right| \Bigg( & \frac{1}{N_{c,12}}\left(\frac{\sigma(m_{12})}{m_{12}}\right)^2 + \frac{1}{N_{c,22}}\left(\frac{\sigma(m_{22})}{m_{22}}\right)^2 \\ & + \frac{1}{N_s}\left(\frac{\sigma(s_{y,1}(0,1))}{s_{y,1}(0,1)}\right)^2 + \frac{1}{N_s}\left(\frac{\sigma(s_{y,2}(0,1))}{s_{y,2}(0,1)}\right)^2 \Bigg)^{1/2} \end{aligned} \tag{C.46}$$

using the standard deviation of the mean in $m_{12}$, $m_{22}$, $s_{y,1}(0,1)$ and $s_{y,2}(0,1)$.
expanded uncertainty

$$U\left(\left.\frac{s_{y,2}}{s_{y,1}}\right|_S\right) = 1.96u\left(\left.\frac{s_{y,2}}{s_{y,1}}\right|_S\right) \tag{C.47}$$

**NMR film velocity**

standard uncertainty

$$u(v_{\mathrm{NMR,F}}) = \max(v_{\mathrm{NMR,F}} - \mathrm{lb}(v_{\mathrm{NMR,F}}), \mathrm{ub}(v_{\mathrm{NMR,F}}) - v_{\mathrm{NMR,F}}) \tag{C.48}$$

expanded uncertainty

$$U(v_{\mathrm{NMR,F}}) = 1.96u(v_{\mathrm{NMR,F}}) \tag{C.49}$$

**NMR slug velocity**

standard uncertainty

$$u(v_{\mathrm{NMR,S}}) = \max(v_{\mathrm{NMR,S}} - \mathrm{lb}(v_{\mathrm{NMR,S}}), \mathrm{ub}(v_{\mathrm{NMR,S}}) - v_{\mathrm{NMR,S}}) \tag{C.50}$$

expanded uncertainty

$$U(v_{\mathrm{NMR,S}}) = 1.96u(v_{\mathrm{NMR,S}}) \tag{C.51}$$

**NMR liquid holdup in the film region**

combined standard uncertainty

$$u(\alpha_{\mathrm{NMR,F2}}) = \sqrt{{\alpha_{\mathrm{NMR,F2}}}^2\left(\frac{1}{N_{c,21}}\left(\frac{\sigma(m_{21})}{m_{21}}\right)^2 + \frac{2}{N_s}\left(\frac{\sigma(s_{y,2}(0,1))}{s_{y,2}(0,1)}\right)^2\right)}, \tag{C.52}$$

using the standard deviation of the mean in $m_{21}$ and $s_{y,2}(0,1)$.
expanded uncertainty

$$U(\alpha_{\mathrm{NMR,F2}}) = 1.96u(\alpha_{\mathrm{NMR,F2}}) \tag{C.53}$$

**NMR liquid holdup in the slug region**

combined standard uncertainty

$$u(\alpha_{\mathrm{NMR,S2}}) = \sqrt{{\alpha_{\mathrm{NMR,S2}}}^2\left(\frac{1}{N_{c,22}}\left(\frac{\sigma(m_{22})}{m_{22}}\right)^2 + \frac{2}{N_s}\left(\frac{\sigma(s_{y,2}(0,1))}{s_{y,2}(0,1)}\right)^2\right)}, \tag{C.54}$$

using the standard deviation of the mean in $m_{22}$ and $s_{y,2}(0,1)$.
expanded uncertainty

$$U(\alpha_{\mathrm{NMR,S2}}) = 1.96u(\alpha_{\mathrm{NMR,S2}}) \tag{C.55}$$

**Table C.2**: Standard uncertainty and the corresponding degrees of freedom for the slug flow measurements described in chapter 8. When the degrees of freedom are obtained with Eq. C.1 for a Type B evaluation, the assumed relative uncertainty is given.

| | $T_1$ | $y_{c,1}$ | $\overline{\Delta l}$ | $v_{\mathrm{SL},r}$ | $v_{\mathrm{SL},s}$ | $v_{\mathrm{NMR,\{F,S\}}}$ | $v_{\{F,S\}}$ |
|---|---|---|---|---|---|---|---|
| $u$ | 0.01 s | 0.001 m | 0.003 m | | | | |
| $v$, case 1 – 11 | 39 | 8 | 2 | 959 | 50 | 50 | 50 |
| $v$, case 12 – 14 | 39 | 8 | 2 | 2039 | 50 | 50 | 50 |
| assumed reliability $u$ | | 25% | 50% | | 10% | 10% | 10% |

**superficial NMR velocity**

Omitting the uncertainty in the number of points per cluster, $N_{c,2j},\ j \in \{1,2,3\}$, which is believed to be small compared to the other terms.
combined standard uncertainty

$$u(v_{\mathrm{NMR}}) = \left(\left(\alpha_{\mathrm{NMR,F2}}\frac{N_{c,21}}{N_s}\right)^2 u(v_{\mathrm{NMR,F}})^2 + \left(\alpha_{\mathrm{NMR,S2}}\frac{N_{c,22}+N_{c,23}}{N_s}\right)^2 u(v_{\mathrm{NMR,S}})^2 + \left(v_{\mathrm{NMR,F}}\frac{N_{c,21}}{N_s}\right)^2 u(\alpha_{\mathrm{NMR,F2}})^2 + \left(v_{\mathrm{NMR,S}}\frac{N_{c,22}+N_{c,23}}{N_s}\right)^2 u(\alpha_{\mathrm{NMR,S2}})^2\right)^{1/2} \tag{C.56}$$

expanded uncertainty

$$U(v_{\mathrm{NMR}}) = 1.96u(v_{\mathrm{NMR}}) \tag{C.57}$$

**NMR average liquid holdup**

Omitting the uncertainty in the number of points per cluster, $N_{c,2j},\ j \in \{1,2,3\}$, which is believed to be small compared to the other terms.
combined standard uncertainty

$$u(\alpha_{\mathrm{NMR,2}}) = \sqrt{\left(\frac{N_{c,21}}{N_s}\right)^2 u(\alpha_{\mathrm{NMR,F2}})^2 + \left(\frac{N_{c,22}+N_{c,23}}{N_s}\right)^2 u(\alpha_{\mathrm{NMR,S2}})^2} \tag{C.58}$$

expanded uncertainty

$$U(\alpha_{\mathrm{NMR,2}}) = 1.96u(\alpha_{\mathrm{NMR,2}}) \tag{C.59}$$

**dimensionless NMR film velocity**

combined standard uncertainty

$$u(v^*_{\mathrm{NMR,F}}) = \sqrt{{v^*_{\mathrm{NMR,F}}}^2\left(\left(\frac{u(v_{\mathrm{NMR,F}})}{v_{\mathrm{NMR,F}}}\right)^2 + \left(\frac{u(T_1)}{T_1}\right)^2 + \left(\frac{u(y_{c,1})}{y_{c,1}+\overline{\Delta l}}\right)^2 + \left(\frac{u(\overline{\Delta l})}{y_{c,1}+\overline{\Delta l}}\right)^2\right)} \tag{C.60}$$

effective degrees of freedom

$$\nu(v^*_{\mathrm{NMR,F}}) = \frac{u(v^*_{\mathrm{NMR,F}})^4}{{v^*_{\mathrm{NMR,F}}}^4} \frac{1}{\left(\left(\frac{u(v_{\mathrm{NMR,F}})^4}{v_{\mathrm{NMR,F}}}\right)^4 \frac{1}{\nu(v_{\mathrm{NMR,F}})} + \left(\frac{u(T_1)}{T_1}\right)^4 \frac{1}{\nu(T_1)} + \left(\frac{u(y_{c,1})}{y_{c,1}+\overline{\Delta l}}\right)^4 \frac{1}{\nu(y_{c,1})} + \left(\frac{u(\overline{\Delta l})}{y_{c,1}+\overline{\Delta l}}\right)^4 \frac{1}{\nu(\overline{\Delta l})}\right)} \tag{C.61}$$

expanded uncertainty

$$U(v^*_{\mathrm{NMR,F}}) = t_{\mathrm{ST}\ 0.025}(\nu(v^*_{\mathrm{NMR,F}}))u(v^*_{\mathrm{NMR,F}}) \tag{C.62}$$

**dimensionless NMR slug velocity**

combined standard uncertainty

$$u(v^*_{\mathrm{NMR,S}}) = \sqrt{{v^*_{\mathrm{NMR,S}}}^2 \left(\left(\frac{u(v_{\mathrm{NMR,S}})}{v_{\mathrm{NMR,S}}}\right)^2 + \left(\frac{u(T_1)}{T_1}\right)^2 + \left(\frac{u(y_{c,1})}{y_{c,1}+\overline{\Delta l}}\right)^2 + \left(\frac{u(\overline{\Delta l})}{y_{c,1}+\overline{\Delta l}}\right)^2\right)} \tag{C.63}$$

effective degrees of freedom

$$\nu(v^*_{\mathrm{NMR,S}}) = \frac{u(v^*_{\mathrm{NMR,S}})^4}{{v^*_{\mathrm{NMR,S}}}^4} \frac{1}{\left(\left(\frac{u(v_{\mathrm{NMR,S}})^4}{v_{\mathrm{NMR,S}}}\right)^4 \frac{1}{\nu(v_{\mathrm{NMR,S}})} + \left(\frac{u(T_1)}{T_1}\right)^4 \frac{1}{\nu(T_1)} + \left(\frac{u(y_{c,1})}{y_{c,1}+\overline{\Delta l}}\right)^4 \frac{1}{\nu(y_{c,1})} + \left(\frac{u(\overline{\Delta l})}{y_{c,1}+\overline{\Delta l}}\right)^4 \frac{1}{\nu(\overline{\Delta l})}\right)} \tag{C.64}$$

expanded uncertainty

$$U(v^*_{\mathrm{NMR,S}}) = t_{\mathrm{ST}\ 0.025}(\nu(v^*_{\mathrm{NMR,S}}))u(v^*_{\mathrm{NMR,S}}) \tag{C.65}$$

**NMR liquid flowrate**

Omitting the uncertainty in $D_p$, which is small compared to the other terms.
combined standard uncertainty

$$u(q_{\mathrm{NMR}}) = \frac{\pi}{4} D_p^2 u(v_{\mathrm{NMR}}) \tag{C.66}$$

expanded uncertainty

$$U(q_{\mathrm{NMR}}) = \frac{\pi}{4} D_p^2 U(v_{\mathrm{NMR}}) \tag{C.67}$$

**superficial liquid velocity Krohne Optiflux 2300 C**

systematic standard uncertainty

$$u_s(v_{\mathrm{SL}}) = 0.002 v_{\mathrm{SL}} + 0.001 \text{ m s}^{-1} \tag{C.68}$$

random experimental standard deviation of the mean

$$u_r(\bar{v}_{\mathrm{SL}}) = \frac{1}{\sqrt{N_{LJ}}} \sqrt{\frac{1}{N_{LJ}-1} \sum_{i=1}^{N_{LJ}} (v_{\mathrm{SL}}[i] - \bar{v}_{\mathrm{SL}})^2} \tag{C.69}$$

combined standard uncertainty

$$u(\bar{v}_{\mathrm{SL}}) = \sqrt{u_s(\bar{v}_{\mathrm{SL}})^2 + u_r(\bar{v}_{\mathrm{SL}})^2} \tag{C.70}$$

effective degrees of freedom

$$\nu(\bar{v}_{\mathrm{SL}}) = \frac{u(\bar{v}_{\mathrm{SL}})^4}{\frac{u_s(\bar{v}_{\mathrm{SL}})^4}{\nu(\bar{v}_{\mathrm{SL,s}})} + \frac{u_r(\bar{v}_{\mathrm{SL}})^4}{\nu(\bar{v}_{\mathrm{SL,r}})}}, \tag{C.71}$$

where $\nu(\bar{v}_{\mathrm{SL,s}})$ is determined with Eq. C.1 and $\nu(\bar{v}_{\mathrm{SL,r}}) = N_{LJ} - 1$.
expanded uncertainty

$$U(\bar{v}_{\mathrm{SL}}) = t_{\mathrm{ST}\ 0.025}(\nu(\bar{v}_{\mathrm{SL}}))u(\bar{v}_{\mathrm{SL}}) \tag{C.72}$$

**liquid film holdup wiremesh sensor**

systematic overestimation liquid holdup

$$\delta\alpha_L = 0.04 \tag{C.73}$$

standard deviation

$$\sigma(\alpha_{\mathrm{LF}}) = \sqrt{\frac{1}{N_b - 1} \sum_{i=1}^{N_b} (\alpha_{\mathrm{LF}}[i] - \bar{\alpha}_{\mathrm{LF}})^2} \tag{C.74}$$

half-width of the window that contains 95% of the data

$$U(\alpha_{\mathrm{LF}}) = 2\sigma(\alpha_{\mathrm{LF}}) \tag{C.75}$$

The statistical spread is represented by the asymmetric interval from $\bar{\alpha}_{\mathrm{LF}} - U(\alpha_{\mathrm{LF}}) - \delta\alpha_L$ to $\bar{\alpha}_{\mathrm{LF}} + U(\alpha_{\mathrm{LF}})$.

**liquid slug holdup wiremesh sensor**

systematic overestimation liquid holdup

$$\delta\alpha_L = 0.04 \tag{C.76}$$

standard deviation

$$\sigma(\alpha_{\mathrm{LS}}) = \sqrt{\frac{1}{N_b - 1}\sum_{i=1}^{N_b}(\alpha_{\mathrm{LS}}[i] - \bar{\alpha}_{\mathrm{LS}})^2} \tag{C.77}$$

half-width of the window that contains 95% of the data

$$U(\alpha_{\mathrm{LS}}) = 2\sigma(\alpha_{\mathrm{LS}}) \tag{C.78}$$

The statistical spread is represented by the asymmetric interval from $\bar{\alpha}_{\mathrm{LS}} - U(\alpha_{\mathrm{LS}}) - \delta\alpha_L$ to $\bar{\alpha}_{\mathrm{LS}} + U(\alpha_{\mathrm{LS}})$.

**film velocity**

standard deviation

$$\sigma(v_F) = \sqrt{\frac{1}{N_b - 1}\sum_{i=1}^{N_b}(v_F[i] - \bar{v}_F)^2} \tag{C.79}$$

half-width of the window that contains 95% of the data

$$U(v_F) = 2\sigma(v_F) \tag{C.80}$$

The statistical spread is represented by the asymmetric interval from $\bar{v}_F - U(v_F)$ to $\bar{v}_F + U(v_F) + \delta v_F$, where $\delta v_F$ is defined in Eq. 8.32.

**slug velocity**

standard deviation

$$\sigma(v_S) = \sqrt{\frac{1}{N_b - 1}\sum_{i=1}^{N_b}(v_S[i] - \bar{v}_S)^2} \tag{C.81}$$

half-width of the window that contains 95% of the data

$$U(v_S) = 2\sigma(v_S) \tag{C.82}$$

The statistical spread is represented by the asymmetric interval from $\bar{v}_S - U(v_S)$ to $\bar{v}_S + U(v_S) + \delta v_S$, where $\delta v_S$ is defined in Eq. 8.31.

**dimensionless film velocity**

systematic error due to the overestimation of the liquid holdup

$$\delta v_F^* = \frac{\delta v_F T_1}{y_{c,1} + \overline{\Delta l}} \tag{C.83}$$

combined dispersion

$$u(v_F^*) = \sqrt{v_F^{*\,2}\left(\left(\frac{\sigma(v_F)}{v_F}\right)^2 + \left(\frac{u(T_1)}{T_1}\right)^2 + \left(\frac{u(y_{c,1})}{y_{c,1} + \overline{\Delta l}}\right)^2 + \left(\frac{u(\overline{\Delta l})}{y_{c,1} + \overline{\Delta l}}\right)^2\right)} \tag{C.84}$$

effective degrees of freedom

$$\nu(v_F^*) = \frac{u(v_F^*)^4}{v_F^{*\,4}\left(\left(\frac{\sigma(v_F)^4}{v_F}\right)^4 \frac{1}{\nu(v_F)} + \left(\frac{u(T_1)}{T_1}\right)^4 \frac{1}{\nu(T_1)} + \left(\frac{u(y_{c,1})}{y_{c,1}+\overline{\Delta l}}\right)^4 \frac{1}{\nu(y_{c,1})} + \left(\frac{u(\overline{\Delta l})}{y_{c,1}+\overline{\Delta l}}\right)^4 \frac{1}{\nu(\overline{\Delta l})}\right)} \tag{C.85}$$

half-width of the window that contains 95% of the data

$$U(v_F^*) = t_{\mathrm{ST}\ 0.025}(\nu(v_F^*))u(v_F^*) \tag{C.86}$$

The statistical spread is represented by the asymmetric interval from $\bar{v}_F^* - U(v_F^*)$ to $\bar{v}_F^* + U(v_F^*) + \delta v_F^*$.

**dimensionless slug velocity**

systematic error due to the overestimation of the liquid holdup

$$\delta v_S^* = \frac{\delta v_S T_1}{y_{c,1} + \overline{\Delta l}} \tag{C.87}$$

combined dispersion

$$u(v_S^*) = \sqrt{v_S^{*\,2}\left(\left(\frac{\sigma(v_S)}{v_S}\right)^2 + \left(\frac{u(T_1)}{T_1}\right)^2 + \left(\frac{u(y_{c,1})}{y_{c,1} + \overline{\Delta l}}\right)^2 + \left(\frac{u(\overline{\Delta l})}{y_{c,1} + \overline{\Delta l}}\right)^2\right)} \tag{C.88}$$

effective degrees of freedom

$$\nu(v_S^*) = \frac{u(v_S^*)^4}{v_S^{*\,4}\left(\left(\frac{\sigma(v_S)^4}{v_S}\right)^4 \frac{1}{\nu(v_S)} + \left(\frac{u(T_1)}{T_1}\right)^4 \frac{1}{\nu(T_1)} + \left(\frac{u(y_{c,1})}{y_{c,1}+\overline{\Delta l}}\right)^4 \frac{1}{\nu(y_{c,1})} + \left(\frac{u(\overline{\Delta l})}{y_{c,1}+\overline{\Delta l}}\right)^4 \frac{1}{\nu(\overline{\Delta l})}\right)} \tag{C.89}$$

half-width of the window that contains 95% of the data

$$U(v_S^*) = t_{\mathrm{ST}\ 0.025}(\nu(v_S^*))u(v_S^*) \tag{C.90}$$

The statistical spread is represented by the asymmetric interval from $\bar{v}_S^* - U(v_S^*)$ to $\bar{v}_S^* + U(v_S^*) + \delta v_S^*$.

**liquid flowrate**

Omitting the uncertainty in $D_p$, which is small compared to the relative uncertainty in $\bar{v}_{\mathrm{SL}}$.
combined standard uncertainty

$$u(q_L) = |q_L| \left| \frac{u(\bar{v}_{\mathrm{SL}})}{\bar{v}_{\mathrm{SL}}} \right| \tag{C.91}$$

effective degrees of freedom

$$\nu(q_L) = \nu(\bar{v}_{\mathrm{SL}}) \tag{C.92}$$

expanded uncertainty

$$U(q_L) = t_{\mathrm{ST}\ 0.025}(\nu(q_L))u(q_L) \tag{C.93}$$

**directional bias error** $v_{\mathrm{NMR,F}} - v_F$

combined dispersion

$$u(v_{\mathrm{NMR,F}} - v_F) = \sqrt{u(v_{\mathrm{NMR,F}})^2 + \sigma(v_F)^2} \tag{C.94}$$

effective degrees of freedom

$$\nu(v_{\mathrm{NMR,F}} - v_F) = \frac{u(v_{\mathrm{NMR,F}} - v_F)^4}{(v_{\mathrm{NMR,F}} - v_F)^4 \left( \frac{u(v_{\mathrm{NMR,F}})^4}{\nu(v_{\mathrm{NMR,F}})} + \frac{\sigma(v_F)^4}{\nu(v_F)} \right)} \tag{C.95}$$

half-width of the window that contains 95% of the data

$$U(v_{\mathrm{NMR,F}} - v_F) = t_{\mathrm{ST}\ 0.025}(\nu(v_{\mathrm{NMR,F}} - v_F))u(v_{\mathrm{NMR,F}} - v_F) \tag{C.96}$$

The statistical spread is represented by the asymmetric interval from $v_{\mathrm{NMR,F}} - \bar{v}_F - U(v_{\mathrm{NMR,F}} - v_F) - \delta v_F$ to $v_{\mathrm{NMR,F}} - \bar{v}_F + U(v_{\mathrm{NMR,F}} - v_F)$.

**directional bias error** $v_{\mathrm{NMR,S}} - v_S$

combined dispersion

$$u(v_{\mathrm{NMR,S}} - v_S) = \sqrt{u(v_{\mathrm{NMR,S}})^2 + \sigma(v_S)^2} \tag{C.97}$$

effective degrees of freedom

$$\nu(v_{\mathrm{NMR,S}} - v_S) = \frac{u(v_{\mathrm{NMR,S}} - v_S)^4}{(v_{\mathrm{NMR,S}} - v_S)^4 \left( \frac{u(v_{\mathrm{NMR,S}})^4}{\nu(v_{\mathrm{NMR,S}})} + \frac{\sigma(v_S)^4}{\nu(v_S)} \right)} \tag{C.98}$$

half-width of the window that contains 95% of the data

$$U(v_{\mathrm{NMR,S}} - v_S) = t_{\mathrm{ST}\ 0.025}(\nu(v_{\mathrm{NMR,S}} - v_S))u(v_{\mathrm{NMR,S}} - v_S) \tag{C.99}$$

The statistical spread is represented by the asymmetric interval from $v_{\mathrm{NMR,S}} - \bar{v}_S - U(v_{\mathrm{NMR,S}} - v_S) - \delta v_S$ to $v_{\mathrm{NMR,S}} - \bar{v}_S + U(v_{\mathrm{NMR,S}} - v_S)$.

**directional bias error** $\alpha_{\mathrm{NMR,F2}} - \alpha_{\mathrm{LF}}$

combined dispersion

$$u(\alpha_{\mathrm{NMR,F2}} - \alpha_{\mathrm{LF}}) = \sqrt{u(\alpha_{\mathrm{NMR,F2}})^2 + \sigma(\alpha_{\mathrm{LF}})^2} \tag{C.100}$$

effective degrees of freedom

$$\nu(\alpha_{\mathrm{NMR,F2}} - \alpha_{\mathrm{LF}}) = \frac{u(\alpha_{\mathrm{NMR,F2}} - \alpha_{\mathrm{LF}})^4}{(\alpha_{\mathrm{NMR,F2}} - \alpha_{\mathrm{LF}})^4 \left(\frac{u(\alpha_{\mathrm{NMR,F2}})^4}{\nu(\alpha_{\mathrm{NMR,F2}})} + \frac{\sigma(\alpha_{\mathrm{LF}})^4}{\nu(\alpha_{\mathrm{LF}})}\right)} \tag{C.101}$$

half-width of the window that contains 95% of the data

$$U(\alpha_{\mathrm{NMR,F2}} - \alpha_{\mathrm{LF}}) = t_{\mathrm{ST}\ 0.025}(\alpha_{\mathrm{NMR,F2}} - \alpha_{\mathrm{LF}})u(\alpha_{\mathrm{NMR,F2}} - \alpha_{\mathrm{LF}}) \tag{C.102}$$

The statistical spread is represented by the asymmetric interval from $\alpha_{\mathrm{NMR,F2}} - \bar{\alpha}_{\mathrm{LF}} - U(\alpha_{\mathrm{NMR,F2}} - \alpha_{\mathrm{LF}})$ to $\alpha_{\mathrm{NMR,F2}} - \bar{\alpha}_{\mathrm{LF}} + U(\alpha_{\mathrm{NMR,F2}} - \alpha_{\mathrm{LF}}) + \delta\alpha_L$.

**directional bias error** $\alpha_{\mathrm{NMR,S2}} - \alpha_{\mathrm{LS}}$

combined dispersion

$$u(\alpha_{\mathrm{NMR,S2}} - \alpha_{\mathrm{LS}}) = \sqrt{u(\alpha_{\mathrm{NMR,S2}})^2 + \sigma(\alpha_{\mathrm{LS}})^2} \tag{C.103}$$

effective degrees of freedom

$$\nu(\alpha_{\mathrm{NMR,S2}} - \alpha_{\mathrm{LS}}) = \frac{u(\alpha_{\mathrm{NMR,S2}} - \alpha_{\mathrm{LS}})^4}{(\alpha_{\mathrm{NMR,S2}} - \alpha_{\mathrm{LS}})^4 \left(\frac{u(\alpha_{\mathrm{NMR,S2}})^4}{\nu(\alpha_{\mathrm{NMR,S2}})} + \frac{\sigma(\alpha_{\mathrm{LS}})^4}{\nu(\alpha_{\mathrm{LS}})}\right)} \tag{C.104}$$

half-width of the window that contains 95% of the data

$$U(\alpha_{\mathrm{NMR,S2}} - \alpha_{\mathrm{LS}}) = t_{\mathrm{ST}\ 0.025}(\alpha_{\mathrm{NMR,S2}} - \alpha_{\mathrm{LS}})u(\alpha_{\mathrm{NMR,S2}} - \alpha_{\mathrm{LS}}) \tag{C.105}$$

The statistical spread is represented by the asymmetric interval from $\alpha_{\mathrm{NMR,S2}} - \bar{\alpha}_{\mathrm{LS}} - U(\alpha_{\mathrm{NMR,S2}} - \alpha_{\mathrm{LS}})$ to $\alpha_{\mathrm{NMR,S2}} - \bar{\alpha}_{\mathrm{LS}} + U(\alpha_{\mathrm{NMR,S2}} - \alpha_{\mathrm{LS}}) + \delta\alpha_S$.

# Appendix D

# Spectral Characterization of Stratified Flow Regimes

Different stratified flow sub-regimes are defined according to the different type of waves on the gas-liquid interface. Such differences give rise to wave type specific power spectra of the liquid level fluctuations. As the different peak frequencies carry information about the existing surface waves, the appearance, disappearance and shape changes of the peaks are an indication for the transitions between the wave patterns [12, 67, 228, 238].

## D.1 Why Welch, how does it work?

Welch's periodogram averaging technique [257] is a method to improve the variance of the estimated power spectrum of stationary, long-time signals. Periodograms have the disadvantage that the variance stays the same even though the signal length increases. Since we are especially interested in the lower frequencies of the range measured (between 0 and the Nyquist frequency $f_s/2$), the spectrum of the interface waves is not smooth enough to determine the dominant frequencies with a peak picker. Welch's algorithm successfully reduces those fluctuations in the PSD, however, with a resolution trade-off [189].

The power spectrum is only computed for the fluctuating part of the interface signal. The average liquid level is subtracted to avoid leakage of the associated zero frequency peak into the low-frequency components.

In Welch's method, the data sequence of the liquid level fluctuations $h'_L[n], 0 \leq n \leq N-1$, is first divided into $K$ segments

$$h_{L,r}[n] = h'_L[rR + n]w[n], \qquad 0 \leq n \leq L-1 \tag{D.1}$$

of $L$ elements each that are multiplied by a window $w[n]$ of the same length $L$. $R$ is the number of elements that does not overlap with the previous section. So, $R = L$ if the segments

are contiguous and $R = L/2$ in the case of 50% overlapping segments. By using the FFT algorithm to compute the discrete Fourier transform, the modified periodogram of the r$^{th}$ full-length segment is given by

$$P_{h_L h_L,r}[k] = \frac{1}{LU}\left|H_{L,r}[k]\right|^2, \qquad k = 0, 1, ..., L-1 \tag{D.2}$$

where $H_{L,r}[k]$ is the L-point DFT of $h_{L,r}[n]$ and

$$U = \frac{1}{L}\sum_{n=0}^{L-1}(w[n])^2 \tag{D.3}$$

is a normalizing constant that corrects for the windowing operation. Next, the time-averaged periodogram of the spectral estimate is computed as the arithmetic average

$$\bar{P}_{h_L h_L}[k] = \frac{1}{K}\sum_{r=0}^{K-1} P_{h_L h_L,r}[k], \qquad k = 0, 1, ..., L-1 \tag{D.4}$$

of the periodogram estimates $P_{h_L h_L,r}[k]$ belonging to the $K$ segments. The normalized discrete frequencies, denoted by the index $k$, are equally distributed between $-\pi$ and $\pi$. For even $L$, they correspond to the continuous-time frequencies

$$\omega[k] = \begin{cases} \dfrac{2\pi k f_s}{L}, & k = 0, 1, ..., L/2 \\ -\dfrac{2\pi(L-k)f_s}{L}, & k = L/2+1, ..., L-1 \end{cases} \tag{D.5}$$

where $f_s$ is the sample frequency of the signal. Oppenheim et al. [189] show that the variance of the average periodogram $\bar{P}_{h_L h_L,r}[k]$ is inversely proportional to the number of periodograms averaged. Dividing a fixed-length signal into a larger number of segments will thus result in a smoother periodogram, but with the negative effect of a reduced frequency resolution

$$\Delta f = \frac{f_s}{L} \tag{D.6}$$

as $L$, the number of elements per segment, decreases accordingly. Given a window of a certain length, the best reduction of the variance is achieved by 50% overlapping segments [189].

## D.2 Implementation

In the present study, the interfacial wave power spectrum is computed by averaging $K = 99$ PSD estimates. Welch's method is combined with a 50% overlapping Hamming window

$$w[n] = \begin{cases} 0.54 - 0.46\cos\left(\dfrac{2\pi n}{L-1}\right), & 0 \le n \le L-1 \\ 0, & \text{otherwise} \end{cases} \tag{D.7}$$

**Table D.1:** Parameters for Welch's averaged periodogram estimation.

| $v_{SL}$ [ms$^{-1}$] | $f_s$ [Hz] | $N$ | $K$ | $L$ | NFFT | $\Delta f$ [Hz] |
|---|---|---|---|---|---|---|
| 0.050 | 800 | 80,000 | 99 | 1600 | 2048 | 0.391 |
| 0.100 | 500 | 102,400 | 99 | 2048 | 2048 | 0.244 |
| 0.150 | 800 | 80,000 | 99 | 1600 | 2048 | 0.391 |

and a 2048-point FFT. Dependent on the number of data points, the data sequence is either truncated or zero-padding is applied. This means that in the case of zero-padding, the apparent frequency resolution increases, because $L$ in Eq. D.5 and D.6 should be replaced by the size of the FFT. Since part of the signals is acquired at 500 Hz and part at 800 Hz, their respective spectral resolutions are close but slightly different. The signal analysis parameters are summarized in table D.1.

## D.3 Regime dependent spectral shape

Under the conditions of low gas (below 3 m s$^{-1}$) and low liquid superficial velocities (0.05 – 0.15 m s$^{-1}$), two stratified sub-regimes are found: stratified smooth (SS) and stratified wavy (SW) flow with regular two-dimensional (2D) waves.
Typical time traces of the dimensionless liquid height calculated from the cross-sectional holdup and their corresponding power spectra are shown in Figure D.1 and D.2 in order of increasing wave instability. In case the liquid flowrate would be kept constant, this is the effect of an increasing gas flowrate. Matlab's peak picking function 'findpeaks' is used for determining the peak frequencies, associated with the interfacial waves, from the PSD estimate.

In the stratified smooth regime no significant peaks are observed in the PSDs as the gas-liquid interface is almost undisturbed. Initially the signal is a smooth decaying function (Figure D.1, top), but with increasing gas flowrate, tiny peaks are formed by the ripples on the interface (Figure D.1, middle). As long as those peaks remain well below the initial level of the spectrum, the flow is defined as stratified smooth.

The onset of the stratified wavy flow regime is considered to take place when the primary peak in the power spectrum has risen to about the initial level (Figure D.1, bottom). At this stage, the RMS amplitude

$$A_{rms} = \sqrt{2}\sigma_{h_L} = \sqrt{\frac{2}{N-1}\sum_{i=1}^{N}\left(h_L[i] - \bar{h}_L\right)^2}, \tag{D.8}$$

of the waves is with values below 1.5 mm still very low, as table D.2 illustrates. This is in agreement with the transition criterion as suggested by both Strand [238] and Ayati et al. [12]

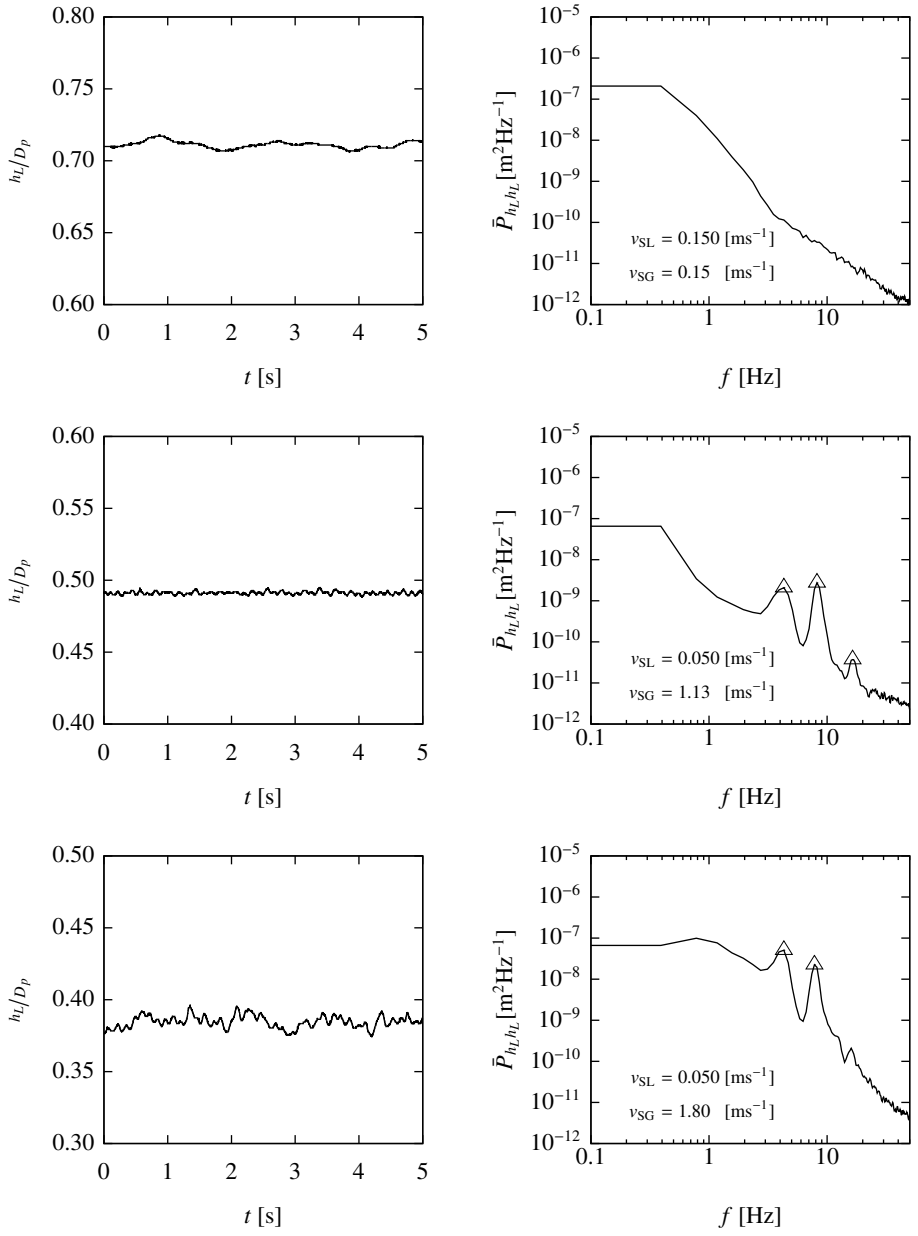


**Figure D.1**: Time traces of the dimensionless liquid height calculated from the cross-sectional liquid holdup and the corresponding PSDs for stratified smooth flow (top, middle) and the transition from stratified smooth to stratified wavy flow (bottom).

**Table D.2**: Sub-regime classification according to the shape of the PSD estimate for the stratified flow measurements presented in chapter 7.

| $v_{SL}$ [m s$^{-1}$] | $v_{SG}$ [m s$^{-1}$] | $v_{BL}$ [m s$^{-1}$] | $\bar{\alpha}_L$ [-] | $\bar{h}_L \pm A_{rms}$ [mm] | $f_p$ [Hz] | |
|---|---|---|---|---|---|---|
| 0.050 | 0.15 | 0.072 | 0.70 | 64.9 ± 0.2 | | SS |
| 0.050 | 0.41 | 0.072 | 0.69 | 64.3 ± 0.2 | | SS |
| 0.050 | 0.87 | 0.092 | 0.55 | 53.0 ± 0.3 | | SS |
| 0.050 | 1.13 | 0.102 | 0.49 | 48.7 ± 0.4 | | SS |
| 0.050 | 1.32 | 0.11 | 0.47 | 47.3 ± 0.4 | | SS |
| 0.050 | 1.61 | 0.13 | 0.38 | 39.7 ± 0.4 | | SS to SW |
| 0.050 | 1.8 | 0.14 | 0.35 | 37.8 ± 0.7 | | SS to SW |
| 0.050 | 2.1 | 0.15 | 0.33 | 36.2 ± 1.4 | | SS to SW |
| 0.050 | 2.3 | 0.16 | 0.31 | 34.6 ± 1.8 | 3.5 | 2D SW |
| 0.050 | 2.6 | 0.16 | 0.32 | 34.8 ± 2.4 | 3.1 | 2D SW |
| 0.050 | 2.7 | 0.16 | 0.31 | 34.3 ± 2.0 | 2.9 | 2D SW |
| 0.099 | 0.61 | 0.15 | 0.66 | 61.9 ± 0.6 | | SS |
| 0.100 | 0.74 | 0.16 | 0.63 | 59.6 ± 0.6 | | SS |
| 0.100 | 0.87 | 0.17 | 0.59 | 56.2 ± 0.5 | | SS |
| 0.099 | 1.00 | 0.17 | 0.59 | 56.0 ± 0.5 | | SS |
| 0.099 | 1.13 | 0.18 | 0.55 | 53.5 ± 0.6 | | SS |
| 0.099 | 1.26 | 0.19 | 0.53 | 51.4 ± 0.8 | | SS to SW |
| 0.099 | 1.47 | 0.19 | 0.53 | 51.6 ± 4.1 | 3.7 | 2D SW |
| 0.099 | 1.61 | 0.19 | 0.51 | 49.9 ± 5.0 | 3.4 | 2D SW |
| 0.150 | 0.15 | 0.20 | 0.76 | 69.8 ± 0.6 | | SS |
| 0.150 | 0.28 | 0.20 | 0.76 | 70.1 ± 0.8 | | SS |
| 0.150 | 0.48 | 0.23 | 0.66 | 61.5 ± 1.6 | 3.9 | 2D SW |
| 0.150 | 0.61 | 0.23 | 0.65 | 60.7 ± 2.4 | 3.9 | 2D SW |
| 0.150 | 0.74 | 0.26 | 0.59 | 56.1 ± 2.7 | 3.9 | 2D SW |

for 10 cm pipes.

For even higher gas flowrates, the spectrum is for the first time dominated by a peak with a center frequency of 3 – 4.5 Hz, see Figure D.2. Judging from the PSD, it is evident that the flow has changed into the stratified wavy regime. The sharp and almost symmetric peak is typical for the near-sinusoidal 2D waves that are the first to occur [228]. Apart from the leading peak, higher order harmonics can be observed, reflecting the different structures that exist at different zones of the interface. Contrary to channel flow [67], the 2D waves in a pipe flow do not simply extend from one wall to the other, but a number of waves with different amplitudes and wavelengths exist near the wall and in the center of the pipe [238]. Since the power spectral density is calculated for the average liquid height in the entire cross-section, we do not differentiate between the different zones, the frequencies corresponding to the less dominant waves are also present in the spectrum.

Calculating the average liquid height over the entire pipe cross-section is also the reason why the detected peak frequencies are specific for 10 cm pipes and the measurements by Shi and Kocamustafaogullari [228] in a 5 cm pipe can not be used for reference purposes. The amplitude and wavelength of the surface waves are largely determined by the dimensions of the pipe.

The subsequent cases in Figure D.2 show that the peaks in the PSD plots get more pronounced with increasing wave amplitudes. Because the research presented here is limited to conditions in the onset stage of the stratified wavy flow regime, only small amplitude waves are observed.
If the superficial gas velocity is somewhat higher, the work of Strand [238] and Ayati et al. [12] shows that also the secondary peak at 7 – 9 Hz will exceed the initial level of the spectrum. This means that two distinct waves are present with each a different wavelength and amplitude. At this stage, the waves are still regular and two-dimensional. Therefore, it is also considered to be the same stratified wavy flow regime.

Initially all waves are small in amplitude. At a fixed superficial liquid velocity, the RMS amplitude of the waves will increase with the gas superficial velocity until the maximum level is reached, the so-called large amplitude waves. This maximum level occurs at higher gas flowrates if the liquid level, $h_L$, is decreased. Strand [238] shows that the superficial gas velocities at which the maximum wave amplitudes are found in a 10 cm pipe comprise a tongue-shaped region ranging from 3.5 m $s^{-1}$ for high liquid flowrates to almost 5 m $s^{-1}$ for a liquid superficial velocity of 0.07 m $s^{-1}$.
Characteristic of the regular 2D waves, discussed so far, is a PSD with one or two peaks and the most energetic wave components distributed in a narrow bandwidth around the dominant wave frequency. This bandwidth remains roughly constant for an increasing gas flowrate. Furthermore, Ayati et al. [12] point out that the primary peak frequency, $f_p$, decreases in the regular 2D wave regime with increasing slip velocity, $v_{BG} - v_{BL}$, which is in conformity with our measurement results, given in table D.2.

Once the maximum wave amplitude is reached, the energy transfer by an even higher gas flowrate has no longer the effect of increasing the wave amplitude, but it starts to disturb the wave interface [12, 228, 238]. More and more irregular wave structures appear, resulting in PSD plots with broadened and flattened peaks. A second criterion that can be used to distinguish the irregular from the regular 2D wave regime is again the primary peak frequency. Ayati et al. [12] show how in the irregular case $f_p$ will start to increase instead of decrease as a function of the slip velocity.

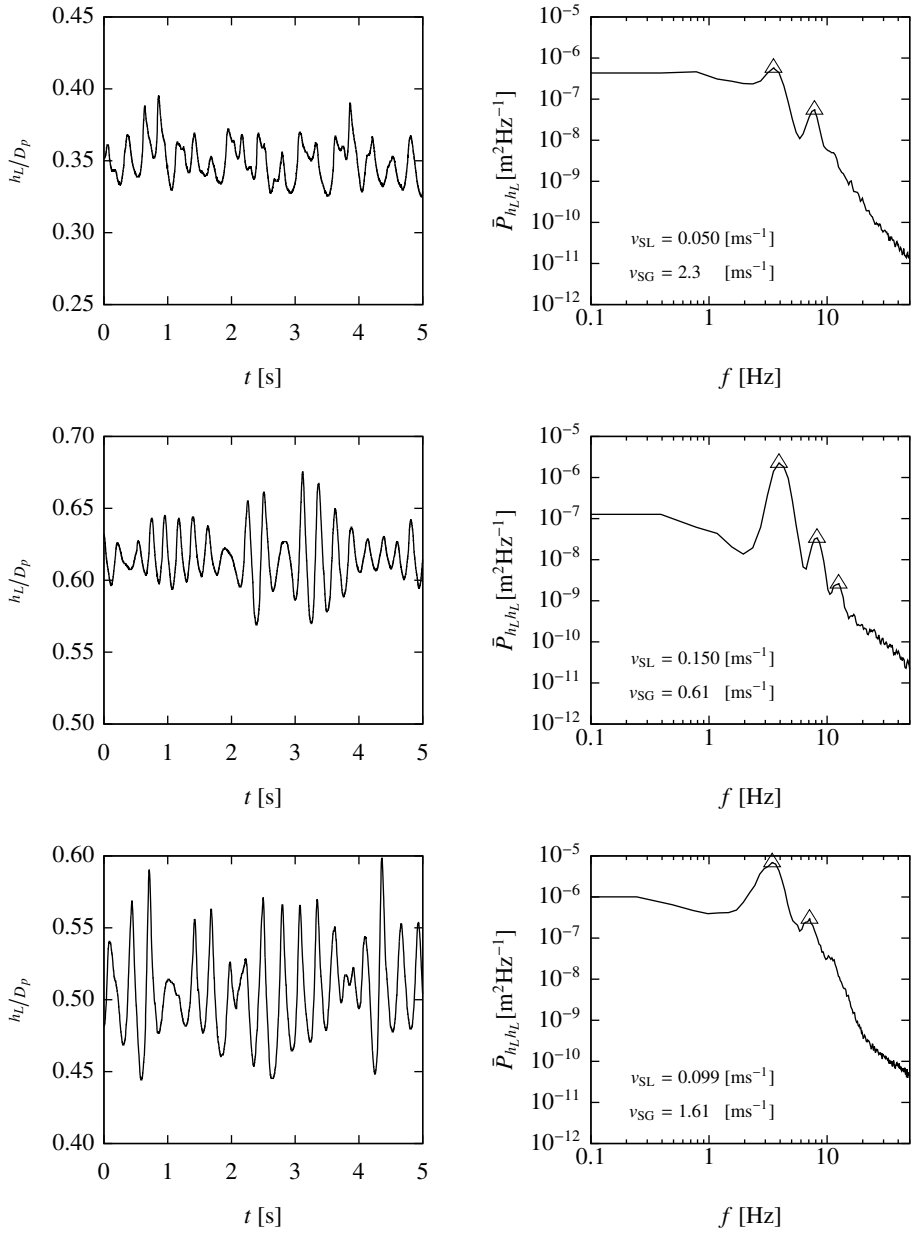


**Figure D.2**: Time traces of the dimensionless liquid height calculated from the cross-sectional liquid holdup and the corresponding PSDs for stratified flow with regular 2D waves (2D SW) in order of increasing RMS wave amplitude.

# Appendix E

# Streamwise Velocity Model for Stratified Flow

This appendix describes how the two-dimensional velocity profile of the liquid phase in turbulent stratified smooth and stratified wavy flow with 2D regular waves is modeled based on the experimental results by Strand [238]. The velocity field is discretized by projecting the pipe's cross-section, as shown in Figure E.1, on a square grid of $N_v \times N_v$ cells, where $N_v$ is even. The position of the node of grid cell [i,j] is defined by

$$xv[i] = \left(i - \frac{1}{2}\right) Dx \tag{E.1a}$$

$$zv[j] = \left(j - \frac{1}{2}\right) Dz \tag{E.1b}$$

where $Dx = Dz = D_p/N_v$. For each cell a weight coefficient $w[i, j]$ is calculated which indicates the percentage of the cell enclosed by the pipe. A cell that is entirely inside the pipe gets a weight coefficient of 1 and a cell that is completely outside the pipe a weight coefficient of 0. It is assumed that the liquid level $h_L$ equals a whole number $NzhL$ of cells.

The construction of the two-dimensional velocity field takes place in 2 steps. First the velocity profile along the vertical axis $vyz0[j]$ is defined, after which the horizontal profile for each $zv[j]$ is scaled with the corresponding center velocity. To this end, first the number of cells $NxhL[j]$ over which the local pipe diameter

$$Dpz[j] = 2\sqrt{zv[j]\left(D_p - zv[j]\right)} \tag{E.2}$$

extends is computed. Subsequently, the cells with $zv[j]$ below the water level ($j \leq NzhL$) are classified according to the following 4 clauses:

1. **IF** $i \leq N_v/2 - NxhL[j]/2$ **THEN** left outside of the pipe

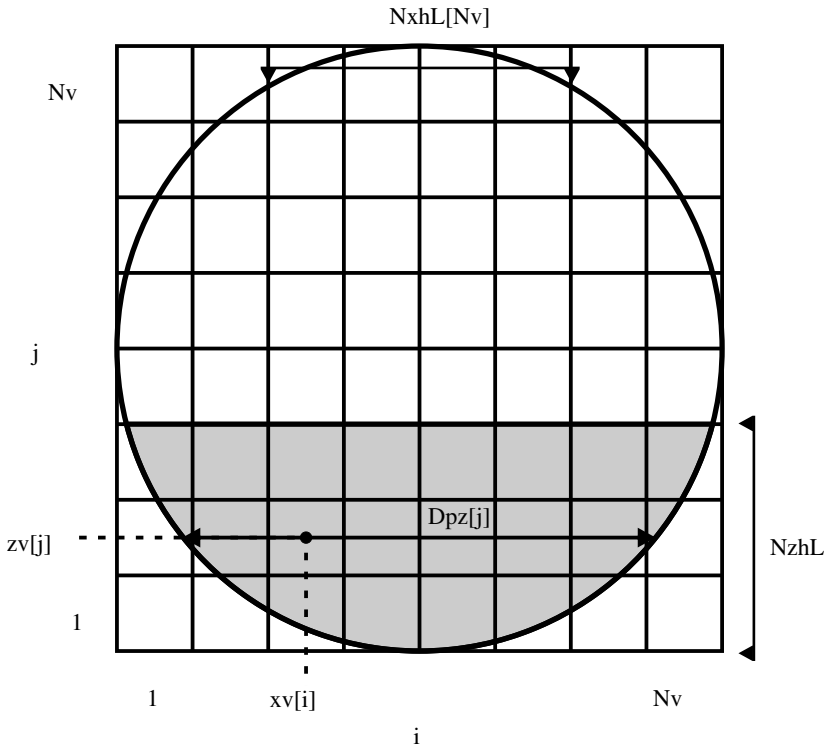


**Figure E.1**: Definition of the discretization scheme used for modeling the two-dimensional velocity field $v_y[i, j]$ in the liquid phase of stratified flow.

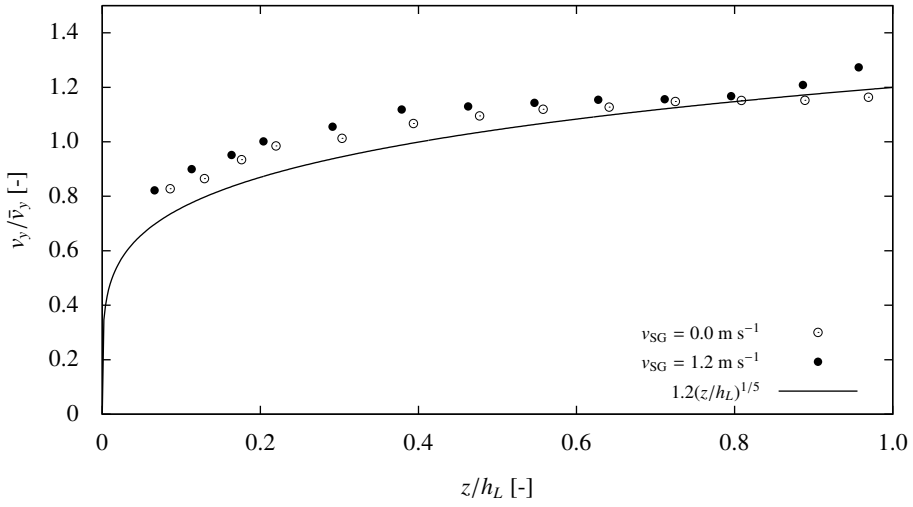


**Figure E.2**: Normalized streamwise velocity along the vertical axis at $v_{SL} = 0.10$ m s$^{-1}$ after Strand [238]. The average water level $h_L$ is 42.9 mm at $v_{SG} = 0$ m s$^{-1}$ and is assumed to be 42.7 mm at $v_{SG} = 1.2$ m s$^{-1}$.

2. **ELSE IF** $i \geq N_v/2 + NxhL[j]/2$ **THEN** right outside of the pipe

3. **ELSE IF** $i \leq N_v/2$ **THEN** in the left half of the pipe

4. **ELSE** in the right half of the pipe

after which the velocity at each node of the row is calculated.

## E.1 Stratified Smooth Velocity Profile

The LDA measurements performed by Strand [238] for $v_{SL} = 0.10$ m s$^{-1}$ and $v_{SG} = 1.2$ m s$^{-1}$ (File UV10A1, UV10A2, UV10A3 and UV10A4) serve as a model for the stratified smooth velocity profile. In figure E.2 the velocity profile along the vertical axis is plotted for both $v_{SG} = 0$ m s$^{-1}$ and $v_{SG} = 1.2$ m s$^{-1}$. In the simulations, this velocity profile is reconstructed by using the power law

$$vyz0[j] = \frac{5+1}{5}\left(\frac{zv[j]}{h_L}\right)^{1/5}, \tag{E.3}$$

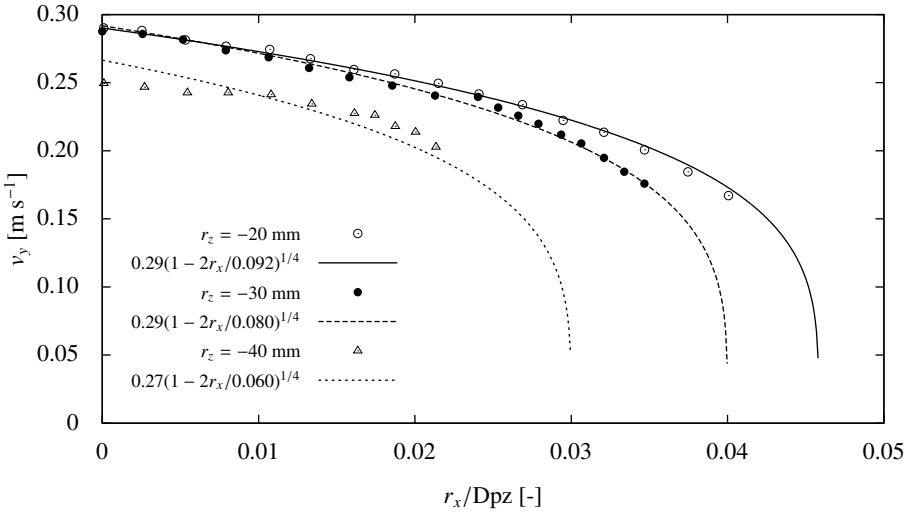


**Figure E.3**: Streamwise velocity along the horizontal chords at $r_z = -20$ mm, $r_z = -30$ mm and $r_z = -40$ mm at $v_{SL} = 0.10$ m s$^{-1}$ and $v_{SG} = 1.2$ m s$^{-1}$ after Strand [238].

which approaches the profile reasonably well. Figure E.3 gives the velocity profile along 3 horizontal chords at $r_z = -20$ mm, $r_z = -30$ mm and $r_z = -40$ mm. The power law

$$v_y(r_x[i]) = vyz0[j]\left(1 - \frac{2r_x[i]}{Dpz[j]}\right)^{1/4} \tag{E.4}$$

with $r_x[i] = |D_p/2 - xv[i]|$ gives the best fit of the data at $r_z = -20$ mm and at $r_z = -30$ mm. Figure E.4 shows the corresponding modeled velocity profile for a liquid holdup of 0.5 and 0.8, the limits of the stratified smooth measurements described in chapter 7. Below a fragment of the Fortran code, used to calculate this 2D velocity matrix is given.

```
pz = 5
py = 4

DO j = 1,NzhL
   vyz0(j) = zv(j)**(1.0/pz)
END DO

wSF = 0.0
vysum = 0.0
wsum = 0.0

DO j = 1,NzhL
```

```
  Dpz(j) = 2.0*SQRT(zv(j)*(Dp-zv(j)))
  NxhL(j) = 2*NINT(Dpz(j)/(2.0*Dx))
  DO i = 1,Nv
    IF (i .LE. (Nv/2 - NxhL(j)/2)) THEN
      vy(i,j) = 0.0
    ELSE IF (i .GT. (Nv/2 + NxhL(j)/2)) THEN
      vy(i,j) = 0.0
    ELSE IF (i .LE. Nv/2) THEN
      vy(i,j) = vyz0(j)*(1.0 - (Dp-2.0*xv(i))/Dpz(j))**(1.0/py)
      wSF = wSF + w(i,j)
      vysum = vysum + vy(i,j)
      wsum = wsum + w(i,j)
    ELSE
      vy(i,j) = vyz0(j)*(1.0 - (2.0*xv(i)-Dp)/Dpz(j))**(1.0/py)
      wSF = wSF + w(i,j)
      vysum = vysum + vy(i,j)
      wsum = wsum + w(i,j)
    END IF
  END DO
END DO

IF (NzhL .NE. Nv) THEN
  DO j = NzhL+1,Nv
    DO i = 1,Nv
      vy(i,j) = 0.0
      wsum = wsum + w(i,j)
    END DO
  END DO
END IF

Avy = wSF/vysum
DO i = 1,Nv
  DO j = 1,Nv
    vy(i,j) = Avy*vy(i,j)
  END DO
END DO

alphaSF = wSF/wsum
```

## E.2 Stratified Wavy Velocity Profile

For the construction of the stratified wavy velocity profile, the measurement data of Strand [238] at $v_{SL} = 0.10$ m s$^{-1}$ and $v_{SG} = 1.7$ m s$^{-1}$ (File UV14A1 and UV14A2) is interpolated over the area containing the liquid phase.

The vertical velocity profile characterized by the typical S-shape is shown in Figure E.5(b). Normalized with the average velocity, the axial velocity profiles at $v_{SG} = 1.7$ m s$^{-1}$ and the much higher $v_{SG} = 3.1$ m s$^{-1}$ have about the same shape. This justifies the use of the obtained velocity profile as template for approaching the stratified wavy flow cases at different liquid velocities.

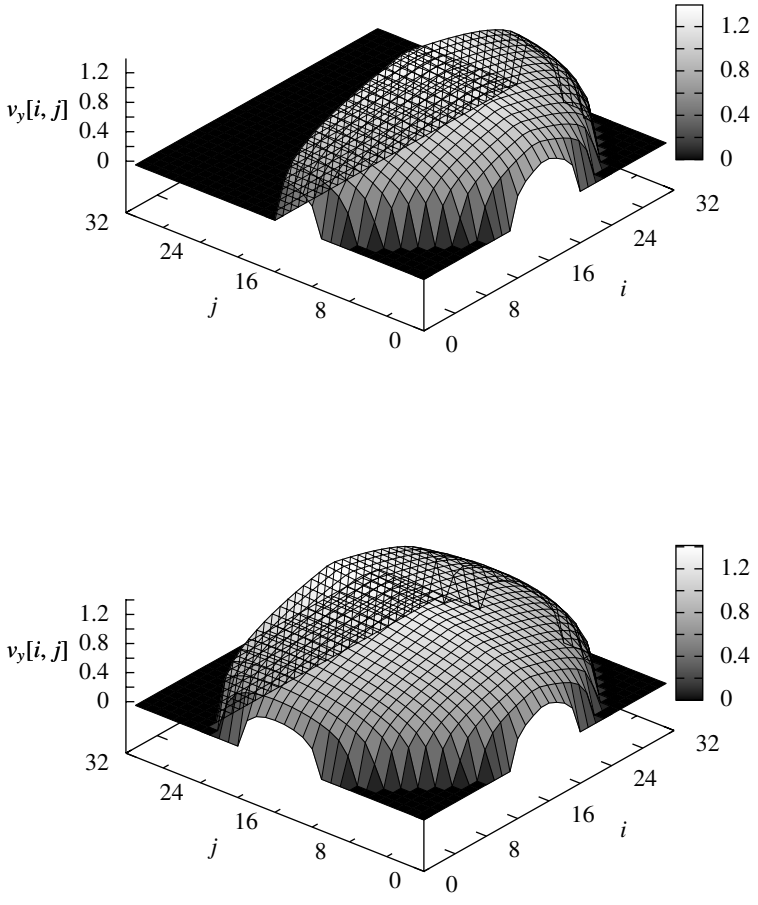


**Figure E.4**: Typical artificial streamwise velocity profile of the liquid phase used to model turbulent smooth stratified flow at (top) $\alpha_L = 0.5$ and (bottom) $\alpha_L = 0.8$.

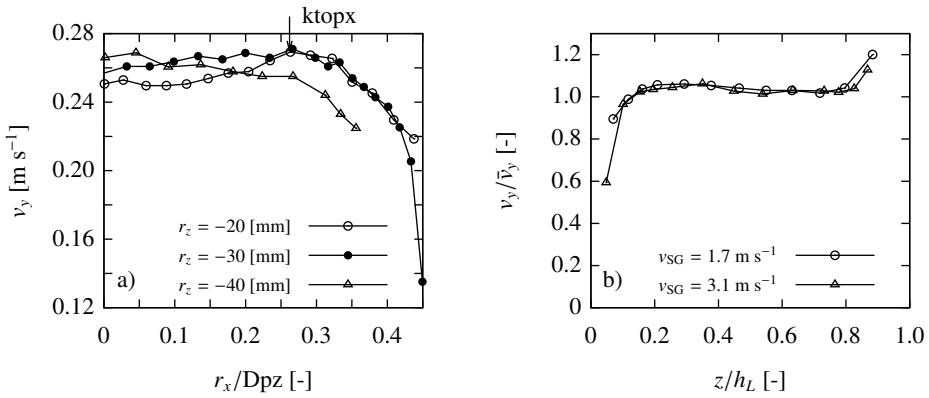


**Figure E.5**: (a) Streamwise velocity along the horizontal chords at $r_z = -20$ mm, $r_z = -30$ mm and $r_z = -40$ mm at $v_{SL} = 0.10$ m s$^{-1}$ and $v_{SG} = 1.7$ m s$^{-1}$ after Strand [238]. ktopx indicates the index of the peak in the velocity profile at $r_z = -20$ mm starting to count at $r_x = 0$ mm. (b) Normalized streamwise velocity along the vertical axis at $v_{SL} = 0.10$ m s$^{-1}$ after Strand [238]. The average water level $h_L$ is 42.5 mm at $v_{SG} = 1.7$ m s$^{-1}$ and is assumed to be 38 mm at $v_{SG} = 3.1$ m s$^{-1}$.

Figure E.5(a) shows the velocity profile along 3 horizontal chords at $r_z = -20$ mm, $r_z = -30$ mm and $r_z = -40$ mm. When the radius $r_x$ is scaled with the local horizontal pipe diameter, the curves for $r_z = -20$ mm and $r_z = -30$ mm coincide in the wall area. Only up to the top, indicated by ktopx, should the velocity be scaled differently. Ignoring the deviating trend for the data at $r_z = -40$ mm, we decided to base the calculation of $v_y[i, j]$ on the velocity profile at $r_z = -20$ mm. To this end, the velocity values between the center of the pipe and the position of the peak at ktopx are multiplied by a sliding scaling factor, which allows the velocity to gradually change between $vyz0[j]$ and the top velocity. The velocities in the wall area are simply interpolated.

The calculated streamwise velocity field for a liquid holdup of 0.3 and 0.7, the limits for the stratified wavy measurements in chapter 7, are given in Figure E.6. A fragment of the Fortran code that models the 2D stratified wavy velocity profile is given below.

```
NULref = 14
hLref = 42.0E-3
zref(1) = 0.0
ULref(1) = 0.0
zref(NULref) = hLref
ULref(NULref) = ULref(NULref-1) + (zref(NULref)-zref(NULref-1))*&
    ((ULref(NULref-1)-ULref(NULref-2))/(zref(NULref-1)-zref(NULref-2)))

DO j = 1,NzhL
  dovyz0 : DO k = NULref,1,-1
```

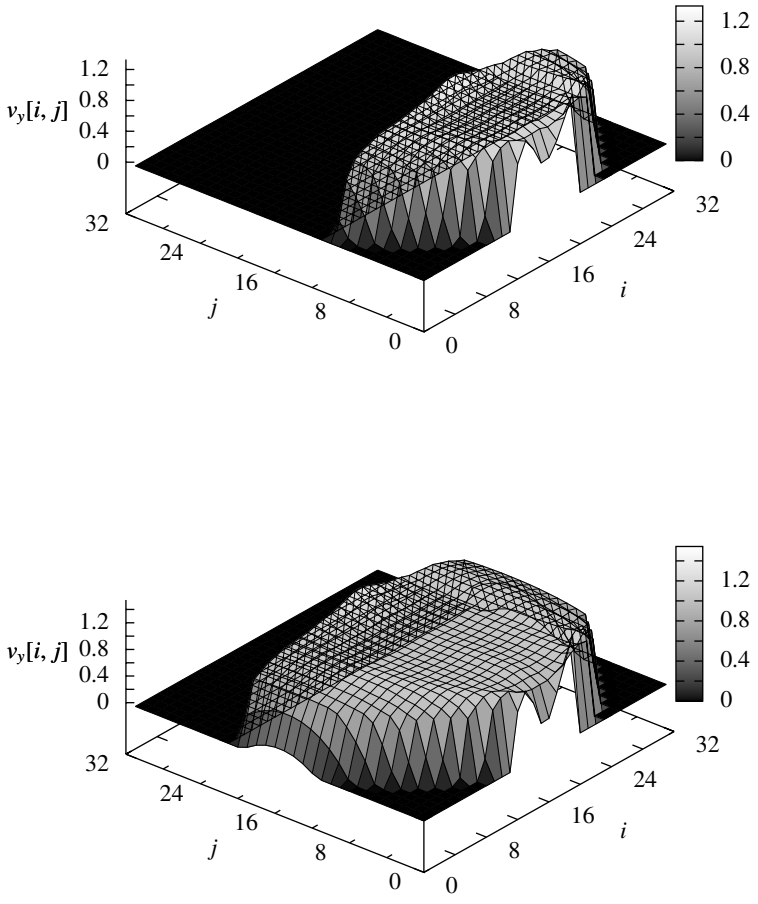


**Figure E.6**: Typical artificial streamwise velocity profile of the liquid phase used to model stratified flow with regular 2D waves at (top) $\alpha_L = 0.3$ and (bottom) $\alpha_L = 0.7$.

```
    kmin = k
    IF ((zv(j)/hL) > (zref(k)/hLref)) EXIT dovyz0
  END DO dovyz0
  vyz0(j) = ULref(kmin)+hLref*((zv(j)/hL)-(zref(kmin)/hLref))*&
      ((ULref(kmin+1)-ULref(kmin))/(zref(kmin+1)-zref(kmin)))
END DO

NULrefx = 17
ktopx = 10
Dprefx = 0.09165

rxref(NULrefx) = 0.5*Dprefx
ULrefx(NULrefx) = 0.0

wSF = 0.0
vysum = 0.0
wsum = 0.0

DO j = 1,NzhL
  Dpz(j) = 2.0*SQRT(zv(j)*(Dp-zv(j)))
  NxhL(j) = 2*NINT(Dpz(j)/(2.0*Dx))
  DO k = 1,(ktopx-1)
    vy0fac(k) = (vyz0(j)/ULrefx(1))-&
      ((rxref(k)-rxref(1))/(rxref(ktopx)-rxref(1)))*&
      ((vyz0(j)/ULrefx(1))-1)
  END DO

  DO k = ktopx,NULrefx
    vy0fac(k) = 1.0
  END DO

  DO i = 1,Nv
    IF (i .LE. (Nv/2 - NxhL(j)/2)) THEN
      vy(i,j) = 0.0
    ELSE IF (i .GT. (Nv/2 + NxhL(j)/2)) THEN
      vy(i,j) = 0.0
    ELSE IF (i .LE. Nv/2) THEN
      dovyx01: DO k = NULrefx,1,-1
        kmin = k
        IF (((Dp-2.*xv(i))/Dpz(j)) > (2.*rxref(k)/Dprefx)) EXIT dovyx01
      END DO dovyx01
      vy(i,j) = ULrefx(kmin)*vy0fac(kmin)+Dprefx*&
          (((Dp-2.*xv(i))/Dpz(j))-(2.*rxref(kmin)/Dprefx))*&
          (ULrefx(kmin+1)*vy0fac(kmin+1)-ULrefx(kmin)*vy0fac(kmin))/&
          (2.*(rxref(kmin+1)-rxref(kmin)))
      wSF = wSF + w(i,j)
      vysum = vysum + vy(i,j)
      wsum = wsum + w(i,j)
    ELSE
      dovyx02: DO k = NULrefx,1,-1
        kmin = k
        IF (((2.*xv(i)-Dp)/Dp) > (2.*rxref(k)/Dprefx)) EXIT dovyx02
      END DO dovyx02
      vy(i,j) = ULrefx(kmin)*vy0fac(kmin)+Dprefx*&
          (((2.*xv(i)-Dp)/Dpz(j))-(2.*rxref(kmin)/Dprefx))*&
```

```
            (ULrefx(kmin+1)*vy0fac(kmin+1)-ULrefx(kmin)*vy0fac(kmin))/&
            (2.*(rxref(kmin+1)-rxref(kmin)))
        wSF = wSF + w(i,j)
        vysum = vysum + vy(i,j)
        wsum = wsum + w(i,j)
      END IF
    END DO
  END DO

  IF (NzhL .NE. Nv) THEN
    DO j = NzhL+1,Nv
      DO i = 1,Nv
        vy(i,j) = 0.0
        wsum = wsum + w(i,j)
      END DO
    END DO
  END IF

  Avy = wSF/vysum
  DO i = 1,Nv
    DO j = 1,Nv
      vy(i,j) = Avy*vy(i,j)
    END DO
  END DO

  alphaSF = wSF/wsum
```

# List of Publications

A. C. L. M. Daalmans, L. M. Portela and R. F. Mudde, "Development of a NMR multiphase flowmeter," in *Proceedings of ICMF 2007* 6th *International Conference on Multiphase Flow*, M. Sommerfeld, Ed., Leipzig, Germany, July 9 – 13, 2007, PS7 11.

R. J. Belt, A. C. L. M. Daalmans and L. M. Portela, "Experimental study of particle-driven secondary flow in turbulent pipe flows," *J. Fluid Mech.*, vol. 709, pp 1 – 36, 2012.

# Acknowledgements

Completion of this thesis was only possible with the support of all those around me.
First of all, I am very grateful to my promotor, Rob Mudde, and copromotor, Luis Portela. Thank you for sticking with me on the bumpy trail, even though the topic and at times management issues were well beyond the comfort zone. Rob, I am extremely grateful for the time you made available in your busy new role as Vice-Rector Magnificus and Vice-President Education in the Executive Board of the University to make the final push. Your tactful support, questions that encouraged me to formulate more clearly and your appreciation for the elegance of a simple model, I experienced as very stimulating. Luis, your keen enthusiasm gave me the impetus to embark on this adventure when you asked me during my graduation project whether I was interested in your recently acquired PhD project. Although our differences in style sometimes got in the way, I look back with pleasure on the scientific and less scientific coffee corner discussions. Unraveling literature on a conceptual level always paid off. I am also very happy that I let you, under the guise of filling the lecture hall, persuade me to participate in your Computational Multiphase Flow course, which was very educational. Special thanks goes to professor Harrie van den Akker. Your playful enjoyment of teaching physical transport phenomena not only aroused my interest in this field, I particularly appreciate your efforts to break the impasse in the project.
Signal analysis is a very important part of any experimental research, but in the curriculum it is unfortunately common to approach it in a purely mathematical way. I'm very thankful for the discussions with Piet Broersen about adjusting the modus operandi in the presence of experimental imperfections. This applied analysis would make the toolbox of all engineering students a lot more useful. I also wish to thank professor Saša Kenjereš from the staff for the always warm interest and encouragement.
An experimentalist is nowhere without the workmanship of the technicians. Jaap van Raamt, Jaap Kamminga and Jan Groeneveld, thank you so much for building the flowloop. I would especially like to thank Jaap Kamminga for smart solutions, sharing practical know-how and for thinking along with us about the design of the constructions. Wouter van Goor, switching to LabJack-cards has been great advice. Evert Wagner, Lodi Schriek and Christiaan Schinkel, because of your unfamiliarity with NMR, I had little need for technical assistance. Nevertheless, you contributed greatly to the positive atmosphere in the lab and it was good to see you enjoying my thank-you-bakes. Many thanks also go to Ben Norder of the 'Applied Soft Matter' section for helping out after our viscometer proved unreliable.

The administrative support provided by all the ladies who have occupied the secretariat over the years is also very much appreciated. I also want to thank Laura van der Meulen. As Rob's PA, it was great that I could always count on your assistance, especially in the final stage.

Within the EET project 'Replacement of offshore separators by NMR multiphase flowmeter technology – EETK03056', initiated by KROHNE, everyone had their own specialism. I would like to thank André Boer and Jankees Hogendoorn (KROHNE Altometer) for keeping sight of the bigger picture and continuing to believe in the successful outcome of the project. Jankees, I have experienced the interest through your spontaneous visits as very pleasant. The development of the composite pipes was far removed from my work, but no less interesting. For someone who can spend hours looking fascinated at a production process to figure out how it works, visiting NLR's advanced composite manufacturing plant was a fun experience. Precisely because of the different backgrounds, project meetings often gave rise to surprising ideas. Laurent Warnet, Salma Hamdi (UT), Walter 't Hart, and Rens Ubels (NLR), thank you for your input and the time you put into the project. In particular, I would like to mention Marc Rhode (KROHNE NMR). Our close cooperation from August 2007, when we received the training from Oxford Instruments as the first step in understanding the black (later yellow) box, I count as the best period of my PhD. It was awesome to have an equal sparring partner. I enjoyed every bit of the numerous discussions we had, not just about science, but about life in general; the puzzling over the trickier aspects of the physics; the creative thinking – who would come up with the brilliant idea of using the jack to remove the pipe socket?; yes, even the joking about women not knowing how to use tools – oh, how wrong you were. Thanks for the great time! Many thanks also go to my BSc student Renée van der Mijle. It was a joy to supervise you and work with you on the development of the bubble sensor, which is the basis for the validation of the slug flow measurements in Chapter 8. Vincent Kampschöer (IMC) is acknowledged for the outstanding bureaucratic support. I also really appreciate the help of professor Ermert, Michael Voigt and Wilko Wilkening from the Ruhr-Universität Bochum in understanding and improving the signal quality of the r.f. probes.

Within the Kramers Laboratory for Physical Technology and later the Multi-Scale Physics and the Transport Phenomena section, I had the opportunity to operate in a colorful international community for quite some years. It gave me great pleasure to hear all your stories about what brought you here, learn from your customs and practices, discover your cuisine and so much more. Thank you all for this inspiring experience that has certainly broadened my horizons.
I have seen many office mates come and go. Our office, W220, became the perfect combination of work and fun. Hugo Hartman, Wouter Harteveld, Jos van 't Westende, Marco Zoeteweij, Özgür Günyol, Maria Silakova, Zaki Saldi, Adrian Toader, Mohammad Kamali, Laurens van Campen, and Anton Kidess: you always made my day, no matter what. Özgür, you navigated alongside me since the early days of this academic journey. How many good memories. I enjoyed your spontaneity and sharing any interesting fun facts you came across in TEDX talks or while playing Clickipedia. I also have a lot of respect for the way you finished your PhD thesis by spending almost all of your free time at the TU next to your job. Zaki, I have always admired the apparent calm with which you pioneered with OpenFOAM.

Adrian, 'Okido' will remind me of you forever. You have the charm and talent to sell everything. I'm sure you'll make it far in this field. Anton K, you are definitely the pizza master! Sending postcards in exchange for your leftover stamps is still a great deal; there is no nicer way to keep in touch than by old-fashioned mail. It is amazing how well you manage to keep your Dutch up to standard. Anton Gryzlov, in order to escape from your own serious office mates you have graced many of our days with lovely anecdotes or *Nederpop* serenades, making it, exceptionally, to the notorious "W220 – Wall of Fame". Another person from this era that I would like to acknowledge is Roel Belt. As supervisor of my MSc project, you showed me with your enthusiasm how much fun it can be to dig deep into a research topic. I benefited a lot from your 'porcupine' code to convert the wiremesh data, not to mention the advice long after you left, which was always just as brilliant as the witty wrapping of the message.
After a series of wanderings, I later had the pleasure of sharing an office with Dries van Nimwegen, Koen Schutte, and Saidah Altway. Dries, you were my most grateful cake consumer, especially when the chocolate content was high. Thanks for putting me on the trail of Welch's periodogram averaging technique; otherwise the power spectra would never have turned out so beautiful. Koen, I especially remember a lot of interesting chats. I will also never forget how you revived my Greece memories with your imported Papadopoulos biscuits surprise.
After moving to TNW-Zuid, my days at the office were brightened up by the company of Snehal Pujar, Hrushikesh Pimpalgoankar, Manas Mandalahalli, Fei Xu, Saeid Khalafvand, Romana Perinajová, Lorenz Baumgartner, Matheus Martinez Garcia, Debasish Sarker, Kostadin Petrov, and a bunch of nice MSc students. Thanks for the good dose of joy and collegiality you provided. Manas, with you around, the fun is never far away. Thank you also for teaming up with Sid and Snehal to fill in the gaps in my knowledge regarding the history of India and Kashmir. Romana and Stefanie Gürzing, even in turbulent times I could always count on your friendly chatter between work. Lorenz, headphones on and go, with your good organization we could simply lean back, knowing that the activities are always arranged down to the last detail. Mattheus, apart from being nice company, thank you for being such a good ally for the past few months when I needed remote assistance.

Thanks also to my colleagues, among whom Michaël Descamps, Marcos Cargnelutti, Usama Kadri, Volkert van Steijn, Xiaogang Yang, Michiel Musterd, Bernhard Righolt, Rudi Kalter, Rajat Bhardwaj, Wenjie Jin, Niels Looije, Anand Ashok, Cees Haringa, Siddharta Mukherjee, Kevin van As, Manu Chakkingal, Maulik Shah, Elin Vesper, Artem Blishchik, Xiaolin Wu, Peng Wei, and Brice Saint-Michel, for making the daily lunches so entertaining with your opinions. All topics could be discussed, ranging from science, current affairs to culture and sports. Volkert, thank you for the great time we had, from team lunch to my partner in crime in the organization of the innumerable PhD songs and gifts, and also for your continuing interest when I ran into you in the hallway. Bernhard, *gozertje*, thanks for reminding us that life cannot always be serious; how we laughed at all your bad jokes. Sid, storyteller pur sang, thank you for sparking the imagination, be it with your photos, algorithmic art or stories. Kevin, with your passion for education and your enthusiastic stories about the CoderDojo, I'm sure that you will become a splendid teacher. Elin, friendly feminist with a strong sense of justice, it is nice to understand through your argument how you arrive at your

principles and I really respect how sincerely you, as a champion of a more beautiful world, practice what you preach. The question '*Hoe gaat het met jou?*' is much more diverse than you might think at first glance. You know how to ask good questions about the Dutch language! May many more emails go back and forth in the future. Manu, I don't think there is a better encyclopedia of Indian cinema. Artem, thanks for your remote help. Xiaolin, always the cheerfulness itself, how often you managed to surprise me with Chinese delicacies and how special it was to enjoy the tea picked by your grandmother.

Of all the people mentioned here, one stands out in particular. Jan Willem Brandenburg, as I have told you before, thank you for so many reasons. Without you, I would not be standing here today. You were always there to listen patiently to all my ideas, act as a sounding board, and to draw my attention to the tricks of pattern recognition. Thank you for your friendship, for being the first to carefully read and correct my texts, for being the biggest cheerleader of my progress, and to remind me over and over to just own my work and be proud of the achievement.

Dear Mom and Dad, you always encouraged me to keep wondering and trying to understand how things work. This has laid an important foundation for everything. It was not always easy to follow all my research stories, but that makes no difference! Thank you for your interest, your unfailing trust, for cheering me up when I needed it most, and for your continued support.

# About the author

Annekatrien Daalmans was born on September 9, 1980 in Delft. In 1998 she received her Gymnasium diploma from the Stanislas College in Delft. In the same year she started studying Applied Physics at the Delft University of Technology. Following an internship at Corus RD&T in IJmuiden, she was given the opportunity to do her MSc graduation project at the Kramers Laboratory for Physical Technology with an experimental LDA study of particle-driven secondary flow in horizontal annular flow. After her cum laude graduation in 2005, she started her PhD research at the same research group under supervision of prof. dr. R.F. Mudde and Dr. Eng. L.M. Portela. This collaborative project with KROHNE Altometer, the Production Technology Group of the University of Twente and the Netherlands Aerospace Centre (NLR) concerned the development of an NMR multiphase flowmeter intended for the petroleum industry as replacement for offshore separators. In 2012, the research group now known as Transport Phenomena moved from the Applied Physics department to the Chemical Engineering department.